Microfluidic Devices For Continuous Liquid-Liquid-Solid Chemical Extractions

A thesis submitted to the University of Wales in accordance with the requirements for the degree of

DOCTOR OF PHILOSOPHY
BY EXAMINATION AND THESIS

By

Oliver Kieran Castell MPharm MRPharmS

Molecular Recognition Research Unit (MRRU)
Drug Delivery Department
Welsh School of Pharmacy
Cardiff University
&
metaFAB
Cardiff School of Engineering
Cardiff University

CARDIFF
UNIVERSITY

PRIFYSGOL
CAERDYⱭ

September 2008

UMI Number: U584612

UMI U584612

Acknowledgements

Summary

In this study the unique properties of microfluidic flow have been exploited to generate efficient mass-transfer in continuous segmented flow to investigate an alternative approach for performing chemical extractions. The concept of extraction-enhancement, by incorporation of a solid absorbent in the extracting phase, was explored. Proof-of-principle studies focused on the use of molecularly imprinted polymers (MIPs) to increase the effectiveness of conventional approaches.

Laser machining and micro-milling were used to prepare PTFE microfluidic separation devices. Importantly, this included the design and integration of a continuous-flow microfluidic liquid phase separator. Propranolol selective molecularly imprinted polymer microspheres (3.6 μm) were prepared by precipitation polymerisation. MIP performance was assessed using conventional (equilibrium batch rebinding) and segmented-flow liquid-liquid systems.

Interfacial mass transfer processes that occur during segmented flow were characterised with respect to flow variables, fluid properties and channel geometries. Segment aspect ratio and flow velocity, together with channel diameter and curvature, were shown to be important. The MIP was shown to possess high affinity and selectivity for the template (propranolol). Incorporation of the MIP into a segmented flow extraction regime was shown to significantly enhance the extent of analyte extraction. Mathematical optimisation approaches showed good correlation with experimental data. On-chip phase separation was demonstrated to be 100% efficient for particle-containing and particle-free immiscible flows. The discovery of soluble MIP species possessing similar binding characteristics to their insoluble counterparts may further improve the kinetics of the reported solid-liquid-liquid extractions.

It was successfully demonstrated that a solid phase material can be incorporated into an organic phase to enhance extraction from an aqueous sample either in continuous segmented flow or under equilibrium conditions. The integration of the segmented flow approach with an on-chip liquid phase separator provides a novel platform for the development of unique and highly-efficient continuous flow devices for molecular enrichments, separations and manipulations.

Contents

Appendix 1. Microfluidic Device Compression and Interfacing Manifold

Appendix 2. Flow Properties and Dimensionless Numbers

Appendix 3. Adaptation of the Predictive MIP Binding Model for Application to a Biphasic Solvent System

Appendix 4. Incorporation of Leaching Fraction into the Predictive MIP Binding Model

Appendix 5. Preliminary Attempts to Harvest a Soluble MIP Prepared at Near-θ Conditions

Appendix 6-14. Publications

   Novel Biphasic Separations Utilising Highly Selective Molecularly Imprinted Polymers as Biorecognition Solvent Extraction Agents

   Microchip Solid-Phase-Enhanced Liquid Liquid Extractions Utilising Highly Selective Molecularly Imprinted Polymers as Chemorecognition Solvent Extraction Agents

   Continuous molecular Enrichment in Microfluidic Systems

   Liquid-Liquid Phase Separation: Characterisation of a Novel Device Capable of Separating Particle Carrying Multiphase Flows

   Microwave Compositional Analysis of Solvent Matrices in Microcapillary Manifold Systems

   Microwave Split Ring Resonator Technique for High Sensitivity Compositional Analysis of Solvents in Microcapillary Systems

   Microwave Technique For Monitoring Phase Separation Of A Multiphase-Flow Regime Utilised For Continuous Molecular Enrichment

   Microfluidic Liquid Separation Device and Methods for Construction and Application. Patent Application Number: 0816001.2

   A Glimpse of the Inner Workings of the Templated Site

Tables

Chapter 1

Chapter 2

Chapter 3

Chapter 7

Chapter 8

Figures

polymerisation of cross-linking and functional monomers.

Chapter 3

Chapter 4   142

although the segmented flow regime is responsible for the majority of the extraction, a significant quantity of propranolol is extracted in the collection vessel. This is reinforced by the observation of increasing extent of extraction with increased collection time, despite a constant segmented flow rate. Experimental conditions: Flow rate of each phase 0.2 ml min⁻¹, where applicable segmented flow generated by a Tefzal T-piece, flowing into 20 cm of 0.5 mm I.D. FEP tubing. Segmented and non-segmented, individual flows, were eluted into a 2 ml eppendorf centrifuge tube of diameter 0.9 cm with collection times of 150, 225 and 330s employed.

Figure 3 Concentration of propranolol remaining in the aqueous phase, following extraction of a 50μM aqueous sample at pH 5.5 with an equal volume of chloroform, containing either MIP, NIP (1 mg ml⁻¹) or no polymer. Extractions conducted by segmented flow extraction in a 5 m length of 0.5 mm I.D. FEP tubing, predominantly coiled (coil diameter 11 cm) at a range of flow rates. ... 153

Figure 4 Mole fraction (*f*) of propranolol extracted from a 50 μM aqueous sample at pH 5.5, following extraction with an equal volume of chloroform, containing either MIP, NIP (1 mg ml⁻¹) or no polymer. Extractions conducted by segmented flow extraction in a 5 m length of 0.5 mm I.D. FEP tubing, predominantly coiled (coil diameter 11 cm) at a range of flow rates. The flow rate dependant extraction time is also depicted. ... 154

Figure 5 Variable map illustrating the velocity dependent secondary mechanisms of mass transfer enhancement in segmented flow regimes. Many of the processes exhibit non-linear behaviour and may be affected by additional variables (e.g. fluid properties, tubing diameter, tubing coiling or channel corners, segmenting architecture etc) ... 156

Figure 6 Calculated extraction rate constant (*k*) for the extraction of a 50 μM aqueous sample of propranolol at pH 5.5 with an equal volume of chloroform, containing either MIP, NIP (1 mg ml⁻¹) or no polymer. Extractions conducted by segmented flow extraction in a 5 m length of 0.5 mm I.D. FEP tubing, predominantly coiled (coil diameter 11 cm) at a range of flow rates. ... 159

Figure 7 Concentration of propranolol remaining in the aqueous phase, following extraction of a 50 μM aqueous sample of propranolol at pH 5.5 with an equal volume of chloroform, containing either MIP, NIP (1 mg ml⁻¹) or no polymer. Individual extraction results for measurements of each of three sequential runs are plotted. The apparent distinction between experimental runs is perhaps indicative of temperature, or other local effect dependencies. Extractions conducted by segmented flow in a 5 m length of 0.5 mm I.D. FEP tubing, predominantly coiled (coil diameter 11 cm) at a range of flow rates. ... 163

Figure 8 Concentration of propranolol remaining in the aqueous phase, following extraction of a 50μM aqueous sample at pH 5.5 with an equal volume of chloroform, containing either MIP, NIP (1 mg ml⁻¹) or no polymer. Extractions conducted by segmented flow in a 15m length of 0.5 mm I.D. FEP tubing, predominantly coiled (coil diameter 11 cm) at a range of flow rates. ... 164

Figure 9 Mole fraction (*f*) of propranolol extracted from a 50 μM aqueous sample at pH 5.5, following extraction with an equal volume of chloroform, containing either MIP, NIP (1 mg ml⁻¹) or no polymer. Extractions conducted by segmented flow extraction in a 5 m length of 0.5 mm I.D. FEP tubing, predominantly coiled (coil diameter 11 cm) at a range of flow rates. The flow rate dependant extraction time is also depicted. ... 165

Figure 10 Calculated extraction rate constants (*k*) for the extraction of a 50 μM aqueous sample at pH 5.5 with an equal volume of chloroform, containing either MIP, NIP (1 mg ml⁻¹) or no polymer. Extractions conducted by segmented flow extraction in a 15 m length of 0.5 mm I.D. FEP tubing, predominantly coiled (coil diameter 11 cm) at a range of flow rates. The calculated extraction rate for extractions attaining equilibrium, or extremely close to attaining equilibrium (chloroform alone), are of limited value due to the ambiguity of the extraction time taken to achieve equilibrium. Additionally, small uncertainties in assay measurements or subtle variations in the equilibrium distribution ratio can induce significant uncertainty in calculation of extraction rate constants (*k*) for extractions close to equilibrium. ... 166

Figure 11 Measured partition coefficient for the extraction of propranolol from a 50 μM aqueous solution (pH 5.5) into an equal volume chloroform containing various masses of added polymer (MIP or NIP). Extractions were conducted using a segmented flow regime in 5 m of 0.5 mm I.D. FEP tubing at flow rates of 0.4 ml min⁻¹, representing an extraction ... 169

Chapter 5

segmented flow stream before aqueous breakthrough occurs.

Figure 11 Micrograph images of laser machined separation ducts branching from the main, micromilled, fluidic channel. Machining damage, or debris, can be observed on the laser machined ducts at high magnification.

Figure 12 Predicted effect of separation duct geometry on separator performance: calculated minimum operating pressure (solid line), aqueous breakthrough pressure (dashed line) and 100% separation efficiency regimes (shaded region). Chloroform/water separation by triangular separation ducts (n = 140) with dimensions w = 15 µm, h = 260 µm and w = 15 µm, h = 520 µm compared to the experimentally evaluated duct of dimensions w = 30 µm, h = 130 µm.

Figure 13 Sequence of still images taken from a video of the phase separator operating with fluorescently labelled polystyrene microspheres (2.0 µm diameter) suspended in the organic phase and passing through the separation ducts, into a second outlet channel. An aqueous fluid packet (dark, non-fluorescent region) can be seen to move progressively closer to the aqueous fluid packet in front due to removal of chloroform from the segmented flow stream (a-f), until complete phase separation, and aqueous phase coalescence occurs (g).

Figure 14 Comparison of the fluidic design of *i*) the device reported by Angelescu et al. [22] which failed to separate segmented flow streams with 100% efficiency, and *ii*) the design constructed and evaluated in the work of this chapter, demonstrated to separate segmented flow streams with 100% efficiency due to appropriately considered geometries of the channels with respect to fundamental fluid properties.

Figure 15 Scale plan and cross sectional schematic diagrams of the fluidic design of the Angelescu et al. (*i*) [22] (dimensions: main channel; w = 100 µm, d = 15 µm, separation ducts; w =15 µm, d = 15 µm square cross section) and the phase separation device constructed and evaluated in the work of this thesis (*ii*) (dimensions: main channel; w = 720 µm, d = 600 µm, separation ducts; w = 36 µm, d = 130 µm high aspect ratio Gaussian cross section).

Figure 16 CAD drawings for optimised phase separation device designs for application in the device manifold illustrated in figure 1. *i*) illustrates a schematic design drawing of an extended path length phase separation module. A segmented flow stream (generated off-chip) enters the device through a dedicated input port (1) which elutes into a main flow channel (2). The shaded region represents an array of high aspect ratio phase separation ducts (3). At the juncture of the multiphase flow carrying channel (2) and the separation ducts (3) phase separation begins to occur with the continuous phase (separated phase) entering the separation ducts (3). The separated phase continues along the separation ducts and empties into the common channel (4), which conducts the separated fluid to a dedicated outlet (5). Removal of the continuous phase through the separation ducts (3), causes coalescence of the disperse phase droplets into a continuous stream which flows to a dedicated outlet (6). The extended path length of the separating portion of the device, allows for a greater number (n) of separation ducts, thus increasing the maximum operable flow rate of the phase separator device. Designs *ii)* and *iii*) demonstrate extended path length phase separation modules suitable for the *passive* separation of multiphase immiscible fluid flows. The difference in resistance of fluid flow, to the two possible fluidic exists (5) and (6), achieved by considered design of the channel geometries (length, width and depth) with respect to the fluid properties and flow characteristics, provides a pressure differential between the fluidic exits (5) and (6) supporting the flow of the separated fluid through the separation ducts (3). This pressure differential (ΔP) is generated wholly or in part by the flow of the immiscible fluid stream and the individual fluid flows in their respective channels. The device illustrated in *iii*) was manufactured in accordance to the channel geometries of the primary device tested in this chapter (Figure 1-14). The device was demonstrated to separate segmented flow streams of chloroform and water (1:1) with 100% separation efficiency at flow rates up to 3.0 ml min^{-1}. The pressure differential (ΔP) across the separation ducts (3), enabling the separation, is provided entirely by the flow of the immiscible fluid stream and the individual fluid flows in their respective channels to their respective outlets.

dramatically with phase ratio, demonstrating the unsuitability of IF as a measure of imprinting efficacy.

Figure 12 Theoretical equilibrium bound and free conditions for MIP. Represented graphically as the solution to the fitted equation describing the measured binding isotherm (red) and the equation representing conservation of ligand for the stipulated conditions (blue). Intersection of the lines described by the respective equations indicates the predicted equilibrium bound and free concentrations for each of the parameter sets modelled, each containing a total of 150 nmol of propranolol ligand. (f1(c) and f2(c) denote the plotted functions described by the Mathcad script detailed in section 6.3.2.4.1 for the stipulated condition set).   248

Figure 13 Theoretical plot illustrating the predicted extent of propranolol binding to the MIP prepared in chapter 2 at a range of polymer masses and chloroform incubation volumes containing a total of 150 nmol of propranolol. The plot illustrates the difficulty in gauging polymer performance expressed as percentage bound due the dependence upon mass and volume incubation parameters. Application of the predictive model to generate such data from a preliminary experimental data set may be of value in optimising binding conditions for an intended application, or comparing the performance of two or more MIPs.   249

Figure 14 Theoretical equilibrium bound and free conditions for NIP. Represented graphically as the solution to the fitted equation describing the measured binding isotherm (red) and the equation representing conservation of ligand for the stipulated conditions (blue). Intersection of the lines described by the respective equations indicates the predicted equilibrium bound and free concentrations for each of the parameter sets modelled, each containing a total of 150 nmoles of propranolol ligand. (f1(c) and f2(c) denote the plotted functions described by the Mathcad script detailed in section 6.3.2.4.1 for the stipulated condition set).   251

Figure 15 Theoretical plot illustrating the predicted extent of propranolol binding to the NIP prepared in chapter 2 at a range of polymer masses and chloroform incubation volumes containing a total of 150 nmol of propranolol. The difference in isothermal shape between the MIP and NIP binding curves manifest as different dependencies of ligand bound upon the variables of mass and volume. Comparison of the equivalent MIP and NIP plots may provide a useful opportunity to optimise conditions of MIP application to maximise specific template binding and minimise non-specific binding, assumed to represented by binding to the NIP.   252

Figure 16 Imprinting factor (IF), modelled for a range of polymer masses and incubation volumes containing 150 nmol of propranolol ligand. The imprinting factor (IF) is seen to vary dramatically with phase ratio, demonstrating the unsuitability of IF as a measure of imprinting efficacy.   254

Figure 17 Three dimensional surface plot illustrating the significance of phase ratio (mass of polymer/volume incubating solvent (mg ml^{-1})) on equilibrium binding for both MIP and NIP for incubation in 150 µM propranolol solution. The intersection of the red plane with the blue (MIP) or green (NIP) isotherm represents theoretical equilibrium binding conditions for ascribed phase ratio. The two plots illustrated represent the same data viewed from different observational angles to convey fully the curvature of red plane and consequently the phase ratio defined equilibrium position.   256

Figure 18 Improved experimental accuracy can be achieved by altering the incubation phase ratio in order to probe different regions of the binding isotherm. The measurement of small concentration depletion from the incubating phase can compound any experimental error or uncertainty in the assumed bound concentration on the polymer. Consequently the employment of high polymer loadings and increased incubation concentrations can assist in determining the near-saturation region of the binding isotherm with improved accuracy.   258

Figure 19 Manual method for estimating equilibrium bound and free values for desired set of incubation conditions from a reported MIP or NIP isotherm. Example illustrated for an incubation system of 4 mg polymer incubated in 2 ml of chloroform containing 300 nmol of propranolol *a)* Calculation of the analyte concentration in the incubating solvent if all analyte were in solution, this is equal to 150 µM, equivalent to the incubation concentration. This value is marked on the x-axis. *b)* Calculation of the concentration of   261

analyte on the polymer, if all the analyte were bound to the polymer present in the incubation system. Equivalent to 75 nmol mg^{-1}, this value is marked on the y-axis. c) Connecting the points made in a) and b) with a straight line defines the maintenance of ligand in the binding system, with the molar sum of propranolol in solution and bound to the polymer equal to the total propranolol in the incubation system (300 nmol) at every point on the line. d) The intersection of the line constructed in c) with the isotherm of the MIP and NIP represents the equilibrium conditions for the hypothetical set of incubation conditions. It should be noted that the isotherm should report the *concentration* of analyte in each phase (solvent or bound to polymer) and not the incubation concentration, the total quantity bound, or the concentration of analyte removed from the liquid phase by the polymer, which are occasionally reported in the context of MIP binding.

Figure 20 Application of the predictive model to five propranolol isothermally reported MIPs prepared by different imprinting methodologies [31-34]. Comparison with binding behaviour of a sixth polymer [30] evaluated non-isothermally. The conditions under which this MIP [30] were evaluated were modelled for the isothermally reported MIPs, namely a polymer loading of 2 mg ml^{-1} and an incubation concentration of 154.2 µM. Where NIP binding isotherm were reported the predicted NIP binding under the stipulated conditions is also illustrated. This comparative methodology enables comparisons to be drawn between imprinting protocols and re-binding media. The addition of the equivalent NIP data is of some assistance in gauging the extent of specific and non-specific binding interactions in the different incubation media.

Figure 21 Distribution ratio (D) plotted against $\log_{10}$ free equilibrium concentration (*log c*). Linear regression produces a line of best fit described by the equation; D = -802.57 (log10 c) + 2464.6.

Figure 22 Distribution ratio (D) plotted against free equilibrium concentration (c).

Figure 23 Comparison of methods. The approach proposed by Horvai et al. [24] (a) and the fitted equation describing the isothermal shape of the MIP (Section 6.2.1.1.1) (b) are compared. In each comparative graph the model generated by the approach of Horvai; fitting a linear equation to the plot of D vs. log c, is illustrated by a dashed red line. The model described by the equation fitted to the isothermal binding data by non-linear regression is described by a solid blue line. The D vs. log c plot (c) suggests that the experiential data is described equally well by the linear fit of D = -802.57 (log10 c) + 2464.6, as it is by the transposed isothermal equation (q = 129.7(1 − e$^{-0.01132}$ x c)) [The transposition is achieved substituting the isothermal equation into equation (6) (D = q/c) with appropriate consideration for the units of q and c]. However, the transposed isothermal equation produces a monotonically decreasing function describing a curve rather than the straight line of the linear fit of the data derived directly from this plot (D = -802.57 (log10 c) + 2464.6). Transposition of this equation onto the binding isotherm (q vs. c) (d) demonstrates that the equation derived from the distribution ratio technique describes the binding behaviour of the MIP well at low free propranolol concentrations. As the isotherm approaches saturation the equation is seen to diverge from the measured results, ultimately overestimating the maximum binding capacity of the MIP before diverging completely from the expected saturable binding behaviour and describing a decrease in binding with further increases in free propranolol concentration, ultimately describing negative values of bound analyte (not shown). This behaviour indicates that the data described by the plot of D vs. log c is not linear and is described more accurately by the transposed curve, derived from the isotherm itself by non-linear regression. However the straight line approximation of the D vs. log c data does describe the binding behaviour adequately for sub-saturation behaviour of MIPs, making it suitable for inter-polymer comparisons and prediction of MIP suitability for potential applications, as intended by the authors [24]. The accuracy of modelled predictions of binding behaviour can be expected to be slightly less accurate than the approach outlined in this chapter due to the linear approximation made when fitting to the D vs. log c plot. However this technique can be conducted manually if the required software for non-linear regression is unavailable. The close agreement of the approach reported by Horvai with the method developed independently in the work of this chapter provides good supporting evidence for the validity of the method and the assumptions made in its development (sections 6.3.1.1.1-6.3.1.1.3).

solvent which is wrongly assumed to be unbound. The effect of increased polymer leachate with increased polymer loading, resulting in a increased experimental measurement of assumed free propranolol and consequently an underestimate in amount bound, can be clearly seen from the intersection of each of the experimentally acquired binding isotherms (dashed lines) with that of the plot describing propranolol conservation within the system (f2(c) blue). Consequently, with knowledge of the 'true' MIP equilibrium binding behaviour (f1(c) (red)), the extent of overestimation of free propranolol can be deduced and an estimation of the extent of leaching of soluble MIP fraction can be made.

Chapter 1

Introduction

1.1 Microfluidics

Microfluidics defines the science and technology of systems that process or manipulate small $(10^{-9}$ to 10^{-18} L) volumes of fluids using channels with dimensions on the micrometer scale [1]. Microfluidics is a comparatively young field of research and technological application that is rapidly generating interest among academics and within industry. The fundamental differences between fluid behaviour on the micro-scale compared to that on the macro-scale gives rise to unique phenomena which provide opportunities for fluid and sample handling unachievable with large scale approaches. It is this key concept, together with the inherent small size of 'lab-on-a-chip' devices, their potential for mass production, high-throughput and automation, together with minimal reagent consumption that makes microfluidics such an appealing platform for chemists, biologists and engineers.

1.1.1 Origins of Microfluidics

The controlled manipulation of fluids within microscale channels has been commonplace in analytical chemistry for decades, notably in the form of gas chromatography (GC) and high performance liquid chromatography (HPLC). Within these fields the ability to analyse sample volumes in the range of 100s to 10s of µl revolutionised analytical chemistry and today such equipment is still the staple of most analytical laboratories. Whether these systems themselves are considered truly microfluidic however is debatable since both tend to possess significant equipment footprints, rely on comparatively large total fluidic volumes and consume large volumes of solvent. Despite this, such systems have been a huge driving force in the conception of the microfluidic discipline. The drive for improved separation performance and decreased analysis time encouraged the use of channels of smaller inner diameter and shorter length, a deliberate exploitation of the behaviour of fluids on the microscale. In 1990 Manz et al., aware of this trend, proposed the concept of miniaturised total chemical analysis systems (µTAS) [2], where all sample handling steps are performed in close proximity to the point of measurement for the *purpose of enhanced analytical performance*. This together with subsequent practical demonstrations [3] contextualised the pioneering work of Terry et al. [4],

who reported a functional gas chromatographic air analyser fabricated on a silicon wafer for portable air quality monitoring. This work was a natural progression for the micromachining and micro-engineering technologies that had already driven the miniaturisation of sensor and transducer technology, having originally arisen in response to the growth of the electronic and integrated circuit market. Furthermore, developments arising from research that strove to miniaturise sensors and transducers would eventually call for the incorporation of fluid phases for analysis in these miniaturised systems, for example in clinical diagnostics. Most notably, at around the same time as Terry was conducting his research, pharmaceutical companies, Ames, now part of Bayer, and Boehringer, now owned by Roche, were independently developing portable devices for home blood glucose monitoring for patients with *diabetes mellitus* [5,6]. A large patient population and growing evidence that improved glycemic control could lead to significant health benefits for patients with type 1 diabetes [7] acted as a huge financial driver for the development of easily operated, portable versions of what were formerly large laboratory housed devices. Their use of small liquid (blood) volumes however bore more relation to patient acceptability than exploitation of fluid properties on the microscale. This, however, was not the case in an alternative commercial sector - print technology, where Ichiro Endo [8] and John Vaught [9], working for Canon and Hewlett-Packard, respectively, independently developed the thermal inkjet mechanism. This relied on thin-film resistors to rapidly vaporise a small volume of ink, the rapid expansion of which caused a small volume to be propelled from tiny etched nozzles at high speed. The development of this system was somewhat serendipitous, with the physics behind its operation initially poorly understood [10]. By the early 1990s inkjet technology (both thermal and piezo) together with glucose biosensors and home pregnancy test kits were commonplace and commercially successful as a result of the huge market forces and consumer market driving their development. The success of these products continues today. However, the relative failure of other biosensors to penetrate potential markets due to a combination of sensitivity, selectivity, stability, cost, and notably market size issues [11-13], added convincing weight to Manz's assertion that miniaturised analytical systems that *gained significant (and numerous) performance advantages over macroscale systems as a result of miniaturisation* [2]

would herald a way forward in analytical science. The opportunities for enhanced performance and efficiency, together with the convenience of small scale, low reagent and sample consumption and potential device integration invited a fresh perspective on fluid handling applications. The development of the field of genomics [14] and the subsequent requirement for high throughput and high sensitivity experimentation from small sample volumes, provided further impetus for the development of microfluidic analytical devices and tools. The DNA microarray enabling expression and monitoring of many, many genes in parallel [15] is one notable example of microfluidic technology addressing the growing needs of the bioscience sphere.

It is apparent that no one individual or singular device was responsible for parenting the field of microfluidics. An intertwined series of events and a steady increase in interest has resulted in the emergence of *microfluidics* as a distinct new technology and field of research. The establishment of the discipline focussed research towards fabrication methods and technologies suitable for substrates, and design features specifically tailored for microfluidic applications. The development of a variety of essential fluidic components for integrated lab-on-a-chip applications, including mixers, filters, pumps, injectors, separators and valves [16-26], subsequently followed, Such fluid handling components often exploit the dominance of viscosity and surface forces on the microscale; as such, the need for understanding the behaviour of fluids on this scale has provided a fresh context for fluid dynamics and the founding theoretical work of Newton, Navier, Stokes, Reynolds, Young and Laplace amongst others [27].

1.1.2 Fluid Behaviour – A Comparison of Fluid Behaviour on the Macro- and Micro-Scale : Observations From the World Around Us

The observed behaviour of fluid(s) in any given system is governed by the forces exerted on the fluid(s). Many of these forces, such as inertial, viscous, gravitational and surface forces, show dependencies on the length scale which defines the geometric fluid volume. On the macroscale we have become accustomed to the relative magnitude of these forces that give

rise to the type of fluid behaviour with which we are familiar. For example if we consider the behaviour of fluids on the scale traditionally employed by a synthetic chemist by considering fluid in a laboratory beaker. On this scale gravitational force plays a dominant role and immiscible fluids (defined partly as a function of entropy) separate on the basis of density. In adding water to an air filled beaker, the water, having a much greater density than air, will occupy the lower portion of the beaker, with the air sitting on top. Similarly when chloroform, immiscible with both water and air and possessing a greater density, is added it will also separate on the basis of density and will form a layer that occupies the lowest possible portion of the beaker. If this simple experiment were to be conducted under low gravity conditions, onboard a space shuttle for example, the same behaviour would not be observed. In the absence of the dominating gravitational force discrete spherical droplets of the liquids would form surrounded by a continuum of air. In this situation the formation of spherical droplets demonstrates the importance of surface forces, with a sphere offering the most compact geometric volume possible (i.e. smallest surface area to volume ratio). Adoption of a spherical shape minimises the unfavourable interactions at the interfacial boundary between the two immiscible fluids (i.e. water and air). The application of motion to the fluid droplet, introduces inertial and viscous forces which enable the deformation in shape of the spherical bubble. This is similarly observed with the application of pressure. Should sufficient force be applied to overcome surface tension, droplet breakup may occur, producing two or more smaller droplets. In proximity to the earth's surface, the earth's mass exerts a gravitational force on the liquid volumes, proportional to the liquid mass. This force can deform or lead to break up of immiscible phase interfaces and gives rise to the fluid behaviour to which we are accustomed. For example, in the situation of the water and chloroform filled beaker, the fluid layers separate on the basis of density, but also form near-flat layers of fluid, rather than the idealised spheres. Droplet breakup is witnessed as the chloroform is added to the water, as it falls through the air when poured from one container to the second, but also when it impacts, and subsequently falls through, the existing water layer. At this scale gravitational forces and inertial forces dictate fluid behaviour, and through experience this is what we have grown to expect. A reduction in scale however, sees a shift in the comparative magnitude of

gravitational and surface forces, together with other forces acting on fluid volumes. A small bubble may appear to defy the dominance of gravity outlined above. For example, should the glass beaker possess surface imperfections (scratches) on the inside surface, a small air bubble may form as a result of dissolution of dissolved gas in the water, and become anchored to this surface. Despite the buoyancy of the air, the bubble may not necessarily rise to the surface and coalesce with the bulk air volume, a counter-intuitive effect following our initial observations. However, on the scale of a small single air bubble, the favourable surface forces acting on the bubble as a result of the contact between the air bubble and the glass surface are greater than the gravitational force difference between the water and the air, whilst surface forces also maintain the bubble as one single confined volume. This results in the intact bubble remaining submerged and attached to the glass surface. If however, the bubble continues to grow, through subsequent dissolution of dissolved gas from the liquid (demonstrated rapidly in carbonated drinks), then the characteristic length scale of the bubble increases. Since gravitational forces, and hence buoyancy effects, act on the volume of the fluid, where as surface force effects act only over the contactable surface area, the initial dominance of surface forces are soon rivalled and then dominated by the increasing significance of gravitational force. This behaviour is exploited by beer manufacturers who produce beer glasses with a micropatterned surface to encourage controlled bubble formation and prolong the time period before the bubbles rise to the surface. This process contributes to the maintenance of the beer's 'head' over the duration which the drink is consumed. This simple example illustrates how the magnitude and significance (or insignificance) of different forces acting on a fluid can change as the characteristic length scale changes. It is the fundamental differences in fluid behaviour, which manifest as a result of these forces on the microscale, which characterise the science of microfluidics. On occasions the dominance of some forces over others can prove problematic, however it is the opportunity to harness this characteristic behaviour which creates many exciting, and otherwise impossible, applications through microfluidic technology.

1.1.3 Dimensionless Analysis

Dimensionless parameters have widely been used to describe the non-linear behaviour of fluids [28,29] The dimensionless comparison of forces acting on a fluid enables assessment of the dominant (or insignificant) forces acting within the fluidic system and prediction and understanding of the fluid behaviour. Several important dimensionless parameters in microfluidics and multiphase microfluidics are outlined in sections 1.1.3.1 – 1.1.3.4.

1.1.3.1 Reynolds Number

One of the most important dimensionless parameters in fluid dynamics is the Reynolds number (Re) [30]. It is used to describe the ratio of inertial forces to viscous forces (Equation 1), expressing the relative significance of each of these forces in determining flow behaviour.

$$\mathrm{Re} = \frac{v\rho L}{\mu} \tag{1}$$

Where μ and ρ represent the fluid properties viscosity (Pa s) and density (kg m^{-3}) respectively, v the flow velocity (m s^{-1}) and L the characteristic length (m) of the channel structure, defined as the hydraulic diameter of the channel. The hydraulic diameter is defined as

$$D = \frac{4A}{U} \tag{2}$$

where A is the cross-sectional area of the channel geometry and U the wetted perimeter. For a cylindrical channel, the hydraulic diameter equates to the diameter of the channel itself. Care should be exercised with many microfluidic fluid dynamic calculations, particularly when comparing between literature examples. For example, the channel radius may frequently be employed, or, incorrectly, the channel diameter in the case of non-cylindrical channels. It should also be noted, for example, that viscosity is also commonly denoted by the symbol η, depending on the context of the equation, and dynamic viscosity (μ or η) should not be

confused with kinematic viscosity, v, defined as the ratio of dynamic viscosity and fluid density (μ/ρ).

The Reynolds number equation describes what is perhaps the most significant feature of microfluidic flows – the dominance of viscous forces over initial forces which gives rise to laminar flow.

1.1.3.2 Capillary Number

The capillary number (Ca) expresses the ratio of viscous forces to surfaces forces acting across a fluidic interface. As such it is an important number in characterising the behaviour of multiphase flows and is applicable to liquid-gas and immiscible liquid-liquid systems.

$$Ca = \frac{\mu v}{\sigma} \tag{3}$$

Where the surface tension between the immiscible fluids is defined by σ (N m^{-1}). In multiphase flows the ratio of fluid viscosities is also important in determining flow regimes and fluid behaviour (section 1.1.6).

1.1.3.3 Weber Number

The Weber number (We) is another dimensionless number used to describe multiphase flows. It characterises the relative importance of inertial forces of a fluid compared to surface forces.

$$We = \frac{v\rho}{\sigma} \tag{4}$$

1.1.3.4 Bond Number

The Bond number (Bo) characterises the significance of gravitational force compared to surface forces. The equation may be applied to any body force acting on the fluid, notably

centrifugal or accelerative forces. However it is most usually applied with gravitational acceleration (*g*) to determine the relative significance of density differences between fluids compared to the surface forces exerted at the interface between the two phases.

$$Bo = \frac{\rho a L^2}{\sigma}$$

(5)

Consequently, to achieve a useful answer in most circumstances, the density difference between the two fluids is used, rather than the absolute density of a single fluid component. In equation 5, *a* represents the accelerative force applied on the fluid (i.e. gravitational acceleration (*g*)) (m s^{-2}), and the characteristic length scale, *L*, in this instance is usually defined by the radius of a spherical droplet, or the radius of a cylindrical channel.

1.1.3.5 Dominant Forces

Figure 1 illustrates the dimensionless values of the Reynolds, Capillary, Weber and Bond numbers. The figure demonstrates the relative magnitude of forces acting on a fluid and the dependency of this on flow velocity and channel diameter (characteristic length scale). The dominance of interfacial forces over viscous, inertial and gravitational forces can clearly be seen, together with the relative dominance of viscous forces over inertial forces (Reynolds number), in the channel size domain and velocity flows typically encountered in the field of microfluidics.
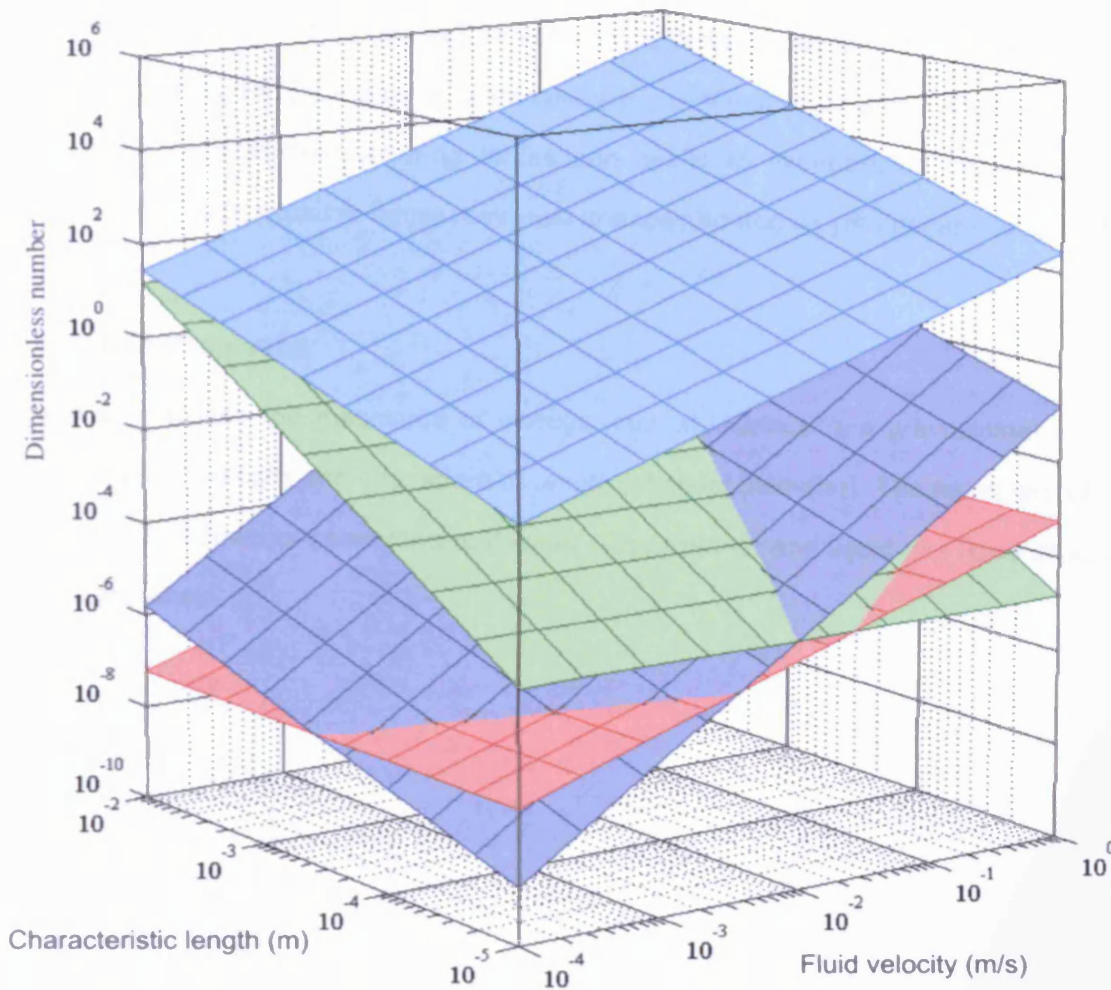
Figure 1 Dimensionless analysis of forces acting on the aqueous fluid of a water and chloroform multiphase flow, with respect to flow velocity and characteristic length (channel diameter for cylindrical channels). Reynolds number (light blue), Bond number (green), Weber number (purple), Capillary number (red).

1.1.3.6 Magnitude of Dimensional Forces - Dimensional Analysis

Although dimensionless analysis of forces is undoubtedly useful in the consideration of microfluidic behaviour, it is also useful to sometimes know, or have an idea of the magnitude of, forces acting on the fluid. This enables consideration or comparison with alternative forces and consequently estimation of their significance, and even predictions of behaviour. For example the anticipated effect of magnetic particles dispersed in a fluid in the presence of a

10

magnetic field can be estimated. Similarly the effect of localised heating of fluidic interfaces and the effect of the Marangoni forces generated can be predicted. Optical interactions (optical tweezers), electrical forces and ultrasonic effects (acoustic force) can all be evaluated for theoretical significance prior to undertaking experimental evaluation. Additionally, realistic expectation of possible interfering forces can assist in experimental design. Imaginative exploration of such possible forces may yield unexpected and as yet uncharacterised effects.

1.1.4 Fluid Properties

Figure 2 illustrates the magnitude of viscous, inertial, surface and gravitational forces with respect to fluid velocity and characteristic length (channel diameter). The forces are calculated for liquid-liquid flows of chloroform and water (upper plane) and liquid-gas flows of water and air (lower plane).
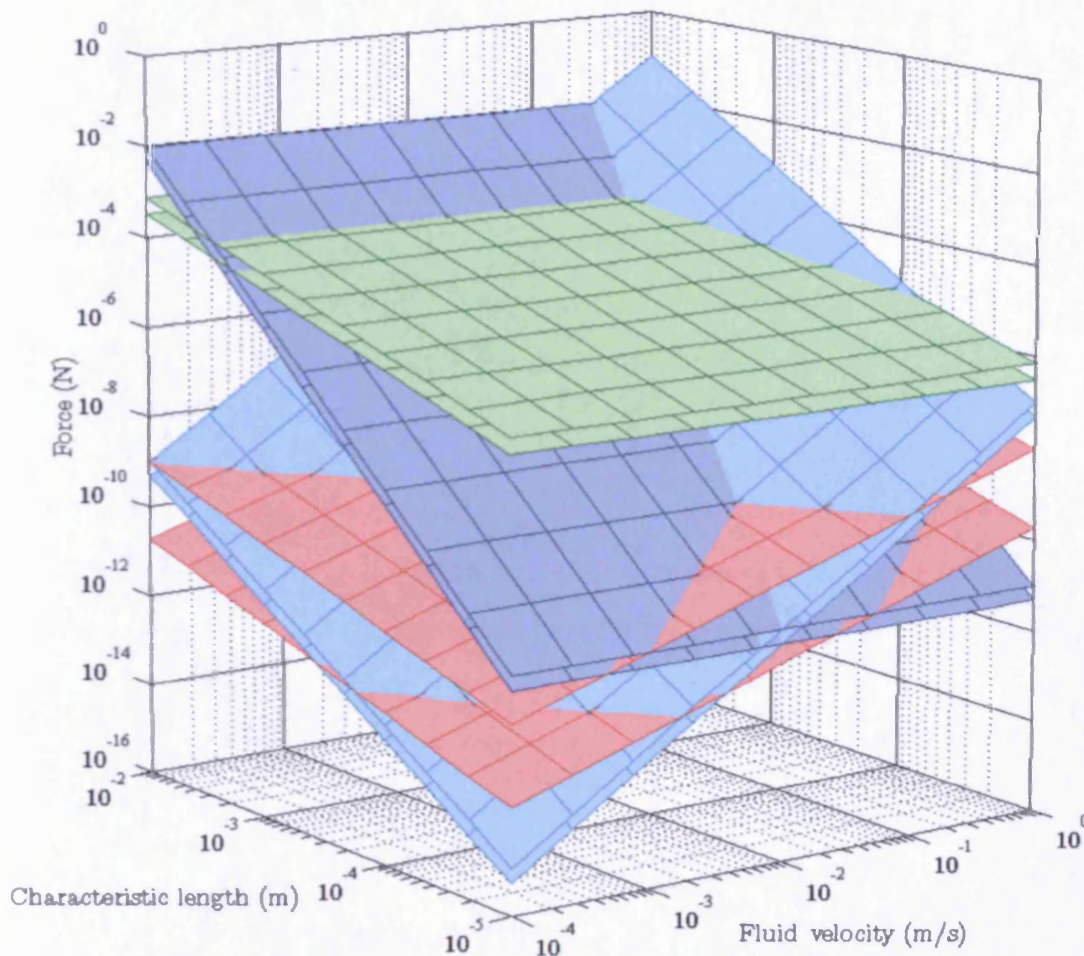
Figure 2 Absolute force exerted on multiphase flow regimes. Both water-chloroform multiphase flows and water-air multiphase flows are considered, with the upper plane of each coloured surface representing the magnitude of force associated with immiscible liquid-liquid flow, and the lower plane representing liquid-gas immiscible flow. The proximity of the generated forces in each instance, demonstrates the similarities in behaviour observed with gases and liquids on the microscale. Very different from our everyday learned experiences of gas and liquid behaviour on the macro-scale. Differential gravitational force (dark blue), interfacial surface forces (green), inertial forces (light blue), viscous forces (red).

The plot illustrates that despite the very different properties of liquids and gases and our experience of their differing behaviour on the macroscale, on the microscale the magnitude of the forces in question shows relatively small variation between the liquid-liquid and liquid-gas flows compared to the difference in magnitude between the different types of force. Consequently liquid and gas microflows can exhibit similar characteristic flow behaviour.

12

Table 1 Fluid properties of chloroform-water and water-air flows, used for calculation of plots illustrated in Figure 1 and Figure 2.

	viscosity Pa s	density Kg m^{-3}	surface tension N m^{-1}	density difference kg m^{-3}
Water	0.0010	997.0		
			0.072	995.9
Air	18 x10^{-6}	1.184		
Water	0.0010	997.0		
			0.032	483.0
Chloroform	0.00058	1480		

Table 2 Fluid properties of alternative multiphase flow regimes for a selection of water immiscible phases.

	surface tension against water N m^{-1}	surface tension against air N m^{-1}	density kg m^{-3}	viscosity Pa s
butanol [a]	0.0021	0.0246	810	0.0029
pentanol [a]	0.0049	0.0254	810	0.0044
hexanol [a]	0.0068	0.0258	810	0.0051
benzyl alcohol [a]	0.0048	0.0397	1040	0.0058
chloroform [a]	0.0328	0.0271	1490	0.0006
hexane [a]	0.0511	0.0184	660	0.0003
ethylene glycol [b]				0.016
olive oil [b]				0.081
glycerol [b]				0.934

[a] [31] [b] [32]

Table 1 and Table 2 illustrate fluid properties for commonly used immiscible solvent systems in analytical and synthetic chemistry. It can been seen that for these solvent systems the variation in fluid densities, surface tensions and viscosity, although variable, tend to span only one order of magnitude, or two when considering liquid-air flows. Oils and glycerol are examples of fluids with greater viscosities, as such the dominance of viscous forces increases,

viscous forces increases, together with pressure drops associated with fluid flow (Chapter 5). As such this should be considered as appropriate when working with these types of fluid flows. Biological samples, such as blood or saliva, where composition and consequently fluid properties can vary greatly between samples may also require additional consideration at the device design stage to ensure repeatable performance of the device.

The plot of figure 2 illustrates that for the fluid systems considered, viscous forces dominate or are approximately on a par with inertial forces for flow in microscale (sub mm) channels. Only in large channels and high flow rates, not often associated with microfluidic applications, do inertial forces dominate and approach values high enough to generate turbulent flow (Re = ~2400). In multiphase fluidic systems surface forces often dominate over gravitational and all other forces in microfluidic flows. As a result these forces play a significant role in defining the behaviour of fluidic systems on the microscale.

1.1.5 Laminar Flow

Laminar flow occurs at low Reynolds numbers where viscous forces dictate fluid behaviour. Flow is characterised by fluid flowing in parallel layers with no mixing of the fluid layers. At larger length scales (channel diameter) and/or flow rates, inertial forces become more influential, at a Reynolds number ~2400 a transition from laminar to turbulent flow occurs. Unlike the predictable nature of laminar flow, turbulent flow regimes appear stochastic and chaotic in their nature owing to the rapid variations in momentum, pressure and velocity in spatial and temporal domains. This gives rise to vortices which interact with each other, further affecting the local fluid momentum, pressure and velocity together with drag and boundary layer effects, creating complex and rapidly changing flow patterns. In microfluidic systems the Reynolds number is usually far less than 100 and may often be less than one, in such situations inertial forces can sometimes be assumed to be negligible and the Navier-Stokes equations can be simplified to give the Stokes equations [33] enabling simplification of some hydrodynamic problems. In a turbulent flow system (e.g. large water pipe) the overall flow outcome is, like laminar flow, that the fluid flows from point A (start) to point B (end) due

to a pressure drop between the two points. However the exact path taken by any given volume of fluid (or solutes contained in the fluid) is almost entirely unpredictable. The high level of momentum transfer causes breakup and mixing of the fluid meaning that a well defined 'slug' of fluid, for example coloured dye, entering the pipe will mix with the fluid bulk and elute as a far more dilute solution over a prolonged period of time. In laminar flow regimes however, the dominance of viscous forces prevents fluid mixing in this sense, resulting in predictable and exploitable fluid behaviour.

1.1.5.1 Exploitation and Limitations of Laminar Flow

1.1.5.1.1 Laminar Flow and Diffusion - Exploitation

Figure 3 depicts an experimental demonstration illustrating the absence of convective mixing of fluid in laminar flow, single phase microfluidics. The figure shows two aqueous streams coloured with dye, eluting into a common duct at a T-junction geometry. The flow can be observed to continue as two parallel flow streams, with minimal observable mixing of the fluid dyes. As a consequence, mixing of liquids or any movement of suspended particles or solutes perpendicular to the flow is governed by diffusion. Einstein's theory of Brownian movement [34], which mathematically defined, in terms of temperature, particle size and fluid properties, what had previously been measured as a diffusion coefficient by Fick, enables calculation of diffusion rates.

$$x(t) = \sqrt{2(\frac{k_B T}{6\pi \rho v R}) \times t}$$

(6)

Where $k_B T$ is the Boltzmann energy (Boltzmann constant [k_B] multiplied by absolute temperature [T]), ρ and v the fluid's density and kinematic viscosity respectively whilst R is the radius of the particle for which diffusion is being calculated. This equation shows that diffusion distance (x) over time (t) for a given species shows an inverse relationship to particle size [35]. This molecular movement can be in any direction and occurs randomly. However, by starting with regions of high and low solute/particle concentrations within a fluid volume, the

molecular 'excess' in the high concentration region results in more molecules randomly migrating into the area of lower concentration than those moving in the opposite direction. Given sufficient time this deficit, or concentration gradient, is gradually reduced until the concentrations are in equilibrium and the net migration is zero. This principle together with the size dependency of diffusion rate and the laminar flow nature of microfluidics were collectively exploited in the invention of the microfluidic H-filter [36]. The H-filter is designed to ease the difficulty in analysing complex biological samples, without employing step-wise sample preparation strategies. The H-filter can be used to limit the size of analytes which are ultimately interrogated. Small molecules are able to diffuse from a biological sample matrix (i.e. blood, urine, etc.) into a co-flowing buffer stream for subsequent analysis. Larger moieties, such as cells or proteins, do not enter the buffer stream due to their slower diffusion speeds as a consequence of their larger size. Channel geometry and flow rate control, enable precise operation of the device for the desired fluids and analytes. Figure 3 shows a schematic illustration of an H-filter, with a green dye diffusing readily into the neighbouring stream whilst the large particles (red blood cells) remain in the original sample flow. This is just one example of many such devices designed specifically to exploit the forces and behaviour of fluids, particles and analytes on the microscale.
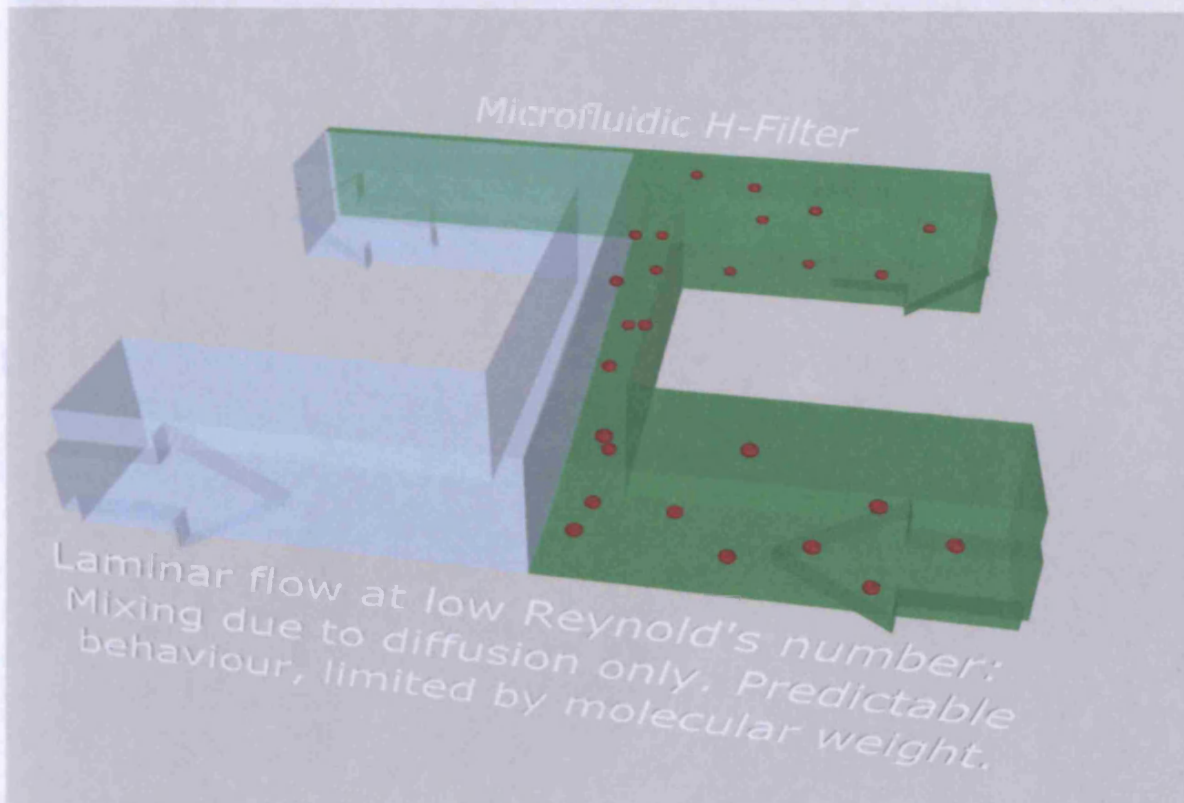
Figure 3 Schematic illustration of an H-filter, with a green dye diffusing readily into the neighbouring stream, for subsequent analysis, whilst the large particles (red blood cells) remain in the original sample flow. Both fluid phases are aqueous based and fully miscible, it is the laminar flow nature of microfluidics that creates the side-by-side flow and prevents the mixing of the two fluid streams.

1.1.5.1.2 Laminar Flow Limitations

In addition to providing novel solutions, the overwhelming laminar nature of single phase microfluidic flows can create its own problems. For example, the absence of mixing can be advantageous, but conversely it may also be problematic. The use of long channels and low flow rates to allow for full diffusive mixing is impractical and the use of excessively long channels compounds the problem of axial dispersion, resulting in broadening of an analyte 'plug' due to a combination of diffusion and the Gaussian velocity flow profile, or Poiseuille flow, of a pressure driven confined laminar flow (Figure 4).
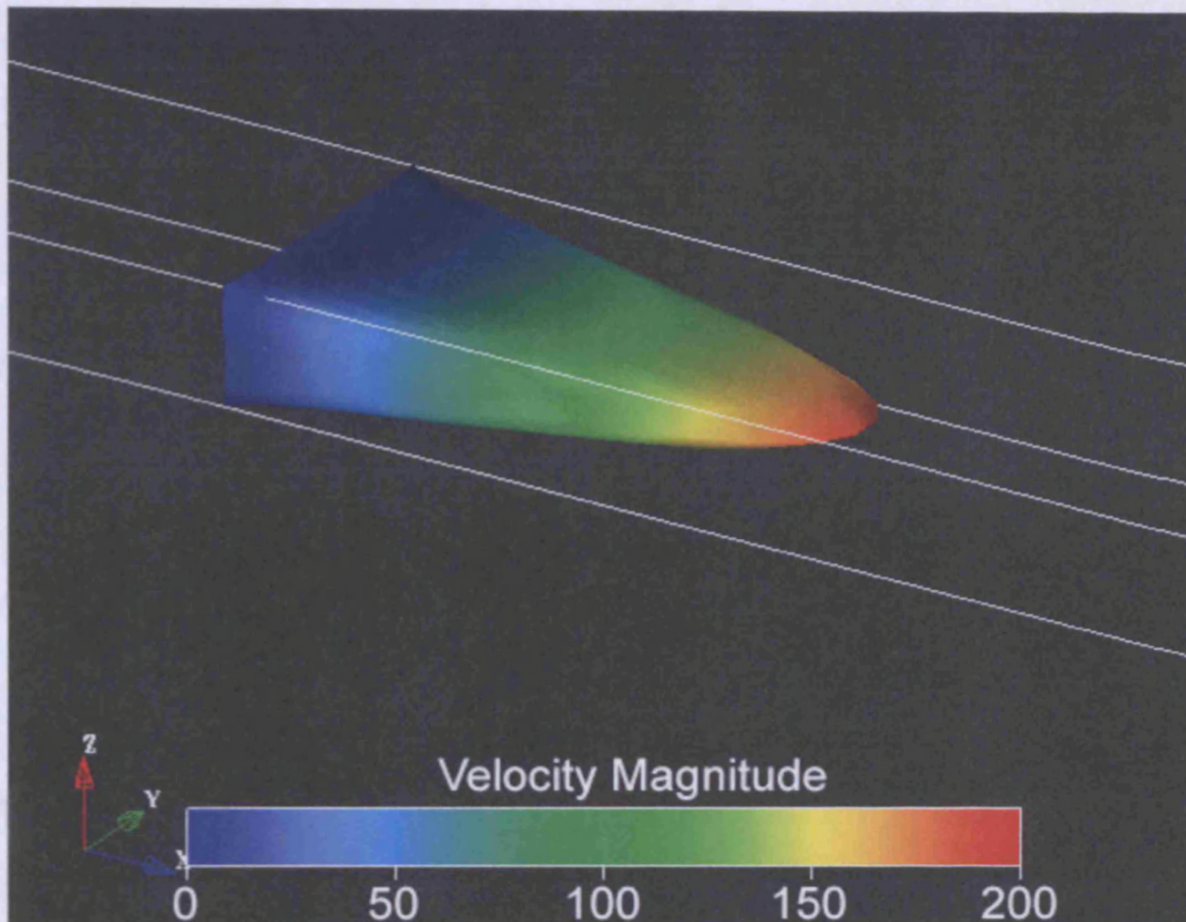
Figure 4 Computational Fluid Dynamic (CFD) model of pressure driven flow within a microchannel [37]. Poiseuille flow, defined by a parabolic velocity flow profile is seen to determine the nature of fluid flow within the channel. The shear force exerted by the channel walls, results in a near stationary layer of fluid at the channel wall, the laminar flow of fluid on the microscale means the effect of viscous shear it transferred between fluid 'layers', exhibiting lowest effect at the channel centre, where the fluid travels at twice the mean fluid velocity. The range of exhibited flow velocities, and absence of convective mixing results in axial dispersions of analyte 'plugs' along the flow path of the fluid. This effect is greatest for longest channels.

Knowledge of the relative significance of different types of forces (Figures 1 and 2) highlights that solutions to microfluidic problems are unlikely to be achieved through miniaturisation of macro-scale fluidic features and that approaches focused on harnessing the dominant forces are required. Many researchers have developed mechanisms for mixing fluids in otherwise laminar flow microfluidic environments [18,20,38]. An intriguing solution can be provided by the introduction of an immiscible fluid phase to *segment* the flow stream. The significant influence of surface forces on the microscale generates internal vortex mixing within *compartmentalised* fluid packets.

1.1.6 Multiphase Microfluidics

Multiphase microfluidics involves the controlled elution or manipulation of two or more immiscible phases within microscale architectures. Multiphase flows are generated when two (or more) immiscible fluids are contacted in a microfluidic flow situation. The flow regimes generated can manifest in different configurations depending on the relative magnitude of the competing forces acting on the fluids. Such flows may include formation of suspended droplets, the generation of channel occluding slugs, or fluid segments, and the generation of pinned interfaces [39]. Pinned interfaces are akin to the side by side, 'layered' flow of laminar flow regimes with similar flow characteristics, where the 'layers' comprise of the immiscible fluids. The dominance of interfacial forces on the microscale (Figure 1) and the energy expense the interface costs the system, provides a drive for the system to minimise the interfacial contact area. For any given volume enclosed by an interface, a sphere offers the most compact shape thus minimising the energy expense to the system most efficiently. Consequently, pinned interfaces, with large, flat interfacial boundaries, are inherently unstable and difficult or impossible to produce without selective surface modification of the channel walls to create selective wetting regions of the duct surface for each of the immiscible fluids [40,41]. Such modifications introduce competing interfacial forces to stabilise the flow regime by effectively pinning the fluid phases to the channel walls. It has been demonstrated experimentally and theoretically that stable pinned interfaces (or vertically stratified flows) are achievable in non-surface modified channels, for immiscible fluid pairs with a low interfacial tension and comparatively high viscosity (e.g. water and butanol), where viscous forces become increasingly more significant over the drive to minimise interfacial area [31]. The dominance of surface forces in multiphase flows makes the formation of stable side by side flows difficult, and encourages the formation of bubbles, droplets and slugs. The exertion of shear stresses and pressure forces by the wetting (continuous) liquid phase can deform the volume of the discontinuous fluid to such a non-idealised extent that interfacial tension favours breakup into smaller drops. If these drops are sufficiently small (diameter < narrowest channel geometry) then (near-) spherical droplets of discontinuous phase are generated dispersed within the continuous phase which wets the channel walls. If, however, the drops are large

enough to fill the channel cross section, elongated slugs form which occlude the channel cross-section with the exception of thin-films of the wetting liquid between the fluid packet edge and the channel walls [42]. The exact mechanism of droplet and slug formation through elution of a discontinuous (non-channel wall wetting) phase into a continuous (channel wall wetting) phase flow stream is a multifactorial process. It is dependent upon channel geometry, fluid properties and flow rates together with downstream events bearing an influence on fluidic resistance. Despite the process being complex, dynamic and dependent upon non-linear interfacial forces, the process is highly reproducible and stable, producing regular flow patterns of sequential fluid packets of identical size, shape and frequency for a given set of flow conditions. Such flow regimes are commonly termed segmented flows (Figure 5) and the disperse phase may be liquid or gaseous. These flows are gaining increasing attention in the field of microfluidics due to the unique opportunities created by such systems. There are two popular methods of segmented and droplet flow formation employed in microfluidic systems; the flow focusing geometry, and a T-junction architecture, resulting in capillary instability and pressure drop induced break up respectively [39].
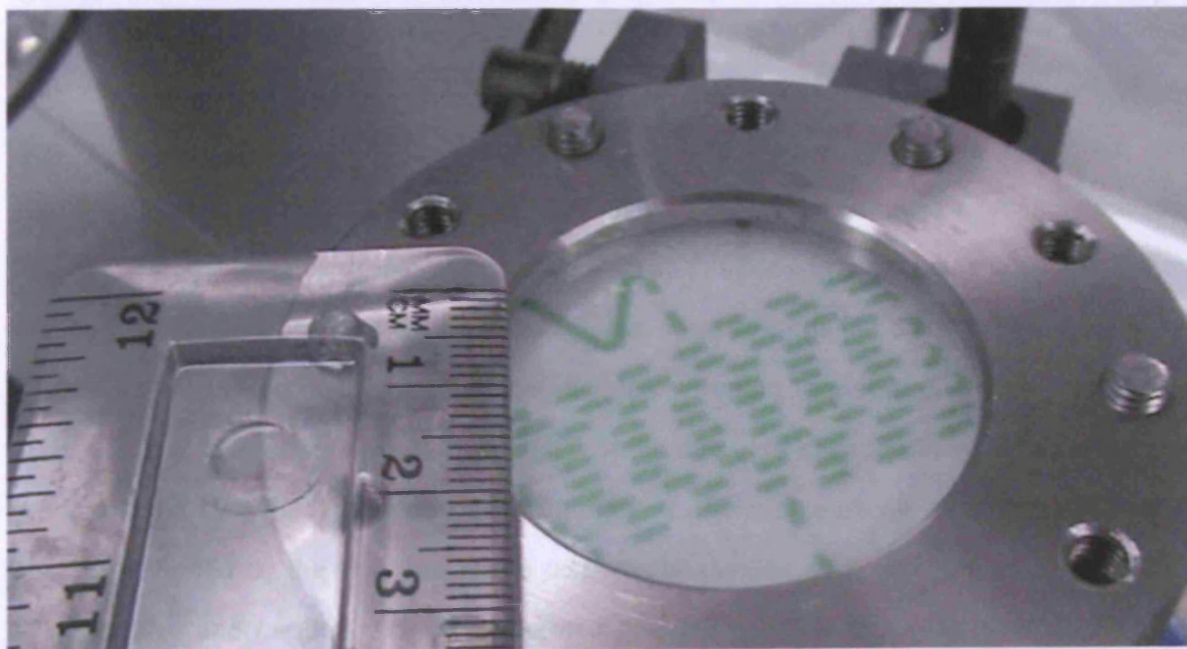
Figure 5 Microfluidic segmented flow regime of chloroform and water. The water phase appears green, due to the presence of aqueous miscible dye.

1.1.6.1.1 Flow Focusing Geometry

A flow focusing geometry (Figure 6) was first demonstrated to produce monodisperse microbubbles in a capillary system, at comparatively high Re numbers ($10^2 - 10^3$) [43], before the group of Howard Stone at Harvard utilised flow focusing geometries in integrated planar microfluidic devices to generate liquid droplets at low Reynolds numbers (<1) [44]. The flow focusing geometry creates a focused fluid sheath of a disperse fluid phase surrounded by a fast flowing continuous liquid film. This flow configuration is produced by the simultaneous elution of three parallel fluid channels into a common duct of minimal length, terminated with a narrow orifice which focuses the flow into a wide outlet channel. The disperse phase flows through the centre feeder channel which is flanked by flow of a continuous, immiscible, liquid phase in the neighbouring channels either side. Droplet formation through breakup of the disperse phase flow stream has been cited as being as a result of capillary instability of the elongated fluidic interface [39] relating to the findings of Plateau and Lord Rayleigh [45] who studied capillary instability of cylindrical interfaces under shear stress in unconstrained flows. A 'pinching' mechanism has also been cited as governing breakup in flow focusing systems, where the dominance of interfacial forces over shear stresses causes the tip of the disperse fluid stream to expand to fill a large portion of the cross-section of the exit of the focusing orifice when the flow slows upon entry into the wide outlet channel. This process restricts the flow of the continuous fluid to narrow films between the interface and the orifice wall, increasing the linear velocity and resistance to flow. This process causes a pressure increase in the continuous fluid upstream of the office exit, as this pressure increases above that of the pressure of the fluid confined by the interface, the neck, towards the tip of the disperse phase stream, is squeezed and the interface eventually breaks generating a disperse droplet [1,46,47]. The rate of squeezing of the neck of the disperse phase is directly proportional to the flow rate of the fluid in the orifice, whilst the flow of disperse phase through the collapsing neck is governed by the flow rate of the disperse phase. As such, extremely precise control over the size and frequency of the generated droplets is achievable [46]. Such devices are able to operate at high rates of droplet generation and are ideally suited for particle manufacture [48] or generation of self assembled foams [46] with droplet production rates of

10^5 bubbles per second with a polydispersity of <2% reported [46]. Importantly, even at these rapid production frequencies, cycling at >100kHz, the flow of fluid through the collapsing neck of the discontinuous stream and the process of squeezing due to the increased resistance of flow caused by the swelling droplet is comparatively slow compared to the equilibration process of adjustment of interface shape to minimise energy, and the transfer of pressure through the system. It is these features of the system that enables the production of virtually identical drops every time and earned comparisons to quasistatic thermodynamic processes [47] and generated interest in the opportunities for complex pattern formation in dynamic systems far from equilibrium [49]. These features have also been exploited to create more complex flow focusing systems, with an array of focussing fluid streams fed from a common duct of continuous fluid. Pressure fluctuations are transmitted near instantaneously to all the channels of the network, in turn affecting the rate of flow of the continuous phase which itself affects the rate of collapse of the interface between the immiscible phases, creating complex, yet reproducible droplet patterns demonstrating emergent behaviour [50].

Flow Focusing Geometry

Continuous Phase (liquid)

Disperse Phase (liquid/gas)

Continuous Phase (liquid)

Increased linear velocity of continuous phase exerts shear stress on disperse phase rupturing fluid filament to produce discrete droplets
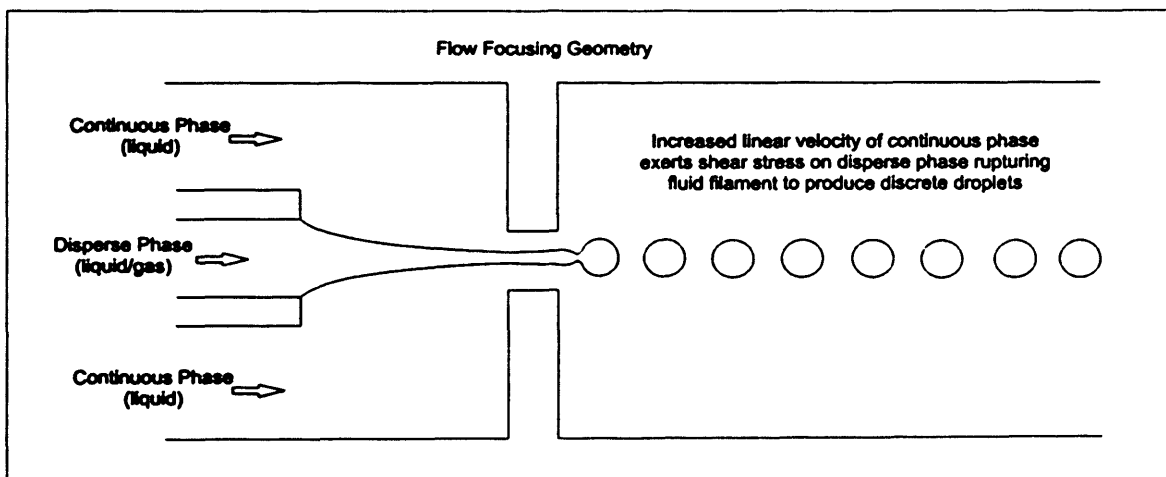
Figure 6 Schematic example of a typical microfluidic flow focusing geometry, used for the production of monodisperse microdroplets.

1.1.6.1.2 T-Junction Geometry

The T-junction is probably the most commonly employed microfluidic geometry for the generation of segmented immiscible fluid flows [49,51,52]. The first reported microfluidic

device with an integrated T-junction used for the generation of segmented flows was by Thorsen et al. in 2001, who postulated a shearing mechanism for droplet breakup [49]. Prior to this, T-junction union connectors and capillary tubing have long been utilised for the creation of segmented flow streams in micro- or milli- bore tubing, long pre-dating the concept of microfluidics. The T-junction is a simple geometry which enables the elution of a disperse immiscible phase (liquid or gas) into an existing flow stream of continuous phase. This is most often through a tributary duct perpendicular to the main channel (Figure 7). Order of magnitude analysis of the relevant forces has shown that pressure imbalance in the two phases at the junction is the dominant factor governing the dynamics of droplet generation in typical T-junction architectures [53], contrary to Thorsen's initial assumptions that shear forces dictated the droplet formation process. Garstecki and co-workers describe the mechanism of droplet formation and propose a mathematical scaling law describing the size of fluid segments generated (equation 7) for a given immiscible fluid system [54].

$$L/w = 1 - \alpha Q_{disperse}/Q_{continuous} \tag{7}$$

The fluid segment aspect ratio (L/w) is described in terms of the flow rate of the disperse phase ($Q_{disperse}$) and continuous phase ($Q_{continuous}$) with α representing a constant related to the T-junction geometry. The mechanism of segmented flow generation at a T-junction geometry proposed by Garstecki et al. is summarised below:

1. As the discontinuous fluid enters the main channel, the interface protrudes into the flow stream of the continuous fluid. The shear stress exerted on the emerging droplet by the flow of continuous fluid and the pressure drop along the length of the main channel deforms the emerging droplet in the downstream direction.

2. Laplace pressure exerted on the discontinuous fluid by the tip of the immiscible interface is against the direction of flow and causes the droplet to expand in the radial direction. In the absence of an immiscible interface, (i.e. elution of miscible fluids) laminar flow would ensue, with the introduced liquid 'pinned' to the lower wall demonstrating the dominance of surface forces over viscous forces.

3. As the drop continues to grow to occupy the majority of the channel cross section, the flow of the continuous fluid is restricted to a narrow film between the immiscible interface and the channel walls. Increasing the resistance to flow of the continuous phase.

4. This increased resistance to flow through the effective narrowing of the cross-sectional area through which the continuous fluid can flow causes an increase in pressure of the continuous fluid upstream of the occlusion, whilst the pressure inside the discontinuous phase remains approximately constant

5. At a critical value of droplet size, the restriction of flow of the continuous phase causes the pressure difference between the continuous and discontinuous phases to reach a value sufficient to overcome the Laplace pressure which had previously pinned the growing droplet in position. The droplet now begins to grow in the axial direction and elongate downstream.

6. Whilst this is occurring the increased pressure of the continuous phase deforms the upstream interface, narrowing it until it is 'pinched off' by the interface contacting the opposite wall of the disperse phase inlet channel. This process also effectively reduces the curvature of the upstream interface in the plane of the device and ultimately affecting the curvature perpendicular to this also. This process also affects the net Laplace pressure on the droplet.
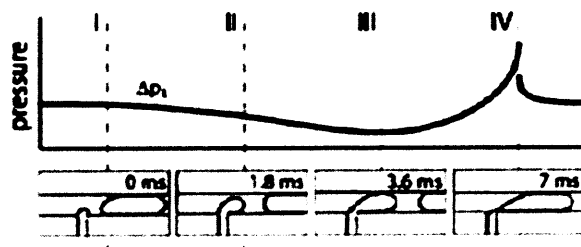
Figure 7 Pressure mediated droplet breakup and segmented flow regime formation at a T-junction architecture [53].

1.1.6.1.3 Recirculatory Flow

The dominance of interfacial forces on the microscale, combined with the viscous force dictated prevalence of Poiseuille flow of liquids in microchannels, gives rise to unique recirculatory flow regimes within each fluid segmented of a segmented flow regime. This highly important feature of such flow regimes has been exploited, in order to overcome the

absence of convective mixing in laminar flows, to accelerate mixing and intensify reaction rates [55] and also to significantly reduce axial dispersion, by largely retaining liquid and dissolved analytes in discrete, time-resolvable, segments [56]. In such flow regimes a recirculatory flow within each fluid segment is adopted [57,58] (Figure 8). The prevalence of Poiseuille-like flow on the microscale results in a parabolic axial flow profile, with the fluid at the centre of the channel travelling at a greater velocity than the upstream interface. Consequently, as the advancing flow approaches the downstream interface, the liquid is deflected towards the channel walls, where the exerted shear force slows the flow significantly. The upstream interfacial boundary then approaches the near stationary fluid near the channel walls, and this fluid is deflected into the channel centre. Here, free from the exerted shear at the channel walls, and subject to a constant pressure, the fluid accelerates and once again approaches the downstream interface. The process is repeated, and a recirculatory flow regime becomes established, symmetrical about the channel central axis. As a consequence of this prevailing flow regime axial mixing within a single fluid segment is very rapid, with reagent mixing within an individual fluid segment achieved on the millisecond time scale [51].

0.0   0.00025   0.0005   0.00075   0.001 m/s
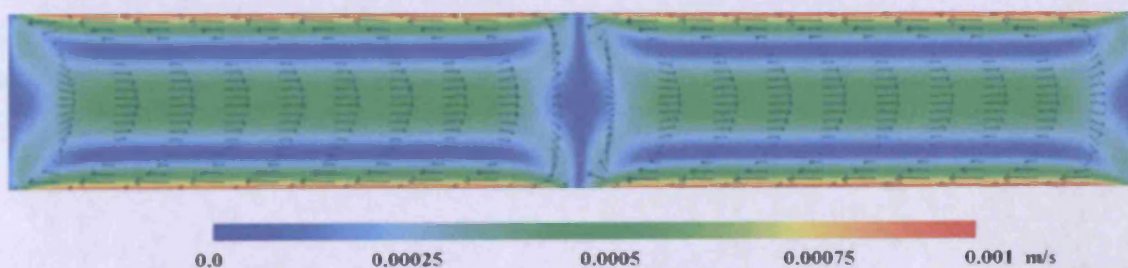
Figure 8 Computation Fluid Dynamic (CFD) vector velocity map of the recirculatory flow within individual fluid segments of a segmented flow regime. Adapted from [57].

This internal recirculatory flow establishes a continually refreshing fluidic interface, thus enhancing mass transfer between contiguous fluid segments [57,59]. Mass transfer occurs both axially into the neighbouring fluid packet, and radially into, and from, the thin film of wetting liquid which exists between the disperse phase and the channel wall [60]. The

continually refreshing fluidic interface provided by the recirculatory flow together with the high surface area to volume ratio afforded by the flow regime facilitate rapid mass transfer. The influence of flow variables on mass transfer effects is discussed in further detail in Chapter 3.

1.1.6.2 History of Segmented Flow: Segmented Flow Analysis & Flow Injection Analysis

In 1957 the AutoAnalyzer was invented by Leonard Skeggs [61] before being commercialised by Technicon Corporation. Termed a segmented flow analyser, segmented flow analysis (SFA) utilised the introduction of a gaseous phase to segment a continuous liquid stream (sample and reagents). The segmentation was utilised to minimise axial dispersion, encourage sample and reagent mixing and maintain separation of sequential samples. This technique enabled high sample throughput under continuous flow operation, thus increasing the efficiency of standard laboratory analysis techniques (i.e. extraction, dialysis, ion exchange, heating, incubation, distillation and analyte quantification [62]). Several years later, Ruzicka and Hansen introduced a related technique, flow injection analysis (FIA) [63], which utilised an immiscible liquid phase as the carrier phase into which the sample phase was segmented. The immiscible carrier liquid would carry the required reagents which would partition into and mix with the injected sample segments. The similar yet distinctly different modes of operation of SFA and FIA are exploited today in on-chip microfluidic multiphase flows, where the continuous and disperse phases can both be active in the chemical system, or alternatively, one phase may be used simply as a passive tool for the purpose of flow segmentation and the associated flow benefits this provides. Both FIA and SFA techniques are conceptually very similar to the multiphase flows receiving broad attention within the microfluidic field today. However unlike the majority of microfluidic devices, FIA and SFA machines tend to operate at high flow rates in comparatively wide capillary tubing (mm scale), resulting in long flow paths, high solvent and reagent consumption and a large equipment footprint. Much of the study utilising multiphase flows on the microscale is further exploiting the dominance of surface forces by working on a reduced scale (spatial and temporal). The development of micromachining techniques, image capture and analysis together with computational fluid dynamics simulation have enabled researchers to explore the fundamental physics

determining fluid behaviour in multiphase fluidics, enabling more refined exploitation of fluid behaviour in segmented flow systems than were offered by either SFA or FIA. This however is perhaps somewhat coincidental as the rapidly growing field of multiphase microfluidics seldom acknowledges the early exploitation of segmented flow regimes in flow injection or segmented flow analysis.

1.1.6.3 Current Applications of Multiphase Microfluidics

Since the conception of the microfluidics discipline, multiphase microfluidics has received ever increasing attention. The application of multiphase flows within microfluidic systems have been numerous, ranging from mass transfer operations similar to those of FIA and SFA for chemical reactions and synthesis, to diverse applications such as particle and fiber production, cell encapsulations, protein crystallisation and chemical logic. Such applications have been the subject of recent reviews [39,64,65]. Examples are illustrated and contextualised in chapter 5.

1.2 Liquid-Liquid Extraction

1.2.1 Principles

Liquid-liquid, or solvent, extraction is a widely employed technique in both synthetic and analytical chemistry. Utilised to separate, remove or isolate compounds on the basis of their relative solubilities in two immiscible liquids; frequently water and an organic solvent. The technique is routinely conducted using a separating funnel which is manually agitated to encourage mixing, whilst avoiding the formation of emulsions which may take considerable time to re-separate into the component phases. Compounds migrate across the interfacial boundary from one phase to the other. This is a dynamic process where at equilibrium the migrational flux of the compound between the phases is equal in both directions. At equilibrium, the extent of extraction is defined by the distribution coefficient (D) [66] which describes the ratio of the concentration of the chemical species in the organic to aqueous

phases. In an efficient extraction D will strongly favour the chemical species residing largely in one of the two phases as dictated by the Gibbs energy of the thermodynamic system. The time taken for the extraction to reach equilibrium is defined by the requirement for analyte diffusion to the interfacial boundary (mixing), together with diffusion across the interface. Additionally it may also be influenced by any necessary chemical reactions or processes which may be required in order to facilitate phase transfer of the chemical species. Such reactions may include protonation/deprotonation, ion pair formation, or complex formation and the rate contribution to the extraction process will depend upon the compound itself and the local chemical environment. Such factors vary considerably from system to system and are also strongly influenced by extraction parameters such as mixing and interfacial area/volume ratio and have been discussed in detail elsewhere [67]. Many extractions generally follow first order reactions kinetics [68] consequently a time/yield trade off can mean that sufficient extraction may be achieved without attaining distribution equilibrium, instead extraction efficiency (yield/time) may be improved through successive extraction procedures on the original sample liquid. Since solvent extraction is widely employed in sample preparation, for example in pharmaceutical and clinical analysis, and as part of the work-up process to isolate and purify the products of chemical reactions, the drive for both time and yield efficiency together with process selectivity is hugely significant.

1.2.2 Segmented Flow Extraction

The first report of liquid-liquid extraction in a segmented flow system was in 1978 [69] following the development of flow injection analysis (FIA) and its establishment as a versatile laboratory technique [62]. The high surface area to volume ratio afforded by the alternating segments of immiscible fluids in segmented flow increases the available interfacial area for extraction. The recirculating flow regime prevalent within each segment [70-73] (Section 1.6.1.3) increases the rate of mixing within each segment, enhancing the rate of mass transfer [74]. Karlberg et al. utilised these features of FIA flow to develop an extraction system which operated through the injection of sequential samples (12 -25 µl) into an aqueous flow stream which was subsequently segmented with chloroform which also acted as the extracting solvent

[69]. Aqueous Caffeine solutions and standards were extracted into chloroform at a total flow rate of 4.2 ml min^{-1} (1 : 1.1 organic : aqueous phase volumetric flow) through a segmented flow stream in 0.8 mm internal diameter Teflon tubing. A portion of the chloroform (35%) was separated from the segmented flow stream and passed through a UV absorption detector which was used to indirectly quantify the caffeine content of the initial aqueous sample solutions. The segmented flow uniquely provided another advantage of segregating sequential sample injection, enabling a high sample analysis throughput (100 samples/hour). This effectively created a semi-automated, high throughput sample analyser. Subsequent demonstrations followed this typical procedure, with some later examples employing a continuous flow of sample into the segmentor creating a continuous extraction technique [75]. Later research investigated the mechanisms of band broadening [60] and the kinetics of FIA solvent extraction, [74,75]. With researchers demonstrating the attainment of equilibrium in the extraction of caffeine within 10 seconds [75]. This research is further described and reviewed in chapter 3. More recently research groups have revisited (or perhaps rediscovered) the application of segmented flow to enhance mass transfer between immiscible phase, applied to integrated microfluidic device flows [55].

1.3 Project Description

It was proposed that the inclusion of solid-phase adsorbent particles in the extracting/segmenting phase of a segmented flow system would enhance the transfer of analyte from a sample phase to the immiscible extracting phase by maintaining a significant concentration gradient between the two immiscible fluid phases. It was envisaged that the enhanced interfacial mass transfer associated with segmented flow as a direct result of the high surface area to volume ratio and the unique recirculating flow patterns within the fluid packets themselves would enhance the time efficiency of the extraction, whilst the suspended solid-phase adsorbent would increase the efficiency of the extent of the extraction. Additionally, it was reasoned that the application of analyte specific adsorbent materials in the form of molecularly imprinted polymers would enhance the extent of extraction *specifically* for the compound of interest (Figure 9). Molecular imprinting is described and reviewed in chapter 2.

- analyte
- selective adsorbent (MIP)
- internal circulation
- aqueous phase
- organic phase
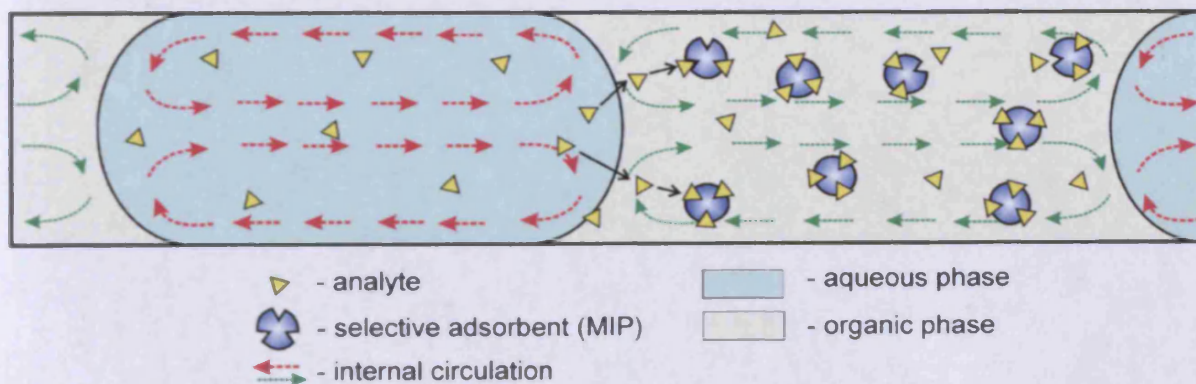
Figure 9 Schematic illustration of the proposed extraction enhancement mechanism achieved through incorporation of a solid affinity medium in the extracting phase of a liquid-liquid extraction, segmented flow regime.

1.4 Aims and Objectives

1.4.1 Aims

The aim of this research was to develop a continuous flow, enhanced efficiency separations platform, utilising microfluidic approaches to harness the unique behaviour of fluids on the microscale, together with incorporated extraction enhancement reagents, to facilitate highly efficient liquid extractions. It was important that a chemically robust affinity phase could be employed to increase analyte extraction and highly desirable that the affinity phase may be analyte specific, or class selective. An integrated approach to chemical separation was sought in order to produce a separation microdevice, with liquid phase separation an inherent challenge in the liquid-liquid extraction methodology. Characterisation of mass transfer behaviour was highly desirable in order to fully understand and optimise extraction performance.

1.4.2 Objectives

- Identification of a suitable inert, chemically resistant affinity phase, for enhancement of liquid-liquid extractions.

- Demonstration of the applicability of the affinity phase to the enhancement of a model liquid-liquid extraction.

- Development of appropriate machining and constructional methodologies for microfluidic device preparation.

- Characterisation of interfacial mass transfer in microfluidic segmented flow regimes, together with investigation into the significance of flow variables, fluid properties and channel geometries on interfacial mass transfer.

- Proof of concept demonstration of microfluidic solid-phase enhanced segmented flow liquid extraction.

- Design, development, and characterisation of an on-chip, integrated, segmented flow, liquid phase separation device, capable of handling flow regimes containing suspended solid phase material.

- Proposition of optimal design structures for enhanced efficiency segmented flow, liquid phase separation devices.

- Characterisation of affinity phase binding behaviour for the development of predictive and comparative performance models.

- Identification of optimisation strategies to enhance temporal separation efficiency and extraction yield efficiency.

1.5 References

[1]   G.M. Whitesides, "The origins and the future of microfluidics," *Nature*, vol. 442, Jul. 2006, pp. 368-373.

[2]   A. Manz, N. Graber, and H. Widmer, "Miniaturized total chemical analysis systems: A novel concept for chemical sensing," *Sensors and Actuators B: Chemical*, vol. 1, Jan. 1990, pp. 244-248.

[3]   A. Manz, D.J. Harrison, E.M.J. Verpoorte, J.C. Fettinger, A. Paulus, H. Lüdi, and H.M. Widmer, "Planar chips technology for miniaturization and integration of separation techniques into monitoring systems : Capillary electrophoresis on a chip," *Journal of Chromatography A*, vol. 593, Feb. 1992, pp. 253-258.

[4]   S. Terry, J. Jerman, and J. Angell, "A gas chromatographic air analyzer fabricated on a silicon wafer," *Electron Devices, IEEE Transactions on*, vol. 26, 1979, pp. 1880-1886.

[5]   A. Clemens, "Reflectance Meter," U.S. Patent SE363902, February 4, 1974.

[6]   J. Hones, P. Muller, and N. Surridge, "The Technology Behind Glucose Meters: Test Strips," *Diabetes Technology & Therapeutics*, vol. 10, 2008, pp. 10-26.

[7]   P.H. Sönksen, S.L. Judd, and C. Lowy, "Home monitoring of blood-glucose. Method for improving diabetic control," *Lancet*, vol. 1, Apr. 1978, pp. 729-32.

[8]   I. Endo, Y. Sato, S. Saito, T. Nakagiri, and S. Ohno, "Liquid Jet Recording Process And Apparatus Therefor," U.S. Patent CA1127227, July 6, 1982.

[9]   J.L. Vaught, F.L. Cloutier, D.K. Donald, C.A. Tacklind, J.D. Meyer, and H.H. Taub, "Thermal Ink Jet Printer," U.S. Patent GB2106039, April 7, 1983.

[10] "Case study: Spitting image," *The Economist print edition*, September 19. 2002.

[11] E. Touloupakis, G. Basile, E. Pace, M. Giardi, and F. Costa, "Successes in the Development and Application of Innovative Techniques," *Biotechnological Applications of Photosynthetic Proteins: Biochips, Biosensors and Biodevices*, 2006, pp. 209-214.

[12] G. Parkinson and B. Pejcic, *Using Biosensors to Detect Emerging Infectious Diseases*, Perth, Australia: Nanochemistry Research Institute, Curtin University of Technology. The Australian Biosecurity Cooperative Research Centre, 2005. http://www1.abcrc.org.au/uploads/a2ab38c8-8eed-4531-b9f7-642691aa2eb2/docs/UsingBiosensors ToDetectEID220306.pdf

[13] B. Pejcic, R.D. Marco, and G. Parkinson, "The role of biosensors in the detection of emerging infectious diseases," *The Analyst*, vol. 131, 2006, pp. 1079-1090.

[14] F. Sanger, G.M. Air, B.G. Barrell, N.L. Brown, A.R. Coulson, C.A. Fiddes, C.A. Hutchison, P.M. Slocombe, and M. Smith, "Nucleotide sequence of bacteriophage phi X174 DNA," *Nature*, vol. 265, Feb. 1977, pp. 687-95.

[18] M.S. Williams, K.J. Longmuir, and P. Yager, "A practical guide to the sta; herringbone mixer," *Lab on a Chip*, vol. 8, 2008, pp. 1121-1129.

[19] C. Kim, K. Lee, J.H. Kim, K.S. Shin, K. Lee, T.S. Kim, and J.Y. Kang, "A serial (microfluidic device using a ladder network generating logarithmic or concentrations," *Lab on a Chip*, vol. 8, 2008, pp. 473-479.

[20] J.D. Toonder, F. Bos, D. Broer, L. Filippini, M. Gillies, J.D. Goede, T. Mol, M. Reij; Talen, H. Wilderbeek, V. Khatavkar, and P. Anderson, "Artificial cilia for active fluidic mixing," *Lab on a Chip*, vol. 8, 2008, pp. 533-541.

[21] M.J. Moehlenbrock and R.S. Martin, "Development of an on-chip injector for mic based flow analyses using laminar flow," *Lab on a Chip*, vol. 7, 2007, pp. 1589-159

[22] G. Chen, F. Svec, and D.R. Knapp, "Light-actuated high pressure-resisting microva on-chip flow control based on thermo-responsive nanostructured polymer," *Lal Chip*, vol. 8, 2008, pp. 1198-1204.

[23] P.A. Willis, F. Greer, M.C. Lee, J.A. Smith, V.E. White, F.J. Grunthaner, J.J. Sp and J.P. Rolland, "Monolithic photolithographically patterned Fluorocur[trade mar PFPE membrane valves and pumps for in situ planetary exploration," *Lab on a Chi* 8, 2008, pp. 1024-1026.

[24] D.B. Weibel, A.C. Siegel, A. Lee, A.H. George, and G.M. Whitesides, "Pumping fl microfluidic systems using the elastic deformation of poly(dimethylsiloxane)," *La Chip*, vol. 7, 2007, pp. 1832-1836.

[25] D.R. Mott, P.B. Howell, Jr., J.P. Golden, C.R. Kaplan, F.S. Ligler, and E.S. "Toolbox for the design of optimized microfluidic components," *Lab on a Chip*, 2006, pp. 540-549.

[26] N. Pamme, "Continuous flow separations in microfluidic devices," *Lab on a Chip*, 2007, pp. 1644-1659.

[27] H. Bruus, *Theoretical microfluidics*, Oxford University Press Oxford, 2007.

[28] G.D. Fulford and J.P. Catchpole, "Dimensionless Groups," *Industrial & Engin Chemistry*, vol. 60, Mar. 1968, pp. 71-78.

[29] D. Janasek, J. Franzke, and A. Manz, "Scaling and the design of miniaturized che analysis systems," *Nature*, vol. 442, Jul. 2006, pp. 374-380.

34

[30] O. Reynolds, "An Experimental Investigation of the Circumstances Which Determine Whether the Motion of Water Shall Be Direct or Sinuous, and of the Law of Resistance in Parallel Channels," *Philosophical Transactions of the Royal Society of London*, vol. 174, 1883, pp. 935-982.

[31] P. Kuban, J. Berg, and P. Dasgupta, "Vertically Stratified Flows in Microchannels. Computational Simulations and Applications to Solvent Extraction and Ion Exchange," *Analytical Chemistry*, vol. 75, Jul. 2003, pp. 3549-3556.

[32] D.R. Lide, *CRC Handbook of Chemistry and Physics*, CRC Press Inc, 1994.

[33] H. A. Stone, A. A. D. Stroock, and A. Ajdari, "Engineering Flows In Small Devices," Jan. 2004.

[34] A. Einstein, R. Furth, and A.D. Cowper, *Investigations on the Theory of the Brownian Movement*, Courier DoverPublications, 1956.

[35] D. Selmeczi, S.F. Tolic-Norrelykke, E. Schaeffer, P.H. Hagedorn, S. Mosler, K. Berg-Sorensen, N.B. Larsen, and H. Flyvbjerg, "Brownian Motion after Einstein and Smoluchowski: Some New Applications and New Experiments," *Acta Physica Polonica B*, vol. 38, Aug. 2007, p. 2407.

[36] J.P. Brody and P. Yager, "Diffusion-based extraction in a microfabricated device," *Sensors and Actuators A: Physical*, vol. 58, Jan. 1997, pp. 13-18.

[37] P. Yager, "Microfluidics Tutorials." Department of Bioengineering, University of Washington http://faculty.washington.edu/yagerp/microfluidicstutorial/tutorialhome.htm

[38] C. Chen, D.N. Breslauer, J.I. Luna, A. Grimes, W. Chin, L.P. Lee, and M. Khine, "Shrinky-Dink microfluidics: 3D polystyrene chips," *Lab on a Chip*, vol. 8, 2008, pp. 622-624.

[39] A. Gunther and K.F. Jensen, "Multiphase microfluidics: from flow characteristics to chemical and materials synthesis," *Lab on a Chip*, vol. 6, 2006, pp. 1487-1503.

[40] K. Ishiguro, M. Iguchi, Y. Mizuno, and Y. Terauchi, "Separation of Gas from Downward Gas-Liquid Two-Phase Flow Using a Y-Junction of Poor Wettability," *JSME International Journal Series B*, vol. 47, 2004, pp. 795-803.

[41] H. Xiao, D. Liang, G. Liu, M. Guo, W. Xing, and J. Cheng, "Initial study of two-phase laminar flow extraction chip for sample preparation for gas chromatography," *Lab on a Chip*, vol. 6, 2006, pp. 1067-1072.

[42] V.S. Ajaev and G.M. Homsy, "Modeling Shapes and Dynamics of Confined Bubbles," *Annual Review of Fluid Mechanics*, vol. 38, 2006, pp. 277-307.

[43] A.M. Gañán-Calvo and J.M. Gordillo, "Perfectly Monodisperse Microbubbling by Capillary Flow Focusing," *Physical Review Letters*, vol. 87, Dec. 2001, p. 274501.

[44] S.L. Anna, N. Bontoux, and H.A. Stone, "Formation of dispersions using "flow focusing" in microchannels," *Applied Physics Letters*, vol. 82, Jan. 2003, pp. 364-366.

[45] H.A. Stone, "Dynamics of Drop Deformation and Breakup in Viscous Fluids," *Annual Reviews in Fluid Mechanics*, vol. 26, 1994, pp. 65-102.

[49] T. Thorsen, R.W. Roberts, F.H. Arnold, and S.R. Quake, "Dynamic Pattern Formation in a Vesicle-Generating Microfluidic Device," *Physical Review Letters*, vol. 86, Apr. 2001, p. 4163.

[50] P. Garstecki, M.J. Fuerstman, and G.M. Whitesides, "Oscillations with uniquely long periods in a microfluidic bubble generator," *Nature Physics*, vol. 1, Dec. 2005, pp. 168-171.

[51] H. Song, J.D. Tice, and R.F. Ismagilov, "A microfluidic system for controlling reaction networks in time," *Angewandte Chemie (International ed. in English)*, vol. 42, Feb. 2003, pp. 768-72.

[52] J.R. Burns and C. Ramshaw, "A Microreactor for the Nitration of Benzene and Toluene," *Chemical Engineering Communications*, vol. 189, 2002, p. 1611.

[53] P. Garstecki, M.J. Fuerstman, H.A. Stone, and G.M. Whitesides, "Formation of droplets and bubbles in a microfluidic T-junction—scaling and mechanism of break-up," *Lab on a Chip*, vol. 6, 2006, pp. 437-446.

[54] P. Garstecki, M.J. Fuerstman, H.A. Stone, and G.M. Whitesides, "Formation of droplets and bubbles in a microfluidic T-junction-scaling and mechanism of break-up," *Lab on a Chip*, vol. 6, 2006, pp. 437-446.

[55] J.R. Burns and C. Ramshaw, "The intensification of rapid reactions in multiphase systems using slug flow in capillaries ," *Lab on a Chip*, vol. 1, 2001, pp. 10-15.

[56] L.R. Snyder and H.J. Adler, "Dispersion in segmented flow through glass tubing in continuous-flow analysis: the ideal model," *Analytical Chemistry*, vol. 48, Jun. 1976, pp. 1017-1022.

[57] N. Harries, J.R. Burns, D.A. Barrow, and C. Ramshaw, "A numerical model for segmented flow in a microreactor," *International Journal of Heat and Mass Transfer*, vol. 46, Aug. 2003, pp. 3313-3322.

[58] A. Gunther, M. Thalmann, M. Jhunjhunwala, M. Schmidt, and K. Jensen, "Micromixing of Miscible Liquids in Segmented Gas-Liquid Flow," *Langmuir*, vol. 21, Feb. 2005, pp. 1547-1555.

[59] B. Ahmed, D. Barrow, and T. Wirth, "Enhancement of Reaction Rates by Segmented Fluid Flow in Capillary Scale Reactors," *Advanced Synthesis & Catalysis*, vol. 348, 2006, pp. 1043-1048.

[60] C.A. Lucy and F.F. Cantwell, "Mechanism of extraction and band broadening in solvent extraction-flow injection analysis," *Analytical Chemistry*, vol. 61, Jan. 1989, pp. 107-114.

[65] H. Song, D.L. Chen, and R.F. Ismagilov, "Reactions in Droplets in Microfluidic Cha *Angewandte Chemie International Edition*, vol. 45, 2006, pp. 7336-7356.

[66] A. Leo, C. Hansch, and D. Elkins, "Partition coefficients and their uses," *Ch Reviews*, vol. 71, 1971, p. 525-616.

[67] J. Pawliszyn, *Sampling and sample preparation for field and laboratory: Fundan and New Directions in Sample Preparation*, Elsevier, 2002.

[68] J. Pawliszyn, *Solid Phase Microextraction: Theory and Practice*, Wiley-VCH, 1997.

[69] B. Karlberg and S. Thelander, "Extraction based on the flow-injection principle : Description of the Extraction System," *Analytica Chimica Acta*, vol. 98, May. 1978, 7.

[70] J.L. Duda and J.S. Vrentas, "Steady flow in the region of closed streamline: cylindrical cavity," *Journal of Fluid Mechanics*, vol. 45, 1971, p. 247.

[71] G. Bugliarello and G.C. Hsiao, "A mathematical model of the flow in the axial pla gaps of the smaller vessels," *Biorheology*, vol. 7, Jun. 1970, pp. 5-36.

[72] H.S. Lew and Y.C. Fung, "The motion of the plasma between the red cells in the flow," *Biorheology*, vol. 6, Aug. 1969, pp. 109-19.

[73] G.I. Taylor, "Deposition of a viscous fluid on the wall of a tube," *Journal ol Mechanics*, vol. 10, 1961, pp. 161-165.

[74] C.A. Lucy and F.F. Cantwell, "Kinetics of solvent extraction-flow injection ana *Analytical Chemistry*, vol. 61, Jan. 1989, pp. 101-107.

[75] L. Nord, K. Bäckström, L-G. Danielsson, F. Ingman, and B. Karlberg, "Extraction liquid-liquid segmented flow injection analysis," *Analytica Chimica Acta*, vol. 194, pp. 221-233.

Molecularly Imprinted Polymer

Production, Assessment and

Application in Single and Multiphase

Incubation Systems

However, in general, the performance of conventional MIPs in aqueous environments is

Likewise, the stability of biologically derived recognition systems (enzymes, antib

receptors etc) is largely poor in organic media, owing to conformational changes that r

binding or recognition capabilities. The customisable nature of MIPs was deemed extr

advantageous, not only in offering the opportunity to influence analyte binding, but a

providing an ability to tune the hydrophilic or hydrophobic nature of the polymer pai

ensuring residence in the extracting phase. As such, MIPs seemed an ideal recognition

for the intended application, whilst the use of a biphasic immiscible solvent system offi

novel approach to interfacing MIPs with aqueous based sample media, which has long

considered a limitation of the molecular imprinting strategy.

This chapter describes a previously unreported use of MIPs as solvent extraction rea

their successful application to aqueous sample media and the opportunities for utilisa

this unique system in novel biosensing and separation procedures. This study demons

the development of a novel biphasic solvent system utilising MIP in the extracting ph

enhance both efficiency and selectivity of a simple two phase liquid extraction.

Monodisperse propranolol imprinted polymer microspheres [poly(divinylbenze

methacrylic acid)] were prepared by precipitation polymerisation. Initially, the affinity

polymers for (R,S)-propranolol was assessed by established techniques whereby th

demonstrated greater affinity for the template than did the non-imprinted control pi

(NIP). Importantly, MIP performance was also assessed using the novel dual-solvent s

The depletion of (R,S)-propranolol from the aqueous phase into the polymer con

organic phase was determined. When compared to control extractions containing no polymer, the presence of MIP in the extracting solvent phase resulted in an increased extraction of (R,S)-propranolol from the aqueous phase. Importantly, this extraction was significantly greater in the presence of MIP when compared to NIP.

This unique principle generates opportunities for MIP-based extractions and chemical enrichments in industrial applications, offering commercial, ecological and practical advantages to traditional solvent extraction techniques. The technique is readily transferable to analytical microsystems utilising MIP recognition elements, generating promising opportunities for MIP based sensing of aqueous sample media.

2.2 Introduction

2.2.1 Molecularly Imprinted Polymers (MIPs)

MIPs offer simple, customisable, rugged and cost effective alternatives to biological recognition systems [1,2]. The technology of molecular imprinting involves the introduction of analyte specific binding sites within rigid, cross-linked, three dimensional polymer matrices [3-5]. This is generally achieved through the formation of pre-polymerisation complexes between the analyte (template) molecule and functionally complementary monomers and their subsequent polymerisation in a porogenic environment in the presence of cross-linking monomer(s). Removal of the template molecule yields a functionally and spatially ordered imprinted site capable of rebinding the template molecule under appropriate conditions (Figure 1). Analyte recognition is achieved through a combination of both spatial and inter-molecular interactions between the analyte molecule and the polymer functionality at the binding site.

40
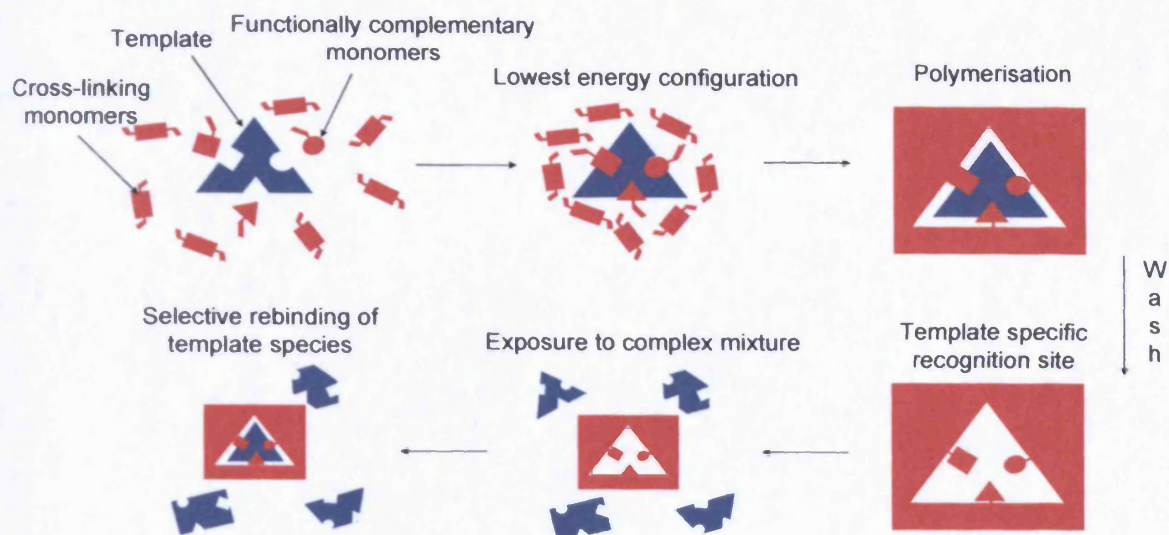
Figure 1 Conceptual schematic cartoon illustrating the molecularly imprinting model.

MIPs have been utilised in a wide variety of applications. Their specific recognition properties have been applied to chromatographic separations including early examples of use in chiral [6] and achiral [7] separations in high performance liquid chromatography (HPLC), solid phase extraction (SPE) [8] and bubble fractionation [9]. MIPs have also been employed as recognition materials for sensors [10] and catalysts in simple organic reactions [11]. Their applications have been widely reviewed [12-17], as have their methods of production [18,19], optimisation [20] and characterisation [19,20].   MIP materials have been the subject of increasing interest in recent years, with several books summarising knowledge of the field [21-24].

2.2.1.1 Aqueous Compatibility

A well documented obstacle to the wider application of MIPs is the issue of aqueous compatibility [25]. Although much progress has been made [26] the performance of MIPs in water is still generally poor when compared to that in non-polar solvents. This is largely attributed to the competition between water and template for functionally important hydrogen bonding sites [25]. The application of MIPs for use in aqueous environments is particularly desirable for the development of MIP based sensors and extractions in biological and

environmental samples. It was anticipated that suspension of MIP material in an immiscible organic phase in contact with an aqueous sample phase would provide a unique way to circumvent this issue and improve application of MIPs to aqueous sample media.

2.2.2 Solvent Extraction

Liquid – liquid extraction, or solvent extraction, has been used for many years for the purification, separation, concentration or removal of desired compounds. Commonly employed as a purification technique in research and production synthetic chemistry, it has also been employed in a wide range of other applications including: examining contaminant levels in water [27], clean-up and recycling of waste water [28], and the recovery of valuable metals [29]. The selectivity of the technique, when used alone, is restricted and only limited specificity can be achieved. However, more recently researchers have extended the range of application, and improved specificity and extraction efficiency, by the incorporation of a solvent extraction reagent into the extracting phase [30-32]. This has been of commercial importance in the extraction of metal ions from an aqueous phase into an organic phase by using ion-selective binding reagents such as oligo-pyridine [30], N-n-octylaniline [33], or crown ethers [34]. Enantioselective partitioning has been demonstrated by the inclusion of small-molecule chiral selectors in the extracting solvent [32]. The approach has also been extended to embrace the specific extraction of organic molecules from an organic solvent into an aqueous phase by utilisation of solubilising reagents such as cyclodextrins [35].

2.2.3 Aims and Objectives

The work of this chapter aims to describe the novel application of MIPs as solvent extraction reagents, their successful application to aqueous sample media and the opportunities for utilisation of this unique system in sensing and separation techniques. This study demonstrates the development of a novel biphasic solvent system utilising MIPs in the extracting phase to enhance both efficiency and selectivity of a simple two phase extraction.

2.3 Precipitation Polymerisation

For the purpose of this study spherical MIP particles, produced by precipitation polymerisation, were preferred as solvent extraction reagents, to those produced by traditional monolithic methods [36]. The small (3-4 µm diameter) and regular particles formed by this technique were able to produce uniform suspensions in the organic solvent. This would have been intrinsically more difficult to achieve with the larger (45 µm diameter) irregular shards of polymer yielded from more traditional monolithic approaches to molecular imprinting. Precipitation polymerisation has recently emerged as a desirable and scalable approach to adopt for the production of high quality, highly uniform, spherical imprinted particles. Unlike the suspension polymerisation approach to generating spherical polymer particles, the precipitation technique does not require the use of surfactant or steric stabilisers. The resulting particles therefore have a clean stabiliser free surface and carry no ionic charge [37,38]. Spherical MIPs were first reported to be prepared using this method in 1999 [39], with the production of sub-micron sized imprinted polymer spheres by the polymerisation of monomers in dilute solutions. Subsequent work [40], utilising an approach first reported by the polymer chemist Stöver [38], tailored MIP particle growth by subtle refinement of the solvent and porogen system to create a polymerisation environment at near θ conditions (Section 2.3.1.1). This enabled the production of larger, imprinted, mono-dispersed microspheres, typically up to 5 µm in diameter, and provided some control over the size and porosity of the resultant polymer. This enabled the production of morphologically favourable, highly expanded, porous polymer networks of high surface area.

2.3.1 Mechanism of Particle Growth

In both the traditional monolithic and precipitation polymerisation approaches to MIP production, early polymer growth occurs in solution, where cross-linked oligomer radicals form. These resulting oligomers grow, cross-link and aggregate to form small, early-stage polymer spheres. In the production of MIP monoliths where high monomer:solvent ratios are used, these spheres continue to grow and coalesce until one continuous macro-porous

polymer network has been formed. However, when the polymerisation is conducted in a large excess of organic solvent, as is the case with precipitation polymerisation where monomer concentrations are typically less than 5%, the initial polymer spheres do not overlap nor coalesce but continue to grow individually by capturing newly formed oligomers and monomers [38]. In a poorly solvating medium, where the growing polymer has little affinity for the surrounding solvent, phase separation occurs early and dense, non-porous polymer microspheres are formed. When the solvating property of solvent media is increased, phase separation is delayed, allowing the entrapment of solvent within the growing polymer prior to precipitation. This results in the formation of many small micro-/meso-pores throughout the forming polymer microsphere [38]. The growth mechanism of particles in suspension polymerisation can be considered as analogous to that of monolith formation, albeit in a substantially restricted volume.

2.3.1.1 Importance of Theta (θ)

The point at which phase separation occurs is governed by the polymer/solvent system's proximity to θ-conditions. In a theta solvent system for the forming polymer, a theta temperature is defined as the temperature at which excess chemical potential and, correspondingly, the excess Gibbs energy of dilution is zero [41], and thus, the solution in the theta state is thermodynamically pseudo-ideal [41]. Therefore, the composition of the polymer, composition of the solvating environment and temperature of the polymerisation, all have an effect on the point of phase separation, and thus, the morphology of the polymer produced. From a practical perspective, polymer microspheres precipitated in near θ-conditions will typically be expanded, porous, and several μm in diameter. In contrast, polymers formed either side of this point will be either non-particulate, continuous and gel like or sub-micron, dense, non-porous, particulates [42]. This influence of theta on polymer growth and morphological characteristics is also relevant to the production of monolithic polymers. However, the high monomer concentration leads to coalescence of the growing polymer spheres regardless of the point of phase separation of the growing polymer from the (non-)solvating environment. Consequently the morphological effects are somewhat less obvious

44

than in a precipitation polymerisation system, with a large contribution of the polymer's porosity contributed by macro-pores created by particle coalescence. To date no study has assessed the influence of theta on monolith formation or recognition performance, or commented on its significance as a variable.

2.4 Polymer Production

2.4.1 Materials

Methacrylic acid (MAA), (R,S)-propranolol hydrochloride, pindolol, naproxen and acebutolol hydrochloride were obtained from Sigma (Gillingham, UK). Divinylbenzene (DVB) technical grade 80 %, was obtained from Aldrich (Gillingham, UK). 2'2-Azobisisobutyronitrile (AIBN) and toluene were purchased from Acros Organics (Loughborough, UK). Vanillic acid was obtained from Fluka (Gillingham, UK), and acetonitrile, chloroform and methanol were purchased from Fisher Scientific (Loughborough, UK). All chemicals and solvents were analytical or HPLC grade and were used without further purification. Fluorescent analysis was performed using a Fluostar Optima 96-well plate reader (BMG Labtech, Aylesbury, UK). HPLC analysis of acebutolol was conducted on a Thermo TSP HPLC system. (Thermo Electron Corporation, Runcorn, UK). Sizing of polymer microspheres was carried out by laser diffraction (Coulter N4 plus, Beckman, High Wycombe, UK).

2.4.2 Method

Uniform imprinted and non-imprinted polymer microspheres were prepared by precipitation polymerisation [40]. (R,S)-Propranolol free base (389.0 mg)(1.5 mmol) (converted from the HCl salt from NaOH solution and subsequent filtration), MAA (509 μL)(6.0 mmol), DVB (4.103 mL)(28.8 mmol), and AIBN (312.0 mg)(1.9 mmol) were dissolved in 128 ml 82.5/17.5 % v/v mixture of acetonitrile and toluene in a 250 ml round-bottomed flask. The solution was sparged with oxygen-free nitrogen for 10 minutes at 0 °C. Subsequently, the sealed flask was rotated at 7½ r.p.m. at 60 °C in a water bath for 24 hours. At the end of the reaction the

polymer microspheres were recovered by filtration and washed successively with acetonitrile (60 ml), toluene (60 ml) methanol/acetic acid 70/30 (120 ml), methanol (40 ml), acetonitrile (40 ml), toluene (40 ml), acetonitrile (40 ml), and methanol (40 ml). The reclaimed microspheres were then dried under vacuum overnight at room temperature. Non-imprinted polymer (NIP) microspheres were prepared in the same way as the MIP microspheres but using 128 ml 90/10 % v/v mixture of acetonitrile and toluene and with the omission of (R,S)-propranolol.

2.4.3 Results and Discussion

In the production of MIP and NIP a white powder was recovered upon filtration. After washing and drying the polymer particles were visualised by light microscopy. Both MIP and NIP particles were observed to be spherical, near-monodispersed, with a narrow size distribution. The mean particle diameter measured by laser diffraction scattering was found to be 3.6 µm (S.D, 1.4 µm) for MIP spheres and 3.9 µm (S.D, 1.6 µm) for NIP spheres. Figure 2 shows an image of the prepared MIP microspheres obtained by Scanning Electron Microscopy (SEM).
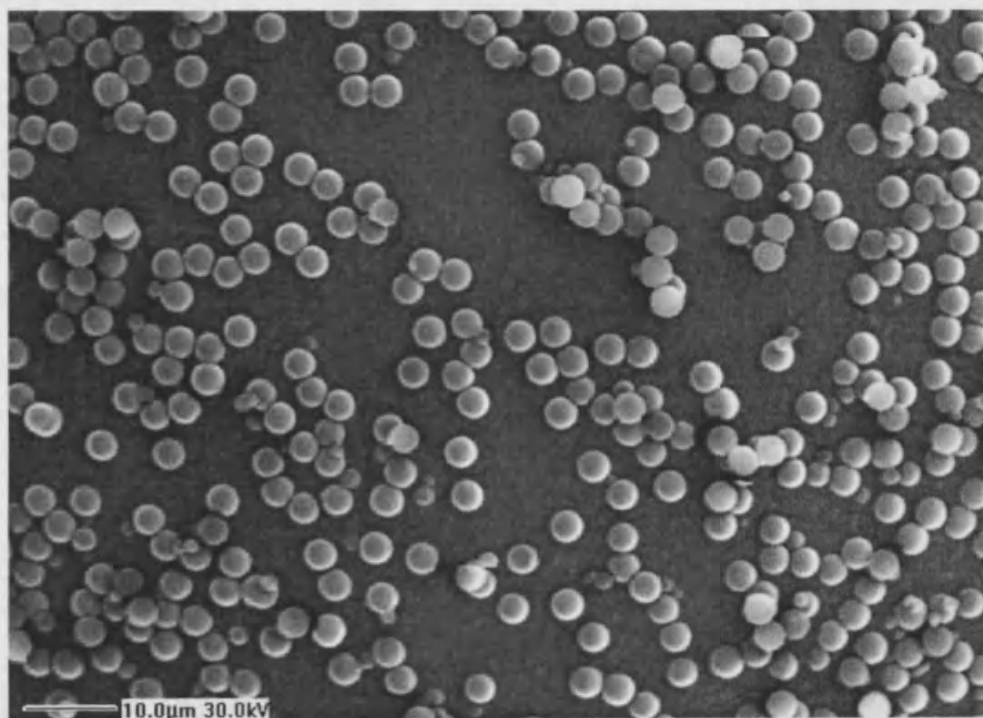
Figure 2 Scanning Electron Microscopy (SEM) image of propranolol imprinted polymer microspheres

In preliminary studies it was observed that when MIP and NIP microspheres were prepared using the same ratio of acetonitrile/toluene, the MIP microsphere were significantly smaller than the NIP microspheres. This indicated that the template was having a significant impact on the solvating properties of the solvent environment for the growing polymer and this was affecting θ-conditions and therefore phase separation. The concern was that there may be a significant difference in the morphology of the two polymers and that this variation would later complicate interpretation of binding data. Therefore, in order to try to obtain morphologically equivalent polymers, it was considered important to attempt to match both the size and growth rate of the MIP and NIP microspheres. In order to compensate for the absence of (R,S)-propranolol in the production of the NIP (control) the toluene and acetonitrile composition of the solvating media was adjusted slightly by decreasing the toluene component from 17.5 % to 10 %. It was reasoned that if phase separation, which occurs when a polymer chain reaches the size where solvent/polymer interactions become unfavourable and the polymer chain precipitates, could be achieved at a comparable point in both the MIP and NIP, the porosity, density and therefore the size of the final microsphere would be comparable. The precise rationale for the effect caused by the presence or absence of template species and the adjustment of solvating media appears to be more complex than simply relating the solubility of the monomers to the solvent media. Exposed, concealed and self-complementary functionality in the evolving MIP and NIP systems, polymer flexibility and also the solvating effect of template molecules remaining in the solvent media itself, may also play an important role.

2.5 Polymer Assessment 1 - Single Phase Studies

2.5.1 Binding Assays

2.5.1.1 Equilibrium Analyte Rebinding

2.5.1.1.1 General Methodology

Polymer microsphere particles (1 mg) were mixed with 2 ml of solvent containing 25 µM concentration of (R,S)-propranolol or cross-reactant species. In the case of saturation binding studies polymer microsphere particles (1 mg) were mixed with 2 ml of solvent containing 25, 50, 100, 250 or 500 µM concentrations of (R,S)-propranolol. Samples were incubated for 24 hours at room temperature and agitated by rocking. The sample mixtures were filtered using PTFE 0.20 µm membrane filters and the filtrate analysed by either HPLC or microplate fluorescence spectroscopy.

2.5.1.1.2 Solvent Screening

The binding of (R,S)-propranolol to both MIP and NIP was assessed in a range of polar, non-polar and intermediate solvents employing the methodology of 2.5.1.1.1.

2.5.1.1.2.1 Results and Discussion

Figure 3 illustrates the binding of propranolol to both MIP and NIP in the range of incubating solvents investigated. In all cases the MIP bound more propranolol than did the NIP. However, in extreme non-polar and polar solvents, i.e. hexane, toluene and water, a large degree of non-specific binding was observed as demonstrated by at least 25 nmol (50%) of the propranolol binding to the NIP in each of the three instances. This was unsurprising due to the extreme nature of the solvent environment and the relatively low solubility of propranolol base in these media. Despite this the MIP appears to show a degree of template recognition in both polar and non-polar environments, suggesting that the recognition mechanisms involve both polar and non-polar interactions between the template and the MIP binding site. In non-polar environments template recognition and binding may occur in part through hydrogen bond

donor and acceptor interactions between the alcohol and ether groups on the propranolol moiety and the carboxylic acid groups of the polymer. Proton transfer and subsequent ionic interactions may also occur through proton donation from the carboxylic acid residue of methacrylic acid to the basic secondary amine of the propranolol molecule. In polar environments hydrophobic interactions such π-π interactions between the aromatic naphthyl moiety of the propranolol structure and the aromatic functionality of divinylbenzene cross-linking monomers may contribute to template recognition. These proposed interactions are illustrated in figure 4. In intermediate environments a combination of these processes may be responsible of binding of propranolol to the MIP. The performance of the MIP in chloroform was particularly noteworthy as although the total amount bound, 20 nmol, was less than in aqueous, hexane or toluene environments it could almost totally be attributed to specific template - binding site recognition mechanisms as just 1.9 nmol (R,S)- propranolol was observed to bind to the NIP microspheres.
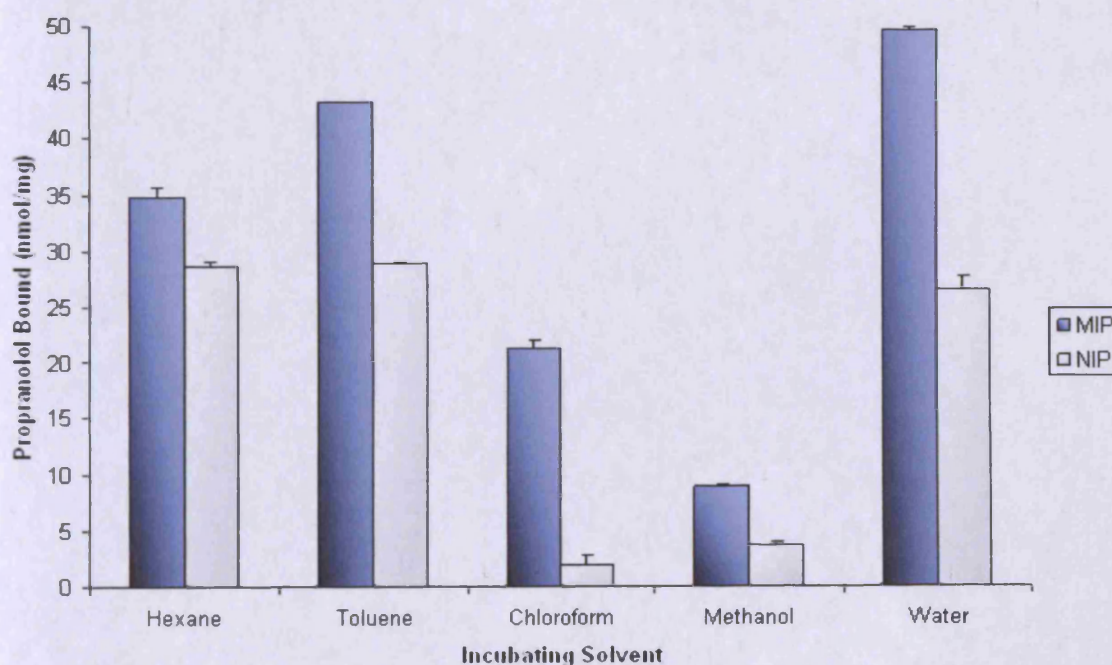
Figure 3 (R,S)-propranolol bound to MIP or NIP in a range of solvents. Conditions: 1 mg polymer, 2 ml incubating solvent containing 25 µM concentration of propranolol. (n=5 ±SEM).

49
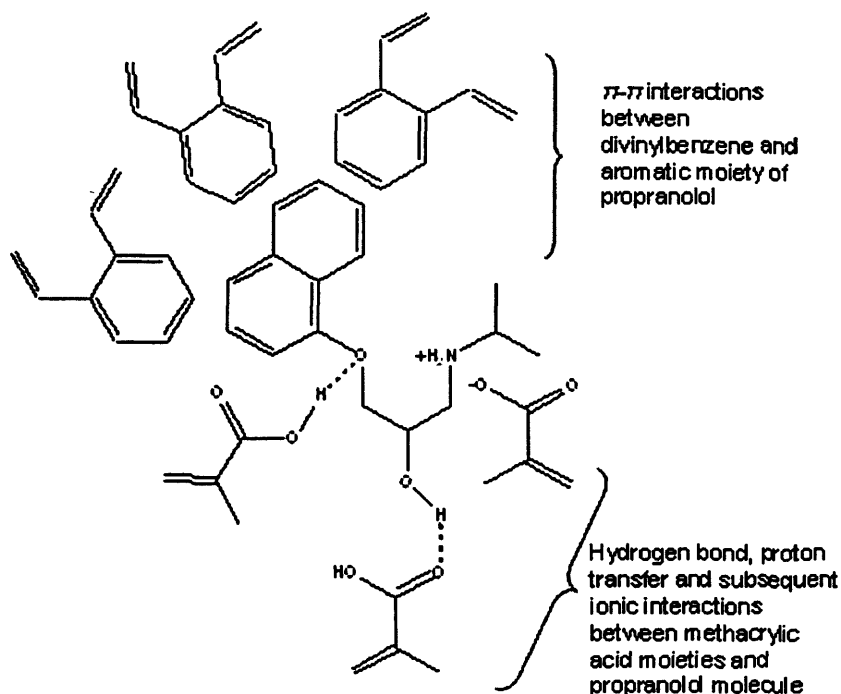
Figure 4 Postulated mechanisms of interaction between propranolol moiety and polymer components, represented and theorised pre-polymerisation complex prior to polymerisation of cross-linking and functional monomers.

2.5.1.1.2.2 Selection of Chloroform as a Candidate Solvent

The initial performance of the MIP in chloroform coupled with the essential immiscible nature of the solvent with water made chloroform a suitable solvent for use in a proof of principle demonstration of the novel two phase MIP binding system. The additional benefit of a high surface tension between chloroform and water was also considered advantageous for subsequent microfluidic segmented flow regimes (Chapter 3 and 4).

2.5.1.1.3 The Effect of Water

The effect on template rebinding to the MIP by the small amount of water that would dissolve in chloroform in a two phase system was investigated by assessing the binding of (R,S)-propranolol to both MIP and NIP microspheres in water saturated chloroform (0.815% H_2O) (Figure 5) employing the batch binding methodology detailed in 2.5.1.1.1.

2.5.1.1.3.1 Results and Discussion

Surprisingly, the presence of water in chloroform had little observable effect on propranolol binding to either the MIP or the NIP. It would be reasonable to predict that the addition of 0.815% water to the chloroform would have some effect on either specific or non-specific polymer-template binding interactions due to competition for hydrogen bond interactions with the polymer [43]. The fact that this was not observed suggests that either recognition is achieved purely through apolar interactions, which considering the complementary functionality of the propranolol moiety and MAA monomers, would seem unlikely. Perhaps more conceivably, the considerably hydrophobic nature of the divinylbenzene based polymers largely inhibits water molecules from entering the pores and template specific binding sites, thus minimising the hydrogen bond disrupting effects of water. This theory is supported by the reported application of mineral oil coatings to MIP particles in order to create a hydrophobic environment for template rebinding in polar media [44].
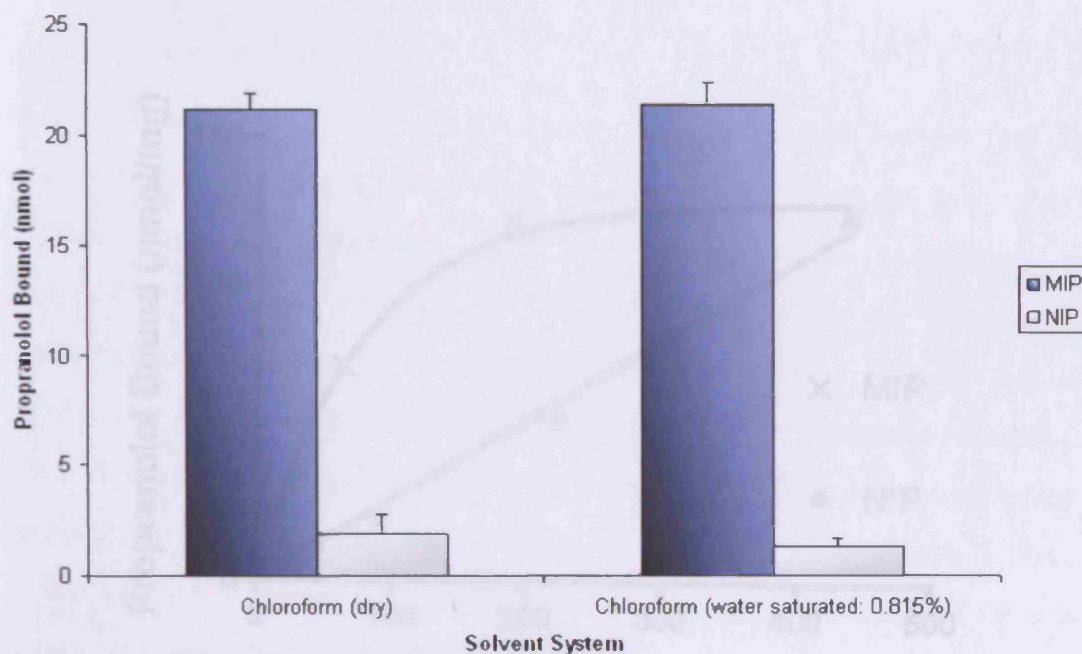
Figure 5 Binding of (R,S)-propranolol to MIP and NIP in dry and water saturated chloroform. (n=5 ±SEM).

51

2.5.1.1.4 Binding Isotherm and Polymer Saturation

MIP saturation binding studies were conducted in accordance with the general binding assessment methodology detailed in section 2.5.1.1. The binding of propranolol to 1 mg of MIP or NIP in water saturated chloroform (2 ml) containing 25, 50, 100, 250 or 500 µM concentrations of (R,S)-propranolol was assessed.

2.5.1.1.4.1 Results and Discussion

A logarithmic like plot characteristic of saturable binding was observed for the binding of propranolol to the MIP microspheres (Figure 6). A linear relationship suggestive of non-specific binding to a large number of non-specific sites was observed over the same concentration range for the NIP microspheres. This data is indicative of a true molecular imprinting effect being observed with the (R,S)-propranolol MIP microspheres. Further studies, quantifying the cross-reactive binding of a number of template related and non-related analytes, were undertaken to confirm the presence of a molecular imprinting effect.
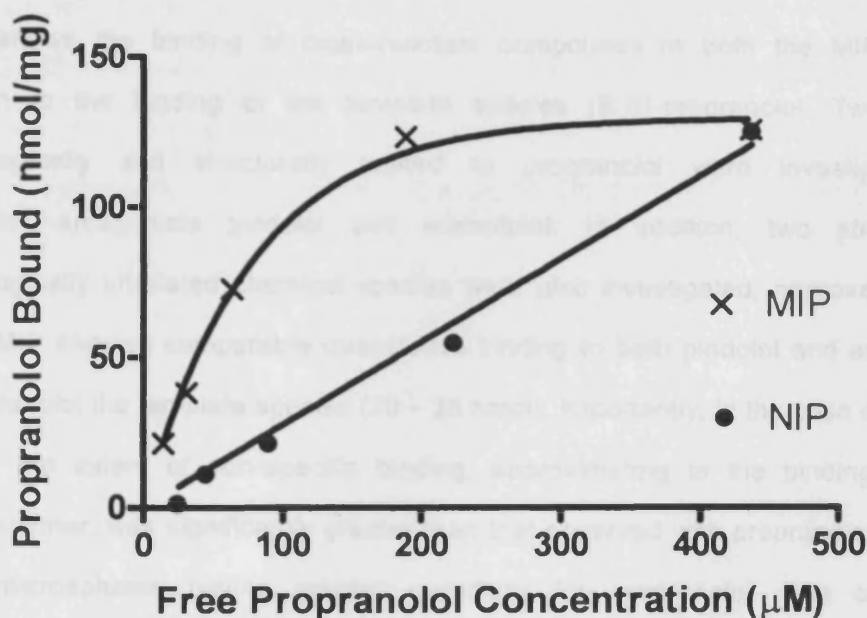
Figure 6 Equilibrium binding of (R,S)-propranolol to MIP or NIP at a range of (R,S)-propranolol concentrations in water saturated (0.815%) chloroform. (n=5).

2.5.1.2 Substrate Cross Reactivity

2.5.1.2.1 Methodology

The binding behaviour of the MIP to a selection of compounds, both related (structurally and pharmacologically) and unrelated to the template species was assessed. Binding assays were conducted in accordance with the methodology of 2.5.1.1.1. Microplate fluorescence spectroscopy was utilised for the detection and quantification of the intrinsically fluorescent ligands; propranolol (excitation λ 290 nm, emission λ 330 nm), pindolol (excitation λ 260 nm, emission λ 310 nm), naproxen (excitation λ 330 nm, emission λ 360 nm) and vanillic acid (excitation λ 290 nm, emission λ 330 nm). Sample volumes of 200 µl were employed and three replicate wells were analysed for each individual experiment. Acebutolol binding was characterised by HPLC analysis. (Column: Genesis C_{18} 4 µm, 15 cm x 4.6 mm Grace Vydac (Worms, Germany). Mobile phase: phosphate buffer 10 mM, pH 6.2 and methanol (1:1), flow rate: 1 mL min^{-1}, UV detection: λ 235 nm, injection volume: 20 µl). Samples in chloroform were evaporated to dryness and reconstituted with equal volumes of methanol.

2.5.1.2.2 Results and Discussion

Figure 7 shows the binding of cross-reactant compounds to both the MIP and NIP in comparison to the binding of the template species (R,S)-propranolol. Two compounds pharmacologically and structurally related to propranolol were investigated, the β adrenoceptor antagonists pindolol and acebutolol. In addition, two structurally and pharmacologically unrelated chemical species were also investigated; naproxen and vanillic acid. The MIP showed comparable quantitative binding to both pindolol and acebutolol as it did to propranolol the template species (20 – 25 nmol). Importantly, in the case of pindolol and acebutolol, the extent of non-specific binding, approximating to the binding to the non-imprinted polymer, was significantly greater than that observed with propranolol, indicative of the MIP microspheres having greater specificity for propranolol. The cross-reactivity demonstrated by the MIP for the compounds structurally related to the template species is unsurprising since pindolol and acebutolol both share structural, positional and functional similarities to propranolol, such as, an aromatic moiety, tertiary alcohol, ether and secondary

amine (Figure 7). This is pharmacologically demonstrated by the ability of all three compounds to act as antagonists to the $\beta 1$ subclass of adrenoceptors and the pharmaceutical application of this activity. The binding of naproxen and vanillic acid to the MIP was substantially less than that seen with propranolol and the other β adrenoceptor antagonists (<2 nmol). The extent of non-specific binding to the NIP microspheres in water saturated chloroform appeared to show a general correlation with calculated logP values for the five compounds. Propranolol and naproxen with logP values of 3.35 and 2.97 respectively demonstrated low levels of non-specific binding to the NIP, whilst vanillic acid (logP = 1.35), pindolol (1.19) and acebutolol (2.02) bound in greater quantities (Figure 7). Naproxen was seen to bind comparably to both the imprinted and non-imprinted microspheres. Interestingly, vanillic acid was found to have greater affinity for the non-imprinted polymer microspheres than it did for the propranolol imprinted polymer microspheres, although binding in both cases was low at 1.7 and 5.6 nmol to the MIP and NIP respectively. The reason for this observation may be explained by the greater presence of surface immobilised methacrylic acid moieties incorporated into the NIP microspheres, which, in the MIP microspheres may often be occluded within template specific binding sites. This phenomenon would expose a greater number of hydrogen bond donor and acceptor species on the NIP microsphere surface which would be available for polar interactions with the ligand, thus potentially increasing non-specific binding to the NIP. This theory, coupled with the necessity to morphologically match the NIP and MIP microspheres, illustrates the inherent difficulties with control experiments in the field of molecular imprinting.
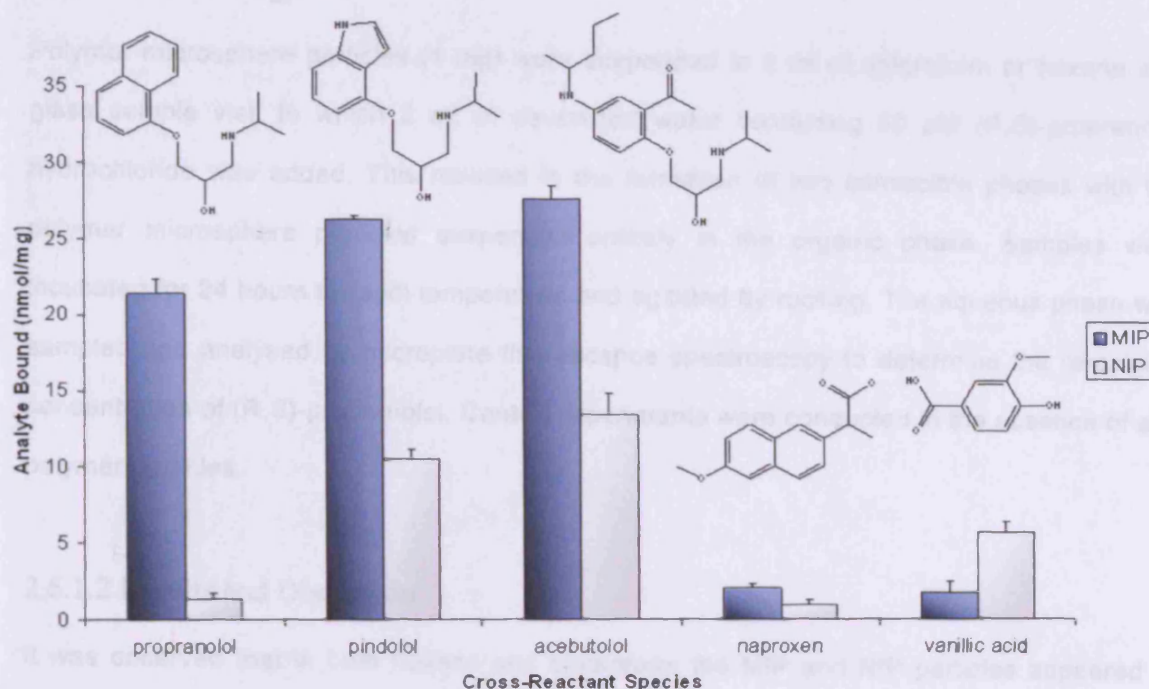
Figure 7 Cross-reactivity binding of structurally related and unrelated compounds to MIP and NIP in water saturated (0.815%) chloroform. (n=5 ±SEM)

2.6 Polymer Assessment 2 - Two Phase Solvent System

2.6.1 Two Phase Depletion Analysis - A Model for Solid Phase Assisted Solvent Extraction

The depletion of (R,S)-propranolol from a 50 μM aqueous sample after extraction with organic solvent (hexane or chloroform) in the absence of polymer, and in the presence of either MIP or NIP microspheres suspended in the organic phase was measured [(MIP/hex/aq), (NIP/hex/aq), (no-polymer/hex/aq), (MIP/chloro/aq), (NIP/chloro/aq) and (no-polymer/chloro/aq)].

2.6.1.1 Methodology

Polymer microsphere particles (1 mg) were suspended in 2 ml of chloroform or hexane in a glass sample vial, to which 2 ml of de-ionised water containing 50 µM (R,S)-propranolol hydrochloride was added. This resulted in the formation of two immiscible phases with the polymer microsphere particles suspended entirely in the organic phase. Samples were incubated for 24 hours at room temperature and agitated by rocking. The aqueous phase was sampled and analysed by microplate fluorescence spectroscopy to determine the remaining concentration of (R,S)-propranolol. Control experiments were conducted in the absence of any polymer particles.

2.6.1.2 Results and Discussion

It was observed that in both hexane and chloroform the MIP and NIP particles appeared to remain solely suspended in the organic phase, with no polymer entering the aqueous layer. This may be attributed to the hydrophobic nature of the largely DVB based polymers. This phenomenon was key in this MIP-based two-phase extraction. However, this is not essential for the application of this principle in biphasic MIP based sensing systems. In such devices the polymer would likely be immobilised on the sensor surface contained within a micro-environment of the partitioning phase.

Table 1 shows the distribution of (R,S)-propranolol between the aqueous, organic and polymer phases. The quantity of (R,S)-propranolol remaining in the aqueous phase was measured, and from this the quantity of (R,S)-propranolol unbound in the organic phase was calculated using a measured partition coefficient of (R,S)-propranolol between aqueous and organic solvents (aqueous/organic). This enabled the quantitative determination of (R,S)-propranolol bound to the MIP and NIP microspheres.

Table 1 Quantity of (R,S)-propranolol (nmol) in each solvent phase or bound to polymer microspheres at equilibrium in two phase binding studies. Results calculated from measurement of propranolol depletion from the aqueous phase due partitioning into immiscible organic solvent (chloroform or hexane) [a], partitioning into immiscible organic solvent (chloroform or hexane) containing suspended NIP microspheres [b] and partitioning into immiscible organic solvent (chloroform or hexane) containing MIP microspheres [c]. (n=5 (CV))

	Location of (R,S)-propranolol by phase (nmol) (100 nmol total)				Binding Ratio MIP/NIP	Binding ratio (MIP/NIP) in organic solvent alone [Figure 1]
	Aqueous phase	Partition coefficient (aq/organic)	Organic phase	Polymer bound		
H_2O	100.00	-	-	-		
H_2O + C_6H_{14} [a]	82.04 (0.04)	4.568	17.96	-		
H_2O + C_6H_{14} + NIP [b]	37.60 (0.26)	4.568	8.23	54.17	1.56	1.22
H_2O + C_6H_{14} + MIP [c]	12.88 (0.35)	4.568	2.82	84.30		
H_2O	100.00	-	-	-		
H_2O + $CHCl_3$ [a]	7.57 (0.28)	0.082	92.43	-		
H_2O + $CHCl_3$ + NIP [b]	7.15 (0.20)	0.082	87.31	5.54	12.21	11.18
H_2O + $CHCl_3$ + MIP [c]	2.45 (0.41)	0.082	29.92	67.63		
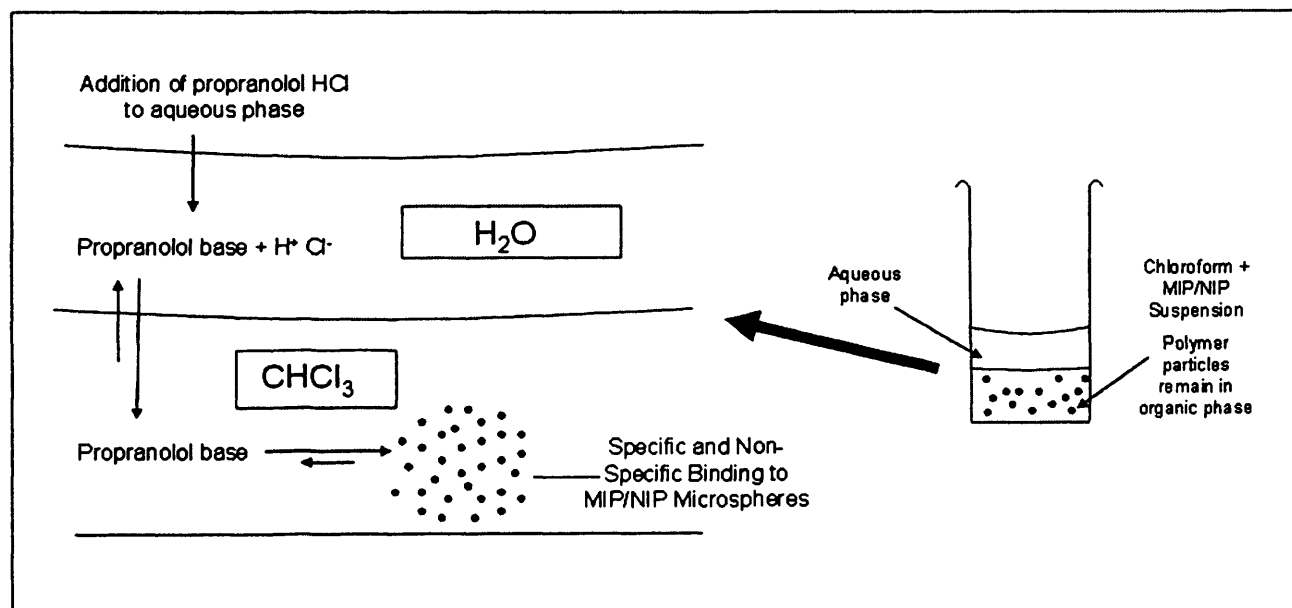
Figure 8 Schematic illustration of enhanced selective extraction utilising MIP microspheres as solvent extraction reagents.

As in traditional batch evaluation of polymer binding, equilibrium is established between bound and free ligand. In the case of this dual solvent and polymer system, equilibrium is established between the three phases (Figure 8). In the organic phase (R,S)-propranolol binds to the polymer as it would in a single phase solvent system (Figure 6), whilst the partition coefficient defining the free (R,S)-propranolol in each solvent phase is maintained. The partition coefficient for the partitioning of (R,S)-propranolol between water and hexane (4.568) and water and chloroform (0.082) represent scenarios where the majority of the analyte will partition into the aqueous phase, in the case of hexane, or into the organic phase in the case of chloroform. The results illustrated in table 1 and figure 9 demonstrate that in either situation the presence of MIP in the organic phase significantly enhances depletion of (R,S)-propranolol from the aqueous phase compared to the extraction seen by organic solvent alone or organic solvent containing suspended NIP microspheres. In both solvent systems the MIP was shown to bind the majority of (R,S)-propranolol present in the system [84.30% (hexane) and 64.63% (chloroform)]. In the single solvent template binding studies (Figure 3) a large amount of non-specific binding to the NIP microspheres was observed in hexane due to its extreme non-polar nature. In the dual solvent NIP/hex/aq system non-specific binding to the NIP resulted in a significant increase in extraction of (R,S)-propranolol from the aqueous phase compared to extraction with hexane alone. However, the amount of (R,S)-propranolol remaining in the aqueous phase in MIP/hex/aq system was significantly lower still, at one third of that seen in the NIP/hex/aq system.

In the case of chloroform as the organic solvent phase, MIP/chloro/aq significantly increased the extent of depletion of (R,S)-propranolol from the aqueous phase. Whilst in the NIP/chloro/aq system only a small increase in removal of (R,S)-propranolol from the aqueous phase was observed when compared no-polymer/chloro/aq. This can be attributed to the high levels of specific binding to the MIP and the very low level of non-specific binding to the NIP observed in batch binding studies conducted in chloroform (Figures 3, 5, 6 and 7). Evaluation of the performance of the MIP microspheres in the biphasic solvent system was conducted by calculating the binding ratio MIP:NIP. For both hexane and chloroform the binding ratio in the

dual solvent environment was found to be extremely close to the ratios calculated for MIP and NIP binding in the organic solvent alone (Figures 3 and 5). The binding ratios shown in figure 6 illustrates that MIP:NIP binding ratio varies with free (R,S)-propranolol concentration. The small changes observed for MIP:NIP binding ratio in the dual solvent system compared to those of the single solvent system may therefore arise due to the difference in free concentration of (R,S)-propranolol in the organic phase at equilibrium in the presence of a second solvent phase.
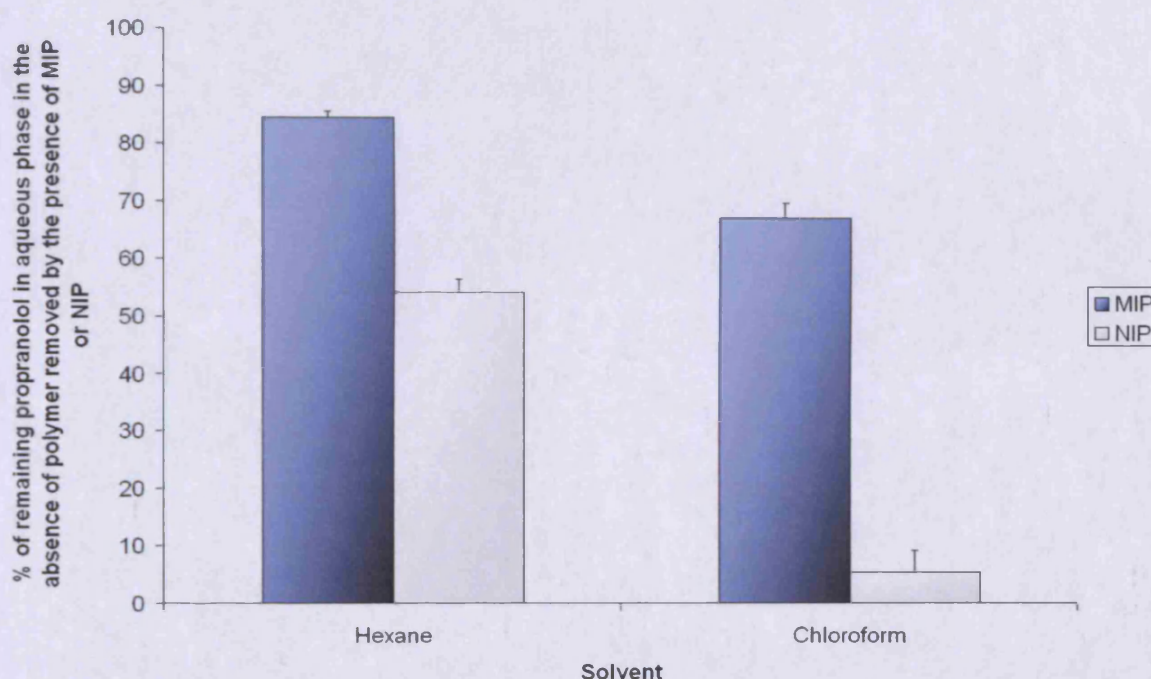
Figure 9 Additional extraction of (R,S)-propranolol from the aqueous phase with the addition of MIP or NIP to the extracting hexane or chloroform component in the two-phase system, expressed as a percentage of (R,S)-propranolol remaining in the aqueous after extraction with organic solvent alone. (n=5 ±SEM).

2.7 Conclusions

2.7.1 Importance of Theta

In the context of polymer formation, the point at which a growing polymer network ceases to remain soluble in the polymerisation media is governed by the polymer/solvent system's proximity to θ-conditions. In precipitation polymerisation the proximity of polymerisation conditions to the theta point has a strong influence on the resultant particle size and pore

structure. These polymer morphology implications also apply to other strategies employed in MIP synthesis, such as monolith production or suspension polymerisation. Results show that small changes in polymerisation environment can affect theta dramatically. Likewise, so can changing polymer components, (monomers etc), and thus theta can vary dramatically between polymerisation systems. Improved knowledge of this process may assist in understanding why some polymers perform better than others, and may partly explain why some cross-linker/functional monomer combinations appear to perform better with regard to template recognition. It was hoped to develop a method for inter-MIP data comparison with the eventual aim of a meta-analysis of reported MIP performance in order to improve understanding and ultimately produce a better MIP, this is discussed further in chapters 6 and 7.

Studies with monolithically prepared MIPs have investigated the effect of preparation temperature on MIP performance, with the hypothesis that inter-molecular interactions of the pre-polymerisation complex will be greater at lower temperatures. The stabilised pre-polymerisation complex is theorised to produce better binding sites, with reduced heterogeneity [45]. The reported data showed some support for the hypothesis, with improved enantiomeric separation achieved with the polymer prepared at low temperature. However, surface area of the polymers, as assessed by nitrogen adsorption porosimetry, was observed to decrease markedly with reduced polymerisation temperature, producing an almost non-porous material. Although perhaps not a surprising observation in itself, it is interesting that despite the reduced surface area of the MIP produced at low temperature, the polymer still performed comparably to high surface area materials of greater porosity, produced at elevated temperatures. This effect is almost certainly theta related and the prospect of adjusting the solvent polymerisation system to produce a theta polymer at reduced temperature, harnessing the enhanced stability of complex formation afforded by low temperatures, whilst producing a highly porous imprinted material with a high surface area and thus a high proportion of exposed binding sites, is an exciting prospect worthy of future study.

2.7.2 MIPs in Multiphase Liquid Systems

A novel, yet simple, method for the application of molecularly imprinted polymer based recognition and extraction systems for analytes in aqueous sample media has been successfully demonstrated. This provides the opportunity for further widening the scope of molecularly imprinted recognition materials in applications such as sensors and assays operating in, or with, aqueous based, biological and environmental media. The prospect of sensors utilising immobilised MIP recognition elements in a micro environment of organic solvent contained within a semi-permeable membrane for sensing in aqueous sample media is a realistic and promising possibility.

2.7.3 MIP Enhanced Solvent Extraction

Demonstration of this unique principle is extremely encouraging in the context of this thesis aim to develop an affinity-phase enhanced, continuous flow microfluidic extraction or enrichment methodology. The inclusion of high affinity and capacity selective MIP binding agents in solvent extraction systems will enable enhancements in extent of extraction whilst enabling application of smaller volumes of organic solvent, offering environmental, commercial and safety advantages. Furthermore, the solid phase MIP included in the extracting phase can subsequently be easily separated from the organic liquid for reclaiming of the analyte, cleaning and recycling of the MIP and organic solvent. Chapter 4 studies the application of the concept demonstrated here on the microscale, in a microfluidic segmented flow system.

2.8 References

[1]   C. Allender, K. Brain, and C. Heard, "Molecularly Imprinted Polymers - Preparation, Biomedical Applications and Technical Challenges," *Progress in Medicinal Chemistry*, vol. 36, 1999, pp. 235-291.

[2]   S.A. Piletsky, S. Alcock, and A.P.F. Turner, "Molecular imprinting: at the edge of the third millennium," *Trends in Biotechnology*, vol. 19, Jan. 2001, pp. 9-12.

[3]   R. Arshady and K. Mosbach, "Synthesis of substrate-selective polymers by host-guest polymerization," *Die Makromolekulare Chemie*, vol. 182, 1981, pp. 687-692.

[4]   M.J. Whitcombe et al., "A New Method for the Introduction of Recognition Site Functionality into Polymers Prepared by Molecular Imprinting: Synthesis and Characterization of Polymeric Receptors for Cholesterol," *Journal of the American Chemical Society*, vol. 117, Jul. 1995, pp. 7105-7111.

[5]   G. Wulff and A. Biffis, *imprinted polymers - Man-made mimics of antibodies and their applications in analytical chemistry*, Oxford: Elsevier, 2001.

[6]   B. Sellergren, B. Ekberg, and K. Mosbach, "Molecular imprinting of amino acid derivatives in macroporous polymers : Demonstration of substrate- and enantio-selectivity by chromatographic resolution of racemic mixtures of amino acid derivatives," *Journal of Chromatography A*, vol. 347, 1985, pp. 1-10.

[7]   M. Kempe and K. Mosbach, "Direct resolution of naproxen on a non-covalently molecularly imprinted chiral stationary phase," *Journal of Chromatography A*, vol. 664, Apr. 1994, pp. 276-279.

[8]   B. Sellergren, "Direct Drug Determination by Selective Sample Enrichment on an Imprinted Polymer," *Analytical Chemistry*, vol. 66, May. 1994, pp. 1578-1582.

[9]   D. Armstrong et al., "Bubble Fractionation of Enantiomers from Solution Using Molecularly Imprinted Polymers as Collectors," *Analytical Chemistry*, vol. 70, Sep. 1998, pp. 3717-3719.

[10] D. Kriz et al., "A Biomimetic Sensor Based on a Molecularly Imprinted Polymer as a Recognition Element Combined with Fiber-Optic Detection," *Analytical Chemistry*, vol. 67, Jul. 1995, pp. 2142-2144.

[11] A. Leonhardt and K. Mosbach, "Enzyme-mimicking polymers exhibiting specific substrate binding and catalytic functions," *Reactive Polymers, Ion Exchangers, Sorbents*, vol. 6, 1987, pp. 285-290.

[12] N. Maier and W. Lindner, "Chiral recognition applications of molecularly imprinted polymers: a critical review," *Analytical and Bioanalytical Chemistry*, vol. 389, 2007, pp. 377-397.

[13] C. Alexander, L. Davidson, and W. Hayes, "Imprinted polymers: artificial molecular recognition materials with applications in synthesis and catalysis," *Tetrahedron*, vol. 59, Mar. 2003, pp. 2025-2057.

[14] A. Hillberg, K. Brain, and C. Allender, "Molecular imprinted polymer sensors: Implications for therapeutics," *Advanced Drug Delivery Reviews*, vol. 57, Dec. 2005, pp. 1875-1889.

[15] K. Haupt, "Molecularly imprinted polymers in analytical chemistry ," *The Analyst*, vol. 126, 2001, pp. 747-756.

[16] B. Sellergren and C.J. Allender, "Molecularly imprinted polymers: A bridge to advanced drug delivery," *Advanced Drug Delivery Reviews*, vol. 57, Dec. 2005, pp. 1733-1741.

[17] K. Haupt, "Molecularly Imprinted Polymers: Artificial Receptors for Affinity Separations," *Handbook of Affinity Chromatography*, 2006. London: Taylor & Francis Group, 2006.

[18] A. Mayes and M. Whitcombe, "Synthetic strategies for the generation of molecularly imprinted organic polymers," *Advanced Drug Delivery Reviews*, vol. 57, Dec. 2005, pp. 1742-1778.

[19] P.A.G. Cormack and A.Z. Elorza, "Molecularly imprinted polymers: synthesis and characterisation," *Journal of Chromatography B*, vol. 804, May. 2004, pp. 173-182.

[20] D.A. Spivak, "Optimization, evaluation, and characterization of molecularly imprinted polymers," *Advanced Drug Delivery Reviews*, vol. 57, Dec. 2005, pp. 1779-1794.

[21] M. Komiyama et al., *Molecular Imprinting*, Weinheim: Wiley-VCH, 2003.

[22] M. Yan and O. Ramström, *Molecularly Imprinted Materials*, London: CRC Press, 2005.

[23] R.A. Bartsch and M. Maeda, *Molecular and ionic recognition with imprinted polymers*, Columbus: American Chemical Society, 2005.

[24] B. Sellergren, *Molecularly Imprinted Polymers: Man-made Mimics of Antibodies and Their Applications in Analytical Chemistry*, Oxford: Elsevier Science, 2001.

[25] O. Ramström and Richard J. Ansell, "Molecular imprinting technology: challenges and prospects for the future," *Chirality*, vol. 10, 1998, pp. 195-209.

[26] B. Dirion et al., "Water-Compatible Molecularly Imprinted Polymers Obtained via High-Throughput Synthesis and Experimental Design," *Journal of the American Chemical Society*, vol. 125, Dec. 2003, pp. 15101-15109.

[27] M.A. Franson, *Standard methods for the examination of water and waste water, 19th ed.*, Washington D.C.: American Public Health Association, 1995.

[28] S.E. Kentish and G.W. Stevens, "Innovations in separations technology for the recycling and re-use of liquid waste streams," *Chemical Engineering Journal*, vol. 84, Oct. 2001, pp. 149-159.

[29] A. Diamantatos, "An integrated scheme for the recovery of the six platinum-group metals and gold after lead fusion and perchloric acid parting and a comparison with the lead cupellation, tin, and nickel sulphide collection schemes," *Analytica Chimica Acta*, vol. 94, Nov. 1977, pp. 49-55.

[30] K. Ishimori et al., "Ion-pair extraction of Am(III) and Eu(III) with oligo-pyridine ligand," *Journal of Alloys and Compounds*, vol. 408-412, Feb. 2006, pp. 1278-1282.

[31] D. Kara and M. Alkan, "Preconcentration and separation of copper (II) with solvent extraction using N,N'-bis(2-hydroxy-5-bromo-benzyl)1,2 diaminopropane," *Microchemical Journal*, vol. 71, Jan. 2002, pp. 29-39.

[32] S.E. Snyder, J.R. Carey, and W.H. Pirkle, "Biphasic enantioselective partitioning studies using small-molecule chiral selectors," *Tetrahedron*, vol. 61, Aug. 2005, pp. 7562-7567.

[33] T.N. Lokhande, M.A. Anuse, and M.B. Chavan, "Extraction and separation studies of platinum(IV) with N-n-octylaniline," *Talanta*, vol. 47, Sep. 1998, pp. 823-832.

[34] K. Kimura, T. Maeda, and T. Shono, "Extraction of alkali metal picrates with poly- and bis(crown ether)s," *Talanta*, vol. 26, Oct. 1979, pp. 945-949.

[35] L.A. Blyshak et al., "Cyclodextrin-modified solvent extraction for polynuclear aromatic hydrocarbons," *Analytical Chemistry*, vol. 60, Oct. 1988, pp. 2127-2131.

[36] S. Piletsky et al., "Polymer Cookery: Influence of Polymerization Time and Different Initiation Conditions on Performance of Molecularly Imprinted Polymers," *Macromolecules*, vol. 38, Feb. 2005, pp. 1410-1414.

[37] K. Li and H.D.H. Stöver, "Synthesis of monodisperse poly(divinylbenzene) microspheres," *Journal of Polymer Science Part A: Polymer Chemistry*, vol. 31, 1993, pp. 3257-3263.

[38] W. Li and H. Stöver, "Porous monodisperse poly(divinylbenzene) microspheres by precipitation polymerization," *Journal of Polymer Science, Part A: Polymer Chemistry*, vol. 36, 1998, pp. 1543-1551.

[39] L. Ye, P.A.G. Cormack, and K. Mosbach, "Molecularly imprinted monodisperse microspheres for competitive radioassay," *Analytical Communications,* vol. 36, 1999, pp. 35-38.

[40] J. Wang et al., "Monodisperse, Molecularly Imprinted Polymer Microspheres Prepared by Precipitation Polymerization for Affinity Separation Applications13," *Angewandte Chemie International Edition,* vol. 42, 2003, pp. 5336-5338.

[41] J. Brandrup and E.H. Immergut, P*olymer Handbook, 3rd ed.,* New York: Wiley-Interscience, 1989 .

[42] J. Downey et al., "Poly(divinylbenzene) Microspheres as an Intermediate Morphology between Microgel, Macrogel, and Coagulum in Cross-Linking Precipitation Polymerization," *Macromolecules,* vol. 34, Jun. 2001, pp. 4534-4541.

[43] C.J. Allender, C.M. Heard, and K.R. Brain, "Mobile phase effects on enantiomer resolution using molecularly imprinted polymers," *Chirality,* vol. 9, 1997, pp. 238-242.

[44] E.V. Piletska et al., "Adaptation of the molecular imprinted polymers towards polar environment," *Analytica Chimica Acta,* vol. 542, Jun. 2005, pp. 47-51.

[45] S. Piletsky et al., "Polymer Cookery: Influence of Polymerization Conditions on the Performance of Molecularly Imprinted Polymers," *Macromolecules,* vol. 35, Sep. 2002, pp. 7499-7504.

Chapter 3

Microfluidic Segmented Flow and

Interfacial Mass Transfer

3.1 Overview

3.1.1 Context

Having prepared and evaluated a molecularly imprinted polymer as a suitable candidate solid-affinity phase for enhancement of a liquid-liquid extraction (Chapter 2), the mechanisms and kinetics of segmented flow phase boundary mass transfer were investigated. Following preliminarily proof of principle demonstration of MIP-assisted segmented flow extraction, both on-chip and in-tube based systems were utilised in conjunction with literature analysis to characterise the variables contributing to mass transfer enhancement in a segmented flow system. Understanding of the influence of channel design and flow regime characteristics on the rate of interfacial mass transfer would be required to ultimately produce an optimised, integrated on-chip extraction platform.

3.2 MIP Binding Kinetics - Sufficiently Fast?

In a microfluidic environment the linear velocity of fluid flow generates a space (channel length) - time (transit time) transformation [1], with the channel cross-sectional geometry defining the volumetric throughput of the device. Integrated microfluidic devices are inherently small in size and therefore the flow path length is limited by the available surface area of the device, when using standard 2.5D machining techniques. As such it was apparent that contact time would be short and therefore rapid binding of the propranolol analyte to the MIP microspheres, in significant quantities, would be required for the demonstrated MIP enhanced biphasic extraction system (Chapter 2) to translate effectively to an accelerated segmented flow microfluidic platform. Since most studies characterise analyte binding to MIPs at equilibrium (reviewed in chapter 6) kinetic binding has not been well characterised. However, it may be reasonable to expect that kinetics may vary considerably between different MIPs, with a high dependency on particle size and the polymer matrix properties such as porosity and pore volume distribution which will affect the diffusional distances required for analytes to reach unoccupied binding sites. Binding site density and non-specific binding interactions of

the polymer matrix may also play a role. However, the successful application of morphologically similar MIP materials as chromatographic stationary phase material [2], demonstrates significant binding in a kinetic application where contact times are limited.

3.2.1 Methodology

MIP and NIP binding kinetics were initially assessed on the macroscale, using the experimental methodology employed in chapter 2 (section 5.1.1.1). Polymer (MIP or NIP) (1 mg) was incubated in 2 ml of chloroform containing 25 μM propranolol in a 22 ml capacity snap cap sample vial. Multiple sample vials were set up and incubated at room temperature on a shaker (frequency 3.33 Hz, amplitude 5 cm). Incubations were prepared by initially aliquoting 1 ml of polymer suspension in chloroform (1 mg ml^{-1}) into each vial, to which 1 ml of chloroform containing 50 μM concentration of propranolol was added. Incubation solutions were prepared sequentially at staggered time intervals and sampled in reverse preparation order for time efficiency purposes. Binding was assessed after incubation periods of 0.5, 1, 1.5, 2, 3, 5, 10, 15, 20, 30 and 60 minutes. After the allotted incubation period, samples were immediately withdrawn with a syringe and needle and filtered through a 0.45 μm pore size PTFE membrane, syringe filter unit. Multiple 200 μl aliquots were assessed for propranolol content by fluorescence microplate analysis (excitation λ: 290 nm, emission λ: 330 nm). The results of the kinetic study are illustrated in Figure 1.

3.2.2 Results and Discussion
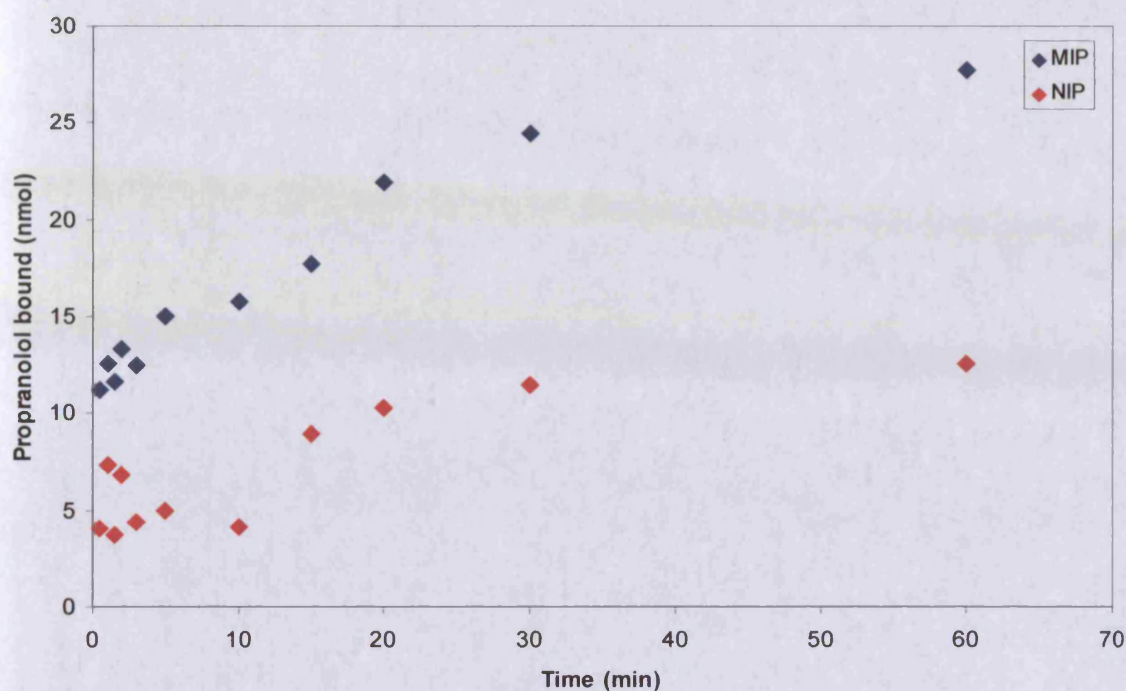
Figure 1 Kinetics of propranolol binding to MIP and NIP. 1 mg of polymer incubated in 2 ml of chloroform containing a 25 µM concentration of propranolol.

It was found that even with short incubation times (30 s), at relatively low polymer loadings, the MIP bound significant quantities of the incubated propranolol ligand. Binding approached equilibrium after approximately one hour, in keeping with the equilibrium binding isotherm reported in chapter 2 (Figure 6), with almost 50% of binding equilibrium reached within 1 minute. At all time points the MIP was observed to bind substantially more propranolol than the non-imprinted counterpart. The spread of data over the short incubation time was considered to be a consequence of uncertainty of contact time introduced through the time requirement for the liquid handling procedures, which becomes less significant as incubation time increases. Despite this the results were encouraging and suggested that MIP binding kinetics for the polymer prepared in chapter 2 are sufficiently fast enough to have a significant effect on the short time scale required in a microfluidic flow device.

It was also proposed that the convenient distance – time proportionality of microfluidics could be used to more precisely characterise MIP binding kinetics, for example, by visualising the phase transfer of a fluorescent substrate for the MIP, for example *N,N*-dimethyl-*N'*-(7-nitro-2,1,3-benzoxadiazol-4-yl)-1,2-ethanediamine [3] in a segmented flow regime. Unfortunately due to time constraints this was not investigated during this project.

3.3 Microfluidic Device Construction Techniques and Preliminary Proof of Concept Demonstration - On-Chip MIP Enhanced Segmented Flow Extraction

3.3.1 Prototype Device – PMMA

Prototype devices for preliminary studies were machined by micromilling in poly(methyl methacrylate) (PMMA). The devices were thermally bonded and a specially designed fluidic manifold used to house the chip and provide fluidic interfacing. Poor chemical compatibility ultimately resulted in the requirement for an alternative approach for device manufacture. However, due to pre-existing expertise within the research group [4] of such PMMA microfluidic devices, it was deemed a suitable starting point for preliminary experimentation.

3.3.1.1 Fluidic Design and Micromachining

3.3.1.1.1 General Procedure

Fluidic circuits were milled, cut and drilled using a circuit board plotter intended for printed circuit board (PCB) prototyping (LPKF ProtoMat C30, Germany). Fluidic circuits were designed in Coral draw 6.0 (Coral Corporation) or AutoCAD LT 2004 (Autodesk) and exported as .DXF files. All fluidic devices were designed to the required specifications for compatibility with the purpose-built fluidic interfacing manifold (Appendix 1):

- 2.0" (50.2 mm) diameter circular substrate,

- 1.6 mm inlet/outlet holes (z-axis), centre point 2.5 mm from outer edge of chip, situated with spacings of multiples of 30° to ensure alignment of each active port with one of the manifold's 12 fluidic interfacing ports.

.DXF design files were imported into CircuitCAM 5.0 (LPKF, Germany) where milling, cutting and drilling procedures were assigned to each line feature of the schematic fluidic design. The resulting file was exported into BoardMaster (LPKF, Germany), where appropriate tools were assigned to each machining procedure, and where necessary, spin and feed rates defined. Micromachining control was also performed through the BoardMaster software interface. The diameter of milled channels, together with drilled hole diameter and the inner and outer edge of cutting processes are defined by the geometry of the selected tool and as such this was considered during the device design stage. Milling, drilling and cutting depth were user defined by manual z-axis control of the machining depth, to attain the desired depth. To improve surface finish and minimise tool breakages multiple machining passes were performed with the machining depth increased incrementally, usually in the order of 10 % of the mill diameter in the milling of fluidic channels and 50 % of the cutting tool diameter for cutting the device from the sheet material. For bonded designs a reciprocal cover plate was machined, in which the inlet and outlet holes were drilled using the milling machine such that they would align with the start and end of channels on the main substrate. To ensure correct alignment, 0.8 mm alignment holes were machined in each substrate layer.

3.3.1.1.1.1 Prototype Device Construction

Transparent PMMA sheet of 2 mm thickness was purchased from RS (Corby, UK). A fluidic design incorporating a variant of the T-junction geometry [5] to generate segmented flow, and a 35 cm segmented flow path length was machined into the PMMA substrate. Fluidic channels were milled with 500 μm 4FM carbide milling cutter (Fetoga: Fenn Tool Ltd, Braintree, UK) to a z-axis depth 500 μm. Inlet and outlet ports to accommodate PEEK tubing of 1/16" outer

diameter (O.D.) were drilled with a 1.5 mm drill bit in the device cover plate. Alignment holes were drilled with a 0.8 mm drill bit and the 50.2 mm diameter fluidic devices cut from the sheet PMMA substrate using a 0.8 mm diamond ground router (M. A. Ford, Davenport, IA, USA). Appropriate steps were undertaken in the CircuitCAM 5.0 software to account for the tool radius in the cutting procedure to ensure the final device was of the desired diameter of 50.2 mm.

50.80 mm
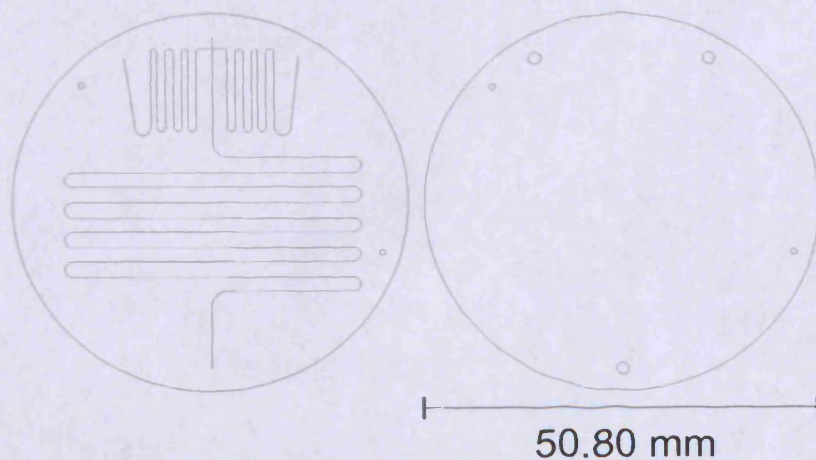
Figure 2 Schematic design of fluid devices machined in PMMA. The milling process is direct write, following the x/y coordinates of the schematic design, with the chosen tool, assigned processing and z-axis tool height adjustment dictating the final device geometries.
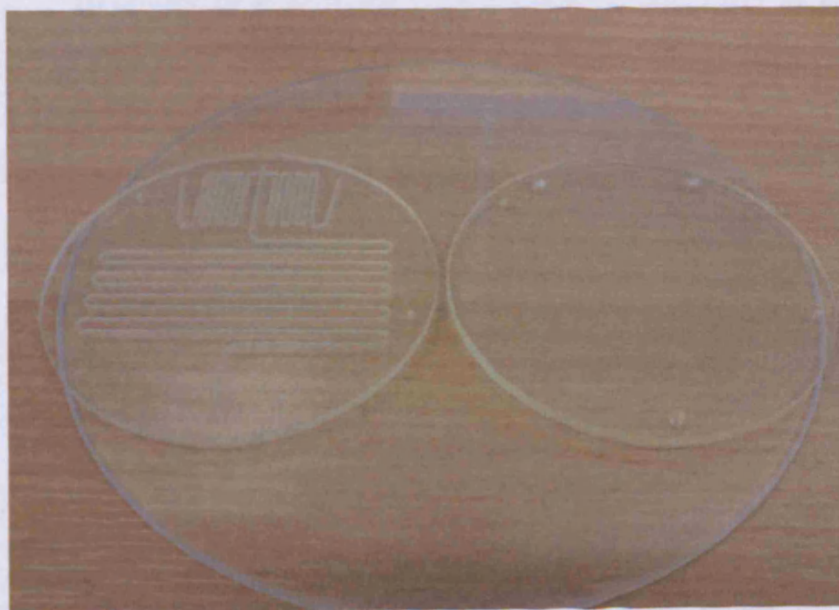
Figure 3 Machined PMMA device prior to substrate bonding.

3.3.1.1.1.1.1 PMMA Device Bonding

The surfaces and channels of machined substrates were washed with soap and water with a standard domestic toothbrush to remove any burr. The two halves of a device were allowed to dry at room temperature before being washed and scrubbed with isopropyl alcohol and a fine cotton cloth to clean the surfaces to be bonded. After drying at room temperature, with the device face to be bonded placed face upwards, the substrate halves were heated to 95 °C for 24 hours to degas the substrate surface. On removal from the oven the substrate halves were placed together with metal pins created from syringe needles placed through the 0.8 mm alignment holes to ensure device alignment was maintained. The assembled device was bonded by heating above the glass transition temperature (Tg) of PMMA, to 127 °C, for 4 hours, whilst placed between two glass plates and sandwiched in a steel compression manifold with weight added to provide a pressure of ~ 60 kPa.
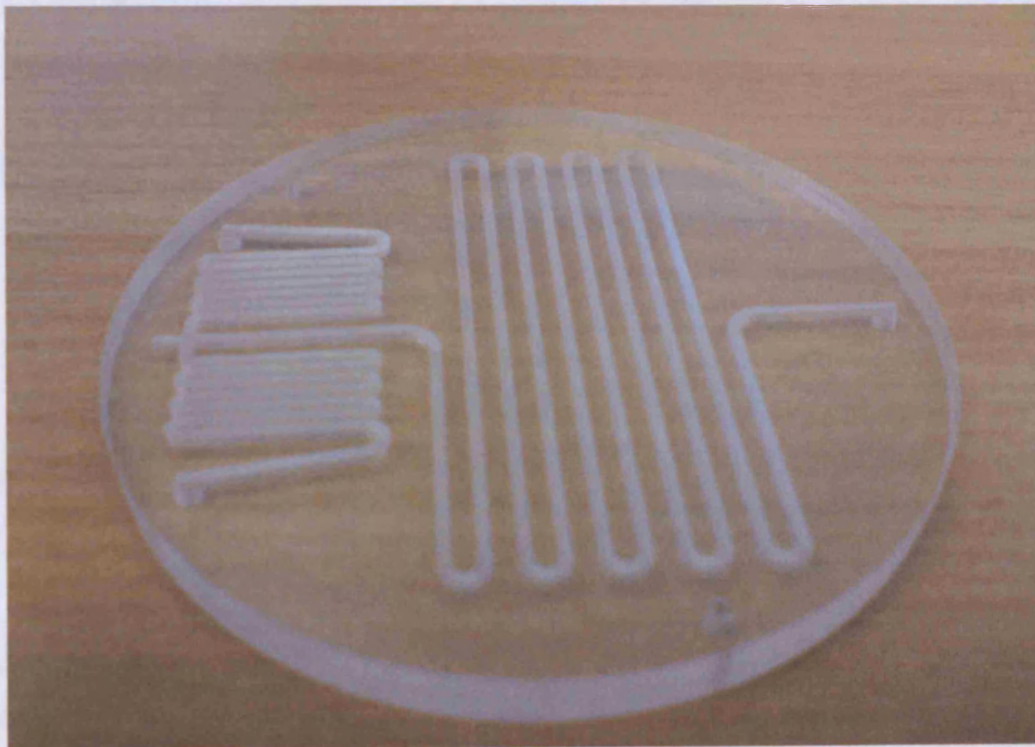
Figure 4 Bonded PMMA microdevice consisting of inlet and outlet ports for interfacing with 1/16" O.D. tubing. Two input ports (left) enable the introduction of two immiscible phases which co-elute into a common flow carrying channel at a segmented flow generating T-junction. The segmented flow regime flows through the 35 cm length channel, enabling phase boundary mass transfer to take place, before flowing to the chip outlet.

several hours of use. Therefore, an extraction system comprising of hexane (±MIP/N

employed for preliminary demonstrations of the technique. It was however apparen1

more robust substrate material would be required for future work. (Section 3.3.1.4)

3.3.1.3 Proof of Concept Demonstration

3.3.1.3.1 Methodology

The constructed PMMA fluidic device outlined in section 3.3.1 was interfaced as

Fluidic inputs were connected to 10 ml plastic disposable syringes via 30 cm of PEEK

(O.D. 1/16", I.D. 500 μm) (Upchurch Scientific, WA, USA). A steel female luer to mal

adapter (Kinesis, Cambridge, UK) connected the inlet tubing to the syringe via a PEE

dead volume union (0.020" through-hole) (Upchurch Scientific, WA, USA) and 10-3

piece, PEEK, fingertight fitting (Upchurch Scientific, WA, USA). The fluidic output

microfluidic device was connected to 10 μl UV flow cell (QS 1.0000 Hellma GmbH

Germany) by 15 cm of PEEK tubing (O.D. 1/16", I.D. 500 μm) (Upchurch Scientific, W/

and a PEEK zero dead volume union (0.020" through-hole) (Upchurch Scientific, W/

with 10-32 one-piece, PEEK, fingertight fittings (Upchurch Scientific, WA, USA). The

the flow cell ran to a waste collection vial. The UV flow cell was interrogated by a

6405 UV/VIS spectrophotometer (Bibby Scientific, Essex, UK) in absorbance mo

wavelength of 290 nm. The analogue voltage output of the device was passed thr

analogue-digital converter, NI-BNC-2110 (National Instruments, Texas, USA), rur

floating source (FS) mode. The processed digital response was recorded by a c

running LabVIEW 7 (National Instruments, Texas, USA) with a custom written data ac

code to plot absorbance against time.

Solutions of propranolol HCl (100 µM) (Sigma-Aldrich, Gillingham, UK) in deionised water were prepared, together with 20 mg ml^{-1} suspension of MIP (as prepared in chapter 2 section 4.2) in hexane (Fisher Scientific, Loughborough, UK). Segmented flow regimes were generated at a combined flow rate of 0.25 ml min^{-1}, with a 1:1 ratio of fluid phase flow, using two rate controllable syringe drivers (KD scientific, MA, USA). The absorbance peak of the aqueous phase was measured to indicate propranolol content remaining in the aqueous phase following segmented flow extraction of 100 µM propranolol solution with hexane alone and the MIP/hexane suspension. The absorbance of deionised water segmented with hexane was recorded to determine base-line response. The suspension of MIP in hexane was briefly ultrasonicated immediately prior to use to ensure dispersion of the polymer microspheres. The uniform suspension was maintained in the delivery syringe through the addition of two magnetic stirrer bars, with an inverted stirrer plate (Fisher Scientific, Loughborough, UK) placed directly above the syringe once mounted in the syringe driver.

3.3.1.3.2 Results and Discussion

A regular and stable segmented flow pattern was achieved in all instances, producing a very regular and consistent UV absorbance pattern, clearly identifying the aqueous and organic phases together with the interfacial boundary as fluid packets passed through the UV flow cell. Several unforeseen difficulties made quantification of extraction difficult. The very narrow aperture of the low volume flow cell meant that transmission of the UV light source was restricted and therefore measurement sensitivity was low. It was also noted that MIP particulates accumulated on the steel adapter and within the PEEK zero dead volume union which connected the delivery syringe to the fluidic device, consequently some uncertainty arose in the exact quantity of MIP solid phase particulates assisting the liquid extraction. Dilution of the polymer suspension to 5 mg ml^{-1} eased this problem, although did not eliminate it entirely. Additionally, it was found that with time the absorbance response due to the hexane fluid packets increased, until zero transmission at 290 nm was observed, this was indicative of highly UV absorbent material leaching from the PMMA device. Although the absorbance of the

aqueous phase remained unaffected by this, the leached material may have impacted on the extent of propranolol partitioning between the aqueous and organic phases and also possibly interfered with propranolol binding to the MIP. Consequently it was not possible to draw quantitative conclusions from the data generated by the experiment. It was however apparent that a significant decrease in aqueous phase absorbance was observed when MIP was added to the extracting hexane phase, indicative of increased removal of propranolol from the aqueous sample, the solid extracting phase enhancing the extent of extraction. A composite image of the absorbance spectra obtained from each of the three investigated segmented flow regimes is illustrated in Figure 5.
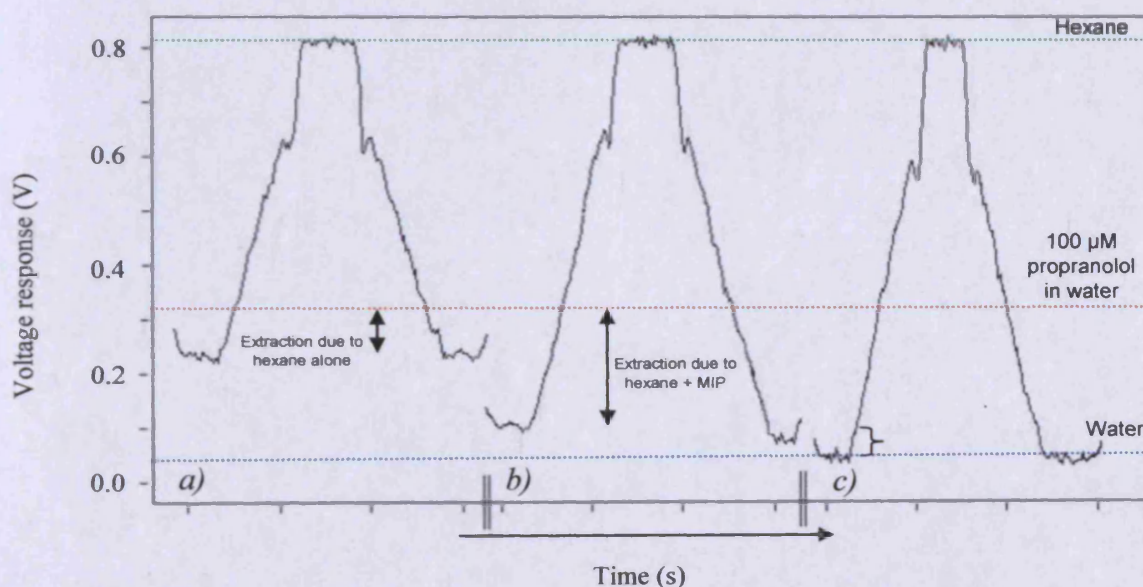
Figure 5 Composite image of measured voltage response traces, proportional to UV absorption, for three segmented flow regimes, demonstrating increased extraction efficiency through incorporation of a MIP solid phase adsorbent into the extracting phase. Peak absorbance is due to a hexane fluid packet passing through the UV detector, the baseline absorbance of each trace is due to analysis of aqueous fluid segments passing through the detector. a) 100 μM aqueous propranolol sample extracted with hexane alone. b) 100 μM aqueous propranolol sample extracted with hexane and MIP 5 mg ml^{-1}. c) Control: Water segmented with hexane and MIP 5 mg ml^{-1} (no propranolol).

The preliminary findings showed promise, however it was apparent that significant improvements in device design together with improved methods of quantitative analysis would be required.

3.3.1.4 Alternative Substrate Materials

Trials were conducted to improve solvent compatibility of the microfluidic device. Initially PMMA chips (as prepared in section 3.3.1) were coated with a Teflon AF coating. This improved the useful lifetime of the device by providing a chemically resistant channel surface. Hpwever, the resistance of the device was limited at the inlet and outlet fluidic interface ports. Alternative thermoplastic polymers were evaluated for solvent resistance, although no suitably resistant and optically transparent, thermoplastic could be identified. Consequently, efforts turned towards alternative methods device design. Since the device was only required to withstand comparatively low pressures, compression sealing, using the existing manifold, was investigated. This created the opportunity to manufacture devices from non-bondable, non-transparent substrate materials. PTFE was chosen for its high chemical resistance and extreme hydrophobic nature (Chapter 5).

3.3.1.4.1 PTFE Device Design

Polished PTFE disks (50.8 mm (2") diameter, 4 mm thick) were purchased from Fluorocarbon Company ltd. (Hertford, UK). Fluidic channels were machined using the milling techniques detailed in section 3.3.1.1. A slight modification of the fluidic channel design (Figure 6) was made from that machined in the PMMA microdevices, due to the tendency for the milling process to produce slightly wider channels in the PTFE substrate material. Additionally a greater channel length was employed to increase transit time. Channels were machined with a 4FM 0.5 mm diameter carbide milling tool, with the machining speed reduced from 17 mm s^{-1} to 6 mm s^{-1} to improve the surface finish of the machined channel walls.

50.80 mm
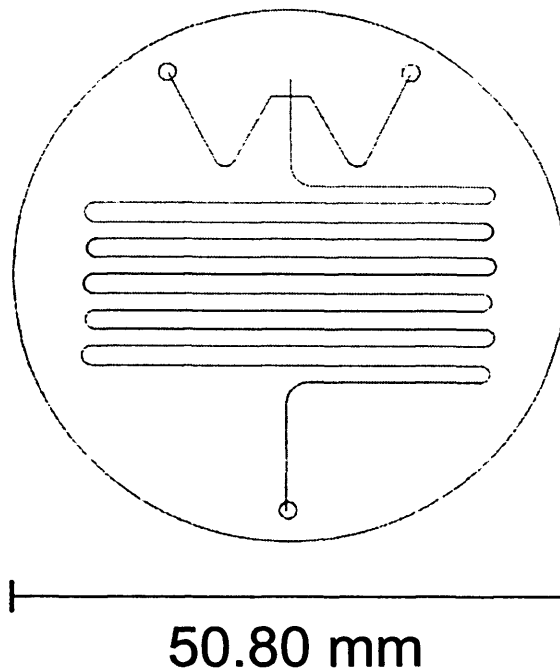
Figure 6 Schematic illustration of the CAD file for fluidic circuits produced in PTFE.

The machined PTFE substrate was gently scrubbed and polished to improve the surface finish, as per the methodology for PMMA devices prior to bonding (section 3.3.1.1.1.1.1). The device was assembled in the fluidic manifold (as per PMMA devices, section 3.1.1.1) with a 100 μm thick amorphous PEEK film lid (Goodfellow, Cambridge, UK) which doubled as a gasket layer between the PTFE substrate and a glass or quartz viewing window (50.8 mm (2") diameter, 4 mm thick) (Edmund Optics, York, UK). Later devices (Chapter 5) utilised an FEP film (100 μm) (Goodfellow, Cambridge, UK) as the intermediary layer. The compression manifold was tightened uniformly around the device, with care taken not to crack the viewing window. Figure 7 shows the assembled PTFE, PEEK and glass composite device assembled in the fluidic manifold.
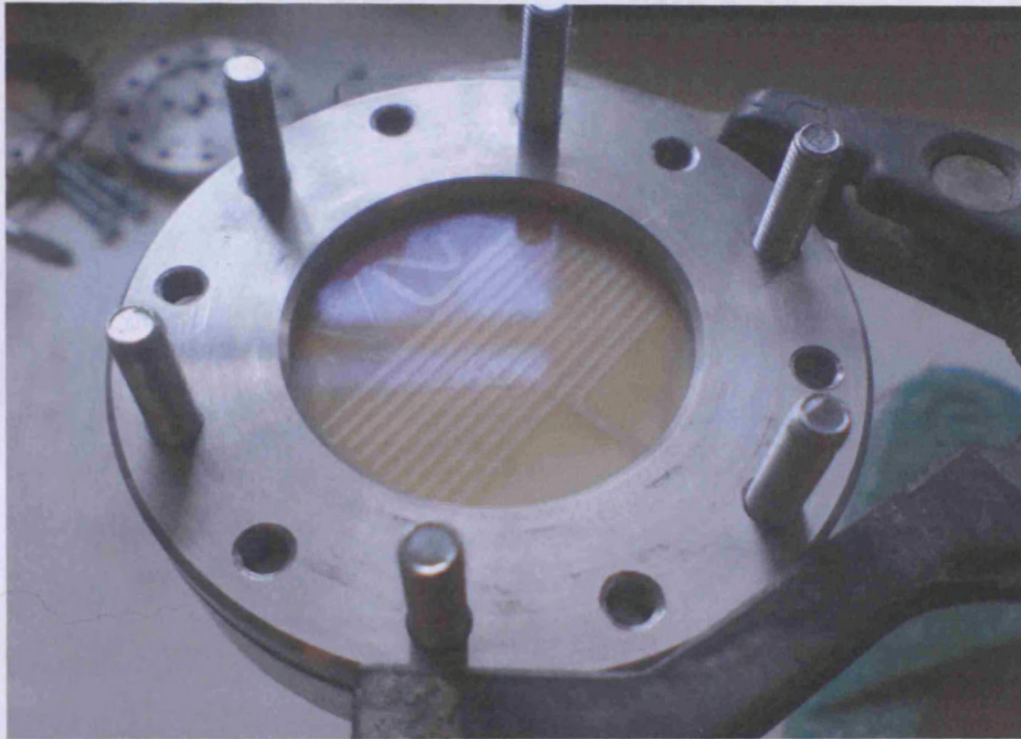
Figure 7 PTFE micromilled device assembled in compression housing with amorphous PEEK intermediary sealing and gasket layer with glass viewing window.

3.3.1.4.1.1 Connectivity

Following the difficulty in uniformly delivering the MIP particulate suspension using the interfacing method outlined in section 3.3.1.3.1, the metal connectors and zero dead volume unions which appeared to be clogging with polymer particles were replaced by a single ethylene tetrafluoroethylene (EFTE) female luer to female 10-32 adapter (Upchurch Scientific, WA, USA). This connected delivery syringes to the PEEK inlet tubing with a PEEK, fingertight fitting (Upchurch Scientific, WA, USA). This setup ensured consistent delivery of particulate suspensions, with no particle accumulation at the connector.

3.4 Segmented Flow Interfacial Mass Transfer Characterisation

3.4.1 Macro Kinetic Assessment as a Comparator

3.4.1.1 Methodology

Initially the kinetics of extraction of propranolol from an aqueous solution of the hydrochloride salt into an equal volume of chloroform was assessed on the macro-scale. A 50 μM stock solution of propranolol hydrochloride in de-ionised water was prepared, 2 ml of the solution was incubated with 2 ml of chloroform in a 22 ml capacity snap cap sample vial. Multiple sample vials were set up and incubated at room temperature on a shaker (frequency 3.33 Hz, amplitude 5 cm). Incubation solutions were prepared sequentially at staggered time intervals and sampled in reverse preparation order for time efficiency purposes. After the allotted incubation period, multiple 200 μl aliquots were removed from the aqueous phase and assessed for propranolol content by fluorescence microplate analysis (excitation λ: 290 nm, emission λ: 330 nm). The results of the kinetic study are illustrated in Figure 8.

3.4.1.2 Results and Discussion
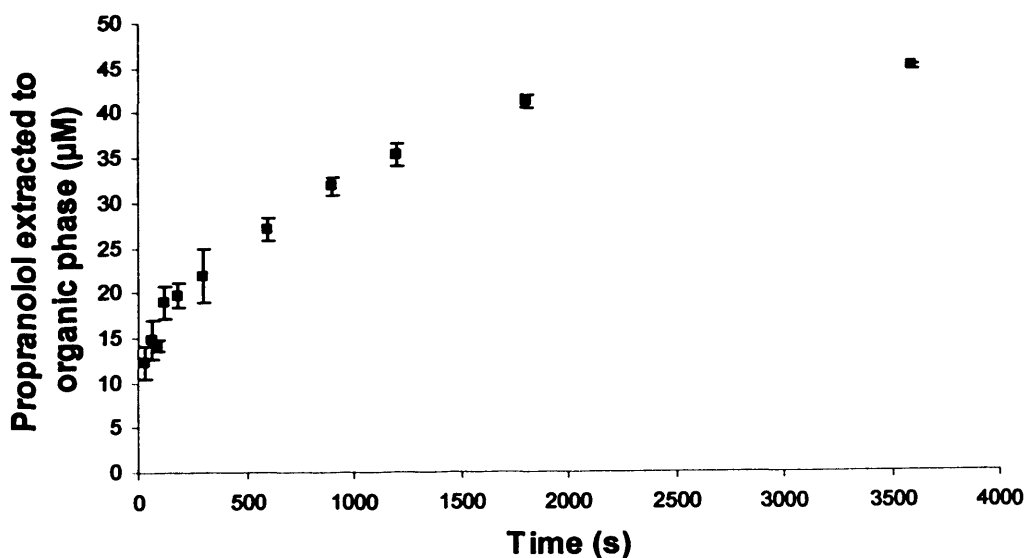
Figure 8 Extraction of propranolol from a 50 μM aqueous solution of propranolol HCl (2 ml) into chloroform (2 ml) in a 2.2 cm diameter cylindrical sample vials shaken at a frequency of 3.33 Hz and amplitude of 5 cm. (n=3 ± S.D.).

3.4.1.2.1 First Order Kinetics

Phase boundary extraction processes usually follow first order reaction kinetics [6]. Integration of the overall extraction rate law, gives the concentration of analyte extracted at time t with the expression

$$C_o = C_{o,eq}(1 - e^{-kt}) \tag{1}$$

where C_o is the number of moles of the extracted species in the organic (extracting) phase at time t, $C_{o,eq}$ is the number of moles of the extracted species in the organic (extracting) phase at equilibrium, k is the overall extraction rate constant and t is time. Pawliszyn presents a detailed derivation of the rate governing equations [7], demonstrating that for a liquid extraction yet to reach equilibrium, the fraction extracted after time t is given by

$$f = \frac{C_o}{C_{aq,initial}} = \frac{D\dfrac{V_o}{V_{aq}}(1 - e^{-kt})}{1 + D\dfrac{V_o}{V_{aq}}} \tag{2}$$

where the fraction extracted f is defined by the ratio of the number of moles of analyte in the extracting phase (C_o) at time t to the total moles of analyte in the system $(C_{aq,initial})$. D is the equilibrium distribution coefficient (*concentration of analyte in the organic phase / concnetration of analyte in the aqueous phase*), k is the overall extraction rate constant and t is time, with V_o and V_{aq} being the volume of the organic and aqueous phases respectively. Rearrangement of this equation, making k the subject can enable calculation of the extraction rate constant for a given data pair:

$$k = \frac{-\ln(-f(\frac{(\frac{V_o}{V_{aq}})D+1}{(\frac{V_o}{V_{aq}})D})+1)}{t} \tag{3}$$

For a 1:1 ratio of phase volumes equation 3 simplifies to

$$k = \frac{-\ln(-\frac{[C_{o,t}]}{[C_{aq,initial}]}(\frac{D+1}{D})+1)}{t} \tag{4}$$

where $[C_{o,t}]$ is the concentration of analyte in the extracting organic phase and $[C_{aq,initial}]$ the starting concentration of analyte in the aqueous sample phase.

3.4.1.2.2 Extraction Rate Constant (k)

Application of equations 1-4 enables the elucidation of extraction rate constants from knowledge of the extent of extraction and extraction time. This is particularly valuable when continual monitoring of the extraction process, for example by spatial imaging analysis [1], is not possible. In an on-chip segmented flow extraction, the channel geometries and flow rate define the extraction time, therefore the interrogation of different time points of a particular extraction regime would otherwise require different path length devices to be constructed. Lucy at al. employed a simplified approximation of equation 4 in an investigation into the kinetics of the solvent extraction of caffeine by flow injection analysis [8]. However, although not implicitly stated, the approximation used by Lucy et al. is only suitable for extraction methodologies where D, the equilibrium distribution of analyte concentration between the extracting and sample phases, is large.

Figure 9 illustrates the calculated extraction rate constant for the experimental data acquired in section 3.4.1.2 for the extraction of propranolol from a 50 μM aqueous solution of

propranolol HCl (2 ml) into chloroform (2 ml) in a 2.2 cm diameter cylindrical sample vials shaken at a frequency of 3.33 Hz and amplitude of 5 cm at room temperature.
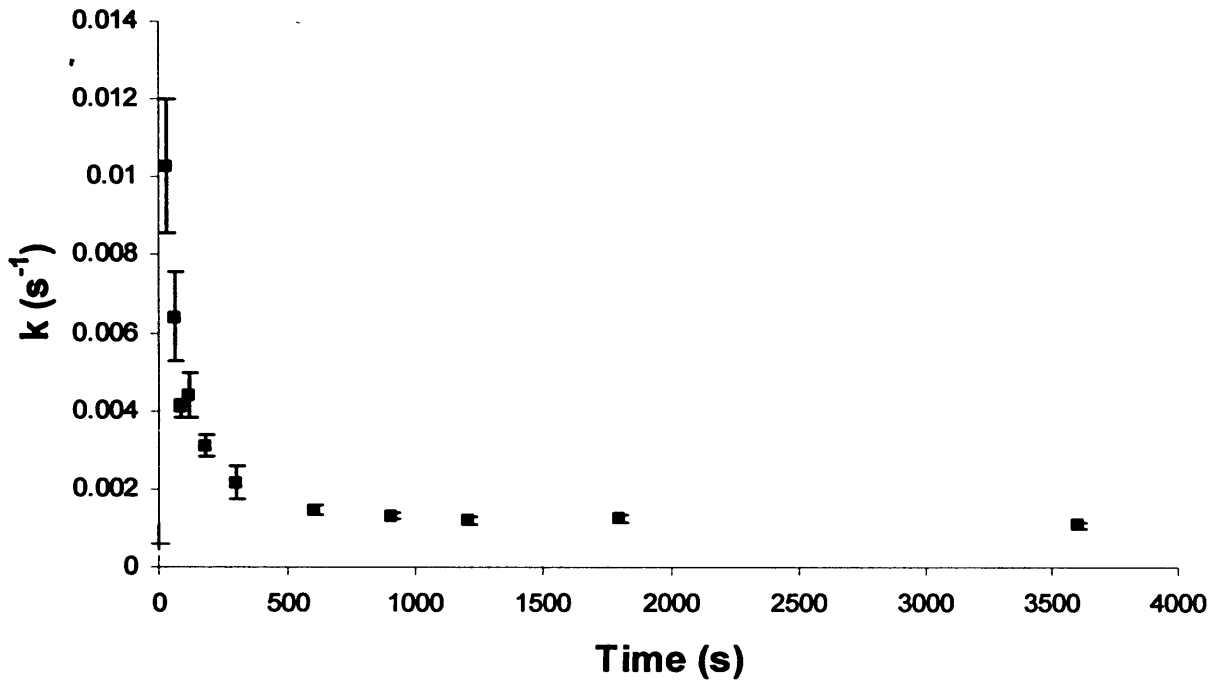
Figure 9 Extraction rate for the extraction of propranolol from a 50 μM aqueous solution of propranolol HCl (2 ml) into chloroform (2 ml) in a 2.2 cm diameter cylindrical sample vials shaken at a frequency of 3.33 Hz and amplitude of 5 cm at room temperature with time. (n=3 ± S.D.).

3.4.1.2.3 Surface Area/Volume Effects

The extraction rate constant (k) is a function of both the mass transfer within the bulk fluid volume, and across the liquid-liquid interface. As such the measured value of k is a function of both the mixing within the fluid volume, and the interfacial area at which extraction can take place. Consequently the interfacial area dependence can be removed by conversion of the observed rate constant into an overall mean mass transfer coefficient [8].

$$\frac{k}{(surfacearea : volume)} \qquad (5)$$

For the 2.2 cm diameter cylindrical sample vials used in this experiment, an assumed horizontal interface between the aqueous sample and extracting chloroform liquid gives rise to

a surface area to volume ratio of 126.7 m^{-1}; this value was used to calculate the $k/$(A:V) value at each time point. The value for the surface area to volume ratio is a significant underestimate since in actuality the phase boundary meniscus displays notable curvature, increasing the contactable surface area. It is also worth noting that the process of vigorous shaking distorts the meniscus and may even lead to discontinuities and break up of the interface, further increasing the surface area to volume ratio. The results are illustrated in Figure 10.
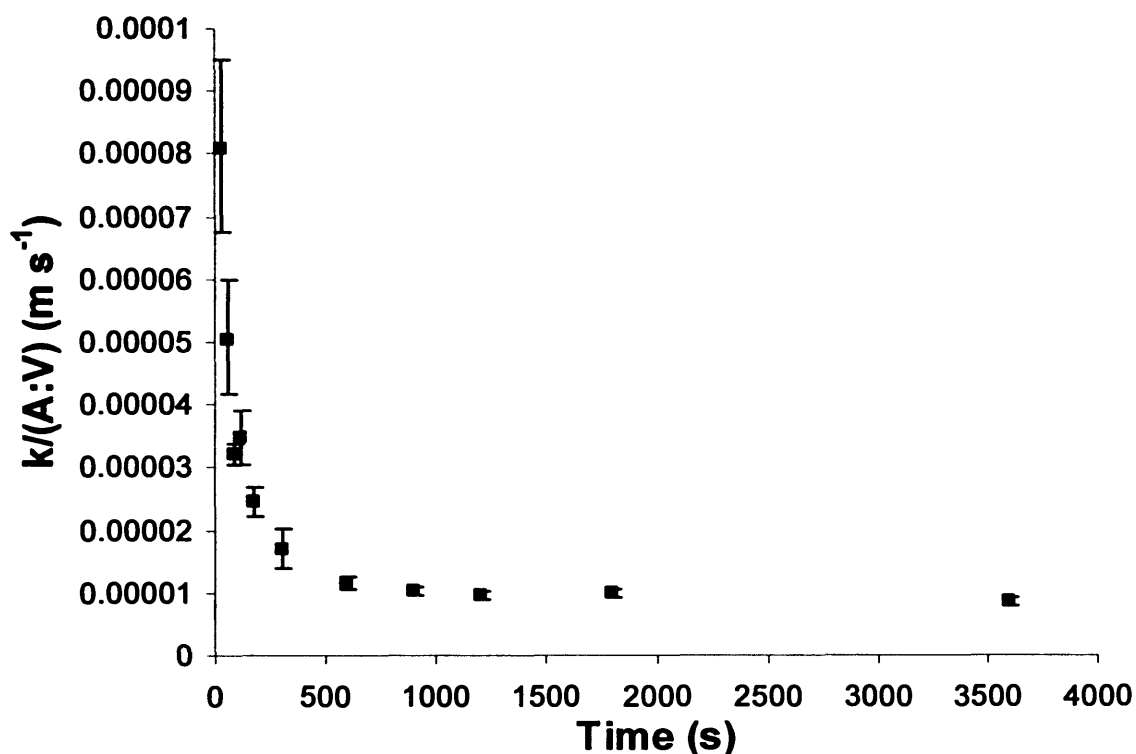
Figure 10 Extraction rate, independent of surface area and volume relationships, for the extraction of propranolol from a 50 μM aqueous solution of propranolol HCl (2 ml) into chloroform (2 ml) in a 2.2 cm diameter cylindrical sample vials shaken at a frequency of 3.33 Hz and amplitude of 5 cm with time. (n=3 ± S.D.).

The magnitude of the of the $k/$(A:V) value can enable comparison between extraction methodologies and flow regimes.

3.4.2 Flow Rate - On-Chip Assessment

3.4.2.1 Methodology

Using the PTFE/amorphous PEEK composite device as described in section 3.3.1.4, the extraction of propranolol from an aqueous solution of the hydrochloride salt into an equal volume of chloroform was assessed using microfluidic segmented flow at a range of flow rates. A 50 µM stock solution of propranolol hydrochloride in de-ionised water was prepared and delivered to the device at flow rates of between 0.05 ml min^{-1} and 5 ml min^{-1}, together with chloroform at the same flow rate. Flow was allowed to stabilise for several minutes, before collection of the combined eluate in a 2 ml eppendorf centrifuge tube for the required time in each instance to collect a total volume of 1.5 ml, Upon collection of 1.5 ml of combined eluate 0.65 ml of aqueous phase was immediately removed from the collecting eppendorf tube to prevent further *in situ* extraction of propranolol from the aqueous phase. This additional sample handling stage constituted an additional *in situ* contact time for the two phases of less than five seconds, supplementary to the flow-rate-dependant collection time for the elution of sufficient volume for analysis (1.5 ml). (The assessment of the effects and consequences of additional off-chip extraction are discussed further in section 4.2). From the 0.65 ml removed aqueous sample three 200 µl aliquots were assessed for propranolol content by fluorescence microplate analysis (excitation λ: 290 nm, emission λ: 330 nm).

3.4.2.2 Results and Discussion
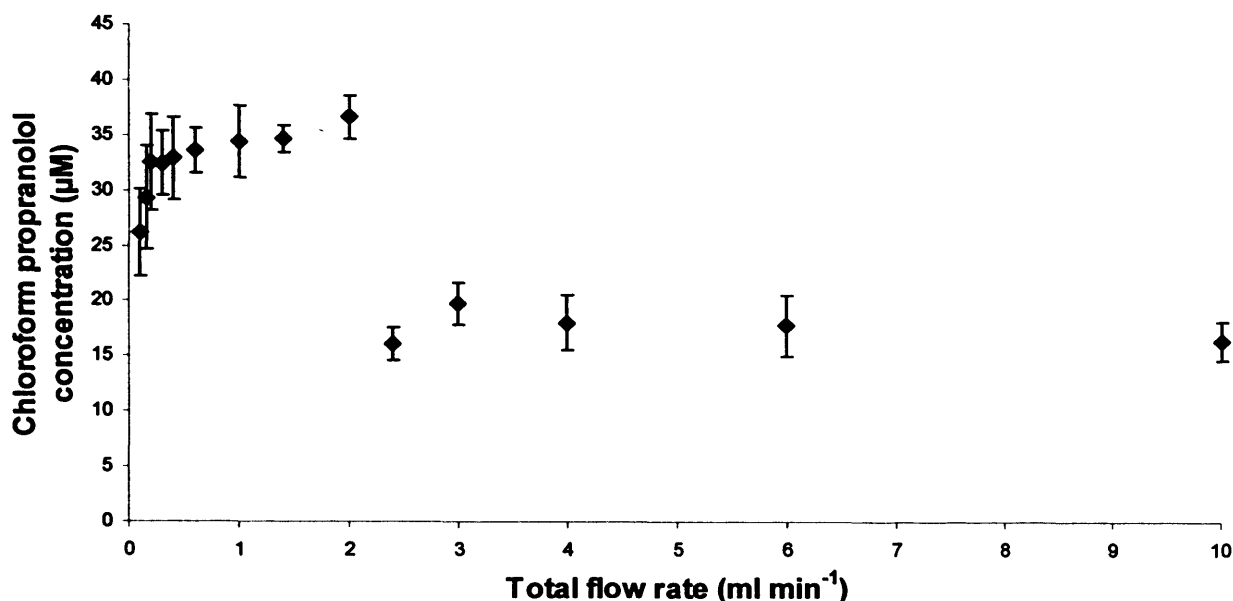
Figure 11 Concentration of propranolol extracted into chloroform from a 50 µM aqueous sample in an on chip segmented flow extraction at a range of flow rates. Channel dimensions: l = 53 cm, w = 600 µm, d = 600 µm. (n=3 ± S.D.).

The results of the investigation into segmented flow rate influence on extent of extraction are discussed with respect to the extraction time in section 3.4.2.2.1.

3.4.2.2.1 Residence Time Consideration

Since the path length of the device together with the channel cross-sectional dimensions and the volumetric flow rate of the fluid define the extraction contact time, investigation into the effect of flow rate on the extent of liquid extraction is less straightforward than it may first appear. Flow velocity affects not only the extent of mixing within fluid segments, but also contact time, together with other dependent variables, such as wetting film thickness, vortex flow and Dean flow which are discussed in detail later in this chapter. The experimental results appeared to show two distinct types of extraction behaviour. The extent of extraction was found to increase with increasing flow rate for total flow rates from 0.1 ml min^{-1} to 2.0 ml min^{-1} (linear velocity 0.00463 – 0.092593 m s^{-1}), despite the decreased residence time associated with increased flow rate (Figure 12). A rapid increase in extraction was observed over the

range of flow rates from 0.1 ml min^{-1} to 0.2 ml min^{-1}, suggesting that at very slow flow rates the mixing within fluid packets is insufficient to offset against the increased residence time afforded by a slower flow rate, limiting the extent of extraction. A maximum extraction of 36.7 μM concentration extracted into the chloroform, leaving a concentration of 13.3 μM remaining in the aqueous phase was recorded. Representing 79.4% of the equilibrium distribution previously measured on the macro scale (D = 12.2, chloroform concentration 46.2 μM, aqueous concentration 3.8 μM) (section 3.4.1).
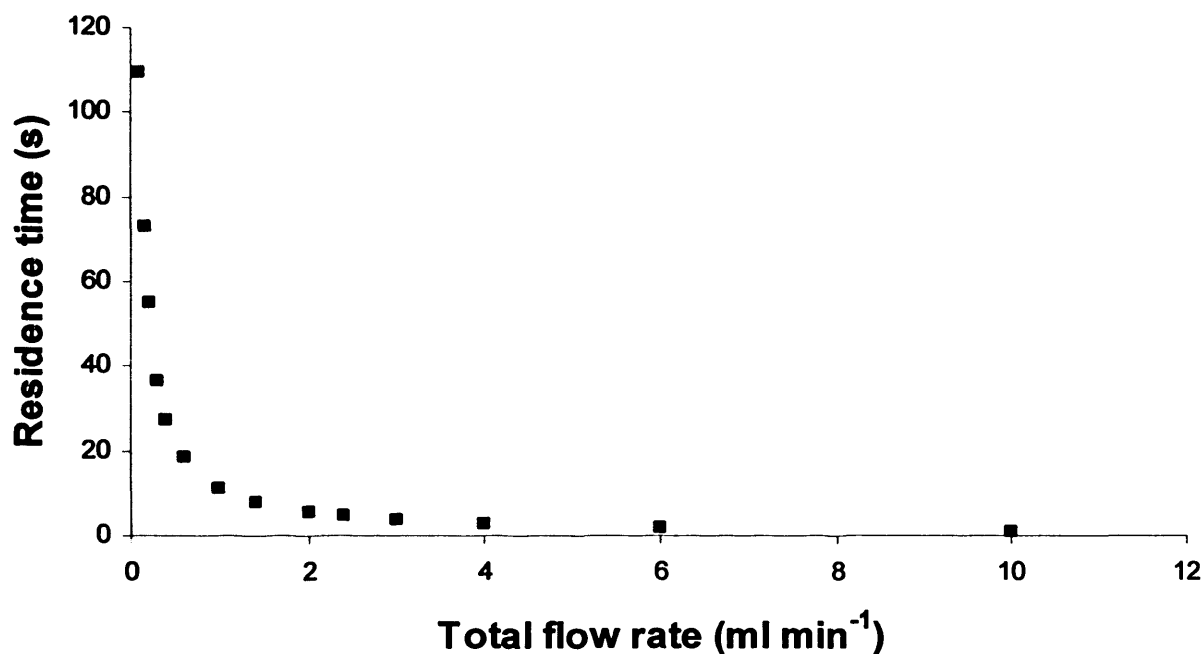
Figure 12 Residence time at each flow rate investigated. Time calculated for microfluidic device with channels of square cross-section (width and depth of 600 μm) and length 43.2 cm with 8.0 cm long, 500 μm I.D. PEEK outlet tubing.

At total flow rates above 2.0 ml min^{-1} (linear velocity 0.092593 m s^{-1}), a distinct change in extent of extraction was observed with extracted concentration dropping to around 15-20 μM in the chloroform phase for flow rates up to 10 ml min^{-1} (linear velocity 0.4630 m s^{-1}). This behaviour was unexpected, with no previous reports of similar associations seen in the literature.

3.4.2.2.2 Extraction Rate Constant (k)

Calculation of the extraction rate constant (k) for each investigated flow rate (Figure 13) highlighted the two different extraction behaviours. For each population, the extraction rate constant was seen to increase near-linearly with increasing flow rate, in keeping with the intuitive observations from Figure 11. This indicates that the efficiency of mixing within individual fluid packets and the associated reduction in diffusional distances through which the analyte is required to travel as part of the extraction process, show a high dependency on linear velocity of the flow stream.
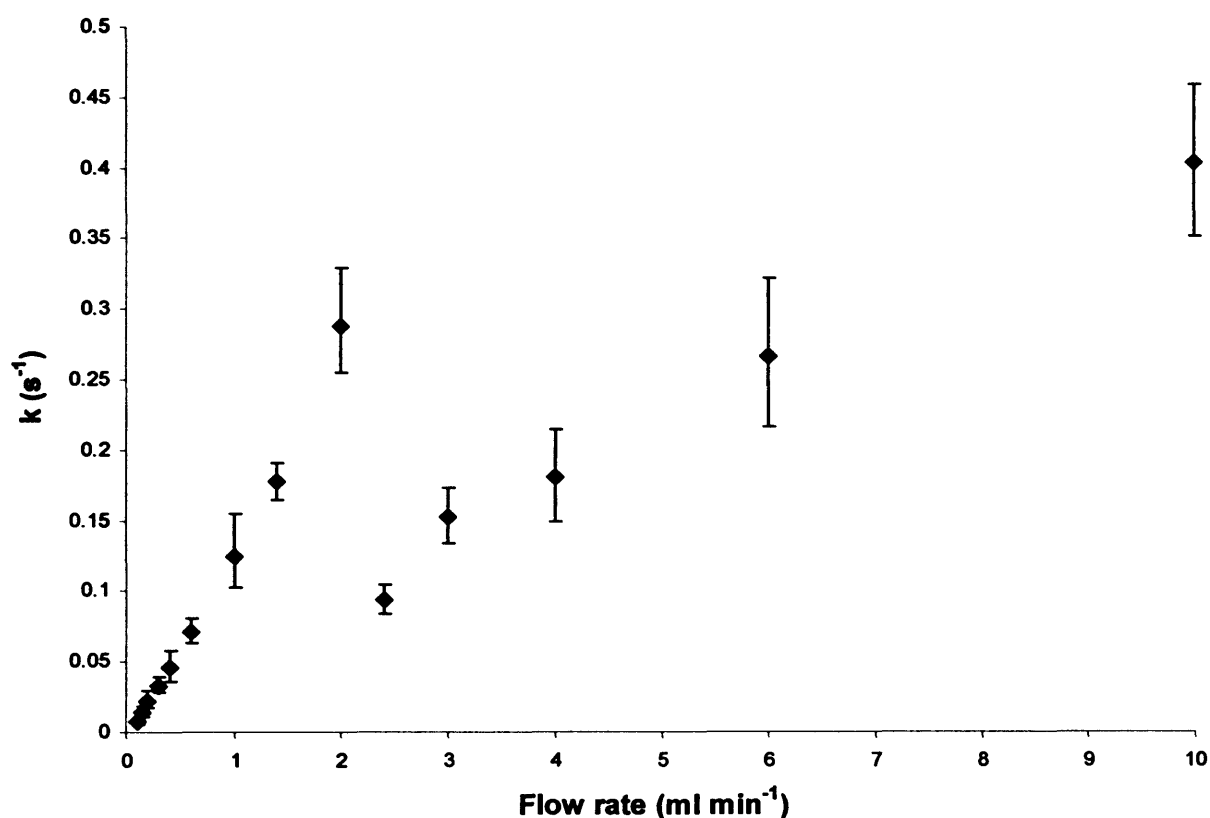
Figure 13 Extraction rate constant (k) for propranolol extraction from a 50 μM aqueous sample into chloroform on-chip, at each investigated flow rate. (n=3 ± S.D.).

It was postulated that an alternative flow regime may be generated in the device at high flow rates, giving rise to different extraction characteristics to those observed in a segmented flow stream. Since the amorphous PEEK intermediary layer was only partially transparent, at high flow rates it was not possible to visually observe the flow regime prevailing within the channels

of the device. It has been reported that immiscible flow regimes of butanol and water form segmented flow regimes at low flow velocities which transforms to a vertically stratified flow regime at higher flow rates. [9]

3.4.2.2.3 Vertically Stratified Flow
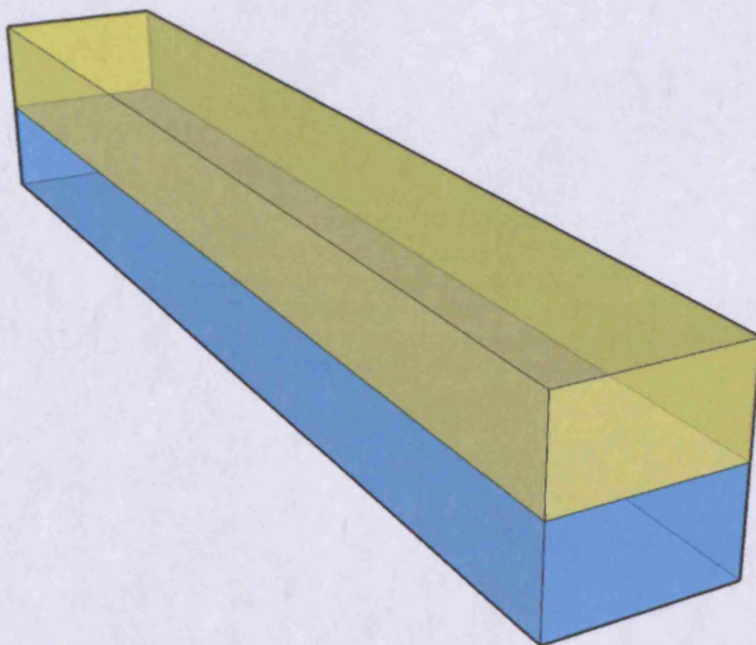
Figure 14 Illustration of vertically stratified flow between two immiscible phases in a micro channel

Kuban et al. reported the transformation of a butanol-water segmented flow stream to a vertically stratified flow regime in a microchannel in a composite glass and polymer gasketted microfluidic device, with a channel width of 2000 μm and depth of 400 μm, as the linear flow velocity increased from 5 mm s^{-1} to 10 mm s^{-1}. This phenomenon was demonstrated both

experimentally and theoretically by computational simulation, where surface forces and viscous forces were shown to be the dominant factors in determining flow regime. The surface tension between butanol and water is significantly lower at 2.1 mN m^{-1}, than that of chloroform and water at a value of 32.8 mN m^{-1}, suggesting that if this flow regime transformation were to occur with a chloroform-water flow stream it would be at a significantly higher linear flow velocity than that which gives rise to the flow regime transition in the butanol and water system. If this flow regime transformation was indeed occurring in the chloroform-water extraction system and giving rise to the discontinuity in the extraction data between the flow rates of 2 ml min^{-1} and 2.4 ml min^{-1}, it would corespond to linear velocities in the range 92.6 – 111.1 mm s^{-1}, significantly higher than the transition in the butanol-water system (between 5 – 10 mm s^{-1}).

3.4.2.2.3.1 Surface Area/Volume Implications

If a vertically stratified flow regime were to manifest, this would have a significant effect on the surface area : volume ratio of the extraction, thus affecting the extraction rate. The surface area : volume ratio was calculated for a stratified flow regime (Table 1), with an assumed flat, horizontal liquid-liquid interface, and also for a segmented flow regime with a slug length of 4 mm, in a 530 x 0.6 x 0.6 mm microchannel. In estimation of the slug surface area and volume, a wetting film of organic solvent of negligible thickness was assumed to exist between the channel wall and the slug sides. The segment ends were represented as hemispherical with a diameter of that of the channel dimension. It was noted that the segment length contributed the majority of the available extraction surface area, suggesting that radial mass transport and wetting film thickness may play significant roles in determining the rate of extraction. This is discussed further in section 3.4.3.

Table 1 Calculated surface area : volume ratio for both stratified flow and segmented flow regimes in a square cross sectional microchannel of width and depth 600 μm and length 53 cm. A segment length of 4 mm was assumed

	surface area:volume (m^{-1})
Vertically Stratified Flow	3333.3
Segmented Flow	8647.4

The extraction rate constants derived in Figure 13 were normalised for the approximated surface area : volume ratio for the two proposed flow regimes, to give kl(A:V). A segmented flow regime was assumed for experimental flow rates of 0.1 ml min^{-1} to 2.0 ml min^{-1}, and a vertically stratified flow regime assumed after the discontinuity in the extraction data, for flow rates of 2.4 to 10 ml min^{-1}. The results are detailed in Figure 15.
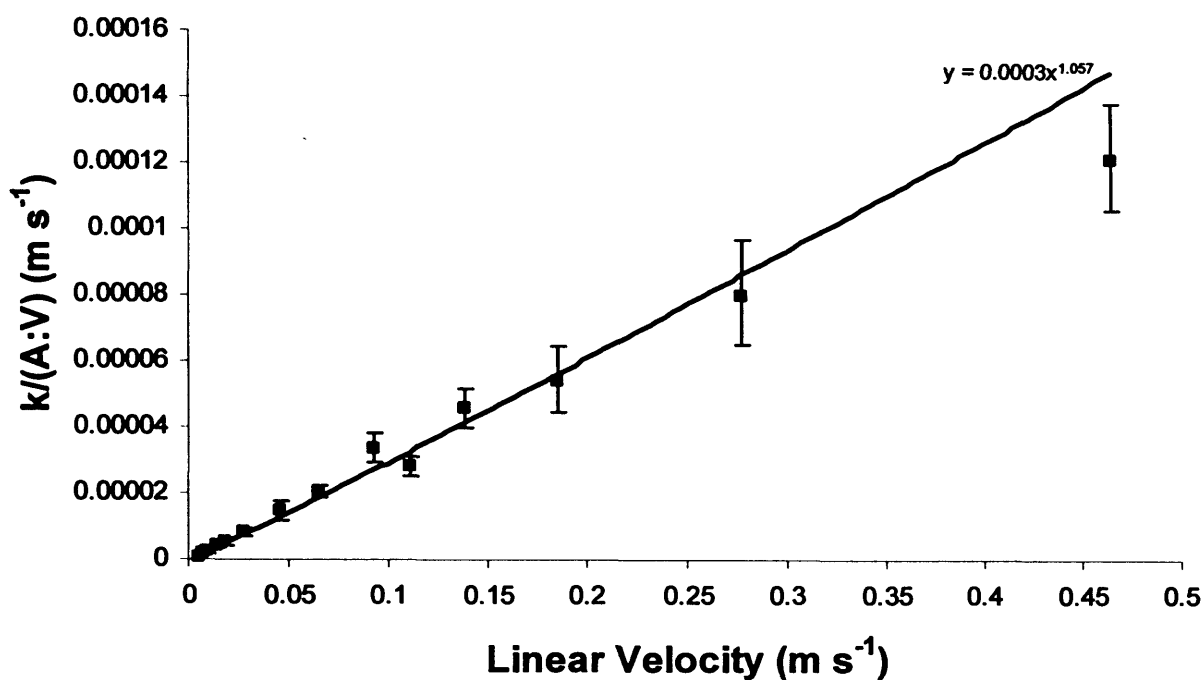
Figure 15 Extraction rate constant (k) normalised for surface to volume ratio (A:V) for two potential flow regimes; segmented flow 0.1 – 2.0 ml min^{-1} and vertically stratified flow 2.4 – 10 ml min^{-1}. For propranolol segmented flow on-chip extraction from a 50 µM aqueous sample into chloroform on-chip. (n=3 ± S.D.).

The effect of normalising the extraction rate constant for the available surface area : volume ratio across which the extraction can proceed for the two proposed flow regimes, had perhaps the surprising effect of eliminating the discontinuity in the rate of extraction with increasing flow rate. This possibly suggests that indeed the extraction flow regime does develop from a segmented flow into a vertically stratified flow at excessive linear velocities, due to the increased contribution of inertial forces. It is important to note that this observation does *not* prove the existence of a vertically stratified flow occurring at the higher flow rates investigated. Further experimentation would be required to conclude with any certainty, the nature of the multiphase flow regime at the high flow rates tested in the microdevice and also elucidate the mechanisms of extraction at these flow rates. High speed video acquisition with improved lighting to give visual clarity through the amorphous PEEK lid of the device, and computation fluid dynamic (CFD) modelling may enable suitable investigation into these effects.

3.4.2.2.3.2 Analysis of Forces Influencing Prevailing Flow Regime

Table 2 Analysis and comparison of the fluid properties and dimensionless analysis of forces acting on the immiscible fluid for the segmented and stratified flow regimes reported by Kuban et al. and proposed flow regime transition in experimental data of section 4.2

		Flow rate	Immiscible phase	Flow regime	Channel geometry	Interfacial tension	Hydraulic diameter[e]	viscosity	Density	Density difference to water	Ca	We	Bo	Combined
		(m s^{-1})			w x d (µm)	(N m^{-1})	(m)	(Pa s)	(kg m^{-3})	(kg m^{-3})	[a]	[b]	[c]	[d]
Kuban et al	experimental	0.0005	Butanol	Segmented	2000 x 400	0.0021	0.000667	0.0029	810	187	0.00069	0.00006	0.388636	0.389391
Kuban et al	experimental	0.001	Butanol	Stratified	2000 x 400	0.0021	0.000667	0.0029	810	187	0.00138	0.00026	0.388636	0.390274
Kuban et al	CFD	0.005	Butanol	Segmented	2000 x 400	0.0021	0.000667	0.0029	810	187	0.00691	0.00643	0.388636	0.401973
Kuban et al	CFD	0.01	Butanol	Stratified	2000 x 400	0.0021	0.000667	0.0029	810	187	0.01381	0.02573	0.388636	0.428173
Castell	experimental	0.0926	Chloroform	Segmented	600 x 600	0.0328	0.0006	0.0006	1490	493	0.00169	0.23371	0.053082	0.288490
Castell	experimental	0.1111	Chloroform	Stratified?	600 x 600	0.0328	0.0006	0.0006	1490	493	0.00203	0.33643	0.053082	0.391542

[a] Ca – Capillary number, ratio of viscous forces to surface forces [viscosity x velocity/surface tension], [b] We – Webber number, ratio of inertial forces to surface forces [(density x velocity^2 x characteristic length)/surface tension], [c] Bo – Bond number, ratio of gravitational forces to surface forces [(Δdensity ¢ H_2O x g x characteristic length^2)/surface tension]. [e] Hydraulic diameter calculated as [4 x cross-sectional area/ wetted perimeter].

Table 2 shows dimensionless analysis of the forces acting on the immiscible organic phase of the segmented and proposed stratified flow streams, for the experimental data of this thesis and the reported observations of Kuban et al. Kuban and co-workers concluded that surface forces, together with viscosity and linear velocity, determined the flow regime in the channel geometry under investigation. The relative importance of these can be quantified by the capillary number (Ca) which expresses dimensionlessly, the relative importance of viscous forces (viscosity x velocity) to surface forces. Comparison of the value of Ca calculated for the experimental data of Kuban et al. either side of the onset of stratified flow, shows a fair correlation with that for the data presented in this thesis. Consideration of other forces, namely inertial and gravitational forces, competing against the surface forces of the immiscible flow though use of the Webber number (We) and Bond number (Bo) when combined with the capillary number (Ca), effectively describe the ratio of the combined viscous, inertial and gravitational forces acting on the fluid to the of surface forces acting on the fluid. This analysis of Kuban et al.'s experimental data suggests that a value of around 0.390 is required for a stable segmented flow regime to breakdown into a stratified flow regime. This value supports the theorised flow transition from segmented flow to stratified flow at the point of extraction discontinuity presented in this chapter. The combined dimensionless analysis approach outlined above for a water-chloroform immiscible fluid system at linear velocities of 0.0926 and 0.1111 m s^{-1}, between which the extraction discontinuity occurs, liberates values of 0.288 and 0.392 respectively, suggesting that breakdown of the segmented flow stream possibly occurs at a similar numeric value for forces opposing interfacial forces in each instance. It should also be noted that the materials used to construct the device will also play an important role in determining the stability of a stratified flow regime, with each liquid's wetting ability of the substrate material introducing additional surface forces where the liquid contacts the channel walls. The experimental device was constructed from a PTFE substrate with amorphous PEEK lid. The amorphous PEEK lid is significantly more hydrophilic than the PTFE base material, thus potentially favouring a vertically stratified flow with water flowing in the upper portion of the device. The experimental investigation device of Kuban et al. consisted of glass upper and lower plates defining the channel top and bottom, with polyester and poly(vinyl chloride)

material defining the channel walls. The authors note a three phase contact angle of water-butanol-glass of 97°, illustrating that the glass substrate is wetted approximately equally by both butanol and water, thus each providing a similar surface force component. However, the comparative wetting ability of the two fluids for the polyester or poly(vinyl chloride) channel walls is not considered. PTFE is wetted much more readily by chloroform than water and thus the preference for a flow regime to prevail where chloroform wets the three PTFE walls should not be overlooked (Figure 16). Detailed three phase contact angle measurements and surface tension measurements would need to be conducted to attempt to elucidate a precise flow regime. However the dimensionless analysis, in comparison to the findings of Kuban et al., suggests that on consideration of liquid properties alone, a segmented flow regime *may* be unstable at the flow rates where the extraction discontinuity was observed. This dimensionless analysis offers further support for the theorised transition from segmented to an alternative flow regime, however the numerical analysis is relatively simplistic and further more rigorous experimentation and calculation would be required to prove or disprove the theory.
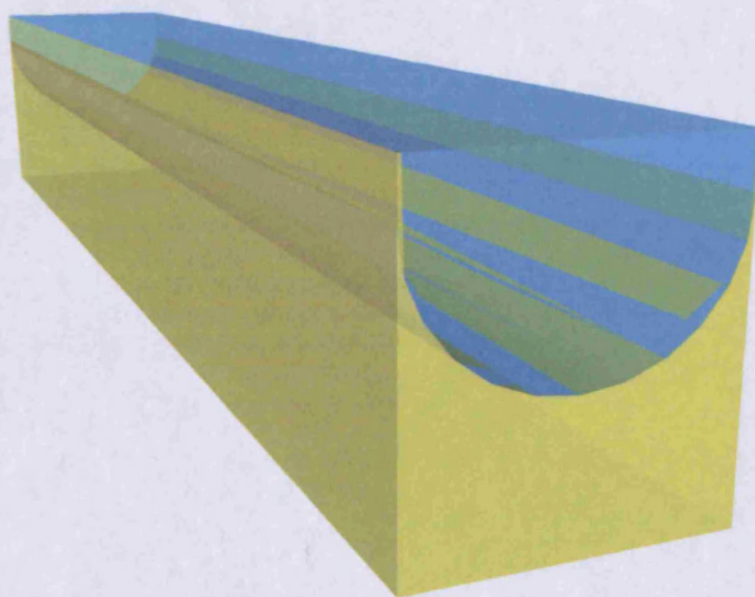
Figure 16 Illustration of vertically stratified flow with a significantly curved interfacial boundary between immiscible fluids. Such a flow regime may prevail due to differential wetting properties of the channel floor and walls (e.g. PTFE) in comparison to the channel lid (e.g. amorphous PEEK), as a result of competing interfacial forces.

3.4.3 Segmented Flow Phase Ratio

3.4.3.1 Methodology

The effect of phase ratio and consequently segment length on the efficiency of a segmented

flow extraction was assessed. Segmented flow was generated using a Tefzel® T-junction with

0.02" (0.5 mm) through hole interfaced with 1/16" O.D. FEP tubing with 0.5 mm I.D. The

segmented flow stream was flowed through 1.5 m of straight, horizontally orientated tubing,

before the combined eluate was collected in a 2 ml eppendorf centrifuge tube. The extraction

of propranolol from an aqueous solution of the hydrochloride salt into chloroform was

assessed at a range of flow ratios, with the total combined flow rate maintained at 0.1 ml

min^{-1}. A 50 μM stock solution of propranolol hydrochloride in de-ionised water was prepared

and delivered to the T-junction at flow rates of between 0.05 ml min^{-1} and 0.09 ml min^{-1},

together with chloroform at the corresponding flow rate to generate a total segmented flow

rate of 0.1 ml min^{-1}. The flow was allowed to stabilise for several minutes (a minimum of twice

the transit time), before proceeding with the collection of the combined eluate. A volume of 1.5

ml of combined eluate was collected in all instances, 0.65 ml of aqueous phase was

immediately removed, from which three 200 μl aliquots were assessed for propranolol content

by fluorescence microplate analysis (excitation λ: 290 nm, emission λ: 330 nm).

3.4.3.2 Results and Discussion

3.4.3.2.1 Analyte Depletion and Mole Fraction Extracted (f)
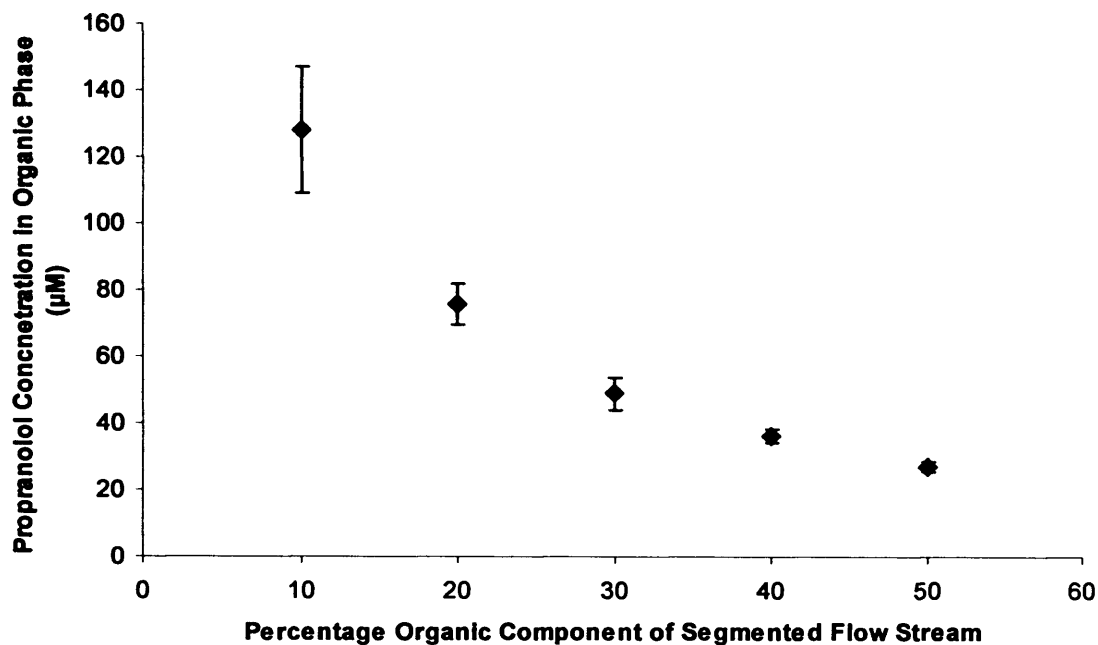
Figure 17 Propranolol concentration extracted into chloroform phase following segmented flow extraction of a 50 µM aqueous propranolol solution with chloroform in 1.5 m of 0.5 mm I.D. FEP tubing at a range of phase ratios at constant total flow rate of 0.1 ml min^{-1}. (n=3 ± S.D.).
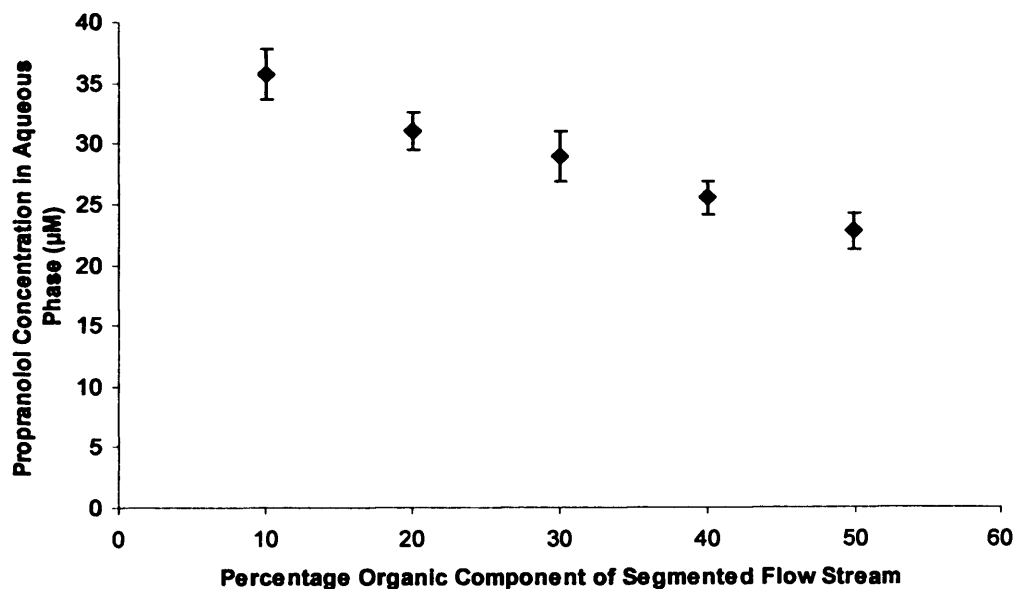
Figure 18 Propranolol concentration remaining in the aqueous phase following segmented flow extraction of a 50 µM aqueous propranolol solution with chloroform in 1.5 m of 0.5 mm I.D. FEP tubing at a range of phase ratios at constant total flow rate of 0.1 ml min^{-1}. (n=3 ± S.D.).

97
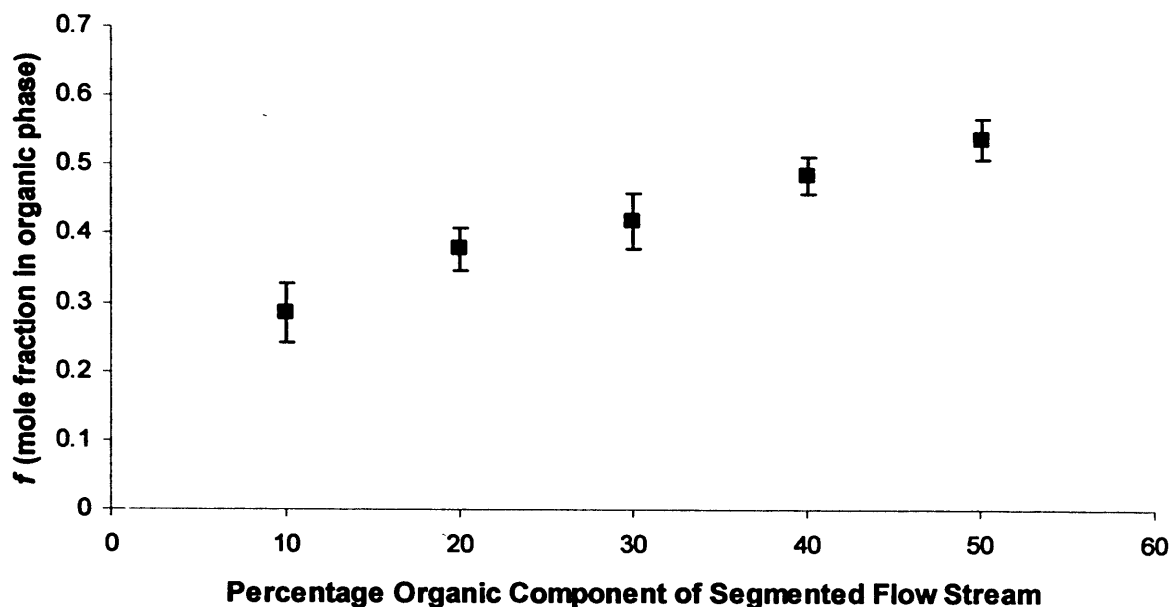
Figure 19 Mole fraction (*f*) of propranolol extracted into chloroform from a 50 μM aqueous propranolol solution through segmented flow extraction in 1.5 m of 0.5 mm I.D. FEP tubing at a range of phase ratios at constant total flow rate of 0.1 ml min^{-1}. (n=3 $\pm$ S.D.).

Figures 17 and 18 illustrate the propranolol concentration in both the aqueous and organic phases after segmented flow extractions at a fixed flow rate of 0.1 ml min^{-1}, with the percentage flow contribution from the extracting chloroform phase varying from 10 - 50 %. It was observed that decreasing the organic component of the segmented flow resulted in a substantial increase in propranolol concentration in the extracting chloroform phase, although the extent of increased concentration was insufficient to prevent a decrease in the extent of concentration depletion from the aqueous sample. This observation is unsurprising since as the flow rate of the segmented flow was maintained, a decrease in organic flow rate had to be offset by an increase in aqueous sample flow rate. Since the aqueous phase contained a fixed concentration of 50 μM propranolol HCl, increasing the flow rate of this phase increased the total moles of propranolol delivered to the segmented flow stream per unit time. Analysis of the extraction data in terms of the mole fraction extracted (*f*) (Figure 19) yields an interesting relationship, showing that the mole fraction extracted increases with increasing percentage of extracting organic component in the segmented flow regime. However, although it is found

that increasing the percentage of organic extracting component for a given segmented flow rate results in a greater proportion of analyte present in the aqueous sample being extracted into the chloroform extracting phase, this is increase is with a diminishing return with respect to reagent consumption and total sample phase throughput. Interestingly, the actual quantity (moles) of propranolol extracted per minute at each of the investigated flow ratios is approximately the same in each instance. These results are illustrated in Table 3 and Figure 20.

Table 3 Total quantity of propranolol extracted (nmol) from a 50 µM aqueous sample by chloroform, in a segmented flow regime for a range of liquid phase ratios at a constant total segmented flow rate of 0.1 ml min^{-1}.

Aqueous Flow Rate	Chloroform Flow Rate	Total Flow Rate	Transit Time	Percentage Choroform in Segmented Flow Stream	Propranolol Extracted	Propranolol delivered in 1 minute	Propranolol extracted in 1 minute
ml min^{-1}	ml min^{-1}	ml min^{-1}	s	%	%	nmol	nmol
0.05	0.05	0.1	180	50	54.2	2.5	1.36
0.06	0.04	0.1	180	40	44.5	3	1.34
0.07	0.03	0.1	180	30	42.1	3.5	1.47
0.08	0.02	0.1	180	20	37.9	4	1.51
0.09	0.01	0.1	180	10	28.5	4.5	1.28
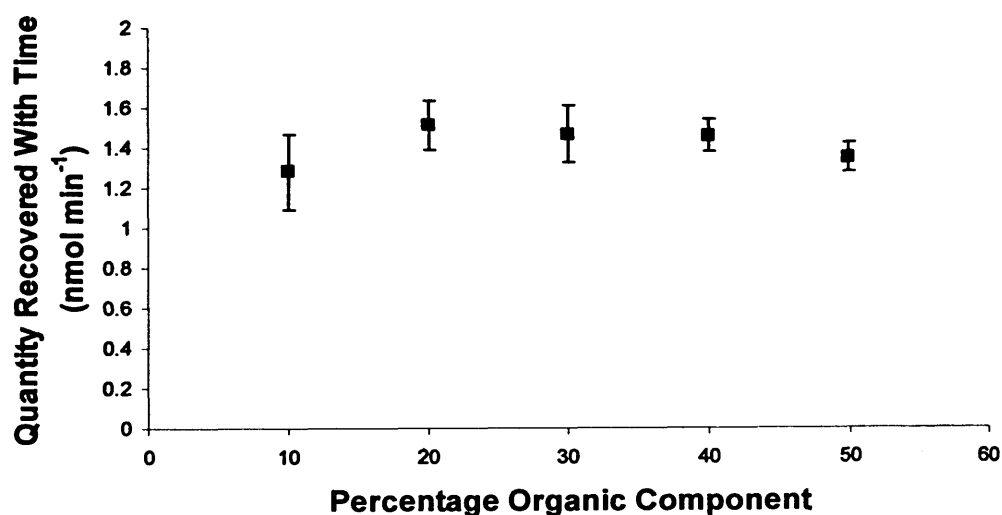
Figure 20 Total quantity of propranolol extracted (nmol) per minute of extraction time, from a 50 µM aqueous sample by chloroform, in a segmented flow regime for a range of liquid phase ratios at a constant total segmented flow rate of 0.1 ml min^{-1}. (n=3 ± S.D.).

volume ratio of the segments decreased only marginally (< 5%) with increasing s(

length. The raw data is contained in Table 4. It has been demonstrated that solutes ex

approximately the same rate per unit area across both the ends and sides of a disperse

segment in a segmented flow regime [10]. As such, the interfacial area dependence o

be removed by conversion of the observed rate constant into an overall mean mass (

coefficient (Figure 22) (as per section 3.4.1.2.3) [8].
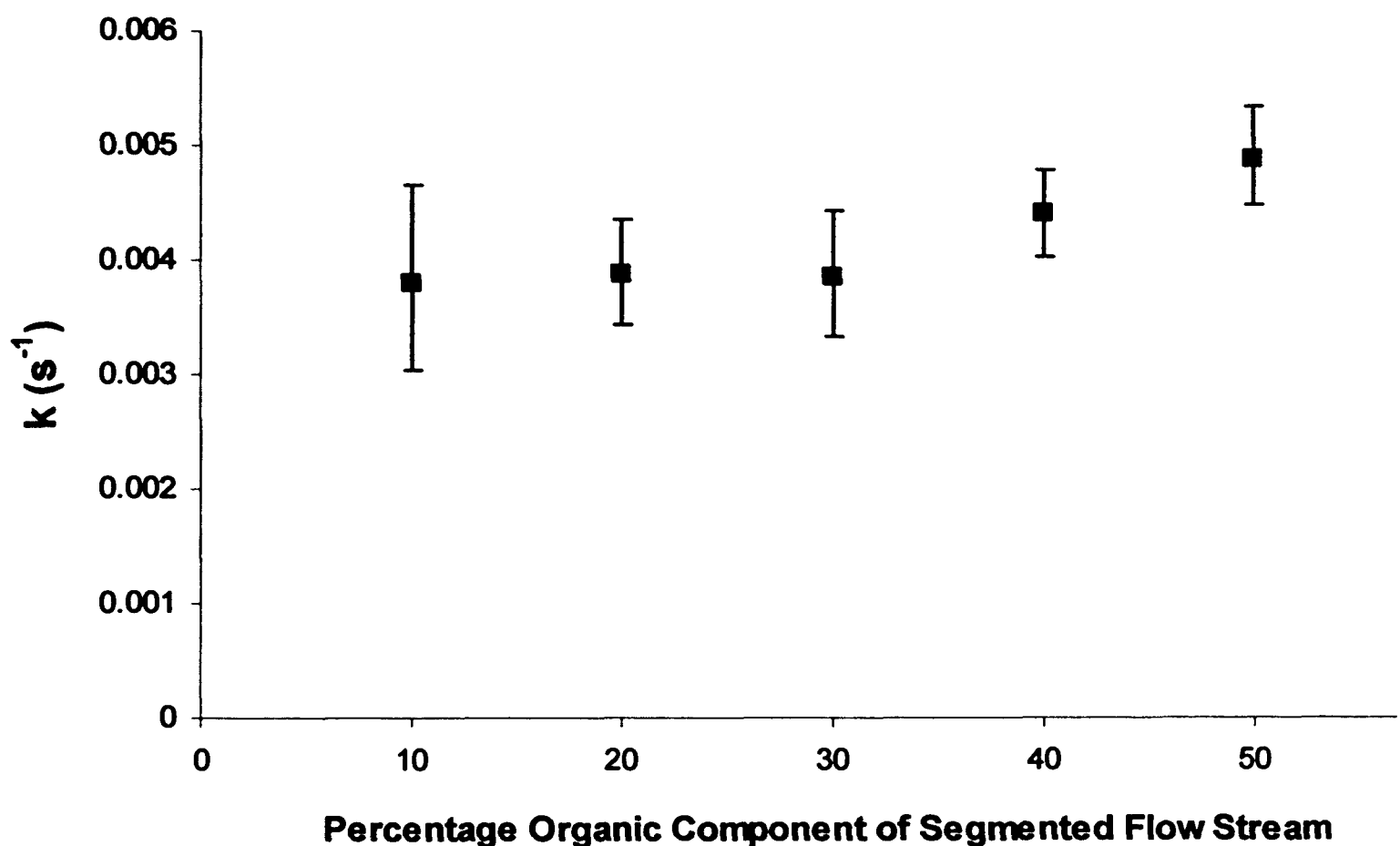
Figure 21 Extraction rate (k) for the extraction of propranolol from a 50 µM aqueous samp chloroform in a segmented flow regime for a range of liquid phase ratios at a constant total segment rate of 0.1 ml min^{-1} in 1.5 m of 0.5 mm I.D. straight FEP tubing. (n=3 ± S.D.).

Table 4 Segment length and corresponding surface area to volume ratio for aqueous segments generated in a segmented flow regime at a range of investigated phase ratios.

Aqueous Flow Rate	Organic Flow Rate	Organic Component of Segmented Flow Stream	Approximate Aqueous Slug Length	Approximate Organic Slug Length	Aqueous Slug Aspect Ratio	Approximate Surface Area : Volume Ratio of aqueous segment
ml min^{-1}	ml min^{-1}	%	mm	mm	length/width	m^{-1}
0.05	0.05	50	4	4	8	8347.8
0.06	0.04	40	6	4	12	8228.6
0.07	0.03	30	9.3	4	18.7	8145.5
0.08	0.02	20	16	4	32	8084.2
0.09	0.01	10	36	4	72	8037.2

3.4.3.2.3 Surface Area/Volume Implications
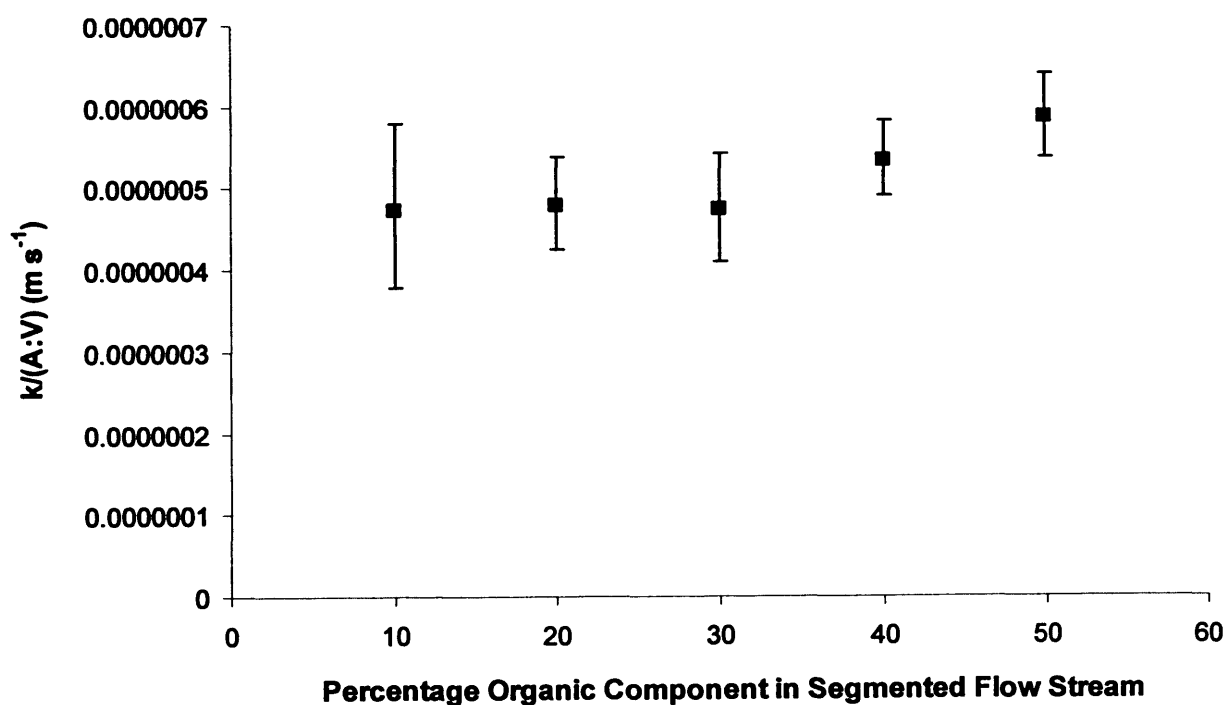
Figure 22 Extraction rate (k) normalised for the surface area : volume ratio (A:V) of the aqueous segment from which extraction occurs. Segmented flow extractions of a 50 µM propranolol aqueous sample into chloroform at a range of phase ratios at a constant total segmented flow rate of 0.1 ml min^{-1}. (n=3 ± S.D.).

101

Figure 22 shows that with the exception of the extraction conducted at a 1:1 ratio of reagent flow, the effect of adjusting the phase ratio of the aqueous sample and organic extracting phase whilst maintaining the overall segmented flow rate and extraction distance has very little, or no, effect on the extraction rate constant normalised for surface area : volume ratio (k/(A:V)). This observation is especially interesting, since several dependent variables of the flow regime are also affected by the manipulation of the phase delivery rates. Most notably this includes the aqueous segment length, which intuitively would be expected to result in a decrease in the mixing within the aqueous segments as the length increases, thus slowing the extraction.

3.4.3.2.4 Dependent Variables

Other important dependent variables also affected by the manipulation of phase ratio of the segmented flow regime, are both the total quantity of analyte in the extraction system and the decreased volume of organic extracting solvent for the analyte to partition into, and subsequently mix and diffuse through, to create a uniform concentration. This in combination with the increased aqueous segment length at high aqueous : organic flow ratios and the equivalent contribution per unit area of axial and radial extraction from the aqueous slug [10], create a possibility of saturation of the stationary, thin films of organic phase separating the aqueous segments from the channel wall. However, since the rate of extraction per unit area was seen to be unaffected by the phase ratio, especially in the case of long aqueous segments, it can be concluded that in this extraction, mass transfer of propranolol in chloroform is not the rate limiting step of the extraction. This process must therefore, be faster than either the mass transfer in the aqueous phase or mass transfer across the liquid-liquid interface, or the deprotonation of the propranolol which takes place to enable phase transfer. Whether this relationship is maintained as the extraction approaches equilibrium, or in extractions which do not strongly favour the analyte residing in the extracting phase, remains to be seen. In this instance, the distribution ratio is comparatively large, favouring propranolol residing in the chloroform phase. The employment of long aqueous segments is likely to restrict mixing and diffusion in the organic phase, due to the extended wetting films and their

requirement to ultimately disperse extracted analyte into the bulk organic phase segment. The large distribution ratio, favouring analyte residing in the organic phase, enables the extracting phase to tolerate significant analyte concentration gradients and act as an 'extraction-sink' for the analyte. Consequently the experimental observations of Figure 22 suggest that mass transfer within the aqueous phase to the interfacial boundary, or interfacial phase transfer, determine the rate of extraction.   Experimentation would be necessary to investigate this relationship further. It would be interesting to evaluate if this phenomenon occurred in an extraction system with a near 1 : 1 equilibrium distribution. It may be conceivable that improvements in intra-segment mixing may be futile if a significant proportion of the extraction is taking place at the channel walls through radial mass transport, if the thin films of near-stagnant extracting solvent become rapidly saturated.

3.4.3.2.5 Literature Comparisons

Lucy et al. reported extraction rate constants in the order of $0.2 - 0.6$ s^{-1} for the extraction of caffeine from an aqueous sample into chloroform in a segmented flow stream in 0.8 mm I.D. Teflon tubing [8]. This value is notably higher than the range of $0.004 - 0.005$ s^{-1} observed in these experiments. It was however noted that in section 3.4.2.2.2, the extraction rate constant approached the magnitude of those reported by Lucy et al. albeit for a different extraction system. It was supposed that the main contributing factor for the difference in measured extraction rate constants was the disparate range of linear flow velocities employed in each study. Lucy et al. employed a volumetric flow rate 4.0 ml min^{-1} resulting in a linear velocity of 0.133 m s^{-1}, compared to a flow rate of 0.1 ml min^{-1} and linear velocity of 0.00849 m s^{-1} reported here. It was originally reasoned that since in the MIP-assisted segmented flow extractions, binding to the MIP would represent the rate limiting stage of the extraction, that a slow flow rate and consequently increased residence time would be preferable to increase extraction efficiency. This was considered particularly important since it was hoped that the final device would take the format of an integrated microfluidic chip, and therefore the path length would be defined by the machinable surface area of the device substrate. As such it was decided to characterise the extraction 'rate' with respect to distance rather than time, an

103

approach adopted by Nord et al. [6].

3.4.3.2.5.1 Extraction Rate Constant With Respect to Distance Travelled (km)

The extraction rate for the results of the phase ratio investigation (Section 3.4.3) was calculated in terms of flow distance rather than time, an approach adopted by Nord et al. [6]. This was done by multiplying the extraction rate constant (k) by time (t) to give the dimensionless kt, which was then divided by the tubing length, representative of the distance travelled after time t. This effectively results in the division of k by the linear velocity (v) of the segmented flow stream, termed here km with the units of m^{-1}.

$$km = \frac{k}{v} \tag{6}$$

km is a measure of the extraction rate of analyte from the aqueous sample with respect to distance travelled by the segmented flow stream. Analysis of both sets of data by this method showed that with respect to path length, the extraction reported in this thesis approached the efficiency seen by Lucy et al., however this comes at the expense of time and hence sample throughput (Table 5). Analysis of the experimental data obtained on-chip with a 1:1 ratio of reagent flow (section 3.4.2.2.1) concluded that at flow rates of 0.1 ml min^{-1} to 0.2 ml min^{-1}, mixing within fluid packets is insufficient to offset against the increased residence time afforded by a slower flow rate, thus limiting the extent of extraction. If this relationship is maintained for the same extraction in cylindrical tubes, it could be anticipated that a higher flow rate might offer advantages in terms of both time and distance efficiency, up to a certain limit. However, with a view to inclusion of suspended MIP particles with comparatively slower binding kinetics and mass transfer it is likely a compromise should be sought, where the reduction in liquid-liquid phase transfer efficiency at a reduced linear velocity is offset by the increased binding to the MIP afforded by the increased residence time within a channel of finite length, as defined by the dimensions of the fluidic chip.

Table 5 Comparison of measured extraction rate constants with respect to time (k) and distance (km) for the segmented flow extractions at a range of flow ratios reported here and by the work of Lucy et al. (Castell: extraction of propranolol from aqueous sample in chloroform in 0.5 mm I.D FEP tubing, Lucy et al.: extraction of caffeine from aqueous sample in chloroform in 0.8 mm I.D Teflon tubing [8].)

	% organic	linear velocity m s^{-1}	k s^{-1}	km m^{-1}
Castell	50	0.008488	0.004909	0.57835
Castell	40	0.008488	0.003848	0.453302
Castell	30	0.008488	0.003864	0.455279
Castell	20	0.008488	0.003882	0.457395
Castell	10	0.008488	0.003798	0.447417
Lucy et al.	66.6	0.133	0.63	4.736842
Lucy et al.	25	0.133	0.25	1.879699
Lucy et al.	20	0.133	0.23	1.729323

3.4.4 Segment Aspect Ratio

In continuation of the data presented in Table 4 and discussed briefly in section 3.4.3.2.4, an obvious consequence of adjusting phase ratio is altering segment length. Additionally, the segment length may also be influenced by pressure, flow rate (Chapter 4) and segmented flow generating geometry (Chapter 1). Lucy and co-workers in their comprehensive study of the kinetics of solvent extraction in segmented flow regimes, studied the effects of segment length in a range of tubing diameters. Caffeine was extracted from an aqueous sample into chloroform with a flow ratio of 1:1, at a linear flow velocity of 0.133 m s $^{-1}$ in straight Teflon tubes of 0.3, 0.5, 0.8 and 1.0 mm I.D. [8]. In analysing the effect of segment length on extraction rate (k), a dependency is observed for both segment length and tubing diameter, with k increasing with decreased segment length and decreased tubing diameter, but as the authors note, in shorter segments, the extraction is fastest in wider tubing, and thus cross over of the respective curves for each tubing diameter is observed. The authors, in an effort to understand this behaviour, consider the consequent effect of increased tubing diameter on the surface area : volume ratio and find that k/(A:V) (equivalently termed β by Lucy and colleagues) shows a more straightforward relationship with segment length. Finding that

irrespective of tubing diameter, for long segments (> 8 mm in their study), the mass transfer coefficient for the extraction converges on a minimum extraction rate, demonstrating that mixing, and consequently mass transfer is more rapid for shorter segments. This trend for increasing mass transfer in shorter segments is, perhaps surprisingly, shown to be greater for wider diameter tubing. The authors cleverly consider this effect with respect to aqueous segment aspect ratio (i.e. segment length divided by tubing diameter), and find that all data converges on a single curve. The reported graph is illustrated in figure 23 (note that β is equivalent to kl(A:V) although units are expressed in cm s^{-1} not m s^{-1}).
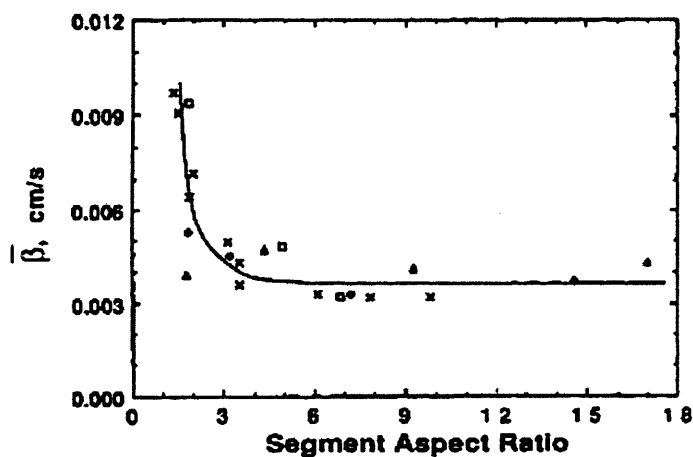
Figure 23 Data reported by Lucy et al. [8] illustrating the dependence of extraction rate, normalised for segment surface area : volume ratio (kl(A:V), termed β by the authors) on segment aspect ratio. Data acquired for the segmented flow extraction of caffeine from an aqueous sample into chloroform with a flow ratio of 1:1, at a linear flow velocity of 0.133 m s^{-1} in straight Teflon tubes of 0.3, 05, 0.8 and 1.0 mm I.D

Figure 23 shows that independent of channel diameter, the mass transfer coefficient (kl(A:V)) is related to segment aspect ratio, and increases significantly for short segments of aspect ratio <4. For segments longer than this, the mass transfer coefficient (kl(A:V)) was found to be constant. Interestingly, these findings suggest that tubing diameter affects the extraction rate constant (k) only by the predictable decrease in surface area : volume ratio of the fluid segments, provided the segment aspect ratio can be controlled.

channel diameter was maintained throughout, and the data in Table 4 illustrate

surface area : volume ratio of the segments is only weakly affected by their leng

variance in the data for the segment sizes studied here), this supports the finding tha

with the exception of the 1:1 ratio of flow, found to be independent of phase ra

consequently segment length when the aqueous segments were long. This data is pr
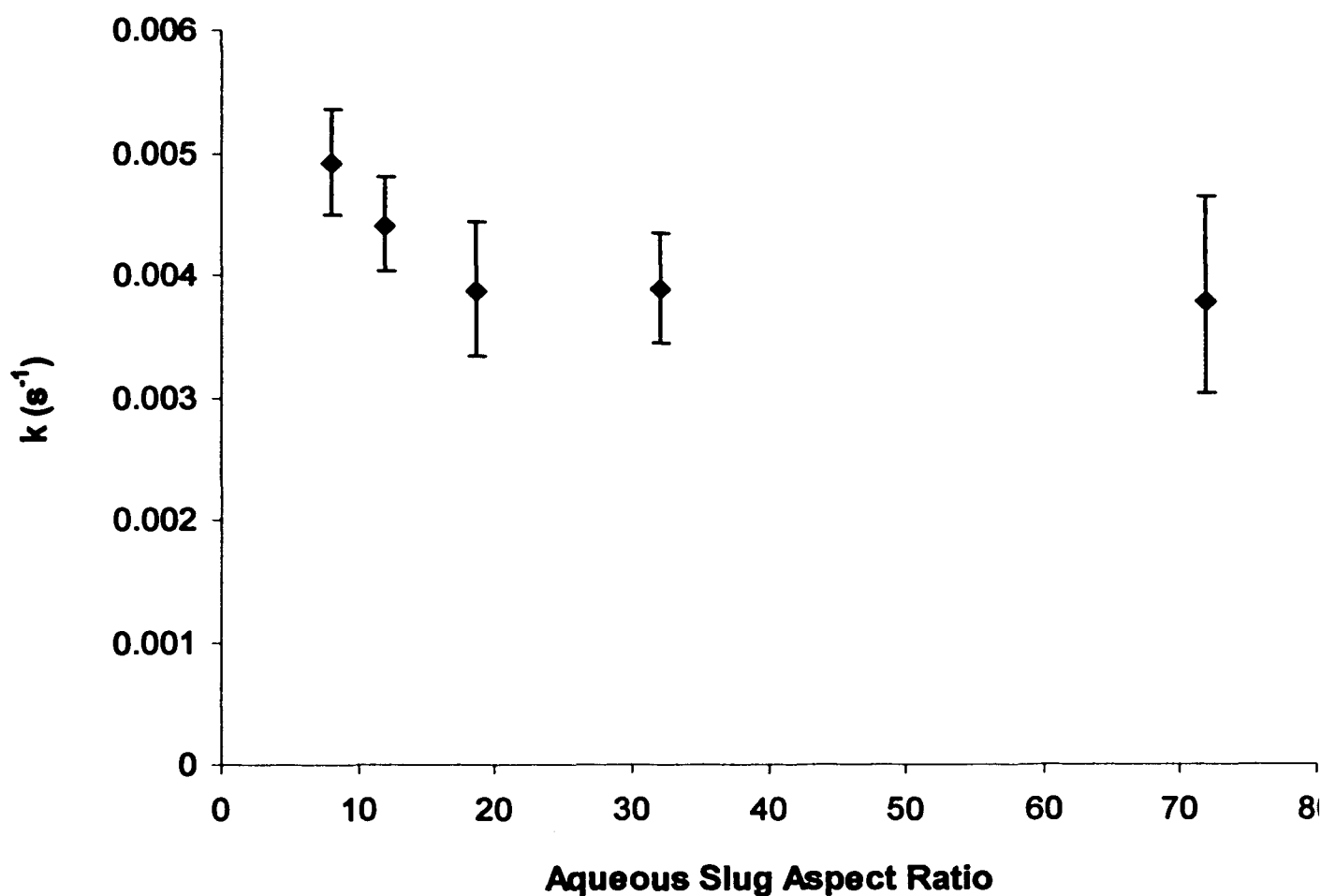
in Figure 24.

Figure 24 Measured extraction rate (k) with varying aqueous segment aspect ratio at a segmented of 0.1 ml min^{-1} in 0.5 mm I.D FEP tubing. In support of data reported by Lucy and co-wor extraction rate is found to be independent of aqueous segment aspect ratio for long segments. (n=3 ±

The data of Figure 24 correlates well with the results reported by Lucy et al. and suggests that formation of shorter segments would improve the extraction efficiency further. It may therefore be beneficial to carefully consider the segmenting geometry independently from the main channel geometry in which segmented flow will take place, in order to decrease the segment length of the segmented flow stream beyond what would typically be generated for a given channel diameter.

Again, the extraction rate constant was defined in terms of linear distance travelled (section 3.4.3.2.5.1) in order to compare the magnitude of the extractions reported by Lucy et al. with that observed in this study. With consideration for segment aspect ratio, this comparison again suggests it may be possible that significantly improved efficiency could be achieved through the employment of shorter aqueous segments. Unfortunately due to time constrains within the project this was ultimately not possible to evaluate, however this will be borne in mind for future work. The comparative data is illustrated in Table 6 and Figure 25.

Table 6 Comparison of measured extraction rate constants with respect to time (k) and distance (km) normalised for varying segment surface area to volume ratios (A:V), for the segmented flow extractions at a range of flow ratios reported here and by the work of Lucy et al. (Castell: extraction of propranolol from aqueous sample in chloroform in 0.5 mm I.D FEP tubing, Lucy et al.: extraction of caffeine from aqueous sample in chloroform in 0.8 mm I.D Teflon tubing.)

	Organic Component Of Segmented Flow %	Aqueous Segment Aspect Ratio	Surface Area : Volume Ratio	Linear Velocity m s^{-1}	k s^{-1}	km m^{-1}	Km/(A:V)
Castell	50	8.0	8347.8	0.0085	0.0049	0.578	6.93×10^{-5}
Castell	40	12.0	8228.6	0.0085	0.0038	0.453	5.51×10^{-5}
Castell	30	18.7	8145.5	0.0085	0.0039	0.455	5.59×10^{-5}
Castell	20	32.0	8084.2	0.0085	0.0039	0.457	5.66×10^{-5}
Castell	10	72.0	8037.2	0.0085	0.0038	0.447	5.57×10^{-5}
Lucy	66.6	1.1	7105.3	0.13	0.63	4.737	66.7×10^{-5}
Lucy	25	3.5	5526.3	0.13	0.25	1.880	34×10^{-5}
Lucy	20	4.1	5439.6	0.13	0.23	1.729	31.8×10^{-5}
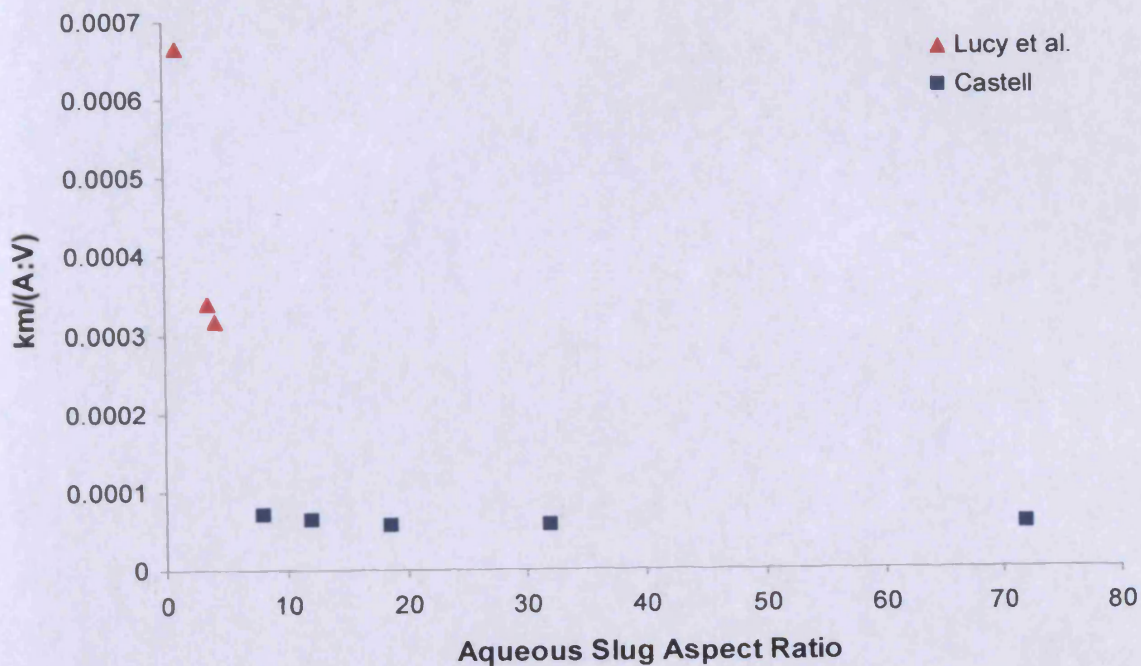
Figure 25 Comparison of measured extraction rate constants with respect to distance (km) normalised for varying segment surface area to volume ratios (A:V), for the segmented flow extractions at a range of flow ratios reported here and by the work of Lucy et al. (Castell: extraction of propranolol from aqueous sample in chloroform in 0.5 mm I.D FEP tubing, Lucy et al.: extraction of caffeine from aqueous sample in chloroform in 0.8 mm I.D Teflon tubing.) Comparison of the data sets suggests that significant performance advantages could be gained through the employment of low aspect ratio segments in the segmented flow extractions reported in the work of this chapter.

Although far from conclusive, the combined plot of Lucy et al.'s data investigating the effect of phase ratio on extraction rate and that obtained in this study, suggests that it is possible that, as assessed by the extraction rate constant with respect to distance travelled, the data combines to form one continuous curve, akin to that of figure 23. This is suggestive that significant performance enhancements in the investigated extraction could be achieved through reduction in aqueous segment length.

3.4.4.2 Segment Aspect Ratio and Velocity - Combined Effect on Extraction Rate Constant (k)

It has also been reported that in straight tubing, the extraction rate constant (k) increases with increasing linear velocity, with increasingly dramatic effect as segment length decreases for a

given tubing diameter [8]. The raw data from Lucy and co-worker's experiment investigating the effects of flow rate and segment length on extraction rate (k) were extracted from their graphic illustration. The data was processed in accordance with the above steps in order to express the data in terms of segment aspect ratio, linear velocity, and k normalised for the approximated surface area : volume ratio associated with various segment aspect ratios to give $k/$(A:V).

3.4.4.2.1 Segment Aspect Ratio and Surface Area/Volume Effects

The general relationship of the surface area : volume ratio (A:V) with channel diameter and segment aspect ratio for cylindrical channels was derived from the method of estimation outlined in section 3.4.2.2.3.1. This approach is defined mathematically in equation 7.

$$A:V = \frac{(l-dia)\pi dia + 4\pi\left(\frac{dia}{2}\right)^2}{\pi\left(\frac{dia}{2}\right)^2(l-dia)+\frac{4}{3}\pi\left(\frac{dia}{2}\right)^3} \tag{7}$$

In equation 7 the segment length (l) is the product of the channel diameter (dia) and the segment aspect ratio. This equation simplifies to a general formula for calculation of a fluid segment area : volume ratio, given in equation 8.

$$A:V = \frac{4 \times aspect\_ratio}{dia(aspect\_ratio - 1/3)} \tag{8}$$

This general formula shows that as the segment aspect ratio approaches one (i.e. segment length = channel diameter) the value of A:V approaches 6/diameter. As segment length increases, the value of A:V approaches 4/diameter. This decrease in A:V with increasing slug aspect ratio occurs rapidly. For example, in a channel of diameter 500 μm, a segment of aspect ratio 1 affords a value for A:V of 12000 m^{-1}, increasing the segment aspect ratio to 4 results in a A:V value of 8727 m^{-1}, close to the theoretical minimum of 8000 m^{-1} for a slug of infinite aspect ratio. After calculation of the segment aspect ratios for each data point, the

corresponding A:V value was derived and applied to elucidate the mass transfer coefficient ($k/$(A:V)). The volumetric flow rate was converted to a linear flow velocity and the data plotted (Figure 26 and 27).
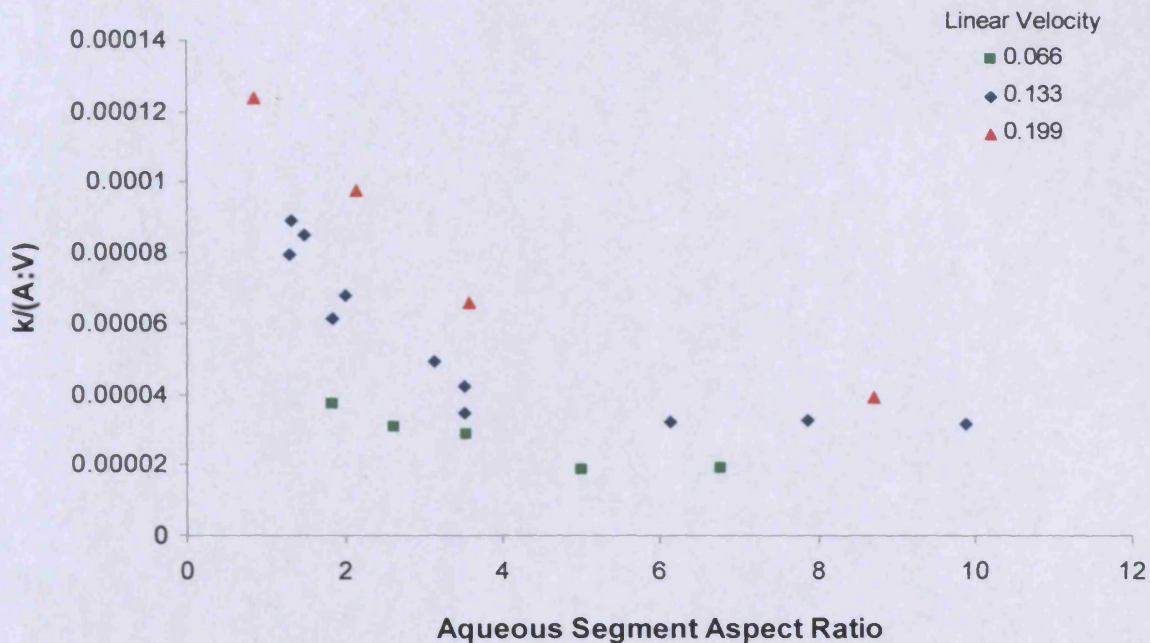
Figure 26 The influence of aqueous segment aspect ratio and linear flow velocity on extraction rate normalised for segment surface area to volume ratio ($k/(A:V)$) extrapolated and calculated from the experimental data presented by Lucy et al. for the extraction of caffeine from an aqueous solution into chloroform in segmented flow regimes with a 1:1 ratio of reagent flow, straight tubing of diameter 0.8 mm [8]

As concluded by the authors, the rate of extraction is seen to increase with respect to time with increased linear velocity and with decreased fluid segment aspect ratio. Interestingly with the data presented in the format of Figure 26, the mass transfer coefficient ($k/$(A:V)) accounts for the increased surface area to volume ratio associated with low aspect ratio segments and thus the divergence of the curves with decreasing segment length and increasing linear velocity is a genuine effect associated with increased mass transfer within the aqueous phase [8]. This can be concluded to be as a result of increased intra-segment mixing and/or a reduction in diffusional distances, either perpendicular to the local vector flow, or across the stationary Nernst-like diffusional layers which characterise a liquid–liquid interface (Section 3.4.4.4.1.2.1). Therefore the plots of Figure 26 can be considered to represent the extent of

mixing within a segmented flow regime, with respect to linear velocity and segment aspect ratio. Short segments and high flow velocity give rise to increased mixing and mass transfer. This is illustrated in the surface plot of Figure 27.
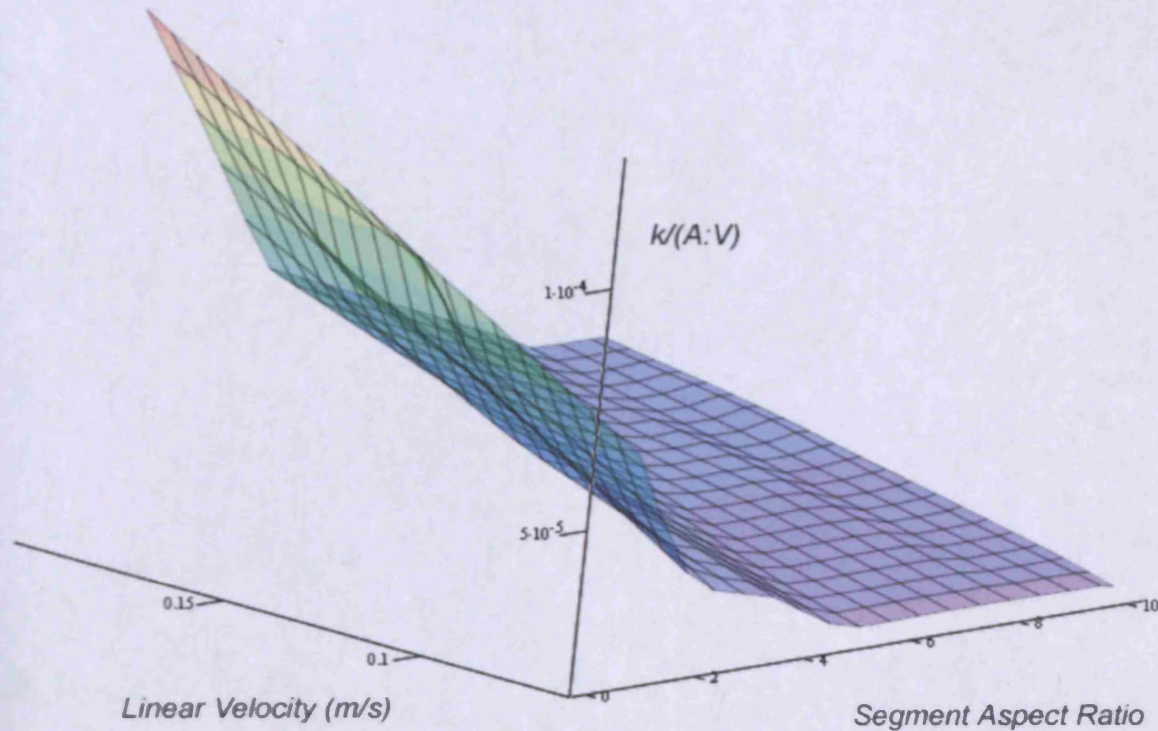
Figure 27 Surface plot illustrating mass transfer coefficient *(k/(A:V))* representing mass transfer within aqueous flow segments (extent of mixing and reduction in diffusional distances) with respect to segment aspect ratio and linear flow velocity. Values calculated from the data presented by Lucy and co-workers for the extraction of caffeine from an aqueous solution into chloroform in segmented flow regimes with a 1:1 ratio of reagent flow, straight tubing of diameter 0.8 mm [8].

3.4.4.3 Segment Aspect Ratio and Channel Diameter - Combined Effect on Extraction Rate Constant (*k*)

Returning to figure 23 which depicts mass transfer coefficient (*k*/(A:V)) against segment aspect ratio for a single linear velocity of 0.133 m s^{-1} in 0.3, 0.5, 0.8 and 1.0 mm diameter tubing. Fitting of the resultant data points to a single curve concludes that tubing diameter affects the extraction rate constant (*k*) only by the predictable decrease in surface area : volume ratio of the fluid segments. Thus for a given segment aspect ratio, the mass transfer

coefficient (k/(A:V)) is independent of channel diameter. This is perhaps a surprising conclusion, since intuitively it might be anticipated that segment width, together with linear velocity, will affect the re-circulatory mixing regime prevailing in the fluid segments, due to the proportional relationship each variable has to the dimensionless Reynolds number, which is sometimes used in characterising such flow regimes [11-14].

3.4.4.4 Reynolds Number Effects: Velocity and Channel Diameter

Several researchers have related extraction rate constants or radial mass transport in segmented flows to either the Reynolds number (Re) [11] or the Peclet number (Pe) [12], although velocity was the main experimental variable governing changes in Re investigated. The Peclet number (Pe) is a dimensionless number characterising the rate of advection of a liquid flow compared to the rate of mass diffusion, its value is equivalent to the product of the Reynolds number (Re) and the Schmidt number (Sc). The Schmidt number dimensionlessly characterises the behaviour of fluids where momentum and mass diffusive convection processes occur simultaneously, it is described by the ratio of momentum diffusivity (*viscosity/density* ≡ *kinematic viscosity*), to mass diffusivity described by the diffusion coefficient of Fick's law (*D*).

$$Sc = \frac{\mu}{\rho D} \tag{9}$$

$$Pe = \mathrm{Re} \times Sc = \frac{Lv}{D} \tag{10}$$

The appropriate characteristic length, L (m), applied in calculation of the Peclet number is the channel diameter for cylindrical channels. The relation of mass transfer or extraction rate directly to Re or Pe, would at first sight suggest a channel diameter influence on extraction comparable to that of velocity (v) (m s^{-1}).

Lucy and colleagues, investigating the dependency of extraction rate on flow velocity,

114

conclude from comparison of their data (represented in Figure 26 and Figure 27) with the findings of other researchers [6,11], that mass transfer in both air and liquid segmented flows is linked to the flow velocity by a power relationship, the power of which is less than one and decreases with increasing segment length. [8]. This conclusion is supported by that of Nord et al. who conclude that increasing flow velocity increases the rate of extraction with respect to time, but not with respect to distance [6], thus indicating a less than linear increase in extraction rate with increased velocity. The independence of ($k/$(A:V)) to channel diameter is also supported by the findings of Nord et al., who conclude that channel diameter has little effect on $k/$(A:V) (termed k_{tot} by the authors), with the difference in measured extraction rate constant (k, termed α by the authors) a consequence of the effect of surface area : volume ratio [6]. However, the experimental data to support this conclusion is limited to one velocity in three tubing diameters for segments of long aspect ratio (>11). Lucy et al.'s investigation into the variables affecting the kinetics of segmented flow liquid extraction, is the only thorough investigation reported in this research area of segmented flow liquid-liquid extractions, yet remains largely uncited (11 citations in the 19 years since publication). Other researchers have explored the effect of some variables on the effects of solvent extraction efficiency, but often with lesser insight into the dependent variables affected by the experiment's operational variables.

3.4.4.4.1 Reynolds Number Effects on Recirculatory Flow

In the context of the Bretherton problem [15], which concerns the mechanism of flow of a long air bubble in a channel filled with viscous fluid, Heil characterised the Reynolds number effect on the flow field ahead of the propagating bubble for low capillary numbers (Ca = 0.05). The flow models are illustrated in Figure 28 [16]. The author found that even at modest values of Re (<230) inertial forces played a significant role in determining the vortex nature of the flow regime. This is important, since inertial effects are often assumed to be of minor importance and consequently may not be considered, probably as a result of the absence of effect on flow

regime in single phase microfluidics, where flow remains laminar until inertial forces dominate viscous forces by the order of 2000-3000. For comparative purposes, a summary of dimensionless number values for the flow regimes employed in the work of this thesis is provided in appendix 2.
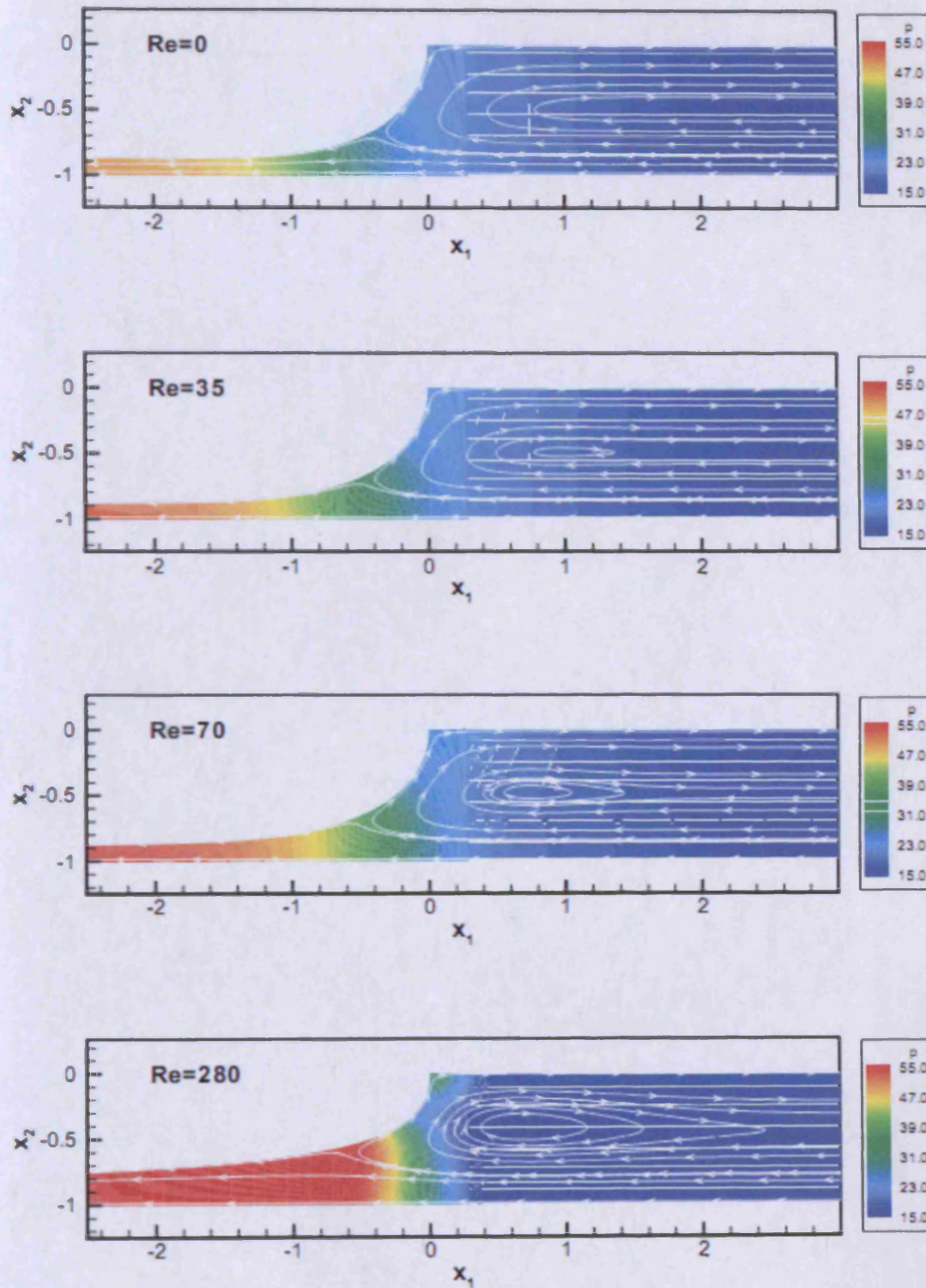
Figure 28 Inertial effects at finite Reynolds number flows induce vortex flow ahead of an advancing immiscible interface. Additionally, wetting film thickness is observed to grow and localised pressure gradients develop as a result. Simulations conducted by Heil [16].

Heil's simulations demonstrate that in the absence of inertial effects (Re = 0), recirculatory flow occurs, as frequently described as being characteristic of segmented or bubble flow streams. The vector flow arrows indicate the direction of fluid flow, relative to the advancing bubble tip. Consequently arrows indicating flow to the left, indicate flow at a lower velocity than the velocity of the advancing bubble tip and arrows indicating flow to the right, indicate flow velocities greater than that of the advancing bubble tip. In frame of reference to the stationary channel walls, all flow is of varying magnitude in the downstream direction (to the right). The viscous shear created by the no-slip conditions at the channel walls and fluidic interfaces creates a velocity gradient across the channel width, encouraging the flow to adopt the characteristic parabolic flow of laminar Poiseuille flow. (Chapter 1). Away from the bubble tip (Re = 0, x_1 = 1) this is well developed and laminar flow ensues, with fluid flowing in the centre of the channel travelling at twice the mean linear velocity of the fluid, (approximately equivalent to the advancing velocity of the immiscible interface). Due to the shear stress induced within the disperse phase by the thin film of continuous phase separating it from the channel walls, the same processes occur in the disperse fluid phase, in the context of Heil and Bretherton's work this is air, and in the context of the work of this thesis, water. In a segmented flow stream, the fluid flow in the channel centre, travelling faster than the downstream interface, approaches and then reaches the immiscible fluid interface. The dominance of surface forces over inertial forces (We) (being zero at Re = 0) and viscous forces (Ca) means that the interface is not ruptured and becomes only marginally deformed. Instead the interface deflects the approaching fluid towards the channel walls, introducing a radial contribution to fluid flow. At the channel walls the imposed shear stress, slows, or stagnates the fluid, depending on its proximity to the channel wall (or interfacial film in the case of the disperse phase). As a result of the shear stress, the liquid deflected by the interface now travels more slowly than the mean fluid velocity and is therefore approached by the upstream interface. When the upstream interface reaches the slow moving fluid near the channel walls, the above process occurs in reverse, with the interface again introducing a radial element to the otherwise Poiseuille like flow, deflecting the slow moving fluid to the centre of the channel. The reduced shear stress at the channel centre reduces resistance to

flow and consequently under the same driving pressure, the fluid now accelerates and the process repeats. It is this continual recirculation of fluid within the fluid segments that has the desired effect of reduced axial dispersion of a liquid flow. Additionally this process cycles the fluid in contact with the fluidic interface, thus increasing mass transfer rate compared to, for example, parallel flowing streams. It is this process which gives rise to the increased mass transfer observed in long fluid segments, with the rate of recirculation a function of velocity. Understanding of this flow regime also demonstrates how the assumption of classical Nernst diffusion layers in analysis of the mass-transfer of a segmented flow regime is not entirely applicable. Unlike parallel flowing streams, single phase flow or well stirred batch vessels, where a boundary layer of (relatively) stationary fluid is assumed, the circulating flow regime of segmented flow means that this layer is continually 'deposited' and removed by the trailing and advancing interface. Diffusion still plays a vital role in such flows however, as this recirculation process inevitably recirculates a large portion of the same fluid, with relatively stagnant regions of fluid travelling at an equal velocity to the interface, largely unaffected by the flow regime (Figure 29). Additionally mixing of fluid between to two sides of the channel axis is limited to diffusion, Ismagilov's research group demonstrated that chaotic advection could be introduced through introducing tight turns into the fluid flow path, thus causing differential mixing between the segment halves and enhancing overall intra-segment mixing [17].

| 0.0 | 0.0025 | 0.005 | 0.0075 | 0.01 |

% concentration of base
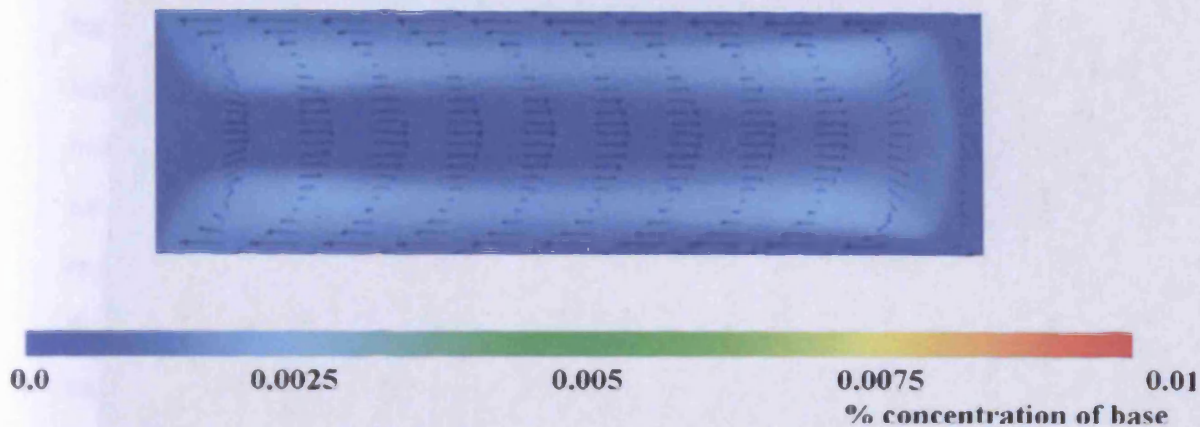
Figure 29 CFD simulation showing solute concentration map within an aqueous fluid segment during partitioning of solute into a neighbouring immiscible phase for an acid-base titration. Zones of higher solute concentration can be seen where fluid velocity is equal to that of the upstream and downstream interface and thus, unlike fluid in the channel centre or channel boundary, no recirculation of flow occurs and mass transfer from this region is governed by diffusion. Consideration of an axially symmetrical solute concentration map in three dimensions suggests that these flow domains may constitute a significant volume of the fluid segment. Simulations conducted by Harries et al. [18].

3.4.4.4.1.1 Significance of Inertial Forces

A significant finding of Heil's studies was the demonstration that the introduction of inertia to the problem has a significant impact on the field flow profile immediately ahead of the fluidic interface. The introduction of inertia by studying finite Reynolds number simulations, creates a closed vortex in the recirculatory flow ahead of the bubble interface. The size of the vortex can be seen to increase with increasing Reynolds number. Heil comments that at Re = 280, the vortex length increases to more than three times the channel half width [16]. The inertia of the fluid has a significant effect as the fluid is displaced by the advancing interfacial boundary, causing the fluid flow to continue on the deflected course, giving rise to the development of the vortex. This curvature of the flow streamlines introduce a centrifugal pressure gradient away from the centre of recirculation. The balance of this effect either side of the interface, governed by the physical properties of the fluids, can affect the interface curvature, causing elongation or flattening of the fluidic interface. This is particularly well observed in gas-liquid flows [19] where significant differences in physical properties exist and the advancing gaseous bubble tip can be seen to elongate and the rear interface flatten, due to the greater inertia of

the liquid phase. Additionally this also affects the deflection of continuous phase fluid away from the channel wall and consequently the liquid flow though, and pressure in, the wetting liquid film increases. These phenomena are probably of minor importance with regard to mass transfer from a disperse phase, unless the analyte concentration in the thin film approaches saturation, although the effect may be more influential if the extraction were reversed and mass transfer was from the continuous phase into the disperse phase. However, these findings by Heil have significant implications with regard to pressure drop due to flow of a multiphase flow stream, which unlike Poiseuille flow of a single phase, is not easily characterised by an empirical rule. Returning to the context of mass transfer, the vortex flow created at finite Reynolds number will contribute to increased radial mass transfer to and from the fluid interface. The vortex flow will also facilitate increased mixing between the recirculating and comparatively stagnant regions of the global recirculating flow within the entire fluid segment, thus reducing diffusional dependencies. Importantly this feature explains the importance of segment aspect ratio on the rate of extraction. In short segments the total contribution of the mass transfer due to the vortex flow will be great compared to that due to the recirculation of Poiseuille like flow (Section 3.4.4.4.1). In comparison, as the segment length increases, the contribution to mass transfer due to the vortex flow becomes small compared to that of the overall global recirculating flow. Thus as segment length is increased, the rate of mass transfer approaches a minimum, equivalent to that where there is no vortex flow (Re = 0). Consequently in short segments, the contribution of velocity to mass transfer rate is two fold, both increasing the rate of global recirculation within the fluid segment and increasing the inertial component of the flow, thus increasing the development of the vortex flow at the segment ends. Since the vortex size illustrated by Heil is expressed dimensionlessly as a function of channel width, it is segment aspect ratio rather than absolute length which is important in determining the relative contribution of the two flow behaviours. Heil comments that the inertial effects are most significant at high values of Reynolds number and small capillary numbers, expressing a Re/Ca value of 5600 required to give rise to the flow regime illustrated in Figure 28. at Re=280. The Re/Ca values for the flows studied in this thesis are all typically >15000, suggestive of a well developed vortex flow at segment ends.

Full details of dimensional and dimensionless properties of the flow regimes investigated can be found in appendix 2.

3.4.4.4.1.2 Diffusional Distances

The Reynolds number (Re) characterises the ratio of inertial to viscous forces. For a given fluid, the Re can be increased by an increase in either velocity or channel diameter, with the velocity increase increasing the inertial component and an increase in channel diameter decreasing the viscous component. It may therefore be anticipated that increasing either variable will result in increased vortex flow. Although not discussed by Heil, the Weber number (We) characterises the ratio of viscous forces to surface forces, consequently, the value of this number may be expected to influence the extent of deflection of fluid by the phase interface and possibly the extent of vortex flow. It is likely that Heil's theoretical approach to fixing Ca and varying Re accounts for this, owing to the intrinsic link of the three dimensionless variables (Re = We/Ca), however from a practical perspective it is unfeasible to maintain Ca whilst evaluating Re effects. The separate effects of inertia and viscosity may contribute to the observed effect of extraction rate normalised for area to volume ratio (k/(A:V)) being independent of channel diameter, despite the Reynolds number implications of this variable. Considerable CFD analysis would be required to further characterise these relationships since this was not the context of Heil's research. Another possible contributing effect for the observed independence of k/(A:V) to channel diameter, is that any vortex or recirculatory mixing improvement afforded by the increase in channel diameter is offset, in whole or in part, by an increase in diffusional distances for the analyte within the recirculating flow regime. This is as a result of diffusive mixing time being proportional to the square of the mixing length (m) for a given diffusion coefficient (D).

$$t = \frac{L_{diffusion}^{2}}{2D} \tag{11}$$

From the experimental data reported in this thesis and that presented in the literature, it is not

possible to entirely rule out a channel diameter contribution to extraction rate outside that of the afforded surface area : volume ratio. This is due to relative lack of sufficient experimental data over a range of channel diameters and flow rates to distinguish any possible weak relationship from experimental error or variance. Additionally the mathematical studies conducted to date have tailored their analysis to different theoretical problems (e.g. Bretherton problem, the radial mass transfer of solutes away from channel walls, or the diffusion of air dissolving from an air plug into a continuous liquid phase). The velocity contribution to mass transfer enhancement is two fold, affecting both the manifestation of vortex flow and the rate of replenishment of the interfacial pseudo-stationary layer at the extraction interface. Any channel diameter mediated effects can, at most, only be considered to enhance the manifestation of vortex flow by the resultant increase in Re, thus a lesser effect can be anticipated. Whether this is offset wholly, or in part by increased diffusional distances is not clear from the presented data. Consideration of dimensionless Sherwood number for mass transfer operations, suggest that complete modelling of the extraction behaviour is non-trivial, owing to the intermediary behaviour of the fluid flow between that of laminar and turbulent systems.

3.4.4.4.1.2.1 Sherwood Number

The Sherwood number (Sh) provides a dimensionless measure of mass transfer mechanisms. In theoretically related fluid dynamics mass transfer studies, Frössling [20] studied gas transfer from gaseous bubbles into surrounding liquid with dimensional analysis, elucidating the empirical formula

$$(Sh) = a \times (\text{Re})^b \times (Sc)^c \tag{12}$$

where (Sh) is the Sherwood number, sometimes referred to as the mass transfer Nusselt number (as a variation on the equivalent dimensionless number for heat transfer). Sh represents dimensionlessly the ratio of convective and diffusive mass transport. The Sherwood number is defined as

$$Sh = \frac{kmtc \times L}{D}$$

(13)

where *kmtc* is the mass transfer coefficient possessing the units of m s^{-1} and defined by the mass transfer rate over an area, driven by a concentration gradient.

$$kmtc = \frac{mass\_transfer\_rate}{A \times \Delta C_A}$$

(14)

where the mass transfer rate, (*mass_transfer_rate*) is measured in mol s^{-1}, A is the area over which mass transfer occurs (m^2) and ΔC_A is the concentration difference (mol m^{-3}) which drives the mass transfer. The general formula proposed by Frössling has been utilised with a variety of values for the parameters *a*, *b* and *c*, depending on application and is also commonly expressed in the form

$$(Sh) = a'\times(Pe)^{b'}$$

(15)

The value of *b'* has been shown to vary from 1/3 to 1/2 for conditions of a rigid spherical bubble and a sphere with a mobile surface, respectively. The range of values for *a'* and *b'* in conjunction with specific scenarios have been outlined [21]. This relationship of Pe raised to a power of less than one, is interesting, since Pe includes a velocity term, and therefore (*Sh*) in the problem of gas dissolution displays a similar dependency to velocity as that concluded by Lucy and Nord for liquid-liquid extraction [8,6]. A more complex but arithmetically similar relationship has also been elucidated for radial mass transfer in a liquid continuous phase, segmented by otherwise passive air segments, with Sh relating to $Pe^{0.599}$ amongst numerous numerical factors and the segment aspect ratio [12]. The authors noted the complex variable set, concluding that even with a dimensionless variable analysis approach an unfeasibly large experimental data set would be required to fully characterise the problem. Consequently a limited experimental data set was obtained to support a large body of theoretical CFD studies in the context of seven dimensionless groups. However experimental validation was limited to

a range of Pe numbers generated in a single tube of 1 mm I.D. It should also be noted that the study concerned only the radial mass-transfer of reagent from the channel walls, into the fluid bulk of the continuous phase. It has however been reported that the axial and radial contribution to extraction from a disperse liquid segment are equal per unit area of the interface [10]. In addition, since comparable recirculatory and vortex flow regimes exist in both the continuous and disperse phases of a segmented flow regime, due to the shear stress induced at the channel wall and interface of the thin wetting film respectively, it is reasonable to draw comparison between the situations. However, direct application of relationships established in studies like those of Gruber and Melin, or those based on the work of Frössling, may be inappropriate for a number of reasons. Firstly, the work of Gruber and Melin [12] considered mass transfer of copper ions from the copper channel walls, and the subject of much of the work following on from the early work of Frössling considers the mass transfer of dissolved gasses originating from the disperse phase bubble into the continuous phase liquid. In both instances a near infinite supply of analyte exists and diffusive relationships can be established with the assumption of a zero concentration at the interface, instead considering the overall bulk concentration in the fluid, which acts as a sink, with the mass-transfer systems often operating far from an equilibrium defined by saturation. Often studies relating Sh to Pe study bubbles in an unrestrained system (i.e. no channel walls), or are applied to liquid-liquid extraction in the context of batch processers, where fluid reservoirs are assumed to be well mixed and the characteristic diffusion length scale is defined by a pseudo-stationary fluid film, or Nernst diffusion layer (Figure 30). This gives rise to a practical approximation representative of a completely stagnant layer at the phase interface, where diffusion completely dominates mass transfer between the interface and the turbulently mixed bulk of the fluid of uniform concentration [22].
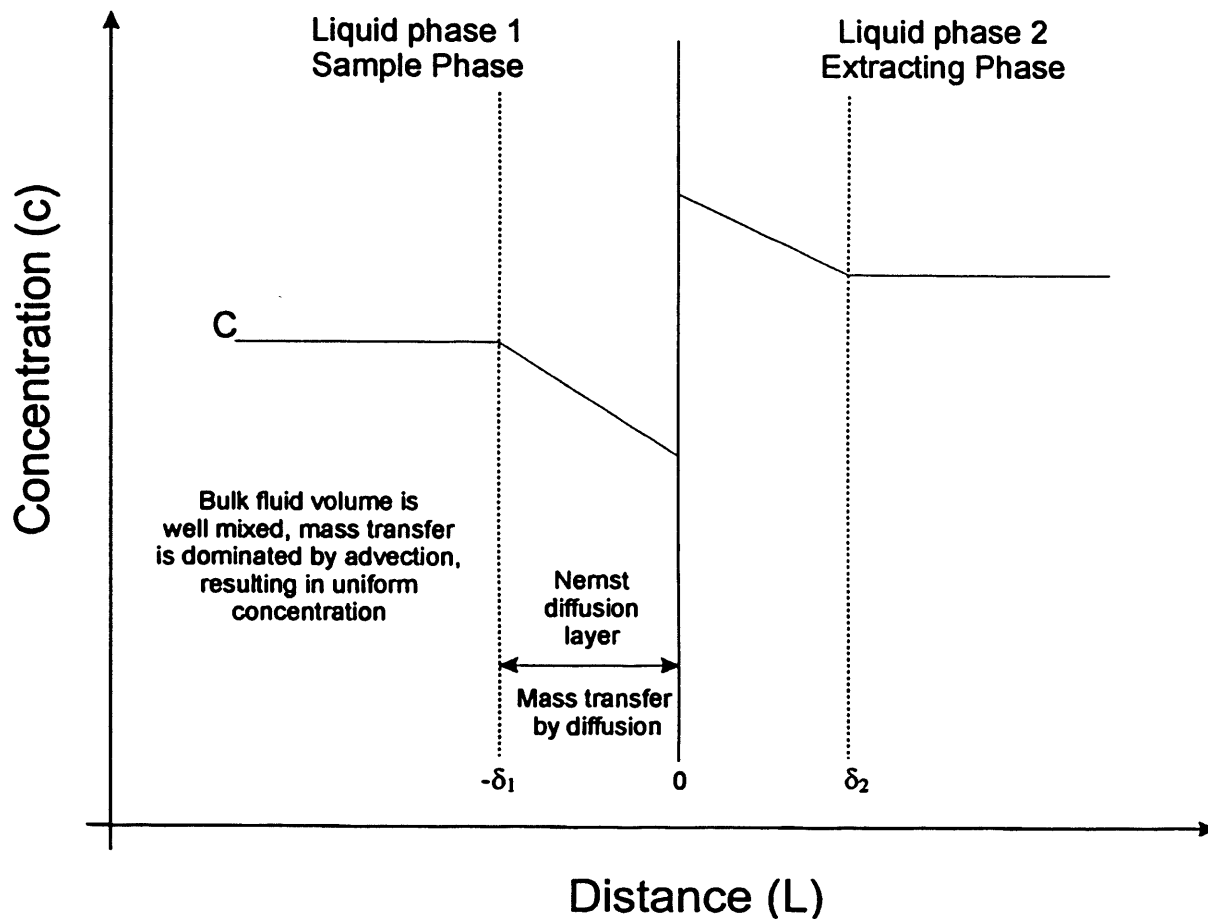
Figure 30 Liquid–liquid interfacial model for typical mass transfer at immiscible interfaces. The model assumes the bulk of the fluid volume is well mixed and of uniform concentration, where mass transfer is dominated by advection. A thin stationary liquid film, or Nernst layer, exists either side of the liquid interface, where mixing is low and fluid is assumed stagnant. In this region diffusion dominates mass transfer processes and as such, concentration gradients develop across the Nernst diffusional layer. In classical liquid-liquid extraction, this model describes the mass transfer of the extraction process, the thickness of the fictitious Nernst layer representing the diffusional length. This layer thickness is defined in part by extent of mixing in the bulk fluid.

Such approximations are difficult to apply to microfluidic flow situations. In single phase microfluidic flow, where Poiseuille, or laminar flow, predominates at low Re numbers, the parabolic flow regime from the channel walls to the channel centre is comparable to the boundary layer, viscous force dominated flow, existing close to channel walls or interfaces in turbulent flows (i.e. pipe flow or air flow over an aeroplane wing). In such turbulent flow examples, the Nernst boundary layer differentiates the regions of diffusion dominated mass transfer (within the boundary layer) and momentum dominated mass transfer (in the turbulent bulk). Consequently in Poiseuille flow, where fluid mixing is poor and no bulk region exists

where momentum dominated mass transfer occurs, the model of Figure 30 can not be applied as no defined region of uniform concentration within the liquid phase exists. Instead, since diffusion dominates radial mass transfer in such single phase flows, the half channel width can be considered akin to the boundary layer, and therefore defining the diffusional length scale.
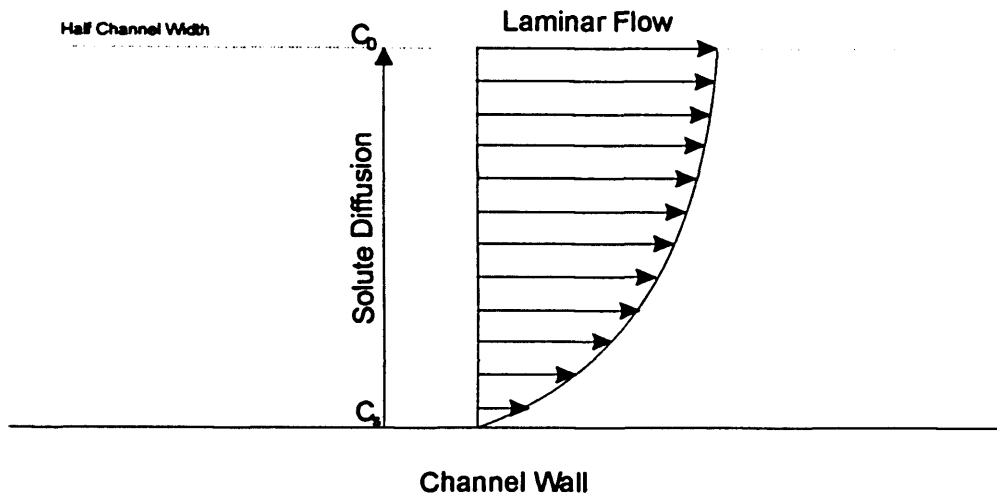
Figure 31 Diffusion dominated radial mass transfer in laminar flow. The figure illustrates the diffusion of solute material from a channel wall to the centre of the channel, perpendicular to the direction of flow. The diffusional distance equates to the channel half width.

3.4.4.4.1.2.1.1 Diffusional Models and Difficulties in Their Application to Segmented Flows

The application of mass transfer models or approximations to multiphase flows is somewhat more complex than the examples illustrated in Figure 30 and Figure 31, for turbulent and laminar systems respectively. In segmented flow, variations of Poiseuille flow and vortex flow co-exist to differing degrees dependent on a number of variables. Within fluid segments of a segmented flow regime regions of diffusion dominated mass transfer are present (Figure 29), together with regions of convective vortex mixing (Figure 28), consequently the segment bulk can neither be considered to be of uniform concentration (akin to the example in Figure 30), nor can a uniform concentration gradient be assumed to exist from the liquid bulk to the interfacial boundary (akin to the example in Figure 31). Additionally, unlike either of the

described models, in segmented flow, the interfacial pseudo-stationary layer at the extraction interface is constantly replenished with fluid from the axial region of the segment. The rate of replenishment of the fluid at the interfacial boundary is a function of the segmented flow velocity. Whilst interfacial mass transfer may only proceed from the fluid in proximity to the interfacial phase boundary, diffusion perpendicular to the flow of parallel flowing fluid layers will take place at all stages of the circulatory flow cycle. Consequently a complex relationship exists, defining the relative contribution of diffusive and advective mass transfer processes within the fluid segment as well as phase boundary transfer. Owing to the combined effect of the above mentioned processes, the diffusional length scale is not clearly defined, making Sh difficult to define or resolve further. In light of this, Horvath and colleague's description of the mass transfer processes of segmented flow lying somewhere between that of laminar flow and turbulent flow [30] would appear an accurate assessment..

Understanding and characterisation of the flow profile in fluid segments is necessary to contextualise the importance of aspect ratio, velocity and channel dimensions on the rate of mass transfer and consequently extraction in such flows. It is important to develop a qualitative understanding of the process variables, even if quantitative elucidation of general numerical solutions proves difficult.

3.4.5 Channel Curvature - Dean Flow

Returning to the data of section 3.4.2 obtained in assessing the on-chip, segmented flow extraction of propranolol from an aqueous solution into chloroform. This established a relationship between the extraction rate coefficient (k) and the on-chip linear flow velocity for both observed extraction behaviours, liberating a v^a relationship in both instances, with the magnitude of a being of the order of one in each instance. It was noted that this velocity dependency was greater than that reported by Lucy et al. in their study of the segmented flow, liquid-liquid extraction of caffeine [8], and also the descriptive relationship of Nord et al. who describe a velocity dependent increase in the rate of extraction with respect to time, but not

distance, implying a less than linear increase [6]. This measured velocity dependency is also greater than the relationship inferred by Gruber et al. in their study of radial mass transfer in air-segmented flow [12]. It was considered a possibility that this finding was a consequence of the tight turns employed in the fluidic channel structure, introduced in order to maximise the segmented flow residence time on the microfluidic chip. Such turns introduce additional mixing enhancements within the segments of the flow stream.

3.4.5.1 Rapid Reorientation

At tight junctures a degree of re-orientation of the fluid segment occurs as the liquid segment navigates the channel curvature (Figure 32). This re-orientation of the fluid in the radial direction promotes mixing within the fluid segment. The characteristic axially recirculating flow pattern associated with segmented flow, tends to discretely recirculate the segment fluid either side of the channel central axis. The radial redistribution of fluid during the rapid re-orientation proccess, facilitates mixing between the segment halves [17]. Song et al. liken this process occurring in a series of winding channels to a 'baker's transformation' of stretching, folding and reorientation, with each successive manipulation reducing the diffusional distances within the fluid segment and reducing the evolution of poorly mixed regions of fluid whilst simultaneously facilitating mixing between the otherwise convectively discrete halves of the fluid segment. This process gives rise to rapid mixing within fluid segments, creating uniform distributions of analyte within individual fluid packets on the millisecond timescale [23]. Whilst this approach to mixing will reduce the time requirement for diffusion to uniformly distribute reagents within an individual fluid segment, the effect on inter-segment mass transfer has not been characterised. It is probable that the process of flow through the curved portion of the channel induces inertially driven Dean-flow, which is described in section 3.4.5.2. This flow regime results in the reported reorientation of segment contents, the interfacial mass transfer enhancement attributed to this flow phenomena is also described in section 3.4.5.2. The more uniform distribution of analyte within the segment volume should eliminate any time dependency in the extraction process for analyte diffusion *within* the fluid segment, thus limiting the rate of extraction to that across the pseudo-stationary fluid layer at the phase

boundary, and consequently this 'layer' thickness and rate of replenishment. A strong radial flow component can be expected to be introduced during the course of flow though the tight turns of the on-chip channel architecture (section 3.4.2), thus enhancing phase boundary mass transfer whilst resident in the curved portion of the channel. On the resumption of characteristic axial recirculatory flow in the straight portion of the channel, it may be expected that improved distribution of analyte within the fluid segment will have a modest effect on interfacial mass transfer, with diffusion through the axially recirculating, Poiseuille-like layers, likely to constitute the rate limiting factor for phase transfer in the absence of radial elements to the flow regime. It should be noted that in very sharp (i.e. 180°) bends the fluid on the inside of the passing segment may approach being stationary and thus for the period of transit both radial and the axial recirculatory flow will enhance extraction on one side of the fluid segment more substantially than the other, thus some limitation or compromise to the afforded performance enhancement may be evident. In conclusion, the presence of tight curvature on the on-chip extraction can be expected to enhance interfacial phase transfer to a comparable extent to that of coiled tube based extraction system (section 3.4.5.2) with extremely tight coils interspersed with straight sections of tubing. The interfacial phase transfer enhancement is not anticipated to be as dramatic as the intra-segment analyte distribution enhancement reported by Song and Ismagilov [23]. It is possible that the extraction enhancement as a result of this mechanism, together with pressure effects affecting segment length (Chapter 4), and thus degree of vortex flow contribution, may account for the greater than expected dependency of extraction rate of linear flow velocity.
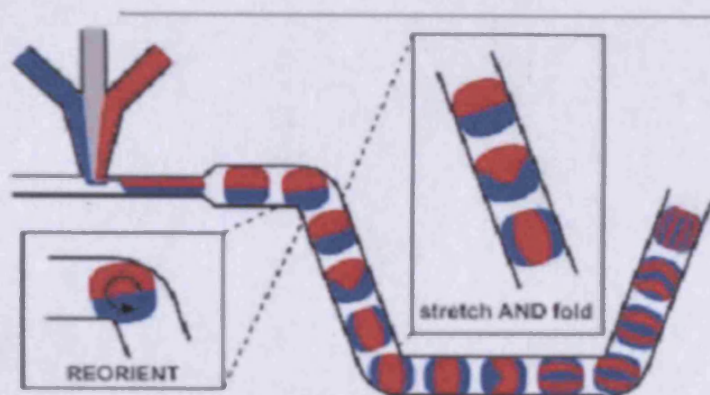
Figure 32 Illustration by Song et al. demonstrating the improved intra-segment mixing resulting from rapid reorientation of fluid segment contents by tight channel curvature, combined with the axially recirculating flow pattern associated with segmented flow. The reduced diffusional requirement for uniform analyte distribution is apparent of several successive re-orientation transformations [17].

3.4.5.2 Dean Flow

The effect of channel curvature on the flow of fluid in channels has long been established and has been well characterised with respect to single phase flows [24,25]. In Poiseuille flow, the axial flow velocity profile together with curvature in the tubing, generates a centrifugal force tangential to the direction of flow. This force is greatest for the fastest moving fluid in the centre of the channel, this fluid therefore advances towards the outer channel wall and is replaced by fluid flowing tangentially from the walls, thus introducing a radial element to the flow. This effect is a function of the inertial and viscous forces of the flow and the degree of curvature, or coiling, of the flow path [26]. These effects are characterised dimensionlessly by the Dean number

$$De = \frac{\rho v L}{\mu}\left(\frac{L}{R}\right)^{0.5} \tag{16}$$

The Dean number is a product of the Reynolds number and the square root length scale ratio of the characteristic length of the channel cross section (i.e. diameter for cylindrical tubes) and the radius of curvature of the path of the channel, (*L/R*). The phenomenon has been exploited

through the use of tightly coiled tubes to minimise axial dispersion in chromatographic applications, and to improve the efficiency of heat exchangers.
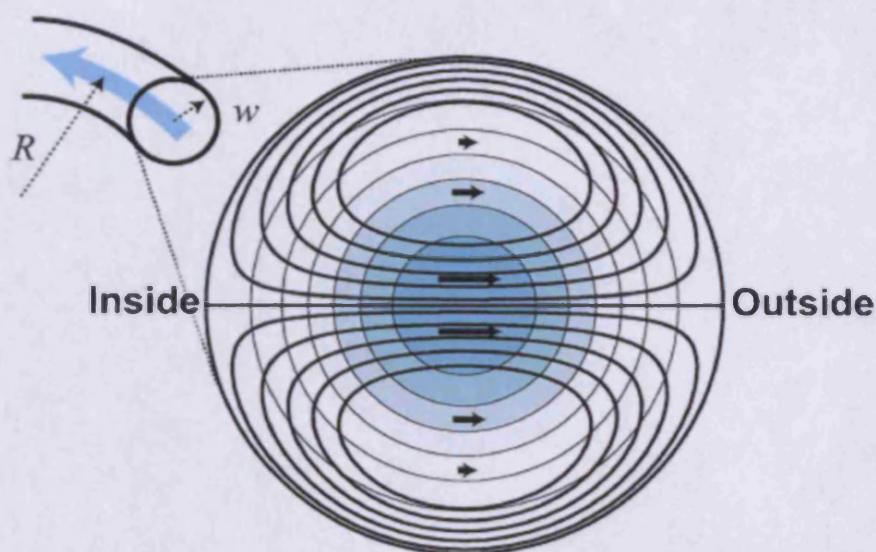
Figure 33 Illustration of the secondary Dean flow induced by inertial forces acting on a fluid flowing in a curved channel. The single phase fluid flow, flowing in an otherwise laminar fashion is forced centrifugally towards the channel outer wall. The effect is greatest for the fastest flowing fluid in the channel centre, resulting in the depicted recirculatory flow illustrated in the plane of the page. [27]

Mass transfer in 'Dean flow' is described by the product of the Schmidt number and the Dean number squared [28] (De^2Sc), and therefore for a given Reynolds number flow, the dimensionless descriptor for mass transfer increases directly with the tightness of the coiling of the tubing or channel. The degree of recirculatory flow increases with increasing Dean number, with elliptical recirculation prevalent at De < 20. At higher Dean numbers (De > 100) inertial forces become increasingly influential over viscous forces and the recirculating flow becomes more pronounced (Figure 34). Fluid flows to the outer channel wall parallel to the plane of the coil, before flowing closely to the channel wall, migrating to the inner most edge of the channel before once again being centrifugally driven to the outer edge. These flow regimes are depicted in Figure 34. The establishment of Dean-flow, also has the effect of increasing pressure drop due to flow along the length of the channel [26], the effect of pressure itself as a variable on the rate of liquid extraction or mass transfer is likely to be insignificant at the relatively low pressure differentials encountered, however the effect of

pressure differentials and local pressure gradients on dependent variables such as wetting film thickness, local flow regimes (i.e. vortex flow), and importantly segment length may play additional roles in determining extraction kinetics.
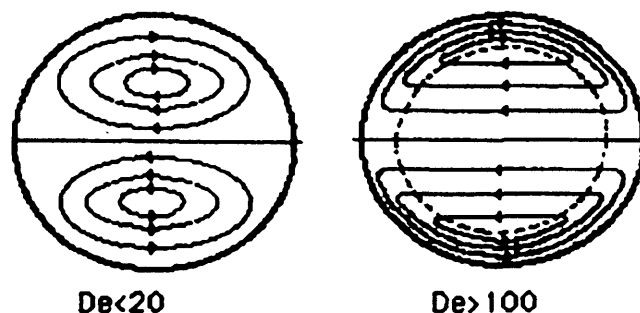
Figure 34 Development of secondary flow at high and low Dean numbers[29].

In segmented flow systems, Dean flow augments the recirculatory flow prevalent in the axial direction to further enhance convective mass transport. This has been demonstrated to be particularly important in long segments [8], where extensive vortex interaction is absent and a high degree of Poiseuille like flow is prevalent. This creates an axial velocity differential across the channel radius, and thus generates a centrifugal force differential as the segmented flow stream flows through the curvature in the channel or tubing. In short segments, vortex interaction generates a significant radial element to flow, reducing the axial velocity differential across the channel radius and therefore the centrifugal force acts more uniformly across the fluid volume, reducing the effect. The data presented by Lucy et al. illustrates a 5 times increase in $k/(A:V)$ for segments of aspect ratio 9.9 and 3.5 in 0.8 mm diameter tubing of coil diameter 6.7 cm and 1.7 cm respectively ($k/(A:V) = 1.5 \times 10^{-4}$ m s^{-1} and 2.0×10^{-4} m s^{-1}), compared to a three times increase for the shorter, aspect ratio = 2, fluid segments at a coiling diameter of 1.25 cm ($k/(A:V) = 2.0 \times 10^{-4}$ m s^{-1}). For each segment length, further decreasing the coil diameter had little or no further effect on rate of extraction. The increased surface area : volume ratio afforded by the very small aspect ratio segments, means that the overall rate constant (k) for the extraction is still greatest for the shortest segments studied (aspect ratio = 2) despite the less substantial increase in mass transfer due coiling the extraction tubing. In Lucy's experiments, a greater degree of coiling was required to observe an extraction rate enhancement in the short aspect ratio segmented flow regime compared to the moderate and

longer segments studies. These extractions, at a flow velocity of 0.133 m s^{-1} (4 ml min^{-1}), considerably higher than flow rates likely to be employed for MIP based extractions, yield a De^2Sc of between 10^5 and 10^6. At lower velocities, a lesser but still significant effect is anticipated. Interestingly, the effect of 'Dean flow' – like radial recirculation provides another mechanism for mass transfer enhancement with a velocity dependency.

3.4.6 Outlook

The complex relationship reported between curvature of the flow path, segment aspect ratio and flow velocity, demonstrate the complex interplay between the multi-dependent variables affecting segmented flow extraction. The difficulty in controlling numerous dependent variables and systematically evaluating the effect of a single parameter presents a near impossible task and an unfeasible amount of experimentation. Consequently, the importance of Lucy and Cantwell's thorough and insightful work should not be overlooked and gives an excellent overview of the variables which should be considered when attempting to either optimise a segmented flow mass transfer operation, or elucidate fundamental parameter effects. The complex variable set, together with the non-linear relationships between many of the variables and their effects, makes it difficult to establish more than general trends of variable effects on the rate of liquid-liquid extraction, whilst literature comparison is often difficult due the absence of influential data (segment length, coiling diameter, coiled or straight tubing etc) from studies. It would appear that fluid dynamics and mass transfer mechanisms fundamental to the problem are sufficiently well characterised for CFD simulation to offer a viable approach to establishing robust empirical mathematical relationships governing the segmented flow extraction process. However these would need to be extremely well thought out to ensure that inappropriate assumptions for the ease of modelling are not made which could massively effect the findings of such studies. Dimensionless analysis offers a extremely useful approach for elucidating variable-effect relationships and easing data handling and visualisation. However, once again, care needs to be taken to ensure the correct dimensionless groups are employed and the analysis is followed through to the dimensionless measure of extraction. Inappropriate selection, or absence of required dimensionless groups may generate error or

ambiguity. Ultimately it would be desirable for individual variable effects (i.e. velocity, channel diameter, etc) to be described, this may increase uptake and encourage effective employment and also reporting of segmented flow mediated mass-transfer enhanced operations. Table 7 illustrates the contribution of several major variables to interfacial mass transfer in segmented flow regimes. It should be noted that many of the definable variables governing segmented flow phase boundary mass transfer, impact upon secondary dependent variables which may also impact upon the mass transfer processes. Figure 35 illustrates the multiple dependent variables present in an outwardly appearing 'simple' segmented flow extraction.

Table 7 Summary of major variables and their contribution to phase boundary mass transfer in segmented flow regimes. Many of the relationships are non-linear and the variables also impact upon other secondary variables influencing mass transfer effects.

Variable	Mass transfer effect	Mechanism
↑ Linear velocity	Increases mass transfer with respect to time Decreases mass transfer with respect to flow distance	Increased recirculatory flow Increased vortex flow Increased contribution from dependent variables
↓ Tubing diameter	Increases mass transfer decreases throughput	Increased surface area to volume ratio
↓ Segment length	Increases mass transfer	Increased contribution of vortex flow Interaction of vortex flow occurring at segment ends Increased surface area to volume ratio (minor effect)
↑ Curvature or coiling	Increases mass transfer	Introduction of Dean flow, enhancing radial extraction and encouraging segment re-orientation
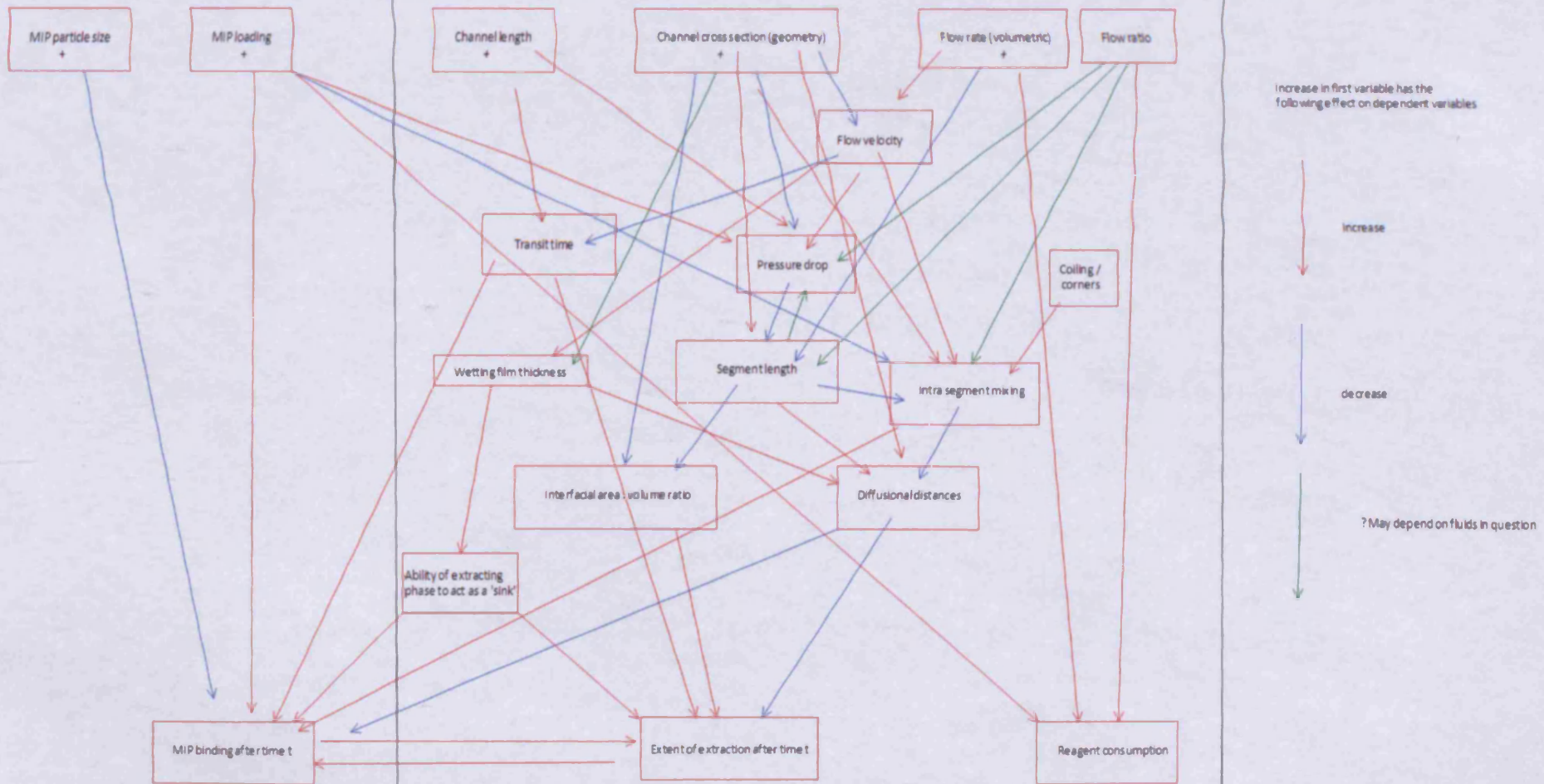
Figure 35 Variable dependency map illustrating the multiple dependencies governing interfacial mass transfer within segmented flow liquid-liquid extraction regimes.

3.5 Conclusions

Whilst segmented flow will almost always offer significant mass transfer advantages over single phase laminar flow [12] or laboratory batch scale mass transfer processes [4], the exact magnitude of enhancement will be dependent upon several key, operator definable variables, most notably segment aspect ratio and flow velocity. The contribution of these and other variables, together with the interplay between them represents a complex process which is not readily quantitatively predictable, however, an understanding of the processes governing mass transfer as identified and discussed here will enable initial qualitative approaches to extraction optimisation. The work of this chapter is continued in chapter 4 with the introduction of MIP material to the extracting phase to enhance the extent of liquid extraction.

3.6 References

[1]   H. Song, J.D. Tice, and R.F. Ismagilov, "A microfluidic system for controlling reaction networks in time," *Angewandte Chemie (International ed. in English)*, vol. 42, Feb. 2003, pp. 768-72.

[2]   J. Wang et al., "Monodisperse, molecularly imprinted polymer microspheres prepared by precipitation polymerization for affinity separation applications," *Angewandte Chemie (International Ed. in English)*, vol. 42, Nov. 2003, pp. 5336-8.

[3]   N. Greene and K. Shimizu, "Colorimetric Molecularly Imprinted Polymer Sensor Array using Dye Displacement," *Journal of the American Chemical Society*, vol. 127, Apr. 2005, pp. 5695-5700.

[4]   B. Ahmed, D. Barrow, and T. Wirth, "Enhancement of Reaction Rates by Segmented Fluid Flow in Capillary Scale Reactors," *Advanced Synthesis & Catalysis*, vol. 348, 2006, pp. 1043-1048.

[5]   J.R. Burns and C. Ramshaw, "The intensification of rapid reactions in multiphase systems using slug flow in capillaries ," *Lab on a Chip*, vol. 1, 2001, pp. 10-15.

[6]   L. Nord et al., "Extraction rate in liquid-liquid segmented flow injection analysis," *Analytica Chimica Acta*, vol. 194, 1987, pp. 221-233.

[7]   J. Pawliszyn, *Sampling and sample preparation for field and laboratory: Fundamentals and New Directions in Sample Preparation*,Oxford: Elsevier, 2002.

[8]   C.A. Lucy and F.F. Cantwell, "Kinetics of solvent extraction-flow injection analysis," *Analytical Chemistry*, vol. 61, Jan. 1989, pp. 101-107.

[9]   P. Kuban, J. Berg, and P. Dasgupta, "Vertically Stratified Flows in Microchannels. Computational Simulations and Applications to Solvent Extraction and Ion Exchange," *Analytical Chemistry*, vol. 75, Jul. 2003, pp. 3549-3556.

[10] C.A. Lucy and F.F. Cantwell, "Mechanism of extraction and band broadening in solvent extraction-flow injection analysis," *Analytical Chemistry*, vol. 61, Jan. 1989, pp. 107-114.

[11] C. Horvath, B.A. Solomon, and J. Engasser, "Measurement of Radial Transport in Slug Flow Using Enzyme Tubes," *Industrial & Engineering Chemistry Fundamentals*, vol. 12, Nov. 1973, pp. 431-439.

[12] R. Gruber and T. Melin, "Radial mass-transfer enhancement in bubble-train flow," *International Journal of Heat and Mass Transfer*, vol. 46, Jul. 2003, pp. 2799-2808.

[13] R. Gruber, "Radial Mass Transfer Enhancement in Bubble-Train Flow," Institut für Verfahrenstechnik der RWTH. 2002.

[14] D. Rosso, D.L. Huo, and M.K. Stenström, "Effects of interfacial surfactant contamination on bubble gas transfer," *Chemical Engineering Science*, vol. 61, Aug. 2006, pp. 5500-5514.

[15] F.P. Bretherton, "The motion of long bubbles in tubes," *J. Fluid Mech.*, vol. 10, 1961, pp. 166-188.

[16] M. Heil, "Finite Reynolds number effects in the Bretherton problem," *Physics of Fluids*, vol. 13, 2001, p. 2517.

[17] H. Song et al., "Experimental test of scaling of mixing by chaotic advection in droplets moving through microfluidic channels," *Applied Physics Letters*, vol. 83, Dec. 2003, pp. 4664-4666.

[18] N. Harries et al., "A numerical model for segmented flow in a microreactor," *International Journal of Heat and Mass Transfer*, vol. 46, Aug. 2003, pp. 3313-3322.

[19] M.T. Kreutzer et al., "Inertial and interfacial effects on pressure drop of Taylor flow in capillaries," *AIChE Journal*, vol. 51, 2005, pp. 2428-2440.

[20] N. Frössling, "Über die Verdunstung fallender Tropfen," *Gerlands Beiträge zur Geophysik*, vol. 52, 1938, pp. 170-215.

[21] P. Somasundaran, *Encyclopedia of Surface And Colloid Science*. London: Taylor & Francis Group, 2004.

[22] J. Rydberg, M. Cox, and J.R. Rydberg, *Solvent extraction principles and practice*, London: CRC Press, 2004.

[23] H. Song and R. Ismagilov, "Millisecond Kinetics on a Microfluidic Chip Using Nanoliters of Reagents," *Journal of the American Chemical Society*, vol. 125, Nov. 2003, pp. 14613-14619.

[24] W.R. Dean, "Note on the motion of fluid in a curved pipe," *Phil. Mag*, vol. 4, 1927, pp. 208-223.

[25] S.W. Jones, O.M. Thomas, and H. Aref, "Chaotic advection by laminar flow in a twisted pipe," *Journal of Fluid Mechanics Digital Archive*, vol. 209, 2006, pp. 335-357.

[26] P. Naphon and S. Wongwises, "A review of flow and heat transfer characteristics in curved tubes," *Renewable and Sustainable Energy Reviews*, vol. 10, Oct. 2006, pp. 463-490.

[27] T.M. Squires and S.R. Quake, "Microfluidics: Fluid physics at the nanoliter scale," *Reviews of Modern Physics*, vol. 77, Jul. 2005, pp. 977-50.

[28] R. Tijssen, "Axial dispersion and flow phenomena in helically coiled tubular reactors for flow analysis and chromatography," *Analytica Chimica Acta*, vol. 114, Feb. 1980, pp. 71-89.

[29] C. Yildiz, Y. Biçer, and D. Pehlivan, "Heat transfers and pressure drops in rotating helical pipes," *Applied Energy*, vol. 50, 1995, pp. 85-94.

[30] C. Horvath, B.A. Solomon, and J. Engasser, "Measurement of Radial Transport in Slug Flow Using Enzyme Tubes," *Industrial & Engineering Chemistry Fundamentals*, vol. 12, Nov. 1973, pp. 431-439.

Chapter 4

Molecularly Imprinted Polymer

Enhanced Segmented Flow Extraction

4.1 Aqueous Buffer Effects

4.1.1 Reproducibility

Following the work of chapter 3, further investigations into extraction rate (k) and flow variable relationships demonstrated some variance in the measured equilibrium distribution coefficient between separate investigations. This was identified as being a result of a difference in pH, together with the absence of buffering capacity in the preparations of the aqueous propranolol hydrochloride solutions in deionised water. In the liquid-liquid extraction process, in order for phase transfer of the propranolol salt to proceed, proton dissociation must occur in the aqueous phase, liberating propranolol free base. It is the free base form of propranolol which displays high solubility in the extracting organic phase, with the protonated form being highly soluble in the aqueous phase.

propranolol base   propranolol hydrochloride
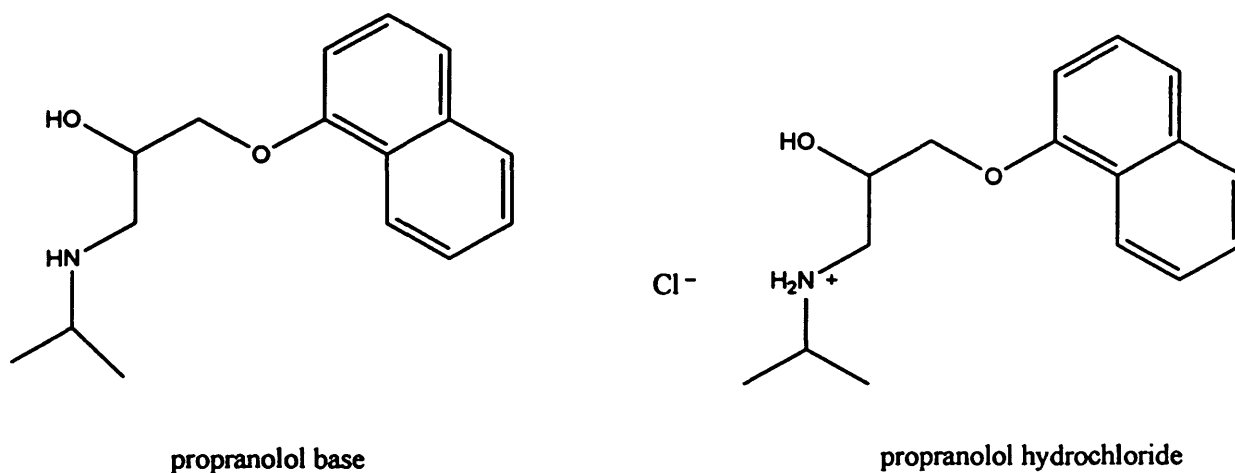
Figure 1 Propranolol base and hydrochloride salt structures. The latter is highly aqueous soluble and poorly soluble in organic media due the presence of the charged amine group. The base species is highly soluble in organic media and poorly soluble in aqueous environments, therefore de-protonation of the propranolol salt is necessary for phase transfer from an aqueous sample into an extracting organic phase.

Consequently, the abundance of H^+ ions in the aqueous phase, affects the relative solubility of propranolol in the two phases, with an acidic environment favouring the likelihood of the propranolol species becoming protonated and residing in the aqueous phase, thus reducing the distribution coefficient (D). Additionally, with the employment of an unbuffered aqueous phase, progression of the extraction results in a decrease in pH of the aqueous phase through

143

the increase in dissociated H^+ ions liberated from propranolol moieties migrating into the organic phase. Consequently, this increase in acidity makes it progressively more difficult for further extraction to occur owing to the decreased likelihood of deprotonation, or conversely, the more rapid reprotonation of uncharged species in the aqueous phase. This dynamic process is therefore highly sensitive to slight changes in de-ionised water quality or pH differences between preparations. This impacts upon the extraction equilibrium, and induces a reduction of extraction rate as the extraction progresses. Owing to the process-dependant feedback nature of pH control, it is conceivable that subtle changes in extraction conditions (temperature, time, etc) may have an enhanced impact on the measured extraction. The employment of buffered aqueous phases maintains a consistent pH throughout the duration of the extraction, thus improving reproducibility and adding a significant degree of control over the equilibrium distribution coefficient through effective pH regulation.

4.1.2 Buffer Screen

The equilibrium distribution coefficient was established for three different buffer conditions. Macro scale equilibrium partitioning studies were conducted in accordance to the methodology described in chapter 3, section 3.4.1.1. The distribution of propranolol from 2 ml of a 50 µM buffered aqueous solution, into an equal volume of chloroform was measured. All propranolol solutions were freshly prepared prior to use to prevent possible acid hydrolysis of the propranolol.

4.1.2.1 Buffer Preparation

Phosphate buffer 10 mM was prepared at pH 7.5 and 6.5, together with a 10 mM acetate buffer at pH 5.5, outside of the effective buffering capacity of phosphate buffer (pKa = 7.2, effective buffer range considered pH = pKa+/- 1). Propranolol solutions (50 µM) were prepared by dilution of a 1000 µM stock solution of propranolol HCl in de-ionised water, with the desired buffer preparation. All solutions were protected from light and stored at 4°C. Table 1 shows the buffer composition and measured pH of prepared solutions.

Table 1 Composition of evaluated buffer systems.

Buffer System			Acid Component		Basic Component		Measured pH	
Buffer concentration (Molar)		pH	Molar		Molar		Buffer	50 µM propranolol solution
10	Phosphate	7.5	0.022	Sodium dihydrogen orthophosphate dihydrate	0.0077	Sodium phosphate dibasic dodecahydrate	7.54	7.545
10	Phosphate	6.5	0.0078	Sodium dihydrogen orthophosphate dihydrate	0.0021	Sodium phosphate dibasic dodecahydrate	6.363	6.415
10	Acetate	5.5	0.00999	Acetic acid	~0.01	Sodium Hydroxide (adjust to desired pH with 1 M NaOH, ~10 ml/L)	5.536	5.531
	De-ionised water							6.351

145

4.1.2.2 Equilibrium Distribution Coefficient in Buffered Extractions

Table 2 illustrates the equilibrium distribution of propranolol between aqueous buffered phases at pH 7.5, 6.5 and 5.5 into an equal volume of chloroform.

Table 2. Equilibrium distribution of propranolol between equal volumes of chloroform and a buffered aqueous phase.

Concentration (mM)	Buffer	pH	Equilibrium Aqueous Concentration (μM)	Equilibrium Chloroform Concentration (μM)	Distribution Coefficient (D)
10	Phosphate	7.5	1	49	49
10	Phosphate	6.5	10	40	4
10	Acetate	5.5	25	25	1

Propranolol partitioned from buffered, aqueous 50 μM propranolol HCl solutions (2 ml) into chloroform (2ml).

As anticipated, the distribution coefficient (D) was seen to reduce with decreasing pH of the sample aqueous phase. The pH 5.5 acetate buffer was identified as providing a promising distribution coefficient for demonstration of model, proof of principle MIP assisted extractions. Although pH reduction limited the extent of extraction, such control provided the opportunity to emulate less readily extracted species to which the enhanced extraction methodology would ultimately be applied. Additionally, deliberate reduction in the extent of analyte extraction eased the process of early stage characterisation of the extraction methodology through retaining a readily and accurately quantifiable analyte concentration in the sample phase.

4.2 Extra-Tubular Extraction

4.2.1 Additional Extraction in Collection Vessel

It was reasoned, that although both the mixing and interfacial area to volume ratio would be substantially greater in the microfluidic segmented flow regime, a degree of additional extraction could take place during the collection process, if the eluate was not already at

extraction equilibrium. This was predicted to occur by two processes, firstly mass transfer across the stationary interface between the two phases separated on the basis of density in the collection vial. The second, occurring during the process of density-based liquid phase separation, the eluted drops falling into the collection vessel with the denser liquid drop (chloroform), sinking though the stagnant aqueous layer residing on top of the previously eluted chloroform. During this process the falling drop would be anticipated to exhibit recirculatory flow and a comparatively high surface area to volume ratio. Consequently a similar extraction process to that occurring in the segmented flow regime may take place, however the falling time for the drop would be extremely limited and so the contribution could be expected to be very small. It was also reasoned that should the outlet tubing be placed at the bottom of the collection vessel, the aqueous sample phase would rise through the eluted chloroform layer with a similarly induced recirculatory flow, however for extractions where D >1 the rate limiting step of the extraction process is likely to be either mass transfer within the aqueous phase or transfer across the interface itself (Chapter 3). As such, recirculatory mixing induced in the rising aqueous phase could be anticipated to result in a greater degree of unwanted, extra-tubular extraction than the scenario of a falling chloroform drop. An additional complication is encountered with respect to the required collection time employed in order to collect an analysable quantity of eluate in experiments where flow rate effects are investigated. With the stationary contact time in the collection vessel decreasing with increased flow rate. Two different experiments were set up to characterise the influence of these two effects. In all segmented flow extraction experiments of this thesis, the same collection method was employed to maintain surface area to volume ratio relationships within the collection vessel, however time dependent effects were unavoidable.

4.2.2 Experimental Design

Two methods were employed to assess the influence of extra-tubular extraction. In each case a 10 mM phosphate buffer pH 7.5 buffer system providing high equilibrium distribution (D) was employed. This resulted in sufficient analyte migration for easily measurable results even if the extent of extraction was far from equilibrium. Propranolol HCl buffered solutions (50 µM) were

extracted with chloroform as described in 4.2.2.1 and 4.2.2.2.

4.2.2.1 Experiment 1

The aqueous sample phase and chloroform were delivered at equal flow rates of 0.2 ml min^{-1} as two individual, non-segmented, flow streams, into a common 2 ml eppendorf collection vial. 1.5 ml combined volume of eluate was collected from which 0.65 ml of aqueous phase was removed immediately for assessment of propranolol content.

4.2.2.2 Experiment 2

The time dependency effect determined by the flow rate - collection time relationship when collecting a fixed volume of eluate was investigated. This was achieved by conducting a segmented flow extraction of propranolol from the pH 7.5 buffered aqueous phase into chloroform and collecting combined volumes of 1, 1.5 and 2 ml of eluate for assessment of extent of propranolol extraction. Since the extraction taking place in the segmented flow stream would be equivalent in each instance, any difference in measured extraction could be attributed to the collection time, correlating to residence time of eluate in the collection vial. Flow rates of 0.2 ml min^{-1} were employed for each phase. Table 3 provides a summary of the experimental conditions investigated.

Table 3 Series of control experiments designed to assess contribution, and time dependency, of extraction occurring in the collection vessel, following the segmented flow extraction.

Experiment	1	2a	2b	2c
Segmented flow prior to collection	No	Yes	Yes	Yes
Total volume collected (ml)	1.5	1	1.5	2
Collection time (s)	225	150	225	300

Flow rate of each phase 0.2 ml min^{-1}, where applicable segmented flow generated by a Tefzal T-piece, flowing into 20 cm of 0.5 mm I.D. FEP tubing. Segmented and non-segmented, individual flows, were eluted into a 2 ml eppendorf centrifuge tube of diameter 0.9 cm

4.2.3 Results

Figure 2 depicts the measured extraction coefficient (concentration ratio) for each of the control studies. It can be seen from the non-segmented flow collection of two individual flow streams in a common collection vial, that extraction does proceed in the collection vessel. However the extent of the extraction is comparatively small (extraction coefficient = 0.6), compared to that of the segmented flow regime with an equivalent collection time (extraction coefficient = 14.5).
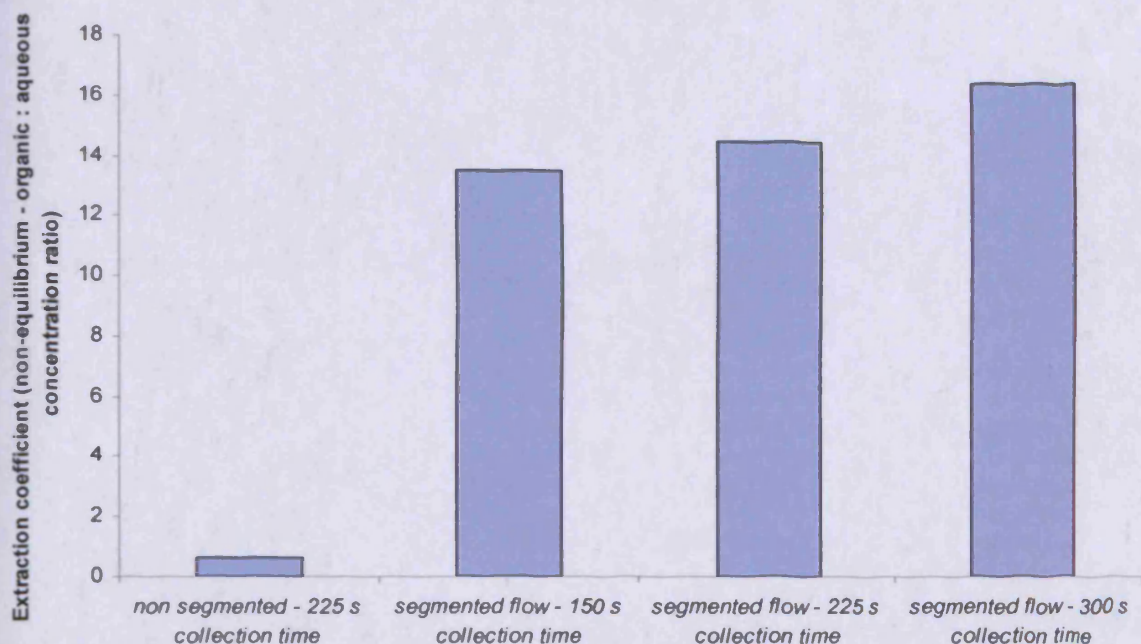
Figure 2 Extraction coefficient of control experiments, characterising the extent of propranolol extraction in the collection vessel. Measured extraction of co-elution of non-segmented flow streams into a common vessel is compared to the extent of extraction measured following segmented flow extraction and collection (non segmented 225 s collection time and segmented flow 225 s collection time). The results indicate that although the segmented flow regime is responsible for the majority of the extraction, a significant quantity of propranolol is extracted in the collection vessel. This is reinforced by the observation of increasing extent of extraction with increased collection time, despite a constant segmented flow rate. Experimental conditions: Flow rate of each phase 0.2 ml min^{-1}, where applicable segmented flow generated by a Tefzal T-piece, flowing into 20 cm of 0.5 mm I.D. FEP tubing. Segmented and non-segmented, individual flows, were eluted into a 2 ml eppendorf centrifuge tube of diameter 0.9 cm with collection times of 150, 225 and 330 s employed.

The extent of extraction can be seen to increase marginally with increased collection time within the collection vessel for segmented flow extractions conducted under otherwise identical conditions (flow rate, phase ratio, transit time etc). Consequently, since a defined volume of eluate is required for analysis of extracted propranolol, this effect of slight

overestimation of analyte extraction will be more pronounced for segmented flow extractions conducted at low flow rates and therefore extended collection times. This effect can not be compensated for by maintaining collection time and collecting various volumes depending on the flow rate under investigation, since this would affect both surface area to volume ratio relationships within the collection vial and also 'drop' time for falling droplets through the existing eluate as collection volume and consequently liquid depth increases. As such it was concluded that for more precise characterisation of extraction mechanisms and evaluation of variable effects and dependencies (Chapter 3), an effective, real-time phase separation mechanism would be required. Such a feature, if integratable onto a planar microfluidic device would be highly desirable for this and numerous other multiphase flow applications. In the context of this thesis an ability of such a liquid phase separator to handle particulate containing flows would be required. The development and characterisation of an integrated on-chip segmented flow phase separation device is the topic of chapter 5.

4.3 MIP Assisted Extraction

The original hypothesis, that solid-phase adsorbent material, specifically a molecularly imprinted polymer, could be included in the extracting phase of a segmented flow extraction, to enhance the extent of extraction was systematically evaluated.

4.3.1 Screening of Buffer Effects on MIP Enhancement of Liquid-Liquid Extractions

In order to evaluate the capability of a MIP assisted system to influence equilibrium extraction under conditions where the solvent-solvent extraction equilibrium was unfavourable a buffer system was employed (10 mM acetate buffer, pH 5.5) that gave a pre-MIP extraction coefficient of ~1 (Table 2). As a demonstration of concept, emulation of a less than desirable extraction and demonstration of its enhancement through the inclusion of an affinity phase was the initial aim, prior to competitive extractions or targeted applications.

Preliminary macro scale extraction experiments were conducted using the methodology of chapter 2 section 2.6.1.1 to measure the equilibrium distribution coefficient (D) for the extraction of propranolol from a 50 μM concentration solution of the hydrochloride salt, in 10 mM pH 5.5 acetate buffer, into an equal volume of chloroform containing either MIP (1 mg ml⁻¹), NIP (1 mg ml⁻¹) or no polymer. The results are illustrated in Table 4.

Table 4 Equilibrium distribution coefficient for propranolol extraction from a pH 5.5 aqueous solution into an equal volume of chloroform ±MIP/NIP.

	Chloroform alone	Chloroform + MIP 1mg ml⁻¹	Chloroform + NIP 1mg ml⁻¹
Equilibrium distribution coefficient (D)	1.2	5.7	2.2

Macro scale extraction of propranolol from a 50 μM concentration solution of the hydrochloride salt, in 10 mmolar pH 5.5 acetate buffer, extracted into an equal volume of chloroform (2 ml), containing either MIP (1 mg ml⁻¹), NIP (1 mg ml⁻¹), or no polymer. (n=5)

As demonstrated in chapter 2, the addition of MIP to the extracting chloroform phase significantly increased the extraction of propranolol from the aqueous sample. Assuming that the addition of polymer had no effect on the distribution coefficient of the *free* propranolol between the aqueous and chloroform phases, calculation of the phase distribution of the propranolol in the system correlates well with the isothermal binding behaviour described for the MIP in chapter 2. This suggests that the presence of the chloroform-miscible acetic acid (from the buffer) in the binding system had little influence on propranolol binding to the MIP. The macro-scale defined equilibrium distribution of propranolol between aqueous and organic phases provided a bench mark for assessment of segmented flow extractions.

4.3.2 MIP Assisted Segmented Flow Extraction

From previous experiments (Chapter 3 section 3.2.) it was concluded that binding to the MIP particles would represent the most significant event in determining the overall rate of attainment of equilibrium. Therefore, segmented flow MIP assisted extractions were initially carried out in 5 m lengths of tubing to provide sizeable transit times to allow for binding of the

propranolol analyte to the polymer microspheres. It was hoped that after further characterisation of the mechanisms and limitations of the approach, optimisation strategies could be employed to enable useful extraction protocols to be carried out on an integrated chip-based fluidic platform.

4.3.2.1 Method

A 50 μM solution of the hydrochloride salt of propranolol was prepared in 10 mM pH 5.5 acetate buffer. Additionally a 1 mg ml^{-1} suspension of either MIP or NIP in chloroform was prepared. The polymer suspensions were briefly ultrasonicated immediately prior to use to ensure dispersion of the polymer microspheres. The uniform suspension was maintained in the delivery syringe through the addition of two magnetic stirrer bars, with an inverted stirrer plate placed directly above the syringe. Flows of aqueous propranolol containing phase were segmented with chloroform containing either MIP, NIP or no polymer, in 5 m of 0.5 mm I.D. FEP tubing using a 0.5 mm through hole diameter Tefzel T-junction. The extended length of tubing was coiled for practical purposes (coil diameter of 11 cm), with the exception of approximately 30 cm of the extraction tubing at the inlet and outlet which remained largely straight in orientation. Flow rates from 0.1 to 0.8 ml min^{-1} with a 1:1 ratio of reagent flow were systematically evaluated for each of the three extraction systems. Due to the observed effect of flow rate on segment size, and the resultant pressure change due to the change in segment size and number of interfacial boundaries present within the tubing length, flow was allowed to stabilise and equilibrate prior to collection of eluate. At each flow rate an equilibration time of twice the transit time was allowed for flow stabilisation, after which collection of 1 ml of combined eluate ensued. Upon collection of 1 ml, 0.45 ml of aqueous phase was immediately removed and two 200 μl aliquots analysed for propranolol content by fluorescence microplate analysis (excitation λ:290nm, emission λ:330nm). Extractions at all six flow rates investigated, for each of the extraction systems (MIP, NIP, no polymer), were repeated on three separate occasions.

4.3.2.2 Results and Discussion

Figure 3 shows the concentration of propranolol remaining in the aqueous phase following segmented flow extraction with chloroform, either alone, or assisted by suspended MIP or NIP microspheres (1 mg ml^{-1}), over a range of flow rates. Figure 4 depicts the same experimental data in the form of mole fraction extracted (f) and linear flow velocity, a major variable in governing the extent of mass transfer in a segmented flow regime, together with extraction time, equivalent to the transit time within the extraction tubing. It can be seen that for each flow rate investigated, addition of the MIP microspheres to the extracting chloroform phase is seen to enhance the extent of propranolol extraction.
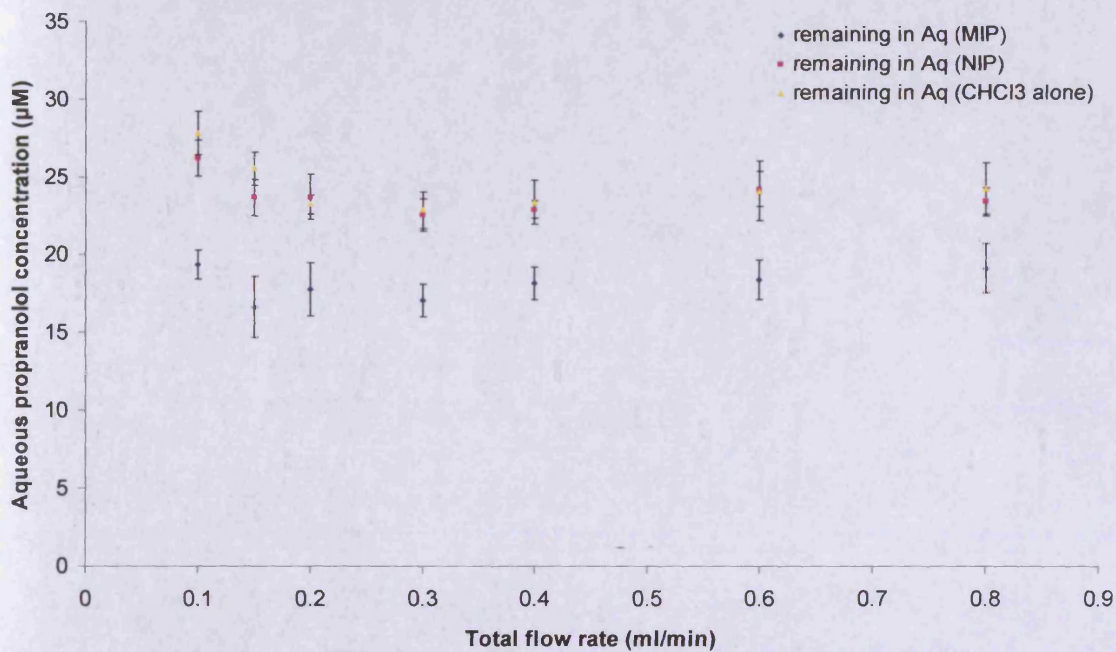
Figure 3 Concentration of propranolol remaining in the aqueous phase, following extraction of a 50 μM aqueous sample at pH 5.5 with an equal volume of chloroform, containing either MIP, NIP (1 mg ml^{-1}) or no polymer. Extractions conducted by segmented flow extraction in a 5 m length of 0.5 mm I.D. FEP tubing, predominantly coiled (coil diameter 11 cm) at a range of flow rates.

Figure 4 Mole fraction (f) of propranolol extracted from a 50 μM aqueous sample at pH 5.5, following extraction with an equal volume of chloroform, containing either MIP, NIP (1 mg ml^{-1}) or no polymer. Extractions conducted by segmented flow extraction in a 5 m length of 0.5 mm I.D. FEP tubing, predominantly coiled (coil diameter 11 cm) at a range of flow rates. The flow rate dependant extraction time is also depicted.

Unfortunately, at the time of conducting the experiment the heavy influence of segment aspect ratio on the rate of mass transfer was not fully appreciated and consequently detailed measurements were not made concerning this (Chapter 3). However it was noted that segment aspect ratios of approximately 8:1 were typical of the slower flow rates, with aspect ratio decreasing with increasing linear velocity. This observation is likely to be as a result of the increased pressure ahead of the advancing bubble tip at higher Reynolds numbers [1] (Chapter 3 section 3.4.4.4.1), thus affecting pressure dominated mechanisms of droplet formation (Chapter 1 section 1.1.6.1.2). This observation was not made by Garstecki et al.[2] despite the author's thorough investigation. However, the studies reported were conducted at lower Reynolds number, with slower flow velocities, narrower channels and significantly more viscous continuous phase fluid. As such inertial forces would be expected to be far less influential in the system evaluated by Garstecki et al.. This reduced inertial effect compared to

the work reported here would be expected to limit the manifestation of the vortex flow ahead of an advancing interface, therefore not affecting wetting film thickness or creation of localised pressure gradients [1] (Chapter 3 section 3.4.4.4.1) which may subsequently affect droplet breakup. As discussed in chapter 3, this observed decrease in segment length will contribute to an enhancement of extraction rate, through increased contribution of the vortex mixing in proximity to the fluid interface compared to the otherwise Poiseuille like axial-recirculatory flow. Additionally shorter segments facilitate interaction of the vortex flow regimes, increasing radial mass transfer and also provide a slightly greater surface area to volume ratio. Consequently at increased flow rates, the extraction rate is increased by several mechanisms. Figure 5 illustrates a simple variable map of secondary velocity dependant effects that contribute to mass transfer enhancement. These are discussed in detail in chapter 3.
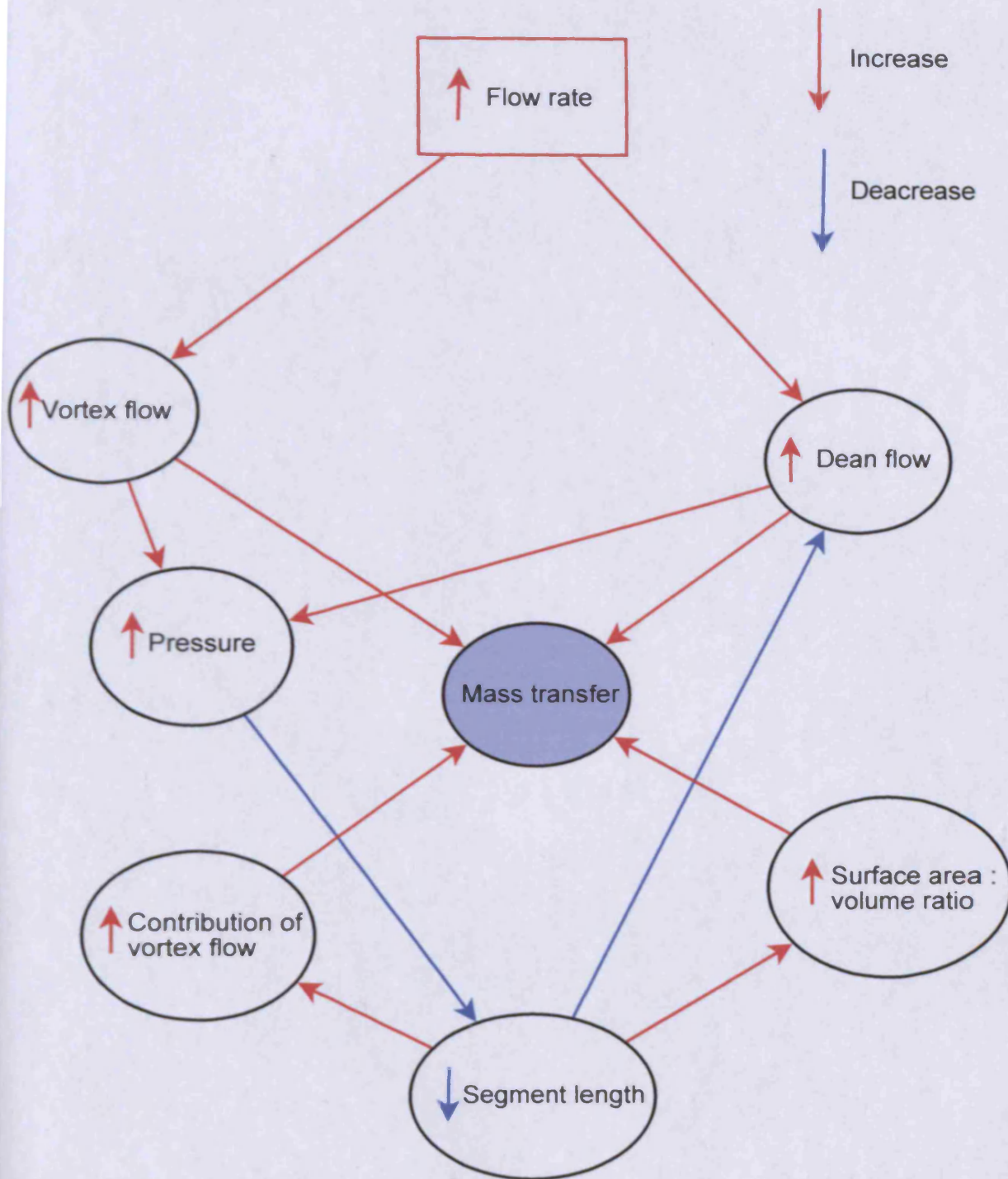
Figure 5 Variable map illustrating the velocity dependent secondary mechanisms of mass transfer enhancement in segmented flow regimes. Many of the processes exhibit non-linear behaviour and may be affected by additional variables (e.g. fluid properties, tubing diameter, tubing coiling or channel corners, segmenting architecture etc)

For the extraction with chloroform alone, which is seen to attain equilibrium (or extremely close to equilibrium) (D = 1.2) at flow rates of 0.2 ml min^{-1} and above, the reduction in

extraction time as a result of increased flow rate is offset entirely by the mixing and mass transfer afforded directly by the increased linear velocity, together with the increased contribution from indirect, dependent effects (Figure 5). The exact extent of enhancement is unclear from this data, since the measured extraction is at, or is extremely close to, equilibrium and therefore the precise point within the 5 m tubing at which equilibrium is obtained can not be identified. For this reason, calculated extraction rate constants (k) for the extractions with chloroform alone are likely to be understimates for situations where equilibrium was obtained (flow rates > 0.2 ml min^{-1}). Interestingly at flow rates of 0.1 and 0.15 ml min^{-1} the rate of extraction through velocity dependent mechanisms was insufficient to offset the increased extraction time afforded by the slow flow rate.

It can be seen from the experimental results that at each flow rate the addition of the MIP to the extracting phase enhanced the extent of extraction compared to chloroform alone. However, perhaps unsurprisingly, unlike the extractions in chloroform alone the extractions with chloroform containing MIP and NIP microspheres did not attain equilibrium. This is a result of the comparatively slow binding kinetics of the polymer, due to the requirement for diffusion through the porous micro-structure of the particle. Additionally, the enhancement of extraction is a dynamic process, with a degree of initial extraction into the chloroform required before binding to the MIP can occur. Binding to the MIP then facilitates further removal of propranolol from the aqueous phase though mass transfer into the chloroform phase re-establishing equilibrium of free propranolol between the two liquid phases. Thus multiple dependencies exist, with mixing and diffusion *within* the extracting phase playing a more significant role in the extraction process than in the liquid-liquid extraction in the absence of polymer. Mixing and mass transfer effects within the extracting liquid phase are required to ensure analyte interaction with the polymer, whilst fluid dynamic properties (viscous and inertial forces) and consequently mass transfer properties are certain to be affected by the presence of particles in the continuous phase of the segmented flow regime. Intuitive estimates may be made based on the consequential effects of parameter changes on the variables discussed in chapter 3, however considerable experimental analysis, possibly in

conjunction with CFD studies would be required to elucidate the exact nature of such effects. From the macro-scale equilibrium distribution studies (Section 4.3.1), where a propranolol concentration of 7.5 µM remained at equilibrium, it could be concluded that in the segmented flow regime of flow rate of 0.2 ml min^{-1}, that propranolol binding to the MIP was approximately 1/3 of the way to equilibrium. With 33.5 nmol mg^{-1} binding to the MIP at equilibrium, compared to 10 nmol mg^{-1} in the case of the segmented flow extraction with a transit time of 147 s. This is suggestive that only a limited penetration depth of analyte into the 3.6 µm diameter MIP spheres is achieved, correlating with approximately 1/3 of the total volume of the sphere, if the microsphere consists of uniform binding site density. Consequently, it was reasoned that employment of smaller MIP particles would enhance the efficiency of the extraction further, enabling attainment of equilibrium, or sizable improvements in extraction yield, for transit times, and flow distances, achievable within an integrated on-chip system. This was considered the most significant limitation of the extraction system evaluated here and would become the focus of later work.

Figure 6 illustrates the calculated extraction rate constant (k) for each of the extraction systems and flow rates investigated. The calculation of k for the extraction in chloroform alone is somewhat superficial owing to the extraction reaching equilibrium during transit through the 5 m tubing. This results in underestimation of the extraction rate constant, as an extraction time (t) equivalent to the residence time is assumed. This factor is also attributed to the poor linearity of the resultant calculated data for k for the extractions into chloroform alone. However these calculated values usefully demonstrate the enhancement in extraction rate compared to the macro-scale studies (0.04 and 0.001 s^{-1} respectively), with the anticipation that this could be significantly improved upon in shorter lengths of tubing employing shorter segment lengths and mass transfer enhancement strategies discussed in chapter 3.
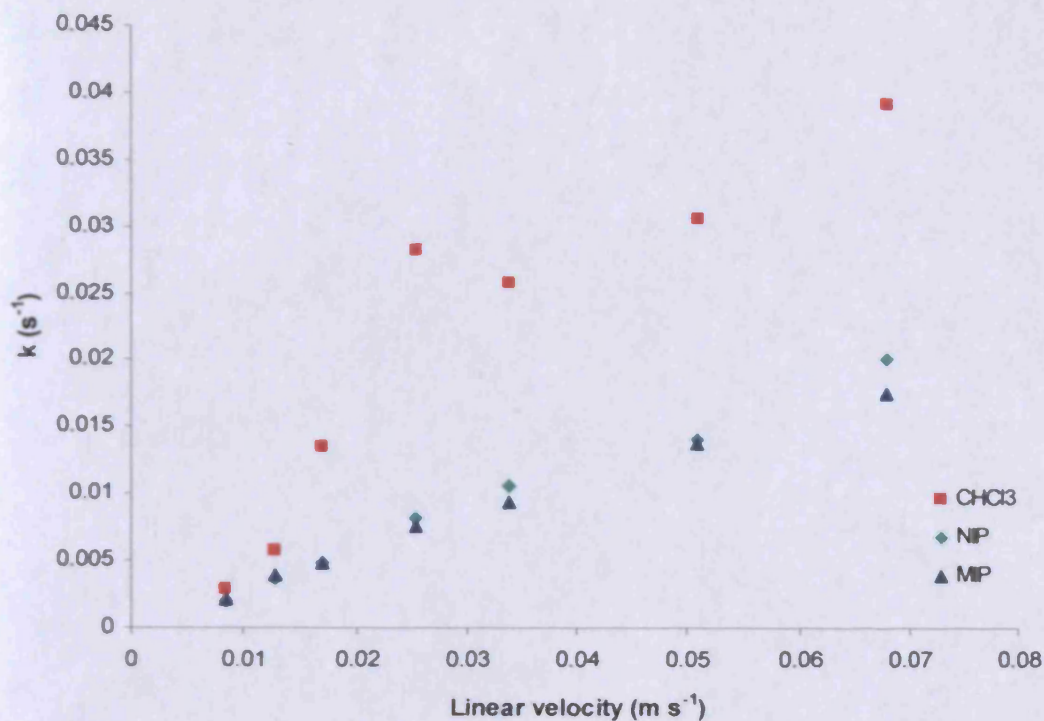
Figure 6 Calculated extraction rate constant (k) for the extraction of a 50 μM aqueous sample of propranolol at pH 5.5 with an equal volume of chloroform, containing either MIP, NIP (1 mg ml^{-1}) or no polymer. Extractions conducted by segmented flow extraction in a 5 m length of 0.5 mm I.D. FEP tubing, predominantly coiled (coil diameter 11 cm) at a range of flow rates.

The extraction rate of the MIP assisted extractions is somewhat lower than the counterpart containing no polymer, this is despite the increased extent of extraction observed with the inclusion of the MIP (Figure 3). This is a result of the extraction rate constant being a measure of the rate of progression of an extraction to equilibrium which, unlike the chloroform only extraction at flow rates of 0.2 ml min^{-1} and higher, the MIP assisted extraction fails to reach. This is a consequence of the rate limiting binding kinetics of the MIP microspheres. However, from a practical point of view, within the same period of time a greater quantity of analyte is extracted by the MIP assisted regime in all cases. This is despite the extraction progressing to equilibrium at a slower rate. The extent of extraction could be increased further by extending the extraction time by increasing the tubing length (Section 4.3.3), by increasing polymer loading (Section 4.4), or by decreasing MIP particle diameter thus reducing the diffusive limitation defined by the particle size (discussed in section 4.4.1 and chapter 7). It is interesting to observe that the calculated extraction rate constant (k) for both the MIP and NIP

are nearly identical at all investigated flow rates. This demonstrates that in the segmented flow regimes tested, both MIP and NIP assisted extractions, at equivalent polymer loadings, progressed to their respective equilibrium distributions at the same rate. It was also found that addition of NIP microsphere to the chloroform extracting phase had no apparent effect on the extent of propranolol extraction form the aqueous phase, despite the difference in equilibrium distribution ratios (D = 2.2 and 1.2 respectively). This suggests that the presence of suspended polymer particles in the continuous phase of the segmented flow stream reduces interfacial mass transfer, but by a small extent which is compensated for by the small amount of non-specific binding which occurs on the polymer surface. Given that the MIP and NIP assisted extractions progress to equilibrium at near identical rates, it is reasonable to expect that this process also occurs in the MIP assisted extractions. This further complicates inter-relationships between the dependent variables governing mass transfer in segmented flow. It is probable that this is a result of viscous and inertial force differences between chloroform and the chloroform plus polymer phases. Further investigation is necessary to confirm or disprove this hypothesis.

The near constant extraction by the MIP at all flow rates (Figure 3), despite not attaining extraction equilibrium, is an interesting feature of the experimental findings. This observation indicates that the combined enhancements in mass transfer due (directly or indirectly) to increase in velocity, counter balance reduced contact time resulting from increased flow rate. This is particularly interesting as it suggests that the rapid mixing associated with increased velocity *may* increase the MIP binding kinetics, by promoting mass transfer of analyte to the polymer surface or through the polymer matrix. Alternatively, it is possible that, the rate of phase transfer of propranolol from the aqueous sample to the chloroform phase within this experimental setup is related to velocity *and* its dependent variables (Figure 5) by a linear (or greater) relationship. Therefore, the increase in velocity accelerates liquid-liquid phase transfer, affording the MIP comparatively more time to bind propranolol. As the MIP depletes propranolol from the chloroform, further extraction of propranolol from the aqueous phase into the chloroform occurs at an increased rate at greater linear velocities. This results in an

increase in the overall rate of attainment of the dynamic equilibrium in the complex three phase system. These observations are supported by the calculated extraction rate constant (k) for the MIP assisted extraction which increases with increasing flow rate (Figure 6).

It should be noted that a number of the velocity dependent variables, contributing to the increased extraction rate with increased velocity, can also be altered by other user definable variables such as coil diameter, to manipulate the contribution of Dean flow, or T-junction geometry to manipulate segment aspect ratio. This offers a degree of flexibility for increasing extraction rates further, or tailoring extraction effects with space-time definable precision with a greater understanding of the mechanisms of the variables involved. This may give rise to exciting extraction mechanisms or molecular manipulations, exploiting the various rate limits within a dynamic system at different points along a pre-defined flow path.

The error bars depicted on Figure 3 illustrate the mean propranolol concentration remaining in the aqueous phase, plus and minus the measured standard deviation for the three repeat experiments conducted on separate occasions for each extracting system. Studying the individual experimental data (Figure 7) suggests that a large contribution of the variance is down to local conditions at the time of conducting the extraction. One set of extraction experiments, consisting of extraction with chloroform alone, chloroform with MIP and chloroform with NIP at seven flow rates were performed in one session (run 1), before repeating the experiment on later days (runs 2 and 3). It can be seen that for each extraction system, run 1 extracts more propranolol than run 2, both of which extract more than run 3. This is true for 60 of the 63 individually collected data points and suggests that systematic changes, such as laboratory temperature on each of the three days when investigations took place, are playing a significant role in inter-run variability. The possibility of degradation of propranolol in the prepared buffer solution was also considered. However, there was no visible evidence of acid hydrolysis (hydrolysed propranolol solutions appear light-brown in colour) over the 5 days that the investigations took place. If acid hydrolysis were to be occurring then the fluorescent naphthalene derivative species would be expected to partition more favourably

into the organic phase, particularly under acid conditions where the tertiary alcohol is unlikely to deprotonate, and thus an apparent increase in extraction would be anticipated in the latter experiments. The opposite of this was observed. Changes in fluorescence as a result of possible degradation could also be ruled out due to the use of reference standards of unextracted propranolol solution in the fluorescence microplate analysis. It can be noted that aside from the effects of extra-tubular extraction (Section 4.2), the segmented flow methodology enables an extremely accurate measurement of extraction. The resulting measurement can be considered a mean of many (dynamically related) replicates of individual fluid segments. A collection volume of 1 ml represents over 1200 individual fluid segments, generating a mean value, considerate of variations in segmented length and flow rate hysteresis. As such, and given the importance of the variables of flow velocity and segment aspect ratio, it may be beneficial to closely monitor, or control, these variables together with other variables known to have an effect on mass transfer or distribution coefficient (e.g. temperature),. It is possible that the extraction system is particularly sensitive to local changes in temperature which not only affect equilibrium distribution coefficient but also mass transfer kinetics, MIP binding, liquid viscosity and interfacial tension. This variation in fluid dynamic properties affects the relative influence of surface forces to viscous forces (Ca) and inertial forces (We). This in turn affects segment formation and the manifestation of vortex flow. The systematic investigation into the effect of temperature on the extent of extraction in a segmented flow extraction system would make for an interesting study. Temperature control could readily be achieved through incubation of the microfluidic device or capillary tubing in a thermostatically controlled water bath. In addition, analysis of perturbation of microwave resonant structures (Appendix 6.5 -6.7) by the segmented flow regime may provide a promising way to closely monitor and measure segment aspect ratio.
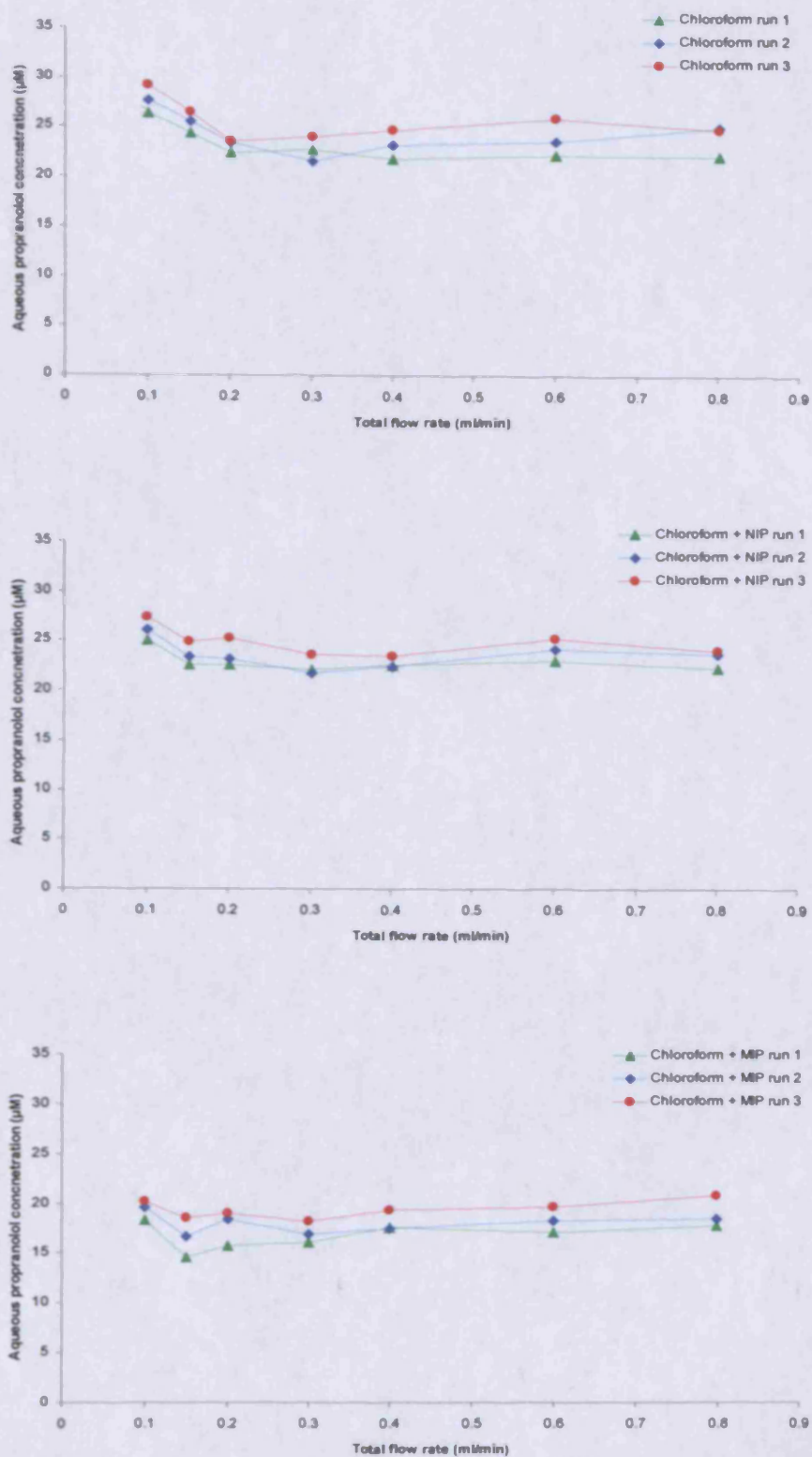
Figure 7 Concentration of propranolol remaining in the aqueous phase, following extraction of a 50 µM aqueous sample of propranolol at pH 5.5 with an equal volume of chloroform, containing either MIP, NIP (1 mg ml^{-1}) or no polymer. Individual extraction results for measurements of each of three sequential runs are plotted. The apparent distinction between experimental runs is perhaps indicative temperature, or other local effect dependencies. Extractions conducted by segmented flow in a 5 m length of 0.5 mm I.D. FEP tubing, predominantly coiled (coil diameter 11 cm) at a range of flow rates.

163

4.3.3 Extended Path Length MIP Assisted Segmented Flow Extraction

The extraction experiments conducted in 5 m lengths of 0.5 mm I.D. tubing were repeated in a 15 m length of coiled tubing (coil diameter 11 cm), all other variables were maintained as described in section 4.3.2.1. Although such a long path length would be impractical from the point of view of an integrated on-chip device, it was reasoned a valuable experiment to enable greater contact time for analyte binding to the MIP. It was hoped that further understanding of the behaviour, of the already otherwise well characterised 3.6 μm MIP microspheres, in a segmented flow extraction environment would provide useful information to assist in addressing the particle size related time limitation. Figure 8 and 9 depict the results graphically.
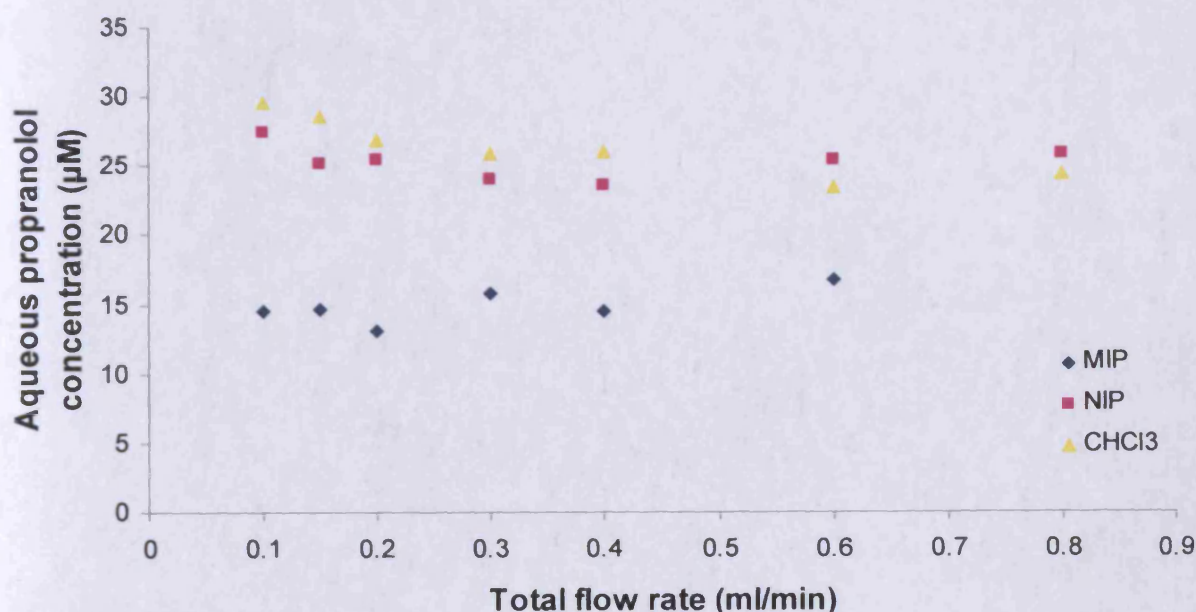
Figure 8 Concentration of propranolol remaining in the aqueous phase, following extraction of a 50 μM aqueous sample at pH 5.5 with an equal volume of chloroform, containing either MIP, NIP (1 mg ml⁻¹) or no polymer. Extractions conducted by segmented flow in a 15m length of 0.5 mm I.D. FEP tubing, predominantly coiled (coil diameter 11 cm) at a range of flow rates.

Figure 9 Mole fraction (*f*) of propranolol extracted from a 50 μM aqueous sample at pH 5.5, following extraction with an equal volume of chloroform, containing either MIP, NIP (1 mg ml^{-1}) or no polymer. Extractions conducted by segmented flow extraction in a 5 m length of 0.5 mm I.D. FEP tubing, predominantly coiled (coil diameter 11 cm) at a range of flow rates. The flow rate dependant extraction time is also depicted.

Segmented flow extraction in a 15 m length of tubing resulted in observation of a similar extraction behaviour to that carried out over 5 m, with the NIP appearing to demonstrate a small element of extraction enhancement at flow rates of 0.4 ml min^{-1} and under. Whilst higher flow rates provide insufficient contact time for the low level of non-specific binding to assist the extraction, with the presence of the polymer particles possibly impeding the liquid-liquid mass transfer process due to the effects of particulate material on fluid dynamic properties. The addition of MIP was seen to enhance the extent of extraction at all flow rates investigated and to a greater extent than over a 5 m extraction distance. This was as expected owing to the increased contact time for polymer binding. At the increased length, extraction rate progression to equilibrium is influenced more greatly by the binding kinetics to the MIP and NIP. This is reflected in the calculated extraction rate constant values (*k*) (Figure 10).

Figure 10 Calculated extraction rate constants (k) for the extraction of a 50 μM aqueous sample at pH 5.5 with an equal volume of chloroform, containing either MIP, NIP (1 mg ml^{-1}) or no polymer. Extractions conducted by segmented flow extraction in a 15 m length of 0.5 mm I.D. FEP tubing, predominantly coiled (coil diameter 11 cm) at a range of flow rates. The calculated extraction rate for extractions attaining equilibrium, or extremely close to attaining equilibrium (chloroform alone), are of limited value due to the ambiguity of the extraction time taken to achieve equilibrium. Additionally, small uncertainties in assay measurements or subtle variations in the equilibrium distribution ratio can induce significant uncertainty in calculation of extraction rate constants (k) for extractions close to equilibrium.

The extraction rate constant (k) is a measure of the rate of progression of extraction to equilibrium for extraction processes following first-order reaction kinetics. Consequently, in the solid-phase assisted extraction system a dynamic system exists composed of two interdependent extraction mechanisms, each with their own inherent k value. As a result, the course of the overall extraction does not follow first order kinetics and the calculation of k becomes somewhat arbitrary. Since the segmented flow, liquid-liquid phase transfer of analyte is comparatively fast compared to binding of analyte to the MIP, an initial portion of the extraction (approximated to that of equilibrium in the extraction system in the absence of polymer), proceeds at a rate in the region of that for the polymer free system. However, additional extraction from the aqueous phase is not possible until binding occurs to the MIP. Likewise, binding to the MIP in sizable quantities is not possible until a degree of extraction

166

from the sample phase has been achieved by the organic liquid. The liquid-liquid phase transfer is relatively fast compared to that of binding to the MIP, however, not so fast that it can be considered negligible. Additionally, in the assessment of the extraction, the extracting phase, consisting of chloroform and MIP is considered as one, as it is effectively the concentration removal from the aqueous sample that is used to measure the extent of extraction, with the equilibrium distribution and time used to calculate the rate. Both the MIP and the chloroform make contributions, albeit inter-dependent, to the extraction in their own right. As a result the extraction rate constant values (k) for the MIP and NIP, measured for 15 m extraction lengths, are seen to fall compared to those measured in 5 m tubing lengths. This is a result of the slower processes of analyte binding to the polymer which dictate the extent of extraction enhancement. This time dependency becomes increasingly more influential in governing the rate at which the extraction progresses to equilibrium as the extent of enhancement is increased. Consequently a time-yield trade-off is likely to be an important consideration in the miniaturisation to an integrated on-chip platform. An approximation of the extraction rate profile to equilibrium in a MIP assisted segmented flow regime can be made. However, in order to achieve this it must be assumed that the rate of extraction from the aqueous phase to the chloroform phase is, from a fluid dynamics perspective, unaffected by the presence of the polymer particles. An assumption which the data from the NIP assisted extraction appears to show is incorrect, however such an approximation may be suitable in assessing the general expected trend. It should also be noted that an additional advantage of employment of small polymer particles, is that together with improved mass transfer, smaller particulate material can be expected to have lesser influence over fluid dynamic properties of the segmented flow.

It was noted that in the longer tubing, segment aspect ratio increased. Whether this is a consequence of pressure effects due to the increased pressure drop induced by the greater flow path, or the result of an imperfect fit at the T-junction union, is unknown. Non-flush, or improper fitting of the segmented flow carrying tubing at the T-piece outlet would create dead volume at the point of droplet formation, possibly increasing segment volume, and therefore

aspect ratio. However, due to the opaque nature of the T-piece, such an effect is difficult to diagnose. This effect may account for the failure of low segmented flow rates (0.1 and 0.15 ml min^{-1}) to attain equilibrium in the extractions with chloroform alone. This is despite the increased transit time compared to segmented flow extractions conducted over a length of 5 m. The effect of the increased pressure on the extraction process is not clear and may also play a contributing role.

4.4 MIP loading

The effect of polymer loading on the extent of extraction in a MIP assisted segmented flow regime was investigated. MIP and NIP loadings of 1, 4 and 8 mg ml^{-1} in chloroform were compared to the extraction achieved by segmented flow extraction with chloroform alone. The experimental procedure was identical to that employed in section 4.3.2.1. A segmented flow rate of 0.4 ml min^{-1} in a 5 m length of 0.5 mm diameter FEP tubing, coiled with a diameter of 11 cm, was employed, resulting in an extraction time of 147 s.

4.4.1 Results

As anticipated increasing the MIP loading was seen to result in a greater enhancement of the extraction, whilst the enhancement due to the inclusion of the NIP did increase slightly with loading but remained modest. Figure 11 illustrates the measured partition coefficient (concentration in extracting phase / concentration in aqueous phase) for MIP and NIP polymer loadings of 1, 4 and 8 mg ml^{-1} compared to chloroform alone.
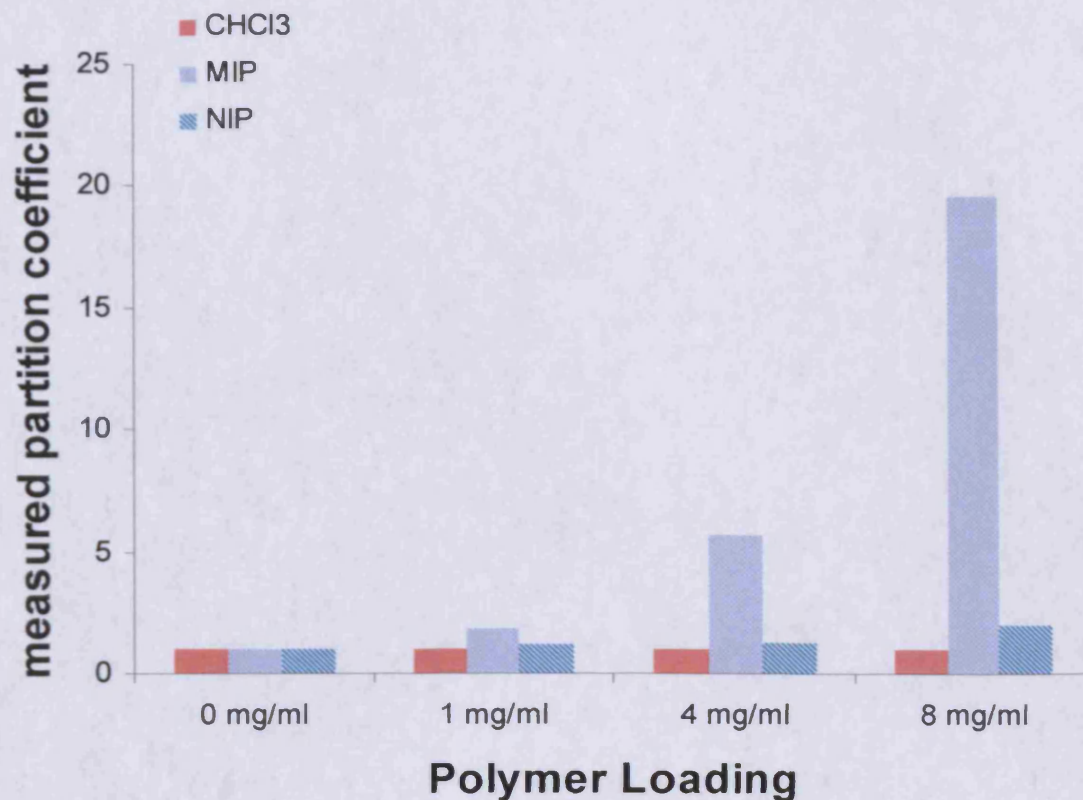
Figure 11 Measured partition coefficient for the extraction of propranolol from a 50 μM aqueous solution (pH 5.5) into an equal volume chloroform containing various masses of added polymer (MIP or NIP). Extractions were conducted using a segmented flow regime in 5 m of 0.5 mm I.D. FEP tubing at flow rates of 0.4 ml min^{-1}, representing an extraction time of 147 s.

It can be seen that despite the limited extraction time (147 s) a MIP loading of 8 mg ml^{-1} was able to enhance the extraction of propranolol from the pH 5.5 buffered aqueous phase, sufficiently to reduce the level of analyte in the aqueous phase to close to the limit of quantification for the method of analysis employed. This enhancement is despite the extraction system not yet attaining equilibrium, demonstrating that for an efficient extraction, equilibrium need not be attained. This result again highlights the desirability for a reduction in MIP particle size, whilst retaining (or improving) the porous open polymeric network structure and binding characteristics. Since diffusion of analyte through the polymer particle is limited by the transit time of the segmented flow stream, failure to attain equilibrium is indicative that a large volume of the spherical MIP particle remains unexposed to analyte. Comparison with equilibrium binding studies (Section 4.3.1) indicates that at a loading of 1 mg ml^{-1}, with

segmented flow extraction at a flow rate of 0.4 ml min^{-1} and an extraction time of 147 seconds results in binding of propranolol to the MIP of approximately one third of the equilibrium value. Attainment of equilibrium, would maximise the potential of the added polymer, this may be achievable through reduction in the redundant volume at the centre of the microspheres, to which analyte has insufficient time to diffuse. At equilibrium, a MIP loading of just over 2.5 mg ml^{-1} (Calculated using 2 phase binding model, Appendix 3) would be expected to attain the same level of extraction as that achieved with the 8 mg ml^{-1} loading demonstrated here. In light of this, a simplified model can be constructed to give an approximate indication of the required MIP particle size required to approach equilibrium binding over the desired time period. Although an approximate model, it gives an indication of the extent of particle size reduction required to optimise the extraction further. Assuming a uniform diffusion rate of analyte through the MIP particle from all outer surfaces of the sphere, it is assumed that the penetration distance from the sphere surface represents one third of the total volume. For the 3.6 μm spheres studied here, this results in an approximate penetration depth of 0.23 μm over 147 s (1.5 x 10^{-9} m s^{-1}), consequently a MIP microsphere of the same macromolecular structure with a diameter of 0.46 μm could be anticipated to be fully diffused by the analyte over the same time period. This approximation represents a gross simplification of the kinetic process, but demonstrates that significant reduction in particle size is required for more efficient application of MIPs to enhance analyte extraction in segmented flow regimes. This is especially important for the application of the technique on-chip, where transit times are likely to be significantly shorter. The production of smaller uniform sub-micron MIP particles possessing an open porous structure through polymerisation at near-theta conditions is perhaps more demanding than first appears. Submicron particles are readily produced by precipitation polymerisation by polymerisation in non-solvating environments, for example acetonitrile [3] However, this migration away from the near-theta conditions will result in a dense polymer microsphere. This would restrict diffusional access to binding sites, resulting in slower than expected kinetics for particle geometry. Particle size may also be limited by early termination of precipitation polymerisation at near-theta conditions. However, the merits of this approach may be limited, with the volume of a sphere being proportional to the radial length

cubed ($4/3\pi r^3$), the volume reduction as spherical particle size decreases is dramatic. Since the number of precipitated particle seeds will be approximately equivalent for the completed reaction and the early terminated reaction, the total number of reclaimed spheres can be expected to be of similar number. Thus the actual reaction yield will be very low. Additionally, with consideration of the particle growth mechanism (Chapter 2) and the relationship of particle radius to particle volume, the polydispersity of the resultant microspheres with respect to particle diameter, is likely to increase for small microspheres in the early stages of growth.

4.5 Conclusion

It has been successfully demonstrated that addition of a solid affinity phase, in this instance a molecularly imprinted polymer, to the extracting phase of a segmented flow regime can significantly enhance the extent of analyte extraction from an aqueous sample. The sequestration by the MIP of propranolol entering the chloroform, through the efficient mass transfer processes associated with segmented flow, maintains a significant propranolol concentration deficit in the chloroform. This continues to drive the extraction from the aqueous phase until a complex three-way equilibrium, in favour of the combined extracting phase, is attained. This significant increase in distribution coefficient enabled the removal of over 95% of the propranolol from the aqueous sample in a single extraction. For an equivalent level of removal to be achieved with chloroform alone, six consecutive extractions would be required, which, if MIP assisted would be expected to extract in excess of 99.99 % of propranolol from the original sample. It is regarded that for distribution coefficients of less than one, solvent extraction can be an ineffective, time consuming and impractical technique [4], and as such the ability to increase the value far above unity by the incorporation of an affinity phase into the extracting solvent is highly desirable. These findings demonstrate a highly promising and simple approach for enhancement of chemical separation, incorporating a solid phase adsorbent into the extracting phase of a liquid-liquid extraction whilst exploiting the rapid mass transfer properties of segmented flow. It is anticipated that through optimised exploitation of the mass transfer relationships detailed in chapter 3, together with optimised, reduced sized

MIP affinity phases, massive advantages in terms of time efficiency and extent of extraction can be achieved over macro-scale and alternative microfluidic extraction methodologies. The continuous flow nature of segmented flow microfluidics allows for continual operation, a distinct advantage of the approach compared to multiple batch manipulations for frequently conducted extraction or separation methodologies. Parallelisation of flow streams holds the potential to increase throughput, ultimately enabling application on an industrial scale, for example in post-synthesis chemical enrichment or contaminant removal. The development and incorporation of a flow-through, liquid phase separator is required for more accurate study of the mass transfer effects of both liquid-liquid and solid-phase assisted liquid-liquid extractions by segmented flow. Integration of such a device into a planar microfluidic chip is desirable for the ultimate aim of this research to produce a continuous flow-separation microdevice. Additionally, phase separation would also allow future studies to perform phase and particle manipulation for analyte recovery and reagent re-use, a further example of the potential flexibility and desirability of the technique. Design, development and evaluation of a segmented flow phase separation microdevice constitutes the work of chapter 5. The opportunity for increased extraction kinetics through the employment of significantly smaller MIP particles is discussed further in chapter 7.

4.6 References

[1] M. Heil, "Finite Reynolds number effects in the Bretherton problem," *Physics of Fluids*, vol. 13, 2001, p. 2517.

[2] P. Garstecki et al., "Formation of droplets and bubbles in a microfluidic T-junction-scaling and mechanism of break-up," *Lab on a Chip*, vol. 6, 2006, pp. 437-446.

[3] L. Ye, P.A.G. Cormack, and K. Mosbach, "Molecularly imprinted monodisperse microspheres for competitive radioassay," *Analytical Communications*, vol. 36, 1999, pp. 35-38.

[4] T.E. Beesley, B. Buglio, and R.P.W. Scott, *Quantitative Chromatographic Analysis*, London: CRC Press, 2001.

Chapter 5

Liquid Phase Separation of

Microfluidic Segmented Flow

5.1 Overview

5.1.1 Context

The requirement for liquid phase separation of the component phases of a segmented flow stream was established in the work of chapter 4. Separation of the component phases of a liquid-liquid extraction is an integral stage of the extraction process. As such, a viable, integrated, on-chip separation technique is highly desirable within the context of producing an integrated micro extraction device. Continuous extraction processes would benefit hugely from continuous liquid phase separation, rather than batch collection and manual separation, similar to that employed in the experiments of chapter 3 and 4. Additionally this would allow greater precision in the assessment of segmented flow extractions in the context of gaining further insight into the fluid dynamics and mass transfer relationships with extraction conditions (Chapter 3.). The presence of suspended molecularly imprinted polymer (MIP) microparticles in the extracting organic phase make it a requirement that the phase separation device is capable of separating particle laden flows. A general purpose microfluidic phase separator for multiphase flow would also be of value in many other multiphase flow applications.

5.1.2 Outline of Reported Work

Capillary forces on the micro-scale are exploited to create a continuous flow liquid-liquid phase separator. Segmented flow regimes of immiscible fluids are generated and subsequently separated into their component phases through an array of laser machined separation ducts (36 μm wide, 130 μm deep) in a planar, integrated, polytetrafluoroethylene (PTFE) microdevice. A controlled pressure differential across the phase separator architecture facilitates the selective passage of the wetting, organic phase through the separator ducts, enabling 100% phase separation. Separation efficiency is quantified over a range of flow rates and applied pressure differentials, characterising device behaviour and limits of operation. Experimental measurements and observations are supported by theoretical hydrodynamic and capillary pressure modelling. The influence of material properties and geometric design

parameters on phase separation is quantified and optimisation strategies proposed. The novel ability of the membrane free device to separate an organic phase containing suspended microparticulates, from an aqueous phase, is also demonstrated.

5.2 Introduction

Exploitation of forces dominant on the microscale in the form of microfluidic technology is empowering scientists to provide solutions for emerging and longstanding challenges alike. Microfluidic systems are widely being developed and applied to multi-step synthetic chemistry [1], separations and enrichments [2], sensing technology [3] and sequential combinations of these activities [4]. Recently, multiphase microfluidics has attracted considerable attention [5] since it provides unique opportunities for liquid- [6] and solid-phase supported micro-separations [7], crystallisations [8], particle synthesis [9], organic micro-synthesis [10], encapsulation [11] and chemical computing [12]. Multiphase flow usually entails the controlled elution of immiscible fluids into a common duct, or system of ducts [13,14] and offers new opportunities over that provided by single phase systems. Segmented flow regimes of alternating immiscible organic and aqueous fluid packets are characterised by each fluid packet exhibiting high internal mixing and there being a continually refreshing fluidic interface between contiguous fluid segments [15]. These important properties allow the rapid attainment of chemical equilibrium between adjacent fluid packages, through highly efficient mass transfer [16]. This enables rapid synthetic chemical migration across interfacial phase boundaries. In many above mentioned applications, it is usually desirable to separate and recover the component immiscible fluids in order to harvest synthesised particles, recover extracted molecular species or products of chemical reactions. Several approaches to liquid phase separation have been reported. Co- and counter-current (side by side) flows of immiscible fluids have been separated through splitting of the two phases at a juncture of appropriate geometry combined with surface modification of exit channels to favourably alter wetting characteristics of the outlets for one of the two immiscible phases [17-19]. Such 'side by side' flow systems lack the rapid mass transfer properties of segmented flow systems and

like single phase microfluidics, mass transfer is limited by diffusion [20]. As a result, extraction methodologies may require several passes to attain chemical equilibrium. Segmented flow regimes generate rapid mixing and efficient mass transfer in discrete droplets. This has enabled massive increases in efficiency of chemical reactions and also provided opportunities for other droplet based chemistries and syntheses. In the majority of cases phase separation has to be performed off-chip by gravimetric approaches which are commonplace on the macro scale. The ability to separate by differences in density on the microscale is much more difficult due the dominance of interfacial forces. However, such forces, which are not immediately obvious when considering the behaviour of fluids on the macro-scale, can be exploited at the micro-scale to enable phenomena and methodologies which would otherwise be unachievable. Capillary forces have been utilised to separate the components of gas-liquid segmented flows through an array of 10 μm wide side channels in a silicon substrate [21]. Angelescu and Siess [22] reported moderate success in adapting this approach to liquid-liquid flows quoting a separation efficiency of ~90% and subsequently demonstrating complete liquid phase separation using a non-wetting membrane to effectively narrow the geometry of the separation ducts. This approach was first adopted by Nord and Karlberg in 1980 [23] and later employed by Jensen's group at Massachusetts Institute of Technology [24].

The work of this chapter documents aqueous and organic phase separation with 100% efficiency in a membrane free, planar microfluidic device, with no additional surface modifications. This is achieved though optimisation of the approach introduced by Angelescu and Siess [22] using capillary forces to bring about total liquid phase separation by removal of the 'wetting' organic phase through a series of narrow side channels. Operating regimes are characterised for the phase separator and compared to predicted behaviour by correlating with modelled hydrodynamic pressure drops and capillary pressures at the separation interface. For the first time the ability of a microfluidic phase separation device to separate an organic phases containing suspended particulate material, from an aqueous phase, is demonstrated, a limitation of membrane based approaches.

5.3 Experimental

5.3.1 Device Production

An integrated planar PTFE microchip device was constructed from a 4 mm thick PTFE base layer, a 100 μm thick FEP intermediary layer and a 2 mm thick glass coverplate, all compression sealed in a stainless steel housing incorporating input-output ports (Figure 1). The separation device was fabricated in PTFE by a combination of micromilling and femtosecond laser ablation. The inlets, segmenting T-junction, main fluidic channel and outlets were micromilled (Protomat C10, LPKF, Garbsen, Germany) at a width of 720 μm and a depth of 600 μm. The separator section of the device consisted of an array of 140 36 μm wide, 130 μm deep and 5 mm long, Gaussian profile, side-channels (Figure 1), each 64 μm apart (top of duct-wall to top of duct-wall), branching from the main fluidic channel. These channels were machined by direct write femtosecond laser ablation (Exitech, Oxford, UK) (λ = 780 nm, 0.55 W, machining speed 50mm/min, 1 pass). Inlet and outlet holes (1/16" O.D.) were drilled in the PTFE substrate to receive equivalent outer diameter transparent FEP tubing (Upchurch Scientific, WA, USA) providing fluidic connectivity. Tubing (500 μm I.D.) of length 255 mm and 148 mm were used on the organic and aqueous outlet respectively. These specific lengths of tubing were employed to provide an equal pressure drop due to flow of the separated fluids through their designated outlets, from the separator to collecting vessel (Chloroform η = 0.00058 Pa s and Water η = 0.001 Pa s). The aqueous outlet was connected to a 50 ml capacity sealed vessel to which a 10 ml air-tight syringe and digital low pressure manometer (DP2-41E 100 kPa, Sunx, Panasonic) were also connected. This arrangement was used to modulate and monitor an applied pressure to this fluidic outlet, creating a pressure differential between the two outlets of the separator and therefore a pressure drop across the phase separator.

Figure 1 Series of schematic diagrams illustrating i) Device construction. ii) Microfluidic channel layout, including aqueous and organic inlets, T-junction for generation of segmented flow, phase separator region of the device consisting of a series of 140 parallel narrow side channels branching form the main fluidic duct leading to a designated organic outlet, with the main fluidic duct continuing to the designated aqueous outlet. iii) Cross-sectional Gaussian profile of a single laser machined separation duct as measured by serial z-axis optical microscopy and the approximated triangular geometry used for modelling calculations. iv) Cartoon illustration of the separator in operation, the organic phase (light) wets the PTFE channel walls and exits through the separation ducts, driven by the applied pressure differential between the two channel outlets. The non-wetting, aqueous fluid segments (dark) do not enter the narrow separation ducts but continue to flow in the main fluidic channel, coalescing into one continuous stream as the organic phase exits the channel.

Figure 2 A portion of the separation architecture, consisting of the main channel (1) and adjoining separation ducts (2). Dimensions; main channel (1) width 720 μm, depth of 600 μm, separation ducts (2) Gaussian profile (approximated to triangular in illustration) 36 μm wide, 130 μm deep, machined on a pitch of 100 μm. The complete device consists of 140 parallel separation ducts, each 5 mm in length, interfaced to a second major outlet channel.

5.3.2 Device Operation

Chloroform (ThermoFisher, Loughborough, UK) and deionised water (18 MΩ cm from a Purelab UHQ II system, ELGA, UK) were delivered to the microfluidic device at equal flow rates of between 0.03 ml min⁻¹ and 0.18 ml min⁻¹ by independent syringe drivers (KD Scientific, Holliston, MA, USA). 5(6)-carboxyfluorescein (Sigma Aldrich, Gillingham, UK) was added to the aqueous phase to assist visualisation (excitation illumination peak λ = 365 nm). The performance of the phase separator was assessed over a range of applied pressure

differentials between the two fluidic outlets, with the designated organic outlet (outlet 2) exiting at atmospheric pressure and the aqueous outlet (outlet 1) exiting to the sealed vial at atmospheric pressure plus the applied pressure due to compression or expansion of the syringe volume. Phase separation efficiency of 100% was confirmed by visual inspection of the outlet fractions and flow within the transparent FEP outlet tubing, additionally conditions resulting in incomplete removal of the organic phase or aqueous breakthrough into the organic outlet were assessed by volumetric measurement of the eluate collected from the organic outlet (outlet 2), using a syringe and needle to remove and quantify the collected phase(s). Figure 3 depicts the described experimental set up. Microscopy at the separating portion of the device was used to observe phase separation and monitor the aqueous breakthrough pressure at the separator. The ability of the device to separate particulate containing phases was studied by the suspension of 2.0 μm fluorescein labelled polystyrene beads (Sigma Aldrich, Gillingham, UK) in the chloroform phase. The hydrophobic nature of the polystyrene beads ensured they remained suspended entirely in the organic phase.
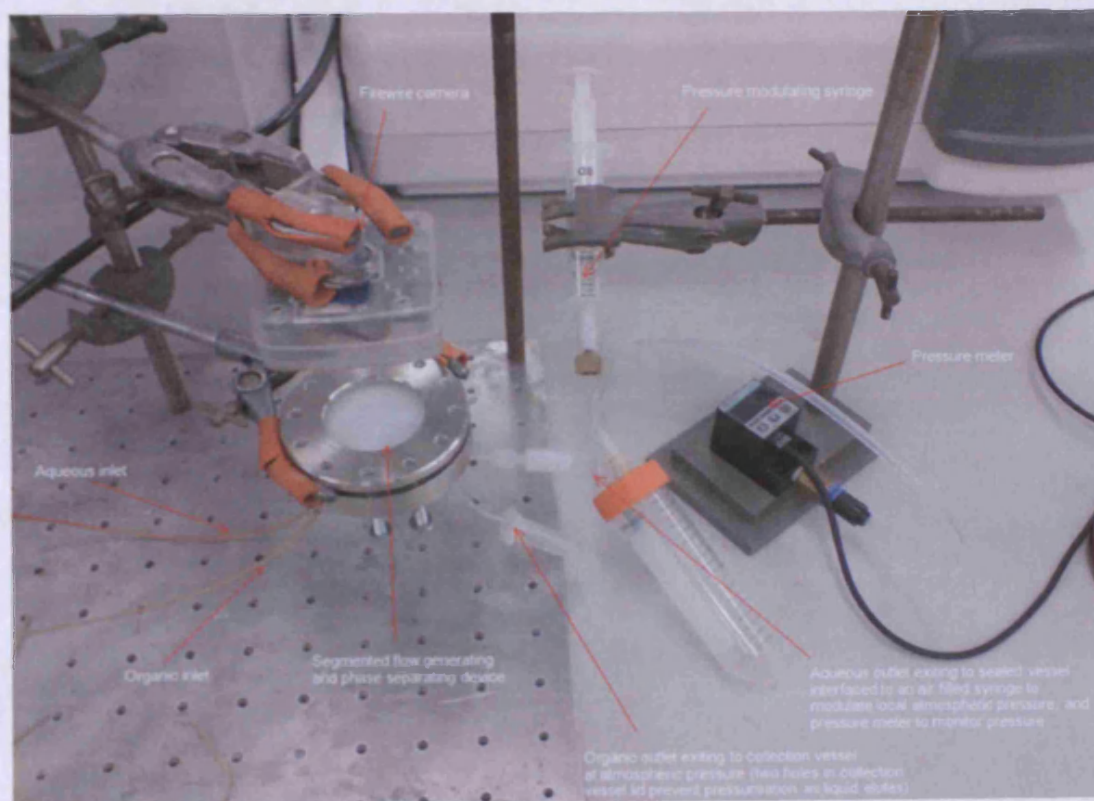
Figure 3 Experimental setup for phase separator operation and evaluation.

5.4 Results and Discussion

5.4.1 Microfluidic Phase Separation

The operation of the phase separator device relies upon a difference in wetting properties between the two liquid phases and the PTFE substrate material. Chloroform is observed to wet the channel walls where as water is repelled by the highly hydrophobic surface of the PTFE. This is easily illustrated by the observed contact angle made by a drop of the two liquids on a PTFE surface (Figure 4).
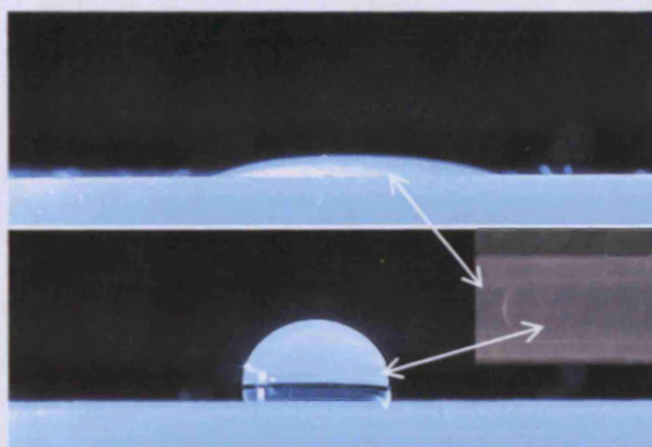
Figure 4 PTFE wettability by chloroform (upper image) and water (lower image), drop volume 10 µl. Co-elution of the two liquids into a PTFE channel results in a segmented flow regime with chloroform wetting the channel walls as the continuous phase and water the disperse, droplet phase (inset image).

The wetting properties of the continuous phase allow it to enter and flow through the narrow separator ducts more readily than the non-wetting, aqueous, dispersed phase. This difference in capillary forces allows the exclusive passage of one phase through the separator ducts by careful control of the pressure drop from the phase separator to each outlet. The Hagen-Poiseuille law enables the calculation of pressure drop due to the laminar flow of Newtonian fluids along a length of tubing or fluidic channel of known geometry:

$$\Delta P = \frac{\alpha \eta Q L}{A^2} \tag{1}$$

where ΔP is the pressure drop due to fluid flow (Pa), α is a numerical prefactor related to the geometry of the channel cross-section, η is fluid viscosity (Pa s), Q is flow rate of the fluid (m^3 s^{-1}), L the channel length (m) and A the cross sectional area of the channel (m^2). For a channel of any geometric cross-section, α is linearly related to the shape's compactness factor, C (C = $perimeter^2$/area) [25-27], Mortensen and Bruus [25] report values of α/C obtained by finite element simulations for a multitude of cross sectional geometries, enabling calculation of pressure drops for a variety of different shaped channels. For a cylindrical tube $\alpha = 8\pi$ and equation 1 simplifies to the commonly given form;

$$\Delta P = \frac{8\eta QL}{\pi r^4} \tag{2}$$

Application of this equation to the outlets either side of the phase separator for their respective fluids gives a nominally equal back pressure of 1.61 kPa ml^{-1} min when the phase separator is operating at 100% efficiency with a 1:1 ratio of fluid flow. (The pressure contribution due to flow within the separation channels was later determined based on subsequent experimental observations of number of ducts required for complete separation). The phase separator device was tested with a 1:1 volumetric ratio of the two liquid phases at combined flow rates of 0.06 ml min^{-1} to 0.36 ml min^{-1}, with additional air pressure applied to the designated aqueous outlet (outlet 1) over the range -1.0 kPa to 10 kPa. Images of the device in operation are illustrated in figures 5 and 6, with the experimental results depicted in figure 7. 100% efficiency separation of the two phases was achieved at all flow rates up to and including an organic flow of 0.18 ml min^{-1} through the separation ducts (0.36 ml min^{-1} segmented flow rate). In keeping with Hagen-Poiseuille law, the minimum applied outlet pressure differential at which phase separation occurs at 100% efficiency with no organic phase remaining in the outlet stream increases linearly with increasing flow rate of the segmented flow stream, as the volume of organic phase required to pass through the separator ducts per unit time increases.
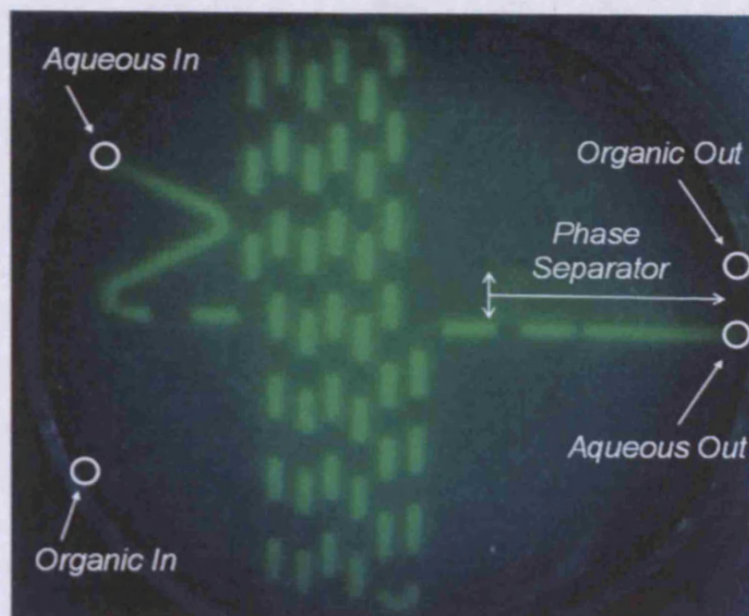
Figure 5 Still image taken from a video of the phase separator in operation. Segmented flow can be seen to be generated through co-elution of the immiscible aqueous and chloroform phases into a common flow channel, via a T-junction geometry. At the phase separation architecture, adjacent aqueous liquid slugs (green) are seen to move progressively closer together and eventually coalesce, as the chloroform exits through the series of narrow separation channels. Complete liquid phase separation occurs and the two fluid streams exit the chip through their respective dedicated outlets. Total flow rate 0.12 ml min^{-1}, 1:1 ratio aqueous/organic flow.
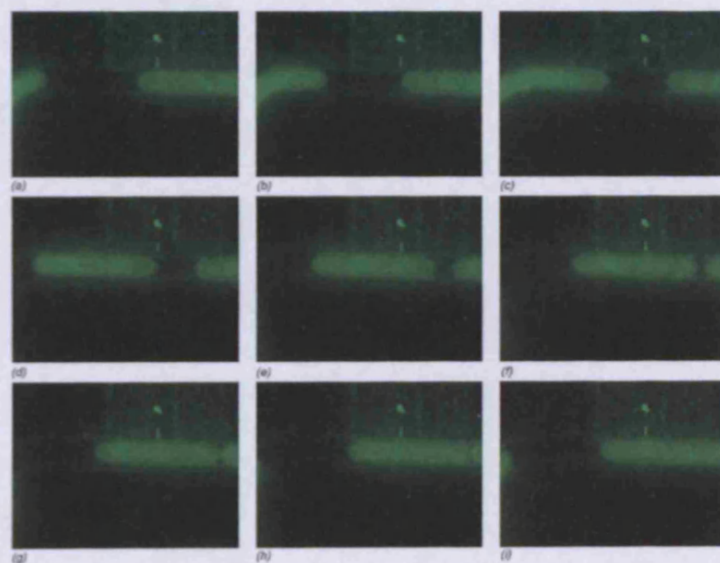
Figure 6 Sequence of still images taken form a video of the phase separator in operation. Adjacent aqueous liquid slugs (green) are seen to move progressively closer together and eventually coalesce, as the chloroform exits through the series of narrow separation channels (top). Total flow rate 0.12 ml min^{-1}, 1:1 ratio aqueous/organic flow.
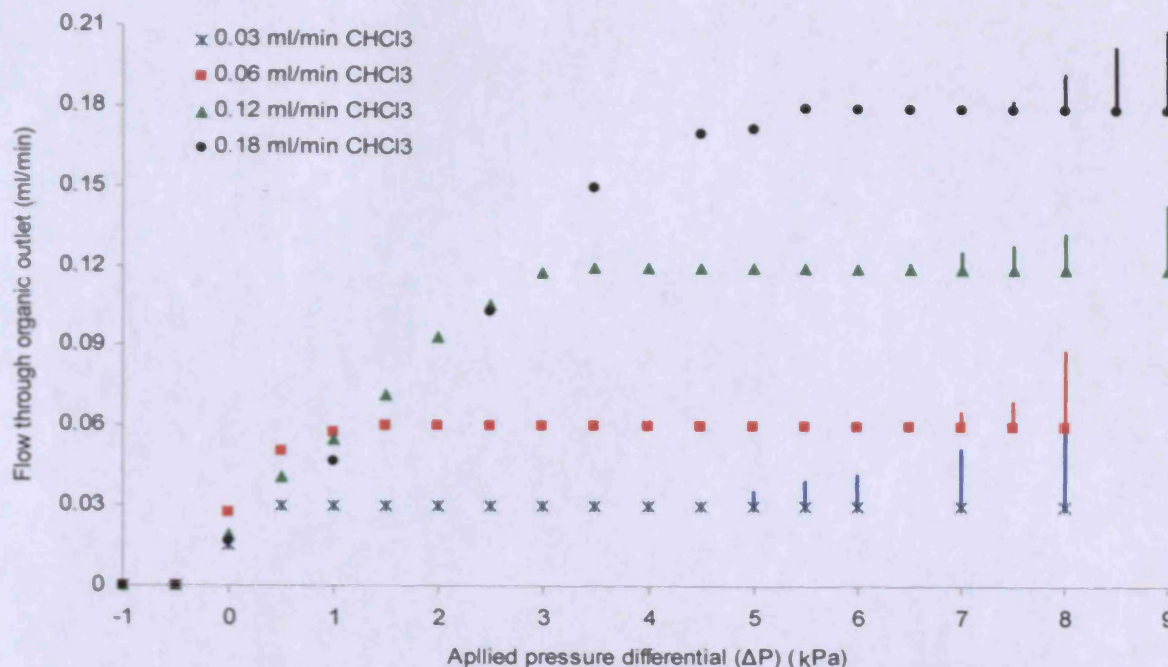
Figure 7 Phase separation performance at four different flow rates over a range of applied pressure differentials across the separator. Segmented flow regimes were generated with a 1:1 ratio of reagent flow and the fluid composition passing through the separator ducts was quantified by measuring the fluid output through the organic outlet over time. Points signify chloroform flow, whilst the height of lines quantify aqueous breakthrough (ml min^{-1}). Note the ability of the device to act as a valve, allowing zero flow, or volumetrically controlled passage of one or both fluid phases.

5.4.2 Limits of Operation

5.4.2.1 Breakthrough Pressure

As the pressure differential between the aqueous outlet and organic outlet increases, the flow rate of chloroform through the separator ducts increases (Equation 1). Total phase separation occurs when the pressure differential across the phase separator is sufficient to support a flow of organic solvent through the separator equal to that in the segmented flow stream (Figure 7). Further increase in the pressure differential supports a greater flow of chloroform though each individual separator duct. Consequently, as the pressure differential increases further, fewer separating channels are required to maintain 100% phase separation. It was observed that as

operating pressure differential increased, coalescence of adjacent aqueous segments occurred progressively nearer the start of the phase separator architecture. This behaviour is described mathematically by the adaptation of Hagen-Poiseuille's law for flow in n parallel channels (Equation 3).

$$\Delta P = \frac{\alpha \eta Q L}{n A^2} \qquad (3)$$

The upper pressure limit of the separation device occurs when a sufficient pressure differential develops to overcome the capillary pressure required to force the non-wetting aqueous phase into the narrow ducts of the separator. This breakthrough pressure (P_b) can be estimated through application of an equation derived from the Young- Laplace equation which governs the capillary rise, or fall, of a wetting or non-wetting liquid in a capillary. Commonly applied as a method for pore size measurement in membrane manufacturing, the bubble point test [28] measures the gas pressure required to force air (non-wetting) through membrane pores filled with a wetting liquid. This enables calculation of pore-size from the equation;

$$P_b = \frac{\alpha \gamma \cos \theta}{r} \qquad (4)$$

where γ is the interfacial surface tension between the two fluids (liquid/liquid or liquid/gas) (N m^{-1}), θ the wetting angle (Figure 8), r the pore radius (m) (cylindrical pores) and α, a numerical prefactor, a value of 2 is used for cylindrical pores. For alternative or irregular geometries α/r can be substituted for the perimeter to area ratio of the pore opening [29]. In the case of the liquid phase separator the non-wetting aqueous phase can be considered analogous to the air in the bubble point test and an estimation for the aqueous breakthrough pressure of the device can be calculated. Approximating the Gaussian geometry of the separation ducts to a triangle (w = 30 μm, h = 130 μm) (Figure 2), giving a perimeter/area measurement of 15x10^4 m^{-1}, and applying a chloroform-water interfacial tension of 32 mN m^{-1} [30] with a wetting angle, θ, of 0° yields a predicted aqueous breakthrough pressure of 4.79 kPa. The equation for capillary

pressure is only valid under capillary equilibrium, (non-flow conditions), but this value acts as an approximate predictor of the upper operating pressure of the device. Validation of this prediction is achieved through extrapolation of the measured, flow-related, trend in aqueous breakthrough pressure to that at a zero flow rate. This is illustrated in figure 9 and results in a static breakthrough pressure of 4.8 kPa, in close agreement with mathematical prediction obtained from equation 4.
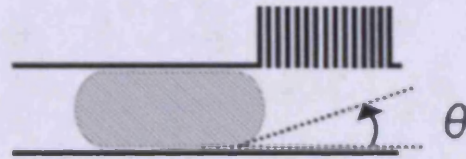
Figure 8 Multiphase flow stream approaching the phase separation duct architecture, the disperse phase approaches with an advancing contact angle of θ, defined by the wetting properties of the fluids with the channel wall.
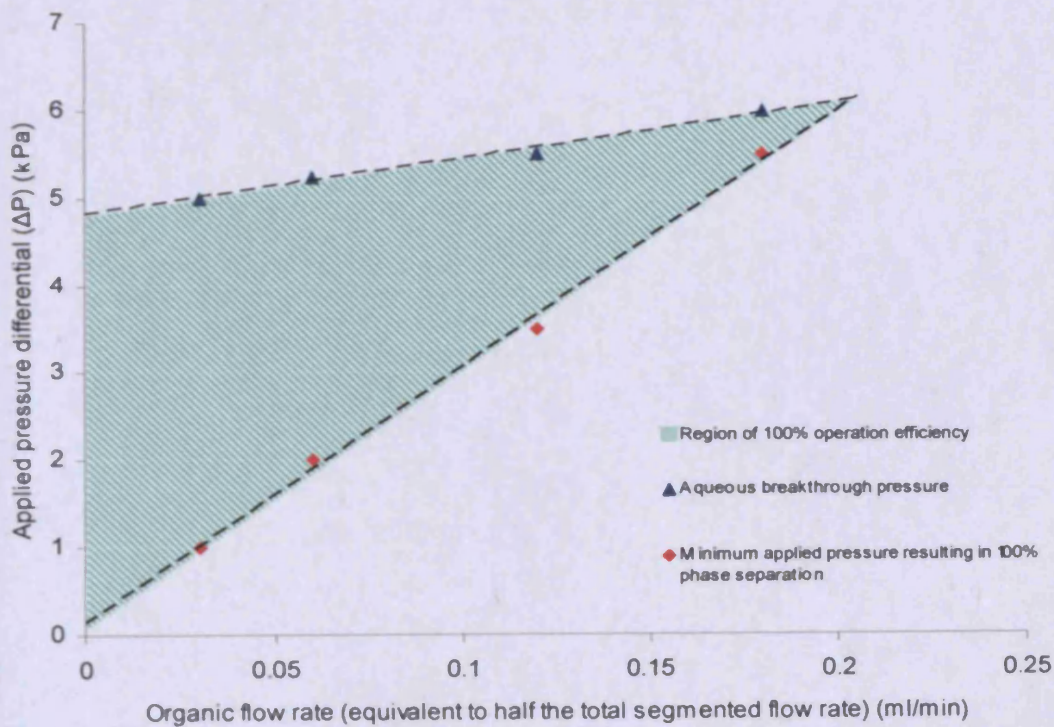
Figure 9 Experimentally defined operating regimes of the phase separator, illustrating minimum applied pressure required to remove all chloroform from the segmented flow stream and applied pressure at which aqueous breakthrough begins to occur. The lower and upper pressure limits for device operation at 100% separation efficiency are illustrated for each flow rate investigated, defining the region of 100% operation efficiency.

The observed increase in breakthrough pressure with increasing flow rate is perhaps a surprising observation. This may be in part a result of a possible reduction in the advancing contact angle of the aqueous fluid packets with increasing flow rate [31], indicative of an increased pressure drop across the fluid packet [32]. Although visual examination confirmed a flattening of the retreating meniscus, it was not possible to observe a change in the advancing contact angle, which approaches 0° when stationary (Figure 4 inset). Another consideration is the force generated which opposes breakthrough as a result of the pressure drop due to flow of organic phase in the separation ducts, described by equation 3. However this would only appear to be applicable to the separation channels through which chloroform was flowing. This assumption is supported by the observation that aqueous breakthrough was largely observed to occur after the point of coalescence of aqueous segments, through otherwise inactive ducts. In order to further understand and explain this behaviour we are currently conducting CFD modelling and simulation studies.

Figure 9 suggests a maximum throughput of just over 0.2 ml min^{-1} per phase (0.4 ml min^{-1} total) with an applied pressure of 6.1 kPa capable of achieving 100% phase separation for this device architecture. This correlates well with experimental observations where the maximum flow rate at which complete phase separation was achievable was 0.2 ml min^{-1} per phase, at an applied pressure of 5.9 kPa. Figure 9 suggests that under these conditions small changes in flow or pressure would result in incomplete separation. This was observed experimentally where small changes in conditions resulted in aqueous breakthrough and/or incomplete removal of chloroform. In such scenarios of incomplete separation the pressure drop due to flow in the designated aqueous and organic outlet tubes ceases to be equal, due to i) the increased fluid flow though one of the channels at the expense of the other, and ii) the presence of immiscible fluid in either outlet stream disrupts laminar flow and generates a pressure drop across the fluidic interface. Therefore at incomplete phase separation $\Delta P_{organic\ out} \neq \Delta P_{aqueous\ out}$, and as a result the pressure at the phase separator does not equate to the applied air pressure at outlet 1 ($\Delta P_{phase\ separator} \neq \Delta P_{applied}$). Consequently further fluctuation in efficiency may be observed as the pressure at the point of phase separation fluctuates due to

incomplete separation. As a result of this the pressure experienced by the segmented flow stream at the phase separator inlets equates to the applied air pressure differential between outlets 1 and 2 only when the phase separator is operating at 100% efficiency. Outside of these limits the pressure at the separator increases above that of the applied air pressure for cases of incomplete removal of organic phase from the segmented flow stream, and is reduced to below that of the air pressure differential in situations where aqueous breakthrough is observed. A range of studies have been conducted investigating pressure drop in segmented or bubble flow [33-41]. The reasoning and estimates vary greatly and the relationship appears to be multi-factorial, with fluidic interfaces [33] and length and number of fluid segments [41] likely to play a key role alongside the properties of the liquids themselves and channel architecture. In multiphase flow droplet formation and break-up at a T-junction geometry has been shown to be governed by pressure fluctuations at the point of generation [31] and thus the effects of pressure changes at the point of phase separation may have implications on the formation of the segmented flow further upstream. As a result, despite being able to easily measure the compositional output from each output of the phase separator the pressure drop this flow provides is not readily predictable except in circumstances of complete phase separation where a single phase flows through each outlet. Further investigation in this area would be required to more accurately understand the behaviour of fluid in the phase separator when operating under conditions of incomplete organic removal or aqueous breakthrough.

5.4.2.2 Active Ducts

At each of the four flow rates investigated the typical number of active separation ducts was recorded at the upper limit of operation of the phase separator (Table 1).

Table 1 Number of active separation ducts at the upper limit of operation at each of the four flow rates investigated, with the calculated pressure drop due to flow of chloroform through the active ducts (Equation 3). Together with comparison to the pressure differential applied across the separator architecture.

Applied air pressure differential (ΔP) = pressure across separator (kPa)	Flow rate of organic phase (ml min^{-1})	Typical no of ducts required for separation	Pressure drop due to flow through active ducts* (ΔP$_{duct\ flow}$) (kPa)	ΔP - ΔP$_{duct\ flow}$ (kPa)
5	0.03	16	1.6	3.4
5.25	0.06	42	1.3	3.95
5.5	0.12	74	1.4	4.1
6	0.18	100	1.6	4.4

* Calculated pressure drop due to organic flow through active separation ducts (equations 3, 5, 6).

The number of active ducts was assumed to be every duct from the entrance of the separator to the point of aqueous phase coalescence. An estimate of the pressure drop as a result of chloroform flow through the active ducts was calculated using equation 3. Mortensen, Okkels and Bruus reported a method for calculation of the numerical prefactor (α) of Hagen-Poiseuille law for any channel geometry, enabling accurate calculation of pressure drop in non-cylindrical channels [27]. Since the separation ducts were machined by laser ablation their cross-sectional profile can be described by a Gaussian curve. Although the mathematics of Gaussian curves are well characterised adaptation of the mathematical expression to give a general formula for the description of a closed (i.e. lid of the channel) Gaussian shape proved difficult. As a result the separation ducts were approximated to be triangular (w = 30 μm, h= 130 μm) (Figure 1). Equation 5 is Mortensen et al.'s general formula for the calculation of α for triangular geometries [27]

$$\alpha = \frac{25C}{17} + \frac{40\sqrt{3}}{17}$$

(5)

where C is the channel shape's compactness factor

$$C = \frac{perimeter^2}{area}$$

(6)

Application of equations 5 and 6 yielded a value for a of 68.26 for the separation ducts. With a = 68.26, η= 0.00058 Pa s for chloroform, Q = the total flow of chloroform (m^3 s^{-1}) cleared through n ducts of length, L= 0.005 m, equation 3 was used to calculate an estimate of the pressure drop due to flow through the active separation channels (Table 1). A linear relationship appears to exist between the minimum number of ducts required for phase separation at the upper limit of operation over the range of flow rates investigated (Figure 10).

Figure 10 Minimum number of active separation ducts clearing chloroform from the segmented flow stream before aqueous breakthrough occurs.

an increase in the typical number of active ducts removing chloroform from the segi

flow stream. This indicates that despite a pressure drop across the separator in the re

4.8 kPa being required to trigger aqueous breakthrough, once the breakthrough pres

exceeded, the force enabling breakthrough is not provided at the expense of the :

chloroform through the separator ducts. This combined with findings in table 1 sugge

the applied pressure (ΔP) across the phase separator is in part responsible for the

chloroform through the separator and in part responsible for the events leading up

eventually resulting in aqueous breakthrough. This may possibly involve clearance

macroscopic organic film which typically surrounds moving slugs of non- wetting liqu

closed channels [42], particularly of square or rectangular geometry [43], or p

overcoming disjoining pressure which exists between the phases and the channel walls

is possible that it is these or other processes which themselves determine the breaktl

pressure with which we are familiar. This perhaps suggests a gradual process of cha

the duct inlet and fluid interface with increasing applied pressure until the breaktl

pressure is overcome. Such factors, which may be influenced by flow velocity and its

on segment length and interfacial contact area [45], may also explain the observed incre

aqueous breakthrough pressure with increasing segmented flow rate. In addition this ma

explain the unsuitability of equation 4 for the estimation of capillary pressure unde

conditions.

It may also be possible that the calculated value for pressure drop due to flow of chlo

through the separation ducts may be significantly underestimated. Although the femtos

pulsed laser ablation process reduces, and for most materials eliminates, conductive tl

192

damage [46], in this case the separation channels machined in the PTFE substrate material appeared to have a rather rough finish when inspected by optical microscopy. This effect may have contributed to an increase in the pressure requirement to support a given rate of flow of organic phase in the laser machined channels. It was also apparent that when in operation, and once aqueous breakthrough into the laser machined separation ducts had occurred, fluorescent regions remained, although entirely static, within the separation ducts (Figure 6). This could be indicative of aqueous residues trapped within the duct, or possibly the machining process giving rise to a change in chemical composition at the machined surface causing the 5(6)-carboxyfluorescein fluorescent probe to be deposited on the machined surface. If, as initially suggested, aqueous residues remained trapped within the separation ducts, this would effectively increase the pressure drop due to flow of chloroform through the channel by both reducing the duct geometry and also providing pressure inducing surface interactions. A further possibility is that the laser ablation process creates a hyper-porous surface which could have the effect of either providing a network of incredibly narrow pores through which a portion of the separated chloroform flows, which, much like a membrane, would provide a greater pressure drop due to flow than an open channel. It is also possible that, should pressure be sufficient, aqueous fluid could enter the hyper-porous structure, where it may well become entrapped or the pore walls become coated with 5(6)-carboxyfluorescein. Therefore, giving rise to the fluorescent regions visible along the path of the separation duct walls. This fluorescent staining of the separation ducts was not cleared following prolonged operation of the phase separator or through flushing the device with either chloroform or water. In additional tests a larger laser machined area of PTFE when exposed to an aqueous dye solution became clearly stained where as virgin areas and micro-milled regions of the PTFE substrate did not experience this phenomenon. It is anticipated that this effect can be reduced or eliminated and the surface finish of the machined ducts improved by submersing the substrate in water during the laser machining process [47]. Figure 11 depicts optical micrographs of a portion of the phase separation architecture, where an array of parallel, narrow, laser machined separation ducts can be seen to branch from the main segmented flow carrying channel.
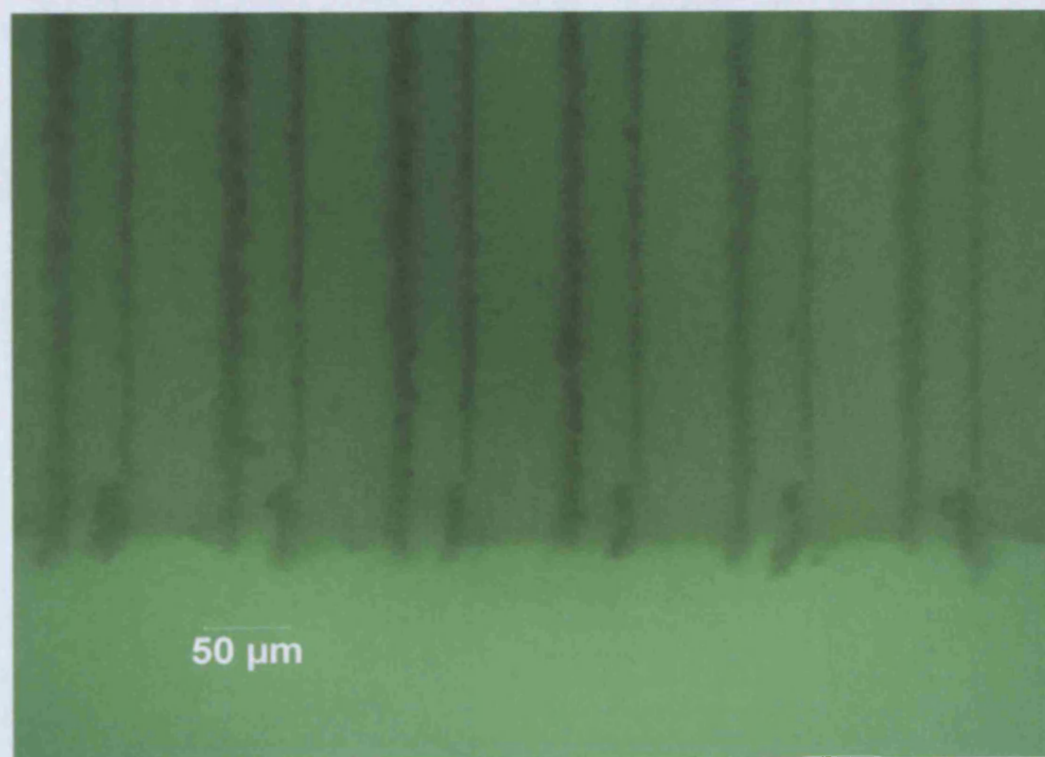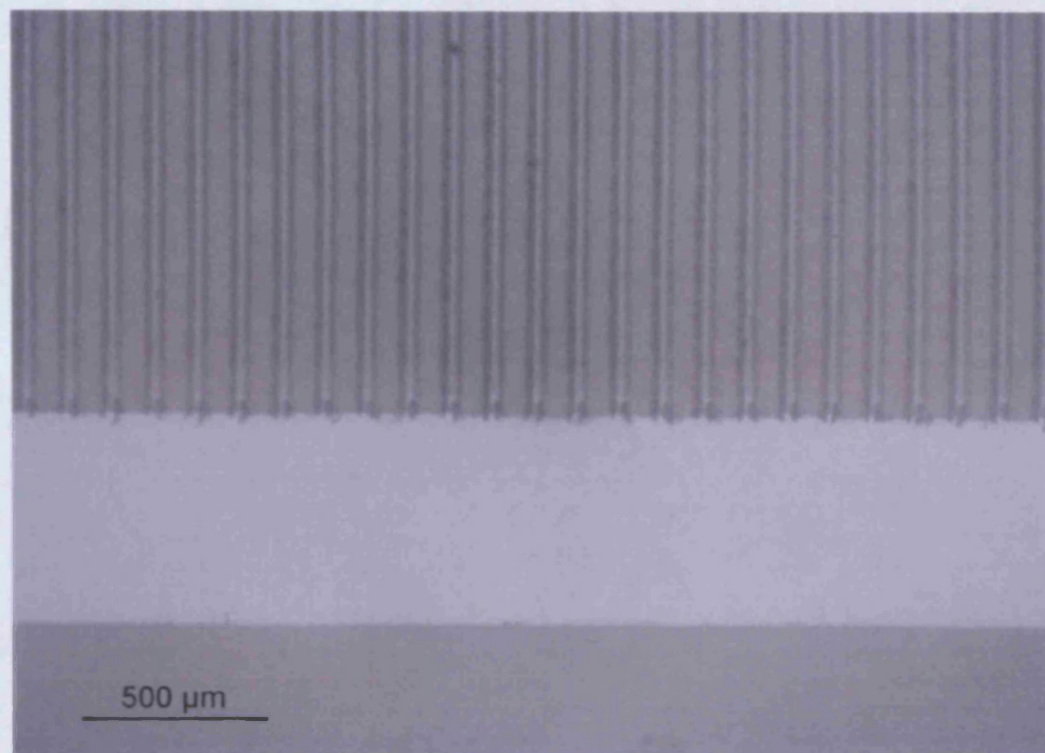
Figure 11 Micrograph images of laser machined separation ducts branching from the main, micromilled, fluidic channel. Machining damage, or debris, can be observed on the laser machined ducts at high magnification.

5.4.3 Design Parameters

5.4.3.1 Mathematical Relationships

Equations 1-6 and the experimental evaluation of the phase separator described illustrate how the operating limits of the phase separator are dependent upon several variables.

The disperse phase breakthrough pressure is governed by the properties of the separator channel as follows;

$$P_b \propto \frac{perimeter}{area} \tag{7}$$

Whilst the pressure drop due to flow of the wetting phase in the separator channels exhibits the following dependencies on separator channel architecture;

$$\Delta P \propto \frac{perimeter^2}{area^3} \qquad \Delta P \propto \frac{1}{n} \qquad \Delta P \propto L \tag{8}$$

The effect of substrate and liquid properties on breakthrough, shows dependencies on the wetting angle and the liquid-liquid interfacial tension;

$$P_b \propto \cos\theta \qquad P_b \propto \gamma \tag{9}$$

With the pressure drop due to flow of the separated fluid in the separator channels proportional to the wetting-fluid's viscosity and flow rate;

$$\Delta P \propto \eta \qquad \Delta P \propto Q \tag{10}$$

Since the choice of fluids employed will largely be governed by the intended application the

scope to tailor the material properties variables is clearly limited, however the ability to predict the feasibility of operation of the phase separator with various flow regimes is undoubtedly useful.

5.4.3.2 Optimisation Strategies

The relationships outlined in equations 7-10 suggest that one of the most effective ways to improve efficiency and provide the opportunity to separate substantially higher flow rates of segmented flow comes from increasing the number of separation ducts (n). For example doubling the number of separation ducts enables twice the flow (Q) of the wetting phase through the separation channels for the same pressure drop across the separator (ΔP). This principle is illustrated by the data in table 1 and figure 6 showing the trend for linear increase in the number of active separation channels with increasing flow rate. Similarly, reducing the length of the separator ducts (L) should have an equivalent effect and thus an array of pillars should provide better results than the relatively long, 5 mm, ducts employed in this device. Less intuitive are the effects of altering the separation channel geometry. Figure 12 illustrates the predicted effect of altering the separation duct geometry relative to the experimental results for the approximated triangular duct cross section (w = 30 µm, h = 130 µm). Based on the relationships 7-10, the anticipated aqueous breakthrough pressure (under static conditions) and the estimated minimum applied pressure differential between the aqueous and organic outlets to achieve 100% phase separation are plotted for triangular ducts of dimensions w = 15 µm, h = 260 µm and w = 15 µm, h = 520 µm.

Figure 12 Predicted effect of separation duct geometry on separator performance: calculated minimum operating pressure (solid line), aqueous breakthrough pressure (dashed line) and 100% separation efficiency regimes (shaded region). Chloroform/water separation by triangular separation ducts (n = 140) with dimensions w = 15 μm, h = 260 μm and w = 15 μm, h = 520 μm compared to the experimentally evaluated duct of dimensions w = 30 μm, h = 130 μm.

Interestingly the aqueous breakthrough pressure shows a heavy dependence on the narrowest geometry of the separation channel, with the depth of the channel having little effect on maximum operating pressure of the device. A finding supported by that of Tsai et al. who showed a similar dependency, albeit by a different method, in estimations of the energy required to deform an air bubble by forcing it into a narrow channel [21]. Despite this dependency, employing narrower and narrower separation ducts may not necessarily improve separation performance, this is as a result of the increased pressure requirement for flow of the organic phase through these ducts due to the increased value of perimeter^2/area^3 for the channel cross section (Figure 12). Additionally the geometry of the main, segmented flow carrying channel should not be ignored. This channel is required to be of suitable dimensions, such that the pressure drop due to flow of the segmented flow stream, along the length of the separator architecture, does not approach the breakthrough pressure of the device. These

197

findings may explain why Angelescu and Siess could not achieve complete phase separation with their device consisting of several 15 x 15 μm square profile separation ducts branching from a main fluidic duct 100 x 15 μm [22]. Clearly a trade off exists between flow rate the phase separator is required to operate at and the tolerance in pressure variations at the point of separation that the device is likely to have to withstand. However with careful design consideration a device suitable for most applications can be envisaged.

5.5 Particulate Carrying Multiphase Flows

A key advantage in employing sufficiently wide separation ducts is their ability to carry solid particulates suspended in the separated organic phase. This would not be possible for a membrane based phase separation approach, since suspended particulates would easily clog the pores. Aside from the requirement for the phase separator device to be capable of separating segmented flow regimes containing suspended MIP particulates (in the context of the work presented in this thesis), solid phase materials may be incorporated in microfluidic systems for a range of applications. For example; separations [48,49], solid support chemistry [50], particle production [9] and particle modification [51]. This enabling methodology holds massive potential, particularly for continuous flow applications combining multiphase flow with an incorporated solid phase.

5.5.1 Methodology

This concept was demonstrated by the separation of a segmented flow stream of water and chloroform containing a 1 mg ml^{-1} suspension of fluorescently labelled 2.0 μm diameter polystyrene beads (Sigma Aldrich, Gillingham, UK) (Figure 8) .The hydrophobic nature of the beads resulted in them remaining suspended entirely in the organic phase as it passed through the separation ducts, with no adverse effects to the device. Complete separation of a segmented flow stream of water and chloroform containing suspended microspheres was achievable with no breakthrough of aqueous phase into the organic stream, or migration of the polystyrene microspheres into the aqueous phase. The presence of the beads suspended in

the chloroform had the effect of increasing the viscosity of the fluid and as such a greater number of separation ducts and a greater pressure drop across the separator was required to achieve complete phase separation compared to the separation of water and chloroform alone. As such, this should be considered when designing a device for such application.

5.5.2 Results

Figure 13 illustrates a series of still images taken from a video recording of the phase separator operating with fluorescent microsphere suspended in the chloroform phase of the segmented flow stream.
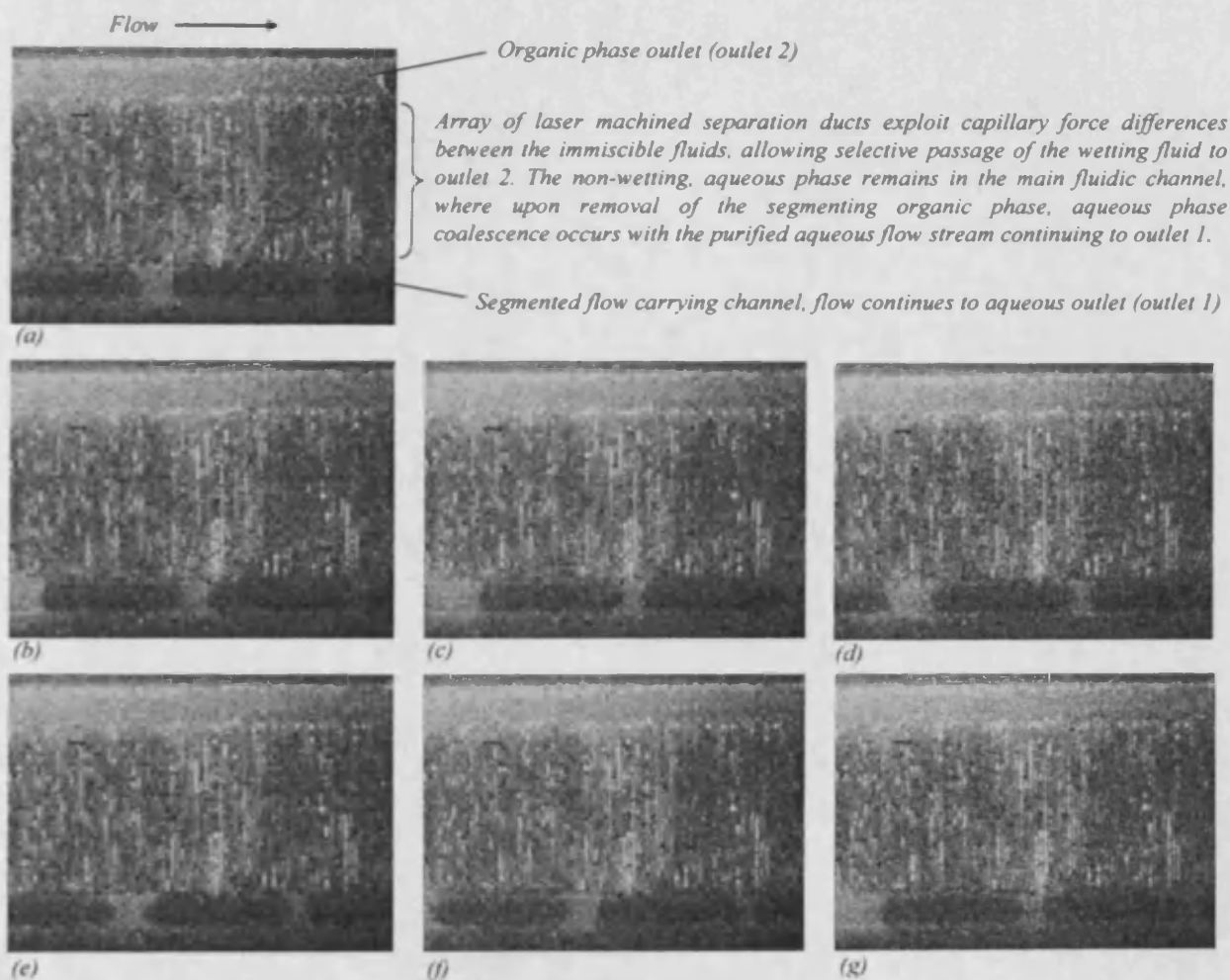
Flow ⟶

— *Organic phase outlet (outlet 2)*

Array of laser machined separation ducts exploit capillary force differences between the immiscible fluids, allowing selective passage of the wetting fluid to outlet 2. The non-wetting, aqueous phase remains in the main fluidic channel, where upon removal of the segmenting organic phase, aqueous phase coalescence occurs with the purified aqueous flow stream continuing to outlet 1.

— *Segmented flow carrying channel, flow continues to aqueous outlet (outlet 1)*

(a) (b) (c) (d) (e) (f) (g)

Figure 13 Sequence of still images taken from a video of the phase separator operating with fluorescently labelled polystyrene microspheres (2.0 µm diameter) suspended in the organic phase and passing through the separation ducts, into a second outlet channel. An aqueous fluid packet (dark, non-fluorescent region) can be seen to move progressively closer to the aqueous fluid packet in front due to removal of chloroform from the segmented flow stream (a-f), until complete phase separation, and aqueous phase coalescence occurs (g).

5.6 Device Design Strategies

5.6.1 Contrast with Angelscu et al.'s Device

The only other reported attempt to utilise a channel array to exploit capillary force differences to separate a segmented flow stream was unsuccessful, leading the authors to adopt a membrane based separation device [22]. The device design of Angelescu et al. assumed that the separation channel geometry must be narrow in all cross-sectional dimensions and, importantly, that the main segmented flow carrying channel should be the same depth as the narrow separation ducts to encourage flow of the wetting phase though the separation ducts. This, however, is not the case. The geometry of the main segmented flow carrying channel has important implications for the operation of the phase separator. The main segmented flow carrying channel must be sufficiently narrow in both cross sectional directions for surface forces to dominate over other forces acting on the fluid(s). Yet it must also be sufficiently wide in all directions to prevent the generation of excessive pressure drop due to flow of the segmented, or separated, flow streams along the length of the complete phase separator architecture. In a laminar flow environment the pressure drop along the length of a channel is given by Hagen-Poiseuille law (Equation 1). In segmented flow regimes the pressure drop due to flow is significantly more complex, as a consequence of the increased pressure generated as a result of interfacial forces and the induced pressure gradients as a result of re-circulating and vortex flow patterns. However, the general relationship is maintained, which for a given volumetric flow, sees the pressure drop generated increase dramatically with reduction in channel diameter. Consequently, the effect of having a main channel of insufficient width or depth is that the pressure generated due to flow of the segmented flow stream in the channel, is sufficiently large that it approaches the breakthrough pressure of the separator, as defined by equation 4, and results in device failure. This oversight constitutes a fundamental flaw in Angelescu et al.'s device design. This is understandable, since it is non-intuitive that a main channel of increased cross-sectional area, consequently carrying an increased volume of fluid, can not only facilitate the increased clearance of wetting fluid through the separation ducts, but that this increase in efficiency outweighs the increased fluid volume present as a

consequence of the increased channel dimensions.

1) 100 x 15 μm

r 2) 15 x 15 μm

i)

r 4) 36 x 130 μm Gaussian cross sectional profile

3) 720 x 600 μm

ii)

Figure 14 Comparison of the fluidic design of *i)* the device reported by Angelescu et al. [22] which failed to separate segmented flow streams with 100% efficiency, and *ii)* the design constructed and evaluated in the work of this chapter, demonstrated to separate segmented flow streams with 100% efficiency due to appropriately considered geometries of the channels with respect to fundamental fluid properties.

Figure 15 Scale plan and cross sectional schematic diagrams of the fluidic design of the Angelescu et al. (*i*) [22] (dimensions: main channel; w = 100 μm, d = 15 μm, separation ducts; w =15 μm, d = 15 μm square cross section) and the phase separation device constructed and evaluated in the work of this thesis (*ii*) (dimensions: main channel; w = 720 μm, d = 600 μm, separation ducts; w = 36 μm, d = 130 μm high aspect ratio Gaussian cross section).

The device design of Angelescu et al. assumed that the separation channel geometry must be narrow in all cross-sectional dimensions (Figure 14 and Figure 15). In fact, the upper operating pressure limit, defined by the aqueous breakthrough pressure (Equation 4) shows only a heavy dependence upon the narrowest of the two cross-sectional geometries (width or depth), and only a weak dependency on the larger of the two length scales. This is because for non-cylindrical geometries a/r in equation 1 can be substituted for the perimeter to area ratio of the pore opening [29]. Consequently, narrow, high-aspect ratio channels (as employed in the device developed and reported within the research of this thesis) enable much greater

separation efficiency. An increase in the depth of the separation duct has very little difference on the pressure required for device failure through the non-wetting phase entering the separation ducts. However, high-aspect ratio separation ducts offer a marked increase in volume of wetting phase the separator is able to clear for any given pressure differential across the phase separator. This is a result of the increased cross-sectional area of each separation duct and the subsequent reduction in pressure required for flow of the wetting phase though the duct (Equation 1). This reduces the force requirement for phase separation; i.e. enabling increased clearance of the wetting phase through the separation ducts for the same pressure differential across the separator. This ensures that the breakthrough pressure is not breached. As such, clearance of the wetting phase through the separation ducts has a strong dependency on both width and height of separation ducts.

Laser machining enables the creation of narrow, high aspect ratio, structures in PTFE and other fluoropolymers. The extremely hydrophobic nature of PTFE, maximises the difference in wetting properties between the two immiscible liquid phases and the device channel walls. This decreases the advancing contact angle (θ) of the disperse (non-wetting) phase droplets as they approach the phase separation ducts, to a value approaching $0°$. This is unlike the mildly hydrophilic properties of silicon, or the variable hydrophilic/hydrophobic properties of polydimethylsiloxane (PDMS), consequently increasing the aqueous breakthrough pressure, and therefore the upper operating limit of the device.

5.6.2 Optimised Designs

The considered design of the complete phase separator architecture, including main fluidic duct and outlet geometries and lengths, can enable production of devices where the pressure differential driving the liquid-liquid separation is provided passively by the pressure differential between the flow of liquid either side of the phase separator ducts. Schematic examples are illustrated in Figure 16.

Figure 16 CAD drawings for optimised phase separation device designs for application in the device manifold illustrated in figure 1. *i)* illustrates a schematic design drawing of an extended path length phase separation module. A segmented flow stream (generated off-chip) enters the device through a dedicated input port (1) which elutes into a main flow channel (2). The shaded region represents an array of high aspect ratio phase separation ducts (3). At the juncture of the multiphase flow carrying channel (2) and the separation ducts (3) phase separation begins to occur with the continuous phase (separated phase) entering the separation ducts (3). The separated phase continues along the separation ducts and empties into the common channel (4), which conducts the separated fluid to a dedicated outlet (5). Removal of the continuous phase through the separation ducts (3), causes coalescence of the disperse phase droplets into a continuous stream which flows to a dedicated outlet (6). The extended path length of the separating portion of the device, allows for a greater number (n) of separation ducts, thus increasing the maximum operable flow rate of the phase separator device. Designs *ii)* and *iii)* demonstrate extended path length phase separation modules suitable for the *passive* separation of multiphase immiscible fluid flows. The difference in resistance of fluid flow, to the two possible fluidic exists (5) and (6), achieved by considered design of the channel geometries (length, width and depth) with respect to the fluid properties and flow characteristics, provides a pressure differential between the fluidic exits (5) and (6) supporting the flow of the separated fluid through the separation ducts (3). This pressure differential (ΔP) is generated wholly or in part by the flow of the immiscible fluid stream and the individual fluid flows in their respective channels. The device illustrated in *ii)* was manufactured in accordance to the channel geometries of the primary device tested in this chapter (Figure 1-14). The device was demonstrated to separate segmented flow streams of chloroform and water (1:1) with 100% separation efficiency at flow rates up to 3.0 ml min^{-1}. The pressure differential (ΔP) across the separation ducts (3), enabling the separation, is provided entirely by the flow of the immiscible fluid stream and the individual fluid flows in their respective channels to their respective outlets.

5.6.2.1 Optimised Separation Module - Production and Evaluation

The optimised design illustrated in Figure 16 *ii)* was manufactured using the techniques detailed in section 3.1 (Device Production). The device was designed as a phase separation module, for the separation of segmented flow regimes generated on either a separate device or within capillary tubing. A main segmented flow carrying channel of width and depth of 600 μm was machined with multiple arrays of laser machined narrow separation ducts (30 μm x 60 μm due to reduced laser power). Each array of separation ducts eluted into a separate collection duct which all flowed into a common outlet channel. The constructed device was supplied with a segmented flow stream of chloroform and water generated by a Tefzal T-piece connected with 0.5 mm I.D. FEP tubing. The two outlets of the phase separation device were each interfaced with 15 cm of 0.5 mm I.D. FEP tubing. This on-chip design (Figure 16 *ii)* created a pressure differential between the two fluid outlets, through velocity, viscous, and channel length differences between the flow paths and flow regimes within the device channels. This passive generation of the pressure differential driving the separation (ΔP) eliminates the need for manual regulation of the local atmospheric pressure at which the flow streams elute. Additionally the design was such that as flow rate increased, the flow generated pressure differential also increased, enabling greater clearance of the wetting organic phase. The device was found to passively separate chloroform and water segmented flow streams, with a 1:1 phase ratio, at total flow rates of 0.05 to 3.00 ml min^{-1} with 100% efficiency.

5.7 Conclusions

The development of a planar, membrane free, liquid phase separation microfluidic architecture offers substantial advantages over previously reported membrane based approaches to segmented flow liquid phase separation. Membrane based approaches have several limitations, the membrane itself is fragile, lacking in physical stability. The membrane can also become easily spoiled or clogged and needs frequent replacement [52]. This leads to challenging design requirements when manufacturing a device. Additionally, membrane separators are typically a sandwich composition of an upper and lower substrate material

containing machined micro-channels, with the PTFE membrane separating them. This design specification therefore requires fully 3-D fluidic devices. This creates an integration difficulty with standard, planar, machining techniques where fluidic channels are typically created on a single surface, where channel depth provides the only z-axis component. Importantly, the phase separation device reported here provides exciting potential for separations and enrichments in synthetic chemistry and for multi-stage processing in multiphase microfluidics. The ability to achieve continuous flow separation of a segmented flow stream provides opportunities for the development of continual operation, high throughput, integrated lab-on-a-chip devices to conduct multi-step synthetic chemistry, separations and enrichments, and sequential combinations of these activities. This work demonstrates that capillary forces in a multiphase flow system are sufficiently dominant to separate the component liquids of a segmented flow regime through an array of narrow channels over a range of flow rates. This is achieved by appropriate control of pressure drops from the separator to the fluidic outlets. In this illustration this was achieved by controlling the atmospheric pressure at which the aqueous outlet exited, in order to interrogate the behaviour of the separator over a range of operating conditions. However, precise control over pressure drop may also be achieved by considered design of outlet length and geometry to provide an appropriate operating pressure differential across the separator. The relationship of design variables such as separator channel geometry, number and length, together with fluid properties, flow rates and applied pressure differentials were examined mathematically and linked to experimental findings together with predicted and observed limits of operation of the separator. This systematic study of phase separator performance together with examination of the mathematical relationships governing liquid-liquid separation and device failure, will enable optimal device design and provide the opportunity to predict the influence of fluid manipulation and events downstream of the separator (e.g. re-segmentation and separation). The demonstration of the separation device to operate with microparticulates suspended in the organic phase paves the way for on-chip multi-fluid phase, solid-phase assisted reactions, separations and manipulations. The inherent properties of segmented flow streams to give rise to highly efficient mass transfer and rapid mixing of chemical species, generates the potential to mix

and transfer chemical species between phases and immediately separate the fluid components in a single 'always-on' device, offering massive efficiency advantages over traditional batch techniques.

5.8 References

[1] C. Lee et al., "Multistep Synthesis of a Radiolabeled Imaging Probe Using Integrated Microfluidics," *Science*, vol. 310, Dec. 2005, pp. 1793-1796.

[2] N. Pamme, "Continuous flow separations in microfluidic devices," *Lab on a Chip*, vol. 7, 2007, pp. 1644-1659.

[3] J. Wang, A. Ibanez, and M. Chatrathi, "On-Chip Integration of Enzyme and Immunoassays: Simultaneous Measurements of Insulin and Glucose," *Journal of the American Chemical Society*, vol. 125, Jul. 2003, pp. 8444-8445.

[4] H.R. Sahoo, J.G. Kralj, and K.F. Jensen, "Multistep Continuous-Flow Microchemical Synthesis Involving Multiple Reactions and Separations," *Angew. Chem., Int. Ed*, vol. 46, 2007, pp. 5704–5708.

[5] S. Teh et al., "Droplet microfluidics," *Lab on a Chip*, vol. 8, 2008, pp. 198-220.

[6] B. Karlberg and S. Thelander, "Extraction based on the flow-injection principle : Part I. Description of the Extraction System," *Analytica Chimica Acta*, vol. 98, May. 1978, pp. 1-7.

[7] O.K. Castell, C.J. Allender, and D.A. Barrow, "Novel biphasic separations utilising highly selective molecularly imprinted polymers as biorecognition solvent extraction agents," *Biosensors and Bioelectronics*, vol. 22, Oct. 2006, pp. 526-533.

[8] C.J. Gerdts et al., "Time-Controlled Microfluidic Seeding in nL-Volume Droplets To Separate Nucleation and Growth Stages of Protein Crystallization," *Angewandte Chemie International Edition*, vol. 45, 2006, pp. 8156-8160.

[9] T. Nisisako and T. Torii, "Microfluidic large-scale integration on a chip for mass production of monodisperse droplets and particles," *Lab on a Chip*, vol. 8, 2008, pp. 287-293.

[10] B. Ahmed, D. Barrow, and T. Wirth, "Enhancement of Reaction Rates by Segmented Fluid Flow in Capillary Scale Reactors," *Advanced Synthesis & Catalysis*, vol. 348, 2006, pp. 1043-1048.

[11] A. Huebner et al., "Quantitative detection of protein expression in single cells using droplet microfluidics," *Chemical Communications*, 2007, pp. 1218-1220.

[12] M.J. Fuerstman, P. Garstecki, and G.M. Whitesides, "Coding/Decoding and Reversibility of Droplet Trains in Microfluidic Networks," *Science*, vol. 315, Feb. 2007, pp. 828-832.

[13] J. Ruzicka and E.H. Hansen, "Flow injection analyses : Part I. A new concept of fast continuous flow analysis," *Analytica Chimica Acta*, vol. 78, Aug. 1975, pp. 145-157.

[14] A. Gunther and K.F. Jensen, "Multiphase microfluidics: from flow characteristics to chemical and materials synthesis," *Lab on a Chip*, vol. 6, 2006, pp. 1487-1503.

[15] N. Harries et al., "A numerical model for segmented flow in a microreactor," *International Journal of Heat and Mass Transfer*, vol. 46, Aug. 2003, pp. 3313-3322.

[16] J.R. Burns and C. Ramshaw, "The intensification of rapid reactions in multiphase systems using slug flow in capillaries ," *Lab on a Chip*, vol. 1, 2001, pp. 10-15.

[17] K. Ishiguro et al., "Separation of Gas from Downward Gas-Liquid Two-Phase Flow Using a Y-Junction of Poor Wettability," *JSME International Journal Series B*, vol. 47, 2004, pp. 795-803.

[18] Y. Kikutani et al., "Temperature Dependent Phase Behaviour of N-Cyclohexyl-2-pyrrolodone/Water System in a Microchannel and Phase Separation Using Viscosity Difference," *The Proceedings of μTAS 2007 Conference*, Paris, France: 2007, pp. 955-957.

[19] H. Xiao et al., "Initial study of two-phase laminar flow extraction chip for sample preparation for gas chromatography," *Lab on a Chip*, vol. 6, 2006, pp. 1067-1072.

[20] J. Atencia and D.J. Beebe, "Controlled microfluidic interfaces," *Nature*, vol. 437, 2005, pp. 648-655.

[21] J. Tsai and L. Lin, "Active microfluidic mixer and gas bubble filter driven by thermal bubble micropump," *Sensors and Actuators A: Physical*, vol. 97-98, Apr. 2002, pp. 665-671.

[22] D. Angelescu and D. Siess, "Microfluidic phase separation," *Proc. Sensors 2005 IEEE*, 2005, p. 4 pp 175-178.

[23] L. Nord and B. Karlberg, "Extraction based on the flow-injection principle : Part 5. Assessment with a Membrane Phase Separator for Different Organic Solvents," *Analytica Chimica Acta*, vol. 118, Aug. 1980, pp. 285-292.

[24] J.G. Kralj, H.R. Sahoo, and K.F. Jensen, "Integrated continuous microfluidic liquid-liquid extraction," *Lab on a Chip*, vol. 7, 2007, pp. 256-263.

[25] N.A. Mortensen, L.H. Olesen, and H. Bruus, "Transport coefficients for electrolytes in arbitrarily shaped nano- and microfluidic channels," *New Journal of Physics*, vol. 8, 2006, p. 37.

[26] N.A. Mortensen and H. Bruus, "Universal dynamics in the onset of a Hagen-Poiseuille flow," *Physical Review E (Statistical, Nonlinear, and Soft Matter Physics)*, vol. 74, Jul. 2006, pp. 017301-4.

[27] N.A. Mortensen, F. Okkels, and H. Bruus, "Re-examination of Hagen-Poiseuille flow: Shape dependence of the hydraulic resistance in microchannels," *Physical Review E (Statistical, Nonlinear, and Soft Matter Physics)*, vol. 71, May. 2005, pp. 057301-4.

[28] M.C. Porter, *Handbook of Industrial Membrane Technology*, Berkshire: Noyes Publications, 1990.

[29] A. Jena and K. Gupta, "Characterization of Pore Structure of Filtration Media," *Fluid/Particle Separation Journal*, vol. 14, 2002, pp. 227-241.

[30] O.V. Nechypor et al., "The influence of weakly polar solvent chloroform on the state of water adsorbed by serum albumin," *Biopolimery I Kletk*, vol. 22, 2006, p. 375.

[31] P. Garstecki et al., "Formation of droplets and bubbles in a microfluidic T-junction-scaling and mechanism of break-up," *Lab on a Chip*, vol. 6, 2006, pp. 437-446.

[32] A. Hazel and M. Heil, "The steady propagation of a semi-infinite bubble into a tube of elliptical or rectangular cross-section," *Journal of Fluid Mechanics*, vol. 470, 2002, pp. 91-114.

[33] T. Cubaud, "Transport of bubbles in square microchannels," *Physics of Fluids*, vol. 16, 2004, pp. 4575-4585.

[34] A. Kawahara, P.M.-. Chung, and M. Kawaji, "Investigation of two-phase flow pattern, void fraction and pressure drop in a microchannel," *International Journal of Multiphase Flow*, vol. 28, Sep. 2002, pp. 1411-1435.

[35] P.M.Y. Chung and M. Kawaji, "The effect of channel diameter on adiabatic two-phase flow characteristics in microchannels," *International Journal of Multiphase Flow*, vol. 30, 2004, pp. 735-761.

[36] M.J. Fuerstman et al., "The pressure drop along rectangular microchannels containing bubbles," *Lab on a Chip*, vol. 7, 2007, pp. 1479-1489.

[37] H. Chio et al., "On the Motion of a Bubble through Microchannel Contractions," *Proceedings of NSTI-Nanotech 2006*, Boston, USA. : Technical University of Denmark, , pp. 497-500.

[38] M.N. Kashid and D.W. Agar, "Hydrodynamics of liquid–liquid slug flow capillary microreactor: Flow regimes, slug size and pressure drop," *Chemical Engineering Journal*, vol. 131, 2007, pp. 1-13.

[39] H. Chio et al., "Transient pressure drops of gas bubbles passing through liquid-filled microchannel contractions: an experimental study," *Journal of Micromechanics and Microengineering*, vol. 16, 2006, pp. 143-149.

[40] B.J. Adzima and S.S. Velankar, "Pressure drops for droplet flows in microfluidic channels," *Journal of Micromechanics and Microengineering*, vol. 16, 2006, pp. 1504-1510.

[41] T. Cubaud, U. Ulmanella, and C. Ho, "Two-phase flow in microchannels with surface modifications," *Fluid Dynamics Research*, vol. 38, Nov. 2006, pp. 772-786.

[42] Vladimir S. Ajaev and G. M. Homsy, "Modeling Shapes And Dynamics Of Confined Bubbles," *Annual Review of Fluid Mechanics*, vol. 38, 2006, pp. 277-307.

[43] H. Wong, S. Morris, and C.J. Radke, "Three-dimensional menisci in polygonal capillaries," *Journal of Colloid and Interface Science*, vol. 148, Feb. 1992, pp. 317-336.

[44] N.V. Churaev, "Derjaguin's disjoining pressure in the colloid science and surface phenomena," *Advances in Colloid and Interface Science*, vol. 104, Jul. 2003, pp. xv-xx.

[45] M. Abkarian and H.A. Stone, "Microfluidic flow focusing: Drop size and scaling in pressure versus flow-rate-driven pumping," *Electrophoresis*, vol. 26, 2005, pp. 3716-3724.

[46] M.D. Shirk and P.A. Molian, "A review of ultrashort pulsed laser ablation of materials," *Journal of Laser Applications*, vol. 10, Feb. 1998, pp. 18-28.

[47] A. Kruusing, "Underwater and water-assisted laser processing: Part 2--Etching, cutting and rarely used methods," *Optics and Lasers in Engineering*, vol. 41, Feb. 2004, pp. 329-352.

[48] O.K. Castell, C.J. Allender, and D.A. Barrow, "Continuous molecular Enrichment in Microfluidic Systems," *Lab on a Chip*, vol. 8, pp. 1031-1033.

[49] L.R. Huang et al., "Continuous Particle Separation Through Deterministic Lateral Displacement," *Science*, vol. 304, May. 2004, pp. 987-990.

[50] S.A. Kulkarni, S.B. Ogale, and K.P. Vijayamohanan, "Tuning the hydrophobic properties of silica particles by surface silanization using mixed self-assembled monolayers," *Journal of Colloid and Interface Science*, vol. 318, Feb. 2008, pp. 372-379.

[51] R. Tornay et al., "Dielectrophoresis-based particle exchanger for the manipulation and surface functionalization of particles," *Lab on a Chip*, vol. 8, 2008, pp. 267-273.

[52] A.N. Anthemidis et al., "On-line liquid-liquid extraction system using a new phase separator for flame atomic absorption spectrometric determination of ultra-trace cadmium in natural waters," *Talanta*, vol. 62, Feb. 2004, pp. 437-443.

Chapter 6

Molecularly Imprinted Polymer Binding Isotherm Modelling - Predicting Binding for Performance Comparisons and Application Optimisation

6.1 Context

Following the results of chapter 4, it was apparent that an extensive variable set influenced the extraction efficiency of a segmented flow extraction, even in the absence of suspended MIP particles for extraction enhancement. As such, greater understanding of MIP binding behaviour would assist in optimisation strategies for the solid-phase assisted segmented flow extraction platform. As demonstrated experimentally (Chapter 4 Figure 11), and as would be expected, the extent of analyte removal from the sample aqueous phase increased with increased MIP loading. However, due to the nature of the three-phase competitive partitioning of analyte in the MIP assisted liquid-liquid extraction system, and the non-linear concentration dependent binding of analyte to the MIP microspheres (Chapter 2 Figure 6), the relationship between extraction efficiency, polymer loading, sample volume and analyte concentration would be less than straightforward. Consequently, a trade-off would exist between increased polymer loading and enhancement of the extraction. This is particularly important from both a practical and resource economics perspective. This problem was approached initially from a theoretical examination of the variables, this was then used to construct a mathematical model to approximate analyte binding to the MIP for a desired set of incubation conditions. Initially this was carried out for a small preliminary data set in a single solvent system. This model would subsequently be expanded upon to estimate phase distribution of analyte at equilibrium for a dynamic two phase system, (Appendix 3). The ability to predict MIP-analyte binding under any desired set of incubation variables (polymer mass, incubation volume and analyte concentration) would also be of extensive value in comparing the efficacy of different polymers reported in the literature. In order to identify promising approaches to molecular imprinting and assist in the development of fundamental knowledge within the molecular imprinting community.

6.2 Background

It is apparent from the literature in the molecular imprinting field and through the minimal uptake of MIP materials in commercially available products that molecular imprinting has yet

to fulfil its early promise. This may in part be due to a lack of fundamental understanding of the workings of the imprinted site since many researchers have taken a 'black box' approach to application driven application of imprinted materials. The investigation of the chemical structure and distribution of binding sites within imprinted matrices have not proved successful with conventional spectroscopic techniques [1]. This is largely due to the large and insoluble nature of MIP particles and the well documented, perceived heterogeneity of binding sites within the polymer matrix [2]. In addition to this lack of understanding of the imprinted site itself, different researchers have adopted different approaches for polymer evaluation and the assessment of imprinting performance (Section 6.2.1). Such techniques, usually adapted from neighbouring fields of research vary in their suitability and usefulness as a global measure of assessing imprinting performance. The relatively small research community of molecular imprinting has yet to adopt a standard approach, or method of data presentation, that enables easy comparison of polymer binding performance for different polymers, imprinting methodologies and application environments. Much analysis of polymer performance is directed towards the intended application and, as such, a collective understanding of the science of molecular imprinting has not been maximised.

6.2.1 Evaluating MIP Binding Performance : Commonly Employed Methods for Assessment of Analyte Recognition and Rebinding

There are several generally applied techniques for assessing MIP analyte recognition performance; these can broadly be categorised as either kinetic or equilibrium analysis. Depending on the application of the polymer or the discipline of the research, the techniques may be closely related to those of the field of chromatography (i.e. HPLC in the case of MIP stationary phase analysis), or pharmacology and the study of biological receptor affinity studies (i.e. use of Scatchard plots), or unique to molecular imprinting (e.g. imprinting factor). In most cases the degree of analyte recognition is assessed *via* direct comparison to binding to a non-imprinted polymeric material, assumed to be representative of non-specific affinity interactions. The specificity of the recognition may be assessed in much the same way through comparison of binding of various species to the MIP, in either a non-competitive or

competitive environment.

6.2.1.1 Equilibrium Analysis

Equilibrium binding analysis is perhaps the most useful approach for generating comparative data as it removes any time dependency. Equilibrium binding analysis can give indicators to both the affinity and capacity of an imprinted matrix. The process usually involves incubation of a known mass of polymer in a known incubation volume, containing a measured quantity of analyte. The suspension is agitated, usually overnight, to allow analyte distribution to reach equilibrium, after which the suspension is usually filtered or centrifuged and the liquid phase assayed to determine the free analyte content. The concentration deficit from the incubation concentration is assumed bound to the polymer (Chapter 2). This methodology is the basis for generation of the raw data, which may then be expressed or processed by a variety of means.

6.2.1.1.1 Binding Isotherm

The binding isotherm is perhaps the most simple depiction of equilibrium analysis binding data over a range of analyte concentrations. It is also possibly the most useful measure in terms of making comparisons between polymers or ligands and also for estimating binding behaviour. This is discussed further in section 6.3. Figure 1 shows the binding isotherm for the MIP and NIP prepared and evaluated in chapter 2.
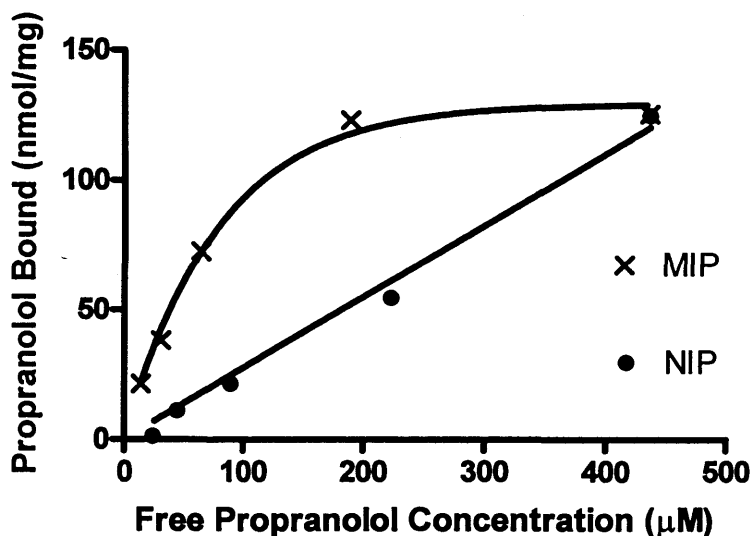
Figure 1 Binding Isotherm for MIP and NIP prepared and evaluated in chapter 2

The isotherm plots the equilibrium concentration of analyte on/in either phase, either in solution (i.e. µM) or bound to the polymer (i.e. nmol mg^{-1} or moles kg^{-1}) and may be referred to as a plot of [bound] verses [free]. It is important that the isotherm plots the equilibrium measured concentration, and not the incubation concentration which is sometime mistakenly plotted. As can be seen from the isotherms of Figure 1 the adsorption isotherm for the MIP is markedly non-linear, unlike that observed, as a measure of non-specific binding, for the NIP (this type of behaviour is similar to that observed for analytes interacting with conventional chromatographic stationary phases e.g. silica or C_{18}). This has significant implications for the employment of MIP materials as chromatographic stationary phases, or their performance evaluation by such methods [3]. This is discussed further in section 6.2.1.2.2, and is essential for the application of MIPs in competitive binding assays [4].

6.2.1.1.1.1 Isothermal Models

In order to further characterise prepared imprinted materials, many researchers have applied various isothermal models to their experimentally derived binding isotherms [5-10]. Such analysis assumes a binding model to elucidate the parameters such as affinity, number of sites, and site distribution, etc. through parameter fitting of the measured isothermal curve to the selected iosthermal model. The application of different isothermal models to MIP

217

isotherms has been reviewed [2,7], a brief summary of the model assumptions and fitting

parameters is detailed in Table 1.

Table 1 Commonly employed isothermal models applied to MIPs.

Model	Major assumptions	Discrete populations?	Continuous distribution?	Saturable?	Equation	Parameters	Note	reference
Langmuir	One finite population of binding site of equal affinity	yes one	N/A	Yes	$B = NKC/1+KC$	N = number of homogenous binding sites, K = adsorption constant, B = Bound concentration, C = Free concentration	will yield linear Scatchard plot if model is correct	[2]
Bi-Langmuir	Two populations of sites, high affinity and low affinity	yes two	N/A	Yes	$B = N1K1C/1+K1C + N2K2C/1+K2C$		Scatchard approximated as two straight lines	[7]
Freundlich	Exponential distribution of binding sites, number of sites increases indefinitely with decreasing association constant	No	Yes - Infinite	No	$B = aF^m$	a = combined measure of capacity (N) and average affinity (k), m = heterogeneity index (0 = heterogeneous, 1=homogenous)	Implies infinite number of sites, applicable only for certain concentration limits for MIPs, deviation at high concentrations. Successfully applied to heterogeneous non-specific materials, activated carbon, silica, clays, metals, polymers	[5-7]
Langmuir-Freundlich	Can behave like Langmuir or Freundlich at either extreme	yes/no	yes/no	yes/no	$B = NaF^m/1+aF^m$	N = total number of binding sites, a is related to the median binding affinity (Ko) via Ko = a^(1/m), with m representing the heterogeneity index of the MIP		[8]

6.2.1.1.1.1.1 Scatchard Plot

The Langmuir model assumes that adsorption takes place at homogenous sites within the adsorbent material, often a valid assumption for biological recognition material, such as enzymes or receptors, where, protein folding produces highly reproducible binding sites between molecules. The Scatchard plot is a transformation of the binding isotherm which linearises Langmuir binding behaviour, from which affinity (K) and binding site numbers can easily be derived. Scatchard plots for non-covalently imprinted polymers fail to linearise the isotherm data, indicating that the Langmuir model is inappropriate, most likely due to heterogeneity of binding sites.

Many researchers have interpreted the non-linearity of the Scatchard plot as being indicative of high and low affinity sites [11,12], adopting the bi-Langmuir model. However this assumption is based more on the visual appearance of the Scatchard plot than any theoretical basis. This approach is reasonably more successful than the single site model in describing the MIP binding behaviour, however the derived values for K and Bmax are largely influenced by interpretation of the Scatchard plot and care should be taken to note that in a true two site binding model, the linear lines representing binding to each of population of binding sites are not asymptotes of the curve [13]. It is known that even for true single binding site populations that extrapolation of binding parameters through linearisation of a binding curve can liberate poor estimates of the binding parameters [14] and as such the methodology has become somewhat obsolete owing to the ease with which computer software can conduct non-linear regression on the original isotherm. Consequently, it should be realised that the error associated with estimation of binding parameters for a quasi-bi-modal binding site distribution through interpretation of a non-linearised plot is likely to be significantly more inaccurate. Difficulties in interpretation of the assumed populations of sites, together with the high dependency of binding parameters on concentration, can lead to dramatic variability in the calculated binding parameters. This makes meaningful inter-polymer comparisons extremely difficult.

6.2.1.1.1.1.2 Heterogeneity of Binding Sites

Due to the method of production of MIPs it should perhaps be expected that a range a binding sites should exist within the material, varying in affinity, accessibility, and number. The polymerisation process in the production of MIPs aims to make rigid permanent cavities based on pre-polymerisation complex formation. However the process of polymerisation is far from instantaneous and the relatively high temperature at which polymerisation is initiated renders the template and monomer components of the system energetic, promoting movement and destabilisation of pre-polymerisation complexes. The reliance on free radical polymerisation means it is conceivable that complexes may move or re-orientate prior to formation of the complete binding site. Additionally some cavities may be relatively open, where others may be occluded, making it difficult for the analyte to dissociate once bound. As such it is probably reasonable to assume that a broad range of binding sites exist in any non-covalently imprinted polymer. This conclusion has been discussed by a several groups [10,15-17] and much work has been undertaken by the group of Shimizu [5,6,8,16] and others [18] in attempt to understand and characterise the heterogeneity of MIP binding sites.

This has led to the application of Freundlich isothermal models, which assume an exponential distribution of binding sites, with decreasing affinity. This model introduces a heterogeneity index to the fit and has been employed by the group of Shimizu to try and understand binding site heterogeneity [5]. However, the Freundlich model employs a parameter which combines both measures of capacity and affinity, thus making useful comparisons between MIPs more difficult. The model is also only effective to a certain concentration limit, where the MIP isotherm and Freundlich model are seen to diverge; this is due to the model's implicit assumption that an infinite number of sites exist. Comparisons of fitting models have produced equally good fits for both Freundlich and bi-Langmuir models [10], therefore providing little supporting evidence for any one particular theory of binding site distribution, other than eliminating a single site model, which was demonstrated to fit poorly. Inherent problems arise when applying binding models which make implicit assumptions as to the binding site mechanisms and distributions when these are in fact unknown. The introduction of multiple

parameters to fitting models and the power of computational non- linear regression may enable inappropriate models to accurately describe the experimental data. In such cases the numeric value of the fitting parameters may not accurately describe the binding site populations. Attempts to measure binding site heterogeneity in terms of characterising the number of sites possessing different affinities, has suggested that different imprinted materials can posses very different affinity populations [8]. This suggests that a single, straight-forward, all purpose MIP binding model may not be easily derived, and highlights the potential for error though application of inappropriate isothermal models. A combined Langmuir-Freundlich approach has been shown to produce good fitting coefficients for a range of polymers [8]. However like the Freundlich model this approach employs a combined parameter for capacity and affinity, thus making useful comparisons between MIPs more difficult. This isothermal model can behave like either the Langmuir or the Freundlich models at its extremes. The application of theoretical binding site models to MIPs is a useful technique for increasing understanding of MIPs and theorising about possible binding site morphologies. However, the relative complexity required to apply an appropriate model has meant that researchers have been slow to adopt the approach.

In the pharmacological field concern has arisen as to the appropriateness of model interpretations of binding isotherms for ligand - receptor binding, where a significant fraction of the added (radiolabeled) ligand becomes bound [19]. This is due to the interdependency of variables compounding error in calculations, biasing the resultant parameter estimates. Since this is a common feature of the methodologies frequently employed in quantifying analyte binding to MIPs, the same mathematical implications are likely to exist for application of binding models to MIPs, and should possibly be considered in the application of isothermal models to imprinted matrices.

6.2.1.1.2 Imprinting Factor

The imprinting factor (IF) is a measure of specific template recognition effect (imprinting effect) in the imprinted matrix. The imprinting factor is defined as the ratio of analyte binding to

the MIP to that of the NIP following incubation of equal masses of polymer in identical conditions of solvent volume, analyte concentration and temperature. A kinetic method for deriving imprinting factors is also widely employed and is described as the ratio of retention time (k) of the analyte on MIP and NIP stationary phases respectively (Section 6.2.1.2.2). It is assumed that the binding of the analyte to the NIP is representative of non-specific binding as a result of favourable interactions between the analyte and the 'disordered' functional groups on the surface of the polymer, whilst the binding to the MIP is representative of specific, recognition based binding events at imprinted sites, with a high imprinting factor demonstrating the effective introduction of recognition properties into the imprinted polymer. Whilst the imprinting factor may be said to usefully demonstrate this effect, it is not a useful tool for comparing between MIPs. As can be seen from the MIP and NIP isotherms, which display markedly different concentration dependent binding, the ratio of binding to the MIP and NIP is dependent on the free concentration, and hence incubation conditions. Figure 2 illustrates the imprinting factor for the MIP and NIP prepared and evaluated in chapter 2, at each of the 5 incubation concentrations evaluated to constructed the respective binding isotherms.
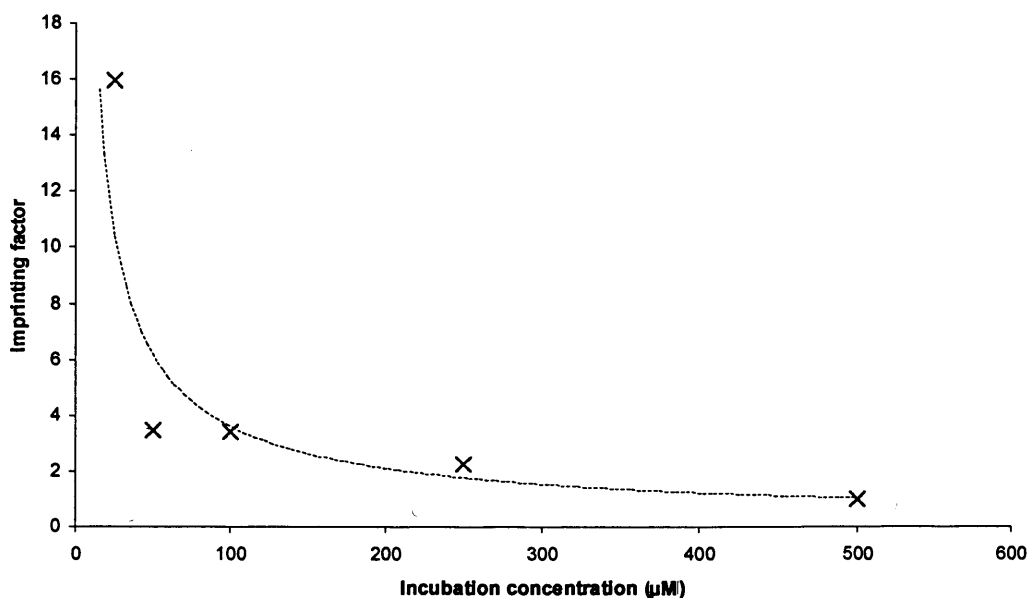
Figure 2 The Imprinting factor for the MIP/NIP pair synthesised and evaluated in chapter 2. The value of the resultant imprinting factor shows a marked concentration dependency as a result of the non-linear binding behaviour of the MIP compared to the near linear behaviour of the NIP as a function of free concentration. (Imprinting factor = bound to MIP / Bound NIP following incubation under equivalent conditions).

The imprinting factor is seen to decrease as the binding to the MIP approaches saturation. As such the value of IF obtained is relatively meaningless as a comparative tool for comparing between MIPs, other than under the exact conditions of the incubation. The effects of depletion of free analyte from the incubation solvent has a significant effect on the resulting imprinting factor, and thus polymer mass, solvent volume and analyte concentration at which the comparison is made has a large influence on the resulting value.

6.2.1.1.3 Percentage Bound

The expression of analyte binding to either MIP or NIP as a percentage of total analyte in the incubation system may be a simplistic approach for conveying the working concept of molecular imprinting. From an application perspective, it can undoubtedly be useful to measure the extent of analyte removal from a sample, such as in solid-phase extraction (SPE) or applications such as those of the subject of this thesis. However, similarly to the imprinting factor, the percentage bound varies dramatically with incubation concentration (Figure 3) together with polymer mass and incubation volume making it an unreliable comparative measure.
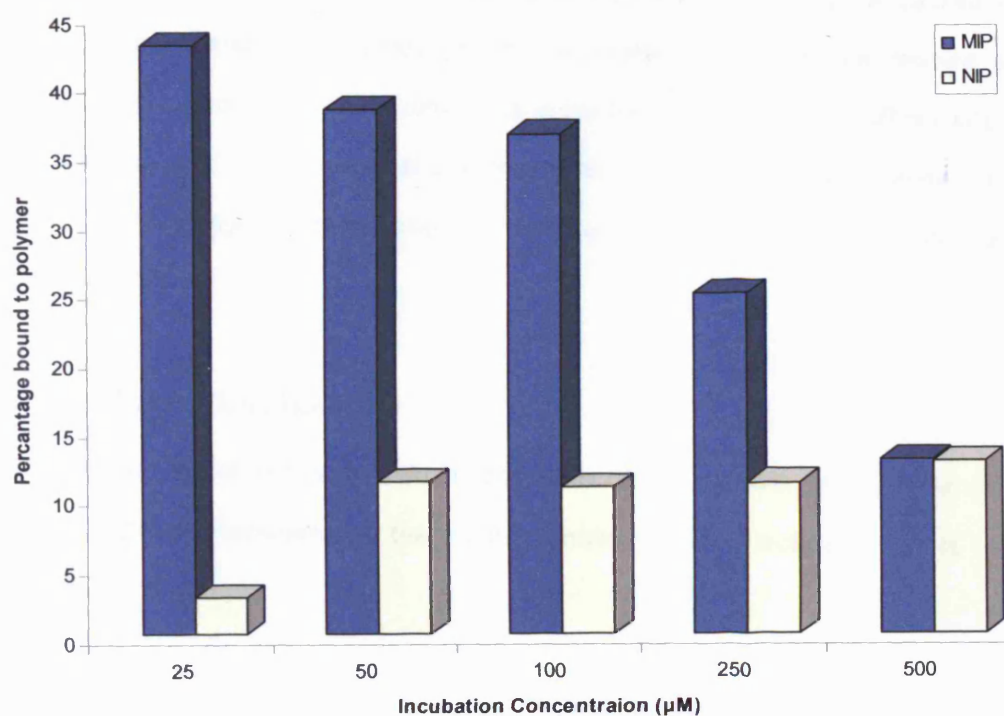
Figure 3 The percentage of analyte bound to the MIP and NIP synthesised and evaluated in chapter 2. The value of the reported percentage bound is seen to show a marked concentration dependency. Affected by both phase ratio and analyte concentration.

6.2.1.2 Kinetic Analysis

Analyte recognition and binding properties of imprinted materials have been frequently assessed by non equilibrium means, most commonly by employment as HPLC stationary phase material [9,17]. Retention times for injected samples of template or related species onto MIP and NIP columns are used to calculate retention factors (k') and selectivity factors (α) for the MIP material.

6.2.1.2.1 HPLC Theory

HPLC is a non-equilibrium chromatographic process, primarily utilised for the batch separation of chemical mixtures, typically for quantification in analytical chemistry, or purification in preparative synthetic chemistry. Upon the introduction of a slug of the analyte mixture into a

continuous flow stream of solvent (mobile phase) passing through a packed bed of solid affinity phase material (stationary phase), separation of the analyte mixture ensues. The separation process relies upon a difference in the sample components affinity interactions with and the stationary phase material and the continually flowing mobile phase. This results in differing partitioning of analyte molecules between the two phases, and consequently differing retention times.

6.2.1.2.1.1 Retention Factor (k')

The retention factor (k') is defined as the ratio of the number of moles of analyte in the stationary phase, compared to that in the mobile phase. Practically, this is calculated by equation 1.

$$k' = \frac{t_R - t_0}{t_0}$$

(1)

In equation 1 k' describes the retention factor of the analyte, where t_R is the retention time of the analyte and t_0 is the mobile phase transit time from the point of sample injection to the point of detection. This is measured practically as the elution time for a non-retained solute (e.g. acetone).

6.2.1.2.1.2 Separation Factor (α)

The separation factor (α) describes the difference in retention of two species. It is defined as the ratio of retention factors for the two species eluted either simultaneously, or under identical conditions.

$$\alpha = \frac{k'_2}{k'_1}$$

(2)

6.2.1.2.2 HPLC Stationary Phase Performance Evaluation

The solid nature of MIPs makes direct evaluation as chromatographic stationary phase material a relatively straightforward and efficient method for assessing imprinting performance. Typically, either MIP microspheres or micron sized, sieved shards of a ground monolithic polymer, are slurry packed under pressure into a stainless steel HPLC column. An identical NIP column is usually prepared for direct comparison. Using standard HPLC injection-retention-detection techniques [20], the ratio of retention factor (k') for an analyte between the MIP and NIP materials is often quoted as an imprinting factor (IF). The difference in retention between the target analyte species and alternative ligands is denoted by (α), the selectivity factor. This is used as a measure of selectivity of the MIP and is described by the ratio of the retention factor of the two species on the MIP column. Typically, to encourage elution of affinity species, modification of the mobile phase is required to weaken binding interactions. This usually involves the addition of a competing hydrogen bonding solvent such acetic acid or water [21]. Due to the marked non-linearity of MIP binding isotherms, chromatographic behaviour is dictated by the principles of non-linear chromatography. This gives rise to the characteristic trailing peak associated with MIP stationary phase chromatography.
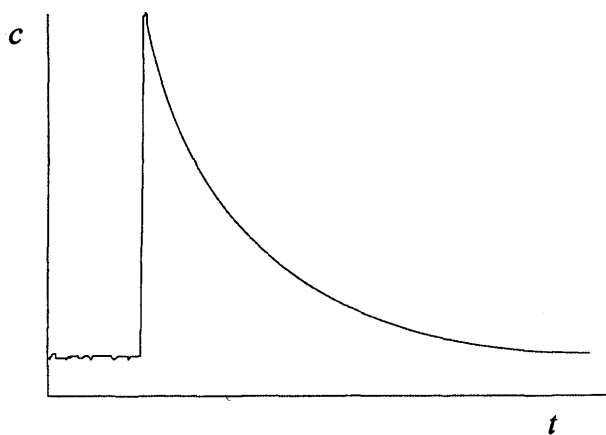
Figure 4 Typical chromatographic peak obtained by MIP stationary phase HPLC.

The research group of Horvai presented an elegant demonstration, with the support of chromatographic theory, illustrating the drawbacks of reporting k', α or IF values for MIP

materials [3]. Citing the work of Guiochon and co-workers, who applied the principles of non-linear chromatography [22] to MIP stationary phases, demonstrating that the peak trailing and peak shape can be calculated directly from the binding isotherm data [23]. The authors were able to demonstrate the mathematical relationship describing the trailing peak shape and its relation to the ratio of bound : free, which is itself a (non-linear) function of free concentration, as described by the binding isotherm. Additionally, the retention time is shown to be concentration dependent, and thus measures such as k', α or IF are therefore not necessarily suitable for assessing MIP performance or comparing between polymers. In a subsequent study [24], the selectivity factor (α) was also shown to be heavily dependent upon column length and diameter, thus making the resultant values non- transferable for inter-MIP comparison. Consequently the authors encourage the reporting of equilibrium binding isotherms, from which application specific comparisons or suitability assessments can be modelled.

6.2.1.3 Application Specific Reporting

Frequently, the performance of novel imprinted materials is reported only with respect to the intended application. Whilst this is obviously useful for the researcher applying the MIP to the tested application, and also serves as a useful demonstration of the versatility of imprinted materials, it is very difficult to gain comparative data. Such examples of application specific reporting include solid phase extraction (SPE) [25], radioassays [26], sensor responses, such as analyte displacement [27], quartz crystal microbalance (QCM) [28] or conductivity measurements [29].

6.3 Binding Isotherms - Tools For Enabling Prediction of MIP Behaviour

6.3.1 Theoretical Basis

As described in 6.2.1.1.1, the binding isotherm describes the binding behaviour of a MIP over a range of equilibrium conditions. Fitting an equation to the acquired data points can describe this behaviour mathematically, without the use of isothermal models. Isothermal models aim to elucidate fitting parameters to a proposed binding model to describe the measured data, in order to impart information on binding site affinities, numbers, distribution and heterogeneity. Whilst such approaches are undoubtedly useful for researchers to attempt to characterise their imprinted materials, the range of applicable models, often displaying equally good fitting characteristics, makes it difficult to hold confidence in the elucidated binding site data. This is particularly true for inter-MIP comparisons where appropriate isothermal models may vary. It may be concluded that in fact the most useful method for comparing MIP behaviour, and thus identifying exceptionally good imprinted materials and the methods of their production, is through the use of the binding isotherm shape itself.

It is proposed here that an accurate mathematical description of the binding isotherm, generated from a small number of initial experiments, can be utilised as a useful comparative tool. In addition, it may also represent a valuable resource for assessing the suitability of a particular polymer for a given application thus enabling the optimisation of experimental conditions required for a desired application.

6.3.1.1 Hypothesis

It is proposed that for any given molecularly imprinted polymer an experimental equilibrium binding isotherm may be utilised to predict the binding behaviour in any permutation of conditions of polymer mass, incubation volume and ligand incubation concentration. This is achieved by the application of three logical assumptions. The resultant predictions may be used to optimise experimental conditions for the MIP's application (i.e. SPE, sensor, HPLC

stationary phase material). Importantly, a broader understanding of the isotherm and its translation and application to alternative methods of assessment will assist in appropriate reporting of the performance of novel imprinted materials and ease the process of inter-polymer comparisons. The binding isotherm can then be utilised to consider mass, volume and analyte concentration effects to enable inter-polymer performance comparisons under theoretical test conditions, even if different from those at which either polymer were evaluated.

6.3.1.1.1 Assumption I - The Binding Relationship Must be Maintained

By fitting an equation to the isotherm this assumption enables the calculation of ligand bound for any defined free ligand concentration at equilibrium, a simple logarithmic association was found to provide a good fit and describe the isotherm shape well including the inherent maximum, equivalent to the capacity of the MIP.
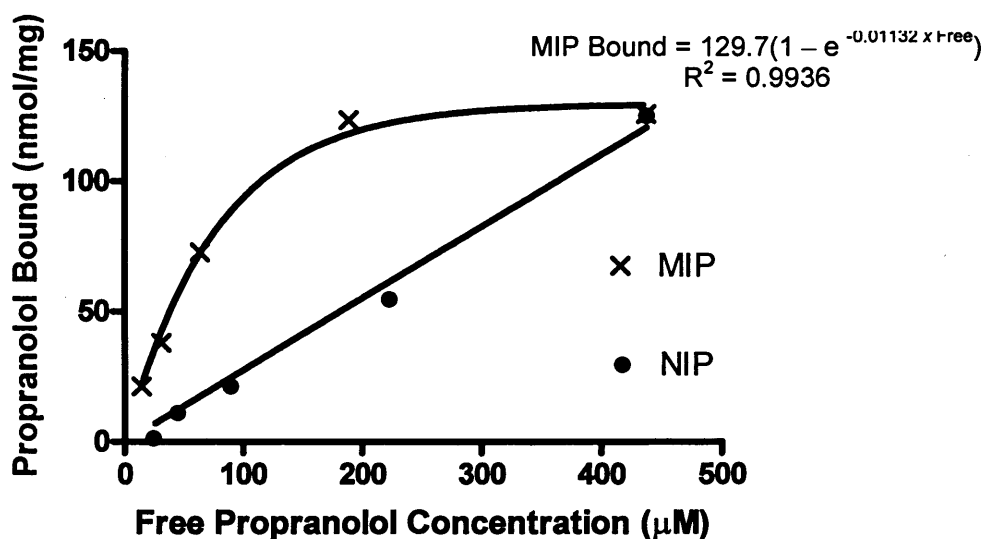
Figure 5 Binding Isotherm for MIP and NIP prepared and evaluated in chapter 2 with fitted equation describing the experimentally observed equilibrium binding behaviour of the MIP.

It can be concluded from this equation that under these conditions of polymer mass and incubation volume the point of equilibrium between the two phases, each with an inherent affinity for the ligand (dependant upon existing amount present in that phase and the surrounding concentration) must lie at some point on the binding isotherm, for this particular

MIP, described by equation 3;

$$bound = 129.7\left(1 - e^{-0.01132 \cdot FreeEquilibriumConcentration}\right) \qquad (3)$$

6.3.1.1.2 Assumption II - Mass of MIP and Volume of Incubating Solvent May be Considered as a Single Variable : Polymer Loading

It is logical to expect the findings of equilibrium binding studies to be entirely scalable providing polymer mass, incubation volume and total amount of ligand are all scaled to the same extent. For example it would be anticipated that 4 mg of MIP incubated in 2 ml of solvent containing 200 nmol of ligand would behave the same as a system which comprised of 2 mg of MIP in 1ml of solvent containing 100 nmol of ligand. Each of these experimental systems would result in the same free equilibrium concentration and the same amount of ligand bound per mg of MIP. This scaling principle can extrapolated to consider a single MIP particle surrounded by solvent.

This allows scaling of the theoretical experimental conditions such that the polymer mass matches that at which the binding isotherm was constructed. In such an experiment equilibrium will be established between the time the ligand resides within binding cavities of the MIP and the time spent free in solution. Much as a liquid-liquid distribution coefficient must be adhered to, the amount of ligand bound to the MIP is dependent upon the free equilibrium concentration (assumption 1) and thus the effect of incubation volume on ligand binding merely affects the extent of concentration depletion from the original incubation conditions (assumption 3) and therefore the point at which equilibrium reached.

6.3.1.1.3 Assumption III – The Logical Effects of Ligand Depletion From the Incubating Solution and the Influence of Volume

As ligand binds to the MIP, and is removed from the incubation solution, concentration depletion occurs. The greater the polymer loading (i.e. mass of polymer/incubation volume)

the greater this effect. It is this effect which is generally utilised to quantify MIP binding experimentally and the dependency on volume : mass ratio highlights why reporting MIP performance in terms of percentage bound is inappropriate.
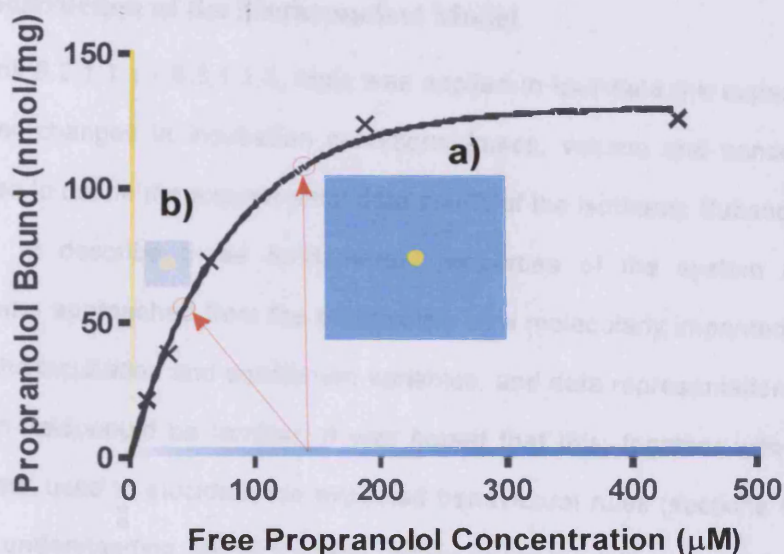
Figure 6 The effect of phase ratio on analyte depletion. An equal mass of polymer is incubated in both a large and small volume of incubating solvent of equal analyte concentration (140 µM). Concentration depletion is considerably greater in the situation of small incubation volume, resulting in a lower free equilibrium concentration (greater extent of analyte depletion). However, the amount of analyte bound is a function of free analyte concentration (assumption 1) and this is consequently lower in the case of small incubation volume also.

As illustrated in Figure 6, when the volume : polymer mass ratio is small, free ligand concentration depletes rapidly as ligand binds to the MIP. Conversely, in situations where the volume : polymer mass ratio is large, removal of ligand from solution has little effect on the overall free concentration and the free ligand concentration at equilibrium is only marginally lower than the initial incubation concentration. In the binding process, equilibrium is established and the amount of ligand bound is dependent upon free equilibrium concentration (Equation 3) and this is therefore affected by the volume of incubating solvent. In the above example, the amount of ligand bound to the MIP will be greater in a) than in b), despite the initial incubation concentration being identical. This demonstrates the important, but entirely predictable, effect incubation volume has on MIP binding. The significant effect this has on the

reporting of binding performance by measures such as percentage bound or imprinting factor is easily extrapolated. Most methods of analysing MIP binding rely upon measuring free ligand concentration, therefore depletion is necessary for MIP assessment

6.3.2 Construction of the Mathematical Model

In sections 6.3.1.1.1 - 6.3.1.1.3, logic was applied to elucidate the expected behaviour of the MIP under changes in incubation conditions (mass, volume and concentration) away from those used to define the experimental data points of the isotherm. Subsequently, the logic was extended to describe these fundamental properties of the system mathematically. The problem was approached from the perspective of a molecularly imprinted polymer chemist, in terms of the incubation and equilibrium variables, and data representation methods with which workers in field would be familiar. It was hoped that this, together with the logical 'thought experiments' used to elucidate the expected behavioural rules (sections 6.3.1.1.1 - 6.3.1.1.3) would aid understanding and encourage uptake of the modelling methodology, should it prove successful.

6.3.2.1 Definition of Terms

m_1 = mass of MIP to be modelled (mg)

m_2 = mass of MIP used to generate binding curve equation (mg)

m_s = scaled mass = m_1/ m_2

v = volume of solvent to be modelled (ml)

v_s = volume scaled = v/ m_s (ml)

P_b = propranolol bound (nmol/mg)

C_{eq} = free propranolol concentration at equilibrium (µM)

C_s = starting propranolol incubation concentration (µM)

P_t = total propranolol in the modelled incubation system (nmol)

P_s = scaled quantity of propranolol in the scaled incubation system (nmol)

6.3.2.2 Ligand Conservation

The fundamental assumption underpinning the equilibrium binding assessment of imprinted polymers is that the total ligand in the system is conserved. Due to the difficulty in analytically measuring the amount of ligand bound to the imprinted material it is commonplace to measure the free equilibrium analyte concentration in the incubation media, with the deficit from the initial incubation concentration considered to be bound to the polymer. The deficit in free ligand concentration is described by equation 4;

$$C_{depletion} = \frac{P_b \times m_2}{V_s}$$ (4)

from this we can derive equation 5 which describes the maintenance of ligand within the system

$$C_{eq} = C_s - \frac{P_b \times m_2}{V_s}$$ (5)

6.3.2.3 Interpretation and Model Generation

Equation 5 can be plotted on the axis of the isotherm, the line it generates describes the conservation of total ligand in the system and as such at every point on the line the sum of analyte on the polymer and analyte in solution equates to the total quantity of analyte in the system. Consequently, the interception of the line described by equation 5 and that describing the binding isotherm (equation 3) represents equilibrium.
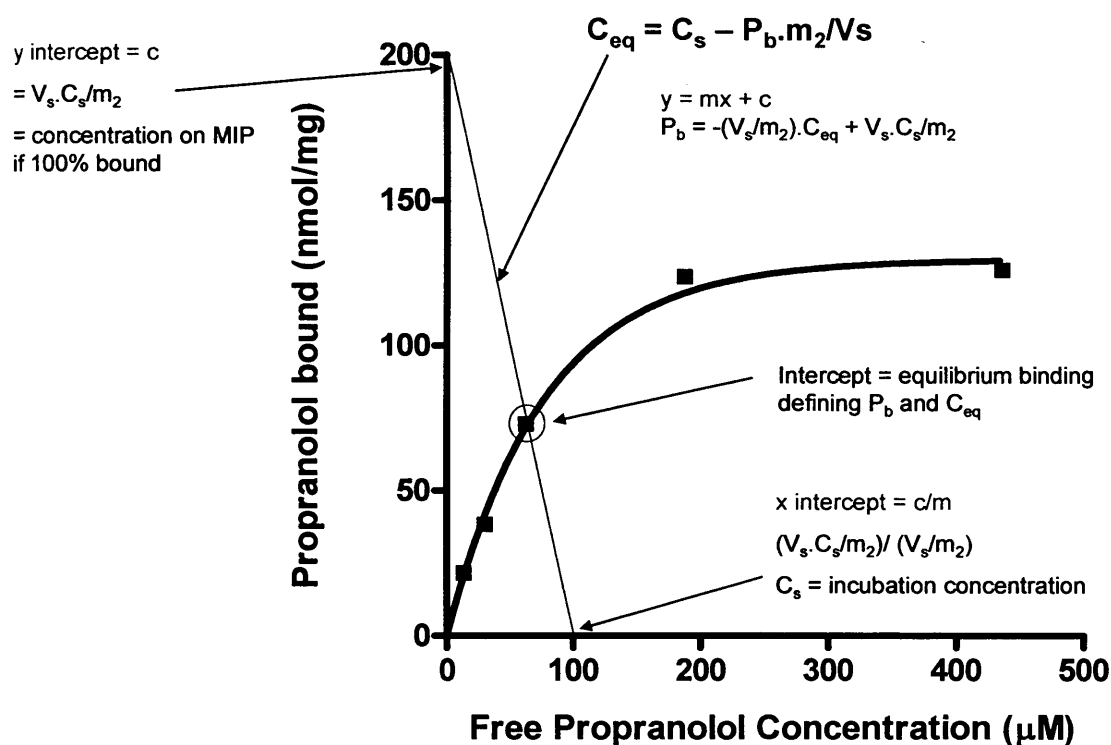
Figure 7 The equation describing conservation of ligand (equation 5) superimposed with the binding isotherm described by equation 3. Values of $C_s = 100$ μM, $V_s = 2$ ml, and $m_2 = 1$ mg are employed, the straight line described by the equation represents the conservation of total ligand in the incubation system for the parameter set (C_s, V_s, m_2), with the equation (5) describing the free ligand concentration (C_{eq}) as a function of ligand bound to the MIP (P_b). Consequently the x-axis intercept represents the free concentration if all ligand were free in solution, with none bound, equivalent to the concentration of the incubation solution. The y-axis intercept represents the concentration of ligand on the polymer if all ligand were bound. The simultaneous solution of equation 5 with that describing the binding isotherm (equation 3) describes the equilibrium bound (P_b) and free (C_{eq}) values for the incubation conditions described by the applied parameter set (C_s, V_s, m_2).

The simultaneous solution of equations 5 and 3 (the binding isotherm) gives the equilibrium condition for the defined set of volume, polymer mass and total ligand. It is therefore possible to model the extent of ligand binding under a series of hypothetically defined scenarios or, conversely, calculate the required conditions which would give rise to a stipulated bound or free quantity of ligand. Such estimations not only enable comparative performance analysis of different MIPs but also enable a rapid route to experimental optimisation.

6.3.2.4 Programming a Model Solver

Section 6.3.1.1.2, considers the effect of scale on the equilibrium binding process. This principle was applied to scale the variables (polymer mass (m_1), volume of incubating solvent

(v) and total amount of propranolol (P_t) such that the modelled polymer mass (m_1) was scaled to that of the mass of polymer under which the binding isotherm data was elucidated (m_2). The scaling factor (m_s) was used to scale the volume of incubating solvent (v) and total amount of propranolol in the incubation system to give (v_s) and (P_s) respectively. Thus maintaining the theoretical incubation concentration (C_s) and matching the mass of polymer to be modelled to that employed in the experiments defining the binding isotherm. As such only concentration depletion from the scaled theoretical incubation volume (v_s) and the equation defining the binding isotherm need be considered in order to predict the equilibrium binding to the MIP for the theoretical conditions stipulated. This was achieved by root solving equations 3 and 5 (isotherm and depletion) containing the scaled terms for the theoretical conditions to be modelled. This gives calculated values for bound and free analyte concentrations. This process was automated to create an interactive model in the mathematical design package Mathcad (v.11.0 PTC ltd (formerly mathsoft)).

6.3.2.4.1 Mathcad

The Mathcad program used to solve equations 3 and 5 with the defined parameter set is detailed below:

mass of MIP to be modelled (mg)   mass of MIP used to generate binding curve equation (mg)

$$m1 := 3$$ $$m2 := 1$$

volume of solvent to be modelled (ml)   Incubation concentration (uM)

$$vol := 1$$

$$Cs := 25$$

MIP binding equation in the
form bound = **a***(1-exp(-**b***Ceq)) $$a := 82.1 \qquad b := 0.05946$$

mass scale ratio

$$ms := \frac{m1}{m2} \qquad ms = 3$$

volume scaled

$$Vs := \frac{vol}{ms} \qquad Vs = 0.333$$

total propranolol in system (nmol)

$$p := Cs \cdot vol \qquad p = 25$$

$$s := \frac{Vs}{m2} \qquad s = 0.333$$

$$f(c) := a \cdot (1 - \exp(-b \cdot c)) + s \cdot c - s \cdot Cs \qquad\qquad f1(c) := a \cdot (1 - \exp(-b \cdot c))$$

$$guess := \frac{Cs}{2}$$

$$f2(c) := -c \cdot \frac{Vs}{m2} + \frac{Cs \cdot Vs}{m2}$$

$$Ceq := root(f(guess), guess)$$

$$c := 0, 0.01 \cdot Cs .. 1 \cdot Cs$$

Free equilibrium concentration (uM) =

$$Ceq = 1.673$$

Ligand bound to MIP (nmol/mg) =

$$f1(Ceq) = 7.776$$

validate total propranolol in system = Tp

$$Tp := (Ceq \cdot Vs \cdot ms) + f1(Ceq) \cdot ms \cdot m2$$

$$Tp = 25$$
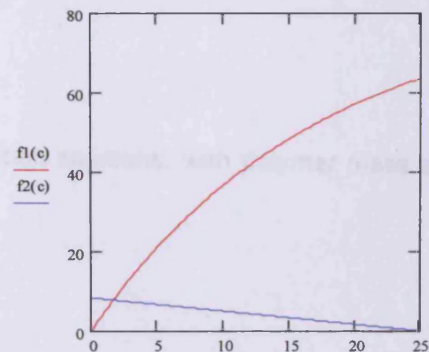
6.3.2.5 Mathematical Analysis of the Model - Cancelation of Scaling Terms: Phase Ratio Independence

Simplification of the expressions in the mathcad model ultimately resulted in the scaling terms cancelling, demonstrating that the isothermal relationship described by equation 3 is *independent of phase ratio*, with phase ratio simply effecting the extent of analyte depletion

237

from the incubation solution (equation 5), and thus the equilibrium condition.

6.3.3 Implications

6.3.3.1 Mass and Volume Effects

Utilising the binding isotherm data for the MIP and NIP produced and characterised in the work of chapter 2, the effect of varying polymer mass and incubation volume in equilibrium batch binding experiments was modelled. The influence of the phase ratio on the extent of analyte binding to the polymer and the subsequent implication on traditionally employed measures of MIP performance were demonstrated.

6.3.3.1.1 Theoretical Experiments

A series of theoretical binding experiments were modelled;

i) Fixed incubation concentration of 50 µM with polymer mass and incubation volume varied

(m = 2, 10, 20 mg, v = 1, 3, 10 ml)

ii) Fixed quantity (150 nmol) of analyte in initial incubation solutions, with polymer mass and incubation volume varied

(m = 2, 10, 20 mg, v = 1, 3, 10 ml).

Each data set was constructed to represent the range of polymer loadings which are frequently encountered in the reporting of evaluation of MIP materials, in conjunction with realistic incubation concentrations for affinity binding studies. For each theoretical experimental condition, equilibrium bound and free concentrations were modelled for both MIP and NIP, from which percentage bound and imprinting factor values were calculated. The isotherm (equation 3) and analyte depletion equation (equation 5) are illustrated for each modelled example, in order to visually demonstrate the significance of each variable on the effect of ligand depletion and the attainment of equilibrium.

6.3.3.1.1.1 Fixed Propranolol Concentration (50 μM)

Table 2 shows the incubation conditions modelled for both MIP and NIP, using the experimental isotherm data investigated in chapter 2, and the interactive mathematical model detailed in section 6.3.2.4.1 The propranolol concentration of the incubation solution was maintained constant with the mass of polymer and volume of incubating solvent, and thus the total quantity of propranolol, varied systematically. The range of values modelled represents typical batch binding incubation conditions reported in the MIP literature

Table 2 Theoretical incubation conditions modelled for both MIP and NIP using the mathcad interactive solver detailed in section 6.3.2.4.1.

incubation concentration (μM)	amount of propranolol (nmol)	mass (mg)	Volume (ml)
50	50	2	1
50	150	2	3
50	500	2	10
50	50	10	1
50	150	10	3
50	500	10	10
50	50	20	1
50	150	20	3
50	500	20	10

6.3.3.1.1.1.1 MIP: Fixed Propranolol Concentration 50 μM Vary Mass and Volume

The theoretical results for MIP binding under the conditions defined by the parameter sets of Table 2 are reported in Table 3. The graphical solutions to the equilibrium conditions are also illustrated in Figure 8.

Table 3 Theoretical equilibrium bound and free conditions, together with percentage bound, modelled for a range of masses of MIP and incubation volumes of $50\mu M$ propranolol solution.

Mass → Volume	2		10		20	
1	Free (µM)	12.3	Free (µM)	2.9	Free (µM)	1.5
	Bound (nmol/mg)	18.9	Bound (nmol/mg)	4.7	Bound (nmol/mg)	2.4
		75.4 %		94.2 %		97.0 %
3	Free (µM)	25.8	Free (µM)	8.0	Free (µM)	4.3
	Bound (nmol/mg)	36.4	Bound (nmol/mg)	12.6	Bound (nmol/mg)	6.9
		48.5 %		84.0 %		91.5%
10	Free (µM)	39.7	Free (µM)	20.3	Free (µM)	12.3
	Bound (nmol/mg)	51.6	Bound (nmol/mg)	29.7	Bound (nmol/mg)	18.9
		20.6 %		59.3 %		75.4 %
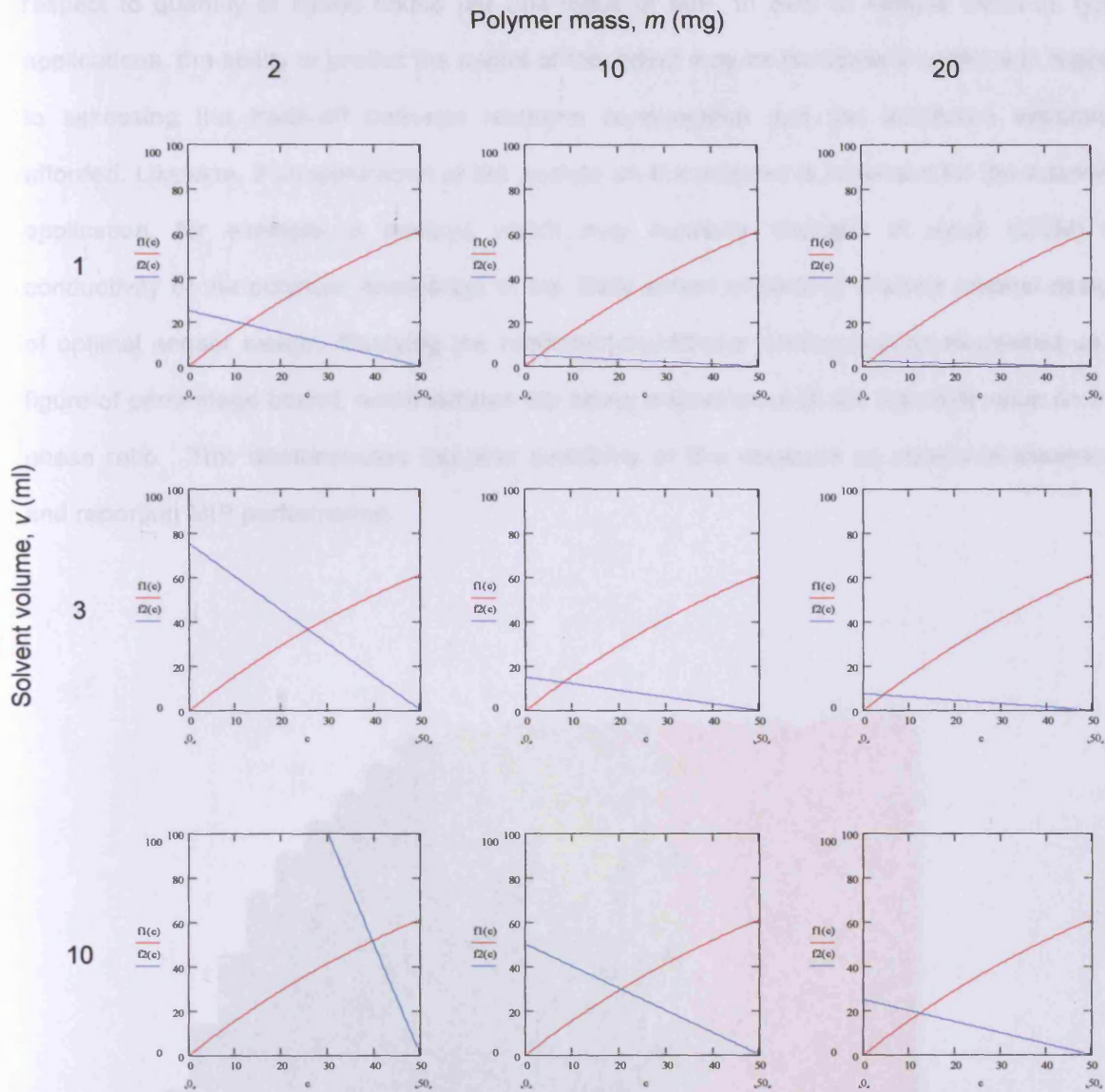
Figure 8 Theoretical equilibrium bound and free conditions. Represented graphically as the solution to the fitted equation describing the measured binding isotherm (red) and the equation representing conservation of ligand for the stipulated conditions (blue). Intersection of the lines described by the respective equations indicates the predicted equilibrium bound and free concentrations. (f1(c) and f2(c) denote the plotted functions described by the Mathcad script detailed in section 6.3.2.4.1 for the stipulated condition set).

It can be seen from the results reported in Table 3 and Figure 8 the importance of phase ratio in governing the point of equilibrium. This is a consequence of the extent of depletion in the experimental system, dictated by the phase ratio, incubation concentration and the binding isotherm shape. It is observed, as might be expected, that increasing the mass of polymer added to the incubation system results in greater removal of the ligand from solution. However, this increase in total quantity of bound ligand is increasingly less efficient with

respect to quantity of ligand bound per unit mass of MIP. In SPE or sample clean-up type applications, the ability to predict the extent of this effect may be particularly useful with regard to assessing the trade-off between resource consumption and the additional extraction afforded. Likewise, if concentration of the analyte on the polymer is important for the intended application, for example in sensors which may measure changes in mass (QCM) or conductivity of the polymer, knowledge of the likely extent of binding enables rational design of optimal sensor design. Studying the modelled equilibrium binding results expressed as a figure of percentage bound, demonstrates the heavy dependence of the resultant value on the phase ratio. This demonstrates the poor suitability of this measure as means of assessing and reporting MIP performance.
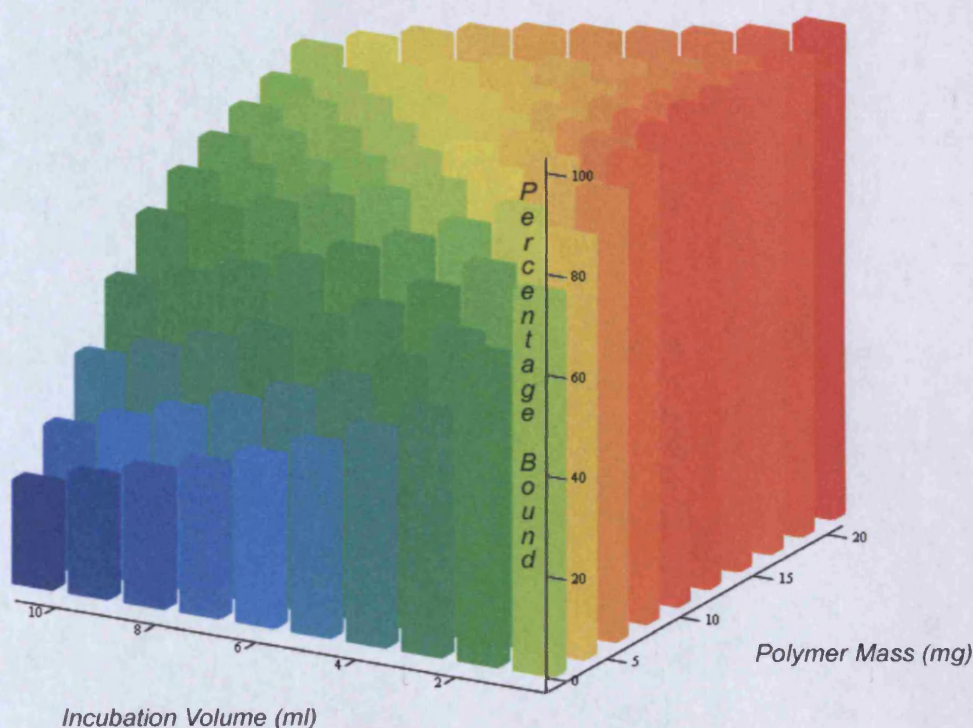
Figure 9 Theoretical plot illustrating the predicted extent of propranolol binding to the MIP prepared in chapter 2 at a range of polymer masses and incubation volumes of 50 µM propranolol solutions in chloroform. The plot illustrates the difficulty in gauging polymer performance expressed as percentage bound due the dependence upon mass and volume incubation parameters. Application of the predictive model to generate such data from a preliminary experimental data set may be of value in optimising binding conditions for an intended application, or comparing the performance of two or more MIPs.

6.3.3.1.1.1.2 NIP: Fixed Propranolol Concentration 50 µM Vary Mass and Volume

The theoretical analysis reported for predicting MIP binding (6.3.3.1.1.1.1) was repeated for

the NIP under identical parameter sets, outlined in Table 2. The predicted bound and free

propranolol concentration for each incubation condition are reported in Table 4. The graphical

solutions to the equilibrium conditions are also illustrated in Figure 10.

Table 4 Theoretical equilibrium bound and free conditions, together with percentage bound, modelled for a range of masses of NIP and incubation volumes of 50µM propranolol solution.

Mass → Volume	2		10		20	
1	Free (µM)	32.2	Free (µM)	13.3	Free (µM)	7.7
	Bound (nmol/mg)	8.9	Bound (nmol/mg)	3.7	Bound (nmol/mg)	2.1
		35.6 %		73.4 %		84.7 %
3	Free (µM)	42.2	Free (µM)	26.0	Free (µM)	17.6
	Bound (nmol/mg)	11.7	Bound (nmol/mg)	7.2	Bound (nmol/mg)	4.9
		15.5 %		47.9 %		64.8 %
10	Free (µM)	47.4	Free (µM)	39.2	Free (µM)	32.2
	Bound (nmol/mg)	13.1	Bound (nmol/mg)	10.8	Bound (nmol/mg)	8.9
		5.2 %		21.6 %		35.6 %
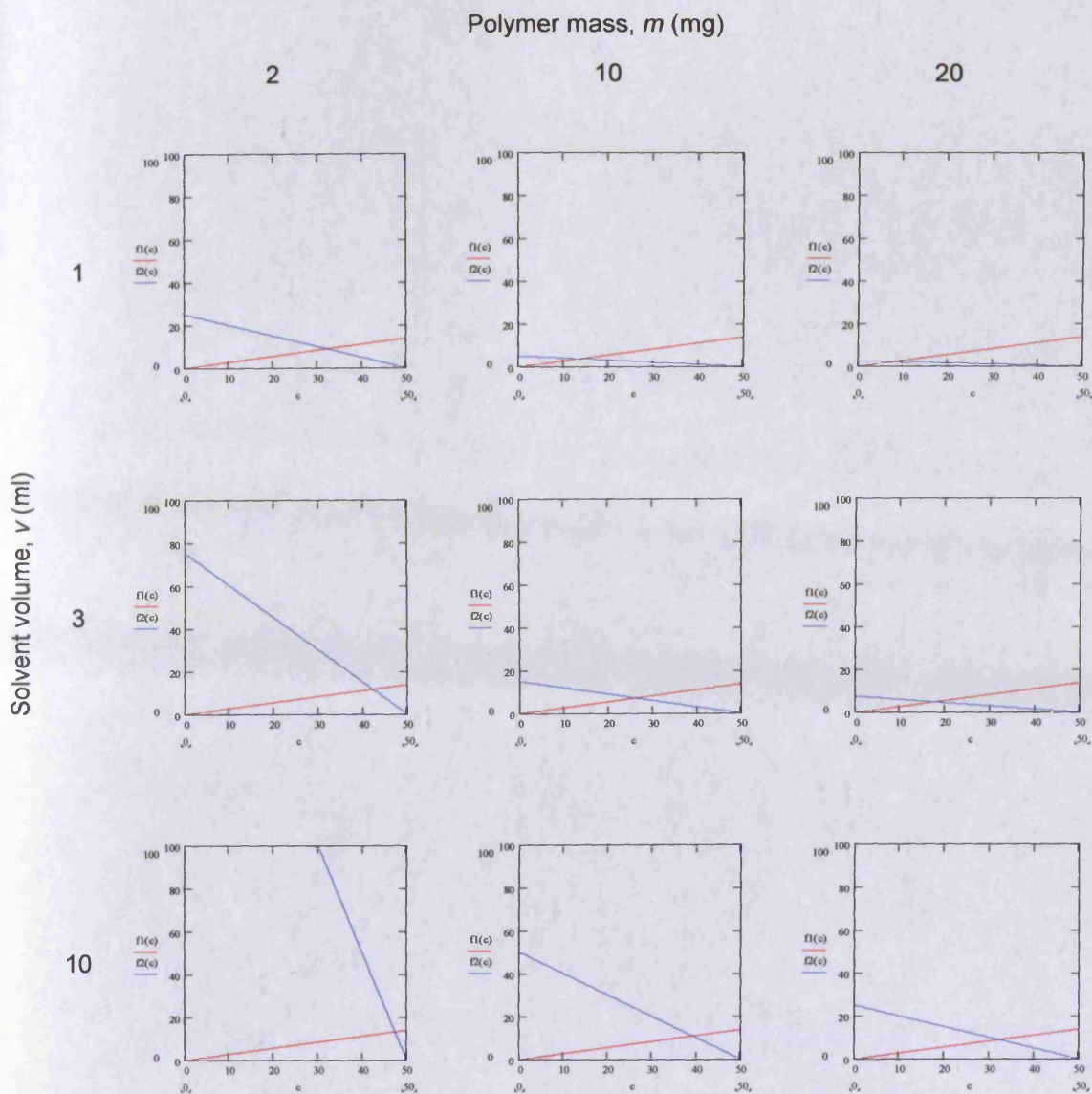
Figure 10 Theoretical equilibrium bound and free conditions for simulated NIP incubations. Represented graphically as the solution to the fitted equation describing the measured binding isotherm (red) and the equation representing conservation of ligand for the stipulated conditions (blue). Intersection of the lines described by the respective equations indicates the predicted equilibrium bound and free concentrations. (f1(c) and f2(c) denote the plotted functions described by the Mathcad script detailed in section 6.3.2.4.1 for the stipulated condition set).

As observed with the modelled MIP incubations, the extent of non-specific binding to the non-imprinted material is seen to depend strongly upon phase ratio. However the linear nature of the binding isotherm, associated with non-specific surface interactions, results in a different relationship to that observed with the MIP. This can be illustrated through the ratio of amount bound to the MIP to that to the NIP under identical incubation conditions, the imprinting factor

(IF). This is illustrated in Table 5 and figure 11 demonstrating a range of imprinting factors from 1.1 to 3.9, for the same MIP and NIP pair incubated in a 50 µM propranolol solution. This large variation in imprinting factor is simply a function of phase ratio and is not related to changes in function of the polymers. This wide range illustrates the poor application of the imprinting factor as a measure of the quality of a MIP material. It is however, sometimes useful to compare specific and non-specific binding, or alternatively a similar analysis may be made to compare alternative binding species to the MIP. It may often be desirable to employ a MIP in an enrichment or separation procedure which may typically contain one or more major impurities. Optimisation of extraction conditions can be approximated theoretically, through application of the measured binding isotherms of the target, and contaminant species, to the MIP with the theoretical binding model demonstrated here. This process would enable theoretical elucidation of optimum parameters of polymer loading and ideal working concentration ranges, in order to maximise separation of the desired species. This approach would be particularly useful as an optimisation strategy with the multiphasic model system (Appendix 3) to optimise a multicomponent separation in a segmented flow MIP assisted extraction regime.

Table 5 Theoretical ratio of bound propranolol to MIP and NIP, commonly known as the imprinting factor (IF). Modelled for a range of polymer masses and incubation volumes of 50 µM propranolol solution. The imprinting factor (IF) is seen to vary dramatically between incubation conditions, demonstrating the unsuitability of IF as a measure of imprinting efficacy.

Mass (mg)	Volume (ml)	IF
2	1	2.12
2	3	3.12
2	10	3.94
10	1	1.28
10	3	1.75
10	10	2.74
20	1	1.15
20	3	1.41
20	10	2.12
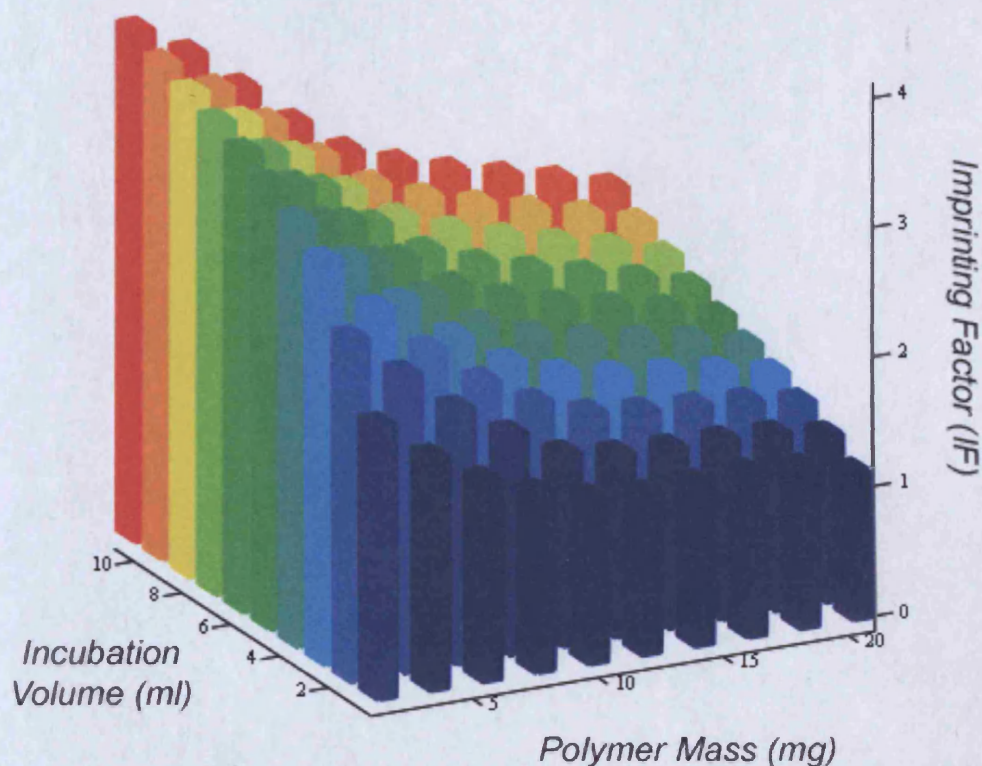
Figure 11 Imprinting factor (IF), modelled for a range of polymer masses and incubation volumes of a 50μM propranolol solution. The imprinting factor (IF) is seen to vary dramatically with phase ratio, demonstrating the unsuitability of IF as a measure of imprinting efficacy.

6.3.3.1.1.2 Fixed Propranolol Quantity (150 nmol)

After investigating the effect of maintaining incubation concentration and varying polymer mass and incubation volume (6.3.3.1.1.1), the effect of varying polymer mass and incubation volume, with a fixed quantity of ligand, was studied. This investigation would therefore result in variance in incubation concentration with changes in modelled volume, in addition to the phase ratio effect previously described (6.3.3.1.1.1). Such a simulation may be useful in comparing or predicting MIP performance where a finite quantity of analyte or interferent is present and conditions may be modulated.

Table 6 Theoretical incubation conditions modelled for both MIP and NIP, using the mathcad interactive solver detailed in section 6.3.2.4.1. A constant quantity of propranolol was maintained in each parameter set.

incubation concentration (µM)	amount of propranolol (nmol)	mass (mg)	Volume (ml)
150	150	2	1
50	150	2	3
15	150	2	10
150	150	10	1
50	150	10	3
15	150	10	10
150	150	20	1
50	150	20	3
15	150	20	10

6.3.3.1.1.2.1 MIP: Fixed Propranolol Quantity 150 nmol Vary Mass and Volume

The theoretical results for MIP binding under the conditions defined by the parameter sets of table 6 are reported in Table 7. The graphical solutions to the equilibrium conditions are also illustrated in Figure 12.

Table 7 Theoretical equilibrium bound and free conditions, together with percentage bound, modelled for a range of masses of MIP and incubation volumes, each containing a total of 150 nmol of propranolol ligand.

Mass → ˙Volume	2		10		20	
1	Free (µM)	42.1	Free (µM)	9.0	Free (µM)	4.5
	Bound (nmol/mg)	54.0	Bound (nmol/mg)	14.1	Bound (nmol/mg)	7.3
		71.9 %		94.0 %		97.0 %
3	Free (µM)	25.8	Free (µM)	8.0	Free (µM)	4.3
	Bound (nmol/mg)	36.4	Bound (nmol/mg)	12.6	Bound (nmol/mg)	6.9
		48.5 %		84.0 %		91.5 %
10	Free (µM)	11.5	Free (µM)	5.8	Free (µM)	3.5
	Bound (nmol/mg)	17.7	Bound (nmol/mg)	9.2	Bound (nmol/mg)	5.7
		23.6 %		61.5 %		76.4 %
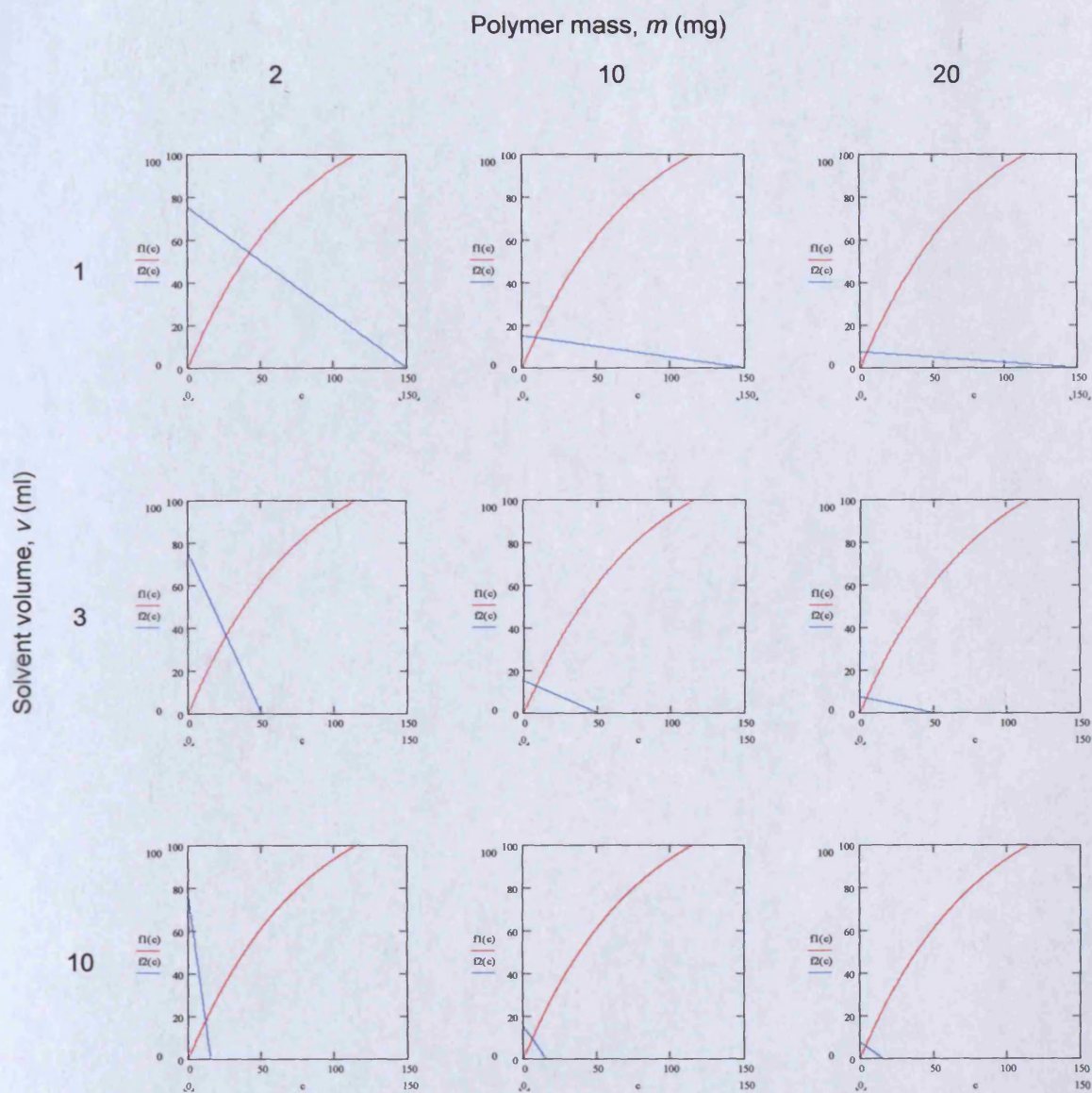
Polymer mass, _m_ (mg)

Figure 12 Theoretical equilibrium bound and free conditions for MIP. Represented graphically as the solution to the fitted equation describing the measured binding isotherm (red) and the equation representing conservation of ligand for the stipulated conditions (blue). Intersection of the lines described by the respective equations indicates the predicted equilibrium bound and free concentrations for each of the parameter sets modelled, each containing a total of 150 nmol of propranolol ligand. (f1(c) and f2(c) denote the plotted functions described by the Mathcad script detailed in section 6.3.2.4.1 for the stipulated condition set).

Figure 13 Theoretical plot illustrating the predicted extent of propranolol binding to the MIP prepared in chapter 2 at a range of polymer masses and chloroform incubation volumes containing a total of 150 nmol of propranolol. The plot illustrates the difficulty in gauging polymer performance expressed as percentage bound due the dependence upon mass and volume incubation parameters. Application of the predictive model to generate such data from a preliminary experimental data set may be of value in optimising binding conditions for an intended application, or comparing the performance of two or more MIPs.

6.3.3.1.1.2.2 NIP: Fixed Propranolol Quantity 150 nmol Vary Mass and Volume

The theoretical analysis reported for anticipated MIP binding (6.3.3.1.1.2.1) was repeated for the NIP under identical parameter sets, outlined in Table 6. The predicted bound and free propranolol concentration for each incubation condition are reported in Table 8. The graphical solutions to the equilibrium conditions are also illustrated in Figure 14.

Table 8 Theoretical equilibrium bound and free conditions, together with percentage bound, modelled for a range of masses of NIP and incubation volumes, containing a total of 150 nmol propranolol ligand.

Mass → Volume	Incubation Concentration	2		10		20	
1	150 µM	Free (µM)	96.6	Free (µM)	39.9	Free (µM)	23.0
		Bound (nmol/mg)	26.7	Bound (nmol/mg)	11.0	Bound (nmol/mg)	6.4
			35.6 %		73.4 %		84.7 %
3	50 µM	Free (µM)	42.2	Free (µM)	26.0	Free (µM)	17.6
		Bound (nmol/mg)	11.7	Bound (nmol/mg)	7.2	Bound (nmol/mg)	4.9
			15.5 %		47.9 %		64.8 %
10	15 µM	Free (µM)	14.2	Free (µM)	11.8	Free (µM)	9.7
		Bound (nmol/mg)	3.9	Bound (nmol/mg)	3.2	Bound (nmol/mg)	2.7
			5.2 %		21.6 %		35.6 %
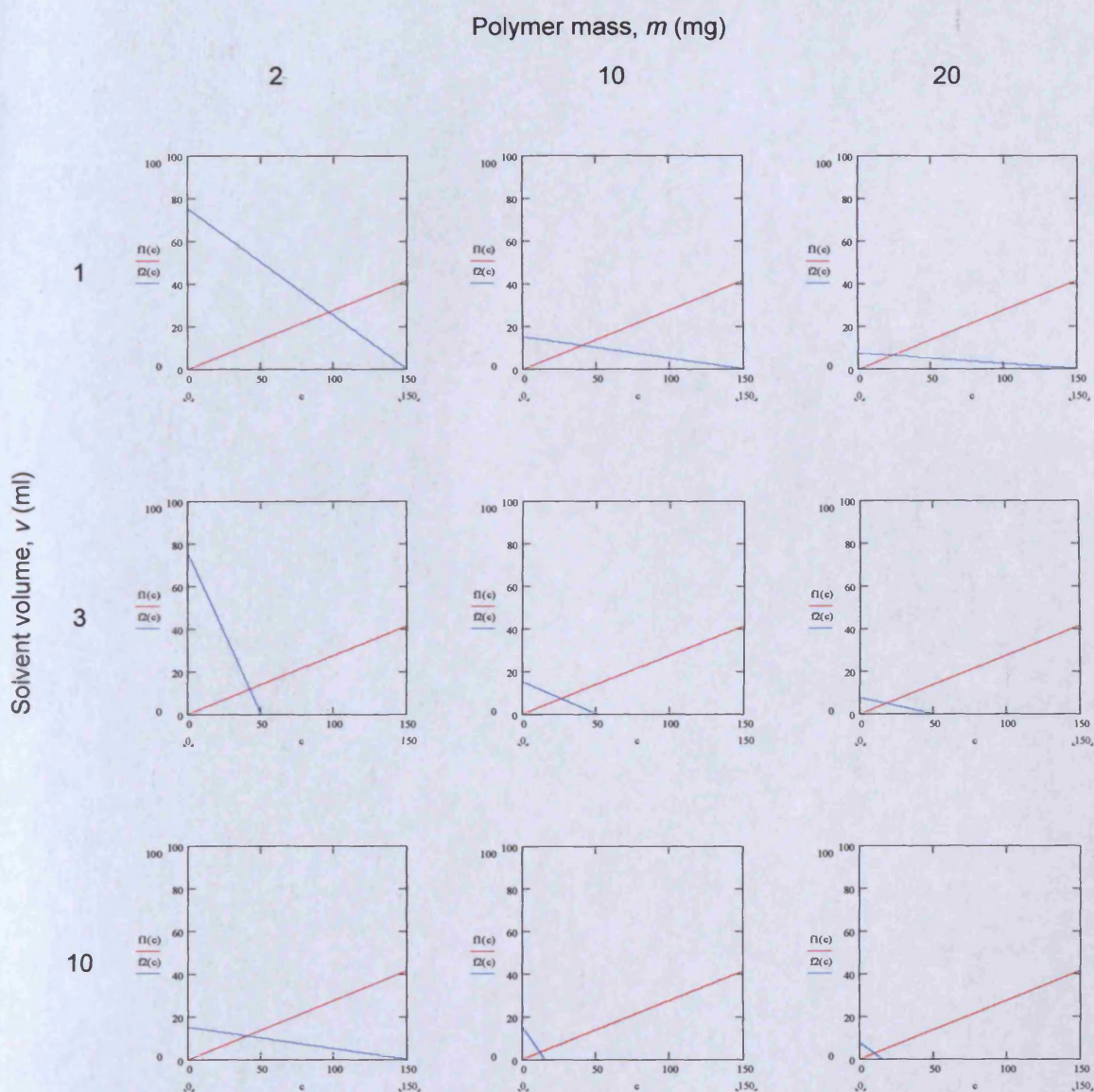
Polymer mass, *m* (mg)

Figure 14 Theoretical equilibrium bound and free conditions for NIP. Represented graphically as the solution to the fitted equation describing the measured binding isotherm (red) and the equation representing conservation of ligand for the stipulated conditions (blue). Intersection of the lines described by the respective equations indicates the predicted equilibrium bound and free concentrations for each of the parameter sets modelled, each containing a total of 150 nmol of propranolol ligand. (f1(c) and f2(c) denote the plotted functions described by the Mathcad script detailed in section 6.3.2.4.1 for the stipulated condition set).

Figure 15 Theoretical plot illustrating the predicted extent of propranolol binding to the NIP prepared in chapter 2 at a range of polymer masses and chloroform incubation volumes containing a total of 150 nmol of propranolol. The difference in isothermal shape between the MIP and NIP binding curves manifest as different dependencies of ligand bound upon the variables of mass and volume. Comparison of the equivalent MIP and NIP plots may provide a useful opportunity to optimise conditions of MIP application to maximise specific template binding and minimise non-specific binding, assumed to represented by binding to the NIP.

A similar trend in analyte binding was observed to that obtained for phase ratios modelled at a fixed propranolol concentration (6.3.3.1.1.1), with the binding to the MIP compared to the NIP seen to vary with polymer loading. Additionally, maintaining the quantity of modelled ligand resulted in alteration of the modelled incubation concentration with changes in incubation volume. This effect, and the differing isothermal shapes (non-linear and linear) of the MIP and NIP, resulted in a greater range of modelled imprinting factors for binding to MIP compared to NIP under identical conditions. These values are shown in Table 9 and illustrated graphically in Figure 16.

Table 9 Theoretical ratio of bound propranolol to MIP and NIP, commonly known as the imprinting factor (IF). Modelled for a range of polymer masses and incubation volumes containing 150 nmol of propranolol ligand. The imprinting factor (IF) is seen to vary dramatically between incubation conditions, demonstrating the unsuitability of IF as a measure of imprinting efficacy.

Mass (mg)	Volume (ml)	Incubation Concentration (μM)	IF
2	1	150	2.02
2	3	50	3.12
2	10	15	4.50
10	1	150	1.28
10	3	50	1.75
10	10	15	2.84
20	1	150	1.15
20	3	50	1.41
20	10	15	2.15
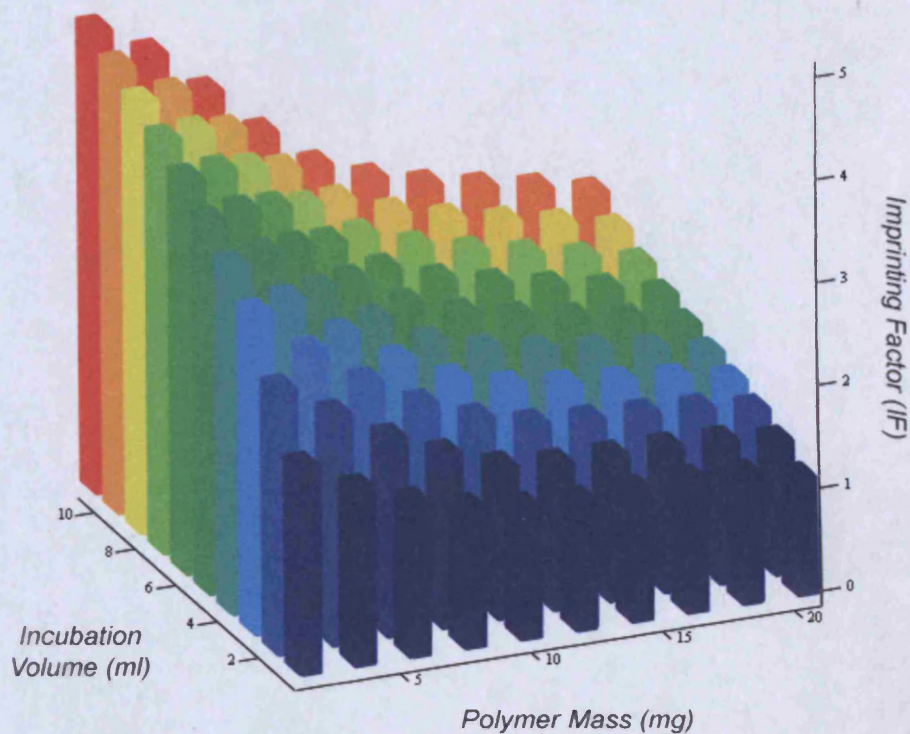
Figure 16 Imprinting factor (IF), modelled for a range of polymer masses and incubation volumes containing 150 nmol of propranolol ligand. The imprinting factor (IF) is seen to vary dramatically with phase ratio, demonstrating the unsuitability of IF as a measure of imprinting efficacy.

6.3.3.2 Phase Ratio

The effect of polymer loading, or phase ratio, on the binding of propranolol to the MIP and NIP has been demonstrated numerically is section 6.3.3.1.1. Figure 17 demonstrates this relationship graphically for both the MIP and NIP. The effect of the chosen polymer loading on the resultant bound/free data pairs is illustrated for 150 µM incubations, for polymer loadings from 0.5 mg ml^{-1} to 10 mg ml^{-1}. Although the 3 dimensional plot is difficult to extract quantitative data from, it usefully depicts the general trend observed as a result of concentration depletion, defined by the phase ratio of the polymer and incubating phase. Every point on the red surface represents the total propranolol in the system per unit volume,

the sum of free concentration in solution, and concentration depleted due to binding to the polymer (bound x mass/volume), (150 µM). The intersection of this surface plot with the planes representing the binding isotherm of the MIP (blue) and NIP (green), is indicative of the equilibrium conditions of bound and free for any given phase ratio. As a result of the initial steeper gradient and non-linear nature of the MIP isotherm, the curvature in the decline of propranolol bound per unit mass of polymer with increased polymer loading (i.e. increased phase ratio), is steeper than that of the corresponding NIP. The isothermal gradient governs the rate of change of the bound/free equilibrium position with increasing phase ratio. The NIP displays linear (or near linear) binding behaviour (thus displaying a constant gradient), where as the binding behaviour of the MIP is markedly non-linear (with the gradient changing with free concentration). Consequently, the relationship of analyte binding as a function of phase ratio is fundamentally different for the two materials. This raises further question of the use of NIP materials as a universal control in the field of imprinting, particularly where MIP : NIP binding ratios (IF) are quoted as a measure of imprinting effect for comparative purposes. Comparisons to non-imprinted materials may still be useful to optimise experimental application of imprinted materials or to better probe and understand their behaviour. For example, in terms of high MIP:NIP binding ratio, figure 17 suggests that greatest specificity may be achieved at low polymer loadings at low, well below saturation, free equilibrium concentrations. Such analysis would be particularly valuable in the assessment of MIP binding of a desired species compared to that of related species or other contaminants present in a typical analytical sample. Similarly, analysis of target and interferent MIP and NIP binding isotherms would enable elucidation of optimal operating conditions to afford, for example, greatest analyte specific sensitivity in sensor applications or most efficient separation of an analyte and contaminant species, in sample preparation or enrichment operations.
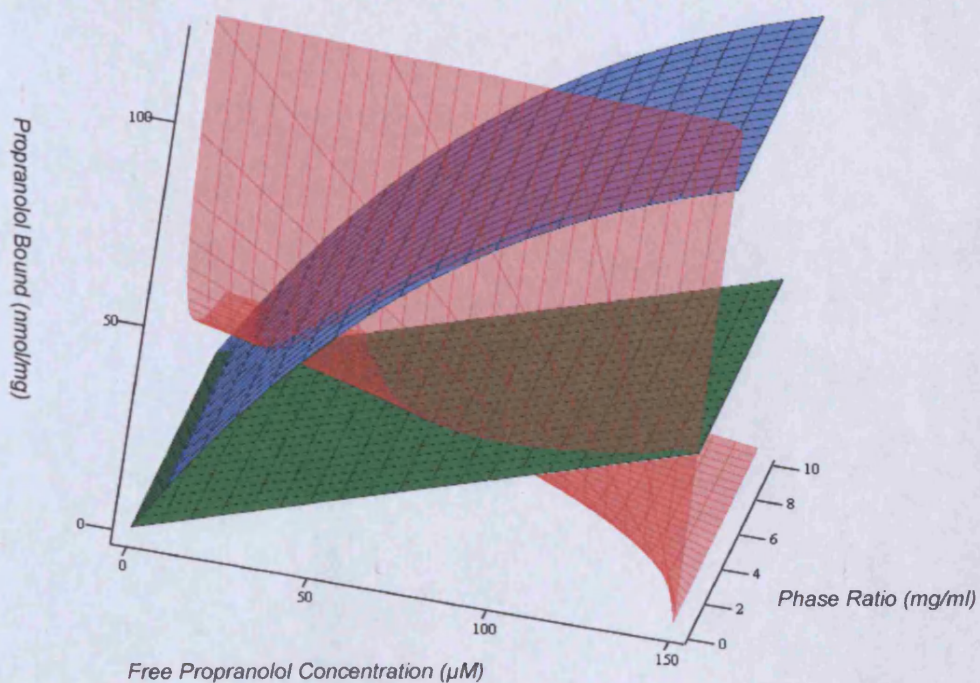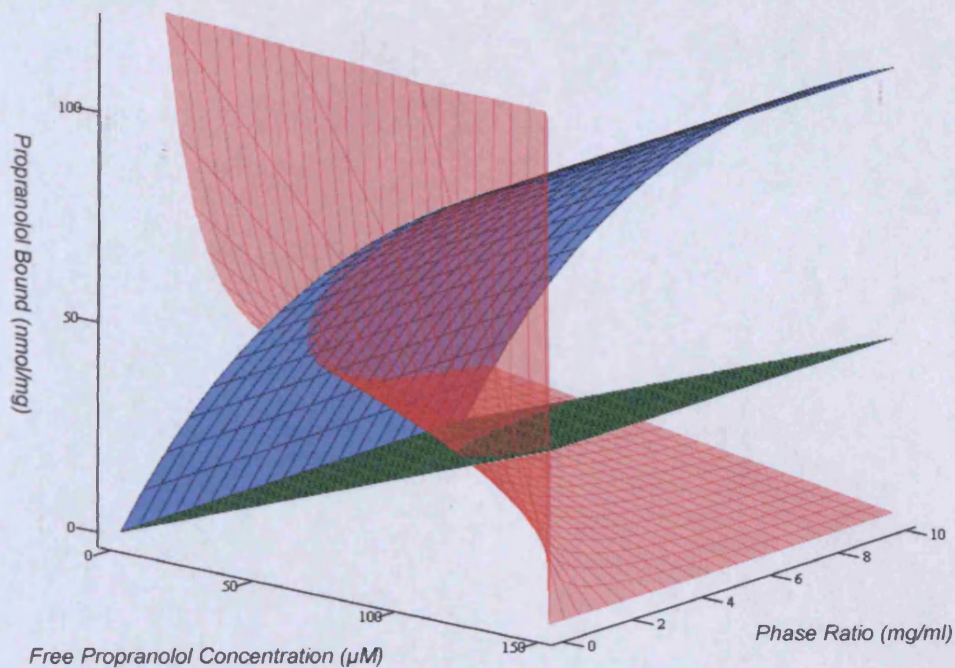
Figure 17 Three dimensional surface plot illustrating the significance of phase ratio (mass of polymer/volume incubating solvent (mg ml^{-1})) on equilibrium binding for both MIP and NIP for incubation in 150 µM propranolol solution. The intersection of the red plane with the blue (MIP) or green (NIP) isotherm represents theoretical equilibrium binding conditions for ascribed phase ratio. The two plots illustrated represent the same data viewed from different observational angles to convey fully the curvature of red plane and consequently the phase ratio defined equilibrium position.

6.3.4 Applications of the Mathematical Model

6.3.4.1 Experimental Design

The fundamental relationships demonstrated by the data presented in section 6.3.3.2 can be applied to optimise the experimental design for the evaluation of MIPs in order to minimise the impact of experimental error on the characterisation of performance.

6.3.4.1.1 Reduction of Error

As discussed in section 6.3.3.2, figure 17 suggests that greatest specificity may be achieved at low polymer loadings at low free equilibrium concentrations. However, care should be taken in selecting the experimental conditions for polymer assessment and indeed application. As discussed in section 6.2.1.1.1.1.2 the vast majority of methodologies employed in the analysis of equilibrium binding experiments rely solely on the measurement of the free analyte concentration (x axis), with the reduction in concentration from the initial incubation concentration attributed to binding to the polymer per unit mass of polymer (y axis). As a result, error in the experimental measurement of free concentration (x axis) is transferred to the y axis calculation of amount bound. As a consequence, the accuracy and precision of assay techniques should be considered, together with limits of accurate quantification. For example the standard deviation on the measurements of free analyte concentration will have a more significant effect on the calculated bound value if the extent of analyte depletion from the incubation concentration is small, compared to if depletion is large. Additionally, this variability is affected by the phase ratio (polymer loading) employed. For low phase ratios (polymer loading), typically of less than about 1 mg ml^{-1}, variability in the measured free equilibrium analyte concentration becomes amplified as error on the y axis, when expressed as bound per unit mass of polymer, due the transformation from concentration depletion to bound concentration (multiplication by volume, division by mass, equivalent to dividing by the phase ratio). The exact extent of this depends upon the capacity of the MIP and sub-saturation free equilibrium concentration. The accuracy and reproducibility of weighing and liquid handling procedures must also be considered. If the investigated phase ratio differs from that intended

257

due to unintentional measurement error, over- and under- estimations of bound and free may be made. This is particularly true at low polymer loading, where the gradient of the plane representing ligand depletion (red surface of figure 17) is steepest and most sensitive to phase ratio variations. This often manifests as uncertainty in the measurement at and around MIP saturation, as researchers understandably maintain the same phase ratio for investigation of the entire binding isotherm. Figure 18 illustrates how high polymer loadings and high incubation concentrations should be employed to elucidate the polymer capacity, so that a significant and accurately measurable depletion of free analyte occurs.
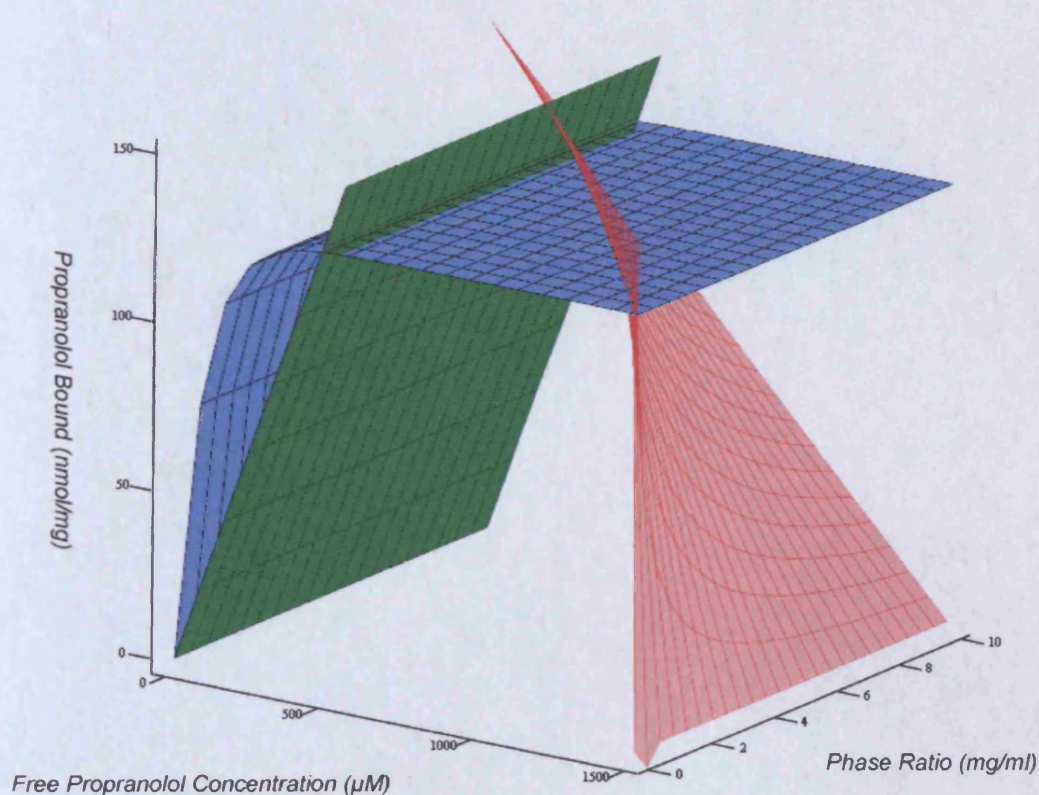
Figure 18 Improved experimental accuracy can be achieved by altering the incubation phase ratio in order to probe different regions of the binding isotherm. The measurement of small concentration depletion from the incubating phase can compound any experimental error or uncertainty in the assumed bound concentration on the polymer. Consequently the employment of high polymer loadings and increased incubation concentrations can assist in determining the near-saturation region of the binding isotherm with improved accuracy.

The dependency of attributed bound concentration value on the measured free concentration,

means the binding isotherm invalidates one of the assumptions of regression; that the data on each axis is independent (usually one value is known and the second measured). Unfortunately this is somewhat unavoidable due the inherent difficulty of accurately quantifying the analyte residing within the solid polymer matrix. However, this effect can be minimised by careful experimental design and by using different polymer loadings to investigate different portions of the binding isotherm. Furthermore it should be noted that subsequent manipulation of the binding data, for example Scatchard plots, (where bound/free is plotted against bound), compounds this uncertainty and therefore regression (linear or non-linear) should be avoided on data presented in this format, and the original isotherm used instead.

6.3.4.2 Application Optimisation

As outlined in section 6.3.3.2 the application of the mathematical model to compare the effects of manipulation of phase ratio, or changes in sample concentration may be extremely useful to enable optimisation of application conditions and parameters. This may be applied to the behaviour of the MIP itself or to comparison between polymers or the binding of different analytes to the same polymer in order to optimise sensor sensitivity ranges or maximise separation efficiencies. The binding isotherm itself has previously been successfully demonstrated to be transferable to model a radioligand competitive assay calibration curve [4] and also in modelling MIP stationary phase HPLC retention data [3].

6.3.4.3 Comparison of Published MIP data

For any MIP with a reported binding isotherm, the predictive model technique can be applied to enable comparisons with other MIPs. This may enable comparative preliminary assessment of the suitability of different MIPs for an intended application, or may facilitate comparisons between different imprinting methodologies. Polymers with a reported isotherm may even be compared to those with reported measures such as imprinting factors, percentage bound or radiolabeled displacement data. Although this approach is limited to the defined set of experimental conditions, some comparison and evaluation is still possible. This transferable

information obtainable from binding isotherms makes comparisons between polymer preparations, or incubation conditions much more meaningful.

6.3.4.3.1 Worked Example

Examples of propranolol MIPs assessed by equilibrium binding methodologies were identified from the literature. The mathematical model was then applied to model comparable incubation conditions to an example polymer where imprinting performance was expressed by percentage bound. In doing so a simple manual technique for predicting binding from reported isotherms is demonstrated. It is proposed that a thorough meta analysis of reported MIP isothermal data may yield interesting relationships and trends in polymer synthesis techniques and the resulting polymer performance.

Hunt and Ansell introduced a novel technique applying fluorescence anisotropy to measure MIP binding, reporting an (S)-propranolol imprinted polymer which bound 30% of incubated (S)-propranolol [30]. Literature analysis identified several reported imprinted materials characterised by a binding isotherm, these together with the MIP prepared and evaluated in the work of this thesis were compared to the result reported for Hunt's MIP [30]. Application of the predictive model enabled prediction of the binding behaviour for the reported MIPs under the same incubation variable set (polymer mass, incubation volume and propranolol concentration) at which Hunt assessed polymer binding (Table 10).

Table 10 Selected propranolol binding analysis reported by Hunt and Ansell [30] in the assessment of a monolithic propranolol imprinted polymer. These conditions of polymer mass, incubation volume and incubation concentration were modelled for a series of propranolol imprinted polymers reported with binding isotherms (Table 11).

Reference	Polymer	Polymer mass (mg)	Solvent volume (ml)	Incubation Concentration (µM)	Incubation media	MIP Percentage bound	NIP Percentage bound
[30]	Monolith	2.8	1.4	154.2	Toluene + 0.5% AcOH	30%	10%

For precision purposes the mathcad model was applied when an equation describing the

binding isotherm was provided, otherwise a rapid manual method was used (Figure 19) Table 11 illustrates the identified MIPs together with reported binding isotherms selected for the comparative study. The modelled results are given in figure 20.

Figure 19 Manual method for estimating equilibrium bound and free values for desired set of incubation conditions from a reported MIP or NIP isotherm. Example illustrated for an incubation system of 4 mg polymer incubated in 2 ml of chloroform containing 300 nmol of propranolol *a*) Calculation of the analyte concentration in the incubating solvent if all analyte were in solution, this is equal to 150 μM, equivalent to the incubation concentration. This value is marked on the x-axis. *b*) Calculation of the concentration of analyte on the polymer, if all the analyte were bound to the polymer present in the incubation system. Equivalent to 75 nmol mg^{-1}, this value is marked on the y-axis. *c*) Connecting the points made in *a*) and *b*) with a straight line defines the maintenance of ligand in the binding system, with the molar sum of propranolol in solution and bound to the polymer equal to the total propranolol in the incubation system (300 nmol) at every point on the line. *d*) The intersection of the line constructed in *c*) with the isotherm of the MIP and NIP represents the equilibrium conditions for the hypothetical set of incubation conditions. It should be noted that the isotherm should report the *concentration* of analyte in each phase (solvent or bound to polymer) and not the incubation concentration, the total quantity bound, or the concentration of analyte removed from the liquid phase by the polymer, which are occasionally reported in the context of MIP binding.

Table 11 Collation of propranolol imprinted polymers with reported binding isotherms, compared using the predictive model approach to the result reported in [30]

Reference	MIP	Binding media	Polymer loading (mg ml^{-1})	Investigated Concentration range	Reporting	Isotherm	Comments
[30]	Monolith	Toluene + 0.5% acetic acid	2	3.9 - 154.2 µM	Percentage bound	MIP: (S)-Propranolol 30% bound of 0.1542 mM incubation solution NIP: (S)-Propranolol 11% bound of 0.1542 mM incubation solution	Incubation conditions to which other polymers will be modelled
Chapter 2 [31]	Precipitation polymerisation	Chloroform (H$_2$O saturated)	0.5	25 - 500 µM	Isotherm		
[32]	Suspension polymerisation	Acetonitrile	0.1	1 - 400 µM	Isotherm		

[32]	Monolith	Acetonitrile	0.1	1 - 400 μM	Isotherm		Monolithic comparator to the suspension polymerised beads
[33]	Particles prepared in supercritical CO_2	50/50 v/v 25 mM Citrate buffer pH6.0 / acetonitrile	0.2	0 - 5000 μM	Isotherm - competitively derived, labelled and unlabelled (S)-Propranolol		Isotherm plotted as total quantity of propranolol bound (nmol) rather than bound per unit mass of polymer (nmol mg^{-1}). Also note for manual application of the predictive methodology that plot origin is inset from where axis cross
[34]	Core-shell particles prepared by aqueous emulsion polymerisation	0.1 M sodium phosphate buffer pH 6.0	~22	0 – 400 μM	Scatchard plot SPE-type analysis		Scatchard plot reported Converted bound vs. free isotherm and concentration of propranolol on polymer calculated (nmol mg^{-1}) from the total binding quantity used to construct the Scatchard plot

						Isotherm appears to display two types of behaviour, typical MIP-like binding at low (< 100 µM) free propranolol concentrations and near linear behaviour thereafter. Suggestive of non-specific binding (akin to the NIP of chapter 2, as modelled in this chapter) following binding site saturation. Full range isotherm inset.
[35]	Sol-Gel thin film	Phosphate buffer pH 7.6	?		Radiolabeled assay		No mass reported for thin films, therefore isotherm, which plots total bound, can not be converted into bound concentration (nmol mg^{-1}). Unsuitable for comparison
[36]	Particles prepared by precipitation polymerisation with sacrificial covalent bond	Hexane(?)	5 (?)	0-15000 µM	Isotherm		Cholesterol MIP prepared and found to display good binding characteristics to propranolol moiety. However, investigated concentration range is too high for useful analysis. Unsuitable for comparison

Figure 20 Application of the predictive model to five propranolol isothermally reported MIPs prepared by different imprinting methodologies [31-34]. Comparison with binding behaviour of a sixth polymer [30] evaluated non-isothermally. The conditions under which this MIP [30] were evaluated were modelled for the isothermally reported MIPs, namely a polymer loading of 2 mg ml^{-1} and an incubation concentration of 154.2 µM. Where NIP binding isotherm were reported the predicted NIP binding under the stipulated conditions is also illustrated. This comparative methodology enables comparisons to be drawn between imprinting protocols and re-binding media. The addition of the equivalent NIP data is of some assistance in gauging the extent of specific and non-specific binding interactions in the different incubation media.

Figure 20 demonstrates how the predictive model may be applied to compare different polymers and incubation systems at a common theoretical condition set of polymer loading and incubation concentration. In processing the data it was noted that binding isotherms were sometimes reported inaccurately as total quantity bound (i.e. nmol), rather than the bound concentration on the polymer (i.e. nmol mg^{-1}). This may in itself be misleading, but in combination with unreported polymer mass, makes the data unsuitable for comparative application. Similarly, with the reporting of total free propranolol (i.e. nmol) in the absence of incubation volume data. It also appeared that several researchers had reported propranolol

265

binding over very wide concentration ranges, perhaps beyond the useful limit of specific analyte recognition, with additional binding occurring due to non-specific surface binding processes, akin to NIPs. Saturation of this non-specific surface binding may mask the binding behaviour at lower analyte concentrations where analyte recognition occurs to a usually small number of templated sites. The comparative plot of figure 20 illustrates the high degree of non-specific binding occurring for some MIPs, this may be suggestive of less than ideal binding environments for the evaluated polymers, despite the measured isothermal difference between prepared MIP and NIP polymers. For example it may be that acetonitrile is a poor rebinding solvent for propranolol MIPs in general, or more specifically trimethylopropane trimethacrylate cross linked polymers, as synthesised in [32]. Although the knowledge gained from this comparative example is limited, it has illustrated points for discussion and potential further investigation. Such comparisons need not be limited to a single template species and the comparison of a large library of synthesised MIPs reported with binding isotherms may help elucidate trends in performance and polymer behaviour to assist in understanding the fundamental processes of molecular imprinting.

6.4 Supporting Literature

During the course of this work the group of Horvai. published work illustrating the use of distribution ratio (*D*) values in the assessment of molecularly imprinted polymers and proposed their use in the characterisation of MIPs [24]. The motivation for Horvai's study, and also for the work in this chapter, was to develop an approach for comparing MIP performance and to encourage the reporting of equilibrium binding isotherms, so that in the future comparative studies would be more easily achieved. The distribution ratio is derived from isothermal binding data and its application in Toth et al.'s research [24] supports the conclusions of sections 6.3.1 - 6.3.3 that the binding described by the isotherm is independent of the phase ratio of polymer and incubating solvent, with the phase ratio simply defining the position on the isotherm at which equilibrium lies.

6.4.1 Horvai

6.4.1.1 Distribution Ratio

The distribution ratio is described as the ratio of analyte concentration on the MIP phase to that in the liquid phase.

$$D = \frac{q}{c} \tag{6}$$

Where q is the concentration of ligand on the MIP (moles kg^{-1}) and c is the concentration in the liquid phase (moles L^{-1}), giving D in L kg^{-1}. The distribution of analyte between the two phases can be calculated as the product of D and the phase ratio. For phases demonstrating linear chromatographic behaviour (e.g. C_{18} silica or non-imprinted polymers) D is a constant for the given phase pair. However for MIPs and other phases displaying non-linear chromatographic behaviour D varies with the value of the free equilibrium concentration (c). As a result the authors propose that the distribution ratio (D) may be plotted against *log c* to approximately linearise the data [24] enabling comparison between different imprinted materials and offering a method that is transferable between applications [24].

The work reports the suitability of different D value MIPs for various applications, illustrating that the requirements for different applications vary significantly. For example MIPs suited for chromatographic applications are poorly suited for application in binding assays and *vice versa* [37].

6.4.1.1.1 Application to Experimental Binding Data

The approach proposed by Horvai was applied to the measured data for the propranolol MIP prepared in chapter 2. Table 11 illustrates the D value for the measured q *and* c data pairs, this is depicted graphically in figure 21 as plot of D *vs. log c* with a straight line describing the relationship of D with respect to log c for the investigated MIP.

Table 12 Distribution ratio (D) values for the MIP prepared and evaluated in chapter 2. Values calculated form the bound (q) and free (c) data points of the binding isotherm.

c (μM)	q (nmol mg^{-1})	D (L g^{-1})	D (L Kg^{-1})
14.32	21.36	1.49162	1491.62
30.94	38.11	1.23	1231.74
63.69	72.63	1.14	1140.37
188.36	123.29	0.65	654.54
437.13	125.74	0.29	287.65
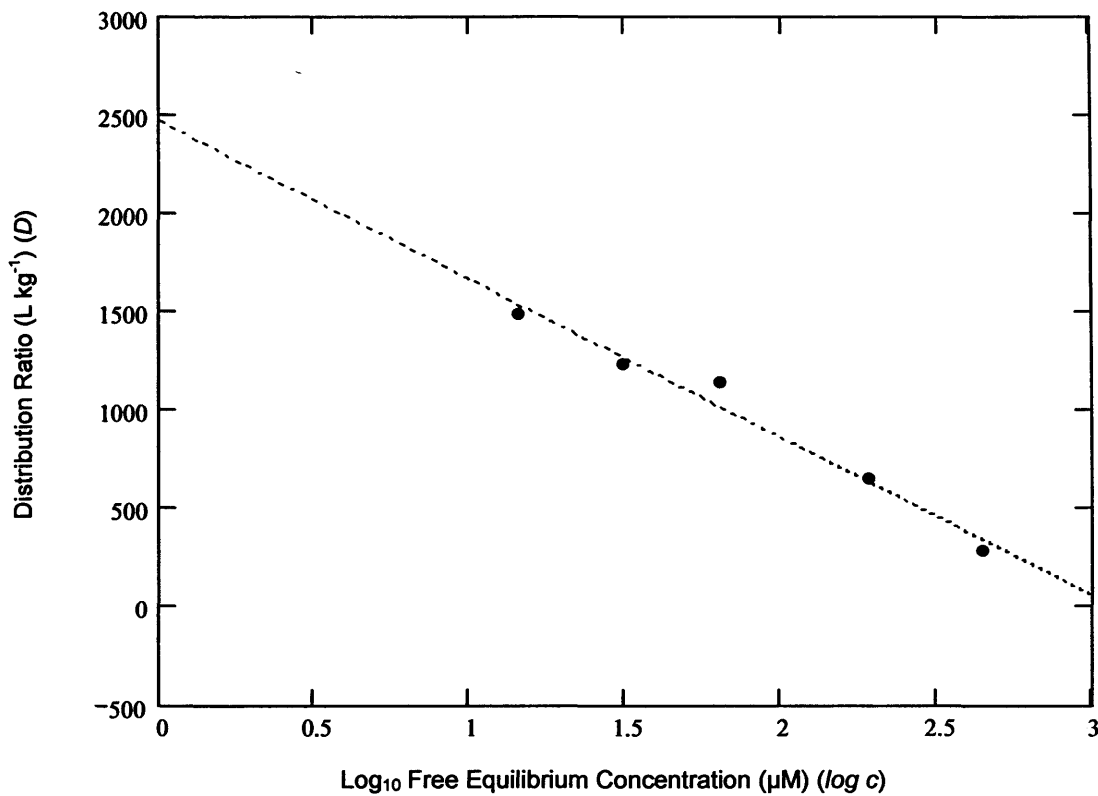
a

Figure 21 Distribution ratio (D) plotted against $\log_{10}$ free equilibrium concentration ($log\ c$). Linear regression produces a line of best fit described by the equation; $D = -802.57\ (\log 10\ c) + 2464.6$.

Linear regression of the data points on the D vs. log c plot appears to give a good fit, suitable for quick estimations or approximate comparisons. The apparent linearization of the data enables simple fitting without the aid of computer software. However, it should be remembered that the log c scale will distort the numeric deviation of the best-fit line from the data points and as such standard linear regression or 'by eye' techniques (sum of squares) will influence the accuracy of the resulting fit. This can be illustrated by de-logging the plot (Figure 22). In addition, much like a Scatchard plot which effectively plots D against q, any uncertainty in data point value is compounded by the q/c data manipulation.
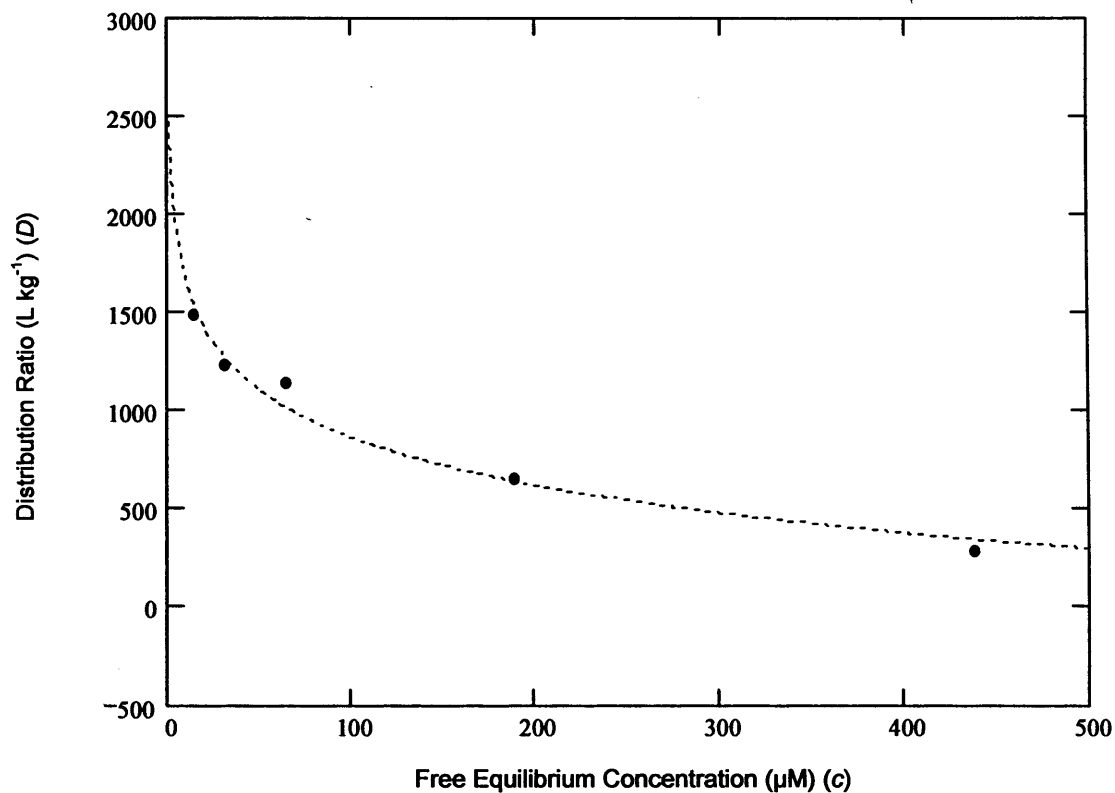
Figure 22 Distribution ratio (D) plotted against free equilibrium concentration (c).

6.4.1.1.1.1 Comparison with Fitted Isotherm Equation

Both of the equations used to describe binding (Equation 3) and the equation describing the relationship between D and $\log c$ were translocated onto each plot's respective axis pairs. This is illustrated in figure 23.

i) D = -802.57 (log10 c) + 2464.6   *ii)* q = 129.7(1 – e$^{-0.01132}$ x c)

Figure 23 Comparison of methods. The approach proposed by Horvai et al. [24] (a) and the fitted equation describing the isothermal shape of the MIP (Section 6.2.1.1.1) (b) are compared. In each comparative graph the model generated by the approach of Horvai; fitting a linear equation to the plot of D vs. log c, is illustrated by a dashed red line. The model described by the equation fitted to the isothermal binding data by non-linear regression is described by a solid blue line. The D vs. log c plot (c) suggests that the experiential data is described equally well by the linear fit of D = -802.57 (log10 c) + 2464.6, as it is by the transposed isothermal equation (q = 129.7(1 – e$^{-0.01132}$ x c)) [The transposition is achieved substituting the isothermal equation into equation (6) (*D = q/c*) with appropriate consideration for the units of *q* and *c*]. However, the transposed isothermal equation produces a monotonically decreasing function describing a curve rather than the straight line of the linear fit of the data derived directly from this plot (D = -802.57 (log10 c) + 2464.6). Transposition of this equation onto the binding isotherm (*q* vs. *c*) (d) demonstrates that the equation derived from the distribution ratio technique describes the binding behaviour of the MIP well at low free propranolol concentrations. As the isotherm approaches saturation the equation is seen to diverge from the measured results, ultimately overestimating the maximum binding capacity of the MIP before diverging completely from the expected saturable binding behaviour and describing a decrease in binding with further increases in free propranolol concentration, ultimately describing negative values of bound analyte (not shown). This behaviour indicates that the data described by the plot of D vs. log c is not linear and is described more accurately by the transposed curve, derived from the isotherm itself by non-linear regression. However the straight line approximation of the D vs. log c data does describe the binding behaviour adequately for sub-saturation behaviour of MIPs, making it suitable for inter-polymer comparisons and prediction of MIP suitability for potential applications, as intended by the authors [24]. The accuracy of modelled predictions of binding behaviour can be expected to be slightly less accurate than the approach outlined in this chapter due to the linear approximation made when fitting to the D vs. log c plot. However this technique can be conducted manually if the required software for non-linear regression is unavailable. The close agreement of the approach reported by Horvai with the method developed independently in the work of this chapter provides good supporting evidence for the validity of the method and the assumptions made in its development (sections 6.3.1.1.1-6.3.1.1.3).

271

6.4.1.1.2 Conclusion

The use of the distribution ratio to describe MIP binding is, as the authors who propose the approach suggest, a valuable first approximation for assessing MIP suitability for an intended application or comparing the performance of difference imprinted materials [24]. The application of the distribution ratio to MIPs supports the assumptions of sections 6.3.1.1.1-6.3.1.1.3 that the amount bound to the polymer (q) is only dependant on the free equilibrium concentration and is otherwise independent of the phase ratio of the MIP and the incubating phase. The translation of the line fitted to the D vs. log c plot to a binding isotherm of bound (q) plotted against free (c) shows a good correlation with binding behaviour over the lower concentration range of free analyte, the most useful working area for imprinted materials. However, the relationship starts to break down as binding to the MIP approaches and then reaches saturation. This is a result of the assumed linearity of the D vs log c plot. Translation of the fitted binding isotherm equation to the D vs. log c plot also suggests that the D vs. log c relationship is non linear, however linearisation over the region of acquired data at sub-saturation conditions can produce adequate results for assessing application suitability and provides a comparative measure for different polymers evaluated under different experimental conditions. It should however be remembered that the q/c data manipulation compounds the error dependency of q from the measured bound, c, data and that the logarithmic scale can distort any 'line of best fit' inaccuracy. Pap and Horvai demonstrate the use of the distribution ratio in calculating a calibration plot for a homologous displacement binding assay with MIPs from the binding isotherm alone, negating the requirement for spiked-assay calibration [4].

6.5 Conclusions

The work of this thesis chapter and that of Horvai's research group, support the analysis of binding isotherms for comparative purposes in the field of molecular imprinting, encouraging their reporting in imprinting publications. The marked non-linear binding behaviour of MIPs makes single value (k', IF, α, percentage bound) measures unsuitable for general comparative

purposes. This is especially true given the often linear binding behaviour associated with NIPs which are frequently employed as control materials, whose performance impacts upon generated MIP performance measures. Horvai's findings [3,4,24,37] support the logic employed in formulating assumptions 1-3 (Sections 6.3.1.1.1 – 6.3.1.1.3) and the calculations of the developed mathematical model (Section 6.3.2), ultimately concluding that an appropriately expressed binding isotherm describes the equilibrium binding behaviour of the MIP irrespective of phase ratio. The phase ratio governs the extent of concentration depletion of free ligand from the incubation solution, thus, for a given set of incubation conditions, dictating the point upon the isotherm at which equilibrium lies. This behaviour can be modelled mathematically or estimated by a simple manual method from a binding isotherm. This enables prediction of expected bound and free equilibrium values for any desired combination of polymer mass, incubation volume and incubating ligand concentration for the MIP in the incubation media described by the isotherm. This process can be employed to predict the binding performance of a MIP under a desired set of conditions, to optimise applications of the MIP or to compare between different MIP preparations, where for example binding isotherms have not been reported (Section 6.3.4.3). It is anticipated that greater understanding of the binding behaviour of MIPs and the ability to compare binding behaviour through appropriately reported isotherms, will assist in differentiation between good and poor MIPs and further the knowledge base of the field. Appreciation of the influence of phase ratio on analyte depletion demonstrates the possible influence of error in elucidation of binding data, and as such may lead to more appropriately considered experimental design for characterisation of different regions of the binding isotherm. Similarly, it is apparent that whilst the binding performance of a MIP possessing non-linear binding behaviour is assessed against a non-imprinted comparator demonstrating linear binding behaviour, the reported performance of the MIP will almost always appear 'better' at low free analyte concentrations. As such, there may be an apparent performance bias with traditionally employed reporting measures (k', IF, α) for imprinted species which are readily detectable, for example radiolabeled targets or inherently fluorescent molecules.

The model developed in the work of this chapter can be applied to optimise experimental conditions for extraction or clean up methodologies, or extended to precisely characterise sample analyte content from SPE eluate analysis. An expansion of the model to incorporate the partitioning of unbound analyte between two immiscible phases was easily envisaged. This would be exceptionally useful in the context of the aims of this thesis, in order to assess theoretically the afforded extraction enhancements from manipulation of phase ratios and polymer loadings. This, in conjunction with the knowledge of the kinetics of interfacial mass transfer in a segmented flow system (chapters 3 and 4) would greatly assist in optimisation of the novel technique. This multi partitioning model (Appendix 3) is utilised in chapter 7, assisting with an interesting discovery which was made through application the model described in this chapter. It was also hoped that kinetic terms could be incorporated into both the single and multi phase MIP binding models, in order to characterise binding behaviour and the depletion of the analyte concentration from incubation conditions with respect to time. Preliminary, continually monitored kinetic studies, conducted in 96 well plates were conducted, however, due to time constraints the completion of this aspect of the model was unfortunately not possible.

6.6 References

[1]   C.J. Allender et al., "A Glimpse of the Inner Workings of the Templated Site,"
      Chemical Communications, no. 2, 2009. pp 165-167.

[2]   J. Garcia-Calzon and M. Diaz-Garcia, "Characterization of binding sites in
      molecularly imprinted polymers," *Sensors and Actuators B: Chemical*, vol. 123,
      May. 2007, pp. 1180-1194.

[3]   B. Toth et al., "Nonlinear adsorption isotherm as a tool for understanding and
      characterizing molecularly imprinted polymers," *Journal of Chromatography A*, vol.
      1119, Jun. 2006, pp. 29-33.

[4]   T. Pap and G. Horvai, "Binding assays with molecularly imprinted polymers--why
      do they work?," *Journal of Chromatography B*, vol. 804, May. 2004, pp. 167-172.

[5]   G.T. Rushton, C.L. Karns, and K.D. Shimizu, "A critical examination of the use of
      the Freundlich isotherm in characterizing molecularly imprinted polymers (MIPs),"
      Analytica Chimica Acta, vol. 528, Jan. 2005, pp. 107-113.

[6]   R.J. Umpleby et al., "Application of the Freundlich adsorption isotherm in the
      characterization of molecularly imprinted polymers," *Analytica Chimica Acta*, vol.
      435, May. 2001, pp. 35-42.

[7]   R.J. Umpleby et al., "Characterization of the heterogeneous binding site affinity
      distributions in molecularly imprinted polymers," *Journal of Chromatography B*,
      vol. 804, May. 2004, pp. 141-149.

[8]   R. Umpleby et al., "Characterization of Molecularly Imprinted Polymers with the
      Langmuir-Freundlich Isotherm," *Analytical Chemistry*, vol. 73, Oct. 2001, pp. 4584-
      4591.

[9]   Y. Chen et al., "Influence of Thermal Annealing on the Thermodynamic and Mass-
      Transfer Kinetic Properties of D- AND L-Phenylalanine Anilide on Imprinted
      Polymeric Stationary Phases," *Analytical Chemistry*, vol. 71, Mar. 1999, pp. 928-
      938.

[10] P. Sajonz et al., "Study of the thermodynamics and mass transfer kinetics of two
      enantiomers on a polymeric imprinted stationary phase," *Journal of Chromatography
      A*, vol. 810, Jun. 1998, pp. 1-17.

[11] R. Ansell, O. Ramström, and K. Mosbach, "Towards artificial antibodies prepared by
      molecular imprinting," *Clin Chem*, vol. 42, Sep. 1996, pp. 1506-1512.

[12] A. Bereczki et al., "Determination of phenytoin in plasma by molecularly imprinted solid-phase extraction," *Journal of Chromatography A*, vol. 930, Sep. 2001, pp. 31-38.

[13] H. Motulsky and A. Christopoulos, *Fitting Models to Biological Data Using Linear and Nonlinear Regression: A Practical Guide to Curve Fitting*, Oxford University Press, USA, 2004.

[14] M.L. Johnson, "Why, when, and how biochemists should use least squares," *Analytical Biochemistry*, vol. 206, Nov. 1992, pp. 215-225.

[15] G. Wulff et al., "Enzyme-analogue built polymers, 5. On the specificity distribution of chiral cavities prepared in synthetic polymers," *Die Makromolekulare Chemie*, vol. 178, 1977, pp. 2817-2825.

[16] R.J. Umpleby II, M. Bode, and K.D. Shimizu, "Measurement of the continuous distribution of binding sites in molecularly imprinted polymers ," *The Analyst*, vol. 125, 2000, pp. 1261-1265.

[17] D.A. Spivak, "Optimization, evaluation, and characterization of molecularly imprinted polymers," *Advanced Drug Delivery Reviews*, vol. 57, Dec. 2005, pp. 1779-1794.

[18] H. Kim and D. Spivak, "New Insight into Modeling Non-Covalently Imprinted Polymers," *Journal of the American Chemical Society*, vol. 125, Sep. 2003, pp. 11269-11275.

[19] S. Swillens, "Interpretation of binding curves obtained with high receptor concentrations: practical aid for computer analysis," *Mol Pharmacol*, vol. 47, Jun. 1995, pp. 1197-1203.

[20] L.R. Snyder and J.J. Kirkland, *Introduction to modern liquid chromatography*, Wiley New York, 1979.

[21] C.J. Allender, C.M. Heard, and K.R. Brain, "Mobile phase effects on enantiomer resolution using molecularly imprinted polymers," *Chirality*, vol. 9, 1997, pp. 238-242.

[22] G. Guiochon, S. Golshan-Shirazi, and A.M. Katti, *Fundamentals of Nonlinear and Preparative Chromatography*, Academic Press, Boston, MA, 1994.

[23] H. Kim, K. Kaczmarski, and G. Guiochon, "Isotherm parameters and intraparticle mass transfer kinetics on molecularly imprinted polymers in acetonitrile/buffer mobile phases," *Chemical Engineering Science*, vol. 61, Aug. 2006, pp. 5249-5267.

[24] B. Toth et al., "Which molecularly imprinted polymer is better?," *Analytica Chimica Acta*, vol. 591, May. 2007, pp. 17-21.

[25] F. Breton et al., "Integration of photosynthetic biosensor with molecularly imprinted polymer-based solid phase extraction cartridge," *Analytica Chimica Acta*, vol. 569, May. 2006, pp. 50-57.

[26] L. Ye, P.A.G. Cormack, and K. Mosbach, "Molecularly imprinted monodisperse microspheres for competitive radioassay," *Analytical Communications*, vol. 36, 1999, pp. 35-38.

[27] C. Nicholls et al., "Displacement imprinted polymer receptor analysis (DIPRA) for chlorophenolic contaminants in drinking water and packaging materials," *Biosensors and Bioelectronics*, vol. 21, Jan. 2006, pp. 1171-1177.

[28] K. Reimhult et al., "Characterization of QCM sensor surfaces coated with molecularly imprinted nanoparticles," *Biosensors and Bioelectronics*, vol. 23, Jul. 2008, pp. 1908-1914.

[29] K. Ho et al., "Amperometric detection of morphine based on poly(3,4-ethylenedioxythiophene) immobilized molecularly imprinted polymer particles prepared by precipitation polymerization," *Analytica Chimica Acta*, vol. 542, Jun. 2005, pp. 90-96.

[30] C.E. Hunt and R.J. Ansell, "Use of fluorescence shift and fluorescence anisotropy to evaluate the re-binding of template to (S)-propranolol imprinted polymers," *The Analyst*, vol. 131, 2006, pp. 678-683.

[31] O.K. Castell, C.J. Allender, and D.A. Barrow, "Novel biphasic separations utilising highly selective molecularly imprinted polymers as biorecognition solvent extraction agents," *Biosensors and Bioelectronics*, vol. 22, Oct. 2006, pp. 526-533.

[32] H. Kempe and M. Kempe, "Development and Evaluation of Spherical Molecularly Imprinted Polymer Beads," *Analytical Chemistry*, vol. 78, Jun. 2006, pp. 3659-3666.

[33] L. Ye et al., "Preparation of molecularly imprinted polymers in supercritical carbon dioxide," *Journal of Applied Polymer Science*, vol. 102, 2006, pp. 2863-2867.

[34] S. Carter and S. Rimmer, "Surface Molecularly Imprinted Polymer Core-Shell Particles," *Advanced Functional Materials*, vol. 14, 2004, pp. 553-561.

[35] S. Marx and Z. Liron, "Molecular Imprinting in Thin Films of Organic-Inorganic Hybrid Sol-Gel and Acrylic Polymers," *Chemistry of Materials*, vol. 13, Oct. 2001, pp. 3624-3630.

[36] S. Boonpangrak et al., "Molecularly imprinted polymer microspheres prepared by precipitation polymerization using a sacrificial covalent bond," *Journal of Applied Polymer Science*, vol. 99, 2006, pp. 1390-1398.

[37] B. Toth, V. Horvath, and G. Horvai, "Which MIP is Better," *Molecularly Imprinted Polymer Science and Technology IV*, Cardiff: STS Publishing, UK, 2006.

Chapter 7

Experimental Validation of the MIP

Binding Mathematical Model Leads to

an Interesting Discovery

7.1 Overview

Continuing from the work of chapter 6, which demonstrated a novel mathematical model for assessing, predicting and comparing MIP binding behaviour, a series of experiments were conducted to validate the theory. Predictions over a range of polymer loadings were conducted and compared to experimental data. The model showed a reasonable correlation with the experimentally measured results. It was however noted that the deviation of the modelled result from the experimental result was greatest under conditions of high polymer loading. This apparent relationship was investigated by further experimentation covering the full isothermal range at three different phase ratios. HPLC analysis of free propranolol was introduced in place of the 96-well plate fluorescence analysis employed previously, to improve the precision of the experimentally measured data. Each phase ratio studied was found to have a different isothermal curve, with affinity and capacity reducing with increased polymer loading. This observation went against all expectation and against the assumptions outlined in chapter 6 and by Horvai at al.'s application of distribution ratios to calculate MIP binding [1]. These works concluded that binding to the MIP is dependant only on the free ligand concentration and is otherwise independent of the polymer/solvent phase ratio. Template leaching, a commonly experienced problem in molecular imprinting [2], was investigated. The experimental studies concluded this was not responsible for the observed disparity between the binding curves. It was proposed that the observation of an apparent decrease in isotherm gradient and reduction in binding capacity was a result of over-estimation of free propranolol in the equilibrium binding experiments. This systematic overestimation in measured 'free' propranolol was theorised to be as a result of soluble imprinted polymer fraction leaching from the MIP microspheres into the incubating chloroform, it was proposed that this soluble fraction possessed template recognition properties, effectively competing with the insoluble MIP microspheres to bind the propranolol in the incubation system.

Consideration of the accepted theories of polymer growth processes during precipitation polymerisation, (Chapter 2) support the theory of formation of a significant soluble polymer

fraction which becomes incorporated into the growing precipitated polymer network [3]. It was considered possible that template specific binding sites were introduced into the polymer in this early stage of growth, whilst the polymer remains soluble. The theta solvent conditions of the polymerisation (Chapter 2) creates a highly porous and open structure in the precipitated microsphere; it is possible that early stage soluble fraction could become non-covalently trapped or entangled within the growing polymer. It was also considered possible that during the polymer washing procedure the wash solvents employed precipitated the remaining soluble fraction causing it to stick to the surface of the microspheres. It is only later when incubated in a solvating solvent, such as chloroform, that this soluble polymer fraction leaches from the polymer microspheres, into solution in the incubating solvent. It is suggested that following incubation the soluble MIP fraction passes through the filter membrane, propranolol bound to the soluble MIP fraction is subsequently removed during the sample preparation and/or analysis stages resulting in the measurement of additional propranolol in the sample and hence an overestimation of free propranolol at equilibrium, and consequently an underestimate in the actual amount bound. The greater the polymer loading in the incubation system the greater quantity of this soluble MIP fraction is leached and the greater this effect becomes, explaining the apparent measurement of decreasing isotherm gradient and reduction in capacity with increased polymer loading.

Mathcad and the predictive MIP binding model (Chapter 6) were utilised to quantitatively estimate the magnitude of the perceived overestimation in unbound equilibrium propranolol concentration from one polymer loadings to the next. Through regression of these resultant estimates, and the assumption that the soluble fraction followed the same binding behaviour as its insoluble counterpart, a proposed relationship linking leaching of soluble MIP fraction with polymer loading was approximated. This enabled extrapolation of a theorised 'true' binding isotherm for the MIP, as if no polymer leaching were occurring. This isotherm together with the proposed relationship for leaching of a soluble MIP fraction were incorporated into the predictive model developed in chapter 6, generating a model capable of accounting for this behaviour. This was utilised to predict the so called 'true' bound and free equilibrium

concentrations and additionally the experimentally measured values, including the overestimation in free propranolol concentration due to the presence of the soluble polymer fraction. This theory was tested by application of the leaching-model to the data obtained from the original validation studies conducted at the outset of the work or this chapter. (Data which was not utilised in the formulation of the mathematical theory and which itself covered a range of polymer loadings). An excellent correlation between the measured experimental results and the predicted results was obtained, supportive of the polymer leachate theory.

Further polymer leachate was harvested, dissolved in chloroform and assessed in a segmented flow regime (Chapter 3 and 4). The presence of the soluble MIP fraction was found to significantly enhance the partitioning of propranolol from the aqueous phase into the leachate-containing organic phase. The significant enhancement in removal of propranolol in comparison to that measured in the presence of a NIP soluble fraction was indicative of a template recognition effect by the soluble imprinted polymer fraction. The extent of binding was found to be in close keeping with that which would be expected from an equivalent mass-loading of insoluble polymer, further supporting the soluble polymer fraction hypothesis.

7.2 Experimental Validation of the Predictive Model

A series of experiments were conducted in an attempt to validate the predictive mathematical model introduced in chapter 6. Predictions over a range of polymer loadings were tested in order to demonstrate the phase ratio independence of the binding isotherm.

7.2.1 Experimental Design

The binding of propranolol to 1.5 mg of imprinted polymer microspheres, incubated in range of volumes of chloroform containing varying amounts of propranolol was investigated. The free equilibrium concentration was measured and the resultant polymer bound value calculated. The measured results were compared to the predicted outcome using the mathematical model introduced in chapter 6. A mass of 1.5 mg was utilised (since this amount had not been used

in earlier studies) with a range of incubation volumes, thus investigating the application of the model over a wide range of polymer loadings. A range of conditions were selected to initially investigate the model validity at relatively low equilibrium concentrations, where the MIP binding isotherm exhibits high sensitivity to variations in free concentration.

Experiments (n = 5) were carried out in accordance with the methodology described in chapter 2 (Section 5.1.1.1.). Incubation was performed in water saturated chloroform in keeping with the experimental conditions at which the binding isotherm was elucidated. Table 1 gives experimental conditions and results.

Table 1 Experimental MIP incubation conditions for validation of the predictive binding model developed in the work of chapter 6, together with the measured experimental equilibrium binding bound and free data.

	m1	v	Pr	p0	Cs	Free	Bound
	polymer mass	volume	Phase ratio	total propranolol	incubation concentration	Measured equilibrium concentration	Measured equilibrium concentration
	(mg)	(ml)	(mg ml^{-1})	(nmol)	(µM)	(µM)	(nmol mg^{-1})
exp 1	1.5	11.29	0.13	300	26.57	22.61	29.86
exp 2	1.5	4.93	0.30	150	30.43	22.28	26.80
exp 3	1.5	3.87	0.39	125	32.31	21.60	27.62
exp 4	1.5	2.81	0.53	100	35.60	23.90	21.91
exp 5	1.5	1.75	0.86	75	42.88	23.49	22.61
exp 6	1.5	0.69	2.18	50	72.57	35.10	16.80

7.2.2 Application of the Predictive Model

The model described in chapter 6 was applied to each of the six experimental conditions (Table 1) using the equation fitted to the experimentally derived binding isotherm (Chapter 6) (equation 1).

$$bound = 129.7 \left(1 - e^{-0.01132 \cdot FreeEquilibriumConcentration} \right) \tag{1}$$

The predicted equilibrium binding conditions are illustrated in table 2.

Table 2 Predicted bound and free equilibrium conditions for MIP binding under a range of experimental conditions. Predicted estimates were made from the previously acquired binding isotherm and mathematical model described in chapter 6.

	m1	v	Pr	p0	Cs	Ceq	f1
	polymer mass	volume	Phase ratio	total propranolol	incubation concentration	Predicted free concentration	Predicted bound concentration
	(mg)	(ml)	(mg ml^{-1})	(nmol)	(µM)	(µM)	(nmol mg^{-1})
exp 1	1.5	11.29	0.13	300	26.57	22.3	32.16
exp 2	1.5	4.93	0.30	150	30.43	21.10	30.66
exp 3	1.5	3.87	0.39	125	32.31	20.65	30.08
exp 4	1.5	2.81	0.53	100	35.60	19.99	29.24
exp 5	1.5	1.75	0.86	75	42.88	18.95	27.90
exp 6	1.5	0.69	2.18	50	72.5	17.11	25.47

7.2.3 Comparison of Experimental and Predicted Results

The measured experimental results and the predicted equilibrium binding conditions are compared in Figure 1.
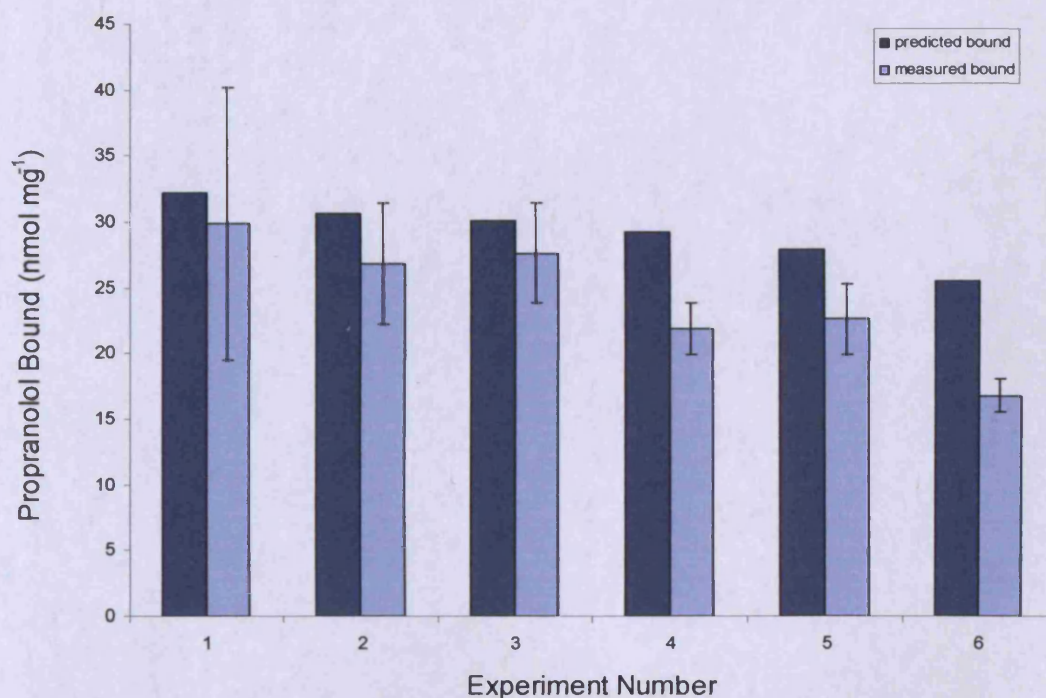
Figure 1 Comparison of experimental and predicted bound and free equilibrium conditions for MIP binding under a range of experimental conditions. Predicted estimates were made from the previously acquired binding isotherm and mathematical model described in chapter 6. (n=5 ±S.D.)

The correlation between the measured and predicted bound values was fair, however, predictive accuracy was seen to decrease for experiments four, five and six, with the main example being experiment six, that of the highest polymer loading, where the measured free equilibrium concentration was approximately twice that of the predicted value (Tables 1 and 2). This corresponds to a large overestimation in the predicted amount bound to the polymer. The observed binding may have been expected to be slightly lower than the predicted values due to increased ambient temperature in the laboratory in the summer months when the validation experiments were conducted, compared to that of the winter months when the binding isotherm generating experiments were conducted. This is as a result of the increase in entropy of the analyte species with increased temperature, thus reducing the favourability of template-binding site interactions. If such an effect were entirely responsible for the discrepancy in measured and predicted results, a near uniform translation of the adsorption isotherm over the lower free concentration region of the isotherm would be expected based on previous experimental investigations [4]. This would therefore be expected to manifest as a consistent overestimation in predicted bound, independent of the polymer loading. It appeared from the data that the margin of error in the predicted equilibrium conditions showed a tendency to increase with increased polymer loading.

7.3 Expansion and Clarification of the Predictive Model's Inaccuracy: Investigation into the Effect of Polymer Loading - Construction of Binding Isotherms at Three Polymer Loadings

In order to investigate further the observed discrepancy between the measured and predicted MIP binding behaviour, binding was quantified over the entire isothermal range at three different polymer loadings. Three discrete masses were chosen, together with three discrete incubation volumes, in order to uncover any potential mathematical frailties in the proposed predicted model (Chapter 6). It was anticipated that the isotherms measured at each of the three phase ratios would be superimposable due to the equilibrium independence of phase

ratio, as described in chapter 6, and by the previous application of distribution ratio values to MIP binding [5]. The difference in phase ratio was expected to affect the extent of analyte depletion from the incubation solution and therefore determine *only* the equilibrium position on the binding isotherm curve.

7.3.1 Experimental Design and Rational

Polymer loadings of 1mg/4ml, 3mg/3ml and 4mg/2ml were studied and binding quantified to incubations at propranolol concentrations of 25, 50, 100, 250 and 500 µM. Each experiment was conducted in replicates of 5, following the general methodology outlined in chapter 2. The binding experiments were conducted in HPLC grade chloroform which was not water saturated. Saturation of the chloroform with water was omitted for this investigation in effort to afford greater precision to experimental results, since the temperature dependency of water solubility in chloroform was not known it was thought this could vary from batch to batch. It was expected that MIP binding behaviour would be subtly different between the water saturated, and dry, chloroform environments, as such it was intended to compare only the 3 isotherms generated from current investigation. Since precision and confidence in the measurements were paramount for this comparison, all 3 polymer loadings were incubated simultaneously at each of the investigated incubation concentrations, in order to minimise the possible effect of temperature variation. For any given incubation concentration all investigations were conducted using the same prepared stock solution to minimise error due to variance in incubation concentration. Free propranolol quantification was conducted by HPLC analysis, rather than the previously employed 96-well plate fluorescence analysis, in order to afford greater precision in the quantification of free propranolol. Free propranolol concentrations were determined by integration of the propranolol peak with the area under the curve being proportional to the propranolol concentration, this relationship was quantified by construction of a standard curve through analysis of prepared standards. The concentration of each of the nominally prepared 25, 50, 100, 250 and 500 µM incubation solutions was also quantified by this method to elucidate an accurate value for the total propranolol in each of the incubation experiments. Due to the relatively limited yield achieved by precipitation

polymerisation compared to monolithic polymerisation, and the desire to ensure all necessary experimental investigations could be conducted from a single polymerisation batch, investigations were conducted in the region of relatively low polymer loading to conserve polymer material.

7.3.1.1 HPLC Analysis

Polymer incubation filtrate (1 ml) was transferred to an HPLC vial and evaporated to dryness before being reconstituted with HPLC mobile phase (1 ml) prior to analysis. Quantification of propranolol content was made by HPLC analysis (TSP SpectraSYSTEM P4000, AS3000, UV3000, SN4000, Runcorn, UK). A mobile phase of 55% 20 mM ammonium acetate buffer, pH 3.5, 45% acetonitrile running at 1.0 ml min^{-1} was employed, with a stationary phase of C_{18} (column: Genesis 4µm, 15 cm, 0.5 cm I.D.). The HPLC system was operated and data acquired through a PC running ChromQuest 1.0 (ThermoQuest, UK). Control experiments confirmed no sublimation of propranolol during the evaporative sample preparation procedure.

7.3.2 Isotherm: Results and Analysis

For each of the investigated incubation concentrations at each of the three polymer loadings detailed in section 3.1, the concentration of propranolol on the polymer was calculated from the measured free equilibrium concentration. The results are illustrated in Figure 2.
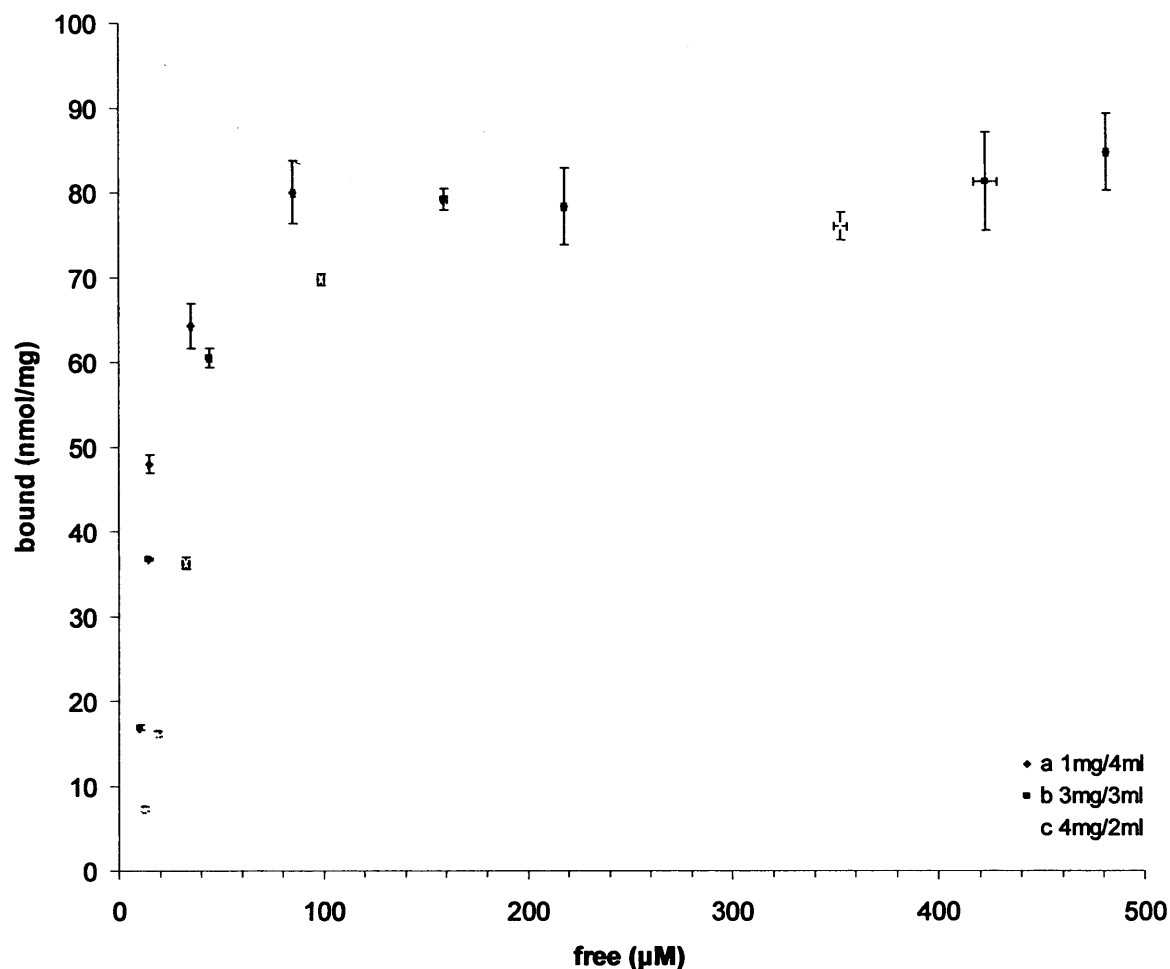
Figure 2 Experimentally derived binding isotherms for propranolol binding to MIP in chloroform, investigated at three different polymer loadings (1mg/4ml, 3mg/3ml and 4mg/2ml). (Error = ± S.D, n =5)

As predicted theoretically (chapter 6), uncertainty in the location of data points defining the isotherm is increased when analyte depletion form the incubation solvent is low. This is reflected by the increasing size of the error bars (± S.D.) at high free equilibrium concentrations. This, again in keeping with the theoretical observations of chapter 6, is true for the lowest polymer loading (a 1mg/4ml). Due to the quantity of polymer remaining (from the batch under investigation) higher mass loadings could not be used. It was noted the data appeared to characterise three distinct isotherms, rather than being super-imposable as one. It was observed that as the polymer loading increased, the amount bound for any given free ligand concentration appeared to decrease with increased polymer loading. This unexpected observation was contrary to that predicted from the theory outlined in chapter 6 and to that of

Horvai's work [5]. It was anticipated that binding to a MIP must be dependant only on the free ligand concentration and is otherwise independent of the polymer/solvent phase ratio (Chapter 6). That the data appeared to describe three non-superimposable isotherms was most clearly observable at the low concentrations, where analytical precision was greatest. The data indicates a reduction in gradient of the initial slope of the isotherm with increasing polymer loading, an apparent decrease in affinity for the same free equilibrium concentration. Figure 3 plots the measured data for each of the 5 replicates for each polymer loading over the free concentration range 0 – 200 μM. The reproducibility within each group of 5 replicates was extremely close in all instances. with virtually no variation within the replicates of the data sets acquired at low incubation concentrations for polymer loadings b (3mg/3ml) and c (4mg/2ml). This level of reproducibility, with no overlap in data points between the three polymer loadings, strongly suggests that at each phase ratio a different binding isotherm applies.
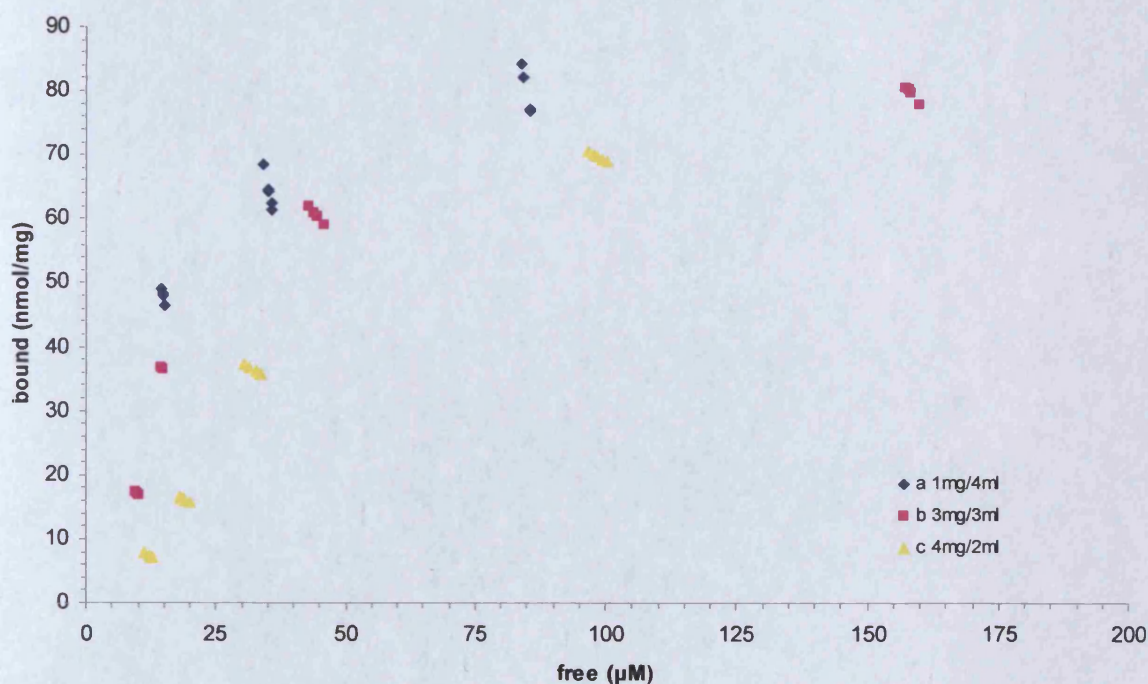
Figure 3 Experimentally derived sub-saturation portion of binding isotherms for propranolol binding to MIP in chloroform, investigated at three different polymer loadings (1mg/4ml, 3mg/3ml and 4mg/2ml). Data points are plotted for each of the 5 replicates for each of the investigated incubation conditions.

This experimental data suggests a decrease in the binding of propranolol to the MIP with increased polymer loading for the same free equilibrium concentration. This effect is clearly demonstrated at low free equilibrium concentrations, for example at a free propranolol concentration of 12.5 µM, apparent binding to the MIP varies from ~7 nmol mg^{-1} (loading c 4mg/2ml) to ~47 nmol mg^{-1} (loading a 1mg/4ml) with a variance of less than 1 and 3 nmol mg^{-1} within the replicate data sets respectively (Figure 3).

Comparison of the isothermal shapes of Figure 2 to that measured in water saturated chloroform (chapter 2), illustrated an apparent decrease in capacity from ~ 130 nmol mg^{-1} to ~85 nmol mg^{-1} as result of analyte binding in non-water saturated chloroform. It was proposed that this was a result of a slight increase in non-specific binding in the water saturated chloroform environment, particularly at high analyte concentrations, due to the decreased solubility of the propranolol base species in the more polar H_2O environment.

7.3.3 Divergence of Isotherms with Increased Polymer Loading

7.3.3.1 Template Leaching

The problem of template becoming entrapped within the polymer matrix during the polymerisation process and later leaching from the polymer is well documented within the field of molecular imprinting [2]. This phenomenon represents a significant obstacle to commercialisation of imprinted materials. Some commercially available MIP based separation materials are prepared through the imprinting of compounds related to the target species in an effort to get around the problem of inadvertently introducing additional analyte into the analysis system [10]. During the imprinting process, it is thought that template molecules becomes entrapped within very high affinity binding sites with little access in or out of the cavity due to spatial hindrance by the surrounding polymer matrix. As a result, despite thorough washing, either by column or packed bed methods, template species may leach on prolonged incubation, particularly in a swelling solvent. Due to the ease of formation of disperse polymer suspensions in chloroform, indicative of highly favourable solvent - polymer interactions, chloroform was considered likely to induce swelling of the polymer microspheres.

This was confirmed qualitatively through microscopic observation of discrete MIP microspheres which were observed to shrink on drying following suspension in chloroform.

7.3.3.1.1 Extent of Template Leaching

To assess whether template leaching could be responsible for the isotherm divergence with increased polymer loading (Figure 3), the extent of propranolol leaching at each of the investigated polymer mass/solvent incubation volume ratios was investigated. It was reasoned that should propranolol be leaching from the polymer, total propranolol in the incubation system would be greater than that provided by the incubation solution alone. This would subsequently result in an under calculation of the propranolol bound to the MIP. Increasing the polymer loading would be expected to result in an increase in quantity of leached propranolol, thus having a greater impact on the deviation of the isotherm at higher polymer loadings. Using the HPLC methodology detailed in 7.3.1.1 the free propranolol liberated from 1, 3 and 4 mg of polymer, incubated in 4, 3 and 2 ml of chloroform respectively, for 24 hours, was assessed (Table 3).

Table 3 Free propranolol leached from MIP microspheres into chloroform, at three different incubation loadings.

polymer mass (mg)	Volume (ml)	polymer loading (mg ml^{-1})	Free Leached Propranolol (µM)
1	4	0.25	0.46
3	3	1	0.61
4	2	2	1.19

Due to the passage of time since preparation of the MIP several very small degradation peaks, absorbing at the characteristic wavelength of 290 nm of the naphthalene moiety present in the propranolol species, were detected in the washing solutions. Consequently, the certainty of quantifying the amount of propranolol, or other potentially interfering binding species, was somewhat reduced. However, further experimental analysis demonstrated that template leaching could not be responsible for the divergence of the measured isotherms

(7.3.3.1.1.1).

7.3.3.1.1.1 Estimated Effect of Template Leaching on the Binding Isotherm

The impact of template leaching on the experimental data used to construct the isotherms at each of the 3 polymer loadings was estimated. An equation (Equation 2), as described in chapter 6, with the value of a describing the isothermal curves maximum (i.e. MIP capacity) and the value of b, describing the isothermal gradient, was fitted to the isotherm for each polymer loading.

$$bound = a(1 - e^{(-bxC_{eq})})$$ (2)

Fitting was conducted using every acquired data point, rather than the mean values of replicates, to give equal weighting to each replicate using the curve fit regression. This results in the sum-of-the-squares regression analysis for curve-fitting recognising the greater reproducibility of the data at the low concentration end of the binding curve giving a more accurate fit over the region where most confidence in the data lies. Conversely regression of the mean data values of each experimental incubation concentration would produce a fit where deviation from the mean data points would be weighted equally, regardless of the variance in measured data comprising the mean value. The fitted isotherms are described mathematically in table 4.

Table 4 Fitting parameters for equation 2, describing the measured binding isotherm for each of the three experimentally investigated polymer loadings.

polymer mass (mg)	Volume (ml)	polymer loading (mg ml⁻¹)	a	b
1	4	a: 0.25	80.74	0.0541
3	3	b: 1	80.39	0.0331
4	2	c: 2	79.00	0.0171

Fitting parameters (a and b) elucidated by non-linear regression using the computer program GraphPad Prism 4 (GraphPad Software inc.). Isothermal data fitted to the equation $bound = a(1 - e^{(-bxC_{eq})})$.

It was assumed that any leached propranolol would, once free, be able to rebind to the MIP and thus an equilibrium would exist between bound and free propranolol. It was assumed that the number of additional sites made available for binding due to the eventual removal of the previously entrapped template would be minimal compared to the total number of sites. It would be anticipated that such processes would also occur to the same or to a similar degree in the presence of propranolol in the incubating solvent, and as such the binding to the MIP of the leached propranolol would be expected to follow that of the binding isotherm. With respect to this, the measured free leached propranolol was considered as the free equilibrium concentration. In order to estimate the quantity of bound propranolol, and consequently the total potentially leachable propranolol introduced by the MIP, this value was substituted into the mathematical equation describing the binding isotherm for the relevant polymer loading (Table 4). The results are illustrated in Table 5.

Table 5 Estimated total quantity of leachable propranolol remaining on the MIP microspheres after washing.

polymer loading	Zero incubation measured free (μM)	calculated bound from isothermal equation (nmol mg^{-1})	total leached propranolol (nmol)	total pre-existing concentration on MIP (nmol mg^{-1})
1mg / 4ml	0.46	1.97	3.80	3.80
3mg / 3ml	0.61	1.59	6.60	2.20
4mg / 2ml	1.19	1.59	8.76	2.19
			mean	2.73

The total quantity of propranolol removable from the MIP was low but, particularly at the lower incubation concentrations investigated, represented a significant addition to the total propranolol in the incubation systems. The amount of propranolol bound in each of the equilibrium binding experiments was recalculated from the measured free concentration using a readjusted value for the total propranolol in the incubation system; the estimated propranolol introduced on the polymer, in addition to that provided by the incubating solution. The re-

evaluated, slightly elevated value for bound propranolol was plotted against the measured free equilibrium concentration. For each polymer loading, the isothermal data was re-fitted to equation 2, to achieve a leaching-adjusted isothermal equation. The re-fitted isothermal equation for each polymer loading describes more accurately the binding behaviour of the MIP due to the additional propranolol introduced to the binding system on the MIP itself. These re-fitted equations (Table 6) were re-applied to the free concentration measured under zero concentration incubation (Table 3), thus arriving at a more accurate estimate for the total leachable propranolol introduced to the binding systems by the MIP. This approach was repeated, with the more accurate estimate for the additional propranolol introduced by the MIP, for each of the incubation systems. Re-evaluation of the amount of propranolol bound and re-fitting of the isothermal equation enabled an even more accurate description of MIP binding behaviour at each of the three polymer loadings investigated. This iterative process was repeated, with subsequent iterations converging quickly on a solution for the equation describing the binding isotherm, to take into account of the effect of template leaching. Table 6 illustrates the calculated propranolol bound to the MIP, from the measured free equilibrium concentration, for each iteration of the above process. The values are rapidly seen to converge on a description of binding behaviour accounting for the leachable template remaining on the polymer upon incubation. Figure 4 and 5 illustrate this effect graphically. Table 7 gives the fitting parameters for equation 2, describing the binding isotherm shape mathematically, for each iteration and for each of the three polymer loadings

Table 6 Successive iterations of isothermal correction for leaching propranolol from the MIP microspheres rapidly converge on a solution. Adjustment of measured binding isotherms to consider template leaching at each of the investigated polymer loadings maintains three non-superimposable binding isotherms. This indicates that the effect of template leaching is not responsible for the measured divergence of the binding isotherm with increased polymer loading.

polymer loading	nominal incubation concentration	measured incubation concentration	measured equilibrium free (mean)	Bound original: template leaching not considered	Bound – template leaching considered			
					Template leaching iteration 1	Template leaching iteration 2	Template leaching iteration 3	Template leaching iteration 4
	µM	µM	µM	nmol/mg	Nmol/mg	nmol/mg	nmol/mg	nmol/mg
1mg / 4ml	25	26.81	14.81	47.98	51.78	51.98	51.99	52.00
1mg / 4ml	50	51.20	35.13	64.26	68.06	68.26	68.27	68.27
1mg / 4ml	100	104.93	84.91	80.06	83.86	84.06	84.07	84.07
1mg / 4ml	250	238.04	218.44	78.38	82.18	82.38	82.39	82.39
1mg / 4ml	500	504.13	482.93	84.80	88.60	88.80	88.81	88.81
3mg / 3ml	25	26.81	9.90	16.91	19.11	19.23	19.24	19.24
3mg / 3ml	50	51.20	14.49	36.71	38.91	39.03	39.04	39.04
3mg / 3ml	100	104.93	44.42	60.50	62.70	62.82	62.83	62.83
3mg / 3ml	250	238.04	158.76	79.28	81.48	81.60	81.61	81.61
3mg / 3ml	500	504.13	422.74	81.39	83.59	83.72	83.72	83.72
4mg / 2ml	25	26.81	12.20	7.30	9.49	9.62	9.63	9.63
4mg / 2ml	50	51.20	18.80	16.20	18.39	18.52	18.52	18.52
4mg / 2ml	100	104.93	32.40	36.26	38.45	38.58	38.59	38.59
4mg / 2ml	250	238.04	98.50	69.77	71.96	72.09	72.09	72.10
4mg / 2ml	500	504.13	351.96	76.09	78.28	78.40	78.41	78.41
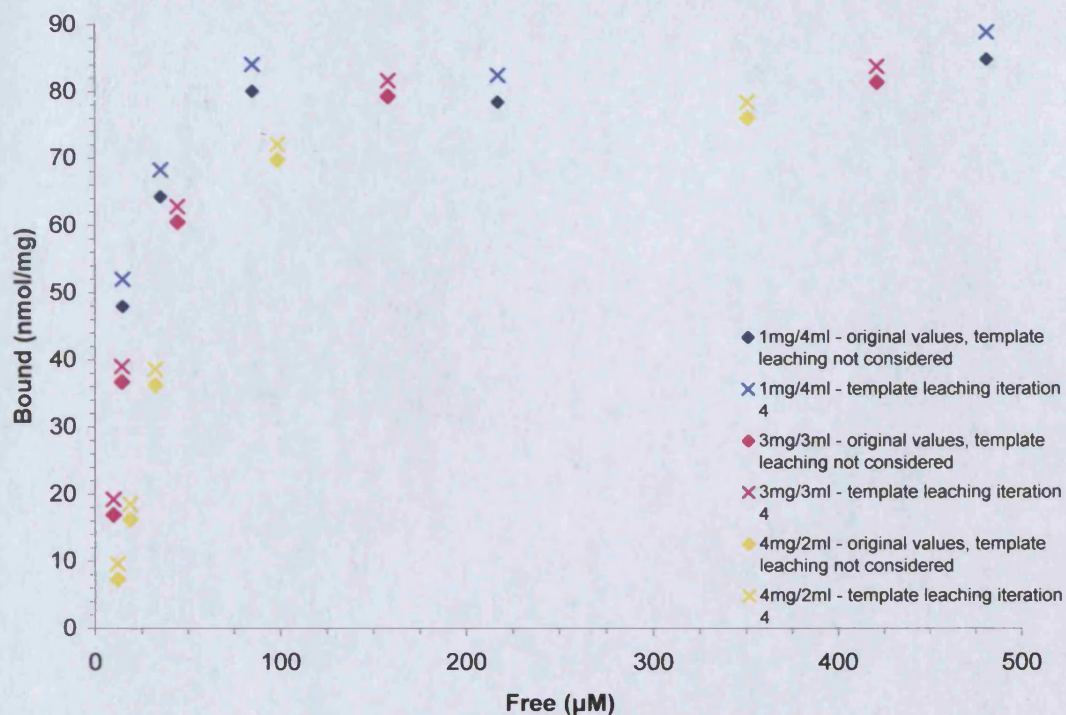
Figure 4 Adjustment of measured binding isotherms to consider template leaching at each of the investigated polymer loadings maintains three non-superimposable binding isotherms. The effect is minimal and results in an approximately equal increase in equilibrium bound at each of the three polymer loadings. This indicates that the effect of template leaching is not responsible for the measured divergence of the binding isotherm with increased polymer loading.
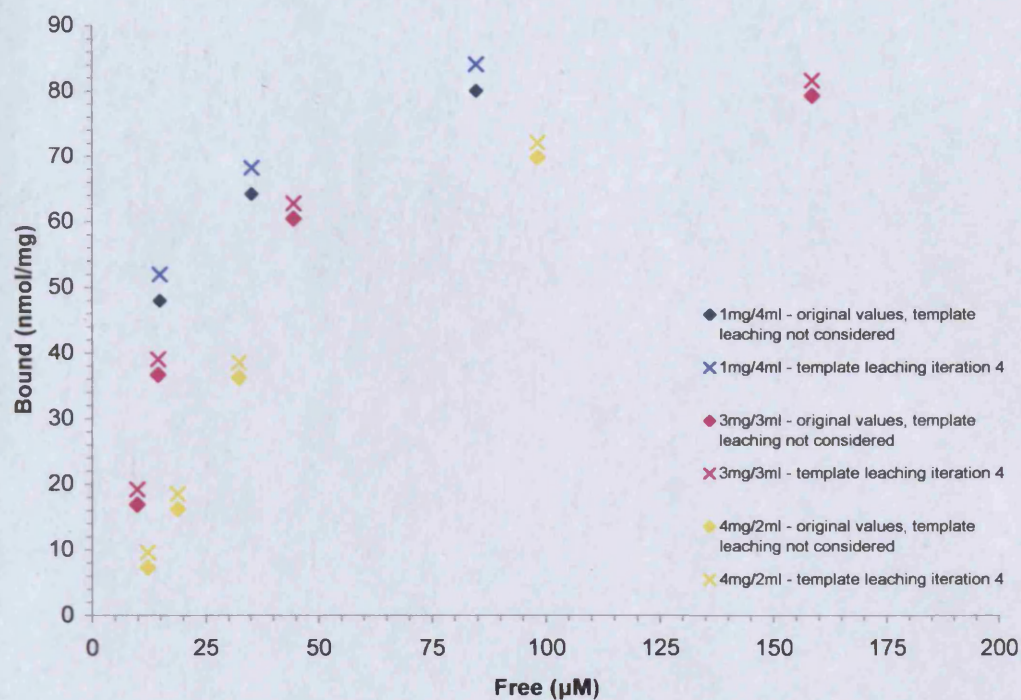
Figure 5 Adjustment of measured binding isotherms to consider template leaching at each of the investigated polymer loadings maintains three non-superimposable binding isotherms. The effect is minimal and results in an approximately equal increase in equilibrium bound at each of the three polymer loadings. This indicates that the effect of template leaching is not responsible for the measured divergence of the binding isotherm with increased polymer loading.

Table 7 Fitting parameters describing the measured binding isotherm for each investigated polymer loading. The shift in isothermal shape can be seen with successive iterations considering the effect of template leaching on the measured binding equilibrium, to converge on a more accurate description of the MIP binding behaviour. The effect of template leaching on the fitted isothermal equation can be seen to be minimal compared to the measured difference in isothermal shape between the three polymer loadings investigated. This indicates that the effect of template leaching is not responsible for the measured divergence of the binding isotherm with increased polymer loading.

polymer loading	original		iteration 1		iteration 2		iteration 3		iteration 4	
	a	b	a	b	A	b	a	b	a	b
1mg / 4ml	80.74	0.0541	84.38	0.05703	84.57	0.05718	84.58	0.05719	84.58	0.05719
3mg / 3ml	80.39	0.0331	82.39	0.0348	82.5	0.0349	82.51	0.03491	82.51	0.03491
4mg / 4ml	79	0.01706	80.95	0.01798	81.06	0.01803	81.07	0.01804	81.07	0.01804

Fitting parameters (a and b) elucidated by non-linear regression using the computer program GraphPad Prism 4 (GraphPad Software inc.). Isothermal data fitted to the equation $bound = a(1 - e^{(-bxC_{eq})})$.

This analysis shows that the effect of template entrapped during the polymerisation process, which subsequently leaches upon incubation, does appear to have a slight effect on the binding isotherm characterised by equilibrium binding experiments. This effect however appears to be fairly constant across the 3 polymer loadings investigated, resulting in a small increase (~3 nmol/mg) in the quantity of propranolol bound to the MIP (Figure 4 and Figure 5). The effect on the amount bound is an approximately equal increase of bound values across all three polymer loadings. It does not suggest that the isotherms of the three polymer loading converge to a common data fit. This effect is seen mathematically with the equations describing the isothermal shape (Table 7). The effect of template leaching on the isothermal equation variables (*a* and *b)* is minimal (Table 7), maintaining the suggestion of three distinct isothermal fits. In fact with consideration of template leaching fitting parameter *b* (defining the initial gradient of the isotherm) is observed to increase further with decreasing polymer loading. Consequently, it may be expected that if sufficient quantities of propranolol were introduced on the polymer itself the actual isotherm divergence would increase further (Table 7). The extent of template leaching is interesting since following their preparation (Chapter 2) the imprinted polymer microspheres were washed in solvents over a range of polarities, together with acetic acid as an acidic modifier to discourage binding of the template through proton transfer and subsequent charge interactions at the binding site. The washing was performed equally or more rigorously than examples of similarly prepared polymers [6]. Analysis of the wash solvents indicated that, for later washes, the propranolol concentration was below detectable limits. This suggests effective removal of leachable template. However the polymer wash was performed by pressure driven flow of washing solvent though a packed bed of polymer. These experimental observations suggest that such a kinetic style of washing is insufficient to remove all potential leaching template, batch equilibrium washing, for example under reflux with a swelling solvent may afford more complete removal of template species.

7.3.3.2 Experimental Reproducibility

Investigations into pipetting and weighing reproducibility and accuracy over the range of operation employed in the experiments described in this chapter were conducted. The accuracy and precision of both measuring techniques was found to be very good and as such could be ruled out as being responsible for isotherm divergence.

7.3.3.3 Hypothesis: Leaching of Soluble Polymer Fraction

7.3.3.3.1 Basis of Hypothesis

It was proposed that the apparent decrease in isotherm gradient, together with the possible reduction in maximum capacity observed with increased polymer loading, was a result of over-estimation of the measured free propranolol. It was reasoned that this over-estimation increased with increasing polymer loading. A hypothesis was developed with consideration of the precipitation polymerisation growth mechanism, where growing polymer chains are 'captured' from solution and incorporated into a growing precipitated microsphere [3,7,8] (chapter 2). It has been reported that in general the microsphere yield from precipitation polymerisation reactions, where total polymerisable monomers constitute ~4% of the reaction volume, is around 50%. This type of polymerisation also gives rise to a soluble polymer product typically with a yield of between 3% and 20%, dependent on the solvating strength of the reaction media [7]. This soluble polymer fraction remains in solution since it is below the critical molecular size where Gibbs' free energy disfavours polymer–solvent interactions and precipitation of the polymer occurs in the theta-solvent environment (Chapter 2). It was theorised that a portion of this soluble polymer fraction may become entrapped within pores of the precipitated microspheres without becoming covalently incorporated into the larger polymer network. It may also be possible that during the polymer washing procedure the reduction in temperature and change of solvent environment away from theta conditions results in its precipitation where it subsequently binds non-specifically to the surface of the polymer microspheres. This is a likely result as polymer-polymer interactions become favoured over polymer-solvent interaction at the reduced temperature. The large porous nature of the microspheres formed by precipitation polymerisation at near theta conditions offers a large

298

surface area for the potential deposition of the freshly precipitated soluble polymer fraction. It was proposed that through such mechanisms a portion of potentially soluble, small chain length, polymer networks are deposited on or within the MIP microspheres. On incubation in a suitable solvent, such as chloroform, where solvent-polymer interactions are favourable, (indicated by microsphere swelling and stability of suspension), all, or a portion, of this polymer fraction may leach from the polymer and pass into solution.

It was hypothesised that the three distinct binding isotherms observed, for the three different polymer loadings, resulted from a systematic overestimation of measured 'free' propranolol as a result of analyte binding to a soluble polymer fraction leaching from the incubated MIP microspheres. It was proposed that this soluble MIP fraction possessed template recognition and rebinding ability, effectively competing with the insoluble polymer microspheres to bind the propranolol in solution. Upon filtration of the polymer suspensions, this soluble MIP fraction passes through the filter membrane and as a result is subsequently measured as additional 'free' propranolol after becoming unbound during the sample preparation and HPLC analysis. This effect would result in an overestimate of the unbound equilibrium concentration and therefore an underestimation in amount bound. The greater the microsphere loading, the greater the quantity of the soluble MIP fraction giving rise to a systematic overestimation of the free propranolol. This theory would account for the apparent measurement of decreasing isotherm gradient and reduction in capacity with increased polymer loading.

7.3.3.3.2 Supporting Observations

The hypothesis of a soluble polymer fraction leaching from the MIP was supported by observations made during HPLC analysis (Section 7.3.1.1.). It was noted that after the evaporative step of the sample preparation procedure (section 7.3.1.1.) prior to HPLC analysis, a transparent, glassy, crystalline frosting was deposited on the inside of the HPLC sample vial. This residue, present in the incubation filtrate, was initially assumed to be crystalline propranolol. However, the visible quantity of the deposit appeared greatest for the highest polymer loading (4mg / 2ml) where the quantity of propranolol remaining unbound

was, as would be expected, at its lowest. Upon reconstitution of the chloroform-evaporated sample with mobile phase (55% 20 mM ammonium acetate buffer, pH 3.5, 45% acetonitrile) and subsequent ultrasonication, the deposited layer appeared, in some instances, to be only partially soluble. Analysis of the HPLC peak data acquired at λ = 254 nm, particularly towards the end of long runs of consecutive samples, showed broad, erroneous peaks, in the chromatogram. These peaks occurred at inconsistent retention times, indicative of artifactual sample components residing on the column for periods greater than the analysis run time. The HPLC column was new prior to the analysis so as such the peaks were unlikely to be a remnant from prior experimental studies. The unexpected chromatographic elution was undetectable at 290 nm, the peak absorbance wavelength of propranolol, and as such did not interfere with analysis. Absorbance at λ = 254 nm is indicative of aromatic conjugation. This qualitative evidence and observation is supportive of the theory proposed in section 3.3.3.1, of small, chloroform soluble, polymer networks leaching from the solid MIP microspheres upon incubation.

7.3.3.3.3 Confirmation of the Leaching of a Soluble Polymer Fraction and Characterisation of the Binding Effect

Having established analyte binding to a leached soluble fraction as a viable hypothesis for the divergence in the experimentally measured binding isotherms, further experimentation was required to prove the theory. It could be anticipated that a similar soluble polymer fraction should leach from the non-imprinted polymer microspheres, and as such a comparative experiment with NIP could further support the theory. Additionally, results from such a study may suggest whether the proposed binding of propranolol to the leached soluble MIP fraction was binding to specific binding sites, akin to the traditional, insoluble MIP particles, or binding non-specifically to the functionality of the sol-polymer network. Such conclusions could impart valuable information on the formation of binding sites during the imprinting process, relevant to not only precipitation polymerisation but also to traditional monolith preparative methods and alternative methodologies. The introduction of template recognition properties into relatively low molecular weight, soluble, polymer networks could have a significant impact on

future approaches to molecular imprinting. Whilst the presence within imprinted polymer particulates of a leaching polymeric fraction may have significant implications on the application and commercialisation of currently studied imprinted materials.

7.3.3.3.3.1 Experimental Design Considerations

It was deemed that characterisation of the NIP isotherm over a range of polymer loadings with a view to observing a similar effect would be difficult and most probably inconclusive. The shallow gradient of the NIP isotherm with the low quantity of binding measured to the NIP at low free propranolol concentrations would make any overestimation in measured free propranolol difficult to confidently identify. This would be especially true if binding to any leached non-imprinted polymer fraction were also low. The high binding at low free concentrations associated with the MIP meant that the initial steep gradient of the binding isotherm made the effect easily observable as can be seen from Figure 3. The inherent difficultly of quantifying binding to a soluble moiety meant that even if the soluble MIP and NIP fraction could be separated from the insoluble material and collected, traditional binding analysis techniques relying on separation of bound and free could not be applied. However, the segmented flow application of MIP microspheres suspended in the organic phase introduced in chapter 3 and 4, would allow analysis of propranolol binding through analysis of depletion enhancement of propranolol from an aqueous sample phase.

7.3.3.3.3.2 Segmented Flow Analysis

7.3.3.3.3.2.1 Recovery of Soluble Polymer Fraction

Insufficient MIP remained on completion of the isothermal binding experiments to conduct many more binding experiments or to incubate the remaining polymer and harvest a reasonable quantity of soluble polymer leachate. As a result more imprinted polymer microspheres were prepared in accordance with the methodology detailed in chapter 2. All quantities were scaled to three times the quantity previously employed. After polymerisation, the polymer was washed in situ, initially with 2 x 150 ml aliquots of acetonitrile/toluene (82.5% / 17.5%), equivalent to that of the polymerisation solvent environment. The acetonitrile/toluene

ratio was adjusted to 50:50 for a further 2 x 150 ml aliquot washings. It was anticipated that the increased toluene content would offset the temperature drop from 60 °C to ~25 °C, providing near-theta conditions for the polymer, closer to those of the polymerisation environment. Further washing with 2 x 150 ml aliquot of 50:50 acetonitrile/toluene with 25 % acetic acid for template removal were conducted before preparing a slurry of approximately ¾ of the polymer yield (equivalent to a bed volume of 12 ml) in chloroform (providing a total volume of 21 ml). It was noted that despite the low volume, the polymer microspheres suspended readily in the chloroform, far more so than the higher volume toluene/acetonitrile (50:50) washings. A 22 cm long x 1.0 cm I.D. column with 2 μm frit was packed using an HPLC column packer (Jones Chromatography, Hengoed, UK). The column was packed at a pressure of 4000 psi using chloroform as packing solvent providing a flow of ~ 2 ml min^{-1} through the column. Initially, the eluate was observed to contain some polymer as the eluted chloroform was slightly opaque, probably as a result of elution of sub 2 μm spheres, or inconsistencies in the frit specification which rapidly became occluded by sufficiently large microspheres. Following 10 ml elution volume, the eluate became completely clear at which point 50 ml fractions were collected sequentially. Fractions 2-4 were evaporated to dryness by rotary evaporation. A small quantity of a glass-like material remained coated on the inside of the round bottom flask. The flask was sealed and stored at -20 °C. This procedure was repeated in the preparation and recovery of a non-imprinted polymer leaching fraction.

7.3.3.3.3.2.2 Segmented Flow Analysis

The collected polymer leachate fraction for both MIP and NIP was re-dissolved in a minimum amount of chloroform to create a concentrated solution of the soluble polymer fraction. The partitioning of propranolol from an aqueous sample into this immiscible polymer-containing chloroform phase was assessed utilising segmented flow extraction (chapter 3 and 4). It was proposed that any increase in partitioning of propranolol from the aqueous phase into the organic phase, compared to the equivalent extraction with chloroform alone, could be attributed to binding to the soluble polymer fraction.

7.3.3.3.3.2.2.1 Methodology

The leachate from both the MIP and NIP were dissolved in 4 ml of chloroform. The polymeric residue was observed to dissolve readily. 2 ml of the MIP and NIP polymer leachate containing solution were utilised to generate a segmented flow regime with an aqueous phase of pH 5.5 acetate buffer (10 mM) containing 50 µM propranolol HCl, using a tefzal T-piece eluting into a 25 cm length of 0.5 mm I.D. FEP tubing (Chapter 3). A 1:1 ratio of organic to aqueous flow was employed and the depletion of propranolol from the aqueous phase was measured following collection of 1 ml of combined eluate at total flow rates of 1, 0.2 and 0.06 ml min^{-1}. Two 200 µl aliquots of aqueous eluate were immediately removed and the propranolol content determined by fluorescent microplate spectroscopy. The comparative enhancement of partitioning of propranolol from the aqueous phase was compared for both MIP and NIP to that measured due to chloroform alone.

7.3.3.3.3.2.2.2 Results and Discussion

The addition of the recovered soluble MIP fraction to the extracting chloroform phase was found to significantly enhance the partitioning of propranolol from the aqueous phase into the leachate-containing organic phase. As observed with the insoluble polymer microspheres (Chapter 4), the addition of the equivalent NIP phase to the extracting chloroform was seen to exert little effect on the partitioning of propranolol from the aqueous sample, with the extent of extraction similar to that seen with chloroform alone. The significant enhancement in removal of propranolol by the addition of the soluble MIP fraction, in comparison to that measured in the presence of a soluble NIP fraction, is suggestive of a template recognition effect. Figure 6 illustrates graphically the distribution of propranolol species between the extracting phase and the sample aqueous phase after the segmented flow extraction.
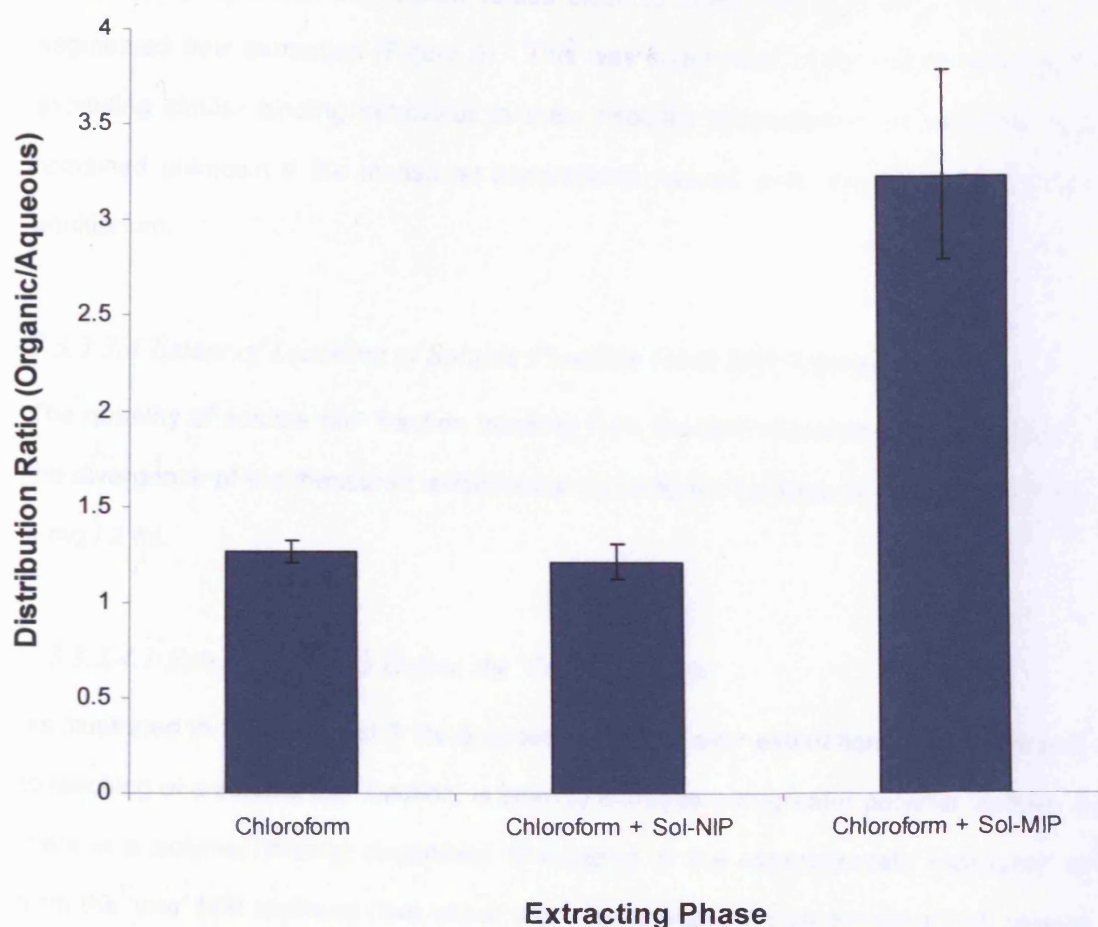
Figure 6 Segmented flow extraction of propranolol from an aqueous sample (10mM acetate buffer pH 5.5 acetate buffer containing 50 μM propranolol HCl) into an equal volume of chloroform, either alone or containing soluble MIP or NIP fraction. Segmented flow rate 0.06 ml min^{-1}, over a path length of 25 cm in 0.5 mm diameter FEP tubing. (n=2 ±S.D.)

Following extraction, the remaining MIP and NIP sol-fraction solutions were evaporated to dryness and the residue weighed in order to approximate the sol-fraction loading of the extraction experiments. It was approximated that both the MIP and NIP chloroform solutions contained 3 mg ml^{-1} of soluble polymer material. An adapted version of the MIP predictive binding model (Chapter 6) was developed, designed to consider the three way partitioning of propranolol between two immiscible liquid phases and incubated MIP residing in one liquid phases only. This two phase predictive model is detailed in Appendix 3. Application of this two phase equilibrium binding and partition model with the measured binding isothermal behaviour of the insoluble MIP and NIP microspheres in water saturated chloroform, suggested

equilibrium propranolol distribution values close to those measured experimentally following segmented flow extraction (Figure 6). This was suggestive of the soluble polymer fractions exhibiting similar binding behaviour to their insoluble microsphere counterparts. However it remained unknown if the measured experimental values were representative of distribution equilibrium.

7.3.3.3.4 Extent of Leaching of Soluble Fraction From MIP Microspheres

The quantity of soluble MIP fraction leaching from the MIP microspheres was estimated from the divergence of the measured isotherms at the polymer loadings of 1 mg / 4 ml, 3 mg / 3 ml, 4 mg / 2 ml.

7.3.3.3.4.1 Extrapolation to Define the 'True Isotherm'

As illustrated in Figure 2 and 3 the proposed effect of over-estimation of free propranolol due to leaching of a soluble MIP fraction, is seen to increase with greater polymer loading. As such there is a polymer loading dependent divergence of the experimentally measured isotherm from the 'true' MIP isotherm (that which would be expected to be obtained if all polymer were separable from the incubating solvent). It was anticipated that the leaching of the soluble polymer fraction from the MIP microspheres would observe linear binding behaviour, with the soluble polymer expected to exhibit a non-specific affinity to both the polymer and chloroform phases. This relationship was scrutinised by investigating the variation in bound over a range of values of free propranolol for the equations fitted to binding isotherms of each of the three polymer loadings investigated. For each of four sub-saturation free equilibrium concentrations, the corresponding equilibrium bound value, defined by the fitted isothermal equations, was calculated for each of the three investigated polymer loadings. The results are illustrated graphically in Figure 7. The decrease in propranolol bound (nmol/mg) with increased polymer loading appears to follow a linear relationship.

Free concentration: 12.5 µM   Free concentration: 25 µM

Free concentration: 50 µM   Free concentration: 100 µM
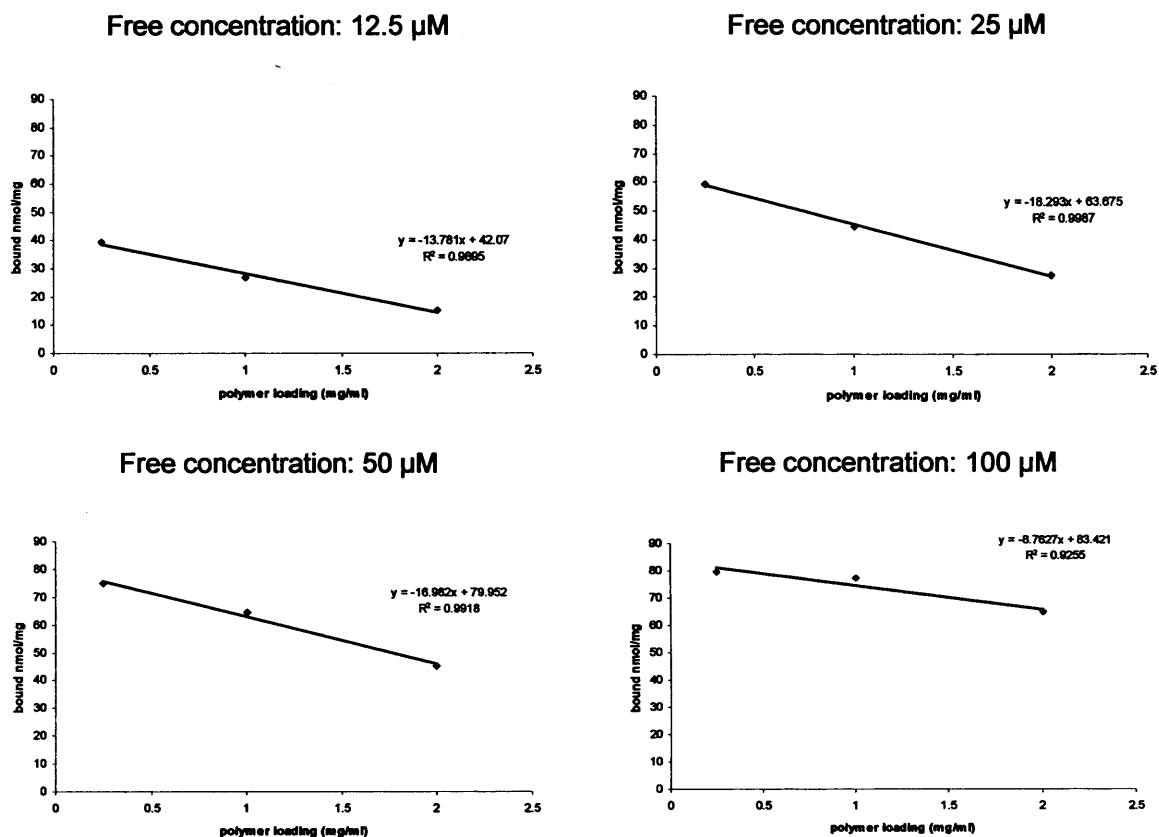
Figure 7 Calculated equilibrium bound values, as defined by the fitted isothermal equations, for each of the three investigated polymer loadings, at four sub-saturation free equilibrium concentrations (12.5, 25, 50 and 100 µM). Although the data set is limited to three polymer loadings, a linear relationship appears to exist, with each of the fitted isotherms describing a linearly decreasing bound equilibrium value with increasing polymer loading, for each of the four theoretical free equilibrium concentrations.

Although the data set is limited to three points, a linear relationship appears to exist between polymer loading and the *expected* measure of the 'bound' value for the defined 'free' equilibrium concentration. This is suggestive of a linear link between over-estimation in measured 'free' propranolol concentration and polymer loading, a result of polymer-loading dependent leaching of the competing soluble fraction. As polymer loading approaches zero (pl → 0) the over-estimation in measured 'free' propranolol, due to polymer leaching, also approaches zero, and the isotherm approaches that of the 'true' binding isotherm, as if no leaching were occurring.

To estimate this 'true' binding isotherm the linear relationship between the *expected* measure of the 'bound' value and polymer loading (Figure 7) was extrapolated to theoretically estimate

the anticipated bound result at an infinitely small polymer loading, i.e. where polymer loading approximates to 0 mg ml^{-1}. This is equivalent to the y-axis intercept of the plots of Figure 7. This process was repeated and a 'true' binding value extrapolated over a range of free concentration values. This established approximations for data points of the 'true' binding isotherm over a range of free equilibrium propranolol concentrations. An equation was fitted to this data using the techniques described previously (Section 3.3.1.1.1). The results are illustrated in full in Table 8 and the extrapolated 'true' isotherm depicted graphically in Figure 8.

Table 8 Equilibrium bound and free concentration data pairs calculated from each of the three experimentally derived isothermal equations (polymer loadings of 0.25, 1 and 2 mg ml⁻¹). For each of the free equilibrium concentration values listed the corresponding bound value for each of the three polymer loadings was plotted, as per the illustrated examples in figure 7. The y-axis intercept was extrapolated for each plot. This value represents the anticipated measured equilibrium bound concentration for an infinitely small incubated polymer loading (i.e. pl $\rightarrow$ 0). These values are listed at the bottom of this table, together with the corresponding fitting parameters describing this 'true' binding isotherm, equivalent to the expected MIP binding behaviour if leaching of a soluble MIP fraction were not occurring.

equation form:

$$bound = a(1 - e^{(-b \times C_{eq})})$$

free equilibrium concentration value (µM) (C_{eq}) and corresponding polymer bound concentration (nmol mg⁻¹)

polymer loading	a	b	3.125	6.25	12.5	25	37.5	50	100	150	200	250	300
0.25	80.15	0.0542	12.48799	23.03025	39.44301	59.47552	69.64974	74.81707	79.79516	80.12639	80.14843	80.1499	80.14999
1	80.25	0.0326	7.772819	14.79278	26.85876	44.72819	56.61694	64.52665	77.16933	79.64641	80.13174	80.22683	80.24546
2	79.54	0.01687	4.084635	7.959511	15.12252	27.36987	37.2887	45.32172	64.81922	73.20709	76.81557	78.36794	79.03578

Extrapolated 'true' polymer bound concentrations (nmol mg⁻¹), expected if no polymer leaching were occurring

polymer loading	a	b	3.125	6.25	12.5	25	37.5	50	100	150	200	250	300
pl$\rightarrow$0	82.1[a]	0.05946[a]	13.252	24.486	42.07	63.675	74.6	79.952	83.421	82.089	81.17	80.734	80.534

[a] Fitting parameters for 'true' binding isotherm derived by non-linear regression of the extrapolated equilibrium data points for the theoretical infinitely small polymer loading (see section 3.3.3.4.1)
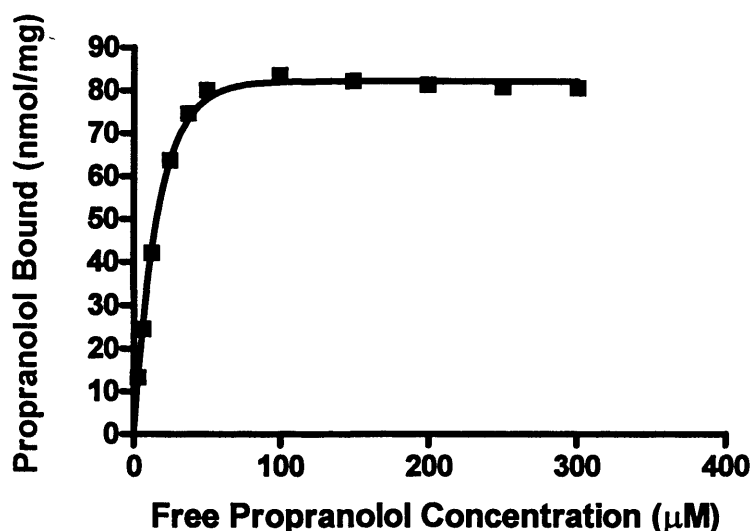
Figure 8 Extrapolated 'true' binding isotherm for the tested MIP, equivalent to what would be expected to be measured if no soluble polymer fraction leaching were occurring.

It was noted that as the theoretical free equilibrium concentration was increased, the linear relationship between polymer loading and the expected measured bound (Figure 7) exhibited a reduction in gradient. It is possible that this may be indicative of the soluble MIP fraction possessing slightly different binding behaviour to the insoluble counterpart. Additionally, this observation may also be a result of the decreased precision of experimental measurements as the MIP approaches saturation (chapter 6), reducing the accuracy of the equation describing the isothermal shape at conditions of saturation.

7.3.3.3.4.2 Estimated Extent of Leaching of Soluble Polymer Fraction

The mathematical model constructed in chapter 6 was applied over a range of theoretical incubation concentrations to all three experimentally obtained isothermal equations in addition to the idealised equation representative of no polymer leaching (Figure 8). The over-estimation in free propranolol was estimated for each polymer loading at each theoretical incubation concentration. This was calculated as the difference in equilibrium free concentration between the idealised, 'true' isotherm and the fitted isotherm at the given polymer loading. A theoretical incubation volume of 1ml and polymer mass of 1 mg were applied to the model. The principle is demonstrated graphically in Figure 9 for incubation in a

309

50 µM concentration propranolol solution. The increase in the expected measured free propranolol concentration for each of the isotherms describing increased polymer loading is easily observed.
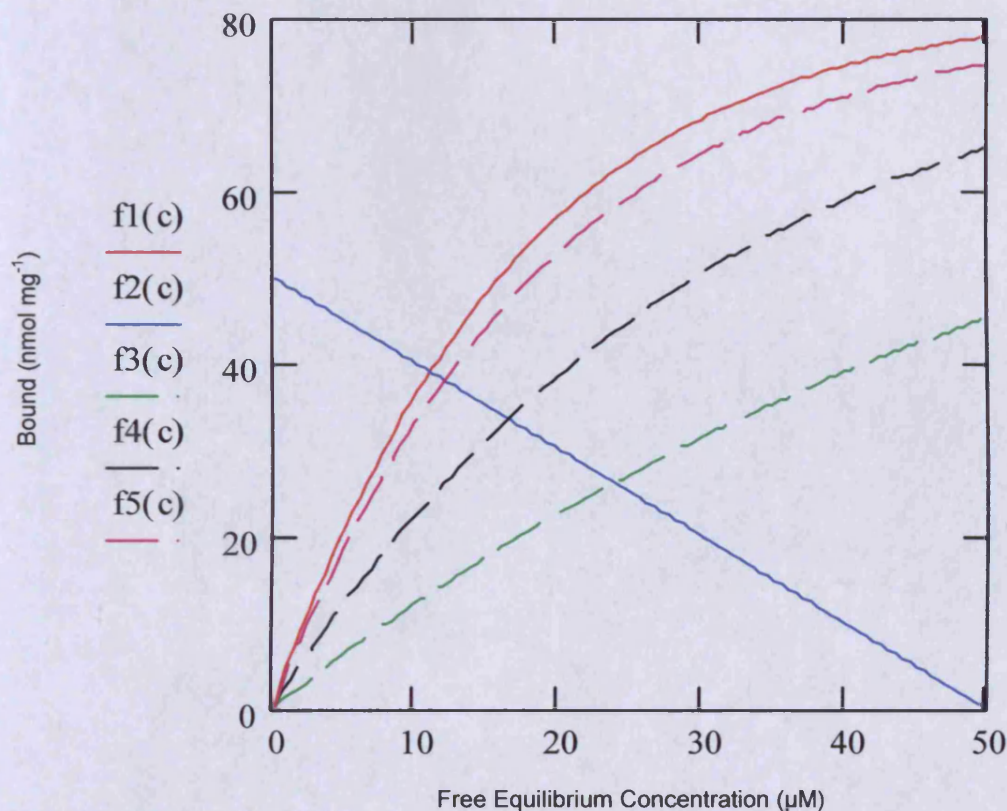
Figure 9 Application of the MIP predictive binding model developed in the work of chapter 6 to each of the three experimentally measured binding isotherms, and the extrapolated 'true' isotherm representing *actual* MIP binding, free from underestimation due to the leaching of the soluble MIP fraction. Modelled incubation conditions of 1 mg of polymer incubated in 1 ml of chloroform at an initial incubation concentration of 50 µM. The blue plot (f2(c)) represents the conservation of propranolol in the incubation system, with every point on the line representing a sum total of 50 nmol of propranolol distributed between being in solution (free x-axis (µM)) or bound to the polymer (bound y-axis (nmol mg^{-1}). The intersection of this line with each of the four isothermal curves, represents the theoretical equilibrium situation for the specified incubation conditions, for a binding material possessing the binding behaviour described by each of the four isothermal equations. (f1(c) (red) = 'true' binding isotherm, f5(c) (pink dashed) = MIP isotherm measured at a polymer loading of 0.25 mg ml^{-1}, f4(c) (black dashed) = MIP isotherm measured at a polymer loading of 1 mg ml^{-1}, f3(c) (green dashed) = MIP isotherm measured at a polymer loading of 2 mg ml^{-1}). None of the measured isotherms (dashed lines) accurately describe the binding behaviour of the MIP, this is result of a leaching soluble fraction, causing the measurement of additional propranolol in the incubating solvent which is wrongly assumed to be unbound. The effect of increased polymer leachate with increased polymer loading, resulting in a increased experimental measurement of assumed free propranolol and consequently an underestimate in amount bound, can be clearly seen from the intersection of each of the experimentally acquired binding isotherms (dashed lines) with that of the plot describing propranolol conservation within the system (f2(c) blue). Consequently, with knowledge of the 'true' MIP equilibrium binding behaviour (f1(c) (red)), the extent of overestimation of free propranolol can be deduced and an estimation of the extent of leaching of soluble MIP fraction can be made.

As an approximation, it was assumed that the binding of propranolol to the soluble MIP fraction demonstrated comparable binding to that of the insoluble microsphere counterparts. This approximation was applied to calculate an apparent quantity of soluble MIP fraction leaching from the MIP in each of the three polymer loadings studied. Having defined the overestimation in measured free for each of the three polymer loadings (Table 9 and Figure 10) and defined a 'true' binding isotherm for the MIP (Table 8 and Figure 8) an approximation of leached soluble polymer could be calculated. Since binding to the soluble MIP fraction was assumed to follow the same behaviour as that of the insoluble microspheres, and thus the idealised, or 'true' binding isotherm modelling the behaviour of the MIP, if leaching were not occurring, could be assumed to describe the binding of propranolol to the soluble MIP fraction. For each the of the theoretical incubation concentrations an approximation of the overestimation of free propranolol for each polymer loading was calculated, using the technique illustrated in Figure 9, together with an estimated value for polymer bound propranolol at the truly free (bound to neither soluble or insoluble polymer) propranolol equilibrium concentration. These values were defined by the equilibrium solution to the idealised binding isotherm. As such an estimate of the mass of soluble polymer present in each situation could be calculated by simply dividing the observed overestimate in free propranolol (equivalent to propranolol bound to the soluble MIP fraction) by the anticipated bound concentration (nmol mg^{-1}) at the truly free equilibrium propranolol concentration, as described by the idealised binding isotherm. This, therefore, calculates an approximate mass of polymer leachate responsible for the overestimation in measured free, for each polymer loading at each of the theoretical incubation concentrations. The results and intermediate calculated values are detailed in Table 9 and figure 10.

Table 9 Estimated apparent mass of leached soluble MIP. Calculated by quantification of the overestimate in measured free propranolol at each of the three investigated polymer loadings through comparison with previously extrapolated 'true' binding isotherm over a range of modelled incubation conditions.

	$bound = a(1 - e^{(-bxC_{eq})})$		'true' MIP binding	Measured at 0.25 mg ml^{-1} polymer loading	Measured at 1 mg ml^{-1} polymer loading	Measured at 2 mg ml^{-1} polymer loading
incubation concentration (µM)	Fitting parameters	a	82.1	80.15	80.25	79.54
		b	0.05946	0.0542	0.0326	0.01687
	polymer loading (mg ml^{-1})		0	0.25	1	2
5	free (µM)		0.868	0.955	1.406	2.157
	bound (nmol mg^{-1})		4.132	4.045	3.595	2.843
	overestimate in free (µM)		0	0.087	0.538	1.289
	estimated apparent mass of soluble polymer (mg)			0.021055	0.130203	0.311955
10	free (µM)		1.775	1.952	2.859	4.36
	bound (nmol mg^{-1})		8.225	8.048	7.141	5.64
	overestimate in free (µM)		0	0.177	1.084	2.585
	estimated apparent mass of soluble polymer (mg)			0.02152	0.131793	0.314286
17.5	free (µM)		3.215	3.533	5.134	7.751
	bound (nmol mg^{-1})		14.285	13.967	12.366	9.749
	overestimate in free (µM)		0	0.318	1.919	4.536
	estimated apparent mass of soluble polymer (mg)			0.022261	0.134337	0.317536
25	free (µM)		4.76	5.227	7.531	11.25
	bound (nmol mg^{-1})		20.239	19.773	17.469	13.75
	overestimate in free (µM)		0	0.467	2.771	6.49
	estimated apparent mass of soluble polymer (mg)			0.023074	0.136914	0.320668
37.5	free (µM)		7.612	8.343	11.827	17.333
	bound (nmol mg^{-1})		29.888	29.156	25.674	20.167
	overestimate in free (µM)		0	0.731	4.215	9.721
	estimated apparent mass of soluble polymer (mg)			0.024458	0.141026	0.325248
50	free (µM)		10.883	11.901	16.545	23.746
	bound (nmol mg^{-1})		39.117	38.099	33.456	26.254
	overestimate in free (µM)		0	1.018	5.662	12.863
	estimated apparent mass of soluble polymer (mg)			0.026024	0.144745	0.328834
62.5	free (µM)		14.686	16.008	21.746	30.504
	bound (nmol mg^{-1})		47.814	46.492	40.754	31.996
	overestimate in free (µM)		0	1.322	7.06	15.818
	estimated apparent mass of soluble polymer (mg)			0.027649	0.147655	0.330824
75	free (µM)		19.167	20.804	27.496	37.623
	bound (nmol mg^{-1})		55.833	54.196	47.505	37.377
	overestimate in free (µM)		0	1.637	8.329	18.456
	estimated apparent mass of soluble polymer (mg)			0.02932	0.149177	0.330557
100	free (µM)		30.941	33.145	40.902	52.993
	bound (nmol mg^{-1})		69.058	66.855	59.098	47.007
	overestimate in free (µM)		0	2.204	9.961	22.052
	estimated apparent mass of soluble polymer (mg)			0.031915	0.144241	0.319326
150	free (µM)		69.239	71.512	76.399	88.371

	bound (nmol mg^{-1})	80.762	78.488	73.601	61.629
	overestimate in free (µM)	0	2.273	7.16	19.132
	estimated apparent mass of soluble polymer (mg)		0.028144	0.088656	0.236894
200	free (µM)	117.973	119.969	121.289	129.421
	bound (nmol mg^{-1})	82.026	80.03	78.11	70.579
	overestimate in free (µM)	0	1.996	3.316	11.448
	estimated apparent mass of soluble polymer (mg)		0.024334	0.040426	0.139566
250	free (µM)	167.904	169.858	170.064	174.639
	bound (nmol mg^{-1})	82.096	80.142	79.936	75.361
	overestimate in free (µM)	0	1.954	2.16	6.735
	estimated apparent mass of soluble polymer (mg)		0.023801	0.026311	0.082038
300	free (µM)	217.9	219.851	219.812	222.329
	bound (nmol mg^{-1})	82.1	80.149	80.188	77.671
	overestimate in free (µM)	0	1.951	1.912	4.429
	estimated apparent mass of soluble polymer (mg)		0.023764	0.023289	0.053946
400	free (µM)	317.9	319.85	319.752	320.815
	bound (nmol mg^{-1})	82.1	80.15	80.248	79.185
	overestimate in free (µM)	0	1.95	1.852	2.915
	estimated apparent mass of soluble polymer (mg)		0.023752	0.022558	0.035505
500	free (µM)	417.9	419.849	419.75	420.526
	bound (nmol mg^{-1})	82.1	80.15	80.25	79.474
	overestimate in free (µM)	0	1.949	1.85	2.626
	estimated apparent mass of soluble polymer (mg)		0.023739	0.022533	0.031985

313
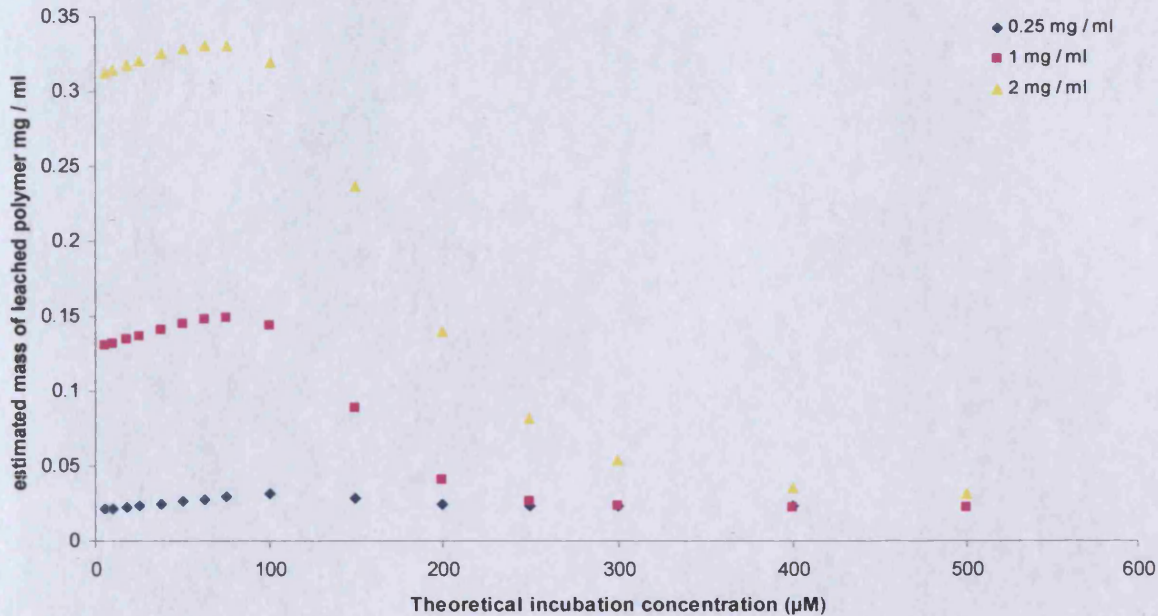
Figure 10 Estimated apparent mass of leached MIP fraction resulting in overestimation of measured free propranolol and hence leading to divergence of the measured MIP binding isotherms with increased polymer loading. Values calculated from the divergence of each of the three measured isotherms from that of the extrapolated 'true' binding isotherm, representative of no soluble MIP leaching. This raw data is illustrated in table 9. The estimated mass of leached polymer can be seen to increase with increased polymer loading, as anticipated.

At each polymer loading a horizontal line would be expected if binding to the soluble and insoluble MIP fractions demonstrated equivalent affinity, the assumption made to elucidate the mass of leached soluble polymer. The observed inflexion of the lines at higher theoretically probed incubation concentrations is not unreasonable since as the binding isotherms approach saturation they approach approximately the same maximum value. This is a result of the difficulty in accurately assessing binding at the high incubation concentrations necessary to probe binding at saturation conditions (as discussed in chapter 6). This is demonstrated in the increased spread of data at the saturated end of the isotherm compared to that measured at more useful lower concentrations (Figure 2). As such, confidence in the isothermal maximum is not sufficient to categorically elucidate a difference in binding as a result of the leaching of the soluble polymer fraction. Figure 2 illustrates that the incubation studies conducted at 500 µM, where binding to the MIP is saturated, follow the trend of the lowest experimental polymer loading possessing the highest mean calculated bound as a result of having the lowest overestimation of free due to leached soluble MIP. However the spread of

314

the replicate data is insufficient for this to be a statistically significant observation. The equation fitting methods used (Section 3.3.1.1.1.) fit more accurately to data points with low variance than those with higher variance, and therefore the fitted equations describe with more confidence the behaviour of the MIP in sub-saturation conditions where experimental methodology enables more precise characterisation of the binding behaviour. This is illustrated numerically in Table 10, which shows the 95% confidence intervals for the values of fitting parameters a (maximum) and b (indicative of apparent affinity) of the isotherms fitted to the experimental data at each of the three investigated polymer loadings. An overlap in confidence intervals of the isotherm maxima can be seen whilst the value for b is distinctly different in each case. Additionally, as illustrated in Figure 8, the 'true' MIP binding isotherm appears very close to saturation at free equilibrium concentrations of around 100 μM, thus, combined with the uncertainty of the isotherm accuracy within the saturable range (Table 10), the theoretically calculated difference in anticipated equilibrium conditions become unreliable.

Table 10 95% confidence interval data for the values of fitting parameters a (maximum) and b (indicative of apparent affinity) for the equations describing the isothermal binding behaviour of each of the three investigated polymer loadings.

polymer mass (mg)	Volume (ml)	polymer loading (mg ml^{-1})	a 95% confidence intervals	b 95% confidence intervals
1	4	a: 0.25	76.61 - 83.68	0.04534 - 0.06307
3	3	b: 1	76.88 - 83.61	0.02831 - 0.03688
4	2	c: 2	73.99 - 85.10	0.01394 - 0.01980

Consideration of the initial portion of the plot of estimated leached soluble polymer fraction (Figure 10), reveals a linear relationship with a near-zero gradient at each polymer loading investigated. (Figure 11).
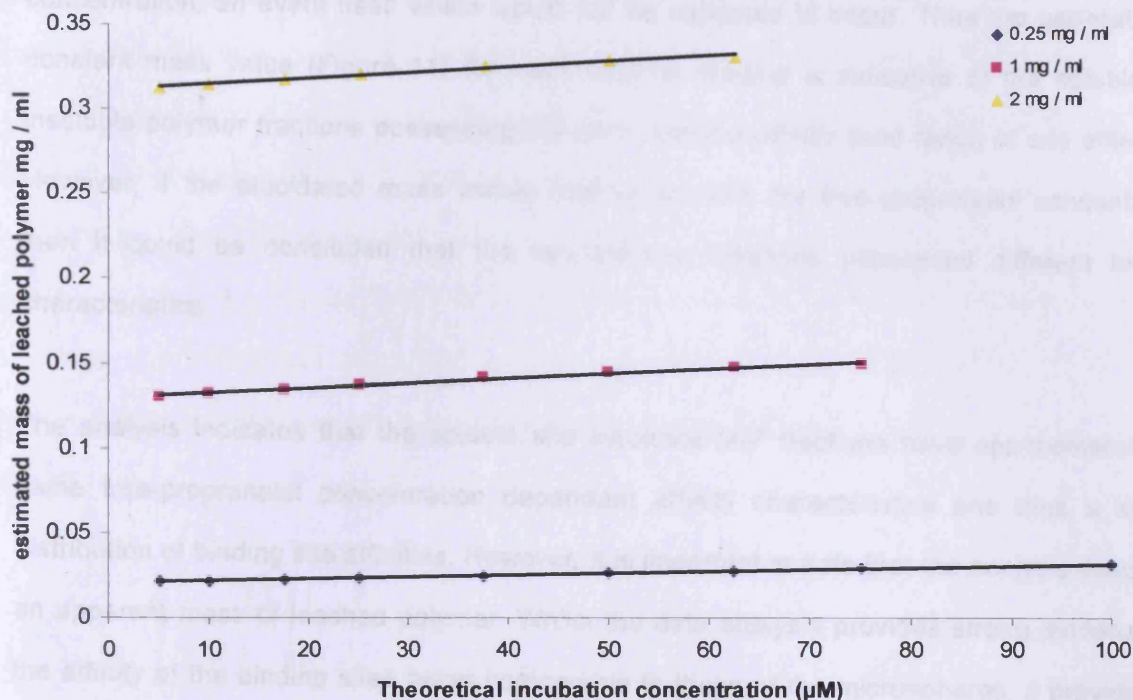
Figure 11 Estimated apparent mass of leached MIP fraction at each of the three investigated polymer loadings. As soluble polymer leaching can be expected to be independent of propranolol concentration, the linear, near zero gradient elucidated for incubation concentrations in the subsaturation region of the isotherm, suggests, as expected, the leaching of a constant mass of soluble polymer at each of the polymer loadings, independent of propranolol incubation concentration. It can therefore be concluded that the soluble, leaching MIP fraction (sol-MIP) possesses similar binding properties to its insoluble counterpart.

The mass of soluble polymer leaching from the solid MIP microspheres would be expected to be dependant upon polymer mass and incubation volume only, and therefore would be expected remain constant regardless of free propranolol concentration. Estimation of the mass of leached soluble fraction was calculated by applying the assumption that the soluble MIP fraction observed the same binding relationship as the insoluble counterpart. This assumption resulted in near constant estimate of leached polymer mass at each polymer loading over the sub-saturation portion of the binding isotherms. This, therefore, is suggestive of the soluble MIP fraction possessing similar affinity for propranolol to that of the insoluble microspheres (as assumed in order to conduct the analysis). Since the soluble and insoluble polymer fractions are essentially competing to bind the propranolol in the incubation solution, if the affinity of the two fractions is not comparable, the analysis employed to estimate the mass of leached polymer would result in a variation in estimated mass leached with changing free propranolol

316

concentration, an event itself which would not be expected to occur. Thus the generation of constant mass value (Figure 11) for each polymer loading is indicative of the soluble and insoluble polymer fractions possessing the same binding affinity (and range of site affinities). However, if the elucidated mass values had varied with the free propranolol concentration then it could be concluded that the two polymer fractions possessed different binding characteristics.

The analysis indicates that the soluble and insoluble MIP fractions have approximately the same free-propranolol concentration dependant affinity characteristics and thus a similar distribution of binding site affinities. However, it is important to note that the analysis describes an apparent mass of leached polymer. Whilst the data analysis provides strong evidence for the affinity of the binding sites being comparable to those of the microspheres, it provides no information on binding site density within the polymer matrix. The calculated mass of the polymer leachate is therefore an apparent mass since it assumes that the density of binding sites in both the soluble and insoluble fractions is the same. The findings of this work demonstrate that binding site formation occurs early during the polymerisation process, whilst the polymer network remains in solution. As such it may be expected that the density of binding sites within the polymer network to be the same on both the soluble MIP fraction and the precipitated polymer microspheres. However, it may also be possible that a significant proportion of binding sites within the core of the precipitated polymer microsphere become occluded during the polymer growth stage of the precipitated polymer and thus are subsequently inactive during rebinding analysis. Such an occurrence would result in a higher binding site density on the soluble MIP fraction than the precipitated microspheres and therefore the mathematical analysis conducted here would result in a overestimate of the physical mass of the soluble MIP fraction. As such the calculated mass of soluble MIP leachate is an apparent mass comparable to that of the insoluble microspheres with an equivalent binding site density.

Despite this uncertainty in actual mass of soluble polymer fraction leached from the MIP microspheres the ratio of leached polymer between each polymer loading investigated will remain constant even if the binding site density on the soluble MIP fraction differs from that on the insoluble counterpart. The apparent mass value can be applied to investigate the relationship of leaching of soluble polymer fraction with polymer loading in the incubating chloroform. The linear portion of the estimated leached polymer mass graph (Figure 11) was considered and the mean calculated estimate for leached polymer at each of the three polymer loadings plotted against the incubation phase ratio (Figure 12).

$$y = 0.1692x - 0.0212$$
$$R^2 = 0.9974$$
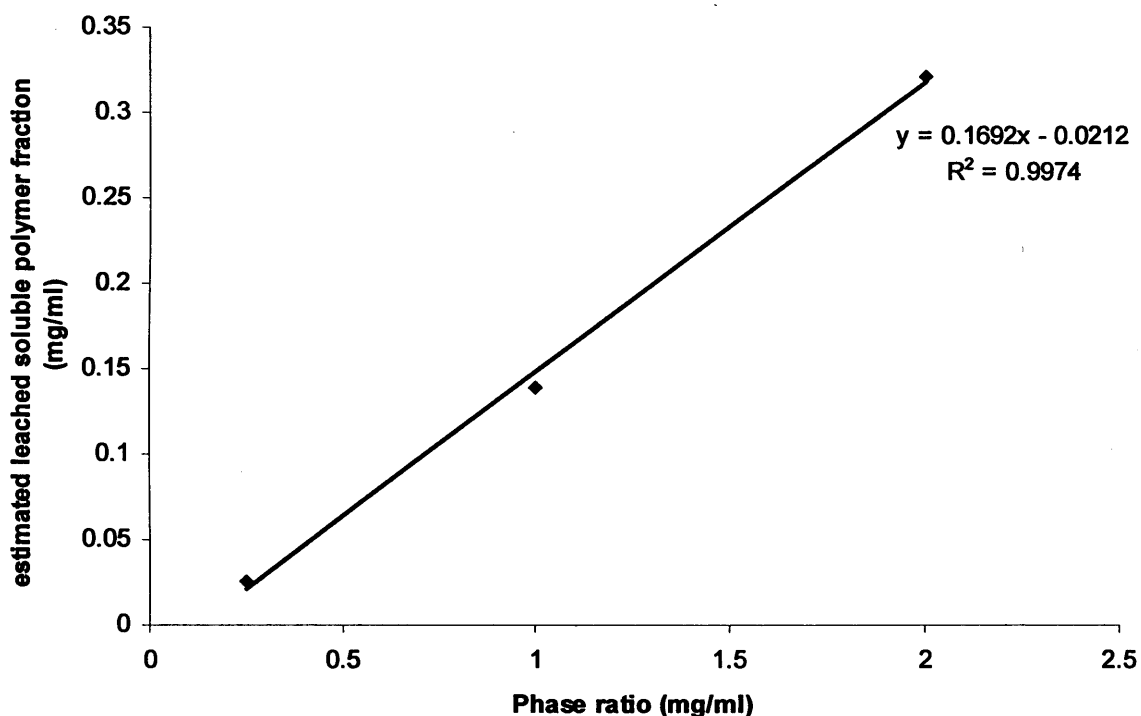
Figure 12 Apparent concentration (mg ml^{-1}) of leached polymer fraction with increased MIP microsphere loading (phase ratio (mg ml^{-1})).

A linear relationship is observed with a near (0,0) intercept. A relationship of this type would be anticipated as a result of non-specific interactions between the soluble polymer and the solid polymer matrix. Leaching of soluble polymer into the incubation media being proportional to the polymer loading, at least while the solubility of the soluble polymer fraction remains far from the limit of saturation in the incubating solvent. The elucidation of this relationship further

supports the proposed theory of a soluble MIP fraction leaching from the MIP microspheres, to cause the isothermal deviation with increased polymer loading.

7.4 Re-evaluation of the Mathematical Model: Consideration of the Proposed Sol-Fraction Effect

The effect of polymer leaching established in section 3.3.3.4.2 was programmed into the mathematical model described in chapter 6. The resultant model (Appendix 4) was applied to predict the anticipated 'measured' and 'true' binding behaviour of the MIP under the original experimental conditions investigated in defining the binding isotherm at three polymer loadings. A good correlation was observed between the measured and predicted results, this is perhaps unsurprising since the data being tested was that used to generate the leaching hypothesis and quantify its effects. As such the model was evaluated against the experimental data in section 7.2.1, which investigated the binding of propranolol to 1.5 mg of MIP over a range of incubation volumes. This data was entirely independent of the quantification of the effect of soluble MIP fraction leaching.

7.4.1 Incorporation of Sol-MIP leaching into the Mathematical Model

The relationship of leached soluble fraction to polymer loading as elucidated in section 7.3.3.3.4.2 was described by the equation;

$$sol - MIP(mg/ml) = 0.1692 \times Polymerloading - 0.0212 \qquad (3)$$

This relationship was programmed into the mathematical model to calculate the apparent mass of sol-MIP leached from the incubated polymer in each of the experimental incubation conditions (Table 1). This subsequently enabled the estimation of the amount of propranolol bound to the quantified, leached soluble fraction. This, therefore, enabled the prediction of the overestimate in free propranolol, which would theoretically be made in each experimental

319

analysis. Consequently, the experimentally measured value for free and bound propranolol respectively could now more accurately be predicted by the mathematical model. Additionally, an estimate of the 'truly' bound and unbound propranolol at each of modelled experimental conditions could be predicted (i.e. the total bound to both soluble and insoluble MIP fractions constituting that which is 'truly' bound, with that unbound to either fraction representing the 'truly' free).

7.4.2 Validation of the Mathematical Model and Proposed Sol-MIP Leaching Effect

The adapted model was evaluated against the experimental data of section 7.2.1. These experiments were conducted in water saturated chloroform and as such the binding isotherm measured in water saturated chloroform was applied to the model:

$$bound = 129.7(1 - e^{(-0.01278 x C_{eq})}) \tag{4}$$

The experimental conditions at which this isotherm was investigated were at a polymer mass of 1 mg and an incubation volume of 2 ml, resulting in a phase ratio of 0.5. This meant that the isotherm which equation 4 describes would be subject to some bias due to leaching of soluble MIP fraction at this phase ratio. This was considered in the modified model and calculations were based upon change in phase ratio (ΔPr) from this initial value. The mathcad model coding is detailed fully in appendix 4.

7.4.2.1 Results and Discussion

Figure 13 and 14 illustrate the measured free and corresponding bound values for each of the experimental incubations investigated (Table 1) compared to the predicted values obtained from the original theoretical model (Section 7.2.2), and the sol-MIP leaching adjusted model. The results are detailed fully in Table 11.

	0.13	0.30	0.39	0.53	0.86	2.18
☐ measured bound	29.86	26.80	27.62	21.91	22.61	16.80
■ original model - predicted bound	32.16	30.66	30.08	29.24	27.90	25.47
☐ sol-MIP leaching model - predicted bound	32.33	29.94	28.95	27.43	24.66	16.90
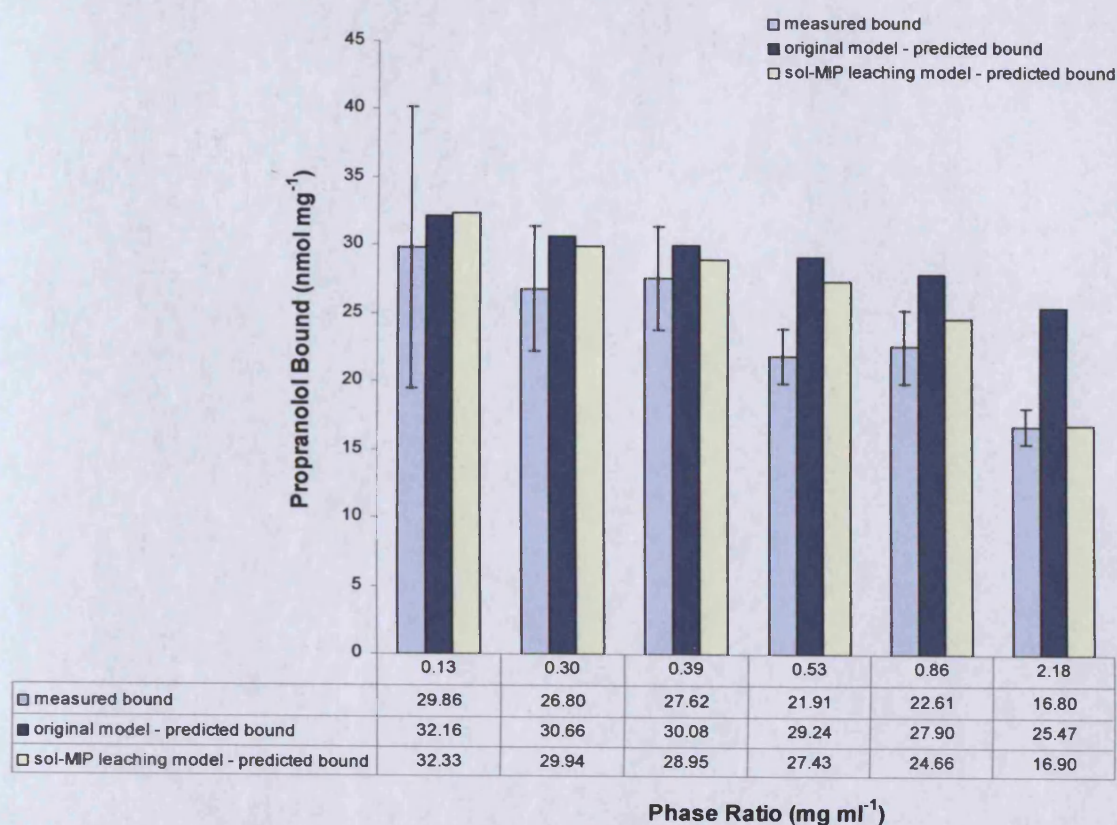
Phase Ratio (mg ml^{-1})

Figure 13 Experimentally elucidated bound propranolol (nmol mg $^{-1}$) at 6 experimental polymer loadings (phase ratio (mg ml^{-1})) compared to the theoretically predicted equilibrium value, calculated by the original MIP binding model (Chapter 6), and also that calculated by the sol-MIP leaching incorporated model. The predicted estimate from this model represents the anticipated measured bound value as a result of overestimation of measure free propranolol as a result of leaching of a soluble MIP fraction. (experimental data n=5 ±S.D.)

	0.13	0.30	0.39	0.53	0.86	2.18
▫ measured free	22.61	22.28	21.60	23.90	23.49	35.99
▪ original model - predicted free	22.30	21.10	20.65	19.99	18.95	17.11
▫ sol-MIP leaching model - predicted free	22.28	21.32	21.08	20.95	21.73	35.78
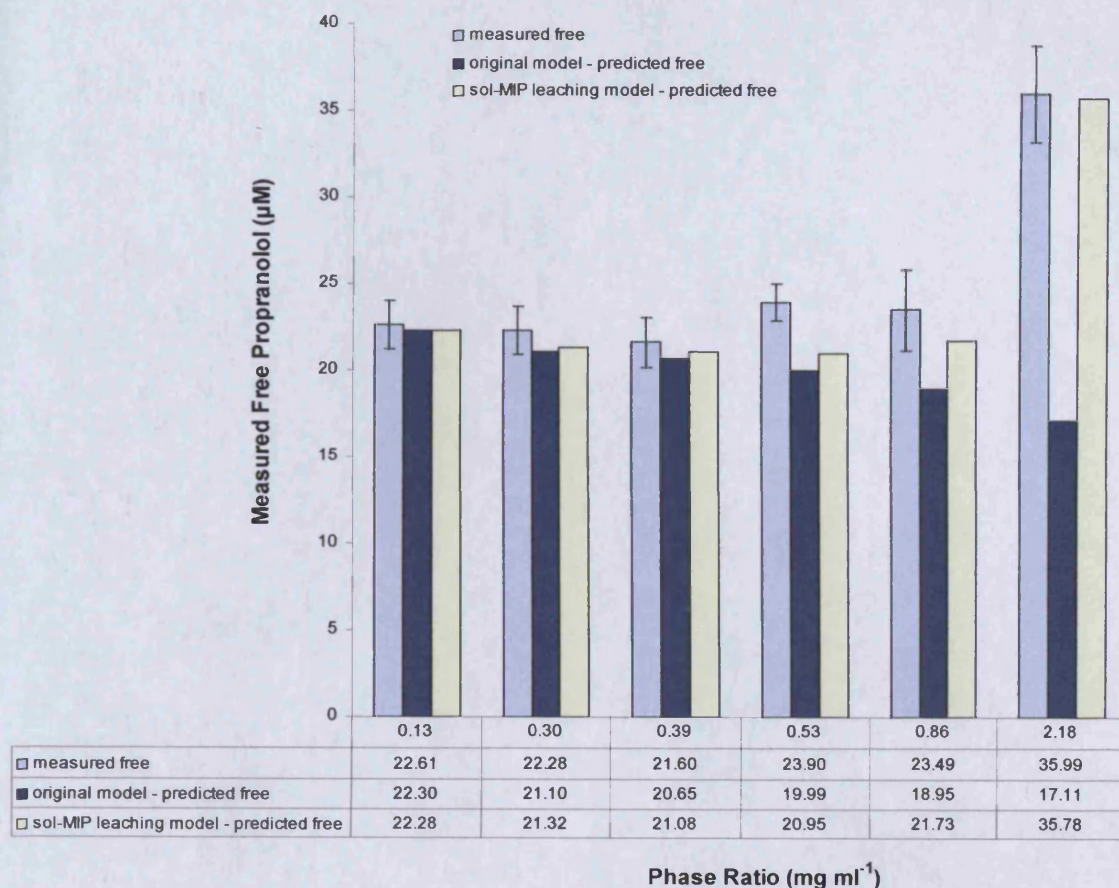
Phase Ratio (mg ml⁻¹)

Figure 14 Experimentally measured free propranolol concentration (μM) at 6 experimental polymer loadings (phase ratio (mg ml⁻¹)) compared to the theoretically predicted equilibrium value, calculated by the original MIP binding model (Chapter 6), and also that calculated by the sol-MIP leaching incorporated model. The predicted estimate from this model represents the anticipated measured free concentration, including the theorised over-estimation as a result of leaching of a soluble MIP fraction. (experimental data n=5 ±S.D.)

Table 11 Full comparative data of the predicted, and experimentally measured, bound and free data pairs for six different polymer incubation conditions of varying phase ratio. Consideration of the sol-MIP leaching effect can be seen to produce a more accurate estimate of expected experimentally measured binding equilibrium values, compared to that of the original theoretical model (Chapter 6).

	m_1	v	p_0	C_s	PI	Measured		Original model		Sol-MIP leaching model	
						Free	Bound	Free	Bound	Free	Bound
	polymer mass	volume	total propranolol	incubation concentration	Polymer loading	Measured equilibrium conc	Measured equilibrium conc	Predicted	Predicted	Predicted	Predicted
	(mg)	(ml)	(nmol)	(μM)	(mg ml^{-1})	(μM)	(nmol mg^{-1})	(μM)	(nmol mg^{-1})	(μM)	(nmol mg^{-1})
exp 1	1.5	11.29	300	26.57	0.13	22.61	29.86	22.3	32.16	22.28	32.33
exp 2	1.5	4.93	150	30.43	0.30	22.28	26.80	21.10	30.66	21.32	29.94
exp 3	1.5	3.87	125	32.31	0.39	21.60	27.62	20.65	30.08	21.08	28.95
exp 4	1.5	2.81	100	35.60	0.53	23.90	21.91	19.99	29.24	20.95	27.43
exp 5	1.5	1.75	75	42.88	0.86	23.49	22.61	18.95	27.90	21.73	24.66
exp 6	1.5	0.69	50	72.5	2.18	35.10	16.80	17.11	25.47	35.78	16.90

The sol-MIP leaching model described in section 7.4.1. predicts more accurately the measured experimental data than the original theoretical model, especially at the investigated high polymer loading (experiment 6) where leaching soluble fraction, and consequently the HPLC measured overestimate in free propranolol concentration, is highest. Expressing the data on a plot of bound against free (Figure 15) suggests that each experimentally measured data point lies on a separate isothermal line, as found to be the case with the full investigation into propranolol binding at the three distinct polymer loadings (Section 7.3). The original mathematical model, constituting the work of chapter 6, predicts the bound and free data pairs for each experimental condition to lie on a single isothermal curve (Figure 15 - open circles), as initially anticipated and theoretically justified [5] (Chapter 6). Incorporation of the soluble MIP fraction leaching theory into the predictive model results in the predicted bound and free data pairs closely following the experimentally measured trend. This manifested as a mass-related deviation from the anticipated isotherm due to the theorised overestimation in free propranolol as a result of binding to the leached polymer fraction. Consequently, a more accurate prediction of the experimentally measured result is achieved. (Figure 15 - filled squares (experimental data), red crosses (sol-MIP leaching considered predictions)).
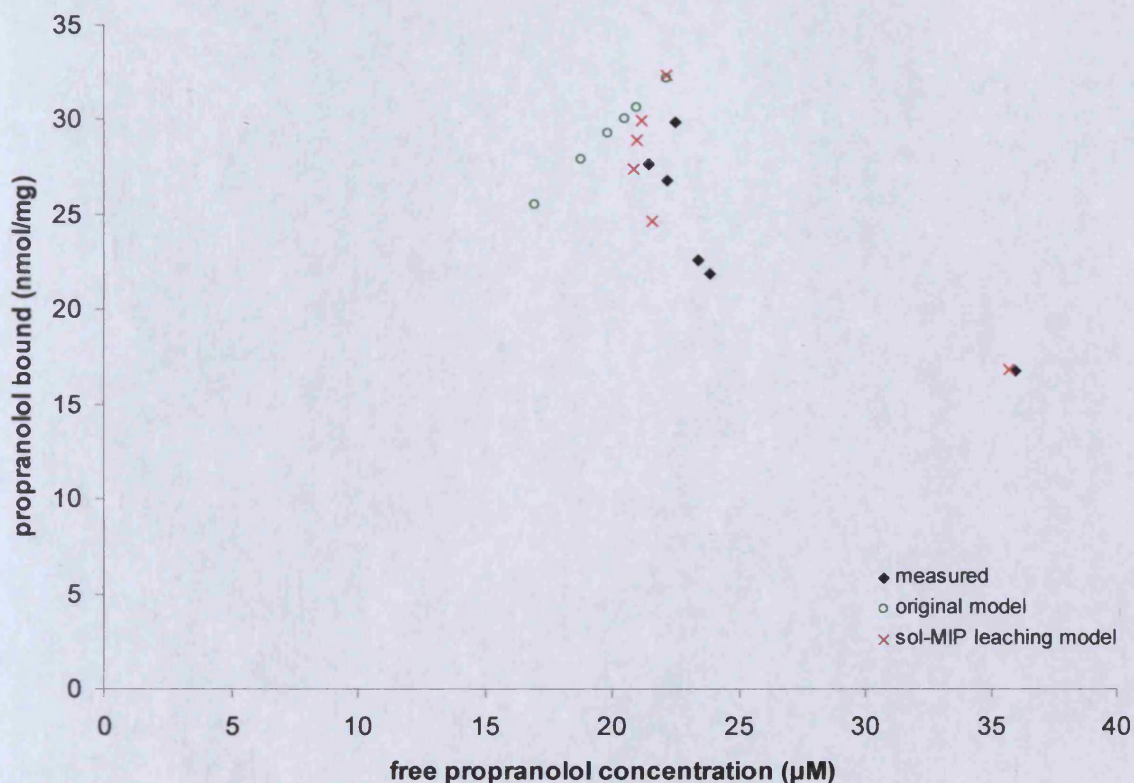
Figure 15 Comparative data of the predicted, and experimentally measured, bound and free data pairs for six different polymer incubation conditions of varying phase ratio. Consideration of the sol-MIP leaching effect can be seen to produce a more accurate estimate of experimentally measured binding equilibrium values, compared to that of the original theoretical model (Chapter 6). This improved correlation can be seen to mirror the observed experimental trend, with the equilibrium data failing to lie on a single isothermal curve, as would be anticipated.

Despite the model's close prediction of the curvature of experimentally measured data points, the sol-MIP leaching model's predicted bound values for each incubation condition are slightly higher than the measured experimental result in each instance. This may be as a result of slight differences in either polymer leaching, or propranolol binding to either polymer fraction, in the water saturated and non water saturated chloroform. Alternatively it may be the result of a temperature effect, with the isothermal equation investigations carried out in the winter months in a colder ambient environment than the particularly hot summer weather experienced when the validation experiments were carried out. An increased incubation temperature would be expected to reduce binding to the MIP [9] and may also affect leaching of the soluble fraction. Additionally, fitting the equation describing sol-MIP leaching with respect to polymer loading (Figure 12) with a 0,0 intercept would be likely to improve the

accuracy of the predicted values of the sol-MIP leaching model for low polymer loadings. Application of the sol-MIP leaching predictive model to this experimental data offers further supportive evidence to the previously elucidated relationships of the effect of polymer loading on experimentally measured binding data (Section 7.3.), further supporting the polymer leachate theory. It is important to note that the experimental data compared to the predictive models here was conducted independently to the investigation of the mathematical relationship of the sol-MIP leaching and the effect on measured binding data. Unfortunately due to the lack of sufficient remaining polymer it was not possible to conduct any further equilibrium binding experiments using polymer prepared from the same batch. As such, it was concluded that since the accuracy and precision required for further validation and investigation into the leaching phenomena was paramount, any inter-batch variation especially as a result of minor differences in washing protocols (vacuum pressure, polymer bed volume etc) could significantly affect the experimental findings. Therefore, without re-characterising the leaching behaviour of a second polymer batch (Section 7.3), which was not feasible within the time constraints of the project, further, more optimised, validation was not possible.

7.5 Conclusion

Although further experimentation is required, the work of this chapter suggests that in the production of MIP microspheres at near-theta conditions, a co-produced soluble MIP fraction is formed, possessing similar binding characteristics to its insoluble microsphere counterpart. The serendipitous discovery of this soluble fraction was found as a result of measured deviation in the binding isotherm of MIP microspheres with increased polymer loading. Were it not for the work of chapter 6 and the understanding gained as to the theoretical independence of the binding isotherm to the experimental phase ratio, such observations may not have been noted. In the context of MIP enhanced segmented flow extraction, the application of soluble polymer affinity species may afford increased kinetic advantages over simple size reduction of insoluble particulate MIP microspheres. The reduced fluid dynamic impact of soluble species compared to suspended particulates may be expected to maintain the inherent segmented

flow interfacial mass transfer mechanisms more closely to those characterised in liquid-liquid flow (Chapter 3).

7.6 References

[1] T. Pap and G. Horvai, "Binding assays with molecularly imprinted polymers--why do they work?," *Journal of Chromatography B*, vol. 804, May. 2004, pp. 167-172.

[2] A. Ellwanger et al., "Evaluation of methods aimed at complete removal of template from molecularly imprinted polymers ," *The Analyst*, vol. 126, 2001, pp. 784-792.

[3] E. Goh and H. Stöver, "Cross-Linked Poly(methacrylic acid-co-poly(ethylene oxide) methyl ether methacrylate) Microspheres and Microgels Prepared by Precipitation Polymerization: A Morphology Study," *Macromolecules*, vol. 35, Dec. 2002, pp. 9983-9989.

[4] Y. Chen et al., "Influence of Thermal Annealing on the Thermodynamic and Mass-Transfer Kinetic Properties of D- AND L-Phenylalanine Anilide on Imprinted Polymeric Stationary Phases," *Analytical Chemistry*, vol. 71, Mar. 1999, pp. 928-938.

[5] B. Toth et al., "Which molecularly imprinted polymer is better?," *Analytica Chimica Acta*, vol. 591, May. 2007, pp. 17-21.

[6] J. Wang et al., "Monodisperse, Molecularly Imprinted Polymer Microspheres Prepared by Precipitation Polymerization for Affinity Separation Applications13," *Angewandte Chemie International Edition*, vol. 42, 2003, pp. 5336-5338.

[7] W. Li and H.D.H. Stöver, "Porous monodisperse poly(divinylbenzene) microspheres by precipitation polymerization," *Journal of Polymer Science Part A: Polymer Chemistry*, vol. 36, 1998, pp. 1543-1551.

[8] O.K. Castell, C.J. Allender, and D.A. Barrow, "Novel biphasic separations utilising highly selective molecularly imprinted polymers as biorecognition solvent extraction agents," *Biosensors and Bioelectronics*, vol. 22, Oct. 2006, pp. 526-533.

[9] Y. Chen et al., "Influence of Thermal Annealing on the Thermodynamic and Mass-Transfer Kinetic Properties of D- and L-Phenylalanine Anilide on Imprinted Polymeric Stationary Phases," *Analytical Chemistry*, vol. 71, Mar. 1999, pp. 928-938.

[10] MIP Technologies, "The MIP Rule of Six," http://www.miptechnologies.com/technology.asp, accessed March 2008.

Chapter 8

General Discussion

8.1 General Discussion

It can be envisaged that solid phase enhanced micro liquid-extractions could be performed utilising many modes of adsorbents, both passive and catalytic, organic, inorganic, and biological moieties in a 'reverse' phase approach. This makes the technique readily applicable and transferable to many areas where chemical separation, enrichment or selective transport of analytes is desirable. Researchers wishing to study affinity based binding events can utilise the technique as a practical and efficient alternative to the macro-scale binding and dialysis studies traditionally employed. This may prove particularly promising for low molecular weight receptor species which are often difficult to manipulate and separate from the incubation media where commonly covalent immobilisation is employed. The technique's successful application is dependent upon careful consideration of the immiscible phases, ensuring the affinity phase resides entirely in one phase, whilst the analyte has a degree of solubility in both. In this particular example molecularly specific adsorbents (e.g. MIPs) (Chapter 4), rather than non-specific adsorbents such as functionalised silica, were used to bring about molecularly specific enhancement of extraction. This important feature of a species or class specific extraction creates opportunities for separation or extraction from otherwise difficult to separate components i.e. those which display similar solvent-solvent distribution ratios. pH adjustment of the aqueous phase can be utilised to restrict the migration of analyte or difficult to separate contaminant species, into the organic phase where, the presence of the MIP is exploited to massively enhance the removal of the desired compound. This results in the partitioning of further analyte and the process continues until dynamic three way equilibrium is established. In a well designed, optimised, system this will result in the majority of the analyte residing on the polymer. The development of an on-chip continuous flow liquid phase separator (Chapter 5) creates the opportunity for post-extraction manipulation of extracted species e.g. re-segmentation of flows or analysis with integrated detection technologies. Additionally it is expected that the segmented flow liquid phase separation will prove valuable in many multiphase flow applications, particularly in the field of flow chemistry.

The main limitation of the work reported here is the time requirement for binding to the MIP although it is predicted that this can be significantly improved by reduction in MIP particle size to sub-micron diameters, to reduce diffusional requirements. It is reasoned that it would be important to retain the porous open structure characteristic of MIPs prepared by precipitation polymerisation at near-θ conditions (Chapter 2), to retain the favourable analyte binding and diffusive qualities of these materials. As discussed in chapter 4, this may be more demanding that simply terminating the reaction early or employing a less solvating reaction media. The discovery of soluble imprinted affinity species formed during the polymerisation process in the preparation of MIP microspheres in Chapter 7, may provide an alternative route to improved binding kinetics compared to that achievable by particle size reduction.

With consideration of the polymerisation process by which the precipitated polymer microspheres form [1,2], it is perhaps unsurprising that a soluble fraction containing imprinted sites should form throughout the course of the polymerisation process (chapter 2). The proximity of the polymerisation system to theta conditions [3] determines the solubility limit of growing polymer chain in the polymerisation environment. It is likely that during this initial growth stage, template-monomer pre-polymerisation complexes cross-link to yield a low molecular weight molecularly imprinted material. Continued polymer growth occurs until the polymer network either grows excessively large, preventing it remaining in solution, or it becomes incorporated into a pre-existing precipitated microsphere (Chapter 2). This polymer growth mechanism is likely to have implications for alterative methods of MIP production. Application of the mathematical model for comparison of MIP binding performance suggests that MIPs prepared by precipitation polymerisation perform comparably to monolithically prepared materials (Chapter 6) (4). This is despite the dilution of templated species in polymerisation environment. This is likely to be, at least in part, a result of the necessity to consider the solubility of the growing polymer when designing the polymerisation system so as to achieve polymerisations at near-theta condition. With the exception of extremely solvating environments, where gels may form, polymerisations conducted with a high concentration of polymerisable moieties will form monolithic materials, due to the coalescence and coagulation

of individually forming precipitated polymer networks. Under such conditions a major contribution to porosity of the MIP are macro-porous structural cavities created in the regions between fused neighbouring microspheres. This process occurs regardless of the inherent micro-porosity, or structural density, of the growing polymer microspheres which will eventually coalesce. Consequently when designing a monolithic MIP system little consideration needs to be given to the precise composition of the polymerisation environment. However, it is possible that performance enhancement may be achieved thorough consideration of the theta point in monolithically prepared imprinted polymers.

The production of soluble imprinted polymer nanogels has been previously reported [5,6], through polymerisation at high dilutions conducted in very solvating media. The molecular recognition performance [5] and the catalytic activity [6] of the resultant materials were found to be relatively poor compared to traditionally prepared MIPs. With the authors concluding in later work that, in general, nanogels of this type appeared unsuitable for molecular imprinting applications [7]. The research group of Wulff explored several optimisation strategies [8] with the aim of achieving improved catalytic activity and reduced polydispersity of the soluble imprinted materials. With an ultimate objective of producing catalytically active particles containing, on average, one active cavity per particle (analogous with biological recognition systems and with comparable molecular weights [7]). This was achieved, demonstrating the promise of soluble imprinted materials, however the reported catalytic activity compared to control nanogels was relatively modest compared to some of the larger, more polydisperse soluble imprinted materials or monolithic preparations [7,8]. In the production and optimisation of these imprinted materials, the effect of theta was not directly considered. In order to produce soluble polymer particles the polymerisations were conducted with consideration of the critical monomer concentration and also solvent solubility parameters for reference polymer materials [8]. The influence of these parameters affects the structural morphology of resulting polymer networks [1]. The morphological structure dictated by polymerisation at near-theta conditions may afford improved imprinting performance due to the controlled balance achieved between solubility, porosity and structural rigidity. As such it is hypothesised

that if it were possible to harvest, or produce, the soluble MIP fraction present in polymerisations conducted at near-theta conditions, a soluble recognition material could be produced with comparable performance to MIPs prepared using established protocols. Excessive dilution of the polymerisation system may restrict oligomer coalescence, increasing the number of potential precipitation seeds and potentially restricting seed growth to sizes below the solubility limit. However, such an approach may be counter productive due to the corresponding dilution in template species, possibly reducing the number of imprinted sites. Early termination of polymerisation, whilst particle size remains small, may enable collection of soluble polymer, however due to the polymerisation kinetics [9] it would be anticipated that the yield would be low. A variation of this approach has been reported where early termination of a high monomer loading polymerisation (which would normally result in monolith formation) was used to harvest a soluble imprinted fraction [10]. The process utilised living polymerisation to afford greater uniformity in the growth rate of the developing polymer networks, however the polymer yield was low (3%).

The serendipitous discovery of the soluble affinity phase (Chapter 7) not only provided valuable insight into the processes occurring in the imprinting process, but may also have provided the basis for the development of techniques to produce and utilise soluble imprinted phases. Provided that solubility is limited to one of the two immiscible phases, segmented flow extraction provides an ideal platform for assessing the binding performance of soluble affinity phases. Employment of this methodology circumvents the difficulties associated with traditional MIP evaluation methodologies that are reliant upon filtration (Chapters 2 and 7). Additionally the binding kinetics for soluble MIP fractions will certainly be higher than for micron sized particles, where analyte diffusion to the particle core is required in order for all available binding sites to be filled. This reduced equilibration time is evident in the high degree of extraction enhancement observed in the segmented flow extraction over a path length of just 25 cm (Chapter 7), compared to the requirement for lengths of ~ 5m when used with the MIP microsphere (Chapter 4). As such a method of harvesting or exclusively producing a soluble MIP fraction would be of great value for application as an affinity medium in on-chip

segmented flow extraction. A preliminary attempt is outlined in appendix 5, however time limitations prevented further development of this approach. Upon achieving this aim and improving MIP binding kinetics, optimisation of the liquid-liquid mass transfer process through exploitation of the relationships characterised and understood in chapter 3, will enable appropriate design of fluidic channel networks for highly efficient on-chip liquid extractions. Segmented flow regimes comprised of short aspect ratio segments, flowing at increased linear velocity through channels of narrow diameter with tightly curved flow paths are theorised to maximise phase transfer efficiency (Chapter 3). Given the transit time limitations of a microfluidic chip device, kinetic enhancement is paramount. Such flow regimes could be realised on chip through the employment of a T-junction geometry of narrower channel diameter than the main extraction channel, in order to generate short aspect ratio fluid segments. Serpentine-like channels will improve intra-segment mixing and interfacial mass transfer through induction of segment reorientation and secondary Dean flows. The employment of narrower channels will also add performance advantages and provide the opportunity to employ greater channel length over an equivalent surface area, thus increasing contact time for MIP binding for a constant linear flow velocity. However this would be at the expense of volumetric throughput and as such an appropriate compromise would need to identified. The ability to predict MIP binding behaviour from a small set of initial experiments (chapter 6) combined with the mass transfer variable dependencies established in chapter 3, creates the opportunity to predict extraction behaviour and therefore reduce the experimental throughput required to optimise extraction methodologies for the intended application. The theoretical insight gained into the processes governing microfluidic liquid phase separation (Chapter 5) also enable such prediction to be made regarding the anticipated performance of the phase separator with alternative candidate flow regimes. Additionally, as detailed in chapter 5, the theory can be employed to design higher efficiency separators or tailor designs to meet specific requirements for the intended application.

The demonstrated concept of high efficiency, solid-phase enhanced liquid-liquid extractions conducted on-chip, in continuous flow, holds massive potential as a configurable platform for molecular separations, enrichments and chemical manipulations. With the integration of the

demonstrated phase separation techniques, post-processing and subsequent chemical and reagent manipulations are readily realisable. Analyte recovery from the solid phase material may be made through co-elution of the particle carrying separated flow with a stream which disfavours binding. After dissociation of analyte from the binding species re-segmentation of the flow with an appropriate immiscible phase can isolate the analyte for collection and return the affinity phase for recycling in the extraction process. The ability to perform single- to multi-phase flow transitions and back again through the introductions of immiscible and co-miscible liquids respectively, creates the opportunity to mix and separate reagents instantaneously. Integration of detection processes or monitoring capabilities (Appendix 12) will enable intelligent feedback regulated control of input variable parameters. Highly reproducible chemical reactions can be achieved with the distance-time proportionality of microfluidic flows enabling reaction control with high space-time definable precision. The potential to combine the demonstrated extraction methodology with on-chip chemical synthesis will create unprecedented opportunities for integrated, continuous chemical synthesis and purification.

References

[1] E. Goh and H. Stöver, "Cross-Linked Poly(methacrylic acid-co-poly(ethylene oxide) methyl ether methacrylate) Microspheres and Microgels Prepared by Precipitation Polymerization: A Morphology Study," *Macromolecules*, vol. 35, Dec. 2002, pp. 9983-9989.

[2] O.K. Castell, C.J. Allender, and D.A. Barrow, "Novel biphasic separations utilising highly selective molecularly imprinted polymers as biorecognition solvent extraction agents," *Biosensors and Bioelectronics*, vol. 22, Oct. 2006, pp. 526-533.

[3] R. Takekoh et al., "Multilayered Polymer Microspheres by Thermal Imprinting during Microsphere Growth," *Journal of the American Chemical Society*, vol. 128, Jan. 2006, pp. 240-244.

[4] J. Hedin-Dahlström, Private Communication, 2007.

[5] A. Biffis et al., "The Synthesis, Characterization and Molecular Recognition Properties of Imprinted Microgels," *Macromolecular Chemistry and Physics*, vol. 202, 2001, pp. 163-171.

[6] S.C. Maddock, P. Pasetto, and M. Resmini, "Novel imprinted soluble microgels with hydrolytic catalytic activity," *Chemical Communications*, 2004, pp. 536-537.

[7] G. Wulff, B. Chong, and U. Kolb, "Soluble Single-Molecule Nanogels of Controlled Structure as a Matrix for Efficient Artificial Enzymes13," *Angewandte Chemie International Edition*, vol. 45, 2006, pp. 2955-2958.

[8] B. Chong, "The Dependence of Polymer Structure and Morphology on Catalytic Activity in Molecularly Imprinted Nanogels," 2005, p. 134.

[9] W. Li and H.D.H. Stöver, "Porous monodisperse poly(divinylbenzene) microspheres by precipitation polymerization," *Journal of Polymer Science Part A: Polymer Chemistry*, vol. 36, 1998, pp. 1543-1551.

[10] K. Karim et al., "Preparation of Soluble and Colloidal Molecularly Imprinted Polymers by Living Polymerisation," 2006. UK Patent GB2006/001986, , July 12 2006.

Appendix 1 Microfluidic Device Compression and Interfacing Manifold

REMOVE ALL SHARP EDGES

TAP M5 X 12 THROUGH ON 63 PCD

Ø 40
Ø 51
Ø 75

REMOVE ALL SHARP EDGES

4
2
1.5 X 45°
1 X 45°
1 X 45°

COPYRIGHT-NOT TO BE USED WITHOUT THE OWNERS PERMISSION

DIMENSIONS IN MM UNLESS OTHERWISE STATED

PREFERRED TOLERANCE
X.X ± 0.3
X.XX ± 0.1
X.XXX ± 0.01

ANGULAR TOLERANCE
± 0.5

3RD ANGLE PROJECTION

REMOVE SHARP EDGES

DO NOT SCALE   IF IN DOUBT "ASK"
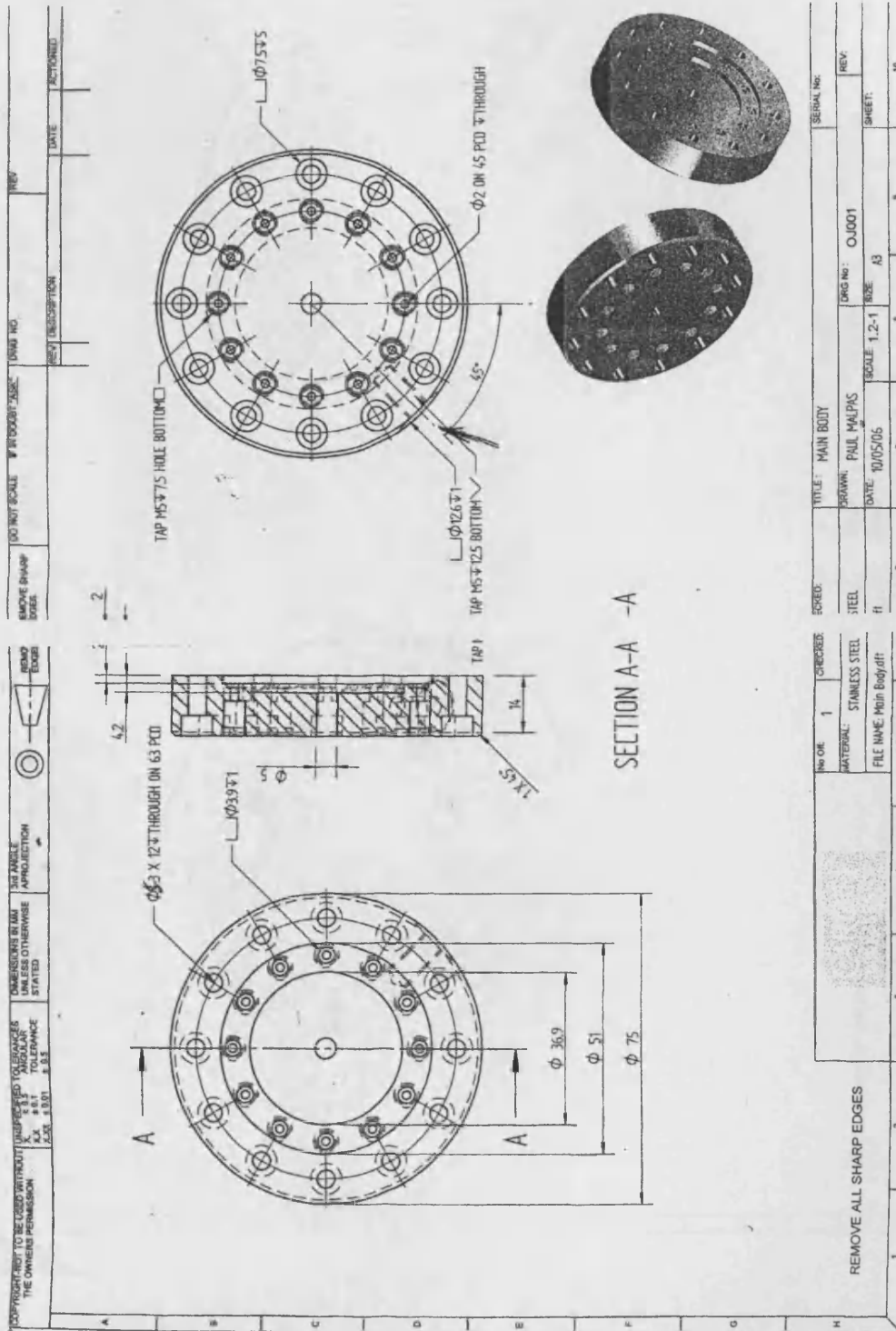
REV   DWG NO   REV DESCRIPTION   DATE   ACTIONED

CHECKED:

ESS STEEL
NTLJH

TITLE: TOP PLATE

DRAWN: PAUL MALPAS

DATE: 10/05/06

SERIAL No

DWG No: OJO03

SCALE: 1.2-1   SIZE   A3

REV

SHEET:

No Off: 1
MATERIAL: STAIN
FILE NAME: TOP PL

Appendix 2 Flow Properties and Dimensionless Numbers

Linear flow velocities and dimensionless numbers were calculated for flow regimes tested in both cylindrical FEP tubing (0.5 mm I.D.) and the square cross section (0.6 x 0.6 mm) channels typical of the evaluated microdevices.

cylindrical tube

flow rate each phase (ml/min)	total flow rate (ml/min)	total flow rate (m3/s)	dia (um)	cross-secti m2	velocity m/s	velocity cm/s	velocity mm/s	area/wetted perimeter hydraulic radius m	um	Water density kg/m3	viscosity Pa s	CHCl3 density kg/m3	viscosity Pa s	Re water	Re CHCl3	Schmidt number water	Schmidt number CHCl3	Peclet number water	Peclet number CHCl3
0.05	0.1	1.67E-09	500	1.96E-07	0.008488	0.848826	8.488264	0.000125	125	997.048	0.001003	1480	0.00058	4.218946	10.82985	10059.7	3918.919	42441.32	42441.32
0.075	0.15	2.5E-09	500	1.96E-07	0.012732	1.27324	12.7324	0.000125	125	997.048	0.001003	1480	0.00058	6.328419	16.24478	10059.7	3918.919	63661.98	63661.98
0.1	0.2	3.33E-09	500	1.96E-07	0.016977	1.697653	16.97653	0.000125	125	997.048	0.001003	1480	0.00058	8.437893	21.65971	10059.7	3918.919	84882.64	84882.64
0.15	0.3	5E-09	500	1.96E-07	0.025465	2.546479	25.46479	0.000125	125	997.048	0.001003	1480	0.00058	12.65684	32.48956	10059.7	3918.919	127324	127324
0.2	0.4	6.67E-09	500	1.96E-07	0.033953	3.395305	33.95305	0.000125	125	997.048	0.001003	1480	0.00058	16.87579	43.31941	10059.7	3918.919	169765.3	169765.3
0.3	0.6	1E-08	500	1.96E-07	0.05093	5.092958	50.92958	0.000125	125	997.048	0.001003	1480	0.00058	25.31368	64.97912	10059.7	3918.919	254647.9	254647.9
0.5	1	1.67E-08	500	1.96E-07	0.084883	8.488264	84.88264	0.000125	125	997.048	0.001003	1480	0.00058	42.18946	108.2985	10059.7	3918.919	424413.2	424413.2
0.7	1.4	2.33E-08	500	1.96E-07	0.118836	11.88357	118.8357	0.000125	125	997.048	0.001003	1480	0.00058	59.06525	151.618	10059.7	3918.919	594178.5	594178.5
1	2	3.33E-08	500	1.96E-07	0.169765	16.97653	169.7653	0.000125	125	997.048	0.001003	1480	0.00058	84.37893	216.5971	10059.7	3918.919	848826.4	848826.4
1.2	2.4	4E-08	500	1.96E-07	0.203718	20.37183	203.7183	0.000125	125	997.048	0.001003	1480	0.00058	101.2547	259.9165	10059.7	3918.919	1018592	1018592
1.5	3	5E-08	500	1.96E-07	0.254648	25.46479	254.6479	0.000125	125	997.048	0.001003	1480	0.00058	126.5684	324.8956	10059.7	3918.919	1273240	1273240
2	4	6.67E-08	500	1.96E-07	0.339531	33.95305	339.5305	0.000125	125	997.048	0.001003	1480	0.00058	168.7579	433.1941	10059.7	3918.919	1697653	1697653
3	6	1E-07	500	1.96E-07	0.509296	50.92958	509.2958	0.000125	125	997.048	0.001003	1480	0.00058	253.1368	649.7912	10059.7	3918.919	2546479	2546479
5	10	1.67E-07	500	1.96E-07	0.848826	84.88264	848.8264	0.000125	125	997.048	0.001003	1480	0.00058	421.8946	1082.985	10059.7	3918.919	4244132	4244132

square microchannels

flow rate each phase (ml/min)	total flow rate (ml/min)	total flow rate (m3/s)	w (um)	d (um)	cross-secti m2	velocity m/s	velocity cm/s	velocity mm/s	hydraulic dia m	hydraulic dia um	area/wetted perimeter hydraulic radius m	hydraulic radius um	Water density kg/m3	viscosity Pa s	CHCl3 density kg/m3	viscosity Pa s	Re water	Re CHCl3	Schmidt number water	Schmidt number CHCl3	Peclet number water	Peclet number CHCl3
0.05	0.1	1.67E-09	600	600	3.6E-07	0.00463	0.462963	4.62963	0.0006	600	0.00015	150	997.048	0.001003	1480	0.00058	2.761294	7.088123	10059.7	3918.919	27777.78	27777.78
0.075	0.15	2.5E-09	600	600	3.6E-07	0.006944	0.694444	6.944444	0.0006	600	0.00015	150	997.048	0.001003	1480	0.00058	4.141941	10.63218	10059.7	3918.919	41666.67	41666.67
0.1	0.2	3.33E-09	600	600	3.6E-07	0.009259	0.925926	9.259259	0.0006	600	0.00015	150	997.048	0.001003	1480	0.00058	5.522588	14.17625	10059.7	3918.919	55555.56	55555.56
0.15	0.3	5E-09	600	600	3.6E-07	0.013889	1.388889	13.88889	0.0006	600	0.00015	150	997.048	0.001003	1480	0.00058	8.283882	21.26437	10059.7	3918.919	83333.33	83333.33
0.2	0.4	6.67E-09	600	600	3.6E-07	0.018519	1.851852	18.51852	0.0006	600	0.00015	150	997.048	0.001003	1480	0.00058	11.04518	28.35249	10059.7	3918.919	111111.1	111111.1
0.3	0.6	1E-08	600	600	3.6E-07	0.027778	2.777778	27.77778	0.0006	600	0.00015	150	997.048	0.001003	1480	0.00058	16.56776	42.52874	10059.7	3918.919	166666.7	166666.7
0.5	1	1.67E-08	600	600	3.6E-07	0.046296	4.62963	46.2963	0.0006	600	0.00015	150	997.048	0.001003	1480	0.00058	27.61294	70.88123	10059.7	3918.919	277777.8	277777.8
0.7	1.4	2.33E-08	600	600	3.6E-07	0.064815	6.481481	64.81481	0.0006	600	0.00015	150	997.048	0.001003	1480	0.00058	38.65811	99.23372	10059.7	3918.919	388888.9	388888.9
1	2	3.33E-08	600	600	3.6E-07	0.092593	9.259259	92.59259	0.0006	600	0.00015	150	997.048	0.001003	1480	0.00058	55.22588	141.7625	10059.7	3918.919	555555.6	555555.6
1.2	2.4	4E-08	600	600	3.6E-07	0.111111	11.11111	111.1111	0.0006	600	0.00015	150	997.048	0.001003	1480	0.00058	66.27105	170.1149	10059.7	3918.919	666666.7	666666.7
1.5	3	5E-08	600	600	3.6E-07	0.138889	13.88889	138.8889	0.0006	600	0.00015	150	997.048	0.001003	1480	0.00058	82.83882	212.6437	10059.7	3918.919	833333.3	833333.3
2	4	6.67E-08	600	600	3.6E-07	0.185185	18.51852	185.1852	0.0006	600	0.00015	150	997.048	0.001003	1480	0.00058	110.4518	283.5249	10059.7	3918.919	1111111	1111111
3	6	1E-07	600	600	3.6E-07	0.277778	27.77778	277.7778	0.0006	600	0.00015	150	997.048	0.001003	1480	0.00058	165.6776	425.2874	10059.7	3918.919	1666667	1666667
5	10	1.67E-07	600	600	3.6E-07	0.462963	46.2963	462.963	0.0006	600	0.00015	150	997.048	0.001003	1480	0.00058	276.1294	708.8123	10059.7	3918.919	2777778	2777778

Appendix 3 Adaptation of the Predictive MIP Binding Model for Application to a Biphasic Solvent System

The predictive MIP binding model developed in the work of chapter 6 was adapted to model the anticipated equilibrium propranolol distribution in a MIP assisted liquid-liquid extraction system. The prediction was made from knowledge of the propranolol distribution coefficient between the two liquid phase alone (i.e. water and chloroform) and the binding isotherm describing MIP binding behaviour in extracting solvent (i.e chloroform). The model performed sequential iterations defining the distribution of propranolol between the three phases, eventually converging on an answer representing the equilibrium of the extraction system.

The model demonstrated good correlation with experimental results, however due to time constrains it was not possible to continue the work further. It was hoped the model would assist in the optimising experimental conditions for conducting MIP assisted segmented flow extractions.

The mathcad code is detailed on the following pages.

Define 'Fixed' Variables
Volume of CHCl3
Volume of H2O
Polymer mass

$m := 1$

$Vc := 1$

$Vw := 1$

Total propranolol
Partition coefficient
organic/aq

$Tp := 50$

$\dfrac{1}{0.85} = 1.176$

$kl := 1.4$

MIP binding equation in the form bound = a*(1-exp(-b*Ceq)

$a := 129.7$

$b := 0.01278$

1. Calculate distribution of propranolol between the aqueous and organic phases

$k := \dfrac{1}{kl}$

descibe for unbound propranolol, initial this will equal Tp but later itterations will require adjustment for total of unbound in Aq and CHCL3
General notation

C = concentration

$Pw(P\_unbound) := \dfrac{P\_unbound \cdot k \cdot Vw}{k \cdot Vw + Vc}$

$Pc(P\_unbound) := P\_unbound - Pw(P\_unbound)$

2. Calculate the concentration of propranolol in CHCl3

$Cc(Pc) := \dfrac{Pc}{Vc}$

For further itterations Tp (i.e. total propranolol) will be replaced by the summ of free popranolol in CHCl3 and H2O after binding to the MIP

$Pw(Tp) = 20.833$

$Pc(Tp) = 29.167$

$Cc(Pc(Tp)) = 29.167$

3. Calculte amount bound to the MIP
From previous notation f1 = bound
f2 = total propranolol intersection line
f = equation equalling zero

$bound(C) := a \cdot (1 - exp(-b \cdot C))$

$P\_conserved(C) := -C \cdot \dfrac{Vc}{m} + \dfrac{Vc \cdot Cc(Pc(Tp))}{m}$

$P\_conserved(100) = -70.833$

Equation which will equal zero when MIP binding is at equalibrium

$f(C) := a \cdot (1 - exp(-b \cdot C)) + C \cdot \dfrac{Vc}{m} - \dfrac{Vc}{m} \cdot Cc(Pc(Tp))$

$guess := \dfrac{Cc(Pc(Tp))}{2}$

$guess = 14.583$

$Ceq := root(f(guess), guess)$

$C := 0, 0.1 .. 100$

$Ceq = 11.475$
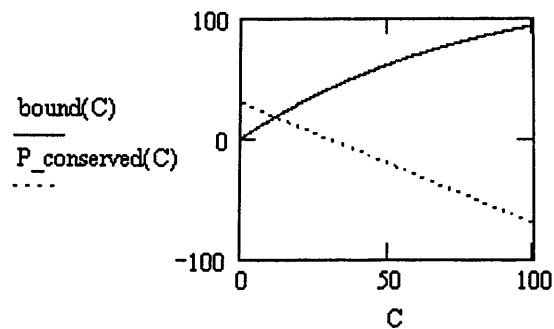
$bound(Ceq) = 17.692$

$P\_conserved(Ceq) = 17.692$

4. Calculate total propranolol unbound in system
Unbound in chloroform (i.e. Ceq) and propranolol partitioned into H2O

$P\_unbound1 := Ceq \cdot Vc + Pw(Tp)$

$P\_unbound1 = 32.308$

5. Calculate distribution of this between Aq and organic phases, using equations generated for 1.

$Pw(P\_unbound1) = 13.462$

$Pc(P\_unbound1) = 18.847$

Check total:

$Pc(P\_unbound1) + Pw(P\_unbound1) = 32.308$

6. Calculate new total of propranolol in chloroform (prevuous bound + newly distributed into CHCl3)
is this a bit muddled?
should this function be made more genral for use later?

$Pc1 := (bound(Ceq) \cdot m) + Pc(P\_unbound1)$

$Pc1 = 36.538$

$Pc\_apparent(bound, free) := bound \cdot m + free$

perhaps this is better?

$Pc\_apparent(bound(Ceq), Pc(P\_unbound1)) = 36.538$

7. Calculate concentration this would give in order to re-solve binding to mip, using equation 2

$Cc(Pc1) = 36.538$

$Cc(Pc\_apparent(bound(Ceq), Pc(P\_unbound1))) = 36.538$

8. Calculate amount that would bind to the MIP

$bound(C) := a \cdot (1 - exp(-b \cdot C))$

$$P\_conserved(C) := -C \cdot \frac{Vc}{m} + \frac{Vc \cdot Cc(Pcl)}{m}$$

$P\_conserved(100) = -63.462$

Equation which will equal zero when MIP binding is at equalibrium

$$f(C) := a \cdot (1 - exp(-b \cdot C)) + C \cdot \frac{Vc}{m} - \frac{Vc}{m} \cdot Cc(Pcl)$$

$$guess := \frac{Cc(Pcl)}{2}$$

$guess = 18.269$

$Ceq := root(f(guess), guess)$

$C := 0, 0.1 .. 100$

$Ceq = 14.542$
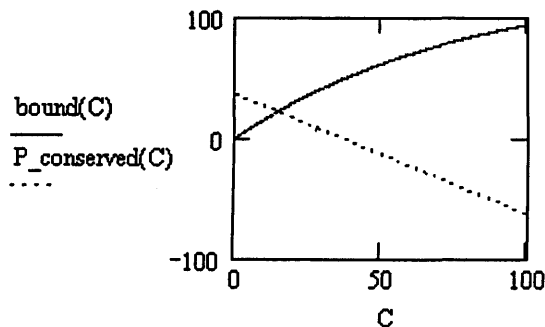
$bound(Ceq) = 21.997$
validate total propranolol in this 'mini syatem'
$P\_conserved(Ceq) = 21.997$

$tot := Ceq \cdot Vc + bound(Ceq) \cdot m$

$tot = 36.538$

9.Repeat steps 4-8
In step 4 the calculation of propranolol in water needs to change from Pw(Tp) to Pw(P_unbound1)
to reflect previous itteration
4. Calculate total propranolol unbound in system
Unbound in chloroform (i.e. Ceq) and propranolol partitioned into H2O
$P\_unbound1 = 32.308$

$P\_unbound1 := Ceq \cdot Vc + Pw(P\_unbound1)$
value for P_unbound1 changes at this point, thereore dont need to define new name for it i.e.P_unbound2
$P\_unbound1 = 28.003$

$P\_unbound1 = 28.003$
5. Calculate distribution of this between Aq and organic phases, using equations generated for 1.
$Pw(P\_unbound1) = 11.668$

$Pc(P\_unbound1) = 16.335$
check overall total:
Check total:
$Pc(P\_unbound1) + Pw(P\_unbound1) = 28.003$

$Pc(P\_unbound1) + Pw(P\_unbound1) + bound(Ceq) \cdot m = 50$
6. Calculate new total of propranolol in chloroform
(prevuous bound + newly distributed into CHCl3)
$Pcl := (bound(Ceq) \cdot m) + Pc(P\_unbound1)$

$Pcl = 38.332$
both 6 and 7 reduced to use more efficient equation for insetion into step 8

i.e Pcl easier to substitute in than
(Pc_apparent(bound(Ceq),Pc(P_unbound1))

also this may not work as introducing old value of Ceq into equation trying to find the new value
7. Calculate concentration this would give in order to re-solve binding to mip, using equation 2
$Cc(Pcl) = 38.332$
8. Calculate amount that would bind to the MIP
$bound(C) := a \cdot (1 - exp(-b \cdot C))$

$$P\_conserved(C) := -C \cdot \frac{Vc}{m} + \frac{Vc \cdot Cc(Pcl)}{m}$$

$P\_conserved(100) = -61.668$
Equation which will equal zero when MIP binding is at equalibrium

$$f(C) := a \cdot (1 - exp(-b \cdot C)) + C \cdot \frac{Vc}{m} - \frac{Vc}{m} \cdot Cc(Pcl)$$

$$guess := \frac{Cc(Pcl)}{2}$$

$guess = 19.166$

$Ceq := root(f(guess), guess)$

$C := 0, 0.1 .. 100$

$Ceq = 15.299$
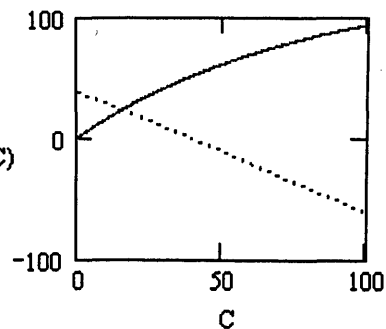
$bound(Ceq) = 23.033$
validate total propranolol in this 'mini syatem'

P_conserved(Ceq) = 23.033

tot := Ceq·Vc + bound(Ceq)·m

tot = 38.332

10. Repeat step 9
In step 4 the calculation of propranolol in water needs to
change from Pw(Tp) to Pw(P_unbound1)
to reflect previous itteration
4. Calculate total propranolol unbound in system
Unbound in chloroform (i.e. Ceq) and propranolol
partitioned into H2O

P_unbound1 = 28.003

P_unbound1 := Ceq·Vc + Pw(P_unbound1)

value for P_unbound1 changes at this point, thereore dont
need to define new name for it i.e.P_unbound2

P_unbound1 = 26.967

P_unbound1 = 26.967

5. Calculate distribution of this between Aq and organic
phases, using equations generated for 1.
look for convergence here

Pw(P_unbound1) = 11.236

Pc(P_unbound1) = 15.731

check overall total:
Check total:

Pc(P_unbound1) + Pw(P_unbound1) = 26.967

Pc(P_unbound1) + Pw(P_unbound1) + bound(Ceq)·m = 50

6. Calculate new total of propranolol in chloroform
(prevuous bound + newly distributed into CHCl3)

Pcl := (bound(Ceq)·m) + Pc(P_unbound1)

Pcl = 38.764

7. Calculate concentration this would give in order to re-
solve binding to mip, using equation 2

Cc(Pcl) = 38.764

8. Calculate amount that would bind to the MIP

bound(C) := a·(1 − exp(−b·C))

$$P\_conserved(C) := -C \cdot \frac{Vc}{m} + \frac{Vc \cdot Cc(Pcl)}{m}$$

C := 0,0.1 .. 100

Equation which will equal zero when MIP binding is at
equalibrium
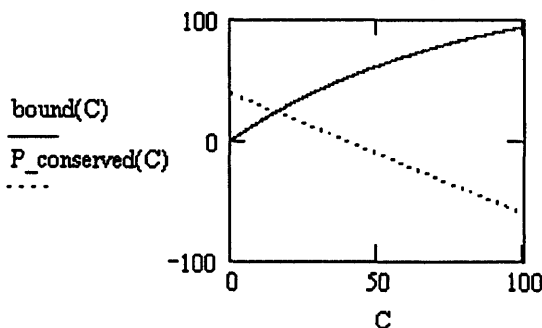
$$f(C) := a·(1 − exp(−b·C)) + C \cdot \frac{Vc}{m} − \frac{Vc}{m} \cdot Cc(Pcl)$$

validate total propranolol in this 'mini syatem'

$$guess := \frac{Cc(Pcl)}{2}$$

tot := Ceq·Vc + bound(Ceq)·m

guess = 19.382

tot = 38.332

Ceq := root(f(guess), guess)

Ceq = 15.481

bound(Ceq) = 23.282

P_conserved(Ceq) = 23.282

11. Repeat step 9
In step 4 the calculation of propranolol in water needs to
change from Pw(Tp) to Pw(P_unbound1)
to reflect previous itteration
4. Calculate total propranolol unbound in system
Unbound in chloroform (i.e. Ceq) and propranolol
partitioned into H2O

P_unbound1 = 26.967

P_unbound1 := Ceq·Vc + Pw(P_unbound1)

value for P_unbound1 changes at this point, thereore dont
need to define new name for it i.e.P_unbound2

P_unbound1 = 26.718

P_unbound1 = 26.718

5. Calculate distribution of this between Aq and organic
phases, using equations generated for 1.
look for convergence here

Pw(P_unbound1) = 11.132

Pc(P_unbound1) = 15.585

check overall total:
Check total:

Pc(P_unbound1) + Pw(P_unbound1) = 26.718

Pc(P_unbound1) + Pw(P_unbound1) + bound(Ceq)·m = 50

6. Calculate new total of propranolol in chloroform
(prevuous bound + newly distributed into CHCl3)

Pcl := (bound(Ceq)·m) + Pc(P_unbound1)

Pcl = 38.868

7. Calculate concentration this would give in order to re-
solve binding to mip, using equation 2

Cc(Pcl) = 38.868

8. Calculate amount that would bind to the MIP

bound(C) := a·(1 − exp(−b·C))

$$P\_conserved(C) := -C \cdot \frac{Vc}{m} + \frac{Vc \cdot Cc(Pcl)}{m}$$

C := 0,0.1 .. 100

Equation which will equal zero when MIP binding is at equalibrium
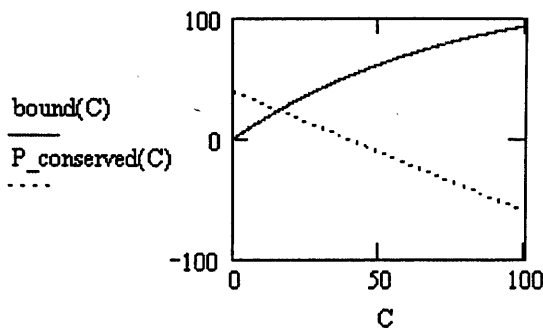
$$f(C) := a \cdot (1 - \exp(-b \cdot C)) + C \cdot \frac{Vc}{m} - \frac{Vc}{m} \cdot Cc(Pc1)$$

validate total propranolol in this 'mini syatem'

$$guess := \frac{Cc(Pc1)}{2}$$

$$tot := Ceq \cdot Vc + bound(Ceq) \cdot m$$

$$guess = 19.434$$

$$tot = 38.764$$

$$Ceq := root(f(guess), guess)$$

$$Ceq = 15.525$$

$$bound(Ceq) = 23.342$$

$$P\_conserved(Ceq) = 23.342$$
12.Repeat step 9
In step 4 the calculation of propranolol in water needs to change from Pw(Tp) to Pw(P_unbound1)
to reflect previous itteration
4. Calculate total propranolol unbound in system
Unbound in chloroform (i.e. Ceq) and propranolol partitioned into H2O
$$P\_unbound1 = 26.718$$

$$P\_unbound1 := Ceq \cdot Vc + Pw(P\_unbound1)$$
value for P_unbound1 changes at this point, thereore dont need to define new name for it i.e.P_unbound2
$$P\_unbound1 = 26.658$$

$$P\_unbound1 = 26.658$$
5. Calculate distribution of this between Aq and organic phases, using equations generated for 1.
look for convergence here
$$Pw(P\_unbound1) = 11.107$$

$$Pc(P\_unbound1) = 15.55$$
check overall total:
Check total:
$$Pc(P\_unbound1) + Pw(P\_unbound1) = 26.658$$

$$Pc(P\_unbound1) + Pw(P\_unbound1) + bound(Ceq) \cdot m =$$

6. Calculate new total of propranolol in chloroform (prevuous bound + newly distributed into CHCl3)
$$Pc1 := (bound(Ceq) \cdot m) + Pc(P\_unbound1)$$

$$Pc1 = 38.893$$
7. Calculate concentration this would give in order to re-solve binding to mip, using equation 2
$$Cc(Pc1) = 38.893$$
8. Calculate amount that would bind to the MIP
$$bound(C) := a \cdot (1 - \exp(-b \cdot C))$$

$$P\_conserved(C) := -C \cdot \frac{Vc}{m} + \frac{Vc \cdot Cc(Pc1)}{m}$$

$$C := 0, 0.1 .. 100$$
Equation which will equal zero when MIP binding is at equalibrium
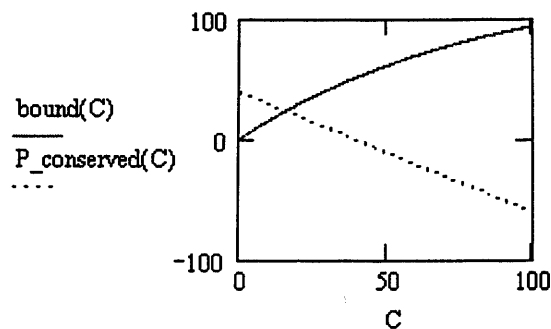
$$f(C) := a \cdot (1 - \exp(-b \cdot C)) + C \cdot \frac{Vc}{m} - \frac{Vc}{m} \cdot Cc(Pc1)$$

validate total propranolol in this 'mini syatem'

$$guess := \frac{Cc(Pc1)}{2}$$

$$tot := Ceq \cdot Vc + bound(Ceq) \cdot m$$

$$guess = 19.446$$

$$tot = 38.868$$

$$Ceq := root(f(guess), guess)$$

$$Ceq = 15.536$$

$$bound(Ceq) = 23.357$$

$$P\_conserved(Ceq) = 23.357$$
13.Repeat step 9
In step 4 the calculation of propranolol in water needs to change from Pw(Tp) to Pw(P_unbound1)
to reflect previous itteration
4. Calculate total propranolol unbound in system
Unbound in chloroform (i.e. Ceq) and propranolol partitioned into H2O
$$P\_unbound1 = 26.658$$

$$P\_unbound1 := Ceq \cdot Vc + Pw(P\_unbound1)$$
value for P_unbound1 changes at this point, thereore dont need to define new name for it i.e.P_unbound2

P_unbound1 = 26.643

P_unbound1 = 26.643
5. Calculate distribution of this between Aq and organic
phases, using equations generated for 1.
look for convergence here

$Pw(P\_unbound1) = 11.101$

$Pc(P\_unbound1) = 15.542$
check overall total:
Check total:

$Pc(P\_unbound1) + Pw(P\_unbound1) = 26.643$

$Pc(P\_unbound1) + Pw(P\_unbound1) + bound(Ceq) \cdot m = 50$
6. Calculate new total of propranolol in chloroform
(prevuous bound + newly distributed into CHCl3)

$Pcl := (bound(Ceq) \cdot m) + Pc(P\_unbound1)$

$Pcl = 38.899$
7. Calculate concentration this would give in order to re-
solve binding to mip, using equation 2

$Cc(Pcl) = 38.899$
8. Calculate amount that would bind to the MIP

$bound(C) := a \cdot (1 - exp(-b \cdot C))$

$P\_conserved(C) := -C \cdot \dfrac{Vc}{m} + \dfrac{Vc \cdot Cc(Pcl)}{m}$

$C := 0, 0.1 .. 100$
Equation which will equal zero when MIP binding is at
equalibrium

bound(C)
———
P_conserved(C)
. . . .
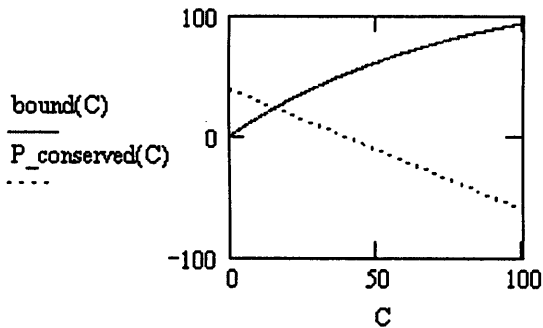
$f(C) := a \cdot (1 - exp(-b \cdot C)) + C \cdot \dfrac{Vc}{m} - \dfrac{Vc}{m} \cdot Cc(Pcl)$

validate total propranolol in this 'mini syatem'

$guess := \dfrac{Cc(Pcl)}{2}$

$tot := Ceq \cdot Vc + bound(Ceq) \cdot m$

$guess = 19.449$

$tot = 38.893$

$Ceq := root(f(guess), guess)$

$Ceq = 15.539$

bound(Ceq) = 23.36

P_conserved(Ceq) = 23.36
14.Repeat step 9
In step 4 the calculation of propranolol in water needs to
change from Pw(Tp) to Pw(P_unbound1)
to reflect previous itteration
4. Calculate total propranolol unbound in system
Unbound in chloroform (i.e. Ceq) and propranolol
partitioned into H2O

P_unbound1 = 26.643

$P\_unbound1 := Ceq \cdot Vc + Pw(P\_unbound1)$
value for P_unbound1 changes at this point, thereore dont
need to define new name for it i.e.P_unbound2

P_unbound1 = 26.64

P_unbound1 = 26.64
5. Calculate distribution of this between Aq and organic
phases, using equations generated for 1.
look for convergence here

$Pw(P\_unbound1) = 11.1$

$Pc(P\_unbound1) = 15.54$
check overall total:
Check total:

$Pc(P\_unbound1) + Pw(P\_unbound1) = 26.64$

$Pc(P\_unbound1) + Pw(P\_unbound1) + bound(Ceq) \cdot m = 50$
6. Calculate new total of propranolol in chloroform
(prevuous bound + newly distributed into CHCl3)

$Pcl := (bound(Ceq) \cdot m) + Pc(P\_unbound1)$

$Pcl = 38.9$
7. Calculate concentration this would give in order to re-
solve binding to mip, using equation 2

$Cc(Pcl) = 38.9$
8. Calculate amount that would bind to the MIP

$bound(C) := a \cdot (1 - exp(-b \cdot C))$

$P\_conserved(C) := -C \cdot \dfrac{Vc}{m} + \dfrac{Vc \cdot Cc(Pcl)}{m}$

$C := 0, 0.1 .. 100$
Equation which will equal zero when MIP binding is at
equalibrium

bound(C)
———
P_conserved(C)
. . . .

$f(C) := a \cdot (1 - exp(-b \cdot C)) + C \cdot \dfrac{Vc}{m} - \dfrac{Vc}{m} \cdot Cc(Pcl)$

validate total propranolol in this 'mini syatem'

$$guess := \frac{Cc(Pcl)}{2}$$

$$tot := Ceq \cdot Vc + bound(Ceq) \cdot m$$

$$guess = 19.45$$

$$tot = 38.899$$

$$Ceq := root(f(guess), guess)$$

$$Ceq = 15.539$$

$$bound(Ceq) = 23.361$$

$$P\_conserved(Ceq) = 23.361$$
15.Repeat step 9
In step 4 the calculation of propranolol in water needs to
change from Pw(Tp) to Pw(P_unbound1)
to reflect previous itteration
4. Calculate total propranolol unbound in system
Unbound in chloroform (i.e. Ceq) and propranolol
partitioned into H2O
$$P\_unbound1 = 26.64$$

$$P\_unbound1 := Ceq \cdot Vc + Pw(P\_unbound1)$$
value for P_unbound1 changes at this point, thereore dont
need to define new name for it i.e.P_unbound2
$$P\_unbound1 = 26.639$$

$$P\_unbound1 = 26.639$$
5. Calculate distribution of this between Aq and organic
phases, using equations generated for 1.
look for convergence here
$$Pw(P\_unbound1) = 11.1$$

$$Pc(P\_unbound1) = 15.54$$
check overall total:
Check total:
$$Pc(P\_unbound1) + Pw(P\_unbound1) = 26.639$$

$$Pc(P\_unbound1) + Pw(P\_unbound1) + bound(Ceq) \cdot m = 50$$
6. Calculate new total of propranolol in chloroform
(prevuous bound + newly distributed into CHCl3)
$$Pcl := (bound(Ceq) \cdot m) + Pc(P\_unbound1)$$

$$Pcl = 38.9$$
7. Calculate concentration this would give in order to re-
solve binding to mip, using equation 2
$$Cc(Pcl) = 38.9$$
8. Calculate amount that would bind to the MIP
$$bound(C) := a \cdot (1 - exp(-b \cdot C))$$

$$P\_conserved(C) := -C \cdot \frac{Vc}{m} + \frac{Vc \cdot Cc(Pcl)}{m}$$

$$C := 0, 0.1 .. 100$$
Equation which will equal zero when MIP binding is at
equalibrium

bound(C)
—————
P_conserved(C)
· · · ·

$$f(C) := a \cdot (1 - exp(-b \cdot C)) + C \cdot \frac{Vc}{m} - \frac{Vc}{m} \cdot Cc(Pcl)$$
validate total propranolol in this 'mini syatem'

$$guess := \frac{Cc(Pcl)}{2}$$

$$tot := Ceq \cdot Vc + bound(Ceq) \cdot m$$

$$guess = 19.45$$

$$tot = 38.9$$

$$Ceq := root(f(guess), guess)$$

$$Ceq = 15.539$$
Free In CHCl3
Free In Aq
Bound per mg
$$bound(Ceq) = 23.361$$
CHCl3 conc:
$$Ceq = 15.539$$
Aq conc:
$$\frac{Pw(P\_unbound1)}{Vw} = 11.1$$

$$bound(Ceq) = 23.361$$
CHCl3 amount:
$$Ceq \cdot Vc = 15.539$$

$$P\_conserved(Ceq) = 23.361$$
Aq amount:
$$Pw(P\_unbound1) = 11.1$$

$$total := bound(Ceq) \cdot m + Ceq \cdot Vc + Pw(P\_unbound1)$$

$$total = 50$$
16.Repeat step 9
In step 4 the calculation of propranolol in water needs to
change from Pw(Tp) to Pw(P_unbound1)
to reflect previous itteration
4. Calculate total propranolol unbound in system
Unbound in chloroform (i.e. Ceq) and propranolol
partitioned into H2O
$$P\_unbound1 = 26.639$$

$$P\_unbound1 := Ceq \cdot Vc + Pw(P\_unbound1)$$
value for P_unbound1 changes at this point, thereore dont

need to define new name for it i.e.P_unbound2

$P\_unbound1 = 26.639$

$P\_unbound1 = 26.639$

5. Calculate distribution of this between Aq and organic
phases, using equations generated for 1.
look for convergence here

$Pw(P\_unbound1) = 11.1$

$Pc(P\_unbound1) = 15.539$

check overall total:
Check total:

$Pc(P\_unbound1) + Pw(P\_unbound1) = 26.639$

$Pc(P\_unbound1) + Pw(P\_unbound1) + bound(Ceq) \cdot m =$
6. Calculate new total of propranolol in chloroform
(prevuous bound + newly distributed into CHCl3)

$Pc1 := (bound(Ceq) \cdot m) + Pc(P\_unbound1)$

$Pc1 = 38.9$

7. Calculate concentration this would give in order to re-
solve binding to mip, using equation 2

$Cc(Pc1) = 38.9$

8. Calculate amount that would bind to the MIP

$bound(C) := a \cdot (1 - exp(-b \cdot C))$

$$P\_conserved(C) := -C \cdot \frac{Vc}{m} + \frac{Vc \cdot Cc(Pc1)}{m}$$

$C := 0, 0.1 .. 100$

Equation which will equal zero when MIP binding is at
equalibrium

$$f(C) := a \cdot (1 - exp(-b \cdot C)) + C \cdot \frac{Vc}{m} - \frac{Vc}{m} \cdot Cc(Pc1)$$

validate total propranolol in this 'mini syatem'

$$guess := \frac{Cc(Pc1)}{2}$$

$tot := Ceq \cdot Vc + bound(Ceq) \cdot m$

$guess = 19.45$

$tot = 38.9$

$Ceq := root(f(guess), guess)$

$Ceq = 15.539$

Free In CHCl3
Free In Aq
Bound per mg

$bound(Ceq) = 23.361$

CHCl3 conc:

$Ceq = 15.539$

Aq conc:

$$\frac{Pw(P\_unbound1)}{Vw} = 11.1$$

$bound(Ceq) = 23.361$

CHCl3 amount:

$Ceq \cdot Vc = 15.539$

$P\_conserved(Ceq) = 23.361$

Aq amount:

$Pw(P\_unbound1) = 11.1$

$total := bound(Ceq) \cdot m + Ceq \cdot Vc + Pw(P\_unbound1)$

$total = 50$

17.Repeat step 9
In step 4 the calculation of propranolol in water needs to
change from Pw(Tp) to Pw(P_unbound1)
to reflect previous itteration
4. Calculate total propranolol unbound in system
Unbound in chloroform (i.e. Ceq) and propranolol
partitioned into H2O

$P\_unbound1 = 26.639$

$P\_unbound1 := Ceq \cdot Vc + Pw(P\_unbound1)$
value for P_unbound1 changes at this point, thereore dont
need to define new name for it i.e.P_unbound2

$P\_unbound1 = 26.639$

$P\_unbound1 = 26.639$

5. Calculate distribution of this between Aq and organic
phases, using equations generated for 1.
look for convergence here

$Pw(P\_unbound1) = 11.1$

$Pc(P\_unbound1) = 15.539$

check overall total:
Check total:

$Pc(P\_unbound1) + Pw(P\_unbound1) = 26.639$

$Pc(P\_unbound1) + Pw(P\_unbound1) + bound(Ceq) \cdot m = 50$

6. Calculate new total of propranolol in chloroform
(prevuous bound + newly distributed into CHCl3)

$Pc1 := (bound(Ceq) \cdot m) + Pc(P\_unbound1)$

$Pc1 = 38.9$

7. Calculate concentration this would give in order to re-
solve binding to mip, using equation 2

$Cc(Pc1) = 38.9$

8. Calculate amount that would bind to the MIP

$bound(C) := a \cdot (1 - exp(-b \cdot C))$

$$P\_conserved(C) := -C \cdot \frac{Vc}{m} + \frac{Vc \cdot Cc(Pc1)}{m}$$

$C := 0,0.1 .. 100$

Equation which will equal zero when MIP binding is at equalibrium

bound(C) ———

P_conserved(C) ....

$$f(C) := a \cdot (1 - \exp(-b \cdot C)) + C \cdot \frac{Vc}{m} - \frac{Vc}{m} \cdot Cc(Pcl)$$

validate total propranolol in this 'mini syatem'

$$guess := \frac{Cc(Pcl)}{2}$$

$tot := Ceq \cdot Vc + bound(Ceq) \cdot m$

$guess = 19.45$

$tot = 38.9$

$Ceq := root(f(guess), guess)$

$Ceq = 15.539$
Free in CHCl3
Free in Aq
Bound per mg
$bound(Ceq) = 23.361$
CHCl3 conc:
$Ceq = 15.539$
Aq conc:
$$\frac{Pw(P\_unbound1)}{Vw} = 11.1$$

$bound(Ceq) = 23.361$
CHCl3 amount:
$Ceq \cdot Vc = 15.539$

$P\_conserved(Ceq) = 23.361$
Aq amount:
$Pw(P\_unbound1) = 11.1$

$total := bound(Ceq) \cdot m + Ceq \cdot Vc + Pw(P\_unbound1)$

$total = 50$
18. Repeat step 9
In step 4 the calculation of propranolol in water needs to change from Pw(Tp) to Pw(P_unbound1)
to reflect previous itteration
4. Calculate total propranolol unbound in system
Unbound in chloroform (i.e. Ceq) and propranolol partitioned into H2O
$P\_unbound1 = 26.639$

$P\_unbound1 := Ceq \cdot Vc + Pw(P\_unbound1)$
value for P_unbound1 changes at this point, thereore dont need to define new name for it i.e.P_unbound2
$P\_unbound1 = 26.639$

$P\_unbound1 = 26.639$
5. Calculate distribution of this between Aq and organic phases, using equations generated for 1.
look for convergence here
$Pw(P\_unbound1) = 11.1$

$Pc(P\_unbound1) = 15.539$
check overall total:
Check total:
$Pc(P\_unbound1) + Pw(P\_unbound1) = 26.639$

$Pc(P\_unbound1) + Pw(P\_unbound1) + bound(Ceq) \cdot m = 50$
6. Calculate new total of propranolol in chloroform
(prevuous bound + newly distributed into CHCl3)
$Pcl := (bound(Ceq) \cdot m) + Pc(P\_unbound1)$

$Pcl = 38.9$
7. Calculate concentration this would give in order to re-solve binding to mip, using equation 2
$Cc(Pcl) = 38.9$
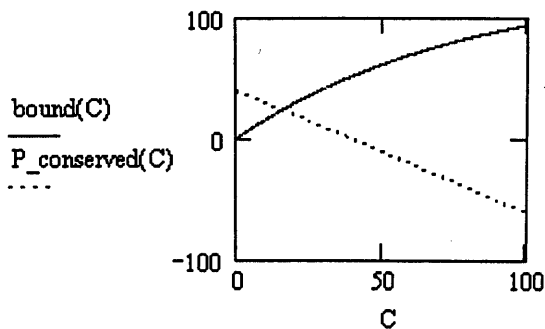8. Calculate amount that would bind to the MIP
$bound(C) := a \cdot (1 - \exp(-b \cdot C))$

$$P\_conserved(C) := -C \cdot \frac{Vc}{m} + \frac{Vc \cdot Cc(Pcl)}{m}$$

$C := 0,0.1 .. 100$
Equation which will equal zero when MIP binding is at equalibrium

bound(C) ———

P_conserved(C) ....

$$f(C) := a \cdot (1 - \exp(-b \cdot C)) + C \cdot \frac{Vc}{m} - \frac{Vc}{m} \cdot Cc(Pcl)$$

validate total propranolol in this 'mini syatem'

$$guess := \frac{Cc(Pcl)}{2}$$

$tot := Ceq \cdot Vc + bound(Ceq) \cdot m$

$guess = 19.45$

$tot = 38.9$

$Ceq := root(f(guess), guess)$

$Ceq = 15.539$
Free in CHCl3
Free in Aq
Bound per mg
$bound(Ceq) = 23.361$
CHCl3 conc:
$Ceq = 15.539$
Aq conc:
$$\frac{Pw(P\_unbound1)}{Vw} = 11.1$$

$bound(Ceq) = 23.361$
CHCl3 amount:
$Ceq \cdot Vc = 15.539$

$P\_conserved(Ceq) = 23.361$
Aq amount:
$Pw(P\_unbound1) = 11.1$

$total := bound(Ceq) \cdot m + Ceq \cdot Vc + Pw(P\_unbound1)$

$total = 50$

$$extraction\_coeff := \frac{(bound(Ceq) \cdot m) + Ceq \cdot Vc}{Pw(P\_unbound1)}$$

$extraction\_coeff = 3.505$

Appendix 4 Incorporation of Leaching Fraction into the Predictive MIP Binding Model

As detailed in chapter 6, the equation describing the apparent mass of soluble leaching fraction was incorporated into the predictive MIP binding model. This enabled a predicted calculation of the overestimate made in experimentally assessing free propranolol concentration when conducting binding assays. The mathcad code used to program this model is detailed below.

mass of MIP to be modelled (mg)
mass of MIP used to generate binding curve equation (mg)

$m1 := 4$

$m2 := 1$

volume of solvent to be modelled (ml)
Incubation concentration (uM)

$vol := 2$

$Cs := 50$

MIP binding equation in the form bound = a*(1-exp(-b*Ceq)

$a := 82.1$

$b := 0.05946$

mass scale ratio

$ms := \dfrac{m1}{m2}$

$ms = 4$

volume scalled
total propranolol in system (nmol)

$Vs := \dfrac{vol}{ms}$

$Vs = 0.5$

$p := Cs \cdot vol$

$p = 100$

$s := \dfrac{Vs}{m2}$

$s = 0.5$

$f(c) := a \cdot (1 - \exp(-b \cdot c)) + s \cdot c - s \cdot Cs$

$f1(c) := a \cdot (1 - \exp(-b \cdot c))$

$f2(c) := -c \cdot \dfrac{Vs}{m2} + \dfrac{Cs \cdot Vs}{m2}$

$guess := \dfrac{Cs}{2}$

$Ceq := root(f(guess), guess)$

$c := 0, 0.01 \cdot Cs .. 1 \cdot Cs$
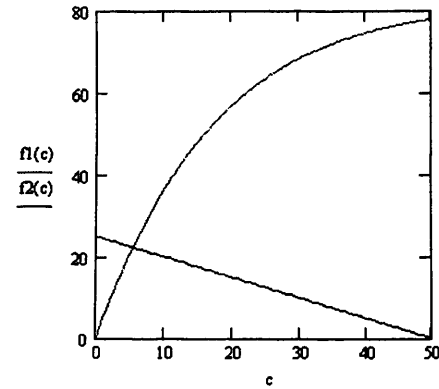
Free equilibrium concentration (uM) =

$Ceq = 5.339$

Ligand bound to MIP (nmol/mg) =

$f1(Ceq) = 22.331$

$\dfrac{Cs \cdot Vs}{m2} = 25$

validate total propranolol in system = Tp

$Tp := (Ceq \cdot Vs \cdot ms) + f1(Ceq) \cdot ms \cdot m2$

$Tp = 100.002$

$v := Vs \cdot ms$

$v = 2$

$m2 = 1$

$v2 := 2$

$Pr_2 := \dfrac{m2}{v2}$

Phase ratio

$Pr_2 = 0.5$

$Pr := \dfrac{m1}{vol}$

$Pr = 2$

Consider effect of leaching enabling extimation of measured
bound/free values from experimentally measured isotherm
where leaching of soluble fraction has occured to some
extent
binding curev equation constructed at a phase ratio of:
mass of MIP used to construct eq = m2
volume of solvent used to construct equation = v2
corrected phase ratio, i.e phase ratio giving rise to
ADDITIONAL leaching

$Pr_c := Pr - Pr_2$

$Pr_c = 1.5$

leached oligomer concentration in incubating solvent

$Cc_{oligfrac} := 0.1712 \cdot Pr_c - 0.015$

$Cc_{oligfrac} = 0.242$

mg per ml (apparent mass assuming equal binding site
density)
Assume soluble fraction binds with same characteristics as
'true' isotherm (extrapolated solid and soluble combined)
total bound and free

$$free_{tot} := Ceq \cdot vol$$

$$bound_{tot} := fl(Ceq) \cdot ml$$

$$bound_{tot} = 89.324$$

$$free_{tot} = 10.678$$

$$tot := bound_{tot} + free_{tot}$$

$$tot = 100.002$$

additioanl leached oligomer

$$oligc_{tot} := Cc_{oligfrac} \cdot vol$$

$$oligc_{tot} = 0.484$$

remaining microsphere mass

$$mipc_{spheremass} := ml - oligc_{tot}$$

$$mipc_{spheremass} = 3.516$$

sol fraction

$$solfractionc := \frac{oligc_{tot}}{mipc_{spheremass}}$$

$$solfractionc = 0.138$$

bound to sol fraction
this represents overestimation in free

$$boundc_{sol} := fl(Ceq) \cdot oligc_{tot}$$

represents additional concentration of:

$$boundc_{sol} = 10.799$$

$$concc_{overestimate} := \frac{boundc_{sol}}{vol}$$

$$concc_{overestimate} = 5.4$$

estimate of measured free conc

$$Ceq = 5.339$$

$$concc_{overestimate} = 5.4$$

$$freec := concc_{overestimate} + Ceq$$

$$freec = 10.739$$

bound to insoluble microspheres
This represents actual bound removed from incubation
solution by filtering

$$boundc_{insol} := fl(Ceq) \cdot mipc_{spheremass}$$

however, experimental analysis will think this is bound to
ALL weighed mass of polymer m1

$$boundc_{insol} = 78.525$$

apparent measured bound nmol/mg

$$boundc := \frac{boundc_{insol}}{ml}$$

$$boundc = 19.631$$
check total

$$checkc_{tot} := boundc \cdot ml + freec \cdot vol$$

check bound total

$$boundc_{totcheck} := boundc_{sol} + boundc_{insol}$$

$$checkc_{tot} = 100.002$$

$$boundc_{totcheck} = 89.324$$
$$p = 100$$

Appendix 5 Preliminary Attempts to Harvest a Soluble MIP Prepared at Near-θ Conditions

Following the findings of this chapter, limited experimental studies were conducted, attempting to harvest a soluble imprinted fraction prepared under the conditions of precipitation polymerisation. Precipitation polymerisation reactions were conducted in accordance with the method detailed in chapter 2 however the reactions were conducted in 50 ml volume centrifuge tubes. The reaction was monitored and polymer precipitation confirmed visually, signified by the reaction mixture beginning to become opaque, the reaction mixture was centrifuged to separate the precipitated and soluble fractions thus preventing the continued capture of growing oligomers by the precipitated spheres therefore increasing the proportion of soluble polymer. The reaction was then restarted and the process repeated several times. Upon quenching the reaction the precipitated material was removed and the solvent volume of the soluble fraction reduced. The soluble MIP fraction was then precipitated through addition of non-solvents; acetonitrile and water. The resultant precipitate could not be separated by centrifugation and intriguingly demonstrated a reversible effect, of displaying increased solubility in the toluene/acetonitrile/water environment at reduced temperatures (4°C). Due to time constraints it was not possible to process the material further, but the completely opaque suspension was indicative of a significant yield of polymer. The solubility of which could be modulated depending on the solvent environment. Development of this methodology may prove valuable in the production of soluble MIP material prepared under near-theta polymerisation conditions. Such a process combined with possible low temperature, near-theta, polymerisation (Chapter 2) is an exciting prospect. Additionally, it was reasoned that if precipitated polymer microspheres could be removed from the reaction media immediately upon their precipitation, the small sized precipitated microspheres would likely be soluble in a more solvating environment (i.e. chloroform). It may be possible to combine such an approach with low temperature near-theta polymerisation and to conduct the polymerisation under an applied external force (i.e. centrifugal), or alternatively the controlled mixing within segmented flow may provide and ideal platform for continuous polymer synthesis.

Appendices 6-14 Publications

[1] O.K. Castell, C.J. Allender, and D.A. Barrow, "Novel Biphasic Separations Utilising Highly Selective Molecularly Imprinted Polymers as Biorecognition Solvent Extraction Agents," *Biosensors and Bioelectronics*, vol. 22, Oct. 2006, pp. 526-533.

[2] O.K. Castell, C.J. Allender, and D.A. Barrow, "Microchip Solid-Phase-Enhanced Liquid Liquid Extractions Utilising Highly Selective Molecularly Imprinted Polymers as Chemorecognition Solvent Extraction Agents," *The Proceedings of µTAS 2006 Conference*, Tokyo, Japan: 2006, pp. 891-893.

[3] O.K. Castell, C.J. Allender, and D.A. Barrow, "Continuous molecular Enrichment in Microfluidic Systems," *Lab on a Chip*, vol. 8, 2008 pp. 1031-1033.

[4] O.K. Castell, C.J. Allender, and D.A. Barrow, "Liquid-Liquid Phase Separation: Characterisation of a Novel Device Capable of Separating Particle Carrying Multiphase Flows," *Lab on a Chip*, vol. 9, 2009, pp. 388-396..

[5] R. Göritz et al., "Microwave Compositional Analysis of Solvent Matrices in Microcapillary Manifold Systems," *The Proceedings of µTAS 2007 Conference*, Paris, France: 2007, pp. 1689-1691.

[6] A. Masood et al., "Microwave Split Ring Resonator Technique for High Sensitivity Compositional Analysis of Solvents in Microcapillary Systems," *The Proceedings of µTAS 2008 Conference*, San Diego, USA: 2008, pp. 1636-1638.

[7] O.K. Castell et al., "Microwave Technique For Monitoring Phase Separation Of A Multiphase-Flow Regime Utilised For Continuous Molecular Enrichment," *The Proceedings of µTAS 2008 Conference*, San Diego, USA: 2008, pp. 137-139.

[8] O.K. Castell, D.A. Barrow, and C.J. Allender, "Microfluidic Liquid Separation Device and Methods for Construction and Application." Patent Application Number: 0816001.2

[9] C.J. Allender et al., "A Glimpse of the Inner Workings of the Templated Site," *Chemical Communications*, 2009, pp. 165-167.

Novel biphasic separations utilising highly selective molecularly imprinted polymers as biorecognition solvent extraction agents

Oliver K. Castell [a,b], Christopher J. Allender [a,*], David A. Barrow [b]

[a] *Molecular Recognition Research Unit, Welsh School of Pharmacy, Cardiff University, Redwood Building,*
King Edward VII Avenue, Cardiff CF10 3XF, United Kingdom
[b] *metaFAB, Cardiff School of Engineering, Cardiff University, 1-5 The Parade, Cardiff CF24 3AA, United Kingdom*

Abstract

Molecularly imprinted polymers (MIPs) represent a class of artificial receptors that promise an environmentally robust alternative to naturally occurring biorecognition elements of biosensing devices and systems. However, in general, the performance of conventional MIPs in aqueous environments is poor. In the study reported here, this limitation has been addressed by the novel application of MIPs as a solvent extraction solid phase in a biphasic solvent system. This paper describes a previously unreported use of MIPs as solvent extraction reagents, their successful application to aqueous sample media and the opportunities for utilisation of this unique system in novel biosensing and separation procedures. This study demonstrates the development of a novel biphasic solvent system utilising MIP in the extracting phase to enhance both efficiency and selectivity of a simple two phase liquid extraction.

Monodisperse propranolol imprinted polymer microspheres [*p*(divinylbenzene-*co*-methacrylic acid)] were prepared by precipitation polymerisation. Initially, the affinity of the polymers for (*R,S*)-propranolol was assessed by established techniques whereby the MIP demonstrated greater affinity for the template than did the non-imprinted control polymer (NIP). Importantly, MIP performance was also assessed using the novel dual solvent system. The depletion of (*R,S*)-propranolol from the aqueous phase into the polymer containing organic phase was determined. When compared to control extractions containing no polymer the presence of MIP in the extracting solvent phase resulted in an increased extraction of (*R,S*)-propranolol from the aqueous phase. Importantly, this extraction was significantly greater in the presence of MIP when compared to NIP.

This unique principle generates opportunities for MIP based extractions and chemical enrichments in industrial applications, offering commercial, ecological and practical advantages to traditional solvent extraction techniques. The technique is readily transferable to analytical microsystems utilising MIP recognition elements generating promising opportunities for MIP based sensing of aqueous sample media.
© 2006 Elsevier B.V. All rights reserved.

Keywords: Liquid–liquid extraction; Solid phase extraction; Solvent extraction; Biosensing; Molecularly imprinted polymers; Molecular recognition; Precipitation polymerisation

1. Introduction

Molecularly imprinted polymers (MIPs) offer simple, customisable, rugged and cost effective alternatives to biological recognition systems (Allender et al., 1999; Piletsky et al., 2001). The technology of molecular imprinting involves the introduction of analyte specific binding sites within rigid, cross-linked, three-dimensional polymer matrices (Arshady and Mosbach, 1981; Whitcombe et al., 1995; Wulff and Biffis, 2001). This is

generally achieved through the formation of pre-polymerisation complexes between the analyte (template) molecule and functionally complementary monomers and their subsequent polymerisation in a porogenic environment in the presence of cross-linking monomer(s). Removal of the template molecule yields a functionally and spatially ordered imprinted site capable of rebinding the template molecule under appropriate conditions. Analyte recognition is achieved through a combination of both spatial and inter-molecular interactions between the analyte molecule and the polymer functionality at the binding site. MIPs have been utilised in wide variety of applications. Their specific recognition properties have been applied to chromatographic separations including chiral (Sellergren et al., 1985) and achiral

(Kempe and Mosbach, 1994) separations in high performance liquid chromatography (HPLC), solid phase extraction (SPE) (Sellergren, 1994) and bubble fractionation (Armstrong et al., 1998). MIPs have also been employed as recognition materials for sensors (Kriz et al., 1995) and catalysts in simple organic reactions (Leonhardt and Mosbach, 1987).

A well documented obstacle to the wider application of MIPs is the issue of aqueous compatibility (Ramström and Ansell, 1998). Although much progress has been made (Dirion et al., 2003) the performance of MIPs in water is still generally poor when compared to that in non-polar solvents. This is largely attributed to the competition between water and template for functionally important hydrogen bonding sites (Ramström and Ansell, 1998). The application of MIPs for use in aqueous environments is particularly desirable for the development of MIP based sensors and extractions in biological and environmental samples.

Liquid–liquid extraction, or solvent extraction, has been used for many years for the purification, separation, concentration or removal of desired compounds. Commonly employed as a purification technique in research and production synthetic chemistry, it has also been employed in a wide range of other applications including; examining contaminant levels in water (Franson, 1995), clean up and recycling of waste water (Kentish and Stevens, 2001), and the recovery of valuable metals (Diamantatos, 1977). The selectivity of the technique, when used alone, is restricted and only limited specificity can be achieved. However, more recently researchers have extended the range of application, and improved specificity and extraction efficiency, by the incorporation of a solvent extraction reagent into the extracting phase (Ishimori et al., 2006; Kara and Alkan, 2002; Snyder et al., 2005). This has been of commercial importance in the extraction of metal ions from an aqueous phase into an organic phase by using ion-selective binding reagents such as oligo-pyridine (Ishimori et al., 2006), *N-n*-octylaniline (Lokhande et al., 1998), or crown ethers (Kimura et al., 1979). Enantioselective partitioning has also been demonstrated by the inclusion of small-molecule chiral selectors in the extracting solvent (Snyder et al., 2005). The approach has also been extended to embrace the specific extraction of organic molecules from an organic solvent into an aqueous phase by utilisation of solubilising reagents such as cyclodextrins (Blyshak et al., 1988).

This paper describes the novel application of MIPs as solvent extraction reagents, their successful application to aqueous sample media and the opportunities for utilisation of this unique system in sensing and separation techniques. This study demonstrates the development of a novel biphasic solvent system utilising MIPs in the extracting phase to enhance both efficiency and selectivity of a simple two phase extraction.

For the purpose of this study spherical MIP particles, produced by precipitation polymerisation, were preferred as solvent extraction reagents, to those produced by traditional monolithic methods. The small (3–4 μm diameter) and regular particles formed by precipitation polymerisation were able to produce uniform suspensions in the organic solvent. This would have been intrinsically more difficult to achieve with the larger (45 μm

diameter) irregular shards of polymer yielded from more traditional monolithic approaches to molecular imprinting. Precipitation polymerisation has recently emerged as a desirable and scalable approach to adopt for the production of high quality, highly uniform, spherical imprinted particles. Unlike the suspension polymerisation approach to generating spherical polymer particles the precipitation technique does not require the use of surfactant or steric stabilisers. The resulting particles therefore have a clean stabiliser free surface and carry no ionic charge (Li and Stöver, 1993; Li and Stöver, 1998). Spherical MIPs were first reported to be prepared using this method in 1999 (Ye et al., 1999), with the production of sub-micron sized imprinted polymer spheres by the polymerisation of monomers in dilute solutions. Subsequent work (Wang et al., 2003), utilising an approach first reported by the polymer chemist Stöver (Li and Stöver, 1998), tailored MIP particle growth by subtle refinement of the solvent and porogen system to create a polymerisation environment at near θ conditions. This enabled the production of larger, imprinted, mono-dispersed microspheres, typically up to 5 μm in diameter, and provided some control over the size and porosity of the resultant polymer.

In both the traditional monolithic and precipitation polymerisation approaches to MIP production, early polymer growth occurs in solution, where highly cross-linked oligomer radicals form. These resulting oligomers grow, cross-link and aggregate to form small, early-stage polymer spheres. In the production of MIP monoliths where high monomer:solvent ratios are used, these spheres continue to grow and coalesce until one continuous macro-porous polymer network has been formed. However, when the polymerisation is conducted in a large excess of organic solvent, as is the case with precipitation polymerisation where monomer concentrations are typically less than 5%, the initial polymer spheres do not overlap nor coalesce but continue to grow individually by capturing newly formed oligomers and monomers (Li and Stöver, 1998). In a poorly solvating medium, where the growing polymer has little affinity for the surrounding solvent, phase separation occurs early and dense, non-porous polymer microspheres are formed. When the solvating property of solvent media is increased, phase separation is delayed, allowing the entrapment of solvent within the growing polymer prior to precipitation. This results in the formation of many small micro-/meso-pores throughout the forming polymer microsphere (Li and Stöver, 1998).

The point at which phase separation occurs is governed by the polymer/solvent system's proximity to θ-conditions. In a theta solvent system for the forming polymer, a theta temperature is defined as the temperature at which excess chemical potential and, correspondingly, the excess Gibbs energy of dilution is zero (Brandrup and Immergut, 1989), and thus, the solution in the theta state is thermodynamically pseudo-ideal (Brandrup and Immergut, 1989). Therefore, the composition of the polymer, composition of the solvating environment and temperature of the polymerisation, all have an effect on the point of phase separation, and thus, the morphology of the polymer produced. From a practical perspective, polymer microspheres precipitated in near θ-conditions will typically be expanded, porous, and several micrometer in diameter. In contrast, polymers formed

* Corresponding author. Tel.: +44 29 20875824; fax: +44 29 20874149.
E-mail address: allenderej@cf.ac.uk (C.J. Allender).

either side of this point will be either be non-particulate, continuous and gel like or sub-micron, dense, non-porous, particulates (Downey et al., 2001).

2. Materials and methods

2.1. Materials

Methacrylic acid (MAA), (R,S)-propranolol hydrochloride, pindolol, naproxen and acebutolol hydrochloride were obtained from Sigma (Gillingham, UK). Divinylbenzene (DVB) technical grade 80%, was obtained from Aldrich (Gillingham, UK). 2'2-Azobisisobutyronitrile (AIBN) and toluene were purchased from Acros Organics (Loughborough, UK). Vanillic acid was obtained from Fluka (Gillingham, UK), and acetonitrile, chloroform and methanol were purchased from Fisher Scientific (Loughborough, UK). All chemicals and solvents were analytical or HPLC grade and were used without further purification. Fluorescent analysis was performed using a Fluostar Optima 96-well plate reader (BMG Labtech, Aylesbury, UK). HPLC analysis of acebutolol was conducted on a Thermo TSP HPLC system (Thermo Electron Corporation, Runcorn, UK). Sizing of polymer microspheres was conducted by laser diffraction (Coulter N4 plus, Beckman, High Wycombe, UK).

2.2. MIP microsphere production by precipitation polymerisation

Uniform imprinted and non-imprinted polymer microspheres were prepared by precipitation polymerisation (Wang et al., 2003). (R,S)-Propranolol base (389.0 mg, 1.5 mmol) (converted from the HCl salt by NaOH solution and subsequent filtration), MAA (509 μl, 6.0 mmol), DVB (4.103 ml, 28.8 mmol), and AIBN (312.0 mg, 1.9 mmol) were dissolved in 128 ml 82.5/17.5% (v/v) mixture of acetonitrile and toluene in a 250 ml round-bottomed flask. The solution was sparged with oxygen-free nitrogen for 10 min at 0 °C. Subsequently, the sealed flask was rotated at 7(1/2) rpm at 60 °C in a water bath for 24 h. At the end of the reaction the polymer microspheres were recovered by filtration and washed successively with acetonitrile (60 ml), toluene (60 ml), methanol/acetic acid 70/30 (120 ml), methanol (40 ml), acetonitrile (40 ml), toluene (40 ml), acetonitrile (40 ml), and methanol (40 ml). The reclaimed microspheres were then dried under vacuum overnight at room temperature. Non-imprinted polymer (NIP) microspheres were prepared in the same way as the MIP microspheres but using 128 ml 90/10% (v/v) mixture of acetonitrile and toluene and with the omission of (R,S)-propranolol.

2.3. Binding assays

Polymer microsphere particles (1 mg) were mixed with 2 ml of solvent containing 25 μM concentration of (R,S)-propranolol or cross-reactant species. In the case of saturation binding studies polymer microsphere particles (1 mg) were mixed with 2 ml of solvent containing 25, 50, 100, 250 or 500 μM concentrations of (R,S)-propranolol. Samples were incubated for 24 h at

room temperature and agitated by rocking. The sample mixtures were filtered using PTFE 0.20 μm membrane filters and the filtrate analysed by either HPLC or microplate fluorescence spectroscopy.

2.4. Two phase depletion analysis

1 mg of polymer microsphere particles were suspended in 2 ml of chloroform or hexane in a glass sample vial, to which 2 ml of de-ionised water containing 50 μM (R,S)-propranolol hydrochloride was added. This resulted in the formation of two immiscible phases with the polymer microsphere particles suspended entirely in the organic phase. Samples were incubated for 24 h at room temperature and agitated by rocking. The aqueous phase was sampled and analysed by microplate fluorescence spectroscopy to determine the remaining concentration of (R,S)-propranolol. Control experiments were conducted in the absence of any polymer particles.

2.5. Substrate and cross-reactant detection and quantification

Microplate fluorescence spectroscopy was utilised for the detection and quantification of the intrinsically fluorescent ligands: propranolol (excitation λ 290 nm, emission λ 330 nm), pindolol (excitation λ 260 nm, emission λ 310 nm), naproxen (excitation λ 330 nm, emission λ 360 nm) and vanillic acid (excitation λ 290 nm, emission λ 330 nm). 200 μl sample volumes were employed and three replicate wells were analysed for each individual experiment. Acebutolol binding was characterised by HPLC analysis [column: Genesis C_{18} 4 μm, 15 cm × 4.6 mm Grace Vydac (Worms, Germany). Mobile phase: phosphate buffer 10 mM, pH 6.2 and methanol (1:1), flow rate: 1 ml min^{-1}, UV detection λ 235 nm, injection volume: 20 μl]. Samples in chloroform were evaporated to dryness and reconstituted with an equal volume of methanol.

3. Results and discussion

3.1. Polymer production

In the production of MIP and NIP a white powder was recovered upon filtration. After washing and drying the polymer particles were visualised by light microscopy. Both MIP and NIP particles were observed to be spherical, near-monodispersed, with a narrow size distribution. The mean particle diameter measured by laser diffraction scattering was found to be 3.6 μm (S.D., 1.4 μm) for MIP spheres and 3.9 μm (S.D., 1.6 μm) for NIP spheres.

In preliminary studies it was observed that when MIP and NIP microspheres were prepared using the same ratio of acetonitrile/toluene, the MIP microspheres were significantly smaller than the NIP microspheres. This indicated that the template was having a significant impact on the solvating properties of the solvent environment for the growing polymer and this was affecting θ-conditions and therefore phase separation. The concern was that there may be a significant difference in the morphology of

the two polymers and that this variation would later complicate interpretation of binding data. Therefore, in order to try to obtain morphologically equivalent polymers, it was considered important to attempt to match both the size and growth rate of the MIP and NIP microspheres. In order to compensate for the absence of (R,S)-propranolol in the production of the NIP (control) the toluene and acetonitrile composition of the solvating media was adjusted slightly by decreasing the toluene component from 17.5 to 10%. It was reasoned that if phase separation, which occurs when a polymer chain reaches the size where solvent/polymer interactions become unfavourable and the polymer chain precipitates, could be achieved at a comparable point in both the MIP and NIP, the porosity, density and therefore the size of the final microsphere would be comparable. The precise rationale for the effect caused by the presence or absence of template species and the adjustment of solvating media appears to be more complex than simply relating the solubility of the monomers to the solvent media. Exposed, concealed and self-complementary functionality in the evolving MIP and NIP systems, polymer flexibility and also the solvating effect of template molecules remaining in the solvent media itself, may also play an important role.

3.2. Evaluation of polymer rebinding performance

The binding of (R,S)-propranolol to both MIP and NIP was assessed in a range of polar, non-polar and intermediate solvents (Fig. 1). In all cases, the MIP bound more propranolol than did the NIP. However, in extreme non-polar and polar solvents, i.e. hexane, toluene and water a large degree of non-specific binding was observed as demonstrated by at least 25 nmol (50%) of the propranolol binding to the NIP in each of the three instances. This was unsurprising due to the extreme nature of the solvent environment and the relatively low solubility of propranolol base in these media. Despite this the MIP appears to show a degree of template recognition in both polar and non-polar environments, suggesting that the recognition mechanisms involve both polar and non-polar interactions between the template and the MIP binding site. In non-polar environments template recognition and binding may occur in part through hydrogen bond donor and acceptor interactions between the alcohol and ether groups on the propranolol moiety (illustrated in Fig. 4) and the

carboxylic acid groups of the polymer. Proton transfer and subsequent ionic interactions may also occur through proton donation from the carboxylic acid residue of methacrylic acid to the basic secondary amine of the propranolol molecule. In polar environments hydrophobic interactions such π–π interactions between the aromatic naphthalene moiety of the propranolol structure and the aromatic functionality of divinylbenzene cross-linking monomers may contribute to template recognition. In intermediate environments, a combination of these processes may be responsible of binding of propranolol to the MIP. The performance of the MIP in chloroform was particularly noteworthy as although the total amount bound, 20 nmol, was less than in aqueous, hexane or toluene environments it could almost totally be attributed to specific template-binding site recognition mechanisms as just 1.9 nmol (R,S)-propranolol was observed to bind to the NIP microspheres.

The initial performance of the MIP in chloroform and the essential immiscible nature of the solvent in water made chloroform a suitable solvent for use in a proof of principle demonstration of the novel two phase MIP binding system. The effect on template rebinding to the MIP by the small amount of water that would dissolve in chloroform in a two phase system was investigated by assessing the binding of (R,S)-propranolol to both MIP and NIP microspheres in water saturated chloroform (0.815% H_2O) (Fig. 2). Surprisingly, the presence of water in chloroform had little observable effect on propranolol binding to either the MIP or the NIP. It would be reasonable to predict that the addition of 0.815% water to the chloroform would have some effect on either specific or non-specific polymer-template binding interactions due to competition for hydrogen bond interactions with the polymer (Allender et al., 1997). The fact that this was not observed suggests that either recognition is achieved purely through apolar interactions, which considering the complementary functionality of the propranolol moiety and MAA monomers, would seem unlikely. Or more perhaps more conceivably, the considerably hydrophobic nature of the divinylbenzene based polymers largely inhibits water molecules from entering the pores and template specific binding sites, thus minimising the hydrogen bond disrupting effects of water. This theory is supported by the reported application of mineral oil coatings to MIP particles in order to create a hydrophobic envi-
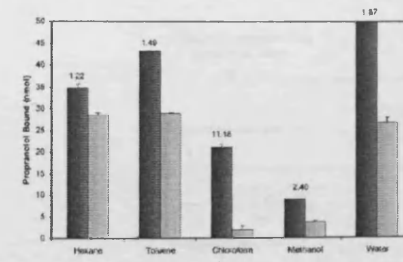

Fig. 1. (R,S)-Propranolol bound to MIP or NIP in a range of solvents with MIP:NIP binding ratios ($n = 5 \pm$ S.E.M.).
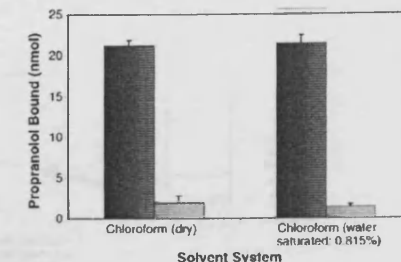

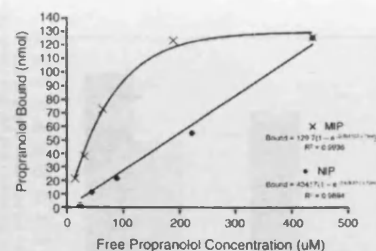Fig. 2. Binding of (R,S)-propranolol to MIP and NIP in dry and water saturated chloroform ($n = 5 \pm$ S.E.M.).

Fig. 3. Equilibrium binding of (R,S)-propranolol to MIP or NIP at a range of (R,S)-propranolol concentrations in water saturated (0.815%) chloroform (n = 5).

ronment for template rebinding in polar media (Piletska et al., 2005).

MIP saturation binding studies were conducted using a range of concentrations of (R,S)-propranolol (Fig. 3). A logarithmic like plot characteristic of saturable binding was observed for the binding of propranolol to the MIP microspheres. A linear relationship suggestive of non-specific binding to a large number of non-specific sites was observed over the same concentration range for the NIP microspheres. This data is indicative of a true molecular imprinting effect being observed with the (R,S)-propranolol MIP microspheres. Further studies, quantifying the cross-reactive binding of a number of template related and non-related analytes, were undertaken to confirm the presence of a molecular imprinting effect.

3.3. Evaluation of cross-reactant binding

Fig. 4 shows the binding of cross-reactant compounds to both the MIP and NIP in comparison to the binding of the template species (R,S)-propranolol. Two compounds pharmacologically and structurally related to propranolol were investigated, the β adrenoceptor antagonists pindolol and acebutolol. In addi-

tion two structurally and pharmacologically unrelated chemical species were also investigated; naproxen and vanillic acid. The MIP showed comparable quantitative binding to both pindolol and acebutolol as it did to propranolol the template species (20–25 nmol). Importantly, in the case of pindolol and acebutolol, the extent of non-specific binding, approximating to the binding to the non-imprinted polymer, was significantly greater than that observed with propranolol, indicative of the MIP microspheres having greater specificity for propranolol. The cross-reactivity demonstrated by the MIP for the compounds structurally related to the template species is unsurprising since pindolol and acebutolol both share structural, positional and functional similarities to propranolol, such as, an aromatic moiety, tertiary alcohol, ether and secondary amine (Fig. 4). This is pharmacologically demonstrated by the ability of all three compounds to act as antagonists to the β₁ subclass of adrenoceptors and the pharmaceutical application of this activity. The binding of naproxen and vanillic acid to the MIP was substantially less than that seen with propranolol and the other β adrenoceptor antagonists (<2 nmol). The extent of non-specific binding to the NIP microspheres in water saturated chloroform appeared to show a general correlation with calculated log P values for the five compounds. Propranolol and naproxen with log P values of 3.35 and 2.97, respectively, demonstrated low levels of non-specific binding to the NIP, whilst vanillic acid (log P = 1.35), pindolol (1.19) and acebutolol (2.02) bound in greater quantities (Fig. 4). Naproxen was seen to bind comparably to both the imprinted and non-imprinted microspheres. Interestingly, vanillic acid was found to have greater affinity for the non-imprinted polymer microspheres than it did for the propranolol imprinted polymer microspheres, although binding in both cases was low at 1.7 and 5.6 nmol to the MIP and NIP, respectively. The reason for this observation may be explained by the greater presence of surface immobilised methacrylic acid moieties incorporated into the NIP microspheres, which, in the MIP microspheres may often be occluded within template specific binding sites. This phenomenon would expose a greater number of hydrogen

Fig. 4. Cross-reactivity binding of structurally related and unrelated compounds to MIP and NIP in water saturated (0.815%) chloroform (n = 5 ± S.E.M.).

Table 1
Quantity of (R,S)-propranolol (nmol) in each solvent phase or bound to polymer microspheres at equilibrium in two phase binding studies

	Location of (R,S)-propranolol by phase (nmol) (100 nmol total)				Binding ratio MIP/NIP	Binding ratio (MIP/NIP) in organic solvent alone (Fig. 1)
	Aqueous phase	Partition coefficient (aqueous/organic)	Organic phase	Polymer bound		
H₂O	100.00	–	–	–	1.56	1.22
H₂O + C₆H₁₄ [a]	82.04 (0.04)	4.568	17.96	–		
H₂O + C₆H₁₄ + NIP [b]	37.60 (0.26)	4.568	8.23	54.17		
H₂O + C₆H₁₄ + MIP [c]	12.88 (0.35)	4.568	2.82	84.30		
H₂O	100.00	–	–	–	12.21	11.18
H₂O + CHCl₃ [a]	7.57 (0.28)	0.082	92.43	–		
H₂O + CHCl₃ + NIP [b]	7.15 (0.20)	0.082	87.31	5.54		
H₂O + CHCl₃ + MIP [c]	2.45 (0.41)	0.082	29.92	67.63		

Results calculated from measurement of propranolol depletion from the aqueous phase due partitioning into immiscible organic solvent (chloroform or hexane) [a], partitioning into immiscible organic solvent (chloroform or hexane) containing suspended NIP microspheres [b] and partitioning into immiscible organic solvent (chloroform or hexane) containing MIP microspheres [c]; n = 5 (CV).

bond donor and acceptor species on the NIP microsphere surface which would be available for polar interactions with the ligand, thus potentially increasing non-specific binding to the NIP. This theory coupled with the necessity to morphologically match the NIP microspheres to the MIP microspheres illustrates the inherent difficulties with control experiments in the field of molecular imprinting.

3.4. Propranolol depletion from an aqueous phase in a two phase solvent system in the presence of MIP microsphere particles

The depletion of (R,S)-propranolol from a 50 μM aqueous sample after extraction with organic solvent (hexane or chloroform) in the absence of polymer, and in the presence of either MIP or NIP microspheres suspended in the organic phase was measured [(MIP/hex/aq), (NIP/hex/aq), (no-polymer/hex/aq), (MIP/chloro/aq), (NIP/chloro/aq) and (no-polymer/chloro/aq)]. It was observed that in both hexane and chloroform the MIP and NIP particles appeared to remain solely suspended in the organic phase, with no polymer entering the aqueous layer. This may be attributed to the hydrophobic nature of the largely DVB based polymers. This phenomenon was key in this MIP-based two-phase extraction. However, this is not essential for the application of this principle in biphasic MIP based sensing systems.

In such devices the polymer would likely be immobilised on the sensor surface contained within a micro-environment of the partitioning phase.

Table 1 shows the distribution of (R,S)-propranolol between the aqueous, organic and polymer phases. The quantity of (R,S)-propranolol remaining in the aqueous phase was measured, and from this the quantity of (R,S)-propranolol unbound in the organic phase was calculated using a measured partition coefficient of (R,S)-propranolol between aqueous and organic solvents (aqueous/organic). This enabled the quantitative determination of (R,S)-propranolol bound to the MIP and NIP microspheres.

As in traditional batch evaluation of polymer binding, equilibrium is established between bound and free ligand. In the case of this dual solvent and polymer system equilibrium is established between the three phases (Fig. 5). In the organic phase (R,S)-propranolol binds to the polymer as it would in a single phase solvent system (Fig. 3), whilst the partition coefficient defining the free (R,S)-propranolol in each solvent phase is maintained. The partition coefficient for the partitioning of (R,S)-propranolol between water and hexane (4.568) and water and chloroform (0.082) represent scenarios where the majority of the analyte will partition into the aqueous phase, in the case of hexane, or into the organic phase in the case of chloroform. The results illustrated in Table 1 and Fig. 6 demonstrate that in

Fig. 5. Schematic illustration of enhanced selective extraction utilising MIP microspheres as a solvent extraction reagent.

Fig. 6. Additional extraction of (R,S)-propranolol from the aqueous phase with the addition of MIP or NIP to the extracting hexane or chloroform component in the two-phase system. Expressed as a percentage of (R,S)-propranolol remaining in the aqueous after extraction with organic solvent alone (n = 5 ± S.E.M.).
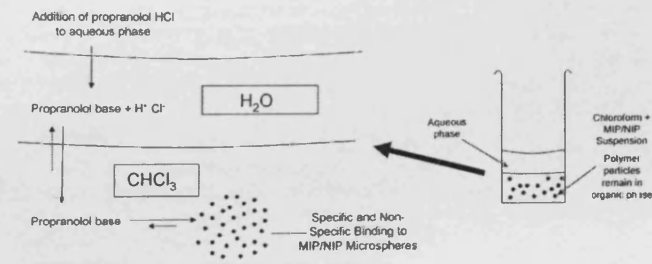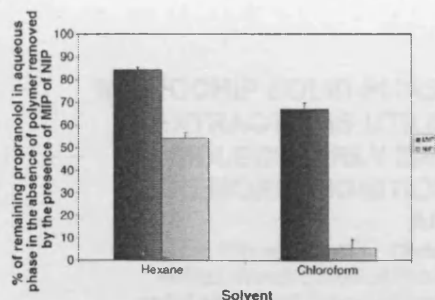
either situation the presence of MIP in the organic phase significantly enhances depletion of (R,S)-propranolol from the aqueous phase compared to the extraction seen by organic solvent alone or organic solvent containing suspended NIP microspheres. In both solvent systems the MIP was shown to bind the majority of (R,S)-propranolol present in the system [84.30% (hexane) and 67.63% (chloroform)]. In the single solvent template binding studies (Fig. 1) a large amount of non-specific binding to the NIP microspheres was observed in hexane due to its extreme non-polar nature. In the dual solvent NIP/hex/aq system nonspecific binding to the NIP resulted in a significant increase in extraction of (R,S)-propranolol from the aqueous phase compared to extraction with hexane alone. However, the amount of (R,S)-propranolol remaining in the aqueous phase in MIP/hex/aq system was significantly lower still, at one-third of that seen in the NIP/hex/aq system.

In the case of chloroform as the organic solvent phase, MIP/chloro/aq significantly increased the extent of depletion of (R,S)-propranolol from the aqueous phase. Whilst in the NIP/chloro/aq system only a small increase in removal of (R,S)-propranolol from the aqueous phase was observed when compared no-polymer/chloro/aq. This can be attributed to the high levels of specific binding to the MIP and the very low level of non-specific binding to the NIP observed in batch binding studies conducted in chloroform (Figs. 1–4). Evaluation of the performance of the MIP microspheres in the biphasic solvent system was conducted by calculating the binding ratio MIP:NIP. For both hexane and chloroform, the binding ratio in the dual solvent environment was found to be extremely close to the ratios calculated for MIP and NIP binding in the organic solvent alone (Figs. 1 and 2). The binding ratios are shown in Table 1. Fig. 3 illustrates that MIP:NIP binding ratio varies with free (R,S)-propranolol concentration. The small changes observed for MIP:NIP binding ratio in the dual solvent system compared to those of the single solvent system may therefore arise due to the difference in free concentration of (R,S)-propranolol in the organic phase at equilibrium in the presence of a second solvent phase.

4. Conclusions

A novel, yet simple, method for the application of molecularly imprinted polymer based recognition and extraction systems for analytes in aqueous sample media has been successfully demonstrated. This provides the opportunity for further widening the scope of molecularly imprinted recognition materials in applications such as sensors and assays operating in, or with, aqueous based, biological and environmental media. The prospect of sensors utilising immobilised MIP recognition elements in a micro-environment of organic solvent contained within a semi-permeable membrane for sensing in aqueous sample media is a realistic and promising possibility. The unique principle generates further possibilities for MIP based extractions or enrichment of chemical species in industrial applications. The inclusion of high affinity and capacity selective MIP binding agents in solvent extraction systems will allow for smaller volumes of organic solvent to be employed offering environmental, commercial and safety advantages, whilst also lowering the potential for cross-contamination of the aqueous source with organic pollutants. Furthermore, the solid phase MIP included in the extracting phase can subsequently be easily separated from the organic liquid for reclaiming of the analyte, cleaning and recycling of the MIP and organic solvent. Ongoing and future work is aimed at utilising this unique and previously unreported principle in the demonstration and optimisation of on-chip microfluidic MIP based template specific extractions.

References

Allender, C.J., Heard, C.M., Brain, K.R., 1997. Chirality 9, 238–242.
Allender, C.J., Heard, C.M., Brain, K.R., 1999. Prog. Med. Chem. 36, 235–291.
Armstrong, D.W., Schneiderheinze, J.M., Hwang, Y.-S., Sellergren, B., 1998. Anal. Chem. 70, 3717–3719.
Arshady, R., Mosbach, K., 1981. Macromol. Chem. Phys. (Makromol. Chem.) 182, 687–692.
Blyshak, L.A., Rossi, T.M., Patonay, G., Warner, I.M., 1988. Anal. Chem. 60, 2127.
Brandrup, J., Immergut, E.H., 1989. Polymer Handbook, third ed. Wiley-Interscience, New York.
Diamantatos, A., 1977. Anal. Chim. Acta 94, 49–55.
Dirion, B., Cobb, Z., Schillinger, E., Andersson, L.I., Sellergren, B., 2003. J. Am. Chem. Soc. 125, 15101–15109.
Downey, J.S., McIsaac, G., Frank, R.S., Stöver, H.D.H., 2001. Macromolecules 34, 4534–4541.
Franson, M.A., 1995. Standard Methods for the Examination of Water and Waste Water, 19th ed. American Public Health Association, Washington, DC.
Ishimori, K.-I., Watanabe, M., Kimura, T., Murata, M., Nishihara, H., 2006. Proceedings of Rare Earths'04 in Nara, Japan, vol. 408–412. J. Alloys Compd., 1278–1282.
Kara, D., Alkan, M., 2002. Microchem. J. 71, 29–39.
Kempe, M., Mosbach, K., 1994. J. Chromatogr. A 664, 276–279.
Kentish, S.E., Stevens, G.W., 2001. Chem. Eng. J. 84, 149–159.
Kimura, K., Maeda, T., Shono, T., 1979. Talanta 26, 945–949.
Kriz, D., Ramström, O., Svensson, A., Mosbach, K., 1995. Anal. Chem. 67, 2142–2144.
Leonhardt, A., Mosbach, K., 1987. React. Polym. 6, 285–290.
Li, K., Stöver, H.D.H., 1993. J. Polym. Sci. Part A Polym. Chem. 31, 3257–3263.
Li, W.-H., Stöver, H.D.H., 1998. J. Polym. Sci. Part A Polym. Chem. 36, 1543–1551.
Lokhande, T.N., Anuse, M.A., Chavan, M.B., 1998. Talanta 47, 823–832.
Piletska, E.V., Romero-Guerra, M., Guerreiro, A.R., Karim, K., Turner, A.P.F., Piletsky, S.A., 2005. Anal. Chim. Acta 542, 47–51.
Piletsky, S.A., Alcock, S., Turner, A.P.F., 2001. Trends Biotechnol. 19, 9–12.
Ramström, O., Ansell, R.J., 1998. Chirality 10, 195–209.
Sellergren, B., 1994. Anal. Chem. 66, 1578–1582.
Sellergren, B., Ekberg, B., Mosbach, K., 1985. J. Chromatogr. 347, 1–10.
Snyder, S.E., Carey, J.R., Pirkle, W.H., 2005. Tetrahedron 61, 7562–7567.
Wang, J., Cormack, P.A.G., Sherrington, D.C., Khoshdel, E., 2003. Angew. Chem. Int. Ed. 42, 5336–5338.
Whitcombe, M.J., Rodriguez, M.E., Villar, P., Vulfson, E.N., 1995. J. Am. Chem. Soc. 117, 7105–7111.
Wulff, G., Biffis, A., 2001. Molecularly Imprinted Polymers—Man-made Mimics of Antibodies and Their Applications in Analytical Chemistry. Elsevier, Oxford.
Ye, L., Cormack, P.A.G., Mosbach, K., 1999. Anal. Comm. 36, 35–38.

MICROCHIP SOLID-PHASE-ENHANCED LIQUID-LIQUID EXTRACTIONS UTILISING HIGHLY SELECTIVE MOLECULARLY IMPRINTED POLYMERS AS CHEMORECOGNITION SOLVENT EXTRACTION AGENTS

Oliver Castell[*,**]   Chris Allender[*]   David Barrow[**]

[*] MRRU, Welsh School of Pharmacy, Cardiff University, Cardiff. UK.
[**] metaFAB, Cardiff School of Engineering, Cardiff University, Cardiff. UK.

Abstract

Molecularly imprinted polymers (MIPs) are a class of artificial receptors that promise an environmentally robust alternative to naturally occurring bio-recognition elements of chemical sensing devices and systems [1]. This work reports for the first time the application of MIPs in microfluidic systems to enhance solvent extraction. This paper describes the use of MIPs as solvent extraction reagents in microfluidic biphasic solvent systems, their successful interface to aqueous sample media and the opportunities for utilisation of this unique system in novel microscale separation procedures. This study demonstrates the development of a novel multiphase flow microfluidic system utilising MIPs in the extracting phase to enhance both efficiency and selectivity of a simple two phase liquid extraction.

Keywords: microscale, liquid extraction, solid-phase-extraction, solvent extraction, biosensing, molecularly imprinted polymers, multi-phase flow.

1. Introduction

Liquid – liquid extraction, or solvent extraction, has been used for many years for chemical and biochemical purifications, separations, and enrichments. In conventional use the efficiency and selectivity of the technique is restricted. Following a recent study in which MIPs were used to enhance macro-scale extraction [2], and with the escalating interest in miniaturised, scalable and automated laboratory processes, this work presents the novel concept of highly efficient on-chip micro-extractions utilising MIPs as artificial receptors in multi-phase flow microfluidic systems.

2. Theory

Molecularly Imprinted Polymers (MIPs) offer simple, customisable, rugged and cost effective alternatives to biological recognition systems [1]. The methodology involves the introduction of analyte specific binding sites within rigid, cross-linked, three dimensional polymer matrices [3]. This is achieved through the formation of pre-polymerisation complexes between the analyte (template) molecule and functionally complementary monomers and their subsequent polymerisation in a porogenic environment in the presence of cross-linking monomer(s). Template removal yields a functionally and spatially ordered imprinted site capable of rebinding the template molecule. Recognition is achieved through a combination of spatial and inter-molecular interactions between analyte and polymer functionality at the binding site.
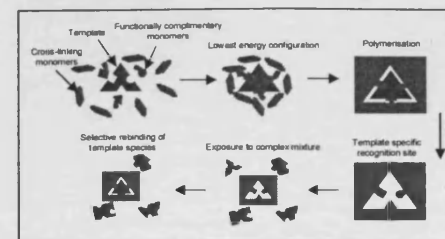
Fig 1. Schematic illustrating molecular imprinting methodology

Segmented flow regimes of alternating immiscible organic and aqueous fluid packets are characterised by each fluid packet having high internal mixing and a continually refreshing fluidic interface between contiguous fluid segments [4] (Fig 2). This unique mixing property is unusual as microfluidic systems overwhelmingly display laminar flow characteristics associated with low Reynolds number channel geometries. This important property allows the rapid attainment of chemical equilibrium between adjacent fluid phases [4].
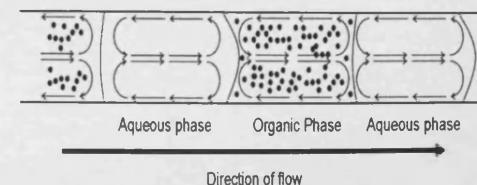
Fig 2. Schematic of on-chip segmented flow regime

Aqueous phase   Organic Phase   Aqueous phase

Direction of flow

The novel presence of solid-phase MIP particles in the organic liquid phase was predicted to enhance the specific transfer of analyte from the aqueous phase to the organic phase by maintaining a significant concentration gradient between the two immiscible fluid phases.

3. Experimental

Monodisperse propranolol imprinted polymer microspheres [p(divinylbenzene-co-methacrylic acid)] were prepared by precipitation polymerisation [2] (Fig 3). The affinity of the polymers for propranolol was
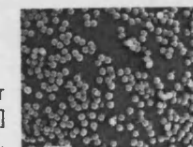
Fig 3. MIP microspheres

assessed by established techniques [2]. Segmented flow regimes were generated in a micromilled PTFE reactor incorporating T-junction geometry and a 35 cm channel length for extraction.

4. Results and Discussion

The MIP particles demonstrated greater affinity for the template species than did the non-imprinted polymer (control) particles (NIP) (Fig 4). On-line flow through UV absorbance spectrophotometry of the microfluidic segmented flow regimes demonstrated a significant increase in removal of propranolol from the aqueous phase in the presence of MIP compared to organic solvent (hexane) alone. UV absorbance data illustrates almost complete removal of propranolol from the aqueous stream. (Fig 6) The key property of this system is that this extraction would be *molecularly selective* [2].

Fig 4. Propranolol bound to MIP and NIP (control)
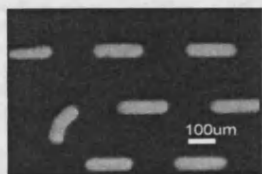
Fig 5. MIP enhanced segmented flow extraction fluorescent image
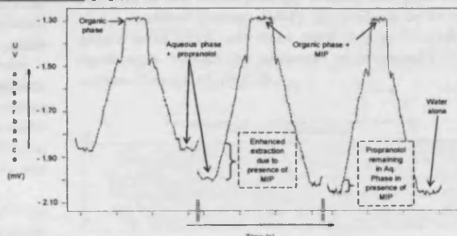
Fig 6. Composite on-line UV absorbance data for propranolol extractions into hexane ±MIP

5. Conclusion

This unique principle generates opportunities for on-chip MIP based extractions and chemical enrichments in industrial applications, offering commercial, ecological and practical advantages to traditional solvent extraction techniques. Ongoing work involves the incorporation of an integrated on-chip capillary force fluid phase separator to allow further analyte manipulations and recovery as well as quantitative analysis of MIP-enhanced extraction efficiencies.

References

[1] C. Allender, C. Heard and K. Brain, *Molecularly imprinted polymers - Preparation, biomedical applications and technical challenges. Progress in Medicinal Chemistry*, 36, pp. 235-291, (1999).
[2] O. Castell, C. Allender and D. Barrow, *Novel biphasic separations utilising highly selective molecularly imprinted polymers as biorecognition solvent extraction agents*, Biosensors and Bioelectronics, in press.
[3] G. Wulff and A. Biffis, *Molecularly imprinted polymers - Man-made mimics of antibodies and their applications in analytical chemistry*. Elsevier, Oxford. (2001).
[4] N. Harries, J. Burns, D. Barrow and C. Ramshaw, *A numerical model for segmented flow in a microreactor*, Journal of Heat and Mass Transfer 46, pp 3313 – 3322, (2003).

Continuous molecular enrichment in microfluidic systems†

Oliver K. Castell,*[a,b] Christopher J. Allender[a] and David A. Barrow[b]

Highly efficient molecular extractions in continuous flow microfluidic systems are demonstrated utilising the rapid mixing properties of biphasic segmented flow in conjunction with suspended micro-particulate adsorbents. A continuous flow technique providing potential for continual on-line sample enrichment, purification and clean-up in chemical synthesis, and sample preparation.

We report a novel strategy for performing highly efficient molecular extractions in continuous flow microfluidic systems. This previously unreported approach utilises the accelerated mass transfer properties of microfluidic segmented flow in conjunction with incorporated adsorbent micro-particulate material to massively enhance the efficiency of traditional solvent–solvent extraction. In this demonstration, a molecularly specific adsorbent, in the form of a molecularly imprinted polymer, is suspended in an extracting organic solvent to facilitate analyte specific enhanced extraction of propranolol from an aqueous sample. The continuous flow nature of the technique provides potential for flow-through sample enrichment, purification and clean-up in chemical synthesis, sample preparation and multiphase chemistry.

In microfluidic systems the flow of a single fluid phase in an open channel is overwhelmingly laminar due to the dominance of viscous forces over inertial forces. This results in mixing being restricted and mass transfer being primarily driven by diffusion.[1] This problem has frequently been addressed through the use of long channels and slow flow rates. An alternative strategy utilises segmented flow regimes of two immiscible fluid phases to bring about efficient mass transfer.[2] Segmented flow regimes of alternating immiscible organic and aqueous fluid packets are characterised by each fluid packet exhibiting high internal mixing and there being a continually refreshing fluidic interface between contiguous fluid segments[3] (Fig. 1). These important properties allow the rapid attainment of chemical equilibrium between adjacent fluid phases.[4]

It was proposed that the inclusion of solid phase adsorbent particles in an extracting/segmenting phase would enhance the transfer of analyte from a sample phase to the immiscible extracting phase by maintaining a significant concentration

[a]Molecular Recognition Research Unit, Welsh School of Pharmacy, Cardiff University, King Edward VII Avenue, Cardiff, UK. E-mail: castellok@cardiff.ac.uk, allendercj@cardiff.ac.uk; Fax: +44 (0)29 208 74149; Tel: +44 (0)29 208 75824
[b]metaFAB, School of Engineering, Cardiff University, The Parade, Cardiff, UK. E-mail: barrow@metafab.net; Tel: +44 (0) 780 983 9979
† The HTML version of this article has been enhanced with colour images.

Fig. 1 Computational fluid dynamic model of the internal vortex flow within each of two immiscible phases of a microfluidic biphasic segmented flow regime. The continually refreshing fluidic interface facilitates rapid mass transfer between the two liquid phases (adapted from ref. 2).

gradient between the two immiscible fluid phases. Herein, we demonstrate this unique principle utilising hydrophobic molecularly imprinted polymer (MIP) microspheres as an analyte specific solid phase adsorbent suspended in chloroform to significantly enhance the extraction of propranolol from an aqueous flow stream (Fig. 2).
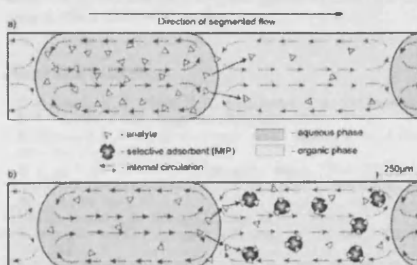
Fig. 2 Schematic illustration of solvent extraction in a biphasic microfluidic segmented flow regime. The analyte species is shown to partition from the aqueous sample into the organic phase at the continually refreshing phase boundary (a). The addition of molecularly-specific solid phase adsorbent micro-particulates to the extracting phase significantly enhances the extent of extraction (b).

The technology of molecular imprinting involves the introduction of analyte-specific binding sites within rigid, cross-linked, three-dimensional polymeric matrices, where analyte recognition is achieved through a combination of spatial and inter-molecular interactions between the analyte molecule and the binding site.[5] Due to their robust and resilient nature MIPs function well in extreme environments e.g. pH, temperature and organic media. However, their application to aqueous sample media has been somewhat less successful due to reduction in substrate affinity in the presence of competing hydrogen bond donor/acceptor species. This study also demonstrates

the successful application of MIPs to aqueous sample media through the application of a second immiscible fluid phase.

In order to demonstrate the rapid mixing properties of the segmented flow system the rate of attainment of equilibrium in partitioning of propranolol from a 50 μM solution in 10 mM acetate buffer pH 5.5 into chloroform was assessed in a segmented flow system and by a macro-scale, traditional, solvent–solvent extraction technique. Organic and aque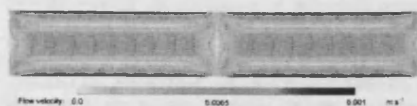ous phases were loaded into separate 10 ml syringes connected via a Tefzel T-piece to generate a segmented flow stream into fluorinated ethylene propylene tubing (500 μm I.D, Upchurch Scientific, Washington, USA). Solvent–solvent extractions were conducted over a range of tubing lengths from 3–100 cm at a rate of 0.2 ml min⁻¹ with a 1 : 1 ratio of reagent flow. 1 ml of combined eluate was collected and two 200 μl aliquots of aqueous sample were immediately removed for quantification of propranolol content by fluorescence microplate analysis (excitation λ: 290 nm, emission λ: 330 nm). The minimum length of tubing required to provide sufficient contact time for the segmented flow regime to establish propranolol distribution equilibrium between the two liquid phases was determined by progressively reducing the tubing length. At tubing lengths of 100, 50, 25, 15, 10 and 5 cm the aqueous propranolol concentration was found to be 27 μM, indicative of attainment of equilibrium since increasing tubing length and consequently increasing transit time caused no further increase in propranolol extraction. Tubing lengths of 4 and 3 cm resulted in greater measured propranolol content in the aqueous phase, indicating that the reduced transit time in the shorter tubing length was insufficient to establish equilibrium. As such, 5 cm was found to be the minimum transit distance required for the segmented flow mixing regime to establish equilibrium, corresponding to a transit time of just 3 s. The method was validated by the collection of 1 ml (combined volume) of two individual non-segmented flow streams in one vial, in which the extraction of propranolol from the aqueous sample was shown to be minimal. The comparative macro-scale solvent extraction was conducted by mechanically shaking (4 Hz, 3 cm amplitude) 2 ml of 50 μM propranolol solution in acetate buffer pH 5.5 with 2 ml of chloroform in an 11 ml glass sample vial. The aqueous phase was sampled at 10 min intervals and assayed for propranolol content, equilibrium was deemed to be established at the time point after which no further reduction in aqueous propranolol content was measured. For each method the distribution coefficient was calculated as the ratio of the concentration of propranolol in the organic phase to that in the aqueous phase. As anticipated, this was identical for both the macro- and micro-scale extractions, since the distribution ratio is independent of the scale or relative volumes of the solutions employed.[6] The time required for attainment of equilibrium was substantially shorter in the segmented flow system equating to a time efficiency increase of 2×10^5 % (Table 1).

Propranolol imprinted polymer microspheres (3.6 μm S.D. 1.4 μm) and non-imprinted (control) polymer (NIP) microspheres (3.9 μm S.D. 1.6 μm) were prepared by precipitation polymerization[7] and an imprinting effect confirmed by standard techniques.[8] Each polymer was suspended in chloroform and this suspension used as the segmenting/extracting phase in the segmented flow system. The solid phase assisted extractions were

Table 1 Time taken to establish equilibrium in the partitioning of propranolol from an aqueous solution into an equal volume of chloroform. Comparison of segmented-flow extraction and traditional low-volume macro-scale solvent-extraction with vigorous shaking

	Microfluidic segmented flow: 0.2 ml min⁻¹	Macro: 2 ml/2 ml vigorous shaking
Distribution coefficient[a]	0.85	0.85
Time to equilibrium (s)	3	~ 6000
Efficiency	~2 × 10⁵ % increase in time efficiency establishing equilibrium using microfluidic segmented flow	

[a] Propranolol partitioned from a 50 μM pH 5.5 acetate buffered aqueous solution into an equal volume of chloroform (CHCl₃) at 25 °C.

conducted with a polymer loading of 8 mg ml⁻¹ added to the organic phase and extractions carried out over a flow distance of 5 m (flow rate 0.2 ml min⁻¹, 1 : 1 ratio of reagent flow) to allow sufficient time for mass transfer of analyte throughout the polymer matrix. In all cases, 1 ml of combined eluate was collected and two 200 μl aliquots of aqueous sample analysed for propranolol content. The extreme hydrophobic nature of the polymer microspheres [p(divinylbenzene-co-methacrylic acid)] ensured they remained suspended entirely in the organic liquid phase, with no migration into the aqueous phase being observed in the collected eluate. The extraction of propranolol from a 50 μM solution (pH 5.5 10 mM acetate buffer) into (i) chloroform alone, (ii) chloroform containing suspended NIP microspheres and (iii) chloroform containing suspended MIP microspheres, was assessed. The presence of the molecularly imprinted polymer microspheres in the extracting organic phase was seen to significantly enhance the extent of propranolol removal from the aqueous sample, to a level close to the limit of quantification for the method of analysis, when compared to the control systems (Fig. 3). The distribution of propranolol between the aqueous phase and the extracting phase was measured by the distribution coefficient, this was observed to increase marginally, from 0.85 to 1.80, when the non-imprinted (control)
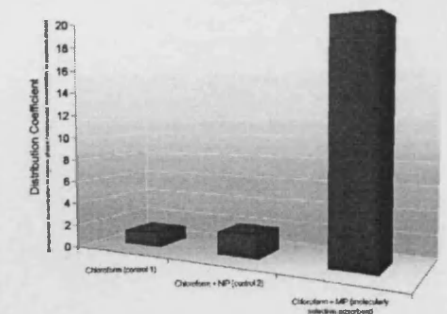

Fig. 3 Solid phase, adsorbent assisted, microfluidic, segmented flow extraction of propranolol from an aqueous sample into an equal volume of chloroform containing no polymer (control 1), non-imprinted control polymer microspheres (NIP) (8 mg ml⁻¹) (control 2), or propranolol-imprinted polymer microspheres (MIP) (8 mg ml⁻¹).

polymer was added to the extracting phase due to non-specific binding to the surfaces of the porous particles, much as would be expected should a non-specific adsorbent, such as silica, be employed in such an extraction. However, on the addition of propranolol MIP microspheres to the extracting chloroform phase the partition coefficient increased substantially to 20, demonstrating that the formation of analyte specific binding sites within the polymer matrix enhances the affinity of the polymer for the propranolol ligand, thus enhancing removal of propranolol from the aqueous sample. The sequestration by the MIP of propranolol entering the chloroform maintains a significant propranolol concentration deficit in the chloroform, continuing to drive the extraction from the aqueous phase until a complex 3-way equilibrium, in favour of the combined extracting phase, is attained. This significant increase in distribution coefficient, enabled removal of over 95% of the propranolol from the aqueous sample in a single extraction. For an equivalent level of removal to be achieved with chloroform alone, six consecutive extractions would be required, which, if MIP assisted, would be expected to extract in excess of 99.99997% of propranolol from the original sample. It is regarded that for distribution coefficients of less than one, solvent extraction can be an ineffective, time consuming and impractical technique,[9] and as such the ability to increase the value far above unity by the incorporation of an affinity phase into the extracting solvent is highly desirable.

These preliminary findings demonstrate a highly original, unique, yet simple approach to chemical separations. Incorporating a solid phase adsorbent into the extracting phase of a liquid–liquid extraction whilst exploiting the rapid mass transfer properties of segmented flow, offers clear advantages in terms of time efficiency and extent of extraction over macro-scale and alternative microfluidic extraction methodologies. The continuous flow nature of segmented flow microfluidics allows for continual operation. Additionally, parallelisation of flow streams holds the potential to increase throughput, potentially enabling application on an industrial scale, for example in post-synthesis chemical enrichment or contaminant removal. The possibility of phase separation by an array of approaches and subsequent phase and particle manipulation for analyte recovery and reagent re-use add further potential flexibility and desirability to the technique. It can be envisaged that solid phase enhanced micro liquid-extractions can be performed utilising many modes of adsorbents, both passive and catalytic, organic, inorganic, and biological moieties in a 'reverse' phase approach, making the technique readily applicable and transferable to many areas where chemical separation, enrichment, or selective transport of analytes is desirable. Researchers wishing to study

affinity based binding events can utilise the technique as a practical and efficient alternative to the macro-scale binding and dialysis studies traditionally employed. This may prove particularly promising for low molecular weight receptor species which are often difficult to manipulate and separate from the incubation media. The technique's successful application is dependent upon careful consideration of the immiscible phases, ensuring the affinity phase resides entirely in one phase, whilst the analyte has a degree of solubility in both phases. In this particular example, the employment of molecularly specific adsorbents (e.g. MIPs) rather than non-specific adsorbents, such as functionalised silica, enables a molecularly specific enhancement of extraction. Current work is directed towards optimising the demonstrated extraction through reduction in MIP particle size in order to reduce the time requirement for analyte diffusion to binding sites within the particle core, the rate limiting step of the solid phase assisted segmented flow extraction reported here. This combined with exploration into the effect of parameters such as flow rates, channel length, geometry, and polymer loading on the kinetics and thermodynamics of the extraction, will further characterise and optimise the novel technique reported.

Acknowledgements

Notes and references

1 C. D. Costin, R. K. Olund, B. A. Staggemeier, A. K. Torgerson and R. E. Synovec, *J. Chromatogr., A*, 2003, 1013, 77–91.
2 N. Harries, J. R. Burns, D. A. Barrow and C. Ramshaw, *Int. J. Heat Mass Transfer*, 2003, 46, 3313–3322.
3 H. Song, J. D. Tice and R. F. Ismagilov, *Angew. Chem.*, 2003, 115, 792–796; H. Song, J. D. Tice and R. F. Ismagilov, *Angew. Chem., Int. Ed.*, 2003, 42, 768–772.
4 J. R. Burns and C. Ramshaw, *Lab Chip*, 2001, 1, 10–15.
5 B. Sellergren and C. J. Allender, *Adv. Drug Delivery Rev.*, 2005, 57, 1733–1741.
6 A. Leo, C. Hansch and D. Elkins, *Chem. Rev.*, 1971, 71, 525–616.
7 J. Wang, P. A. G. Cormack, D. C. Sherrington and E. Khoshdel, *Angew. Chem.*, 2003, 115, 5494–5496; J. Wang, P. A. G. Cormack, D. C. Sherrington and E. Khoshdel, *Angew. Chem., Int. Ed.*, 2003, 42, 5336–5338.
8 O. K. Castell, C. J. Allender and D. A. Barrow, *Biosens. Bioelectron.*, 2006, 15, 526–533.
9 T. E. Beesley, B. Buglio, and R. P. W. Scott, *Quantitative Chromatographic Analysis*, CRC Press, Boca Raton, Florida, 2001, ch, 3, p. 55.

Liquid–liquid phase separation: characterisation of a novel device capable of separating particle carrying multiphase flows†

Oliver K. Castell,[*ab] Christopher J. Allender[a] and David A. Barrow[b]

Capillary forces on the microscale are exploited to create a continuous flow liquid–liquid phase separator. Segmented flow regimes of immiscible fluids are generated and subsequently separated into their component phases through an array of high aspect ratio, laser machined, separation ducts (36 μm wide, 130 μm deep) in a planar, integrated, polytetrafluoroethylene (PTFE) microdevice. A controlled pressure differential across the phase separator architecture facilitates the selective passage of the wetting, organic, phase through the separator ducts, enabling separation of microfluidic multiphase flow streams. The reported device is demonstrated to separate water and chloroform segmented flow regimes at flow rates up to 0.4 ml min⁻¹. Separation efficiency is quantified over a range of flow rates and applied pressure differentials, characterising device behaviour and limits of operation. Experimental measurements and observations are supported by theoretical hydrodynamic and capillary pressure modelling. The influence of material properties and geometric design parameters on phase separation is quantified and optimisation strategies proposed. The novel ability of the membrane free device to separate an *organic phase containing suspended microparticulates*, from an aqueous phase, is also demonstrated.

Microfluidic phase separation

Exploitation of forces dominant on the microscale in the form of microfluidic technology is empowering scientists to provide solutions for emerging and longstanding challenges alike. Microfluidic systems are widely being developed and applied to multi-step synthetic chemistry,[1] separations and enrichments,[2] sensing technology[3] and sequential combinations of these activities.[4] Recently, multiphase microfluidics has attracted considerable attention[5] since it provides unique opportunities for liquid-[6] and solid phase supported micro-separations,[7] crystallisations,[8] particle synthesis,[9] organic micro-synthesis,[10] encapsulation[11] and chemical computing.[12] Multiphase flow usually entails the controlled elution of immiscible fluids into a common duct, or system of ducts[13,14] and offers new opportunities over that provided by single phase systems. Segmented flow regimes of alternating immiscible organic and aqueous fluid packets are characterised by each fluid packet exhibiting high internal mixing and there being a continually refreshing fluidic interface between contiguous fluid segments.[15] These important properties allow the rapid attainment of chemical equilibrium between adjacent fluid packages, through highly efficient mass transfer.[16] This enables rapid synthetic chemical migration across interfacial phase boundaries. In many above mentioned applications, it is

usually desirable to separate and recover the component immiscible fluids in order to harvest synthesised particles, or recover extracted molecular species, or products of chemical reactions. Several approaches to liquid phase separation have been reported. Co- and counter-current (side by side) flows of immiscible fluids have been separated through splitting of the two phases at a juncture of appropriate geometry combined with surface modification of exit channels to favourably alter wetting characteristics of the outlets for one of the two immiscible phases.[17–19] Such 'side by side' flow systems lack the rapid mass transfer properties of segmented flow systems and like single phase microfluidics, mass transfer is limited by diffusion.[20] As a result, extraction methodologies may require several passes to attain chemical equilibrium. Segmented flow regimes generate rapid mixing and efficient mass transfer in discrete droplets. This has enabled massive increases in efficiency of chemical reactions and also provided opportunities for other droplet based chemistries and syntheses. In the majority of cases, phase separation has to be performed off-chip by gravimetric approaches which are commonplace on the macroscale. The ability to separate by differences in density on the microscale is, however, much more difficult due to the dominance of interfacial forces. However, such forces, that are not immediately obvious when considering the behaviour of fluids on the macroscale, can be exploited at the microscale to enable phenomena and methodologies which would otherwise be unachievable. Capillary forces have been utilised to separate the components of gas–liquid segmented flows through an array of 10 μm wide side channels in a silicon substrate.[21] Angelescu and Siess[22] reported moderate success in adapting this approach to liquid–liquid flows quoting a separation efficiency of ~90% and subsequently demonstrating complete liquid phase separation using a non-wetting membrane

[a]Molecular Recognition Research Unit, Welsh School of Pharmacy, Cardiff University, King Edward VII Avenue, Cardiff, UK. E-mail: castellok@cardiff.ac.uk; allenderc@cardiff.ac.uk; Fax: +44 (0)29 208 74149; Tel: +44 (0)29 208 75824
[b]metaFAB, School of Engineering, Cardiff University, The Parade, Cardiff, UK. E-mail: barrow@metafab.net; Tel: +44 (0) 780 983 9979
† Electronic supplementary information (ESI) available: Movies of phase separator in operation. See DOI: 10.1039/b806946h
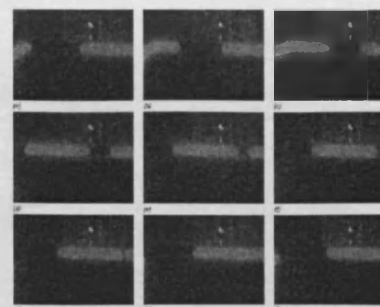
Fig. 1 Sequence of still images taken from a video† of the phase separator in operation. Adjacent aqueous liquid slugs (green) are seen to move progressively closer together and eventually coalesce, as the chloroform exits through the series of narrow separation channels (top). Total flow rate 0.12 ml min⁻¹, 1 : 1 ratio aqueous/organic flow.

to effectively narrow the geometry of the separation ducts. This approach was first adopted by Nord and Karlberg in 1980[23] and later employed by Jensen's group at MIT.[24]

In this manuscript we report aqueous and organic phase separation with 100% efficiency in a membrane free, planar microfluidic device, with no additional surface modifications. We optimise the approach introduced by Angelescu and Siess[22] using capillary forces to bring about total liquid phase separation by removal of the 'wetting' organic phase through a series of narrow side channels (Fig. 1). We measure operating regimes for the phase separator and compare this to predicted behaviour by correlating observed behaviour with modelled hydrodynamic pressure drops and capillary pressures at the separation interface. We also demonstrate for the first time the ability of a microfluidic phase separation device to separate an organic phase containing suspended particulate material, from an aqueous phase, a limitation of membrane based approaches.

Experimental

Device production

An integrated planar PTFE microchip device was constructed from a 4 mm thick PTFE base layer, a 100 μm thick FEP intermediary layer and a 2 mm thick glass coverplate, all compression sealed in a stainless steel housing incorporating input-output ports (Fig. 2). The separation device was fabricated in PTFE by a combination of micromilling and femtosecond laser ablation. The inlets, segmenting T-junction, main fluidic channel and outlets were micromilled (Protomat C10, LPKF, Garbsen, Germany) at a width of 720 μm and a depth of 600 μm. The separator section of the device consisted of an array of 140 36 μm wide, 130 μm deep and 5 mm long, Gaussian profile, side-channels (Fig. 2), each 64 μm apart (top of duct-wall to top of duct-wall), branching from the main fluidic channel. These channels were machined by direct write femtosecond laser ablation (λ = 780 nm, 0.55 W, machining speed 50 mm/min, 1 pass).

Inlet and outlet holes (1/16″ O.D.) were drilled in the PTFE substrate to receive equivalent outer diameter transparent FEP tubing (Upchurch Scientific, WA, USA) providing fluidic connectivity. 500 μm ID tubing of length 255 mm and 148 mm were used on the organic and aqueous outlet, respectively. These specific lengths of tubing were employed to provide an equal pressure drop due to flow of the separated fluids through their designated outlets, from the separator to collecting vessel (chloroform η = 0.00058 Pa s and water η = 0.001 Pa s). The aqueous outlet was connected to a 50 ml capacity sealed vessel to which a 10 ml air-tight syringe and digital low pressure manometer (DP2-41E 100 kPa, Sunx, Panasonic) were also connected. This arrangement was used to modulate and monitor an applied pressure to this fluidic outlet, creating a pressure differential between the two outlets of the separator and therefore a pressure drop across the phase separator.

Device operation

Chloroform (ThermoFisher, Loughborough, UK) and deionised water (18 M′Ω cm from a Purelab UHQ II system, ELGA, UK) were delivered to the microfluidic device at equal flow rates of between 0.03 ml min⁻¹ and 0.18 ml min⁻¹ by independent syringe drivers (KD Scientific, Holliston, MA, USA). 5(6)-carboxy-fluorescein (Sigma Aldrich, Gillingham, UK) was added to the aqueous phase to assist visualisation (excitation illumination peak λ = 365 nm). The performance of the phase separator was assessed over a range of applied pressure differentials between the two fluidic outlets, with the designated organic outlet (outlet 2) exiting at atmospheric pressure and the aqueous outlet (outlet 1) exiting to the sealed vial at atmospheric pressure plus the applied pressure due to compression or expansion of the syringe volume. 100% phase separation efficiency was confirmed by visual inspection of the outlet fractions and flow within the transparent FEP outlet tubing, additionally, conditions resulting in incomplete removal of the organic phase or aqueous breakthrough into the organic outlet were assessed by volumetric measurement of the eluate collected from the organic outlet (outlet 2). Microscopy at the separating portion of the device was used to observe phase separation and monitor the aqueous breakthrough pressure at the separator. The ability of the device to separate particulate containing phases was studied by the suspension of 2.0 μm fluorescein labelled polystyrene beads (Sigma Aldrich, Gillingham, UK) in the chloroform phase. The hydrophobic nature of the polystyrene beads ensured they remained suspended entirely in the organic phase.

Results and discussion

Microfluidic phase separation of segmented flow streams

The operation of the phase separator device relies upon a difference in wetting properties between the two liquid phases and the PTFE substrate material. Chloroform is observed to wet the channel walls, whereas water is repelled by the highly hydrophobic surface of the PTFE. This is easily illustrated by the observed contact angle made by a drop of the two liquids on a PTFE surface (Fig. 3). The wetting properties of the continuous phase allow it to enter and flow through the narrow separator ducts more readily than the non-wetting, aqueous, dispersed
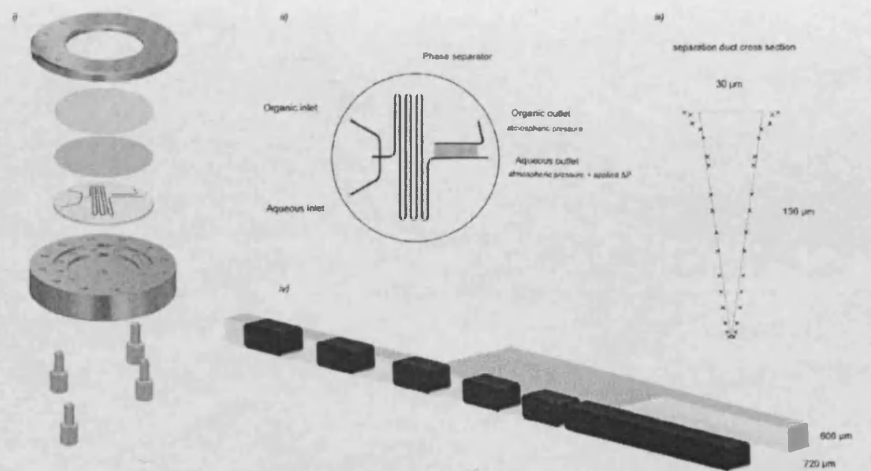
Fig. 2 Series of schematic diagrams illustrating (*i*) device construction. (*ii*) Microfluidic channel layout, including aqueous and organic inlets, T-junction for generation of segmented flow, phase separator region of the device consisting of a series of 140 parallel narrow side channels branching form the main fluidic duct leading to a designated organic outlet, with the main fluidic duct continuing to the designated aqueous outlet. (*iii*) Cross-sectional Gaussian profile of a single laser machined separation duct as measured by serial z-axis optical microscopy and the approximated triangular geometry used for modelling calculations. (*iv*) Cartoon illustration of the separator in operation, the organic phase (light) wets the PTFE channel walls and exits through the separation ducts, driven by the applied pressure differential between the two channel outlets. The non-wetting, aqueous fluid segments (dark) do not enter the narrow separation ducts but continue to flow in the main fluidic channel, coalescing into one continuous stream as the organic phase exits the channel.

phase. This difference in capillary forces allows the exclusive passage of one phase through the separator ducts by careful control of the pressure drop from the phase separator to each outlet. Hagen-Poiseuille's law enables the calculation of pressure

Fig. 3 PTFE wettability by chloroform (upper image) and water (lower image), drop volume 10 μl. Co-elution of the two liquids into a PTFE channel results in a segmented flow regime with chloroform wetting the channel walls as the continuous phase and water the disperse, droplet phase (inset image).

drop due to the laminar flow of Newtonian fluids along a length of tubing or fluidic channel of known geometry:

$$\Delta P = \frac{\alpha \eta Q L}{A^2} \quad (1)$$

where ΔP is the pressure drop due to fluid flow (Pa), α is a numerical prefactor related to the geometry of the channel cross-section, η is fluid viscosity (Pa s), Q is flow rate of the fluid ($m^3 s^{-1}$), L the channel length (m) and A the cross sectional area of the channel (m^2). For a channel of any geometry cross-section, α is linearly related to the shape's compactness factor, C ($C = $ perimeter^2/area),[25-27] Mortensen and Bruus[25] report values of α/C obtained by finite element simulations for a multitude of cross-sectional geometries, enabling calculation of pressure drops for a variety of different shaped channels. For a cylindrical tube $\alpha = 8\pi$ and eqn (1) simplifies to the commonly given form;

$$\Delta P = \frac{8\eta Q L}{\pi r^4} \quad (2)$$

Application of this equation to the outlets either side of the phase separator for their respective fluids gives a nominally equal back pressure of 1.61 kPa ml^{-1} min when the phase separator is operating at 100% efficiency with a 1 : 1 ratio of fluid flow. (The pressure contribution due to flow *within* the separation channels was later determined based on subsequent experimental observations of number of ducts required for complete separation).
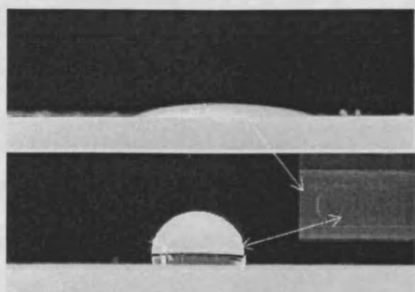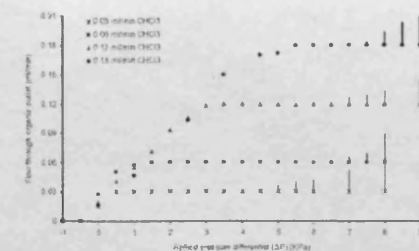
This journal is © The Royal Society of Chemistry 2009

Fig. 4 Phase separation performance at four different flow rates over a range of applied pressure differentials across the separator. Segmented flow regimes were generated with a 1 : 1 ratio of reagent flow and the fluid composition passing through the separator ducts was quantified by measuring the fluid output through the organic outlet over time. Points signify chloroform flow, whilst the lines quantify aqueous breakthrough. Note the ability of the device to act as a valve, allowing zero flow, or volumetrically controlled passage of one or both fluid phases.

The phase separator device was tested with a one to one volumetric ratio of the two liquid phases at combined flow rates of 0.06 ml min^{-1} to 0.36 ml min^{-1}, with additional air pressure applied to the designated aqueous outlet (outlet 1) over the range −1.0 kPa to 10 kPa. The results are illustrated in Fig. 4. 100% efficiency separation of the two phases was achieved at all flow rates up to and including an organic flow of 0.18 ml min^{-1} through the separation ducts (0.36 ml min^{-1} segmented flow rate). In keeping with Hagen-Poiseuille's law the minimum applied outlet pressure differential at which phase separation occurs at 100% efficiency with no organic phase remaining in the outlet stream increases linearly with increasing flow rate of the segmented flow stream, as the volume of organic phase required to pass through the separator ducts per unit time increases.

Limits of operation

As the pressure differential between the aqueous outlet and organic outlet increases, the flow rate of chloroform through the separator ducts increases (eqn (1)). Total phase separation occurs when the pressure differential across the phase separator is sufficient to support a flow of organic solvent through the separator *equal* to that in the segmented flow stream (Fig. 4). Further increase in the pressure differential supports a greater flow of chloroform though each individual separator duct. Consequently, as the pressure differential increases further, fewer separating channels are required to maintain 100% phase separation. It was observed that as operating pressure differential increased, coalescence of adjacent aqueous segments occurred progressively nearer the start of the phase separator architecture. This behaviour is described mathematically by the adaptation of Hagen-Poiseuille's law for flow in *n* parallel channels (eqn (3)).

$$\Delta P = \frac{\alpha \eta Q L}{n A^2} \quad (3)$$

This journal is © The Royal Society of Chemistry 2009

The upper pressure limit of the separation device occurs when a sufficient pressure differential develops to overcome the capillary pressure required to force the non-wetting, aqueous phase, into the narrow ducts of the separator. This breakthrough pressure (P_b) can be estimated through application of an equation derived from the Young-Laplace equation which governs the capillary rise, or fall, of a wetting or non-wetting liquid in a capillary. Commonly applied as a method for pore size measurement in membrane manufacturing, the bubble point test[28] measures the gas pressure required to force air (non-wetting) through membrane pores filled with a wetting liquid. This enables calculation of pore-size from the equation;

$$P_b = \frac{\alpha \gamma \cos\theta}{r} \quad (4)$$

where γ is the interfacial surface tension between the two fluids (liquid/liquid or liquid/gas) (N m^{-1}), θ the wetting angle, r the pore radius (m) (cylindrical pores) and α a numerical prefactor, a value of 2 is used for cylindrical pores. For alternative or irregular geometries α/r can be substituted for the perimeter to area ratio of the pore opening.[29] In the case of the liquid phase separator the non-wetting aqueous phase can be considered analogous to the air in the bubble point test and an estimation for the aqueous breakthrough pressure of the device can be calculated. Approximating the Gaussian geometry of the separation ducts to a triangle ($w = 30$ μm, $h = 130$ μm) (Fig. 2), giving a perimeter/area measurement of 15×10^4 m^{-1}, and applying a chloroform–water interfacial tension of 32 mN m^{-1}[30] with a wetting angle, θ, of 0° yields a predicted aqueous breakthrough pressure of 4.79 kPa. The equation for capillary pressure is only valid under capillary equilibrium, (non flow conditions), but this value acts as an approximate predictor of the upper operating pressure of the device. Validation of this prediction is achieved through extrapolation of the measured, flow-related, trend in aqueous breakthrough pressure to that at a zero flow rate. This is illustrated in Fig. 5 and results in a static breakthrough pressure
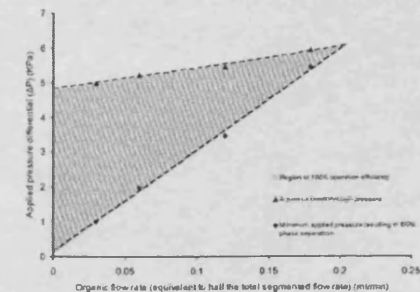

Fig. 5 Experimentally defined operating regimes of the phase separator, illustrating minimum applied pressure required to remove all chloroform from the segmented flow stream and applied pressure at which aqueous breakthrough begins to occur. The lower and upper pressure limits of the device to operate at 100% separation efficiency.

This journal is © The Royal Society of Chemistry 2009

of 4.8 kPa, in close agreement with the mathematical prediction obtained from eqn (4).

The observed increase in breakthrough pressure with increasing flow rate is perhaps a surprising observation. This may be in part a result of a possible reduction in the advancing contact angle of the aqueous fluid packets with increasing flow rate,[34] indicative of an increased pressure drop across the fluid packet.[32] Although visual examination confirmed a flattening of the retreating meniscus, it was not possible to observe a change in the advancing contact angle, which approaches 0° when stationary (Fig. 3 inset). Another consideration is the force generated opposing breakthrough as a result of the pressure drop due to flow of organic phase in the separation ducts, described by eqn (3). However, this would only appear to be applicable to the separation channels through which chloroform was flowing. This assumption is supported by the observation that aqueous breakthrough was largely observed to occur after the point of coalescence of aqueous segments, through otherwise inactive ducts. In order to further understand and explain this behaviour we are currently conducting CFD modelling and simulation studies

Fig. 5 suggests a maximum throughput of just over 0.2 ml min⁻¹ per phase (0.4 ml min⁻¹ total) with an applied pressure of 6.1 kPa capable of achieving 100% phase separation for this device architecture. This correlates well with experimental observations where the maximum flow rate at which complete phase separation was achievable was 0.2 ml min⁻¹ per phase, at an applied pressure of 5.9 kPa. Fig. 5 suggests that under these conditions small changes in flow or pressure would result in incomplete separation. This was observed experimentally where small changes in conditions resulted in aqueous breakthrough and/or incomplete removal of chloroform. In such scenarios of incomplete separation the pressure drop due to flow in the designated aqueous and organic outlet tubes ceases to be equal, due to (i) the increased fluid flow though one of the channels at the expense of the other, and (ii) the presence of immiscible fluid in either outlet stream which disrupts laminar flow and generates a pressure drop across the fluidic interface. Therefore at incomplete phase separation $\Delta P_{organic\ out} \neq \Delta P_{aqueous\ out}$, and as a result the pressure at the phase separator does not equate to the applied air pressure at outlet 1 ($\Delta P_{phase\ separator} \neq \Delta P_{applied}$). Consequently, further fluctuation in efficiency may be observed as the pressure at the point of phase separation fluctuates due to incomplete separation. As a result of this the pressure experienced by the segmented flow stream at the phase separator inlets

equates to the applied air pressure differential between outlets 1 and 2 only when the phase separator is operating at 100% efficiency. Outside of these limits the pressure at the separator increases above that of the applied air pressure for cases of incomplete removal of organic phase from the segmented flow stream, and is reduced to below that of the air pressure differential in situations where aqueous breakthrough is observed. A range of studies have been conducted investigating pressure drop in segmented or bubble flow.[33–41] The reasoning and estimates vary greatly and the relationship appears to be multi-factorial, with fluidic interfaces[33] and length and number of fluid segments[41] likely to play a key role alongside the properties of the liquids themselves and channel architecture. In multiphase flow droplet formation and break-up at a T-junction geometry has been shown to be governed by pressure fluctuations at the point of generation[33] and thus the effects of pressure changes at the point of phase separation may have implications on the formation of the segmented flow further upstream. As a result, despite being able to easily measure the compositional output from each output of the phase separator the pressure drop this flow provides is not readily predictable except in circumstances of complete phase separation where a single phase flows through each outlet. Further investigation in this area would be required to more accurately understand the behaviour of fluid in the phase separator when operating under conditions of incomplete organic removal or aqueous breakthrough.

At each of the four flow rates investigated, the typical number of active separation ducts was recorded at the upper limit of operation of the phase separator (Table 1). The number of active ducts was assumed to be every duct from the entrance of the separator to the point of aqueous phase coalescence. An estimate of the pressure drop as a result of chloroform flow through the active ducts was calculated using eqn (3). Mortensen, Okkels and Bruus report a method for calculation of the numerical prefactor (α) of Hagen-Poiseuille's law for any channel geometry, enabling accurate calculation of pressure drop in non-cylindrical channels.[27] Since the separation ducts were machined by laser ablation their cross-sectional profile can be described by a Gaussian curve. Although the mathematics of Gaussian curves are well characterised, adaptation of the mathematical expression to give a general formula for the description of a closed (i.e. lid of the channel) Gaussian shape proved difficult. As a result, the separation ducts were approximated to be triangular (w = 30 μm, h = 130 μm) (Fig. 2). Eqn (5) is Mortensen et al.'s general formula for the calculation of α for triangular geometries[27]

$$\alpha = \frac{25C}{17} + \frac{40\sqrt{3}}{17} \tag{5}$$

where C is the channel shape's compactness factor

$$C = \frac{\text{perimeter}^2}{\text{area}} \tag{6}$$

Application of eqn (5) and (6) yielded a value for α of 68.26 for the separation ducts. With $\alpha = 68.26$, $\eta = 0.00058$ Pa s for chloroform, $Q =$ the total flow of chloroform (m³ s⁻¹) cleared through n ducts of length, $L = 0.005$ m, eqn (3) was used to calculate an estimate of the pressure drop due to flow through the active separation channels (Table 1). A linear relationship appears to exist between the minimum number of ducts required for phase separation at the upper limit of operation over the range of flow rates investigated (Fig. 6). Intriguingly, the calculated pressure drop due to this flow of chloroform through the separation channels, (eqn (3) and (5)) is substantially lower than the applied pressure differential (ΔP) across the separator (Table 1). The discrepancy between the calculated pressure drop due to flow of organic phase through the separator and the applied pressure (ΔP) across the phase separator was found to be fairly close to the calculated aqueous breakthrough pressure. It was observed that the onset of aqueous breakthrough through the separator ducts did not result in an increase in the typical number of active ducts removing chloroform from the segmented flow stream. This indicates that despite a pressure drop across the separator in the region of 4.8 kPa being required to trigger aqueous breakthrough, once the breakthrough pressure is exceeded, the force enabling breakthrough is not provided at the expense of the flow of chloroform through the separator ducts. This combined with findings in Table 1 suggest that the applied pressure (ΔP) across the phase separator is in part responsible for the flow of chloroform through the separator and in part responsible for the events leading up to and eventually resulting in aqueous breakthrough. This may possibly involve clearance of the macroscopic organic film which typically surrounds moving slugs of non-wetting liquids in closed channels,[42] particularly of

square or rectangular geometry,[43] or possibly overcoming disjoining pressure which exists between the phases and the channel walls.[44] It is possible that it is these or other processes which themselves determine the breakthrough pressure with which we are familiar. This perhaps suggests a gradual process of change at the duct inlet and fluid interface with increasing applied pressure until the breakthrough pressure is overcome. Such factors, which may be influenced by flow velocity and its effects on segment length and interfacial contact area,[45] may also explain the observed increase in aqueous breakthrough pressure with increasing segmented flow rate. In addition, this may also explain the unsuitability of eqn (4) for the estimation of capillary pressure under flow conditions. It may also be possible that the calculated value for pressure drop due to the flow of chloroform through the separation ducts may be significantly underestimated. Although the femtosecond pulsed laser ablation process reduces, and for most materials eliminates, conductive thermal damage.[46] In this case the separation channels machined in the PTFE substrate material appeared to have a rather rough finish when inspected by optical microscopy. It was also apparent that when in operation, and once aqueous breakthrough into the laser machined separation ducts had occurred, fluorescent regions remained, although entirely static, within the separation ducts (Fig. 1). This could be indicative of aqueous residues trapped within the duct, or possibly the machining process giving rise to a change in chemical composition at the machined surface causing the 5(6)-carboxyfluorescein fluorescent probe to be deposited on the machined surface. If, as initially suggested, aqueous residues remained trapped within the separation ducts, this would effectively increase the pressure drop due to flow of chloroform through the channel by both reducing the duct geometry and also providing pressure inducing surface interactions. A further possibility is that the laser ablation process creates a hyper-porous surface which could have the effect of either providing a network of incredibly narrow pores through which a portion of the separated chloroform flows, which, much like a membrane, would provide a greater pressure drop due to flow than an open channel. It is also possible that, should pressure be sufficient, aqueous fluid could enter the hyper-porous structure, where it may well become entrapped or the pore walls become coated with 5(6)-carboxyfluorescein. Therefore, giving rise to the fluorescent regions visible along the path of the separation duct walls. This fluorescent staining of the separation ducts was not cleared following prolonged operation of the phase separator or through flushing the device with either chloroform or water. In additional tests a larger laser machined area of PTFE when exposed to an aqueous dye solution became clearly stained where as virgin areas and micro-milled regions of the PTFE substrate did not experience this phenomenon. It is anticipated that this effect can be eliminated and the surface finish of the machined ducts improved by submersing the substrate in water during the laser machining process.[47]

Design parameters

Eqn (1)–(6) and the experimental evaluation of the phase separator described illustrates how the operating limits of the phase separator are dependent upon several variables.

Table 1 Number of active separation ducts at the upper limit of operation at each of the four flow rates investigated, with the calculated pressure drop due to flow of chloroform through the active ducts (eqn (3)). Together with comparison to the pressure differential applied across the separator architecture

Applied air pressure differential (ΔP) ≡ pressure across separator (kPa)	Flow rate of organic phase (ml min⁻¹)	Typical no of ducts required for separation	Pressure drop due to flow through active ducts[a] ($\Delta P_{duct\ flow}$) (kPa)	$\Delta P - \Delta P_{duct\ flow}$ (kPa)
5	0.03	16	1.6	3.4
5.25	0.06	42	1.3	3.95
5.5	0.12	74	1.4	4.1
6	0.18	100	1.6	4.4

[a] Calculated pressure drop due to organic flow through active separation ducts (eqn (3), (5), (6)).
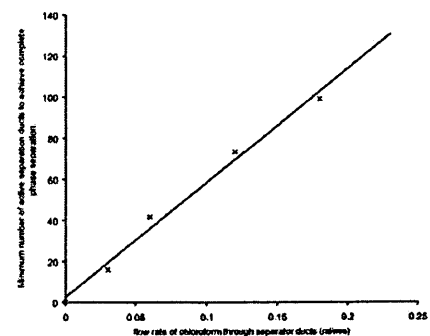

Fig. 6 Minimum number of active separation ducts clearing chloroform form the segmented flow stream before aqueous breakthrough occurs.

The disperse phase breakthrough pressure is governed by the properties of the separator channel as follows;

$$P_b \propto \frac{\text{perimeter}}{\text{area}} \qquad (7)$$

Whilst the pressure drop due to flow of the wetting phase in the separator channels exhibits the following dependencies on separator channel architecture;

$$\Delta P \propto \frac{\text{perimeter}^2}{\text{area}^3} \quad \Delta P \propto \frac{1}{n} \quad \Delta P \propto L \qquad (8)$$

The effect of substrate and liquid properties on breakthrough, shows dependencies on the wetting angle and the liquid–liquid interfacial tension;

$$P_b \propto \cos\theta \quad P_b \propto \gamma \qquad (9)$$

With the pressure drop due to flow of the separated fluid in the separator channels proportional to the wetting-fluid's viscosity and flow rate;

$$\Delta P \propto \eta \quad \Delta P \propto Q \qquad (10)$$

Since the choice of fluids employed will largely be governed by the intended application the scope to tailor the material properties variables is clearly limited, however the ability to predict the feasibility of operation of the phase separator with various flow regimes is undoubtedly useful.

These relationships (eqn (7)–(10)) suggest that one of the most effective ways to improve efficiency and provide the opportunity to separate substantially higher flow rates of segmented flow comes from increasing the number of separation ducts (n), for example doubling the number of separation ducts enables twice the flow (Q) of the wetting phase through the separation channels for the same pressure drop across the separator (ΔP). This principle is illustrated by the data in Table 1 and Fig. 6 showing the trend for linear increase in the number of active separation channels with increasing flow rate. Similarly reducing the length of the separator ducts (L) should have an equivalent effect and
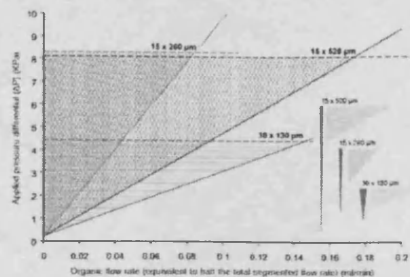
Fig. 7 Predicted effect of separation duct geometry on separator performance: calculated minimum operating pressure (solid line), aqueous breakthrough pressure (dashed line) and 100% separation efficiency regimes (shaded region). Chloroform/water separation by triangular separation ducts ($n = 140$) with dimensions $w = 15\ \mu m$, $h = 260\ \mu m$ and $w = 15\ \mu m$, $h = 520\ \mu m$ compared to the experimentally evaluated duct of dimensions $w = 30\ \mu m$, $h = 130\ \mu m$.

thus an array of pillars should provide better results than the relatively long, 5 mm, ducts employed in this device. Less intuitive are the effects of altering the separation channel geometry. Fig. 7 illustrates the predicted effect of altering the separation duct geometry relative to the experimental results for the approximated triangular duct cross section ($w = 30\ \mu m$, $h = 130\ \mu m$). Based on the relationships eqn (7)–(10), the anticipated aqueous breakthrough pressure (under static conditions) and the estimated minimum applied pressure differential between the aqueous and organic outlets to achieve 100% phase separation are plotted for triangular ducts of dimensions $w = 15\ \mu m$, $h = 260\ \mu m$ and $w = 15\ \mu m$, $h = 520\ \mu m$. Interestingly, the aqueous breakthrough pressure shows a heavy dependence on the narrowest geometry of the separation channel, with the depth of the channel having little effect on maximum operating pressure of the device. A finding supported by that of Tsai *et al.* who showed a similar dependency, albeit by a different method, in estimations of the energy required to deform an air bubble by forcing it into a narrow channel.[21] Despite this dependency, employing narrower and narrower separation ducts may not necessarily improve separation performance, this is as a result of the increased pressure requirement for flow of the organic phase through these ducts due to the increased value of perimeter²/area³ for the channel cross-section (Fig. 7). Additionally, the geometry of the main, segmented flow carrying, channel should not be ignored. This channel is required to be of suitable dimensions, such that the pressure drop due to flow of the segmented flow stream, along the length of the separator architecture, does not approach the breakthrough pressure of the device. These findings may explain why Angelescu and Siess could not achieve complete phase separation with their device consisting of several 15×15 μm square profile separation ducts branching from a main fluidic duct $100 \times 15\ \mu m$.[22] Clearly a trade off exists between the flow rate the phase separator is required to operate at and the tolerance in pressure variations at the point of separation the device is likely to have to withstand. However, with careful design consideration a device suitable for most applications can be envisaged.

Liquid phase separation of particulate suspensions

A key advantage in employing sufficiently wide separation ducts is their ability to carry solid particulates suspended in the *separated* organic phase. This would not be possible for a membrane based phase separation approach, since suspended particulates would easily clog the pores.

Solid materials have been incorporated in microfluidic systems for a range of applications: separations,[7,48] solid support chemistry,[49] particle production[9] and particle modification.[50] This enabling methodology holds massive potential, particularly for continuous flow applications combining multiphase flow with an incorporated solid phase. This concept was demonstrated by the separation of a segmented flow stream of water and chloroform containing a 1 mg ml^{-1} suspension of fluorescently labelled 2.0 μm diameter polystyrene beads (Sigma Aldrich, Gillingham, UK) (Fig. 8). The hydrophobic nature of the beads resulted in them remaining suspended entirely in the organic phase as it passed through the separation ducts, with no adverse effects to the device. Complete separation of a the segmented flow stream
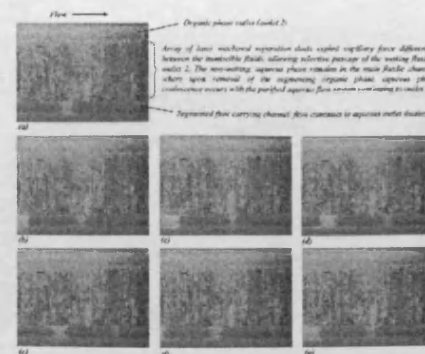
Fig. 8 Sequence of still images taken from a video† of the phase separator operating with fluorescently labelled polystyrene microspheres (2.0 μm diameter) suspended in the organic phase and passing through the separation ducts, into a second outlet channel. An aqueous fluid packet (dark, non-fluorescent region) can be seen to move progressively closer to the aqueous fluid packet in front due to removal of chloroform from the segmented flow stream (a–f), until complete phase separation, and aqueous phase coalescence occurs (g).

of water and chloroform containing suspended microspheres was achievable with no breakthrough of aqueous phase into the organic stream, or migration of the polystyrene microspheres into the aqueous phase. The presence of the beads suspended in the chloroform have the effect of increasing the viscosity of the fluid and as such a greater number of separation ducts and a greater pressure drop across the separator was required to achieve complete phase separation compared to the separation of water and chloroform alone. As such, this should be considered when designing a device for such application.

Conclusion

The phase separation device reported here provides exciting potential for separations and enrichments in synthetic chemistry and for multi-stage processing in multiphase microfluidics. The ability to achieve continuous flow separation of a segmented flow stream provides opportunities for the development of continual operation, high throughput, integrated lab-on-a-chip devices to conduct multi-step synthetic chemistry, separations and enrichments, and sequential combinations of these activities. We have demonstrated that capillary forces in a multiphase flow system are sufficiently dominant to separate the component liquids of a segmented flow regime through an array of narrow channels over a range of flow rates. This is achieved by appropriate control of pressure drops from the separator to the fluidic outlets. In this illustration this was achieved by controlling the atmospheric pressure at which the aqueous outlet exited in order to interrogate the behaviour of the separator over a range of operating conditions. However, precise control over pressure drop may also be achieved by considered design of outlet length and geometry to provide an appropriate operating pressure

differential across the separator. The relationship of design variables such as separator channel geometry, number and length together with fluid properties, flow rates and applied pressure differential were examined mathematically and linked to experimental findings together with predicted and observed limits of operation of the separator. This systematic study of phase separator performance together with examination of the mathematical relationships governing liquid–liquid separation and device failure, will enable optimal device design and provide the opportunity to predict the influence of fluid manipulation and events downstream of the separator (*e.g.* re-segmentation and separation). The demonstration of the separation device to operate with microparticulates suspended in the organic phase paves the way for on-chip multi-fluid phase, solid phase assisted reactions, separations and manipulations. The inherent properties of segmented flow streams to give rise to highly efficient mass transfer and rapid mixing of chemical species generates the potential to mix and transfer chemical species between phases and immediately separate the fluid components in a single 'always-on' device, offering massive efficiency advantages over traditional batch techniques. This will constitute a focus of future work, which aims to utilise segmented flow, together with an optimised phase separation device for liquid–liquid, and solid phase-assisted, continuous flow chemical separations.

References

1 C. Lee, G. Sui, A. Elizarov, C. J. Shu, Y. Shin, A. N. Dooley, J. Huang, A. Daridon, P. Wyatt, D. Stout, H. C. Kolb, O. N. Witte, N. Satyamurthy, J. R. Heath, M. E. Phelps, S. R. Quake and H. Tseng, *Science*, 2005, **310**, 1793–1796.
2 N. Pamme, *Lab Chip*, 2007, **7**, 1644–1659.
3 J. Wang, A. Ibanez and M. Chatrathi, *J. Am. Chem. Soc.*, 2003, **125**, 8444–8445.
4 H. R. Sahoo, J. G. Kralj and K. F. Jensen, *Angew. Chem., Int. Ed.*, 2007, **46**, 5704–5708.
5 S. Teh, R. Lin, L. Hung and A. P. Lee, *Lab Chip*, 2008, **8**, 198–220.
6 B. Karlberg and S. Thelander, *Analytica Chimica Acta*, 1978, **98**, 1–7.
7 O. K. Castell, C. J. Allender and D. A. Barrow, *Lab Chip*, 2008, **8**, 1031–1033.
8 C. J. Gerdts, V. Tereshko, M. K. Yadav, I. Dementieva, F. Collart, A. Joachimiak, R. C. Stevens, P. Kuhn, A. Kossiakoff and R. F. Ismagilov, *Angew. Chem., Int. Ed*, 2006, **45**, 8156–8160.
9 T. Nisisako and T. Torii, *Lab Chip*, 2008, **8**, 287–293.
10 B. Ahmed, D. Barrow and T. Wirth, *Advanced Synthesis & Catalysis*, 2006, **348**, 1043–1048.
11 A. Huebner, M. Srisa-Art, D. Holt, C. Abell, F. Hollfelder, A. J. deMello and J. B. Edel, *Chem. Commun.*, 2007, 1218–1220.
12 M. J. Fuerstman, P. Garstecki and G. M. Whitesides, *Science*, 2007, **315**, 828–832.
13 J. Ruzicka and E. H. Hansen, *Analytica Chimica Acta*, 1975, **78**, 145–157.
14 A. Gunther and K. F. Jensen, *Lab Chip*, 2006, **6**, 1487–1503.
15 N. Harries, J. R. Burns, D. A. Barrow and C. Ramshaw, *International Journal of Heat and Mass Transfer*, 2003, **46**, 3313–3322.
16 J. R. Burns and C. Ramshaw, *Lab Chip*, 2001, **1**, 10–15.
17 K. Ishiguro, M. Iguchi, Y. Mizuno and Y. Terauchi, *JSME International Journal Series B*, 2004, **47**, 795–803.

18 Y. Kikutani, H. Ikeda, M. Harada, Y. Ikeda, M. Tokeshi, and T. Kitamori, in *The Proceedings of µTAS 2007 Conference*, Paris, France, 2007, vol. 2, pp. 955–957.

19 H. Xiao, D. Liang, G. Liu, M. Guo, W. Xing and J. Cheng, *Lab Chip*, 2006, 6, 1067–1072.

20 J. Atencia and D. J. Beebe, *Nature*, 2005, 437, 648–655.

21 J. Tsai and L. Lin, *Sensors and Actuators A: Physical*, 2002, 97–98, 665–671.

22 D. Angelescu and D. Siess, in *Proc. Sensors 2005 IEEE*, 2005, p. 4 pp.

23 L. Nord and B. Karlberg, *Analytica Chimica Acta*, 1980, 118, 285–292.

24 J. G. Kralj, H. R. Sahoo and K. F. Jensen, *Lab Chip*, 2007, 7, 256–263.

25 N. A. Mortensen, L. H. Olesen and H. Bruus, *New Journal of Physics*, 2006, 8, 37.

26 N. A. Mortensen and H. Bruus, *Phys. Rev. E*, 2006, 74, 017301–4.

27 N. A. Mortensen, F. Okkels and H. Bruus, *Phys. Rev. E*, 2005, 71, 057301–4.

28 M. C. Porter, *Handbook of Industrial Membrane Technology*, Noyes Publications, 1990.

29 A. Jena and K. Gupta, *Fluid/Particle Separation Journal*, 2002, 14, 227–241.

30 O. V. Nechypor, V. M. Gun ko, V. M. Barvinchenko and V. V. Turov, *Biopolimery I Kletk*, 2006, 22, 375.

31 P. Garstecki, M. J. Fuerstman, H. A. Stone and G. M. Whitesides, *Lab Chip*, 2006, 6, 437–446.

32 A. HAZEL and M. HEIL, *Journal of Fluid Mechanics*, 2002, 470, 91–114.

33 T. Cubaud, *Physics of Fluids*, 2004, 16, 4575–4585.

34 A. Kawahara, P. M. - Chung and M. Kawaji, *International Journal of Multiphase Flow*, 2002, 28, 1411–1435.

35 P. M. Y. Chung and M. Kawaji, *International Journal of Multiphase Flow*, 2004, 30, 735–761.

36 M. J. Fuerstman, A. Lai, M. E. Thurlow, S. S. Shevkoplyas, H. A. Stone and G. M. Whitesides, *Lab Chip*, 2007, 7, 1479–1489.

37 H. Chio, M. J. Jensen, X. Wang, H. Bruus, and D. Attinger, in *Proceedings of NSTI-Nanotech 2006*, Technical University of Denmark, Boston, USA., pp. 497–500.

38 M. N. Kashid and D. W. Agar, *Chemical Engineering Journal*, 2007, 131, 1–13.

39 H. Chio, M. J. Jensen, X. Wang, H. Bruus and D. Attinger, *Journal of Micromechanics and Microengineering*, 2006, 16, 143–149.

40 B. J. Adzima and S. S. Velankar, *Journal of Micromechanics and Microengineering*, 2006, 16, 1504–1510.

41 T. Cubaud, U. Ulmanella and C. Ho, *Fluid Dynamics Research*, 2006, 38, 772–786.

42 S. Vladimir Ajaev and G. M. Homsy, *Annual Review of Fluid Mechanics*, 2006, 38, 277–307.

43 H. Wong, S. Morris and C. J. Radke, *Journal of Colloid and Interface Science*, 1992, 148, 317–336.

44 N. V. Churaev, *Advances in Colloid and Interface Science*, 2003, 104, xv–xx.

45 M. Abkarian and H. A. Stone, *Electrophoresis*, 2005, 26, 3716–3724.

46 M. D. Shirk and P. A. Molian, *J. Laser Appl.*, 1998, 10, 18–28.

47 A. Kruusing, *Optics and Lasers in Engineering*, 2004, 41, 329–352.

48 L. R. Huang, E. C. Cox, R. H. Austin and J. C. Sturm, *Science*, 2004, 304, 987–990.

49 S. A. Kulkarni, S. B. Ogale and K. P. Vijayamohanan, *Journal of Colloid and Interface Science*, 2008, 318, 372–379.

50 R. Tornay, T. Braschler, N. Demierre, B. Steitz, A. Finka, H. Hofmann, J. A. Hubbell and P. Renaud, *Lab Chip*, 2008, 8, 267–273.

MICROWAVE COMPOSITIONAL ANALYSIS OF SOLVENT MATRICES IN MICROCAPILLARY MANIFIOLD SYSTEMS

R. Göritz[1], A. Masood[1], O. Castell[1,2], D.A. Barrow[1], C. Allender[2] and A. Porch[1]

[1]School of Engineering, Cardiff University, Cardiff, CF24 3AA, United Kingdom
[2]School of Pharmacy, Cardiff University, Cardiff, CF10 3NB, United Kingdom

ABSTRACT

A compact microwave resonator, of resonant frequency 2.8 GHz, is used to measure the complex relative permittivity of an acetonitrile:toluene solvent mixture within a PEEK microcapillary. Experimental results for the change in resonant frequency and transmitted power on resonance (both as a function of composition) are very close to those predicted using cavity perturbation theory from the known dielectric properties of the starting mixtures, measured separately using a coaxial reflectance probe. The combined measurements of frequency shift and transmitted power allow very accurate (< 1% error) and fast (< 0.1s) compositional analysis of polar solvent mixtures.

Keywords: microwave resonator, dielectric measurements, solvent composition

1. INTRODUCTION

In-situ, on-chip, compositional analysis of liquids is desirable in a diverse range of microchemistry applications. Fast, non-invasive, techniques are required for process control but are generally unavailable. Polar liquids interact strongly with microwave electric fields, as is evidenced by the extreme heating of a water-containing substance in a domestic microwave oven operating at 2.45 GHz, so non-contacting, non-invasive microwave techniques hold potential for compositional analysis of polar liquids. Large liquid volumes (i.e. typically a few cm^3 upwards) can be analyzed using a coaxial reflectance probe (e.g. [1]), but measurements of smaller volumes (i.e. mm^3 or less) in arbitrary shaped vessels and ducts are more problematic. Here, we use a quarter-wave copper hairpin resonator for in-situ analysis of a capillary containing mixtures of acetonitrile and toluene, selected as an initial evaluation system due to the large difference in molecular electric dipole moments.

2. EXPERIMENTAL DETAILS

A schematic diagram of the hairpin resonator package is shown in Figure 1. The resonator was a 1 mm thick copper sheet, of width 20 mm, formed into a u-shaped configuration of length 25 mm and plate gap of 5 mm, yielding a resonant frequency of around 2.8 GHz when empty. The resonator is excited magnetically by a pair of loop-terminated, semi-rigid coaxial cables. The transmitted microwave power is measured in the frequency domain using an Agilent 8753 vector network analyzer. This type of resonator has been used extensively for the non-destructive evaluation of the electrical properties of solids [2]. Here, we present a novel adaptation to interrogate a liquid-containing PEEK microcapillary, which passes through the open-end of the hairpin, where the microwave electric field is largest and is approximately uniform. Since the electric field decays very rapidly with distance outside of the hairpin plates, the measurement provides the average dielectric properties of the liquid contained in the 20 mm long section of capillary between the plates, corresponding to an active liquid volume of approximately 15 µl.
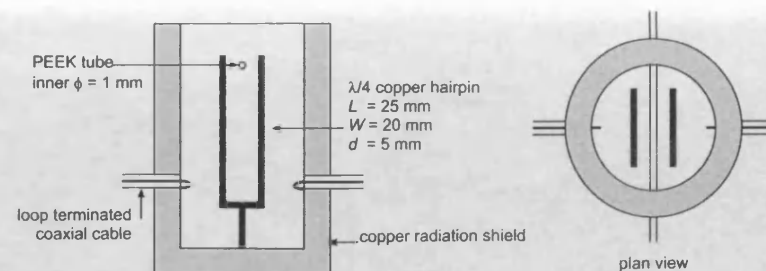
Figure 1. Schematic diagram of the packaged copper hairpin resonator. The resonant frequency when empty is approximately 2.8 GHz. The liquid sample (of active volume 15 µl) is injected into a PEEK microcapillary positioned at the region of maximum electric field at the open end of the resonator.
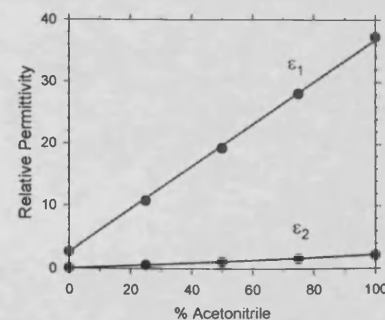
Figure 2. The polarisation ε_1 and loss ε_2 terms at 2.68 GHz of the relative permittivity of an acetonitrile:toluene mixture. Solid lines are the predictions of a simple linear mixing rule.
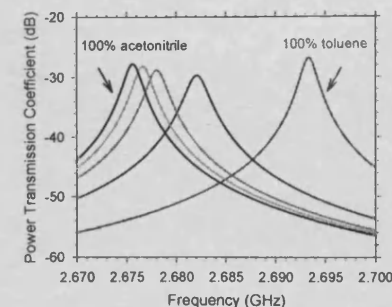
Figure 3. Transmitted power as a function of frequency for acetonitrile:toluene mixtures in the % proportions 100:0, 75:25, 50:50, 25:75 and 0:100 (in the sequence left to right).

3. RESULTS AND ANALYSIS

The real ε_1 and imaginary ε_2 parts of the complex relative permittivity of the component liquids were first measured in the range 2.5 – 3 GHz using a coaxial reflectance probe; the data at 2.68 GHz, appropriate for the experiments reported here, are shown in Figure 2. The measured resonance curves a function of acetonitrile:toluene composition are shown in Figure 3, from which the resonant frequency and transmitted power at resonance (expressed in dB) are determined and are plotted in Figures 4 and 5, respectively. The resonant frequency decreases monotonically as the polar nature of the solvent mix increases. Also shown in Figure 4 is the theoretical prediction (from standard cavity perturbation theory) for a liquid-filled PEEK capillary, based on the measured dielectric properties of the component solvents (Figure 2). The peak transmitted power is minimized (i.e. loss maximized) for small proportions of acetonitrile ($\approx$12%). This curious result is also entirely predicable by theory (the solid curve of Figure 5), its physical interpretation being the competition between the increased dielectric loss and the reduced internal electric field (by depolarization) within the liquid mixture as the proportion of acetonitrile is increased.

Figure 4. The resonant frequency as a function of composition. The theoretical dependence is shown by the solid line.
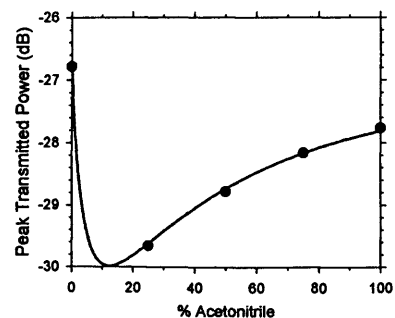
Figure 5. The peak transmitted power (in dB) as a function of composition. The theoretical dependence is shown by the solid line.

4. CONCLUDING REMARKS

There are multiple benefits of this microwave resonant technique over other methods. Firstly, it is fast, with data accumulation on a timescale of less than 0.1 s, thereby enabling compositional analysis in situations where fluid flow and/or chemical reaction are occurring. Secondly, it is non-destructive and applicable to arbitrarily-shaped sample volumes. Using the existing experimental set-up, the proportion of acetonitrile in toluene can be measured to an accuracy of < 0.1%. This work complements works elsewhere on microanalysis involving microwave heating, e.g. polymerase chain reaction [3]. In the near future, we plan to enhance the sensitivity of the measurement system by using microwave host resonators (a) of smaller volumes, and (b) whose electric field is along the axis of the microcapillary, the latter leading to negligible depolarization. Regarding the size reduction (a), the measured sensitivity is inversely proportional to the volume occupied by the microwave electric field energy, so a reduction in effective volume from about 1 cm^3 (as for the hairpin here) to about 1 mm^3 (as can be achieved in a lumped element resonator, whilst maintaining the same resonant frequency) can either give rise to a ×1000 enhancement of measurement sensitivity for the same sample volume, or a ×1000 sample volume reduction for the same measurement sensitivity. These next-generation resonators will enable measurements on microfabricated resonator-capillary systems of much smaller volumes, and/or on liquid mixtures with components more closely matched in terms of their electric dipole moments (e.g. acetonitrile and water).

REFERENCES

[1]   J.P. Grant *et al.*, "A critical study of the open-ended coaxial line sensor technique for RF and microwave complex permittivity measurements", Journal of Physics E – Scientific Instruments, 22 (9) 757-770 (1989)

[2]   M.J. Edmondson *et al.*, "Can alkali metal doped zeolites be metallic? - Microwave conductivity of rubidium doped zeolite rho", Zeitschrift für Physikalische Chemie 217 (8) 939-955 (2003)

[3]   P.-A. Auroux *et al.*, "Microfluidic method for thermal cycling by microwave dielectric heating", Proceedings of MicroTAS2006, Tokyo, pp.1465-1467 (2006)

SPLIT RING RESONATOR TECHNIQUE FOR COMPOSITIONAL ANALYSIS OF SOLVENTS IN MICROCAPILLARY SYSTEMS

A. Masood[1], O. Castell[1], D.A. Barrow[1], C. Allender[2] and A. Porch[1]

[1]School of Engineering, Cardiff Universty, UNITED KINGDOM and
[2]School of Pharmacy, Cardiff University, UNITED KINGDOM

ABSTRACT

A 3.4 GHz split ring resonator has been developed for highly sensitive remote compositional analysis of PEEK microcapillaries containing mixtures of acetonitrile in toluene. As little as 0.1% vol. acetonitrile can be measured in an active volume of around 50 nl. The method is fast (< 0.1 s per measurement) and is adaptable to compositional analysis where fluid flow and/or chemical reactions are occurring.

KEYWORDS: Microwave resonator, dielectric properties, solvent composition

INTRODUCTION

Microwave resonators enable precise, non-invasive and fast compositional analysis of liquid mixtures for a variety of industrial, analytical and quality control applications. Previously, we have demonstrated successfully a hairpin resonator for in-situ analysis of a microcapillary containing a mixture of polar solvents [1]. Here, the use of a split ring resonator has enhanced significantly the measurement sensitivity.

THEORY

The presence of a sample in the high electric field region in the resonator's gap (see Figure 1) will reduce both the resonant frequency f_0 and quality factor Q owing to polarization. These can be expressed using resonator perturbation analysis, giving

$$\frac{\Delta f_0}{f_0} \approx -\frac{\text{Re}(\alpha)}{2V_{\text{eff}}} \quad (1) \qquad \Delta\left(\frac{1}{Q}\right) \approx -\frac{\text{Im}(\alpha)}{V_{\text{eff}}} \quad (2)$$

where α is the sample's electric polarizability (defined by the induced electric dipole moment $p = \alpha\varepsilon_0 E_0$, E_0 being the applied electric field) and V_{eff} is the volume occupied by the electric field energy, essentially the volume of the gap. The split ring resonator is a lumped element structure [2] that can be designed to have a small V_{eff}, resulting in high sensitivity to the sample's dielectric polarization and power loss.

EXPERIMENTAL

The split ring resonator of Figure 1 consists of a copper ring having a length, thickness and inner radius each of 3 mm. The gap was machined mechanically to a width of 400 μm, yielding a resonant frequency of ≈ 3.4 GHz. Transmitted micro-wave power was measured in the frequency domain using a vector network analyzer. The empty resonator has a high quality factor ($Q \approx 1400$) for such a small $V_{\text{eff}} \approx 0.4\times3.0\times3.0$ mm^3 ≈ 3.6 μl. A liquid-containing PEEK microcapillary (inner radius 75 μm) was passed through the gap, where the microwave electric field is uniform and perpendicular to the microcapillary's axis, and the liquid composition varied. The liquid volume is approximately 50 nl in each case. At resonance, less than 10 μW of microwave power is dissipated in the sample, so heating effects are negligible.
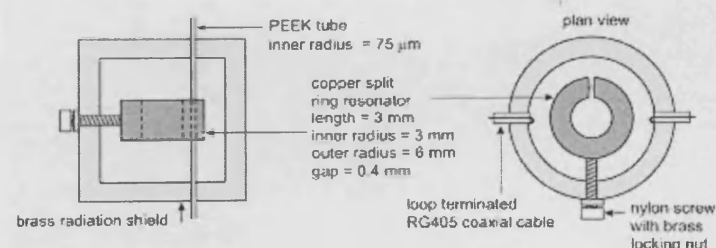
Figure 1. Schematic diagram of the 3.4 GHz split ring resonator package.
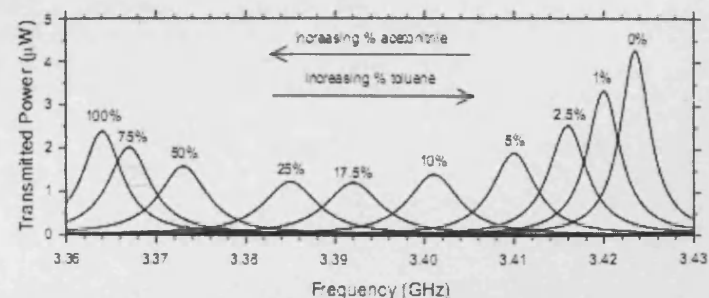
Figure 2. The transmitted power measured as a function of frequency for various acetonitrile:toluene solvent mixtures (volume % of acetonitrile is shown).

RESULTS AND DISCUSSION

Mixtures of acetonitrile in toluene were first measured using a coaxial reflectance probe [1] to establish the variation of complex permittivity with composition. Resonances perturbed by solvent mixtures are shown in Figure 2, from which the change of resonant frequency and unloaded Q factor were measured (Figures 3 and 4, respectively). The resonant frequency decreased monotonically as the polar nature of the solvent mixture increased. Also shown in Figure 3 is the theoretical prediction for a liquid-filled PEEK capillary, based on the measured dielectric properties of the component liquids and PEEK tube. The Q was minimized (i.e. microwave power loss maximized) for small proportions of acetonitrile (≈ 18%). This is entirely predi-

cable by theory (solid curve of Figure 4), its physical interpretation being the competition between the increased dielectric loss and the reduced internal electric field (by depolarization) within the solvent mixture as the proportion of acetonitrile was increased.
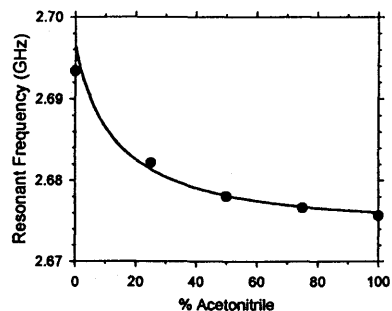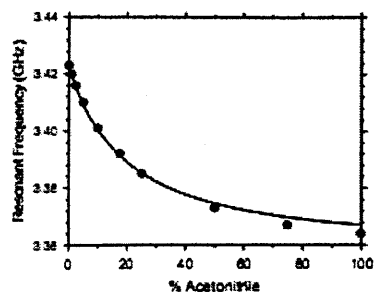

Figure 3. The resonant frequency as a function of fluid composition (the solid line is the theoretical prediction from Eqn. 1, based on the measured dielectric properties of the solvent mixture).
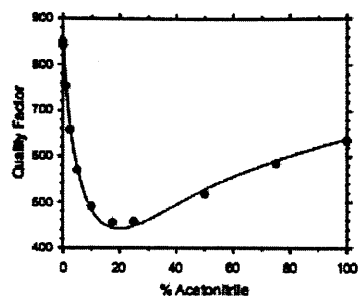
Figure 4. The unloaded quality factor as a function of fluid composition (solid line is the theoretical prediction from Eqn. 2). Note the sensitivity to small % volume of polar species.

CONCLUSIONS

There are numerous benefits of this split ring microwave resonator technique over other methods. Firstly, it is fast, with data accumulation on a timescale of less than 0.1 s, hence enabling compositional analysis in situations where fluid flow and/or chemical reaction are occurring. Secondly, being wavelength independent, the size of split ring resonator can be miniaturized to suit the system under test. Thirdly, the very small volume occupied by the microwave electric field energy (i.e. volume of the gap region) leads to very sensitive compositional analysis compared to resonator techniques where the field energy is distributed over a larger volume [1], [3]; here, less than 0.1% by volume of acetonitrile in toluene can be detected. We plan to further enhance the sensitivity by using microwave resonators whose electric field is along the microcapillary axis, thereby leading to negligible depolarization.

REFERENCES

[1] R. Göritz et al., "Microwave compositional analysis of solvent matrices in microcapillary manifold systems", Proc. MicroTAS 2007, Paris, pp.1689-1691, (2007).

[2] J.S. Hyde and W. Froncisz, "Loop-gap resonator: a lumped mode microwave resonant structure", IEEE Trans. MTT, vol. 83, no. 12, pp.1059-1064, (1983).

[3] K. Saeed et al., "Microstrip Resonator Technique for Measuring Dielectric Permittivity of Liquid Solvents and for Solution Sensing", Proc. IEEE/MTT-S Int. Microwave Symposium 2007, Hawaii, pp.1185-1188, (2007).

[4] P.A. Auroux et al., "Microfluidic method for thermal cycling by microwave dielectric heating", Proc. MicroTAS 2006, Tokyo, pp.1465-1467, (2006).

MICROWAVE TECHNIQUE FOR MONITORING PHASE SEPARATION OF A MULTIPHASE-FLOW REGIME UTILISED FOR CONTINUOUS MOLECULAR ENRICHMENT

O. Castell, A. Masood, R. Göritz, D. Barrow, C. Allender & A. Porch

School of Engineering, Cardiff University, UNITED KINGDOM

ABSTRACT

A 3.0 GHz hairpin microwave resonator has been developed and applied to monitor the liquid compositional output of a multiphase-flow liquid phase separator. An integrated, planar segmented flow generating and separating device is utilised for phase transfer molecular extraction. Extraction efficiency is determined in real time by flow-through UV absorption, whilst microwave resonance analysis simultaneously monitors phase separation efficiency. A promising integrated approach for enhanced efficiency chemical separations and real time performance monitoring.

KEYWORDS: Microwaves, Multiphase Flow, Phase Separation, Liquid Extraction

INTRODUCTION

Solvent extraction is a widely utilised technique to separate or isolate compounds on the basis of their relative solubility in two immiscible liquids. Widely employed in sample preparation (e.g. pharmaceutical and clinical analysis), and as part of the work-up process to isolate products of chemical reactions, the drive for both time and yield efficiency together with process selectivity is huge.

THEORY

Controlled elution of immiscible fluids into a common duct generates segmented flow regimes of alternating immiscible fluid packets, each exhibiting high internal mixing with a continually refreshing interface, together with a large surface area to volume ratio. This enables the rapid attainment of chemical equilibrium between adjacent fluid phases [1]. Consequently, massively accelerated solvent-solvent extractions can be performed, with the extent of analyte removal from the sample enhanced through inclusion of a solid affinity phase suspended in the extracting fluid [2]. Here we demonstrate subsequent on-chip liquid-phase separation of the segmented flow stream through capillary forces [3], enabling continual collection of the desired analyte-purified phase. Microwave resonators [4] [Fig 1] characterise the dielectric properties of the separated liquid streams, continually monitoring phase separator performance. UV interrogation of the aqueous phase assesses extraction efficiency.

EXPERIMENTAL

Segmented flow regimes of aqueous propranolol solutions (50μM) and chloroform (± molecularly imprinted polymer solid phase adsorbent [MIP] 1mg/ml) were generated on-chip by a T-junction geometry flowing into a 35cm long 500x500μm micromilled channel. An array of 140 Gaussian profile (w = 34μm, h = 130 μm),
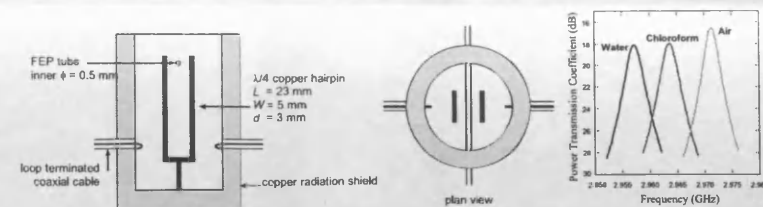
Figure 1: Schematic of the copper hairpin resonator. The phase separated liquid sample flows through the tubing positioned at the region of maximum electric field at the open end of the resonator. The measured resonance responses of the device with the capillary filled with water, chloroform and air are illustrated.
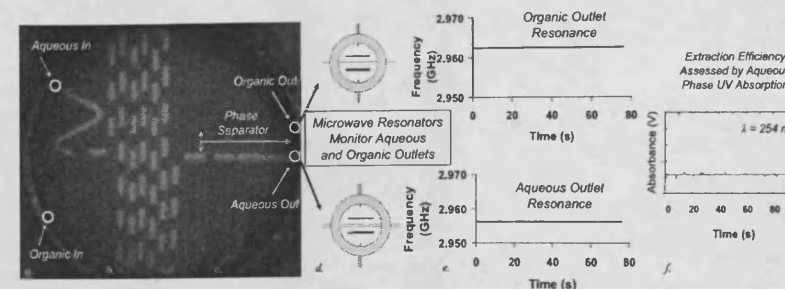
Figure 2: a) Segmented flow generated between the aqueous sample and the extracting chloroform phase (± Molecularly Imprinted Polymer). b) Efficient mixing facilitates rapid mass transfer of analyte from the sample to the extracting phase. c) Phase separation based on capillary forces separates the segmented flow stream into its component fluid phases. d) Microwave resonators interrogate the electrical properties of the two separated streams in real time. e) Experimental data - resonant frequency vs time for the fluid flow from each outlet of the separator, confirming 100% phase separation efficiency. f) flow cell UV absorbance of the aqueous phase is used to calculate the concentration of analyte remaining in the aqueous phase.

laser machined, side channels, branch from the main fluidic duct to elute into a second exit channel. The pressure differential between the two fluidic outlets was carefully regulated maintaining sufficient pressure to support the flow of the wetting organic phase through the separation ducts, whilst not breaching the aqueous breakthrough pressure. The organic and aqueous outlets exited the chip through FEP tubing (I.D. 500μm), which was interrogated by a hairpin resonator (Fig. 1). The capillary passed through the open-end of the hairpin where the microwave electric field is largest, and the transmitted microwave power over a range of frequencies measured. The aqueous outlet was interfaced with an HPLC UV detector to continually assess the analyte concentration remaining in the aqueous phase. Extraction of propranolol from the aqueous sample was assessed over a range of flow rates and validated by microplate fluorescence spectroscopy of collected fractions.

RESULTS AND DISCUSSION

Microwave interrogation in the frequency domain of fluid flowing from the phase separator outlets confirmed complete phase separation (Fig 2) and instances where ineffective pressure regulation caused the separator to fail (Fig 3). UV absorption confirmed an extraction of $20\mu M$ propranolol from the aqueous sample, independent of the flow rates employed (Fig 4), indicative of attainment of equilibrium. The addition of MIP to the extracting phase was seen to enhance the extent of extraction (Fig 4).
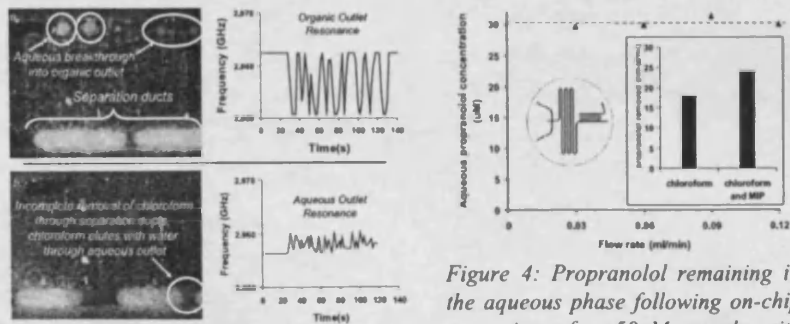
Figure 3: Microwave resonance response to inefficient phase separation. a) Too great applied pressure differential. b) Too low applied pressure differential.

Figure 4: Propranolol remaining in the aqueous phase following on-chip extraction of a $50\mu M$ sample with chloroform. Inset: Schematic of extraction chip and enhanced efficiency of extraction by incorporation of MIP affinity phase.

CONCLUSIONS

Segmented flow and liquid phase separation on the basis of capillary forces, enables the continuous on-chip extraction of analyte species from an aqueous sample. Microwave resonators provide an ideal method for the assessment of liquid phase separation performance. The frequency dependant transmission of microwave power can be assessed rapidly (<10ms), enabling continual, non-contact analysis. Unlike optical approaches the technique can be applied to opaque matrices, as reported here with the use of suspended MIP particles which enhance extraction efficiency. The possibility of resonator feedback pressure regulation of the phase separator is easily envisaged, which together with MIP optimisation is a focus of ongoing work.

REFERENCES

[1]   N. Harries et al., A numerical model for segmented flow in a microreactor, Int. J. Heat Mass Transf. 46, 3313 – 3322, (2003).

[2]   O.K. Castell et al., Continuous molecular Enrichment in Microfluidic Systems, Lab on a Chip, 10.1039/b800521d, (2008).

[3]   O.K. Castell et al., Microfluidic liquid-liquid phase separation: Characterisation of a membrane free and surface modification free microfluidic phase separator, Lab on a Chip, accepted, (2008).

[4]   R. Göritz et al., Microwave compositional analysis of solvent matrices in microcapillary manifold systems, Proc. µTAS 2007, Paris, pp.1689-1691, (2007).

Microfluidic Liquid Separation Device and Methods for Construction and Application

Field of Invention

The present invention relates to microfluidic liquid separation devices and assemblies, methods for their construction with preferred embodiments and methodologies for the functional operation of such.

Background

Microfluidics defines the science and technology of systems that process or manipulate small (10^{-9} to 10^{-18} L) volumes of fluids using channels with dimensions on the micrometer scale (Whitesides 2006). The fundamental differences between fluid behaviour on the micro-scale compared to the macro-scale, gives rise to unique phenomena, creating opportunities for fluid and sample handling in space and time which would otherwise be unachievable with large scale approaches. The inherent small scale of such technology lends itself to device integration, with Philips®, amongst others, demonstrating successful commercial application of microfluidic technology with liquid lenses for camera phones and miniature cameras (Graham-Rowe 2006).

Since the conception of the microfluidic discipline the interest in multiphase microfluidics, which entails the controlled manipulation of two, or more, immiscible fluids on the microscale, has been growing exponentially. The dominance of surface forces on the small scale enables the generation of unique flow regimes of alternating immiscible organic and aqueous fluid packets, often termed, segmented flow or slug flow.

Segmented flow regimes have many desirable characteristics, including; Highly reproducible, and tuneable drop size; high surface area:volume ratio; rapid mixing due to recirculating flow pattern within fluid segments; rapid mass transfer; compartmentalisation of chemical species; low diffusion time. These characteristics are subject of much interest due to the opportunity to both improve efficiency of processes traditionally carried out on the macro-scale and also to enable novel and unique processing which would be otherwise impossible. Such applications of multiphase microfluidics include; accelerated chemical reactions; vastly increased efficiency of chemical reactions (yield); chemical separations; interfacial chemistry (i.e. catalysis); particle production; encapsulation (e.g. biological cells, molecular reagents, quantum dots); crystallisations; chemical computing. In many above mentioned applications, it is usually desirable to separate and recover the component immiscible fluids in order to harvest synthesised particles, recover extracted molecular species or products of chemical reactions. Consequently the development of a high efficiency, multi-purpose, liquid-phase separating device is highly desirable.

Prior to the establishment of the field of microfluidics, segmented flow was being utilised in the filed of analytical chemistry, albeit on a significantly larger scale. Unlike the drive for device miniaturisation and integration associated with modern microfluidic applications, affording both performance and footprint advantages, segmented flow analysis was conducted in several meters of tubing, with an inner diameter of typically 0.5 – 3 mm, at flow rates typically faster than those used in microfluidic applications. Segmented flow

analysis utilised the introduction of a gaseous phase to segment a continuous liquid stream (sample and reagents). The segmentation was utilised to minimise axial dispersion, encourage sample and reagent mixing and maintain separation of sequential samples. This technique enabled a high sample throughput under continuous flow operation, thus increasing the efficiency of standard laboratory analysis techniques (i.e. extraction, dialysis, ion exchange, heating, incubation, distillation and analyte quantification). This led to the development of a closely related technique; flow injection analysis (FIA), which utilised an immiscible liquid phase as the carrier phase into which the sample phase was segmented. The immiscible carrier liquid would carry the required reagents which would partition into, and mix with, the injected sample segments.

Most applications of F.I.A. are analytical. As such complete phase separation is not usually necessary, as only a portion of the purified phase need be separated from the segmented flow stream to pass to a suitable detector to quantify analyte concentration. Typically, phase separators may operate at 35% separation efficiency, (Karlberg & Thelander 1978) and used either gravimetric (Anthemidis et al. 2004) or membrane (Nord & Karlberg 1980) based approaches.

Immiscible liquids may be separated on the basis of density difference. However, on the microscale, gravitational forces are dominated by surface forces. Consequently, separation by this means is not possible on the low volume scale required for microfluidic applications.

A membrane based approach to phase separation utilises a difference in capillary forces between the two immiscible fluids with a selectively wetting material to separate a segmented flow stream into its component fluid phases. Reported devices use a porous fluoropolymer membranes (pore size usually < 1μm). A pressure differential is applied across the membrane, sufficient to enable the passage of the wetting phase through the membrane pores, but insufficient to exceed the breakthrough pressure required for the non-wetting phase to enter the pores, defined by the Young-Laplace equation. This was independently developed (and patented) by three researchers (Nord & Karlberg 1980; D.E. Angelescu & Siess 2005; Kralj, Sahoo & Jensen 2007). With the methodology first reported in the context of flow injection analysis (Nord & Karlberg 1980), then subsequently reported in the context of the field of microfluidics, without reference to previous membrane based phase separators (D.E. Angelescu & Siess 2005; Dan Eugen Angelescu et al. 2006; Kralj, Sahoo & Jensen 2007).

Membrane based phase separation is utilised by Syrris® in the FRX FLLEX product designed for conducting chemistry in a flow-though, microfluidic context.. Additionally, Dolomite® also manufacture a unit for liquid phase separation utilising the membrane based approach to liquid phase separation. These products demonstrate the commercial market for phase separation of segmented flow streams. The membrane based approach to segmented flow liquid phase separation has several limitations. The membrane itself is fragile, lacking in physical stability. The membrane can also become easily spoiled or clogged and needs frequent replacement (Anthemidis et al. 2004). This leads to challenging design requirements when manufacturing a device. Additionally, membrane separators are typically a sandwich composition of an upper and lower substrate material containing machined micro-channels, with the PTFE membrane separating them. This design specification, therefore, requires fully 3-D fluidic devices. This creates an integration difficulty with standard, planar, machining techniques where fluidic channels are typically created on a single surface, where channel depth provides the only z-axis component.

Capillary forces have been utilised to separate the components of gas-liquid segmented flows through an array of 10 μm x 50 μm wide side channels branching from a 200 μm x 50 μm main fluidic channel machined in a silicon substrate (Fig 2) (Tsai & Lin 2002). Gas – Liquid segmented flow streams however are inherently easier to separate than liquid-liquid segmented flows due to (*i*) the significantly greater surface tension (γ) between the phases (typically one order of magnitude), (*ii*) the difference in 'wetting' ability between liquid and gaseous phases to wet most solid materials, and (*iii*) the reduced pressure drop generated by gaseous flow.

Angelescu *et. al* attempted to adapt the concept of microchannel separation ducts to separate a liquid-liquid segmented flow stream using a device consisting of 15 x 15 μm square profile separation ducts branching from a main fluidic duct 100 x 15 μm in PDMS (polydimethyl siloxane) substrate (D.E. Angelescu & Siess 2005). However *complete phase separation could not be achieved with this architecture and the authors utilised a non-wetting membrane approach* to effectively narrow the geometry of the separation ducts. This increased the breakthrough pressure of the separator, and enabled complete phase separation of wetting phase flow rates of 0.03 ml min⁻¹.

Statement of invention

In accordance with a first aspect, a fluid manipulation device is described, which comprises device, most preferably constructed from, or coated with a film of, a fluoropolymer, less preferably constructed from other materials such as non-fluorinated polymers, silicon, glass metals, graphite, and silanised silicon and glass, consisting an input port leading to a flow channel of dimensions ranging in diameter, width or depth most preferably from 100 microns to 1mm leading to an output port or fluidic feature, a second, flow channel, of dimensions ranging in diameter, width or depth most preferably from 5 microns to 1mm, leading to an output port or fluidic feature, the first and second channels are in fluidic communication via one or more smaller separation ducts, each preferably of aspect ratio greater than 2, and preferably possessing a narrow cross-sectional length, less than 25% of that of the first channel, and preferentially being substantially rectangular, triangular or Gaussian in cross-section. The substantially planar microfluidic device is capable of separating fluid flows that incorporate two or more substantially immiscible fluids with 100% efficiency, over a range of flow rates (0-3 ml/min demonstrated). This capability is as a result of several unique features not considered by those previously attempting liquid-liquid phase separations by the employment of microchannel separation ducts.

Additionally, in accordance with this first aspect, the device is constructed from a fluoroploymer such as PTFE to ensure maximum difference in wetting properties between the two liquid phases and the device channel walls. This decreases the advancing contact angle (θ) of the disperse (non-wetting) phase droplets as they approach the phase separation ducts, to a value approaching 0°. This is unlike the mildly hydrophilic properties of silicon, or the variable hydrophilic/hydrophobic properties of polymethyldisiloxane. The upper operating limit of any phase separation device utilising capillary forces is dependant upon the pressure differential (ΔP) between the two fluidic pathways (separation ducts and main channel) at which the non-wetting phase enters the separation ducts or membrane pores. This is defined by the equation for calculation of capillary pressure (1), derived from the Young-Laplace equation:

$$P_b = \frac{\alpha \gamma \cos \theta}{r} \tag{1}$$

where γ is the interfacial surface tension between the two fluids (liquid/liquid or liquid/gas) (N m⁻¹), θ the wetting angle, r the pore radius (m) (cylindrical pores) and α a numerical prefactor, a value of 2 is used for cylindrical pores. The equation demonstrates that the point of entry of the non-wetting liquid into the separation duct, the breakthrough pressure of the device, has a strong correlation with advancing contact angle (θ) and separation channel geometry (r = radius of circular cross sectional channel). Consequently significant performance advantage is gained from utilising a substrate material with maximal difference in wetting properties between the two liquid phases. Additionally, unlike both PDMS and silicon whose surface chemistry can change with prolonged chemical contact, PTFE and other hydrophobic fluoropolymers are extremely chemically resistant maintaining their surface properties and thus device performance.

The device design of Angelescu *et. al* constructed from cross-linked polydimethylsiloxane (PDMS) assumed a narrow separation channel geometry in all cross-sectional dimensions (see later) and, importantly, a main segmented flow carrying channel of the same depth as the narrow separation ducts, to encourage flow of the wetting phase though the separation ducts. This, however, counter-intuitively, restricts the performance efficiency of the device. The geometry of the main segmented flow carrying channel has important implications for the operation of the phase separator.

It is a non-intuitive design enhancement that a wider and/or deeper main fluidic channel, should facilitate an increase in phase separation efficiency with respect to both volumetric clearance **and** in terms of a percentage measure of the overall separation efficiency. This is non-intuitive since this design alteration results in an increase in the volume of fluid required to be separated, as a result of the increased volume of the main segmented flow carrying channel. In addition this also increases the distance the wetting fluid is required to be drawn by surface forces to reach the separation ducts, to subsequently be removed from the multiphase flow stream.

The main segmented flow carrying channel must be sufficiently narrow in both cross sectional directions for surface forces to dominate over other forces acting on the fluid(s) (i.e. ideally < 1 mm). Yet, also sufficiently wide (i.e. ideally > 100 μm) in all directions to prevent the generation of excessive pressure drop due to flow of the segmented, or separated, flow streams along the length of the complete phase separator architecture. In a laminar flow environment (single phase microfluidic flow) the pressure drop along the length of a channel is given by Hagen-Poiseuille's law (2):

$$\Delta P = \frac{\alpha \eta Q L}{A^2} \tag{2}$$

where ΔP is the pressure drop due to fluid flow (Pa), α is a numerical prefactor related to the geometry of the channel cross-section, η is fluid viscosity (Pa s), Q is flow rate of the fluid (m³ s⁻¹), L the channel length (m) and A the cross sectional area of the channel (m²). For a channel of any geometry cross-section, α is linearly related to the shape's compactness factor, C (3). (Niels Asger Mortensen, Okkels & Henrik Bruus 2005; N. A. Mortensen, Olesen & H. Bruus 2006; Niels Asger Mortensen & Henrik Bruus 2006)

$$C = \text{perimeter}^2/\text{area} \tag{3}$$

In segmented flow regimes the pressure drop due to flow is significantly more complex. This is due to the increased pressure generated as a result of interfacial forces and the induced pressure gradients as a result of re-circulating and vortex flow patterns. However, the general relationship is maintained, which for a given volumetric flow, sees the pressure drop generated increase 16 times when a channel radius is halved. Consequently, the effect of having a main channel of insufficient width or depth is that the pressure generated due to flow of the segmented flow stream in the channel, is sufficiently large that it approaches the breakthrough pressure of the separator. This is defined by equation 1, and results in device failure. This oversight constitutes a fundamental flaw in the device design of Angelescu *et al.*

The device design of Angelescu *et al.* assumed that the separation channel geometry must be narrow in all cross-sectional dimensions (figure 3 & figure 4A). In fact, the upper operating pressure limit, defined by the aqueous breakthrough pressure (equation 1) shows only a heavy dependence upon the narrowest of the two cross-sectional geometries (width or depth), and only a weak dependency on the larger of the two length scales. This is because for non-cylindrical geometries a/r in equation 1 can be substituted for the perimeter to area ratio of the pore opening (Jena & Gupta 2002).

Consequently, narrow, high-aspect ratio channels (as used in the invented device) enable much greater separation efficiency. An increase in the depth of the separation duct has very little difference on the pressure required for device failure through the non-wetting phase entering the separation ducts. However, high-aspect ratio separation ducts offer a marked increase in volume of wetting phase the separator is able to clear for any given pressure differential across the phase separator. This is a result of the increased cross-sectional area of each separation duct and the subsequent reduction in pressure required for flow of the wetting phase though the duct (equation 2). This reduces the force requirement for phase separation; i.e. enabling increased clearance of the wetting phase through the separation ducts for the same pressure differential across the separator. This ensures that the breakthrough pressure is not breached. As such, clearance of the wetting phase through the separation ducts has a strong dependency on both width and height of separation ducts.
Laser machining (e.g. 157 nm or 795 nm femtosecond pulsed) enables the creation of narrow, high aspect ratio, structures in PTFE and other fluoropolymers. Should material properties and machining techniques allow, optimal performance can be achieved through extremely high aspect ratio duct structures running from the top to the bottom of a main fluidic channel with geometries fulfilling the requirements outlined above.

The pressure requirement for flow of the wetting phase through the separation ducts is directly proportional to the length of the separation duct(s) (equation 2). As such, the length of the separation ducts should not be excessive for maximal operation efficiency (ideally < 5 mm, less ideally < 5 cm). Consequently, an array of narrow, high aspect ratio pillars effectively creating short, narrow, high aspect ratio separation ducts, would afford a high separation efficiency. Additionally an alternative design for separation ducts in a horizontal orientation, maintaining the desired requirements for a narrow cross-sectional dimension and a high cross sectional aspect ratio, is illustrated in figures 8A & 8B.

In many microfluidic applications, the linear flow velocity, distance - time proportionality, is utilised to control or monitor transit or reaction times. As such, high separation efficiency is desirable over the minimum possible length of the main fluidic duct, to maximise temporal resolution of the separation.

Phase separation efficiency also shows a linear relationship to the number of parallel separation ducts making up the phase separator architecture. As such, efficiency can be maximised by having numerous separation ducts in parallel, with minimum substrate pillar width between adjacent separation ducts (as machining techniques and material properties allow). This increases the temporal resolution of the separator. Additionally, separation ducts may branch from both sides of the main fluidic channel. The maximal total flow rate, separable by the phase separator architecture, can be increased by adding more and more separation ducts, increasing the total length of the separator architecture. (Up to a maximum length, where the pressure drop due flow of the segmented flow stream and/or the flow of the isolated non-wetting phase in the main separation channel over the length of the phase separator architecture, exceeds the breakthrough pressure of the non-wetting phase into the separation ducts). This can be compensated for, to some extent, through increasing the width and/or depth of the main fluidic channel, either over all, or part of, the length of the phase separation architecture.

The considered design of the complete phase separator architecture, including main fluidic duct and outlet geometries and lengths, together with fluid properties, can enable production of device(s) where the pressure differential driving the liquid-liquid separation is provided passively by the pressure differential between the flow of liquid either side of the phase separator ducts. Schematic examples are illustrated in figure 7.

The devices described demonstrate very significant non-intuitive advantages over other designs. These include: 100% separation efficiency; high efficiency affords high temporal and spatial resolution of separation; planar, one-step micromachining; readily integrates into complex fluidic systems (unlike membrane based devices); operational with microparticle carrying flows (difficult with membranes); high flow rate operation; robust and no requirement for replacement of separating feature required (unlike membranes); chemically resilient, no surface modification or surface regeneration required (unlike other substrate materials); and, considered design can enable passive operation for a range of conceivable multiphase flow regimes.

Description of the figures

Figs 1A shows a common segmented flow carrying channel (1) ranging, most preferably from 50 micrometres to 1 millimentre in both linear cross-sectional dimensions of diameter, and less preferably larger up to 1cm in either or both cross sectional directions, or smaller down to 1 micrometre in either or both cross sectional directions, through which flows a stream of immiscible fluids. Shown is a perfectly organised segmented flow stream of a first, continuous fluid (2) and a second immiscible, discontinuous fluid (3). However, the flow stream may be less regular ranging from irregular droplets of a disperse phase (3) within the continuous phase (2). Such immiscible flow streams may be caused deliberately or accidentally through ingress of one fluid into another, or be the breakdown product of a physiochemical process undertaken by use of a single phase flow stream in , for instance, a scientific instrument, a washing machine or a transformer cooling coil. Fig 1B shows a multiphase flow stream approaching a phase separation duct (4), the disperse phase (3) approaches with an advancing contact angle of θ, defined by the wetting properties of the fluids with the channel wall. Fig 1C shows a schematic (plan view) of a phase separator incorporated with another example fluid device for undertaking chemical reactions using

multiphase flow. In this example configuration, input port (5) & input port (6) conduct first and second immiscible fluids respectively, and at junction (7), form a segmented flow stream. After meandering the main channel (8) meets with separation ducts (4). At this meeting point phase separation begins to occur with the continuous phase (2), called the separated phase, entering the separation ducts (4). The separated phase continues along the separation ducts and empties into the common separated phase outlet duct (9), which conducts the separated fluid to a dedicated outlet for the separated fluid (10). Removal of the continuous phase (2) through the separation ducts (4), causes coalescence of the disperse phase droplets (3) into a continuous stream which flows to a dedicated outlet (11).

Fig 2A shows a portion of the separation architecture, consisting of a main channel (8) and adjoining separation ducts (4). Fig 2B illustrates the separation of a segmented flow stream of a continuous fluid (2) a discontinuous fluid (3), separating at the separation architecture, consisting of an array of parallel separation ducts (4). The more wetting, continuous phase, moves through the separations ducts (4) to the common separated phase outlet duct (9).

Fig 3 shows the inlet channel (12) and the microfabricated comb filter (13) of the invention reported by Angelescu and Siess (D.E. Angelescu & Siess 2005). The authors design, unlike the presented invention, does not consider the full significance of geometric features on the efficacy of separation, and thus was reported to be unable to achieve complete separation of an immiscible fluid flow. The authors employ a shallow inlet channel (15 μm) (12) of insufficient depth (with respect to the ducts of the microfabricated comb filter (15 μm x 15 μm) (13)) to prevent excessive pressure generation due to the flow of the fluid stream, thus causing breakthrough of the non-wetting, disperse phase, into the ducts of the microfabricated comb filter (13). The assumption that the ducts of the microfabricated comb filter (13) must be narrow in all cross sectional directions, restricts the clearance of the wetting, continuous phase, through the ducts of the microfabricated comb filter (13) and thus at lower operating pressures, breakthrough of the non-wetting, disperse phase, into the ducts of the microfabricated comb filter (13) *may* be avoided, but complete clearance of the wetting, continuous phase, through the ducts of the microfabricated comb filter (13) is not possible, with the authors reporting incomplete phase separation.

Figs 4A-B illustrates the fundamental difference between the invented device and that reported by Angelescu and Siess (D.E. Angelescu & Siess 2005). Fig 4A shows the sectional and plan views of the inlet channel (12) and the microfabricated comb filter (13) of the device reported by Angelescu and Siess (D.E. Angelescu & Siess 2005). Fig 4B illustrates the sectional and plan views of channel (8) and separations ducts (4) of the invention reported here. The non-intuitive design of channel (8) and separation ducts (4) of the invented device afford substantial performance advantages over the device reported by Angelescu and Siess (D.E. Angelescu & Siess 2005) enabling 100% efficiency separation over a range of flow rates. It is non-intuitive that an increase in volumetric capacity of the main immiscible fluid flow carrying channel (≡(12), ≡(8)) of over 280 times [(12) = 100 x 15 μm Fig 4A, (8) = 650 x 650 μm Fig 4B] will facilitate the greater separation of the immiscible fluid flow, in both *real* terms (volumetric) and with respect to separation efficiency (i.e percentage separation), though separation ducts (≡(13), ≡(4)) with an increased volumetric capacity of just under 10 times [(13) = 15 x 15 μm square Fig 4A, (4) = 34 x 130 μm triangular Fig 4B], with the geometric increase in capacity of separation ducts (4) having minimal effect on the operational pressure limit triggering breakthrough of the non-wetting, disperse phase (3), into the separation ducts (4), through the employment of high aspect ratio separation duct structures (4). This later dependency is illustrated graphically in Figure 5

Fig 5 (6A currently) illustrates the dependency of the upper operating limit, the breakthrough pressure of the non-wetting, disperse phase (3), into the separation ducts (4), and the region of 100% phase separation efficiency, on separation duct (4) geometry. The relationships were elucidated through thorough experimentation of the device illustrated in figure 1C, where the number (*n*) of parallel separation ducts (4) is 140 and an immiscible flow stream of chloroform and water (1:1) is employed. The upper operating limit, the breakthrough pressure of the non-wetting, disperse phase (3), into the separation ducts (4) is shown to have a high dependency on the narrowest geometry of the separation duct (4). The maximum volumetric throughput, and consequently maximum operating flow rate shows a high dependency the cross sectional area of the separation duct (4) geometry. Demonstrating the significant design advantage of high aspect ratio separation ducts (4). The theoretical operational limit for separation ducts of square cross-sectional profile with dimensions 15 x 15 μm (13) employed in the device design illustrated in figure 1C, under the afore described conditions, branching from a main channel (8) in accordance with the geometries detailed in the description of figure 4B, is calculated and represented on the figure (14).

Fig 6 (5 currently) shows an example arrangement of the phase separator integrated in a planar fluidic device (Figure 1C), micro-machined within a planar disc (15). This is one of many arrangements that will be clear to those skilled in the art. In the example configuration shown, planar substrate (15) is held within a vertical stack of components, including a baseplate (16), which incorporates sockets (17) for the application of fluid connectors (18), sealing film (19) which may be manufactured from a variety of materials, most preferably fluoropolymers such as polyfluorotetraethylene, perfluoroalkoxy, Teflon AF, fluorinated ethylene propylene, ethylene tetrafluoroethylene, less preferably from other material such as polyvinyl chloride, polycarbonate, polyethylene terephthalate, or amorphous polyetheretherketone, a top coverplate (20) which may be manufactured from a wide variety of substantially stiff materials, most preferably optically transmissive glass, quartz fused silica or sapphire, less preferably other materials such as polyvinyl chloride, polyethylene terephthalate, polycarbonate. Equally, for top coverplate (21) optically opaque and substantially stiff materials such as stainless steel, brass, copper, bronze, polyethetherketone may also be used. Top plate (21) may be provided with a viewing orifice as shown and provided with features, such as bolt sockets (22) to enable the stacked arrangement of components as shown to be tightly clamped to provide a hermetic seal, when used in conjunction with means for clamping, such as bolt holes (23), provided in the base plate.

Fig 6A illustrates a schematic design drawing of an extended path length phase separation module, suitable for application in the configuration illustrated in figure 6/5. A multiphase immiscible fluid flow enters the device through a dedicated input port (24) which elutes to multiphase flow carrying channel (25) equivalent in design specification to the immiscible fluid carrying channel (8) previously described and depicted. The shaded region represents an array of phase separation ducts (26) equivalent in design specification to the immiscible separation ducts (4) previously described and depicted. At the juncture of the multiphase flow carrying channel (25) and the separation ducts (26) phase separation begins to occur with the continuous phase (2), called the separated phase, entering the separation ducts (26). The separated phase continues along the separation ducts and empties into the common separated phase outlet duct (27), which conducts the separated fluid to a dedicated outlet for the separated fluid (28). Removal of the continuous phase (2) through the separation ducts (26), causes coelscence of the disperse phase droplets (3) into a continuous

stream which flows to a dedicated outlet (29). The extended path length of the separating portion of the device, allows for a greater number (n) of separation ducts (4), thus increasing the maximum operable flow rate of the phase separator device.

Fig 6B & C illustrate schematic design drawing of extended path length phase separation modules suitable for the passive separation of multiphase immiscible fluid flows. The difference in path length to fluidic exists (28) and (29) together with design geometries and fluid properties provides a pressure differential between the fluidic exits (28) and (29) supporting the flow of the separated fluid through the separation ducts (4). This is pressure differential (ΔP) is generated wholly or in part by the flow of the immiscible fluid stream and the individual fluid flows in their respective channels. The device of figure 7B constructed in accordance to the geometries specified in the description of figure 4B has been demonstrated by practical experimentation to separate immiscible flow streams of chloroform and water (1:1) with 100% separation efficiency at flow rates up to 3.0 ml min^{-1}, where the pressure differential (ΔP) across the separation ducts (4), enabling the separation, is provided entirely by the flow of the immiscible fluid stream and the individual fluid flows in their respective channels to their respective outlets.

Fig 8 A & B depict alternative arrangements for a substantially planar phase separation geometries for the separation of immiscible fluid flow streams. In these configurations, the phase separation duct(s) (30) branching from the main immiscible fluid carrying channel are substantially horizontal rather than vertical. The design considerations of the previously described separation ducts (4) apply, however, the narrow cross sectional geometry exists in the vertical direction and the wider cross sectional geometry of the duct existing in the horizontal orientation. Such structures may exist singularly as illustrated in figure 8A, or by additive machining processes or otherwise, created in parallel as depicted in figure 8B.

References

Patents:

Angelescu, D.E. et al., filed: 2004, publication: 2006. Patent: Microfluidic separator – US Patent application number 20060008913.

Kralj, J.G., Sahoo, H.R. & Jensen, K.F., filed: 2006, publication 2007. Patent: microfluidic separators for multiphase fluid-flow based on membranes – publictation number WO/2007/006033.

Research Publictaions:

Angelescu, D. & Siess, D., 2005. Microfluidic phase separation. In *Proc. Sensors 2005 IEEE*. p. 4 pp.

Angelescu, D.E. et al., 2006. Microfluidic separator.

Anthemidis, A.N. et al., 2004. On-line liquid-liquid extraction system using a new phase separator for flame atomic absorption spectrometric determination of ultra-trace cadmium in natural waters. *Talanta*, 62(3), 437-443.

Graham-Rowe, D., 2006. Liquid lenses make a splash. *Nat Photon*, sample(sample), 2-4.

Jena, A. & Gupta, K., 2002. Characterization of Pore Structure of Filtration Media. *Fluid/Particle Separation Journal*, 14(3), 227-241.

Karlberg, B. & Thelander, S., 1978. Extraction based on the flow-injection principle : Part I. Description of the Extraction System. *Analytica Chimica Acta*, 98(1), 1-7.

Kralj, J.G., Sahoo, H.R. & Jensen, K.F., 2007. Integrated continuous microfluidic liquid-liquid extraction. *Lab on a Chip*, 7(2), 256-263.

Mortensen, N.A., Olesen, L.H. & Bruus, H., 2006. Transport coefficients for electrolytes in arbitrarily shaped nano- and microfluidic channels. *New Journal of Physics*, 8(3), 37.

Mortensen, N.A. & Bruus, H., 2006. Universal dynamics in the onset of a Hagen-Poiseuille flow. *Physical Review E (Statistical, Nonlinear, and Soft Matter Physics)*, 74(1), 017301-4.

Mortensen, N.A., Okkels, F. & Bruus, H., 2005. Reexamination of Hagen-Poiseuille flow: Shape dependence of the hydraulic resistance in microchannels. *Physical Review E (Statistical, Nonlinear, and Soft Matter Physics)*, 71(5), 057301-4.

Nord, L. & Karlberg, B., 1980. Extraction based on the flow-injection principle : Part 5. Assessment with a Membrane Phase Separator for Different Organic Solvents. *Analytica Chimica Acta*, 118(2), 285-292.

Tsai, J. & Lin, L., 2002. Active microfluidic mixer and gas bubble filter driven by thermal bubble micropump. *Sensors and Actuators A: Physical*, 97-98, 665-671.

Whitesides, G.M., 2006. The origins and the future of microfluidics. *Nature*, 442(7101), 368-373.

Claims

1. A device for the separation of two, or more, immiscible fluids, consisting of one or more, fluid input ports leading to a common flow channel which carries multiphase fluid flow, the channel continues to an output port, between the input and output ports exist a series of n separation ducts, where n is a positive integer, in fluid communication with the common flow channel and additional output port(s), and with each duct possessing at least one narrow dimension in the cross-sectional profile at the juncture with the common flow channel, the geometry of the common flow channel is, under consideration of the properties of the fluid(s) employed and conditions of operation, sufficiently narrow in both cross sectional dimensions that surface forces dominate over other forces acting on the fluids, whilst also being sufficiently sizable in width and depth, that along the length of the separation feature, defined by n and the duct spacing, the pressure generated due to flow of fluids in the common flow channel is insufficient to exceed the capillary pressure for at least one of the fluids present in the common flow channel in the context of entry into one or more of the smaller separation ducts, as defined largely by the wetted perimeter to cross sectional area of the small duct at the juncture with the common flow channel, together with fluid and material properties.

2. The device of claim 1, where the device is constructed from, or at least a portion of the device is constructed from or coated with a film of, a fluoropolymer.

3. The device of claim 1, where any number of the fluid phases contain suspended particles

4. The device of claim 1, where any number of the fluid phases contain suspended biological material.

5. The device of claim 1, where the common flow channel has a width from about 100 μm to 1 mm

6. The device of claim 5, where the common flow channel has a depth from about 100 μm to 1 mm

7. The device of claim 6, where the small separation ducts have a width and/or depth of less than about 50 μm

8. The device of claim 1, where the small separation ducts have a width and/or depth of less than about 50 μm

9. The device of claim 1, where the common flow channel has a width from about 1 μm to 100 μm

10. The device of claim 1, where the common flow channel has a depth from about 1 μm to 100 μm

11. The device of claim 1, where one or more of the separation ducts have an aspect ratio greater than 2.

12. The device of claim 1, where one or more of the separation ducts are substantially rectangular, triangular or Gaussian in cross-sectional shape.

13. The device of claim 1, where a pressure differential exists between the fluidic pathways at the juncture of the common flow channel with at least one of the adjoining separation ducts.

14. The device of claim 13, where the pressure differential is created wholly or in part through compression or evacuation of the atmosphere into which fluid elutes from the device.

15. The device of claim 13, where the pressure differential is created wholly or in part through a compressible channel structure.

16. The device of claim 13, where the pressure differential is created wholly or in part through a pressure regulating feature.

17. The device of claim 13, where the pressure differential is created wholly or in part through either a pump or vacuum, used alone, together or in combination with other mechanisms for pressure regulation.

18. The device of claim 13, where the pressure differential is created wholly or in part through consideration of channel geometries, including length, width and depth, and/or shape, fluidic features, flow regimes and channel arrangement with respect to the properties of the fluid flowing within the channels, the fluid flow rate and the fluid flow regime.

19. The device of claim 1, where one or more of the separation ducts meet a third channel containing a previously segregated, or otherwise, fluid flow stream.

20. The device of claim 1, where n is greater than 50.

21. The device of claim 1, where n is less than 50.

22. The device of claim 1, where n is less than 10000000.

23. The device of claim 1, where the separation ducts meeting the common flow channel are substantially horizontally orientated.

24. The device of claim 1, where the ducts meeting the common flow channel are substantially vertically orientated.

25. The device of claim 1, where the ducts meeting the common flow channel are substantially diagonally orientated.

26. The device of claim 1, where the multiple separation ducts form a juncture with the common flow channel on more than one of the common flow channel's surfaces

27. The device of claim 1, where the device is constructed using a subtractive machining process.

28. The device of claim 1, where the device is constructed using an additive construction process.

29. The device of claim 1, where the device is constructed using a combination of subtractive machining and additive construction methodologies.

30. The device of claim 1, where the device features are created wholly or in part using ablative laser machining processes.

31. The device of claim 1, where the constructed device is substantially planar.

32. The device of claim 1, constructed from a substantially incompressible material.

33. The device of claim 1, constructed from a substantially or in part from a substantially compressible or flexible material.

34. The device of claim 1, where additional fluidic features or manipulations occur prior the juncture of the common flow channel with at least one of the adjoining separation ducts.

35. The device of claim 1, where additional fluidic features or manipulations occur after the juncture of the common flow channel with at least one of the adjoining separation ducts.

36. A device consisting of one or more of the devices described in claims 1-35, in fluidic communication or otherwise.

37. A device consisting of one or more of the devices described in claims 1-35, with one or more of the input ports or output ports of each device connected together.

38. A device consisting one or more of the device assemblies described in claims 1-35 stacked one on top of the other.

39. A device as described in claims 1-35, with one or more detectors situated within or on the output channels, separation ducts, main fluidic channel or output ports.

Abstract

Microfluidic liquid separation device and methods for construction and application

A planar, fluoropolymeric microfluidic device for the separation of immiscible fluids (2, 3)
consisting of a common flow channel (8) carrying multiphase flow, in fluid communication
with a series of separation ducts (4). Each separation duct (4) possesses at least one narrow
dimension in the cross-sectional profile at the juncture with the common flow channel (8).
The geometry of the common flow channel (8) is, under consideration of the properties of
the fluid(s) employed and conditions of operation, sufficiently narrow in both cross
sectional dimensions that surface forces dominate over other forces acting on the fluids,
whilst also being sufficiently sizable in width and depth, that pressure generated due to
flow of fluids in the common flow channel (8) is insufficient to exceed the capillary
pressure required for the non-wetting fluid (2) in the common flow channel (8) to enter into
one or more of the smaller separation ducts (4).
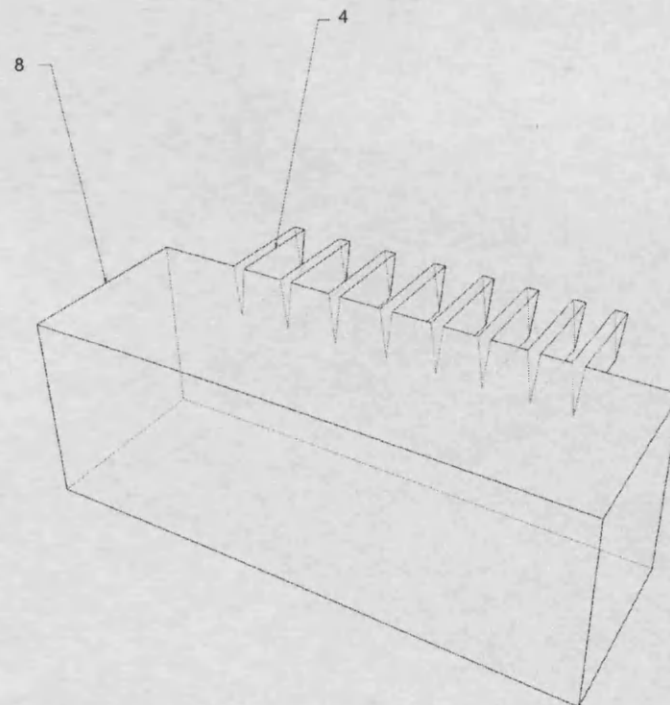
Figure 2B to accompany abstract
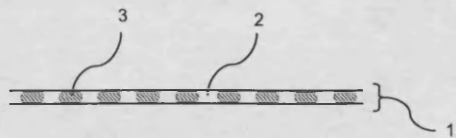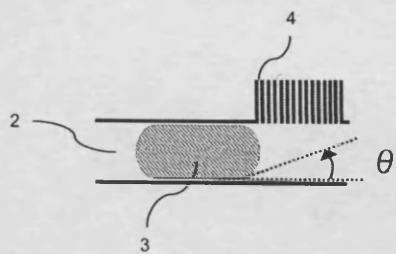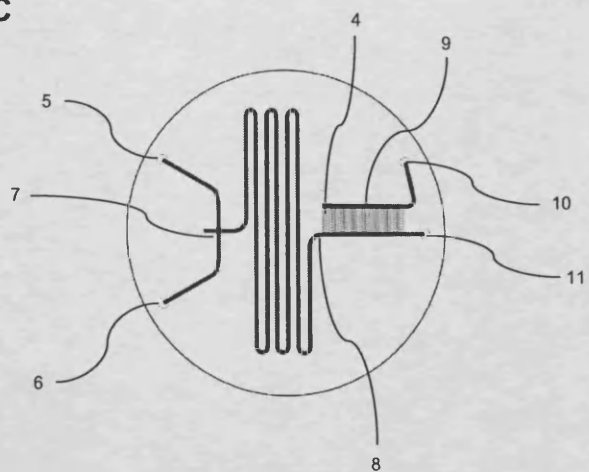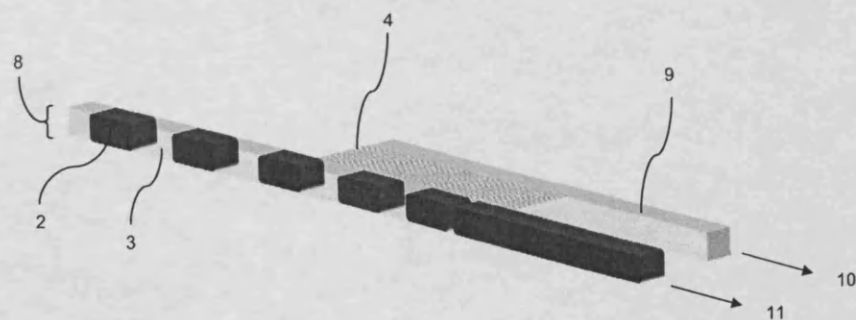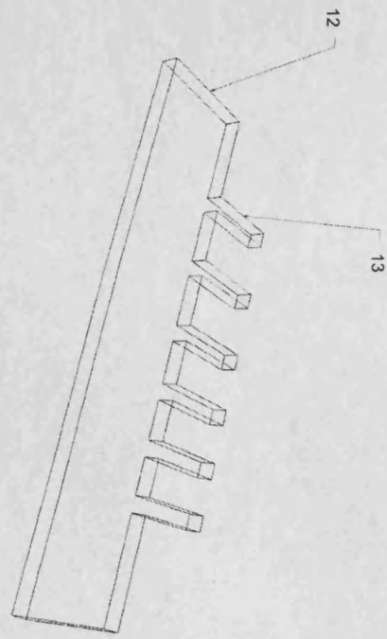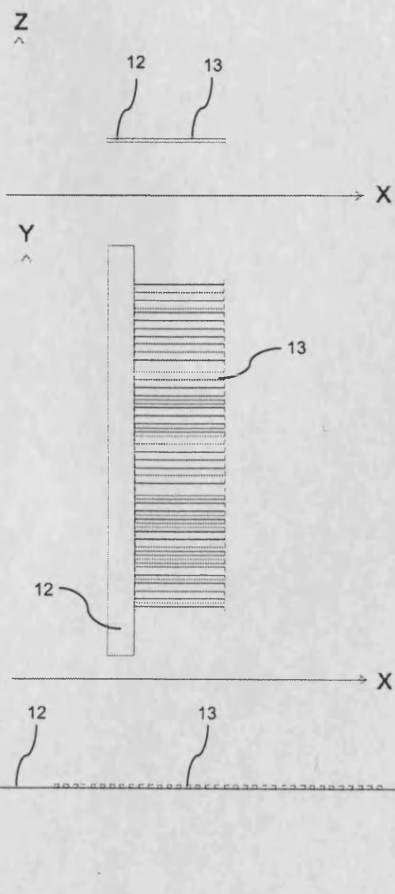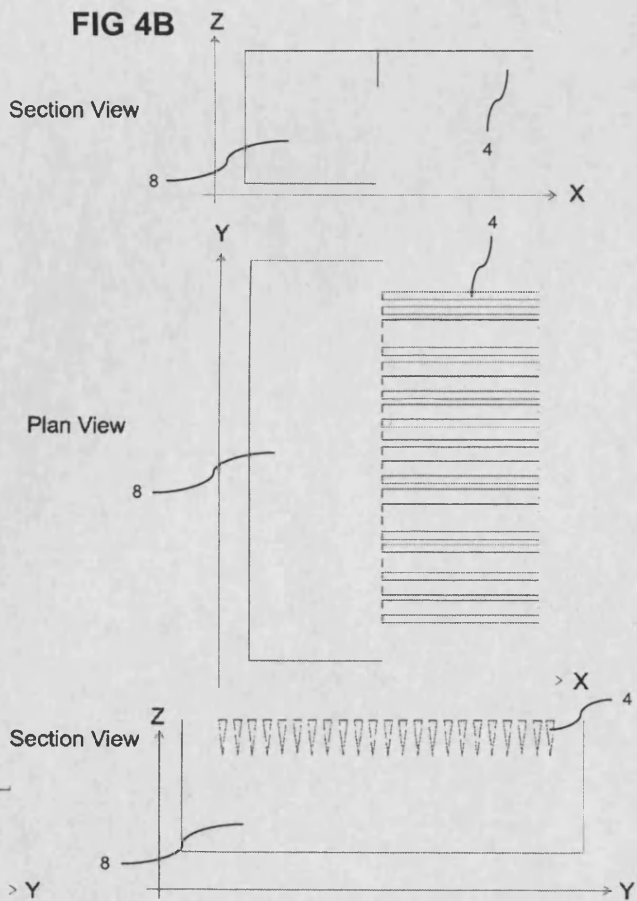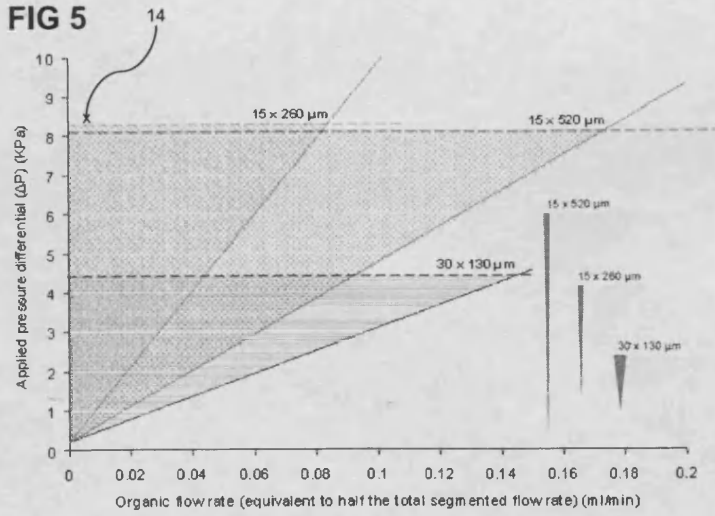
FIG 2A

FIG 1A

FIG 1B

FIG 1C

FIG 2B

FIG 3

12

13

FIG 4A

Z

12   13

X

Y

13

12

X

Z

12   13

X

FIG 4B

Z

Section View

8

4

X

Y

4

Plan View

8

X

Z

Section View

8

4

> X

Y

FIG 5

FIG 6

FIG 7A

26
24
29
25
28
27

FIG 7B

26
24
25
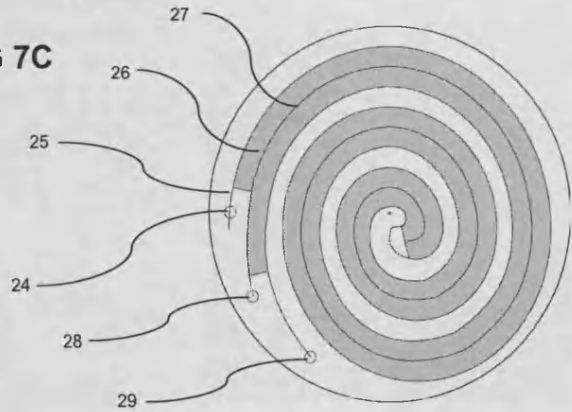29
27
28

FIG 7C

27
26
25
24
28
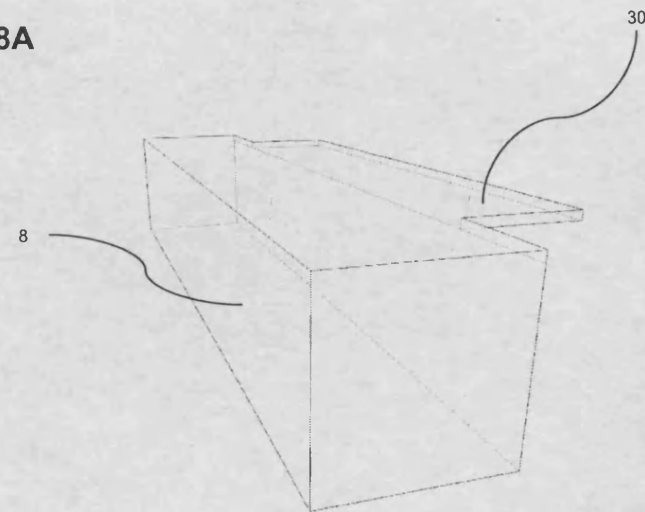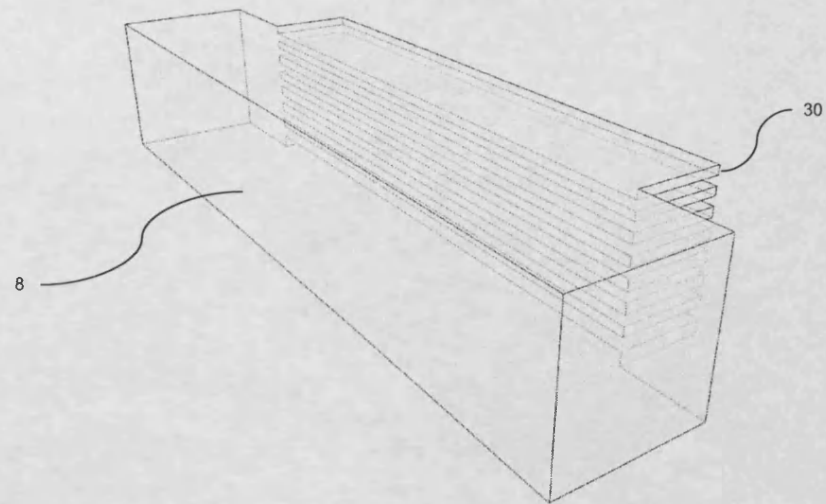29

FIG 8A

30
8

FIG 8B

8
30
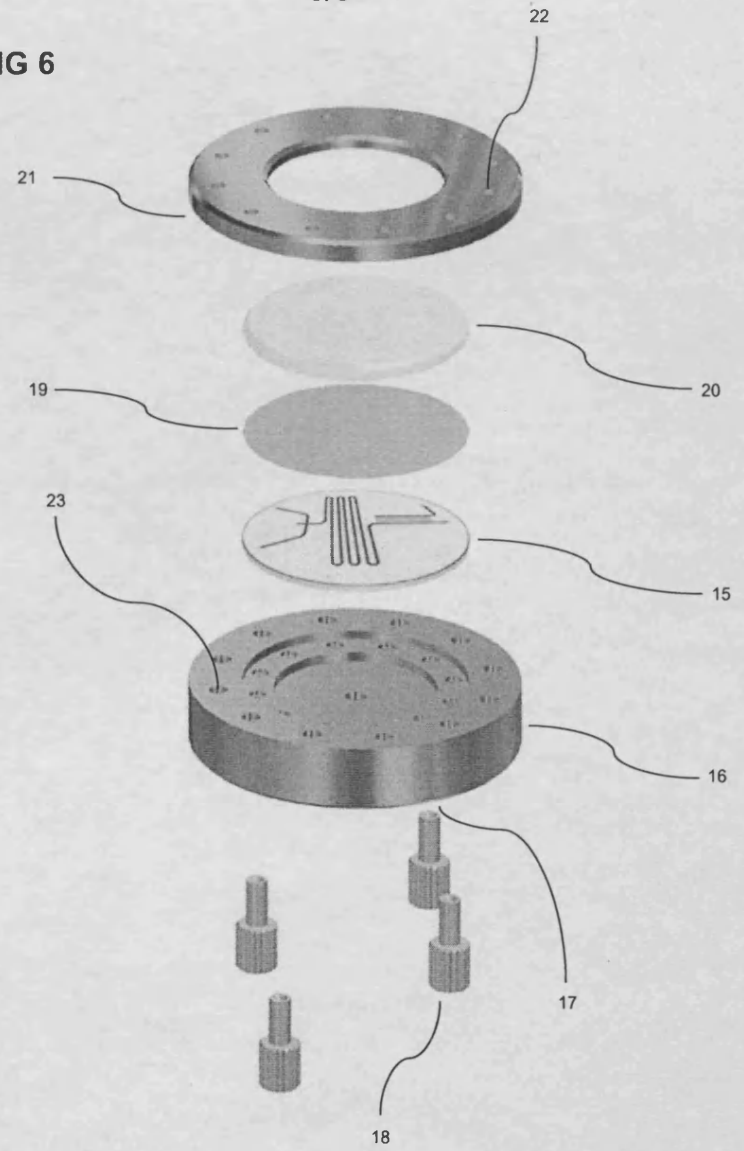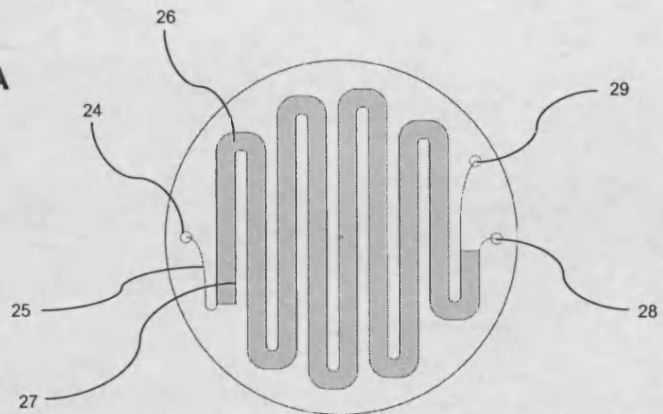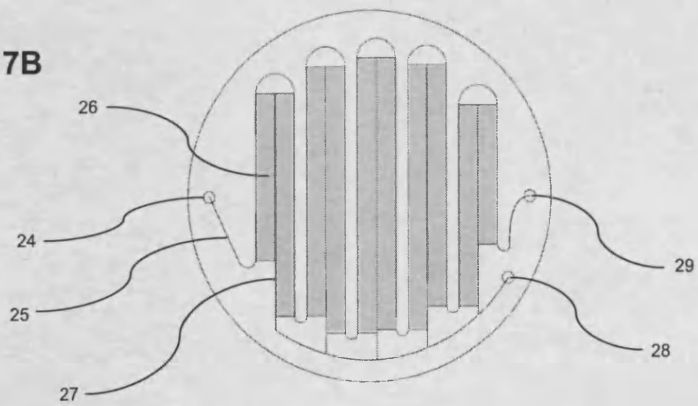
A glimpse of the inner workings of the templated site†

Christopher J. Allender,[a] Oliver K. Castell,[a] Philip R. Davies,[b] Steven Fiddy,[c] Jimmy Hedin-Dahlström[a] and Michael Stockenhuber[d]

This is the first direct experimental probe, using EXAFS, of the active site within molecularly imprinted polymers and paves the way to a more detailed understanding of the inner workings of molecular imprinting.

Robust, engineering friendly alternatives are needed for applications that currently rely on specific molecular recognition by macrobiomolecules such as enzymes, antibodies and nucleic acids. At present practical applications using these molecules are limited by issues of availability, stability, reproducibility and cost. It has been suggested that molecular imprinted polymers (MIPs) could deliver the required molecular selectivity and affinity.

The MIP approach (recently reviewed by Wulff[1] and others[2,3]) has been used extensively in applications where antibody-like recognition is required within an engineerable synthetic material. However, despite initial promise, commercialisation of MIP technology has been hampered by poorly-defined materials possessing unpredictable affinities, selectivities and capacities, issues which appear to be intrinsic to conventional imprinting approaches. To progress MIP technology, a better understanding of the factors that determine imprinting performance is required but this has been difficult to obtain because of the amorphous nature of the polymers which prevents analysis by most structural tools.

This paper describes preliminary experiments that establish the feasibility of using EXAFS[4] to explore the active imprinting site within specifically designed MIPs. The results provide a glimpse of the detailed structure of the template–polymer interactions at the heart of one particular MIP.

We selected a 4-vinyl pyridine–styrene–divinylbenzene copolymer imprinted with dibenzoylmethane (DBM) and cobalt (Co^{2+}); a system studied by Matsui et al.[5] as a shape selective catalyst with DBM as an analogue aldol condensation intermediate.

[a] Welsh School of Pharmacy, Cardiff University, Redwood Building, King Edward VII Avenue, Cardiff, UK CF10 3NB.
E-mail: AllenderCJ@cardiff.ac.uk; E-mail: CastellOK@cardiff.ac.uk; E-mail: Hedin-DahlstromJA@cardiff.ac.uk;
Fax: +44 (0)29 2087 4149; Tel: +44 (0)29 2087 5824
[b] School of Chemistry, Cardiff University, Main Building, Cardiff, UK CF10 3AT. E-mail: DaviesPR@cardiff.ac.uk;
Fax: +44 (0)29 2087 4030; Tel: +44 (0)29 2087 4072
[c] CCLRC Daresbury, Warrington, Cheshire, UK WA4 4AD
[d] University of Newcastle, Chemical Engineering, NSW 2308 Callaghan, Australia.
E-mail: michael.stockenhuber@newcastle.edu.au
† Electronic supplementary information (ESI) available: FTIR analysis of washed and re-impregnated MIP and NIP. See DOI: 10.1039/b811578h

Fig. 1(a) shows the proposed DBM–cobalt complex from Matsui et al.[5] Our aim was to determine whether the binding of the DBM in the polymer could be identified by EXAFS through changes in the coordination shell of the cobalt.

Two types of sample were prepared:‡ a molecularly imprinted polymer (MIP) and a non-imprinted polymer (NIP), the latter being synthesised in the presence of cobalt acetate but not DBM. IR and UV-Vis data were used to support the EXAFS data.

As expected, the as prepared samples contained a wide distribution of different Co^{2+} environments resulting in complex EXAFS spectra which could not be analysed satisfactorily in terms of individually identifiable binding sites. These samples will be the subject of future studies when we have a more detailed understanding of control systems. Initial experiments therefore concentrated on powdered samples in which all but the most strongly bound cobalt had been removed. These were washed until no further colour could be removed from the polymer and no adsorption bands
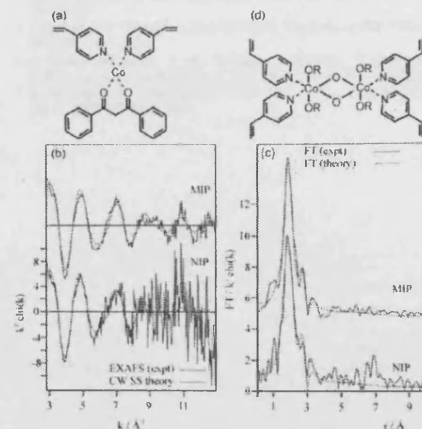

Fig. 1 (a) Proposed[5] template complex between dibenzoylmethane (DBM), cobalt and 4-vinyl pyridine (4-VP). (b) Comparison of EXAFS data from the cobalt adsorption edge of a vinyl pyridine–styrene copolymer (spectra are offset for clarity); MIP imprinted with dibenzoylmethane (DBM) and Co^{2+}; NIP imprinted with Co^{2+} only. Model fits are created with a curved-wave single-scattering model (CW SS) using the parameters given in Table 1. (c) Fourier transforms (FT) of theory and data in (b). (d) Proposed structure of strongly bound dimeric cobalt species.

assignable to the DBM were evident in either the UV-Vis or infrared spectra.

Despite the rigorous washing both NIP and MIP samples gave good adsorption signals at the cobalt edge indicating a very strongly bound cobalt state. Fig. 1(b) and (c) show EXAFS data for these samples, with the parameters used to create the fits given in Table 1. Significantly, we observe near identical spectra for the strongly bound Co^{2+} fraction in the NIP and MIP. (Note that the increased noise in the NIP spectrum results from a reduced number of scans and not from a lower concentration of cobalt.)

Surprisingly neither the MIP nor the NIP samples could be fitted successfully using a monomeric cobalt species such as that previously proposed.[5] Instead, and in both cases, the data strongly suggest a dimeric species with a cobalt–cobalt spacing of ~2.75 Å, Fig. 1(d).

To differentiate between the two models, the experimental data were also fitted to a model with fixed coordination numbers (2N, 2O and 2N, 4O). For the MIP, R-factors of 26.1 and 24.1 and for the NIP R-factors of 42.6 and 41.8 were observed. For the MIP, this suggests strongly that the dimeric model more accurately reflects the structure of the binding site. For the NIP the evidence is slightly weaker probably due to the higher noise level in the data. Please note that significant improvements in the fits were achieved with free fits of the coordination number, suggesting somewhat heterogeneous sites.

We subsequently explored whether less strongly held sites would show similar behaviour. Fig. 2 shows EXAFS spectra for the MIP and NIP samples re-impregnated with the cobalt acetate–DBM mixture.‡ Although the NIP is not expected to absorb the DBM–Co^{2+} complex in significant quantities it has previously been demonstrated that cobalt rebinding is much more extensive in the NIP than the MIP.[6] This suggests that whilst this polymer can be regarded as a NIP for a DBM–Co^{2+} complex, it could also be viewed as an imprinted polymer that specifically binds cobalt, i.e. a Co^{2+} MIP.

In contrast to the washed samples, the EXAFS data obtained from the re-impregnated samples do not contain any evidence for Co–Co coordination, with a 1% significance level,[7] indicating that a monomeric species dominates both re-impregnated samples (Table 1). Instead, the highest quality
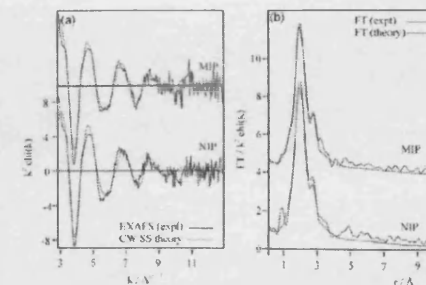

Fig. 2 (a) EXAFS spectra and fits of vinyl pyridine–styrene copolymer (MIP) imprinted with dibenzoylmethane (DBM) and Co^{2+}, (NIP) imprinted with Co^{2+} only. (Parameters used to derive model fits are given in Table 1.) (b) Fourier transforms (FT) of theory and data in (a).

fits were obtained by replacing the Co neighbour with C. The inner shell in the re-impregnated MIP and NIP fits is nitrogen rich; O and C shells have been fitted, but these resulted in significantly worse fit indices. The best fits for both the re-impregnated MIP and NIP samples showed similar bond lengths for Co–O and Co–C.

Significant variation was observed in the coordination numbers for Co–O, Co–N and Co–C between the re-impregnated MIP and NIP samples. As above, two different models with fixed coordination numbers were also investigated for these samples: R-factors of 30.2 and 27.55 were obtained for the re-impregnated NIP with (4N) and (4N, 2O) models, respectively. Similarly, for the re-impregnated MIP, R-factors of 28.7 and 26.1 were found for (4N) and (2N, 4O) models. These results strongly suggest monomeric cobalt species in these samples.

The variation in coordination number provides an insight into the structural differences between the re-impregnated NIP and MIP samples. Most apparent is that the Co–N coordination is significantly lower for the MIP (1.7) than for the NIP (2.7) whilst Co–O coordination increases from 2.4 for the NIP to 3.6 for the MIP (Table 1). These numbers are consistent with a heterogeneous population of complexes perhaps including both tetrahedral and octahedral coordinations, Fig. 3(a) and (b). Similarly there is a reduction in Co–C coordination for the MIP (1.9) compared to the NIP (2.6) although Co–C distances were similar (~2.8 Å). These data correlate well with a structure in the MIP which involves coordination of the Co to the carbonyl oxygens of the template whereas the NIP is predominantly coordinated to the pyridine groups.
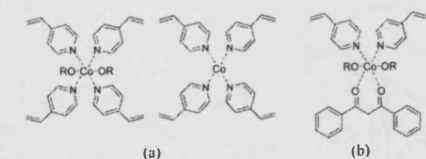
Table 1 Fitting parameters used for the curved-wave single-scattering (CW SS) models of the EXAFS data shown in Fig. 1 and 2

Atom	Coordination	Distance/Å	Debye–Waller factor
MIP (washed)			
N	2.2	1.83	0.043
O	2.8	1.91	0.014
Co	2.2	2.76	0.023
NIP (washed)			
N	2.3	1.85	0.013
O	2.4	1.96	0.012
Co	1	2.75	0.019
MIP (re-impregnated with DBM and Co^{2+})			
N	1.7	1.83	0.039
O	3.6	1.97	0.022
C	1.9	2.86	0.015
NIP (re-impregnated with DBM and Co^{2+})			
N	2.7	1.88	0.027
O	2.4	1.98	0.015
C	2.6	2.82	0.018

Fig. 3 Possible cobalt complexes in (a) re-impregnated NIP, (b) re-impregnated MIP.

On the basis of these data, we suggest for the re-impregnated NIP polymers a 6-coordinate model with 4 nitrogen and 2 oxygen neighbours and for the re-impregnated MIP a 6-coordinate model with 4 oxygen and 2 nitrogen neighbours.

Comparing the washed samples with the re-impregnated samples, the oxygen coordination number increases at the expense of the nitrogen for the MIP but remains roughly equivalent in the NIP. These observations are consistent with the signature of DBM bound to the cobalt in the MIP which is absent in the strongly held complex found in the 3-day washed samples and in the NIP where the polymer selectively adsorbs the cobalt ion at the expense of the template.

IR studies of the pre-polymerisation complexes suggested that pyridine competitively eliminates acetate from cobalt complexes. We have also investigated the identity of the oxygen ligand in the complex using a simple energy minimisation procedure to compare binding strength of the four different oxygen containing ligands present during the re-impregnation of the polymers (acetate, DBM, water and methanol). The calculations showed that methanol, which is present at high concentration during template rebinding, gave the best correlation with the observed Co–O bond length.

In summary, we have established that the template binding site for selected polymers can be successfully probed using EXAFS, enabling an unprecedented insight into the nature of the binding site. Our results suggest that at least two very different binding sites exist in the present system: the most strongly bound state being a cobalt dimer in which the DBM present in the MIP has been replaced by pyridine groups. Re-impregnation with the DMB–Co^{2+} template results in a more weakly bound monomeric cobalt state associated with DBM in the MIP but only the polymer in the NIP.

This new information demonstrates not only that a variety of binding strength sites are available in MIPs but also that the species bound in these sites may vary widely. The results emphasise the complexity of such systems and also illustrate the dangers of proposing overly simplistic structural models.

Notes and references

‡ Experimental procedures: Polymers were synthesised as described by Matsui et al.[5] After polymerisation the samples were ground and sieved to yield particles in the range of 25–52 μm. Extensive washing was performed using three consecutive MeOH–AcOH (7 : 3) incubations with stirring of at least 16 h each. Finally the polymers were washed with acetone and dried. Re-impregnation procedures: the MIP and NIP polymers (500 mg) were placed in 10 ml glass vials. Methanol (2.5 ml), DBM (5 mg), and cobalt acetate (5 mg) were added and the slurry was stirred for 16 h. The same experiment was repeated without cobalt acetate. The solutions were filtered and the polymers were dried. Data acquisition and analysis X-ray absorption spectroscopy was carried out using dipole radiation on beamline 7.1 at the CCRL Daresbury Laboratory. X-Ray absorption spectra were measured in fluorescence mode by a multi-element, energy-sensitive Canberra solid-state detector. The EXAFS results were analysed using standard procedures. The statistical significance of each shell of neighbours reported has been confirmed by the standard test.[7] Energy minimisation calculations were performed with Chem3D Ultra (version 9) using MM2 force fields. Solid samples of cobalt salts were analysed using a Varian FTIR in ATR mode.

1 G. Wulff, Angew. Chem., Int. Ed. Engl., 1995, 34, 1812–1832.
2 C. Alexander, H. S. Andersson, L. I. Andersson, R. J. Ansell, N. Kirsch, I. A. Nicholls, J. O'Mahony and M. J. Whitcombe, J. Mol. Recognit., 2006, 19, 106–180.
3 N. W. Turner, C. W. Jeans, K. R. Brain, C. J. Allender, V. Hlady and D. W. Britt, Biotechnol. Prog., 2006, 22, 1474–1489.
4 H. Bertagnolli and T. S. Ertel, Angew. Chem., Int. Ed. Engl., 1994, 33, 45–66.
5 J. Matsui, I. A. Nicholls, I. Karube and K. Mosbach, J. Org. Chem., 1996, 61, 5414–5417.
6 J. Hedin-Dahlstrom, J. P. Rosengren-Holmberg, S. Legrand, S. Wikman and I. A. Nicholls, J. Org. Chem., 2006, 71, 4845–4853.
7 R. W. Joyner, K. J. Martin and P. Meehan, J. Phys. C: Solid State Phys., 1987, 20, 4005–4012.